

**An Investigation of Hydro-Geochemical
Processes in Coupled Thermal, Hydraulic,
Chemical and Mechanical Behaviour of
Unsaturated Soils**

MAJID SEDIGHI

Geoenvironmental Research Centre
Cardiff School of Engineering
Cardiff University

*Thesis submitted in candidature for the degree of Doctor of Philosophy at
Cardiff University*

JUNE 2011

UMI Number: U573143

All rights reserved

INFORMATION TO ALL USERS

The quality of this reproduction is dependent upon the quality of the copy submitted.

In the unlikely event that the author did not send a complete manuscript and there are missing pages, these will be noted. Also, if material had to be removed, a note will indicate the deletion.



UMI U573143

Published by ProQuest LLC 2013. Copyright in the Dissertation held by the Author.
Microform Edition © ProQuest LLC.

All rights reserved. This work is protected against
unauthorized copying under Title 17, United States Code.



ProQuest LLC
789 East Eisenhower Parkway
P.O. Box 1346
Ann Arbor, MI 48106-1346

DECLARATION

This work has not previously been accepted in substance for any degree and is not concurrently submitted in candidature for any degree.

Signed  (Majid Sedighi)

Date24/06/2011.....

STATEMENT 1

This thesis is being submitted in partial fulfillment of the requirements for the degree of Doctor of Philosophy (PhD).

Signed  (Majid Sedighi)

Date24/06/2011.....

STATEMENT 2

This thesis is the result of my own independent work/investigation, except where otherwise stated. Other sources are acknowledged by explicit references.

Signed  (Majid Sedighi)

Date24/06/2011.....

STATEMENT 3

I hereby give consent for my thesis, if accepted, to be available for photocopying and for inter-library loan, and for the title and summary to be made available to outside organisations.

Signed  (Majid Sedighi)

Date24/06/2011.....

Acknowledgments

Firstly, I would like to sincerely thank my supervisor Professor Hywel Thomas for his continued support, motivation and invaluable academic guidance throughout this research. I am extremely grateful for the opportunity he has provided me with, allowing me to realise this milestone.

I would also like to express my deepest thanks to my co-supervisor, Dr. Phillip Vardon, for his technical support and guidance during this work. For his contribution, technical comments and encouragement in the early stages of this work, I wish to sincerely acknowledge Dr. Suresh Seetharam.

The invaluable financial support of this research through PhD fellowships from the Overseas Research Students Award Scheme (ORSAS), Cardiff School of Engineering, and the Geoenvironmental Research Centre is gratefully acknowledged.

I also owe gratitude to all my colleagues at the Geoenvironmental Research Centre and the Seren project team for their support; especially, Alex, Snehsias, Talib, Peter, Pauline (Welsh), Rao, Ram, Claire, Hesham, Matthew, Shakil and Pauline (Townsend). I would like to express my deepest thanks to Dr. Rob Francis for his understanding during the write up of this work. I am also grateful to Dr. Roger Philp for assisting me in computer programming challenges, I have faced.

For their invaluable kindness and support during my study in the UK, I am truly thankful to Soroor and Shahab. All my friends who have been so important to finish this work deserve special thanks. I would like to thank Bahador and Foad who have helped me with computer programming challenges. I would also like to acknowledge Professors Dennis and Freda Hawkes for their invaluable friendship and motivation.

I must thank sincerely my family members for their continued support and love, specifically to dearest Mehrdad, Mitra, Saied and Amir. I am also very grateful to beloved Iri and Mr. A. Alavi for their support in the early stages of my academic life.

I would like to especially thank my beloved mother, Mali, whose blessing, persistence and support has been always so inspiring to me. I owe her a great gratitude as without her constant love, encouragement and strong support, none of my achievements would have been possible.

Last but not least, my beloved friend and wife, Mojgan, deserves a considerable recognition for her continuing love, friendship and support. Most importantly, without her love, motivation, and understanding, none of the achievements in this work would have been possible.

Summary

This thesis presents an investigation of hydro-geochemical processes in the framework of coupled thermal, hydraulic, chemical and mechanical (THCM) behaviour of unsaturated soils. Based on a mechanistic approach, several theoretical aspects of the modelling of hydro-geochemical behaviour are advanced.

The hydraulic processes investigated include liquid and vapour transfer due to chemical osmosis. These are addressed via an explicit coupling with chemical variables. The chemical processes accommodate the transport of multicomponent chemicals by advection, diffusion and dispersion mechanisms, subjected to homogeneous and heterogeneous geochemical reactions. Multicomponent diffusive flow is treated with diffusion driven by chemical, electrical and thermal potentials under charge conservation conditions in multiple ionic systems.

A numerical solution based on the use of the finite element method for spatial discretisation and the finite difference method for temporal discretisation is developed to solve the governing equations for flow and deformation.

In terms of chemical reactions, advanced geochemical features are introduced via the coupling of the geochemical model, PHREEQC with the coupled THCM model, COMPASS. Both equilibrium and kinetically controlled geochemical reactions are considered in the reactive transport model. To couple chemical transport and reaction models, a sequential non-iterative approach is adopted. In addition, an algorithm for porosity modification from mineral precipitation/dissolution reactions has been established.

Verification of the approach proposed has been addressed via a series of bench mark tests. Good results have been achieved for the theoretical and numerical implementation of hydraulic and chemical behaviour in the model.

The new model is then used to investigate non-isothermal hydro-geochemical processes under the effects of thermal diffusion. The results reveal the importance of thermal diffusion, the so called Soret effect, on the reactive transport of chemicals.

The new model has then been applied to investigate relevant hydraulic and hydro-geochemical processes in a swelling clay, via a series of simulations of laboratory based experiments. This is supported by the development of a new approach to investigate hydration/dehydration effects on porosity evolution and transport processes. With respect to moisture flow, the results obtained are in close agreement with experimental results from water infiltration tests. The results also indicate that the inclusion of the new hydration/dehydration model significantly improves the prediction of water transport and re-saturation time. Considering the behaviour of dissolved chemicals and the composition of minerals/exchangeable ions, the results obtained are in good agreement with experimental results, providing confidence in the ability of the model to simulate the hydro-geochemical processes.

As the result of this study, it is claimed that a new approach for assessing hydro-geochemical processes in unsaturated soils has been developed, which can be employed under variable THCM conditions. Based on the application of the work to the case of a compacted swelling clay, the developed model is also shown to be an appropriate prediction model for that material.

Contents

Chapter 1 Introduction

1.1	Introduction	1-2
1.2	Study objectives	1-4
1.3	Research background	1-5
1.4	Scopes and limitations	1-8
1.5	Overview of the thesis	1-9
1.6	References	1-11

Chapter 2 Literature Review

2.1	Introduction	2-2
2.2	Physical, chemical and mechanical processes in unsaturated compacted bentonite buffer in geological disposal of HLW	2-3
2.3	Compacted bentonite (micro- and macrostructure evolution)	2-7
2.4	Water uptake and interaction with compacted bentonite	2-11
2.5	Physical state of water in compacted bentonite	2-16
2.6	Moisture transport and microstructure in compacted bentonite	2-20
2.7	Chemical diffusion in compacted bentonite	2-22
2.8	Diffusion under non-isothermal conditions	2-26
2.9	Experimental studies on the coupled thermal, hydraulic, chemical and mechanical behaviour of compacted bentonite	2-28
2.10	Computational studies on the coupled thermal, hydraulic, chemical and mechanical behaviour of compacted bentonite	2-33
2.11	Computational schemes and developments in modelling of the reactive transport of multicomponent chemicals	2-38
2.12	Conclusions	2-43
2.13	References	2-46

Chapter 3 Theoretical Formulation

3.1	Introduction	3-2
3.2	Theoretical formulation-General aspects	3-3
3.3	Moisture flow	3-4
3.3.1	Mechanisms of liquid water flow	3-6
3.3.2	Mechanisms of water vapour flow	3-12

3.3.3	Governing differential equation for moisture flow	3-18
3.4	Dry air transfer	3-23
3.5	Heat transfer	3-27
3.6	Reactive transport of multicomponent chemicals	3-33
3.6.1	Transport processes and mechanisms	3-34
3.6.1.1	Advection	3-35
3.6.1.2	Diffusion	3-35
3.6.1.3	Dispersion	3-43
3.6.2	Geochemical reactions	3-44
3.6.3	Implementation of mass and charge conservation laws	3-47
3.6.4	Governing equations for chemical reactive transport	3-49
3.7	Deformation behaviour	3-53
3.7.1	Constitutive elastic relationship	3-54
3.7.2	Yield function	3-55
3.7.3	Flow rule	3-56
3.7.4	Hardening law	3-57
3.7.5	Governing equation for deformation	3-58
3.8	Summary	3-60
3.9	References	3-62

Chapter 4 Numerical Formulation

4.1	Introduction	4-2
4.2	Spatial discretisation	4-3
4.2.1	Spatial discretisation for chemical flows	4-3
4.2.2	Spatial discretisation for moisture, heat and air transfer-deformation	4-7
4.3	Temporal discretisation	4-10
4.4	Coupling between the transport and chemical reaction model	4-13
4.5	Summary	4-17
4.6	References	4-18

Chapter 5 Verification and Validation

5.1	Introduction	5-2
5.2	Osmotic potential effects on moisture transport	5-5
5.2.1	Osmotic potential under saturated conditions (Test I)	5-5

5.2.1.1	Introduction	5-5
5.2.1.2	Numerical model conditions	5-5
5.2.1.3	Results and discussion	5-6
5.2.2	Osmosis potential under unsaturated condition (Test II)	5-8
5.2.2.1	Introduction	5-8
5.2.2.2	Numerical model conditions	5-9
5.2.2.3	Results and discussion	5-10
5.3	Verification of Multicomponent Chemicals Transport	5-14
5.3.1	Diffusion of binary electrolyte solutions under electrochemical potential (Test III)	5-14
5.3.1.1	Introduction	5-14
5.3.1.2	Numerical model conditions	5-16
5.3.1.3	Results and discussion	5-17
5.3.2	Diffusion of multiple ions in electrolyte solution under electrochemical potential (Test IV)	5-19
5.3.2.1	Introduction	5-19
5.3.2.2	Numerical model conditions	5-19
5.3.2.3	Results and discussion	5-20
5.3.3	Diffusion of multi-ionic components due to thermal gradients-coupled electrochemical and thermal diffusion (Test V)	5-24
5.3.3.1	Introduction	5-24
5.3.3.2	Numerical model conditions	5-24
5.3.3.3	Results and discussion	5-26
5.4	Reactive transport of multicomponent chemicals: verification of the coupling of the COMPASS and PHREEQC models	5-31
5.4.1	Chemical Transport with mineral precipitation/dissolution reaction (Test VI)	5-31
5.4.1.1	Introduction	5-31
5.4.1.2	Numerical model conditions	5-32
5.4.1.3	Analytical solution under equilibrium condition	5-33
5.4.1.4	Analytical solution under kinetically controlled steady-state condition	5-34
5.4.1.5	Results and discussion	5-36
5.4.2	Chemical Transport with multiple Precipitation/Dissolution Front (Test VII)	5-39
5.4.2.1	Introduction	5-39

5.4.2.2	Numerical model conditions	5-39
5.4.2.3	Results and discussion	5-40
5.4.3	Chemical Transport with Multiple Ion Exchange (Test VIII)	5-42
5.4.3.1	Introduction	5-42
5.4.3.2	Numerical model conditions	5-43
5.4.3.3	Results and discussion	5-44
5.5	Modelling feed-back of mineral precipitation/dissolution reactions on flow process	5-46
5.5.1	Chemical Diffusion with mineral precipitation/dissolution reaction with flow modification feed back (Test IX)	5-46
5.5.1.1	Introduction	5-46
5.5.1.2	Numerical model conditions	5-46
5.5.1.3	Results and discussion	5-48
5.6	Conclusions	5-50
5.7	References	5-53

Chapter 6 Simulation of the Reactive Transport of Chemicals under Coupled THC Conditions

6.1	Introduction	6-2
6.2	Model domain and conditions	6-3
6.3	Material parameters and relationships	6-4
6.4	Numerical simulation results	6-9
6.4.1	Temperature and moisture distribution	6-9
6.4.2	Dissolved chemicals and mineral distribution	6-10
6.4.2.1	Analysis results with $\kappa=1$ for both anionic and cationic component	6-10
6.4.2.2	Analysis results with κ equal to 0.1 for anionic and equal to 1.0 for cationic component	6-14
6.5	Conclusions	6-19
6.5	References	6-20

Chapter 7 Transport Processes in Compacted Swelling Clays-Microstructural Effects

7.1	Introduction	7-2
7.2	A geochemical solid-solution model for the hydration/dehydration of smectite	7-4
7.3	Suction and temperature dependency of the hydration/dehydration model	7-9

7.4	Evaluation of the interlayer water content in compacted smectite clays	7-11
7.5	Application and adaptation of the model for compacted Na-smectite clay	7-14
7.5.1	Interlayer porosity of saturated compacted Na-smectite	7-14
7.5.2	Application and Adaptation of the solid solution model for compacted MX-80 bentonite	7-18
7.5.3	Interlayer water variations with suction and temperature for compacted MX-80	7-25
7.6	Proposed approach for representing the interlayer water effects on water transport model (an example application of the model)	7-29
7.6.1	Background of the hypothesis	7-29
7.6.2	Modified hydraulic conductivity relationship	7-31
7.7	Simulation of isothermal and non-isothermal transfer of moisture in compacted smectite clay (FEBEX bentonite)	7-34
7.7.1	Model domain and time-step	7-36
7.7.2	Material parameters	7-36
7.7.3	Initial and boundary conditions	7-39
7.7.4	Simulation results of the isothermal infiltration test	7-41
7.7.5	Simulation results of the non-isothermal infiltration test	7-43
7.8	Conclusions	7-45
7.9	References	7-48

Chapter 8 Numerical Simulation of the Coupled Thermal, Hydraulic and Chemical Behaviour Compacted Bentonite

8.1	Introduction	8-2
8.2	FEBEX bentonite and the pore water chemistry	8-4
8.3	Hydro-geochemical results of the heating and hydration experiments	8-10
8.3.1	Experimental methodologies of post-mortem analyses	8-10
8.3.2	Experimental results of post-mortem analyses	8-11
8.4	Numerical simulation of the heating/hydration test	8-15
8.4.1	Model domain and time-step	8-15
8.4.2	Material parameters and relationships for modelling of thermal and hydraulic processes	8-17
8.4.3	Material parameters and relationships for modelling of the reactive transport of chemicals	8-20

8.4.4	Initial and boundary conditions	8-23
8.5	Simulation results	8-27
8.5.1	Temperature distribution	8-27
8.5.2	Moisture distribution	8-28
8.5.3	Geochemistry and pore fluid composition	8-30
8.5.3.1	Chloride (Cl ⁻) distribution (In-place analysis results)	8-30
8.5.3.2	Chloride (Cl ⁻) distribution (Post-mortem simulation results)	8-31
8.5.3.3	Sulfate (SO ₄ ²⁻) distribution (In-place analysis results)	8-33
8.5.3.4	Sulfate (SO ₄ ²⁻) distribution (Post-mortem simulation results)	8-36
8.5.3.5	Bicarbonate (HCO ₃ ⁻) distribution (In-place analysis results)	8-37
8.5.3.6	Bicarbonate (HCO ₃ ⁻) distribution (Post-mortem simulation results)	8-38
8.5.3.7	Sodium (Na ⁺) distribution (In-place analysis results)	8-40
8.5.3.8	Sodium (Na ⁺) distribution (Post-mortem simulation results)	8-41
8.5.3.9	Calcium (Ca ²⁺) distribution (In-place analysis results)	8-42
8.5.3.10	Calcium (Ca ²⁺) distribution (Post-mortem simulation results)	8-43
8.5.3.11	Magnesium (Mg ²⁺) distribution (In-place analysis results)	8-44
8.5.3.12	Magnesium (Mg ²⁺) distribution (Post-mortem simulation results)	8-45
8.5.3.13	Potassium (K ⁺) distribution (In-place analysis results)	8-47
8.5.3.14	Potassium (K ⁺) distribution (Post-mortem simulation results)	8-48
8.5.3.15	Pore water pH (In-place analysis results)	8-49
8.5.3.16	Pore water pH (Post-mortem simulation results)	8-50
8.5.3.17	Exchangeable ions distribution (In-place analysis results)	8-52
8.5.3.18	Exchangeable ions distribution (Post-mortem simulation results)	8-55
8.6	Conclusions	8-59
8.7	References	8-63

Chapter 9 Conclusions and Suggestions for Further Research

9.1	Conclusions	9-2
9.1.1	Theoretical and numerical formulation	9-2
9.1.2	Verification and validation of the numerical model	9-4
9.1.3	Reactive transport under coupled THC conditions	9-5

9.1.4	Transport Processes in compacted bentonite and microstructure evolution	9-6
9.1.5	Simulation of a heating and hydration experiment of a compacted bentonite	9-8
9.1.6	Overall conclusions	9-10
9.2	Suggestions for further research	9-12

Nomenclature

a_{as}	Defined in equation (7.2)
a_{hs}	Defined in equation (7.3)
a_{H_2O}	Activity of water
\mathbf{a}_{ss}	Defined in equation (4.22)
a'	Defined in equation (3.17)
A_p	Defined in equation (3.213)
A_s	Defined in equation (3.195)
A_s^{int}	Internal specific surface area
A_T	Defined in equation (3.196)
A	Constant value, defined in equation (3.150)
A'	Temperature dependent parameter
A_1, A_2	Defined in equation (6.1)
\mathbf{A}	Defined in equation (4.62)
\mathbf{b}	Body force vector
\mathbf{B}	Defined in equation (3.49)
\mathbf{B}	Defined in equation (4.62)
b'	Defined in equation (3.17)
c_d^i	Dissolved concentration of chemical component i^{th}
\hat{c}_d^i	Approximate value of dissolved concentration of chemical component i^{th}
C_{aa}	Defined in equation (3.92)
C_{ac_d}	Defined in equation (3.93)
C_{al}	Defined in equation (3.90)
C_{aT}	Defined in equation (3.91)
C_{au}	Defined in equation (3.94)
$C_{c_d a}$	Defined in equation (3.172) and (3.184)
$C_{c_d l}$	Defined in equation (3.170) and (3.182)
$C_{c_d c_d}$	Defined in equation (3.173) and (3.185)
$C_{c_d u}$	Defined in equation (3.175) and (3.187)

$C_{c_d T}$	Defined in equation (3.171) and (3.183)
$C_{c_d s}$	Defined in equation (3.174) and (3.186)
C_{la}	Defined in equation (3.69)
C_{lc_d}	Defined in equation (3.70)
C_{ll}	Defined in equation (3.67)
C_{lr}	Defined in equation (3.68)
C_{lu}	Defined in equation (3.71)
C_{pda}	Specific heat capacity of dry air
C_{pl}	Specific heat capacity of liquid
C_{ps}	Specific heat capacity of soil solids
C_{pv}	Specific heat capacity of vapour
C_{Ta}	Defined in equation (3.119)
C_{Tc_d}	Defined in equation (3.120)
C_{Tl}	Defined in equation (3.117)
C_{Tr}	Defined in equation (3.118)
C_{Tu}	Defined in equation (3.121)
C_{ua}	Defined in equation (3.220)
C_{ul}	Defined in equation (3.218)
C_{uT}	Defined in equation (3.219)
C_{uu}	Defined in equation (3.221)
c_d^i	Nodal value of i^{th} chemical component
C	Defined in equation (4.62)
C_{aa}	Defined in equation (4.48)
C_{ac_d}	Defined in equation (4.49)
C_{al}	Defined in equation (4.46)
C_{aT}	Defined in equation (4.47)
C_{au}	Defined in equation (4.50)
$C_{c_d l}$	Defined in equation (4.12)
$C_{c_d T}$	Defined in equation (4.13)
$C_{c_d a}$	Defined in equation (4.14)
$C_{c_d c_d}$	Defined in equation (4.15)

$C_{c,u}$	Defined in equation (4.16)
C_{Ia}	Defined in equation (4.26)
C_{Ic_d}	Defined in equation (4.27)
C_{II}	Defined in equation (4.24)
C_{IT}	Defined in equation (4.25)
C_{Iu}	Defined in equation (4.28)
C_{Ta}	Defined in equation (4.37)
C_{Tc_d}	Defined in equation (4.38)
C_{TI}	Defined in equation (4.35)
C_{TT}	Defined in equation (4.36)
C_{Tu}	Defined in equation (4.39)
C_{ua}	Defined in equation (4.59)
C_{ui}	Defined in equation (4.57)
C_{uT}	Defined in equation (4.58)
C_{uu}	Defined in equation (4.60)
$d_{2-layer}$	Defined in equation (7.27)
$d_{3-layer}$	Defined in equation (7.27)
d_e	Defined in equation (5.27)
d_{II}	Defined in equation (7.26)
d_x	Defined in equation (8.1)
D_{atms}	Molecular diffusivity of vapour in air
D_i^0	Tracer diffusion coefficient of the i^{th} component in water
D_i^{eff}	Defined in equation (8.5)
D_{ij}^0	Defined in equation (3.145)
D_i^T	Defined in equation (3.146)
D_m	Coefficient of mechanical dispersion
D	Stiffness matrix
D_{ep}	Elasto-plastic matrix
e	void ratio
e_0	Initial void ratio
E	Young's modulus
E_{ss}	Sink or Source
f	Flow area factor in vapour flux

f_l	Total moisture flux
f_T	Total heat flux
f_c	Clay fraction in soil
f_{IL}	Volume fraction of the interlayer water in compacted smectite
$f_{c,d}$	The approximate chemical solute flux normal to the boundary
F	Applied Force
F	Faraday constant
F_1	Yield function as defined in equation (3.209)
F_2	Yield function as defined in equation (3.210)
f_a	Defined in equation (4.55)
$f_{c,d}$	Defined in equation (4.21)
f_l	Defined in equation (4.33)
f_T	Defined in equation (4.44)
f_a	Defined in equation (4.61)
g	Gravitational constant
g_k	Defined in equation (7.28)
g_s	Defined in equation (7.28)
G_v	Defined in equation (3.50)
G	Shear modulus
G_s	Specific weight
h	Relative humidity
h_m	Relative humidity due to matric potential
h_π	Relative humidity due to osmotic potential
H_c	Heat capacity of the soil
H_s	Henry's volumetric coefficient of solubility
i	Iteration level
I	Ionic strength
J_a	Defined in equation (3.99)
J_i^{Adv}	Advective flux of i^{th} chemical component
$J_{c,d}$	Defined in equation (3.179)
J_i^{Diff}	Diffusive flux of i^{th} chemical component
J_i^{Disp}	Dispersive flux of i^{th} chemical component
J_l	Defined in equation (3.76)

J_T	Defined in equation (3.126)
J_i	Total flux of i^{th} chemical component
k_f	Unsaturated hydraulic conductivity
k_{sat}	Saturated hydraulic conductivity
k_a	Unsaturated conductivity of air
K_0	'at rest' stress state
k	Kinetic rate constant
K	Bulk modulus
K_{∞}	Defined in equation (3.97)
$K_{\infty c_d}$	Defined in equation (3.98)
K_{al}	Defined in equation (3.95)
$K_{\sigma T}$	Defined in equation (3.96)
$K_{c_d l}$	Defined in equation (3.176)
$K_{c_d T}$	Defined in equation (3.177)
$K_{c_d c_d}$	Defined in equation (3.178)
K_{eq}	Equilibrium constant of chemical reaction
K_f	Intrinsic hydraulic conductivity
$K_{f\sigma}$	Defined in equation (3.74)
K_{k_d}	Defined in equation (3.75)
K_{ll}	Defined in equation (3.72)
K_{TT}	Defined in equation (3.73)
$K_{T\sigma}$	Defined in equation (3.124)
K_{Tc_d}	Defined in equation (3.125)
K_{Tl}	Defined in equation (3.122)
K_{TT}	Defined in equation (3.123)
K_{∞}	Defined in equation (4.53)
K_{al}	Defined in equation (4.51)
$K_{\infty c_d}$	Defined in equation (4.54)
$K_{\sigma T}$	Defined in equation (4.52)
$K_{c_d l}$	Defined in equation (4.17)
$K_{c_d T}$	Defined in equation (4.18)
$K_{c_d \sigma}$	Defined in equation (4.19)

K_{c,c_d}	Defined in equation (4.20)
K_{ln}	Defined in equation (4.31)
K_{k_d}	Defined in equation (4.32)
K_{ll}	Defined in equation (4.29)
K_{TT}	Defined in equation (4.30)
K_{T_s}	Defined in equation (4.42)
K_{T_c}	Defined in equation (4.43)
K_{Tn}	Defined in equation (4.40)
K_{TT}	Defined in equation (4.41)
L	Latent heat of vapourisation
L	Defined in equation (4.70)
L_{ii}	Phenomenological transport coefficient due to electrochemical potential for the i^{th} chemical component
L_{iq}	Phenomenological coefficient of thermally induced chemical diffusion for the i^{th} chemical component
m_{IL}	Defined in equation (7.28)
m_{as}	Number of moles of anhydrous smectite
m_{hs}	Number of moles of hydrous smectite
m_{sm}	Molar mass of dry smectite
M_{dry}^{sm}	Total mass of dry smectite
M	Molecular weight of water
M_s	Molecular weight of smectite
M	Slope of the critical state line
\mathbf{m}	Unit vector
\mathbf{m}^T	Differential operator, defined in equation (3.191)
n	Porosity
n_0	Saturate available porosity
\underline{n}	Direction cosine normal to the surface
n_{IL}	Interlayer porosity, Defined in equation (7.24)
nc	Total number of chemical components
n_c	Mole number of interlayer hydrate water
n_{DDL}	Porosity associated with developed diffusion layer
n_{eff}	Effective porosity for diffusion of ionic species
N_r, N_s	Shape functions
\mathbf{N}	Shape function matrix
p_{atms}	Atmospheric pressure

p_c	Reference stress
$p_{H_2O}^0$	Partial pressure of water in a pure solution
p_{H_2O}	Partial pressure of water in soil
p_s	Parameter controlling suction effect on cohesion
p_0	Critical Pre-consolidation stress
p_0^*	Saturated pre-consolidation stress
\mathbf{P}	Strain matrix
q	Deviatoric stress
q	Number of occupied octahedral sites per mole of the mineral
Q	Heat flux
Q_i^*	Heat of transport of i^{th} chemical component
Q_i^{*0}	Heat of transport of i^{th} chemical component in a dilute solution
Q_1	Defined in equation (3.201)
Q_2	Defined in equation (3.202)
r	Defined in equation (3.200)
r_{AB}	Defined in equation (5.12)
R	Defined in equation (4.71)
R	Interlayer cations
R	Universal gas constant
R_Ω	Residual error introduced due to approximation
R_{da}	Specific gas constant for dry air
R_v	Specific gas constant for water vapour
RH	Relative humidity
s	matric suction
s_i	Geochemical sink/source term for i^{th} chemical component
s_r	Suction at reference temperature (T_r)
s_0	Critical value of suction - suction hardening parameter
S^T	The Soret coefficient
S_a	Degree of saturation of pore air
S_l	Degree of saturation of pore water
S_{l0}	Residual degree of saturation
S_l^c	Percolation threshold for degree of saturation
S_{lmax}	Maximum degree of saturation
S_{ro}	Initial degree of saturation of pore-liquid
t	Time

T	Temperature
T_r	Reference temperature
\hat{T}	Approximate value of temperature
$(\nabla T)_o/\nabla T$	Microscopic pore temperature gradient factor
T_i	Nodal value of temperature
TL_{abs}	Matrix of absolute tolerances
TL_{rel}	Matrix of percentage tolerances
u_a	Pore-air pressure
u_{da}	Partial pressure of dry air
u_l	Pore-water pressure
u_v	Partial pressure of water vapour in pore space
\hat{u}_a	Approximate value of pore-air pressure
\hat{u}_l	Approximate value of pore-water pressure
\hat{u}	Approximate value of displacement
u	Displacement vector
$u_{a,s}$	Nodal value of pore-air pressure
$u_{l,s}$	Nodal value of pore-water pressure
u_s	Nodal value of displacement
v	specific volume
$ v $	Absolute average velocity of advection flow
v_v	Mass flow factor
V_l	Pore velocity
V_l^{II}	Defined in equation (7.14)
V_m	Defined in Table (5.8)
V_T	Total volume of the dry smectite
V_s	Volume of Solids
v_a	Velocity of air
v_l	Velocity of liquid water
v_v	Velocity of water vapour
w	Water content
W_s	Margules parameter for a binary regular solid solution of hydrous and anhydrous smectite components
x_0	Defined in equation (8.1)

X_{as}	Mole fraction of anhydrous smectite
X_{hs}	Mole fraction of hydrous smectite
X_{sm}	Mass fraction of smectite in clay
x, y, z	Global coordinates
z	Elevation from the reference level
z_i	Charge of i^{th} chemical component
α	Power number
α_L	Longitudinal dispersivity parameter
α_q	Parameter for non-associated flow rule, defined in equation (3.203)
α_T	Transversal dispersivity parameter
α_T	Coefficient of thermal expansion
β_0	Defined in equation (5.26)
ΔC_p^0	Standard change of heat capacity of the reaction at constant pressure
ΔG_r^0	Standard change of Gibbs free energy of the chemical reaction
ΔH_r^0	Standard change in enthalpy of the chemical reaction
γ_i	Activity coefficient of the i^{th} chemical component
γ_l	Unit weight of liquid
χ_1, χ_2	Fluidity parameters controlling the plastic flow rate (plastic multipliers)
δ	Constrictivity coefficient
δ_{ij}	Kronecker's delta function
∂	Differential
δV	Incremental volume
ε	Total strain
ε^e	Elastic component of strain
ε^p	Plastic component of strain
ε_s^p	Plastic strain increments due to stress and suction changes
ε_q^p	Plastic deviatoric strain
ε_p^e	Elastic component of strain due to stress changes
ε_s^e	Elastic component of strain due to suction changes
ε_T^e	Elastic component of strain due to temperature changes
ε_v	Volumetric strain
ε_v^p	Total volumetric plastic strain

ε_{vp}^p	Volumetric plastic strain due to stress changes
ε_{vs}^p	Volumetric plastic strain due to suction changes
ε_{σ}^e	Elastic component of strain due to stress changes
η	Viscosity of solvent
η_1	Material dependent factor for vapour flux
η_2	Material dependent factor for vapour flux
κ	Stiffness parameter for changes in net mean stress in the elastic region
κ_i	Defined in equation (6.6)
κ_s	Stiffness parameter for changes in suction in the elastic region
λ_1, λ_2	Defined in equation (5.28)
λ_a	Thermal conductivity of pore air
λ_{as}	Activity coefficient of anhydrous smectite
λ_{hs}	Activity coefficient of hydrous smectite
λ_l	Thermal conductivity of pore liquid
λ_r	Thermal conductivity of soil
λ_v	Thermal conductivity of pore vapour
$\lambda(0)$	Stiffness parameter for changes in net mean stress for saturated soil
$\lambda(s)$	Stiffness parameter for changes in net mean stress for virgin states of the soil
μ_a	Viscosity of air
μ_i	Chemical potential of i^{th} chemical component
μ_i^0	Chemical potential of i^{th} chemical component at reference state
μ_l	Absolute viscosity of liquid
θ	Volumetric water content
θ_a	Volumetric air content
θ_l	Volumetric liquid content
θ_l^{IL}	Volumetric content of the interlayer water
θ_r	Defined in Table 5.2
θ_s	Defined in Table 5.2
θ_v	Volumetric vapour content

ξ	Surface energy (tension) at temperature T
ξ_r	Surface energy (tension) at reference temperature T_r
$\xi_{2\text{-layer}}$	Defined in equation (7.27)
ρ_0	Density of saturated water vapour
ρ_d	Bulk dry density of the clay
ρ_{da}	Density of dry air
ρ_d^{sm}	Partial bulk dry density of smectite
ρ_l	Density of liquid water
ρ_s	Density of non-smectite minerals or impurities
ρ_s	Density of soil solids
ρ_v	Density of water vapour
σ	Specific surface area
σ	Total stress
σ^n	Net stress
τ	Tortuosity factor in chemical diffusion flux
τ_v	Tortuosity factor in vapour flux
ν	Poisson's ratio
v_{il}	Molar volume of interlayer water
v_w	Molar volume of water
ω_{abs}	Defined in equation (7.32)
ω_x	Osmotic efficiency coefficient
ω	Defined in equation (4.1)
$\hat{\omega}$	Defined in equation (4.1)
ψ	Defined in equation (5.16)
ψ	Total water potential
ψ_m	Matric potential
ψ_g	Gravitational potential
ψ_π	Osmotic potential
∇	Gradient operator
Γ^e	Element boundary surface
\mathcal{G}	Defined in equation (4.64)
Θ	Defines the type of integrating scheme, defined in equation (4.63)
Ω	Heat content of soil per unit volume
Ω^e	Element domain

ϕ	Variable vector, defined in equation (4.64)
Φ	Electrical potential of the solution
Φ	Defined in equation (7.8)
ζ	Defined in equation (4.69)

Chapter 1

Introduction

1.1 Introduction

Geoenvironmental engineering faces serious challenges with the management of ground and water contamination, waste disposal, energy demand and greenhouse gas emissions due to anthropogenic activities and their consequences (Thomas, 2006). In fact, sustainability of the geoenvironment is highly affected by the continued depletion of non-renewable natural resources and imposing physical, chemical and biological impacts to the geoenvironment from the various anthropogenic stress generators, representing an increasing threat to the subsurface environmental quality and the public health (Yong et al., 2006). Hence, there is a pressing need to develop a better appreciation of the anthropogenic stresses imposed on the geoenvironment and to improve the knowledge and technology for appropriate management of our geoenvironmental resources (Yong et al., 2006).

Understanding hydro-geochemical processes in subsurface soil and groundwater is essential in order to approach the sustainable engineering solutions for the management of the environmental contaminants. The investigation of the various anthropogenically-induced contaminations in subsurface soil and groundwater, such as the accidental release of contaminants, disposal of hazardous wastes, agricultural and soil management practices may involve complex transport and geochemical reactions in the soil-water-chemical system, usually defined as reactive transport of chemicals. This area of research can also include the irreversible changes to the properties of soil material induced by chemical reactions (Yaron et al., 2008) and requires advanced understanding of the hydro-geochemistry and interactions in the soil-water-chemical system.

Modelling of the reactive transport of chemicals inherit all of the difficulties associated with the individual disciplines of hydro-chemical transport and geochemistry which can involve multiple chemicals, reaction heterogeneities and various time-scales. In many geoenvironmental challenges, hydro-geochemical processes are also coupled with physical, chemical and mechanical behaviour. The study of the reactive transport of chemicals under coupled physical, chemical and mechanical problems has been the interest of many studies and evolved with developments in various disciplines due to the various challenges, e.g. ground contaminants, energy demand, anthropogenic atmospheric carbon dioxide and global warming (e.g. Stephansson et al., 2004; Thomas, 2006; Datta et al., 2010). The degree of

complexity due to the coupling phenomena between physical, chemical and mechanical behaviour depends on the geo-material and the conditions related to the engineering case.

The developments in numerical modelling capabilities for simulating hydro-geochemical processes under coupled behaviour and conditions are among the most important steps forward in the assessment and prediction of geoenvironmental solutions. Such models provide an integrating focus for the wide range of geo-engineering disciplines and represent the basic physical, chemical and mechanical processes which can include the effects of heat, water, chemistry and mechanics. It is well accepted that numerical simulation can be used to illustrate technical understanding, via development of conceptual models and validation with experimental data. Numerical simulation can then be used to test various scenarios at a fraction of real cost and predict future behaviour. Computer modelling is also non-destructive; data can be easily produced at all locations and can be produced in reduced time periods compared to experimentation. However, it is critical that models and processes are correctly understood and used only in relevant circumstances; otherwise important processes may be omitted from simulations which can yield to incorrect interpretation.

The overall aim of this research is to advance the numerical simulation of hydro-geochemical processes in unsaturated soils under coupled thermal, hydraulic, chemical and mechanical modelling framework. The research also aims to develop the theoretical understanding and include advances in the experimental knowledge of the hydraulic and chemical/geochemical behaviour in the coupled numerical modelling platform. The specific emphasis is on the developments to the hydraulic and chemical reactive transport processes in compacted swelling clays (smectite clays) under coupled THCM behaviour.

The developed coupled numerical model would be of particular interest in simulation of the coupled physical and chemical behaviour of compacted swelling clays (bentonite) as proposed for the buffer material in geological containment of high level radioactive waste. Engineered Barrier Systems are likely to be subject to thermal, hydraulic, chemical and biogeochemical processes, such as heat release due to radionuclide decay, multiphase flow, swelling of buffer material, radionuclide diffusive transport, waste dissolution and chemical reactions. Hence, the performance assessment of the compacted clay buffer, as a component of the Engineered Barriers System (EBS), includes analysing complex interacting and coupled thermal, hydraulic, chemical/geochemical and mechanical processes (Yong et al., 2010). In

addition, the properties and characteristics of compacted bentonite, i.e. smectite dominated clay, are highly affected by the microstructure of the swelling minerals constituents which in fact, control the transport properties of water and chemicals in the system (Pusch and Yong, 2006).

Understanding the highly complex hydro-geochemical behaviour of compacted clay buffer in high level radioactive waste (HLW) repository is a challenging problem and requires advanced conceptual and theoretical models, comprising multiphase, multicomponent processes and the multilevel structural material effects. In particular, studies related to the smectite mineral hydration and the long-term chemical and mechanical stability of the barrier are among the key issues in the long-term performance of multiple barrier HLW repositories.

There are still essential research and development required for modelling the coupled processes in compacted swelling clays as the buffer candidate. Inclusion of processes such as bentonite hydration mechanism, microstructure evolution, existence of different states of water in the bentonite, existence of a threshold hydraulic gradient for water flow and thermo-osmosis has been suggested in conventional formulation of THM models (Steefel et al., 2010). In terms of chemical/geochemical and biological processes, the models need still more development to reach the stage of sophistication to be coupled with THM platforms (Pusch, 2008). Further integration of C and THM models and processes for simulating coupled THMC processes has been also suggested as a critical research and developments required in this field (Steefel et al., 2010).

The study objectives of the thesis are presented in section 1.2. In section 1.3 the background of the research is presented. The scopes of the work and limitations are discussed in section 1.4. Finally an overview of the structure of the thesis and the chapters is given in section 1.5.

1.2 Study objectives

Within the development of the numerical simulation of the coupled thermo-hydro-chemo-mechanical behaviour of unsaturated soils, the research presented in this thesis focuses, on the advanced modelling of the moisture flow and the reactive transport of chemicals. In

particular, the hydro-geochemical behaviour of compacted bentonite suggested as the buffer in geological disposal of HLW is studied as an application cased of the developed model.

The main objectives of this study are to:

- i) Develop a theoretical framework for the transport of multiple chemicals under variable saturated and non-isothermal conditions and the key coupling effects between chemical/geochemical processes (C) and THM processes.
- ii) Integrate an advanced geochemical model into the coupled THCM numerical model to calculate the chemical reaction under both equilibrium and kinetically controlled conditions.
- iii) Include the impacts of microstructure evolution of compacted swelling clays, in particular, smectite rich clays, in the modelling the transport processes.
- iv) Investigate the hydro-geochemical behaviour of compacted swelling clays under coupled THC effects and compare with experimental results.

1.3 Research background

This work is undertaken at the Geoenvironmental Research Centre at Cardiff University where considerable research, including the development of the numerical computer code COMPASS (COde for Modelling PARTially Saturated Soils), has been performed prior to the study. This section provides the context to this work, and is not intended to replace more detailed reviews of literature in chapter 2 or the theoretical formulation in chapter 3.

A theoretical model of coupled transient heat and moisture transfer in unsaturated soil was developed by Thomas (1985). In this model the vapour flow was modelled by incorporating the diffusive flow proposed by Philip and de Vries (1957) and de Vries (1958), and the latent heat of vaporisation was also introduced following Luikov (1966). The principle of mass conservation was employed for moisture flow and the conservation of energy used for heat transfer. Non-linearity of material parameters was then incorporated in the works presented by Thomas (1987), Thomas, (1988a) and Thomas, (1988b). Revised time-stepping schemes were

investigated under the mentioned coupled TH model by Thomas and Rees (1988) and Thomas and Rees (1990).

Following an experimental investigation into the behaviour of unsaturated sand surrounding a heating rod, Ewen and Thomas (1987) and Ewen and Thomas (1989) amended the vapour transfer diffusivities of the numerical model to simulate coupled heat and moisture transfer processes in unsaturated soil. A numerical simulation in terms of moisture content and temperature was carried out by Ewen and Thomas (1989) including vapour transport via a diffusive mechanism. Thomas and King (1991) presented a theoretical heat and moisture formulation cast in terms of capillary potential and temperature and found good agreement with the Ewen and Thomas (1987) experiments. Thomas and Sansom (1995) extended this formulation to include elevated pore-air pressures and validated via comparison to experimental works on sand and clay. This formulation was presented in three-dimensions including work on pre and post-processing, visualisation and parallel computation by Sloper (1997) and Thomas et al. (1998).

Mechanical behaviour and deformation was introduced examining seasonal ground movements by Thomas and Rees (1990; 1993), with an isothermal coupled hydro-mechanical numerical model presented by Thomas et al. (1992) utilising the non-linear elastic state-surface approach proposed by Lloret and Alonso (1985). This model was applied to seasonal ground movements in the work presented by Thomas and Zhou (1995). An elasto-plastic coupled Thermo-Hydro-Mechanical (THM) model was presented by Thomas and He (1994) and Thomas and He (1995) using the elasto-plastic model of Alonso et al. (1990). Ramesh (1996) applied the THM model to simulate temperature, moisture and void ratio distributions of montmorillonite subjected to heating/hydration. The work also involved investigation of isothermal volume change behaviour of compacted kaolinite in suction controlled tests. Thomas and Cleall (1999) extended the THM model to include highly expansive behaviour. Using the developed model, a numerical simulation of large scale experiments were presented by Mitchell (2002), Thomas et al. (2003), Melhuish (2004) and Cleall et al. (2006) which included investigation into the microstructure behaviour of bentonite and the effects on resaturation of the buffer.

Chemical processes were first introduced as non-reactive chemical solute transport for a single species (Thomas and Cleall, 1997). Hashm (1999) developed the model to two-

dimensional coupled moisture and reactive multiple chemical solute transport by linking the non-reactive transport code with the geochemical model, MINTEQA2 (Allison et al., 1991). The model was applied to simulate a series of leaching cell experiments to study the migration/sorption behaviour of some of the heavy metals. Seetharam (2003) developed the multicomponent chemicals reactive transport module of the coupled THCM model. The geochemical reactions were calculated by the geochemical model, MINTEQA2 using two different coupling schemes to solve transport and reaction equations. The coupled THCM model was used to simulate the reactive transport of chemicals in a small scale laboratory on compacted bentonite under heating and hydration (Seetharam et al., 2006; Cleall et al., 2007).

A number of theoretical and computational developments have recently been made in the model focusing mainly on the behaviour of compacted bentonite as the buffer in HLW geological repository and to model the large scale THM behaviour of the repository. Sing (2007) presented an experimental and numerical investigation on the heat and moisture transfer in compacted bentonite and kaolinite with special attention to the vapour transfer in compacted clays. Modifications to the existing vapour theory were suggested and introduced in existing THM behaviour. Siddiqua (2008) presented an investigation into the elevated temperature effects (70-200 °C) on the THM processes in the model. A pore gas transfer equation and thermo-osmotic effect was developed to account for elevated temperature. Vardon (2009) extended the COMPASS model to accommodate three-dimensional THM behaviour in geological repository, including the development of a high-performance computing algorithm using both multi-threaded and message-passing programming paradigms to enable simulations to be completed in significantly reduced time. The model was utilised for simulation of the THM behaviour of a large-scale experiment, carried out at an underground research laboratory in Sweden. More recently, Thomas et al. (2011) presented the inclusion of biological aspects to the coupled THCM model. The work deals with early developments to include some biological impacts on coupled transport phenomena through unsaturated porous media. The THCMB model presented incorporates biodegradation kinetics of organic substrates.

1.4 Scopes and limitations

The scope of the work undertaken in this thesis and in particular the limitations that are anticipated are listed below:

- Numerical approximation is used to find a solution to the system of coupled differential equations. In particular, the finite-element method is used to provide a spatial solution and the finite-difference method used to provide a temporal solution.
- Soil is assumed as a homogeneous medium acknowledging the fact that that soils exhibit some degree of heterogeneity, and this may be partly accommodated in this study as the assumption of homogeneity only applies within an individual element. Therefore, different soil types may be used within an analysis.
- The chemical transport equation is applicable for miscible chemical flow only. Immiscible chemical flow is not considered.
- Soil hysteresis behaviour such as found in the moisture retention behaviour in wetting/drying paths has not been included in the model. This is due in part to a lack of experimental evidence and potentially complex wetting/drying path.
- The effect of osmotic potential on the deformation behaviour is not considered.
- Vapour transport is assumed to be diffusive. At higher temperatures, elevated air pressure gradients may occur, leading to increased vapour movement. This has not been included in the theoretical formulation. Hence the temperature range, which can be modelled, is between 0 and 100 °C in accordance with the moisture flow formulation. However, the range of temperature validity in the geochemical model depends mainly on the limitation of the thermodynamic data for reactions.
- The constitutive model implemented for stress/strain behaviour is valid for slightly and moderately expansive soils.

1.5 Overview of the thesis

A brief description of each chapter is presented below.

Chapter 2 contains a selective review of the current literature salient to the work contained in the developments presented in the remainder of the thesis, including a review of the recent coupled THCM experimentation and modelling aspects of compacted bentonite buffer behaviour. A targeted review of the development of numerical strategies to efficiently solve coupled transport and geochemical problems is also presented.

The theoretical formulation for thermal, hydraulic and mechanical behaviour and geochemical reactions of the linked geochemical model is presented in chapter 3. The main focus is to present the development in the governing equations for the reactive transport of multicomponent chemicals. In chapter 4 the numerical formulation of the solution of the governing differential equations representing heat, moisture, air, multicomponent chemical and deformation behaviour is presented. The coupling scheme adopted for solving the chemical transport and reaction problems is also presented in this chapter.

Chapter 5 presents the verification and validation of the numerical model against analytical solutions, alternative numerical solutions and experimental results. This chapter will only focus on the verification and validation related to the developments made in the scope of this thesis, in particular in the chemical reactive transport. It is noted that the numerical model has already been verified for a number of test cases involving coupled moisture flow, air flow, heat transfer, chemical transport, and deformation.

Chapter 6 presents a numerical simulation of the reactive transport of chemicals under coupled thermal, hydraulic, chemical framework. In particular, based on the development of the theoretical formulation, presented in chapter 3, the effects related to the combined electrochemical and thermal diffusion potentials on the reactive transport of ionic species in compacted clays are investigated. The simulations have aimed to initially test the numerical model behaviour under coupled THC condition and more importantly to investigate how the coupled electrochemical and thermal diffusion affects the distribution of chemicals in the system.

In chapter 7, a theoretical model is presented to include the microstructural evolution of smectite minerals (as the major clay component of compacted bentonite) in modelling of the transport processes. The hydrate water in the microstructure of compacted bentonite and its variation is evaluated and modelled with an approach proposed based on a geochemical solid-solution reaction. The inclusion of the effects of the hydrate water located in the microstructure on the flow behaviour of confined compacted bentonite is presented. Two series of simulations are reported, the first under isothermal conditions and the second under thermal gradients using the proposed model. The results are compared and validated against experimental results.

Chapter 8 presents the results of an application of the model via simulation of a laboratory experiment reported on the hydro-geochemical response of compacted unsaturated smectite clay subjected to heating and hydration. The problem considered in the simulation is a thermo-hydraulic laboratory test on a sample (600×70 mm) of compacted bentonite for relatively long term (7.6 years) and reported by Villar et al. (2008) and Fernández and Villar (2010). The sample is subjected to heating at 100 °C on the bottom side and hydration through the top surface with granitic water at 1.2 MPa. The focus is to simulate the reactive transport behaviour of major ionic species and the variations in the geochemistry of aqueous-clay system under the influence of opposing thermo-hydraulic gradients. The major geochemical reactions including precipitation/dissolution of multiple minerals and ion exchange process are investigated. The results of simulation are compared with the experimental data providing a validation test on the model for complex and coupled behaviour similar to the condition of the buffer in HLW repository condition.

Chapter 9 presents the conclusions drawn from this work, and suggestions are made for further research.

1.6 References

- Allison, J.D., Brown, D.S., and Novo-Gradac, K.J. (1991). *MINTEQA2 user manual version 3.0*. Environmental Research Laboratory, US EPA.
- Alonso, E.E., Gens, A., and Josa, A. (1990). A constitutive model for partially saturated soils. *Géotechnique*, 40(3), 405-430.
- Cleall, P.J., Melhuish, T.A., and Thomas, H.R. (2006). Modelling the three-dimensional behaviour of a prototype nuclear waste repository. *Engineering Geology*, 85(2), 212-220.
- Cleall, P.J., Seetharam, S.C., and Thomas, H.R. (2007). On the inclusion of some aspects of chemical behaviour of an unsaturated soil in thermo-hydro-chemical-mechanical models: II Application and transport of soluble salts in compacted bentonite. *Journal of Engineering Mechanics, ASCE*, 133, 348-356.
- Datta, M., Srivastava, R.K., Ramana, G.V., and Shahu, J.V. (edt.) (2010). Environmental Geotechnics for Sustainable Development. *Proceeding of the 6th International Congress on Environmental Geotechnics*, New Delhi, India.
- de Vries, D.A. (1958). Simultaneous transfer of heat and moisture in porous media. *Transaction American Geophysical Union*, 39(5), 909-916.
- Ewen, J., and Thomas, H.R. (1987). The thermal probe—a new method and its use on an unsaturated sand. *Géotechnique*, 37, 91-105.
- Ewen, J., and Thomas, H.R. (1989). Heating unsaturated medium sand, *Géotechnique*, 39(3), 455-470.
- Fernández, A.M., and Villar, M.V. (2010). Geochemical behaviour of a bentonite barrier in the laboratory after up to 8 years of heating and hydration. *Applied Geochemistry*, 25, 809-824.
- Hashm, A.A. (1999). *A study of the transport of a selection of heavy metals in unsaturated soils*, Ph.D. Thesis. University of Wales, Cardiff.
- Lloret, A., and Alonso, E.E. (1985). State surfaces for partially saturated soils. *Proceedings of the 11th International Conference of Soil Mechanics and Foundation Engineering*, San Francisco, 2, 557-562.

- Luikov, A.V. (1966). *Heat and Mass Transfer in Capillary Porous Bodies*, Pergamon Press, Oxford.
- Melhuish, T.A. (2004). *An investigation of the three-dimensional thermo/hydro/mechanical behaviour of large scale in-situ experiments*. PhD Thesis, Cardiff University, Cardiff, UK.
- Mitchell, H.P. (2002). *An investigation into the thermo/hydro/mechanical interactions involved in high level nuclear waste disposal*. PhD Thesis, University of Wales, Cardiff, UK.
- Philip, J.R., and de Vries, D.A. (1957). Moisture movement in porous materials under temperature gradients. *Transaction American Geophysical Union*, 38(2), 222-232.
- Pusch, R. (2008). *Geological Storage of Highly Radioactive Waste*, Springer, New York.
- Pusch, R. and Yong, R.N. (2006). *Microstructure of Smectite Clays and Engineering Performance*. Taylor and Francis, New York.
- Ramesh, A.D. (1996). *Modelling the thermo/hydraulic/mechanical behaviour of unsaturated soil using an elasto-plastic constitutive relationship*, Ph.D thesis. University of Wales Cardiff, UK.
- Seetharam, S.C., Thomas, H.R., and Cleall, P.J. (2007). Coupled thermo-hydro-chemical-mechanical model for unsaturated soils-Numerical algorithm. *International Journal of Numerical Methods in Engineering*, 70, 1480-1511.
- Seetharam, S.C. (2003). *An investigation of the thermo/hydro/chemical/mechanical behaviour of unsaturated soils*. Ph.D. Thesis, Cardiff University, Wales, UK.
- Seetharam, S.C., Cleall, P.J., and Thomas, H.R. (2006). Modelling some aspects of ion migration in a compacted bentonitic clay. *Engineering Geology*, 85, 221-228.
- Siddiqua, S. (2008). *An investigation of the influence of elevated temperatures on the thermal-hydraulic-mechanical response of unsaturated soils*. PhD Thesis, Cardiff University, Wales, UK.
- Singh, R.M. (2007). *An experimental and numerical investigation of heat and mass movement in unsaturated clays*. PhD Thesis, Cardiff University, Wales, UK.
- Sloper, N.J. (1997). *The development of a new three dimensional numerical model for fully coupled heat, moisture and air flow in unsaturated soil incorporating scientific visualisation and parallel computing techniques*, PhD Thesis, University of Wales, Cardiff.

Steeffel, C.I., Rutqvist, J. Tsang, C-F., Liu, H-H., Sonnenthal, E., Houseworth J., and Birkholzer, J. (2010). *Reactive Transport and Coupled THM Processes in Engineering Barrier Systems (EBS)*. Technical Report, LBNL-3901E, Lawrence Berkeley National Laboratory.

Stephansson, O., Hudson, J.A., and Jing, L. (edt.) (2004). *Coupled Thermo-Hydro-Mechanical-Chemical Processes in Geo-systems: Fundamentals, Modelling, Experiments and Applications*. Geo-Engineering Book Series, Elsevier.

Thomas, H.R. (1985). Modelling two-dimensional heat and moisture transfer in unsaturated soils, including gravity effects. *International Journal of Analytical Methods in Geomechanics*, 9, 573-588.

Thomas, H.R. (1987). Non-linear analysis of heat and moisture transfer in partly saturated soil, *Journal of Engineering Mechanics, American Society of Civil Engineering*, 113, 1163-1180.

Thomas, H.R. (1988a). A non-linear analysis of two-dimensional heat and moisture transfer in partly saturated soil. *International Journal of Analytical Methods in Geomechanics*. 2, 31-44.

Thomas H.R. (1988b). The influence of non-linear thermal parameters on moisture content distributions in unsaturated soil. *International Journal of Analytical Methods in Engineering*, 26, 263-279.

Thomas, H.R. (2006). *5th ICEG Environmental Geotechnics; Opportunities, Challenges and Responsibilities for Environmental Geotechnics*. Thomas Telford.

Thomas, H.R., and Rees, S.W. (1988). The use of Lee's algorithm in the analysis of some ground heat and mass transfer problems. *Proceedings of the 6th International Conference on Numerical Methods in Geomechanics*, Innsbruck, Austria.

Thomas, H.R., and Rees, S.W. (1990). An examination of the performance of a 3-level time stepping algorithm—Coupled heat and mass transfer computing. *Proceedings of the 1st International Conference, Advances in Computer Methods in Heat Transfer*, Southampton, U.K.

Thomas, H.R., and King, S.D. (1991). Coupled temperature/capillary potential variations in unsaturated soil. *Journal of Engineering Mechanics, American Society of Civil Engineers*, 117, 2475-2491.

Thomas, H.R., Zhou, Z., and He, Y. (1992). Analysis of consolidation of unsaturated soils. *Proceedings of the 2nd Czechoslovak Conference on Numerical Methods in Geomechanics*, Prague, Dolezalova, M., eds., vol.1, 242-247.

Thomas, H.R., and Rees, S.W. (1993). The numerical simulation of seasonal soil drying in an unsaturated clay soil. *International Journal of Numerical and Analytical Methods in Geomechanics*, 17 (1), 119-132.

Thomas, H.R., and He, Y. (1994). An elasto-plastic analysis of the thermo/hydraulic/mechanical behaviour of unsaturated soil. *Proceedings of the 8th International Conference on Computer Methods and Advances in Geomechanics*, Morgantown, Siriwardane, H.J. and Zaman, M.M. eds., Balkema, Rotterdam, 1171-1176.

Thomas, H.R., and He, Y. (1995). Analysis of coupled heat, moisture and air transfer in a deformable unsaturated soil. *Géotechnique*, 45(4), 677-689.

Thomas, H.R., and Sansom, M.R. (1995). Fully coupled analysis of heat, moisture and air transfer in unsaturated soil. *Journal of Engineering Mechanics., American Society of Civil Engineers*, 121(3), 392-405.

Thomas, H.R., and Zhou, Z. (1995). A comparison of field measured and numerically simulated seasonal ground movement in unsaturated clay. *International Journal for Numerical and Analytical Methods in Geomechanics*, 19, 249-265.

Thomas, H.R., and Cleall, P.J. (1997). Chemico-osmotic effects on the behaviour of unsaturated expansive clays. *Geoenvironmental Engineering, Contaminated Ground; Fate of Pollutants and Remediation*, Yong, R.N. and Thomas, H.R., eds., Thomas Telford, London, 272-277.

Thomas, H.R., Rees, S.W., Sloper, N.J. (1998). Three-dimensional heat, moisture and air transfer in unsaturated soils. *International Journal of Numerical and Analytical Methods in Geomechanics*, 22(2), 75-95.

Thomas, H.R., and Cleall, P.J. (1999). Inclusion of expansive clay behaviour in coupled thermo hydraulic mechanical models. *Engineering Geology*, 54, 93-108.

Thomas, H.R., Cleall, P.J., Chandler, N., Dixon, D., and Mitchell, H.P. (2003). Water infiltration into a large-scale in-situ experiment in an underground research laboratory. *Géotechnique*, 53(2), 207-224.

Thomas H.R., Seetharam, S.C., and Vardon, P.J. (2011). On the inclusion of some biological impacts and influences in coupled transport phenomena in unsaturated soil, *Geotechnical and Geological Engineering*, 29, 181-191.

Vardon, P.J. (2009). *A three-dimensional numerical investigation of the therm-hydro-mechanical behaviour of a large-scale prototype repository*. Ph.D. Thesis, Cardiff University, Wales, UK.

Villar, M.V., Fernández, A.M., Martín, P.L., Barcala, J.M., Gómez-Espina, R., Rivas, P. (2008). *Effect of Heating/Hydration on Compacted Bentonite: Tests in 60 cm Long Cells*. Publishing House CIEMAT. Madrid.

Yaron, B., Dror, I and Berkowitz, B. (2008). Contaminant-induced irreversible changes in properties of the soil–vadose–aquifer zone: An overview. *Chemosphere*, 71, 1409-1421.

Yong, R.N., Mulligan, C.N., and Fukue, M. (2006). *Geoenvironmental Sustainability*. CRC Press, Taylor and Francis.

Yong, R.N., Pusch, R., and Nakano, M. (2010). *Containment of High-Level Radioactive and Hazardous Solid Wastes with Clay Barriers*. Spon Press, New York.



Chapter 2

Literature Review

2.1 Introduction

The nature, functionality, properties and the behaviour of soils have been the subject of numerous studies for a long time in various fields of science and engineering. Hence, many of the processes are well established in the literature. In terms of the coupled physical, chemical and mechanical behaviour of unsaturated soils, this study focuses mainly on the behaviour of compacted swelling clays and in particular compacted smectite clays (bentonite), as an application case of the developments made in this research. Compacted bentonite has been suggested as the buffer candidate in relation to the underground disposal of high level nuclear waste (HLW). The modelling of the hydro-geochemical behaviour of compacted bentonite under geological repository conditions is a challenging task which involves difficulties related to the material and to the various processes and time scales involved. This chapter mainly aims to provide a state of the art review on the coupled physical, chemical and mechanical properties and behaviour of compacted smectite clays and the research programs including experimental and numerical investigations.

The advances in the understanding of the key processes related to the thermal, hydraulic, chemical and mechanical behaviour of compacted bentonite in repository conditions has been utilised in developing numerical modelling as an assessment tool of the performance and the quantification of uncertainty, risk and reliability. In this chapter a selective review is presented of the recent developments in the experimental works and the numerical modelling of the behaviour of compacted bentonite.

In section 2.2 the key elements of the physical, chemical and mechanical processes involved in evolution of compacted bentonite as the buffer candidate in repository conditions are briefly reviewed.

The microstructure evolution of compacted bentonite has a profound effect on hydraulic and chemical flow behaviour due to the presence of smectite minerals as the primary solid component of the most of the commercially available bentonite clays. Section 2.3 provides a review on the micro- and macrostructure and the fabric of compacted bentonite. The basic microstructure of smectite minerals is briefly reviewed in this section.

The process of water uptake and hydration/dehydration is discussed in section 2.4. Section 2.5 deals with the water and the physical state of pore water in compacted bentonite. As an

important issue of the modelling of the water and chemical flow, the physical state of water located in different levels of pore scale in compacted bentonite is also concerned. The developments in the modelling of the moisture transport in compacted bentonite and its linkage with the microstructure evolution is presented in section 2.6.

Diffusion acts as the major mechanism of chemical transport, especially in compacted swelling clays. Section 2.7 reviews the current knowledge of the ionic diffusion and effective parameters in compacted smectite clays (bentonite). Temperature effects on the diffusion of ionic species with special focus on thermal diffusion i.e. Soret effect, are also dealt with in section 2.8.

Sections 2.9 and 2.10 present reviews on the recent experimental and numerical investigation of the coupled thermal, hydraulic, chemical and mechanical behaviour of compacted bentonite under similar conditions to the buffer in repository conditions.

Section 2.11 covers some of computational aspects and recent developments of the reactive transport modelling of multicomponent chemicals in porous media. Different schemes for coupling chemical transport and reactions to efficiently solve coupled transport and geochemical problems are also reviewed in this section.

Finally, in section 2.12, summary and conclusions are drawn from the above discussions.

2.2 Physical, chemical and mechanical processes in unsaturated compacted bentonite buffer in geological disposal of HLW

According to most concepts proposed by the organisations responsible for disposal of HLW, the radioactive waste canisters will be placed at several hundred meters depth in crystalline rock, salt, argillaceous rock or clay deposits. Compacted smectite clay (i.e. compacted bentonite) has been suggested as the buffer candidate that provides the embedded medium for canisters with very high tightness for minimizing percolation of groundwater, with sufficient bearing capacity for minimizing movement of the heavy canisters and being sufficiently soft to transfer only a fraction of the stresses generated by tectonic movements to the canisters (e.g. Pusch, 1994; SKB, 1999; Posiva, 2006; Pusch, 2008; Yong et al., 2010). The main

attributes making compacted smectite clays suitable for use as buffer in EBS are (Yong et al., 2010; Steefel et al., 2010):

- Adequate thermal conductivity to transfer heat away from the canister so that the canister can be maintained at a temperature equal to 100°C or below.
- Very low hydraulic conductivity that prevents percolation of the ground water around canister and limits the rate of canister corrosion.
- High swelling potential, that provides the self-sealing and tightness that makes possible self sealing of openings within the Engineered Barrier System and of gaps between the bentonite with the rock and with the radioactive waste canister.
- Low diffusion coefficient and high buffering/attenuation capacity which are essential for reduction and control the transport of radionuclides, and to attenuate the transport of corrosion promoting ions from the rock.
- Low microbial activity in highly compacted bentonite which reduces the impact on clay minerals with respect to transmission through mechanisms of weathering and dissolution over long time period.

Three major phases in the evolution of the bentonite buffer in geological HLW repository conditions can be identified (Pusch and Yong, 2006; Pusch, 2008; Steefel et al., 2010). The compacted bentonite buffer is initially partly saturated when installed around waste canisters in a repository. The first phase is the initial water uptake after emplacement which can take place over a period of 0 to 100 years dependent on repository design (Wersin et al., 2007). The re-saturation phase is under the thermal effects, sourcing from the canister. Processes involved in the evolution of the bentonite buffer include thermally induced distribution of initial pore water in the clay during the early thermal phases (Tong et al., 2009; Thomas et al., 2009). The second phase is dominated by heat input from the waste canister with a significant time-varying temperature gradient, with the temperature initially increasing and then returning to ambient over a period of 100 to 10,000 years. The third phase is the long-term hydro-geochemical period with tectonic or glacial processes under ambient or reduced temperature conditions from a thousand to a million years. The possible external changes that the groundwater might undergo in the long-term, can affect the geochemistry of the bentonite

buffer. Major chemical processes that may affect the chemical stability of the bentonite buffer after water saturation include dissolution and precipitation, conversion of smectite in the buffer to non expansive mineral forms, and cementation by precipitated complexes (Pusch and Yong, 2006).

The engineered barriers around the waste will provide a long period of containment, depending on the environment and the materials used, during which much of the radioactivity of the waste will decay. The engineered barriers hinder the mobilisation of radioactive contaminant generated from the waste for hundreds of thousands of years. It is expected that the transport of chemical species occurs very slowly by the diffusion mechanism in compacted clay buffer.

At the canister side, compacted clays buffer will be exposed to the heat released from radioactive waste. As a result, the heat flux is transferred through the three phase system of solid-water-gas which induces a moisture re-distribution from the initial pore water distribution in the clay during the early thermal phases (e.g. Thomas et al., 2009). At the other side of the buffer (at the clay/rock interface), water uptake and saturation can occur as a result of water flow through the fractures in rock or the water which exists in the host geological medium. Due to the low permeability of compacted bentonite, the process of water uptake and re-saturation is considered as a slow process which has been estimated to take place during the first hundred year of the repository life-time (SKB, 1999; Nagra, 2002; Wersin et al., 2007; Yong et al., 2009).

Figure 2.1 presents a schematic of key processes related to thermal, hydraulic, chemical and mechanical behaviour of compacted bentonite buffer under repository conditions. A source of water is shown to be found in the Excavated Disturbed Zone (EDZ) of the host rock. The location of the canister is shown schematically with the three phase conceptual diagram adjacent to the canister. The various processes associated with the THCM behaviour are coupled in a complex manner. In addition, all the processes operate at different time scales and intensities which make the problem of prediction and modelling difficult (Yong et al., 2009).

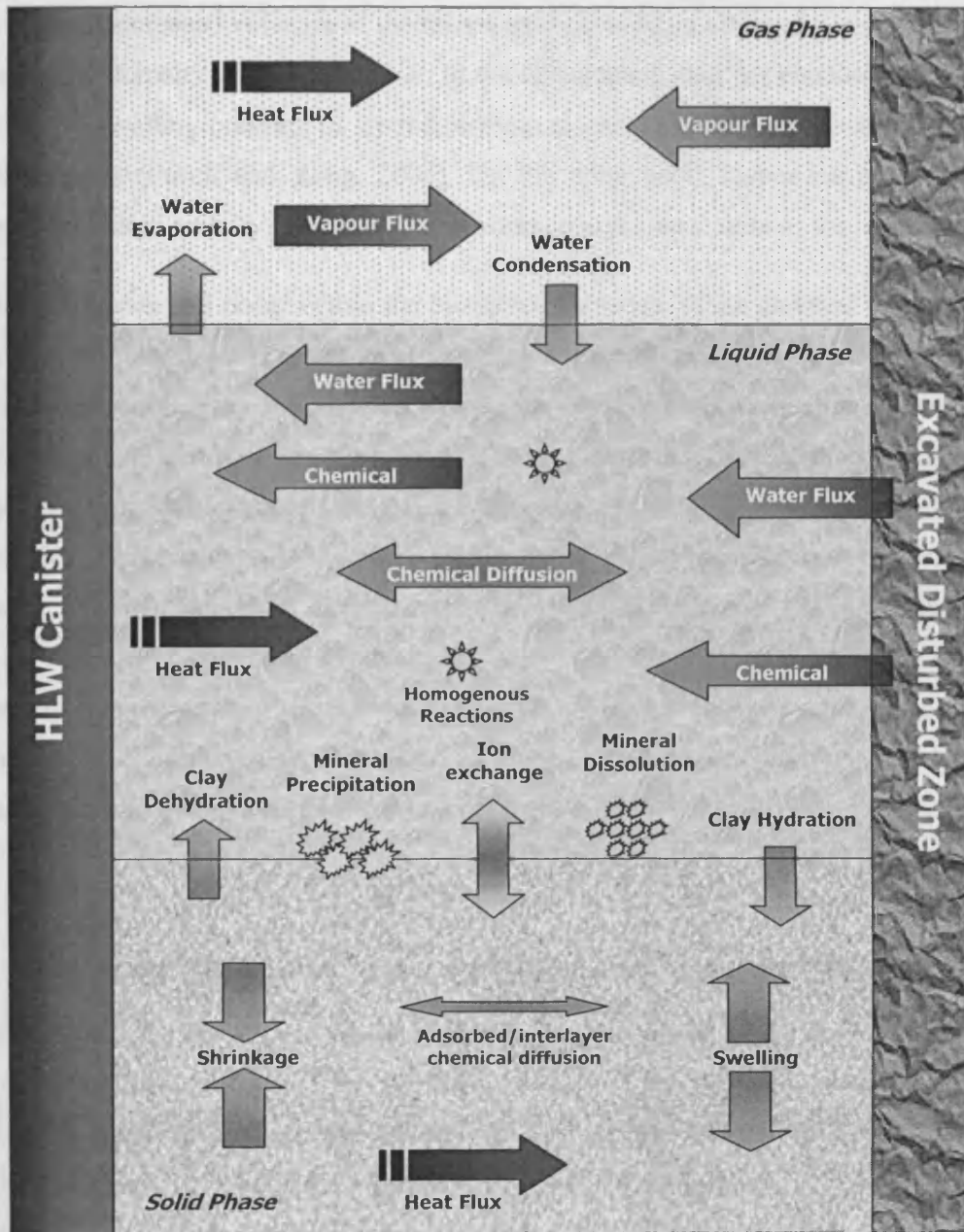


Figure 2.1 Schematic of coupled THCM processes related to the solid, liquid and gas phases in compacted bentonite as the buffer material in repository condition (Adopted and re-produced from Pusch and Yong, 2006; Jullien et al., 2005; Bear and Gilman, 1995)

The hydration process is important for understanding the evolution of the waste repository and plays a significant role in the maximum temperature experienced by the canister (Tong et al., 2010). Also, if hydration occurs slowly, it may influence the chemical state of the buffer. Interaction of smectite minerals, as the major mineral component of bentonite, during water

uptake leads to increased volumes of the microstructure units in terms of density increase and decrease in the porosity of wetted portion. In the constrained swelling condition of the buffer, increasing the swelling pressure of wetted portion causes the local compression of un-wetted portion elements (Pusch and Yong, 2006). On the other hand, higher temperature and the induced dehydration and drying cause local shrinkage in the area close to the heater.

Chemical processes will occur within the buffer as the results of the elevated temperature, re-distribution of moisture and water intrusion from the surrounding geological formation. The pore fluid composition can be affected due to the exposure to the host rock water with a different chemical composition. Pusch and Yong (2006) has described the migration of calcium, chloride and sulphate ions, which increase the salinity in the hot part or cause accumulation of minerals such as halite and gypsum which contribute to corrosion of the canister as the most important chemical processes within the buffer and at the interface of buffer and canister. Concerning geochemical reactions related to the compacted clay buffer, dissolution and precipitation of minerals, ion-exchange reaction (for example conversion of Na-bentonite to Ca-bentonite), illitisation and dissolution of smectite mineral have been reported as the major reactions (Seetharam et al., 2007; Steefel, 2010).

2.3 Compacted bentonite (micro- and macrostructure evolution)

A representative element of partly saturated compacted bentonite can be considered to consist of fabric units (i.e. geometrical arrangement of soil fractions) with associated pores in different size and structure separating them. At macroscopic level, the solid-pore system of a compacted bentonite is a complex of clay aggregates or peds with the associate macropores between them. Inside each ped or aggregate, the system consists of several particle clusters and the micropores between particles. Each particle includes stacking of individual unit layers of smectite minerals (Yong, 1999; Hueckel et al., 2002; Pusch and Yong, 2006; Likos and Wayllace, 2010). The different fabric units and associate pores are shown schematically in figure 2.2.

At the molecular level, smectite unit layers are made up of series of two basic crystal structural units (e.g. Grim, 1962; Yong and Warkentin, 1975, Mitchell, 1993; Sposito, 1984):

- Silica tetrahedral sheet (also known as silica sheet) which consists of two dimensional arrays of silicon-oxygen tetrahedral.
- Aluminium or magnesium octahedral sheet which consists of two dimensional arrays of aluminium/magnesium-oxygen-hydroxyl octahedral.

The unit layer of smectite clay minerals has two tetrahedral sheets that sandwich an octahedral sheet (figure 2.3, represented as the basic unit cell). Montmorillonite is the most common mineral of the smectite group (Mitchell and Soga, 2005).

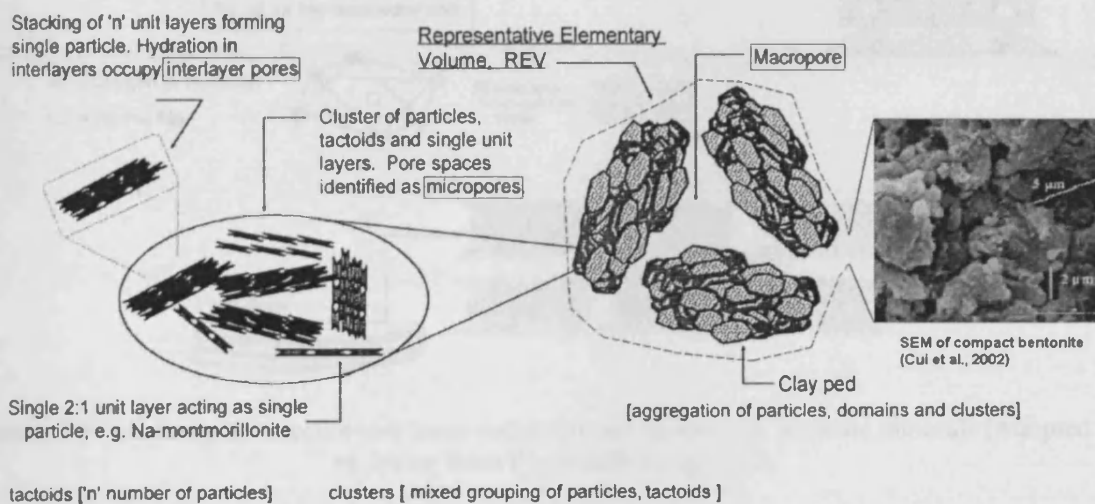


Figure 2.2 Schematic of hierarchy of fabric units and pore spaces in compacted bentonite (Adopted from Yong, 1999), Scanning Electron Microscope image of compacted bentonite (Kunigel bentonite) has been adopted from Cui et al. (2002)

As schematically presented in figure 2.3, the tetrahedral sheet has the oxygen atoms located on the four corners of a regular tetrahedron with the silicon atom in the centre. The octahedral sheet also known as alumina (Gibbsite) sheet or magnesia (Brucite) sheet, depending upon the type of central atom either aluminium or magnesium, has six oxygen or hydroxyl (OH) groups which are coordinated at the six corners of a regular octahedron. In the silica sheet, three of the four oxygen atoms of each tetrahedron are shared by three neighbouring tetrahedral sheets. The oxygen atoms and hydroxyl groups in the octahedral sheet lie in two parallel planes with aluminium or magnesium atoms between these planes (Grim, 1962). The fourth oxygen atom protruding from the tetrahedral sheet is shared by the other octahedral sheet.

The simplified views of the tetrahedron and octahedron are commonly used to represent the elements of a basic unit cell (middle schematic in figure 2.3). The unit cells are joined in spatial articulation to form basic unit layers as shown in figure 2.3. It is noted that in the literature both layer and lamellae has been used interchangeably.

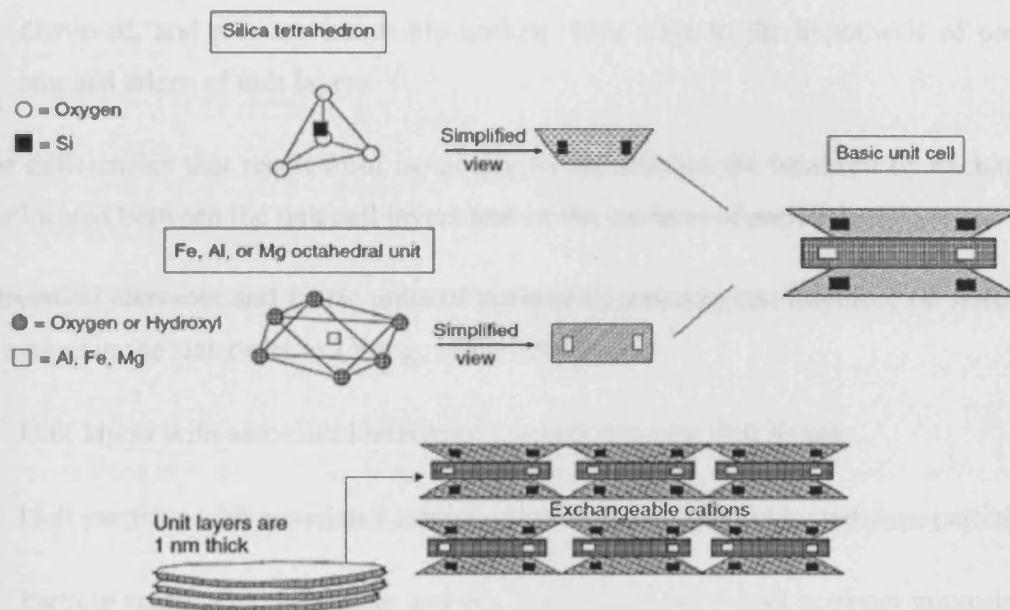


Figure 2.3 Schematic of smectite unit layer and structural elements of smectite minerals (Adopted and re-drawn from Pusch and Yong, 2006)

It is generally believed that there are replacements of the ions in the ideal smectite by ones that have different valences. The result of these is the development of a net negative charge associated with the particles, and is the reason for adsorption of cations that can be more or less strongly hydrated. In other words, unit layers are not electrically neutral, but carry an unbalanced electrical charge on the surfaces and edges (Grim, 1962). Possible sources of unbalanced electrical charge are:

- In any unit layer positively charged ions are generally within the interior of the layer, whereas the oxygen or hydroxyl ions on the surface of the unit layer are negatively charged. This spatial distribution of the positive and negative charges results in a net negative charge on the surface of a unit layer.

- Partial replacement of Si^{4+} by Al^{3+} in a tetrahedral sheet or of Al^{3+} by Mg^{2+} in an octahedral sheet (a process known as isomorphous substitution) results in a net negative charge on the unit layers.
- At the edges of unit layers, tetrahedral silica sheets and octahedral sheets are disrupted, and primary bonds are broken. This leads to the hypothesis of positively charged edges of unit layers.

Charge deficiencies that result from isomorphous substitution are balanced by exchangeable cations located between the unit cell layers and on the surfaces of particles.

The structural elements and fabric units of compacted smectite can therefore be summarized and arranged in the size order as (Yong, 1999, 2003):

- Unit layers with associated interlayer porosity between unit layers
- Unit particles with associated micropores or intra-layer porosity between particles
- Particle aggregates or clusters and the associated macropores between microstructural units

In accordance with the concept presented above, three porosity scales can be identified in compacted smectite clays:

- The interlayer porosity corresponding to the interlayer space which contain cations and water molecules (generally <2 nm),
- The micro/mesoscopic porosity corresponding to the space existing between particles (in the range of 2–50 nm),
- The macroscopic porosity corresponding to the inter-aggregate voids (>50 nm),

There are different statements about the number of individual layers in a stable particle of smectite and it generally depends on the type of interlayer cations and suction value. Sposito (1984) stated that one to sixteen unit layers can be stacked; face to face, to form a unit particle, depending on the interlayer exchangeable cation and the estimation method. van Olphen (1977) estimated that typical sodium montmorillonite particle consists of 2-3 lamellas

or unit layers. Marcial et al. (2002) reported that in Na-smectite, the stacked clay layers which form the wall of inter-particle pores contains 4-10 layers. However, the number of lamellas in a typical particle depends on the electrolyte concentration in the liquid phase as well (Yong and Warkentin, 1975).

The compaction of smectite clays by applying external stress results primarily in the reduction of macro- and micropores. Therefore the ratio of total macro- and micro porosity to the interlayer porosity decreases considerably in compacted smectite clays (Likos and Lu, 2006). In fact, the contribution of the interlayer porosity to the overall porosity increases with the partial smectite dry density.

In one-dimensionally compacted smectite clays, the unit layers or lamellas are oriented preferentially in a direction normal to that of sample compaction. However the effect may be less marked in the presence of non-smectite particles (Bourg et al., 2006). The charge conditions within the stacks, which contain 3–5 unit layers in Na montmorillonite and about 10 unit layers in Ca montmorillonite, are different from those at the external surfaces of the stacks in the sense that only cations are present in the interlayer space while complete electrical double-layers are formed at the outer surfaces (Pusch, 2001).

2.4 Water uptake and interaction with compacted bentonite

Water uptake into anhydrous smectite microstructure units starts via hydration forces initially and continues subsequently via diffuse double layer forces (van Olphen, 1977; Pusch and Yong, 2006). The first mechanism of water uptake referred to as hydration or crystalline swelling is a process whereby initially dry expansive clay minerals sequentially adsorb a limited numbers of discrete layers of water into the mineral interlayer. Hydration process is driven primarily by the energy associated with the initial hydration of exchangeable interlayer cations and hydrogen bonding or charged surface-dipole attraction effects associated with solid-liquid interactions, occurring in the immediate vicinity of the clay particle surfaces (Likos, 2004). Interlayer hydration is determined by the layer charge, inter-layer cations, properties of adsorbed water and particle size (Yong, 2003).

Water uptake beyond the hydration is related to the swelling force related to the development of electrical diffuse layer between particles (van Olphen, 1977; Likos, 2004; Pusch and Yong, 2006). In a clay–water electrolyte system, the adsorbed cations near the surface of the clay particles produce a much higher concentration as compared with the ion concentration in free water away from the surfaces. Ions diffuse away from the surface opposing electrostatic attraction lead to ion distribution adjacent to a clay particle in suspension. The charged clay surface and the distributed charge in the adjacent phase are together termed the diffuse double layer or DDL (van Olphen 1977; Mitchell 1993; Tripathy et al., 2004).

In smectite clay, during the hydration process, discrete layers of water molecules are adsorbed into the individual interlayer positions within a smectite particle. The adsorbed numbers of zero, one, two, three and four layer(s) of water molecules have been reported for smectite clays which are associated with the basal spacing of approximately 1.0, 1.25, 1.50, 1.70 and 2.0 nm, respectively (Laird, 2006). Figure 2.4 shows a schematic of zero to three layers water adsorption during hydration of a single smectite particle.

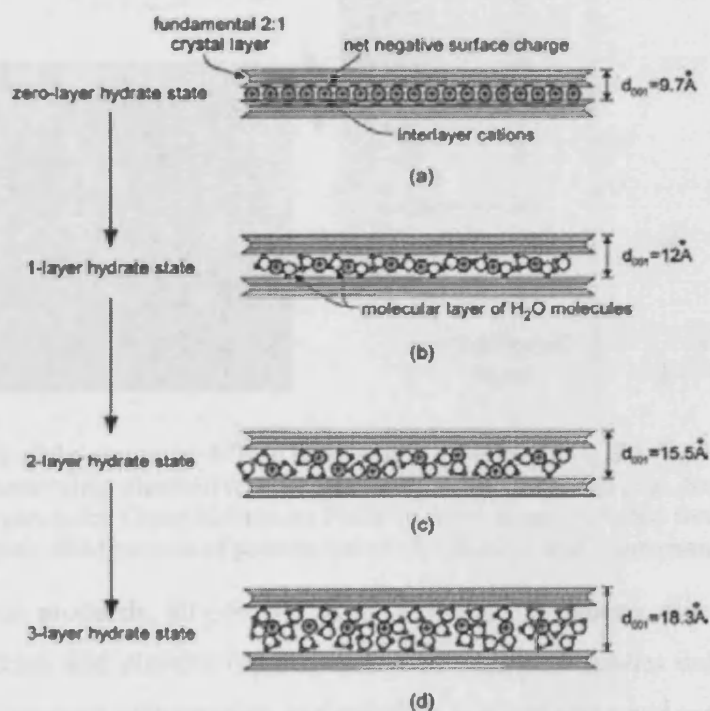


Figure 2.4 Conceptual model of the sequential hydration and crystalline swelling of smectite particle (Adopted from Likos 2004)

In contrast to the hydration, further water uptake due to the double-layer swelling is a process that occurs between individual particles (Laird, 2006). The hydrated cations dissociate from the surface of the clay particle into the solution to form the electrical diffuse double layer. The water uptake and consequently further volume change of the clay beyond the interlayer hydration is due to the osmotic phenomenon and is associated with the interactions of the diffuse double layers (van Olphen, 1977; Yong, 1999). Figure 2.5 shows the distribution of ions in developed diffuse layer adjacent to the surface of smectite particle. The SEM image in figure 2.5, presents the particles of montmorillonite consisting of several unit layers stacked together in a saturated sodium bentonite which has been included in the figure to illustrate the location of developing DDL between the individual particles.

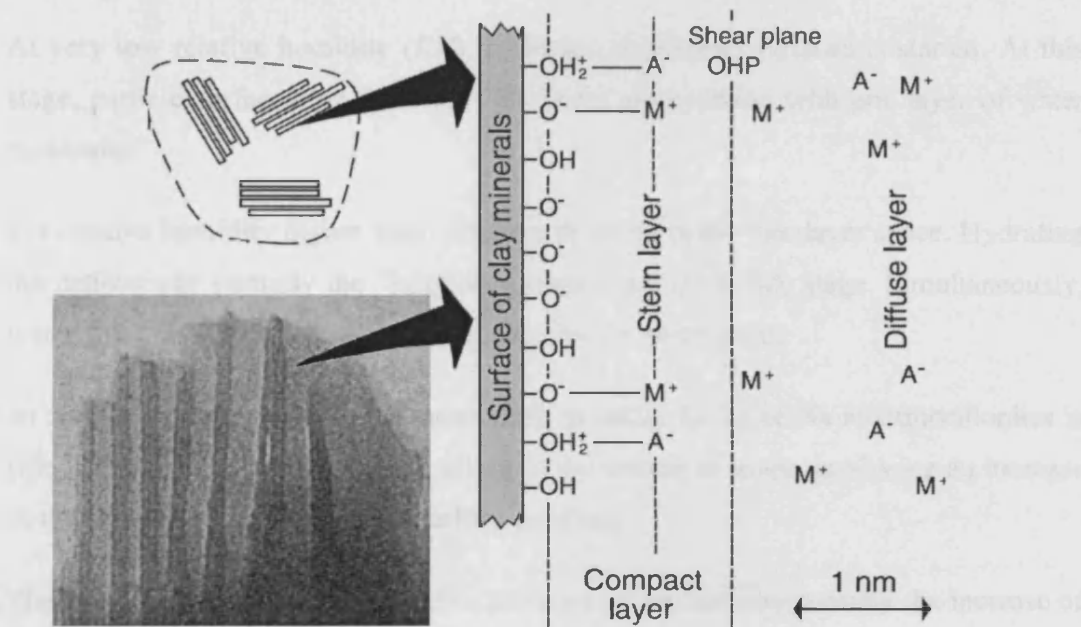


Figure 2.5 Sketch of the electrical diffuse layer and its components at the clay basal surface in the case of a binary monovalent electrolyte, M^+ represents the metal cations (e.g. Na^+) and A^- the anions (e.g. Cl^-). OHP represents the Outer Helmholtz Plane or shear plane (Adopted from Revil and Leroy et al., 2004); SEM picture of sodium bentonite (Barclay and Thompson, 1969).

As water adsorption proceeds, all porosity scales including interlayer, micro- and macropores are affected. Particles and clusters (aggregates) break up into smaller units, generating new void spaces. The sequence of hydration and swelling was observed and reported by Suzuki et al. (2005) for a Na-smectite clay (Kunipia-F bentonite) using laser scanning microscopy (LSM) combined with digital image analysis. Accordingly, the interlayer space between smectite unit layers of a particle is occupied first by adsorbed water under moderate humidity

conditions while the micropores among particles remain dry. After contacting with the water solution, the particles swell and fill the micropores, the aggregates or clusters also swell following the swelling of particles further after filling micropores. During this process, initially thick unit particles may split into several thinner units comprising fewer layers while maintaining a constant interlayer distance.

Salles et al. (2008; 2009) provided a multiscale understanding of the hydration of smectite saturated with sodium or other cations using thermoporometry in combination with X-ray diffraction. Based on the results of the aforementioned study and comparison with other results reported in the literature, they proposed the following hydration sequence picture for smectite clays (Salles et al. 2009):

1. At very low relative humidity (RH), hydration of particle surfaces is started. At this stage, particle surfaces (or “external” surfaces) are hydrated with one layer of water molecules.
2. For relative humidity higher than 10%, water enters in the interlayer space. Hydrating the cations and partially the “internal surfaces” occurs at this stage. Simultaneously, water fills completely the mesoscopic porosity, i.e. micropores.
3. At 54 % relative humidity, the mesoscopic porosity for Li or Na-montmorillonites is filled. The next step is the further filling of the interlayer space, producing an increase of the interlayer distance, i.e. crystalline swelling.
4. The breaking of particles into smaller particles occurs and concurrently the increase of the volume of the mesoscopic porosity.

Figure 2.6 present a schematic of the water uptake sequences presented by Salles et al. (2009) and discussed in the above statements. The mechanisms of hydration/swelling of clays, and particularly the equilibrium between the filling of the mesopores and the filling of the interlayer space, are strongly dependent on the interlayer cation (Salles et al, 2009).

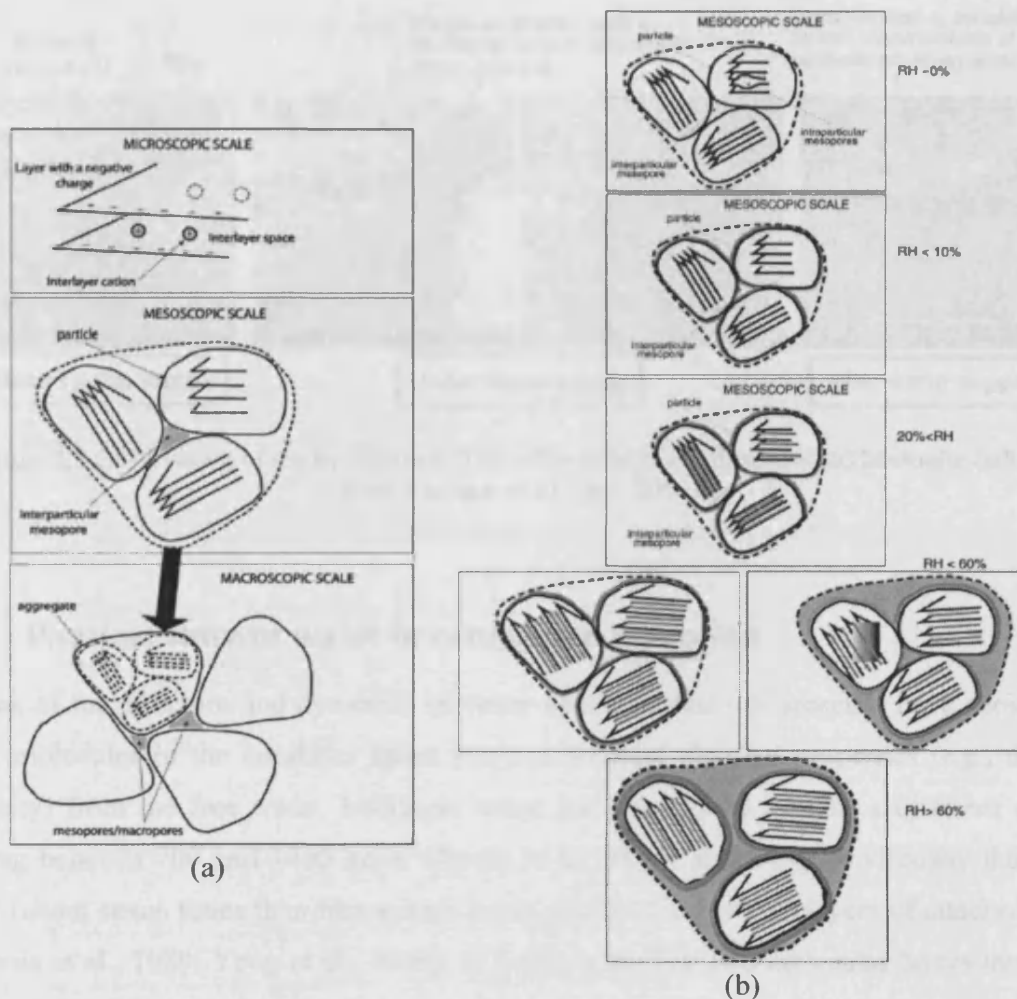


Figure 2.6 A complete hydration sequence for sodium smectite. (a) shows different scales of fabrics and (b) represents schematically the equilibrium condition of water at different range of relative humidity (adopted from Salles et al., 2009)

In compacted bentonite, during the water uptake, particles expand upon the hydration into the macropores through the formation of diffuse layer (or gel) and occupy the macropores gradually until full saturation of the pores. Figure 2.7 shows the swelling of bentonite taken by scanning electron microscope in a controlled temperature and vapour pressure around a sample (Komine and Ogata, 2004). Kozaki et al. (2001) and Liu et al. (2003) studied the fabric of compacted Na-montmorillonite and montmorillonite/silica sand mixtures before and after hydration. The results indicated that even at full hydration, regions of relatively high montmorillonite density persisted in the compacted clay, indicating an incomplete breakup of the aggregate structure of the dry bentonite.

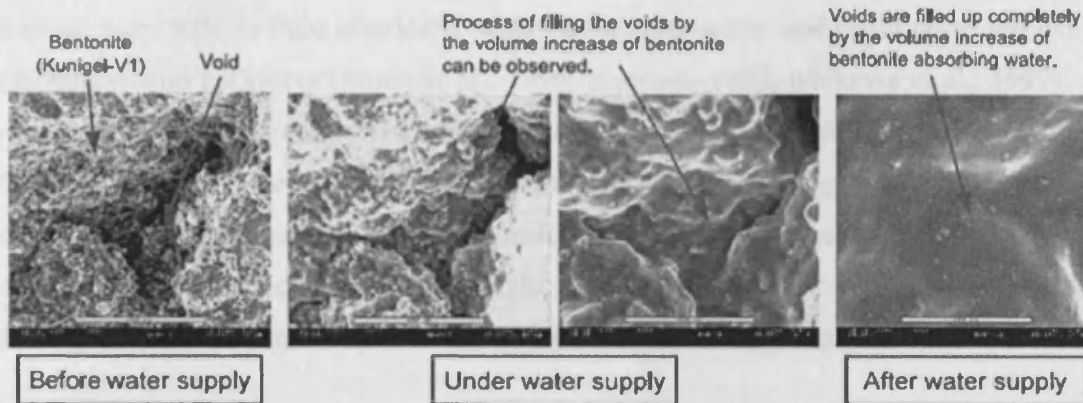


Figure 2.7 Observation of the hydration and swelling behaviour of compacted bentonite (adopted from Komine and Ogata, 2004)

2.5 Physical state of water in compacted bentonite

Studies of the structure and dynamics of water on the surfaces of smectite have shown that water molecules in the interlayer space possess different physical properties (e.g., density, viscosity) from the free water. Interlayer water has been found to pose a different density ranging between 700 and 1400 kg/m³ (Pusch et al., 1990) and a higher viscosity than bulk water (about seven times than free water), especially for the first two layers of attached water (Homola et al., 1989; Yong et al., 2009). At least, in the first two molecular layers located in the interlayer or on the external surfaces, water is structured by the exchangeable cations, and to a lesser extent, by the smectite mineral surface. Beyond these first two molecular layers, the properties of surface water rapidly approach those of bulk water (e.g. Pusch and Yong, 2006). Thermodynamically, the adsorbed water has a lower chemical potential than water located increasingly far from the particle surface or perfectly free water. Physically, the adsorbed water is less mobile than free water (Lu and Likos, 2004). Low and Anderson (1958), and Zhang and Low (1995) have also shown through experimental studies that the thermodynamic, hydrodynamic and spectroscopic properties of water in the montmorillonite-water system differ from those of pure bulk water.

The water within the interlayer, combined with a small portion of water in the micropores, i.e. close to the particle surface, constitutes water that is relatively immobile rather than water in the macropores, making this portion of water a part of solid phase (Pusch et al., 1990; Hueckel, 1992; Hueckel et al., 2002). Therefore the interlayer pores between clay layers

contribute very little to fluid migration, whereas the micropores and macropores are likely to act as major fluid pathways (Pusch et al., 1990; Hueckel, 1992; Ichikawa et al., 1999). As a result, the available pore water for movements of water and ionic-species in compacted bentonite is practically reduced to the pore water in intralayer/micropore between the particle and those in the macropores. From a modelling view point, the hydrated water in the interlayer (immobile water) is attributed to the solid phase and its transport should be considered concurrent with the particles deformation (Hueckel, 1992).

With regards to the physical state of water and chemical ions in compacted bentonite, three types of water can be identified (Bradbury and Bayenes, 2003; Bourg et al., 2003; Wersin et al., 2004; Steefel et al., 2010), including:

- Interlayer water containing only water and cations. The cations balance the fixed charge of the unit layers.
- Diffuse double layer containing cations and anions. Excess amount of cations normally exists to balance the charge of the clay surface.
- Bulk or free pore water. This portion is charge balanced as aqueous solutions. This fraction of pore water can be also regarded as the available geochemical porosity in which the aqueous geochemical reactions take place.

Figure 2.8 shows a schematic of different water in compacted saturated bentonite.

As mentioned previously, compaction process of bentonite results primarily in the reduction of macro porosity (Likos and Lu, 2006), hence by increasing dry density of compacted bentonite, the contribution of interlayer porosity to the overall porosity increases. In other words, major fraction of the pore water in compacted bentonite is located in the interlayer pore space and in micropores between the unit particles which is affected by the diffuse double layer or the electrified surface reactions (Wersin et al., 2004; Pusch and Yong, 2006; Van Loon et al., 2007; Murrinen et al., 2007). The proportion of each kind of above-mentioned water depends on the compaction degree of bentonite, but also on the ionic strength through its effect on the thickness of the diffuse double layer (Van Loon et al., 2007).

Pusch and Hökmark (1990) stated that for an artificial saturated Na-montmorillonite with bulk density of 1800 kg/m^3 ; more than 60 % of the water is immobile. Kozaki et al. (2001) stated that only interlayer water can remain in compacted water saturated bentonite at dry densities more than 1750 kg/m^3 . However, it has been suggested that in practice a small number of larger pores can exist due to the non-systematic character of the clay fabric (Dixon et al., 1992). Suzuki et al. (2001) estimated that the interlayer pore proportion of Na-montmorillonite is 61 % and 22 % for dry densities 900 and 1350 kg/m^3 , respectively. Sato and Suzuki (2003) suggested that impurities (i.e. non-montmorillonite particles) may prevent stacking of unit layers or lamellae from parallel association and orientating normal to the direction of compaction, based on observations on two bentonites with different Na-montmorillonite purities of 99% and approximately less than of 50%.

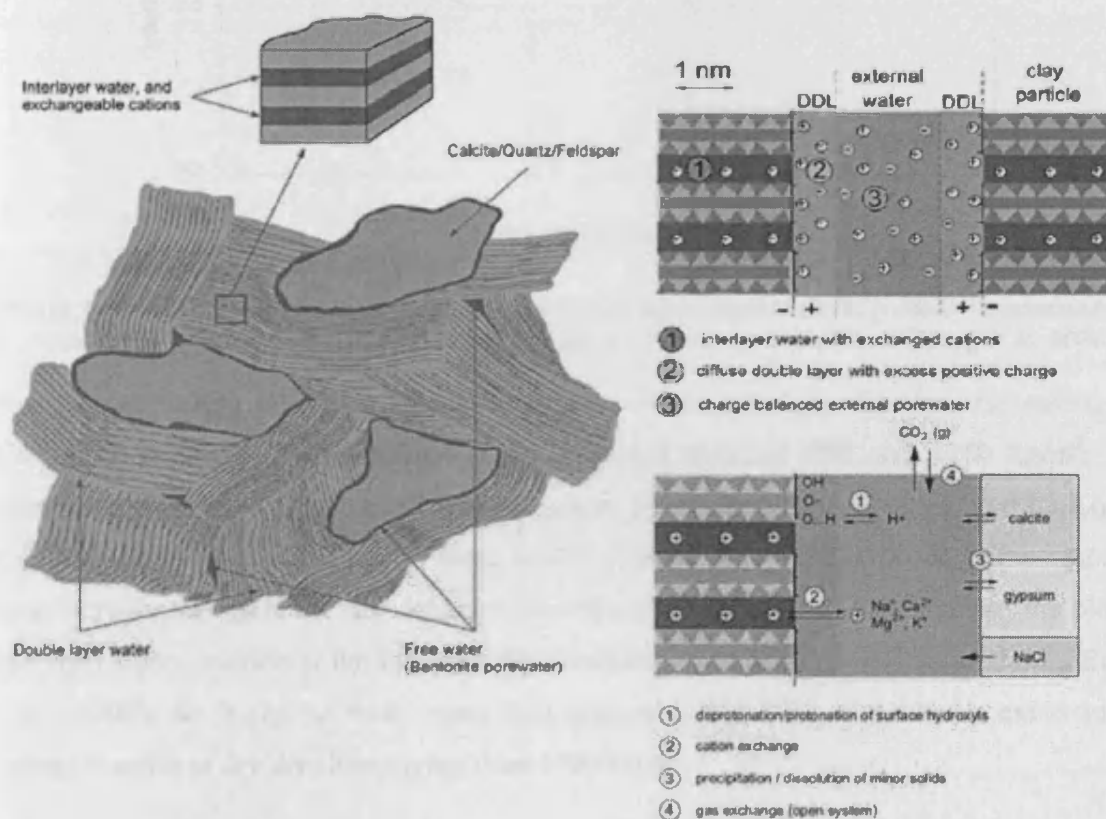


Figure 2.8 Different types of water in compacted re-saturated bentonite (adopted from Bradbury and Bayenes, 2003; Wersin et al., 2004)

Based on XRD observations of the basal spacing of individual layer of Na-bentonite, Kozaki et al. (2001) reported that only two and three hydrated water layers can be located in the

interlayer at dry densities 1570-1760 kg/m³ and at dry densities 980-1570 kg/m³, respectively. The contribution of interlayer porosity to the total porosity increases with the dry density until only interlayer pores are present for the dry densities more than 1750 kg/m³ (Kozaki et al., 2001; Bourg et al., 2006).

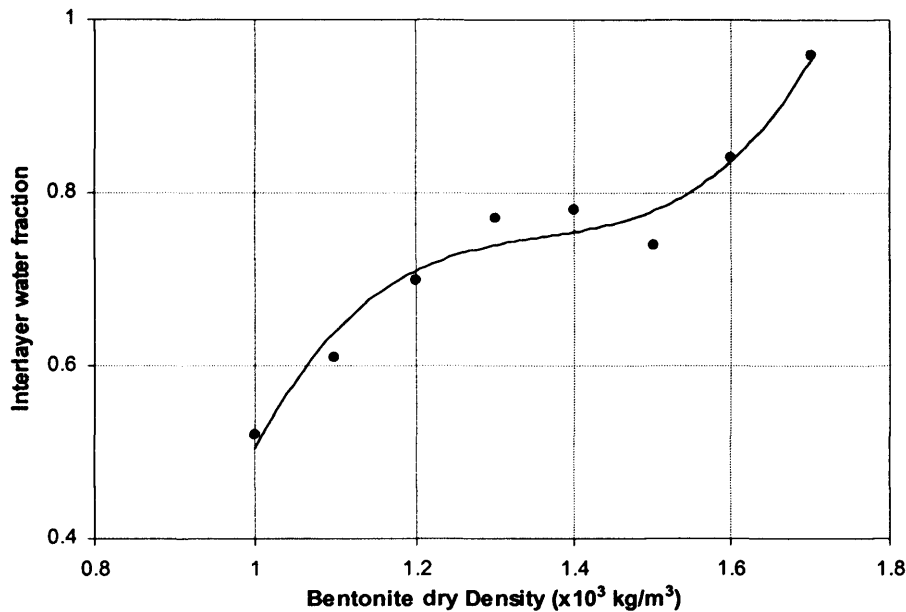


Figure 2.9 Model prediction of the volume fraction of the average interlayer porosity in saturated Na-bentonite as a function of partial montmorillonite dry density (Adopted from Bourg et al. 2006)

Bourg et al. (2006) derived a relationship between the interlayer fraction and partial dry density of saturated Na-bentonite for dry densities between 980 and 1750 kg/m³. The calculation was based on the specific surface area of the clay originally presented by Kozaki et al. (2001). In this model, two or three layers of water have been assumed as the adsorbed water between layers in the dry densities less than 1750 kg/m³. Figure 2.9 shows the plotted interlayer water fraction at the different dry densities based on the proposed model by Bourg et al. (2006). As it can be seen, more than approximately 80% of the water exists in the interlayer space at dry densities higher than 1500 kg/m³.

The structure and other properties of adsorbed water would change with temperature resulting in transferring the interlayer water to the macro/micro porosity under non-isothermal conditions (Ma and Hueckel, 1993; Villar and Lloret, 2004). Accurate estimation of the amount of available pore water or porosity for the transport of water and chemical species is

an important issue in order to model the hydro-geochemical behaviour of compacted bentonite under unsaturated and non-isothermal conditions in HLW repository.

2.6 Moisture transport and microstructure in compacted bentonite

The moisture flow in unsaturated compacted bentonite is strongly influenced by processes taking place within the microstructure of the clay grains during the hydration (e.g. Thomas et al., 2003; Kröhn, 2003). Although the general two-phase moisture flow (liquid water and vapour) assumptions and consideration are normally applied for describing the hydraulic behaviour of compacted bentonite, water migration between the micro/macropores and interlayer space due to the hydration acts as a sink or source for the pore water in a variable suction or temperature environment. As stated previously, the water is immobilised in the interlayer space and swell at the same time, thereby reducing the available pore space in a constrained condition (Pusch and Yong, 2003).

Concerning the understanding of moisture process in compacted bentonite, for some experiments, modelling of the moisture transport tends to over-predict the rate of saturation. As an example, Thomas et al. (2003) showed that the modelling of moisture transport using traditional unsaturated hydraulic conductivity, which assumed an increase in hydraulic conductivity with increasing water content, over-predicts the rate of saturation of the buffer in a full-scale experiment conducted at Atomic Energy of Canada Limited's (AECL's) underground research laboratory. They found that the experimental results could be in agreement with the numerical modelling results through modification of the hydraulic conductivity and flow rate. The study suggested that the expansion of the microstructure of the bentonite, as the material becomes saturated, would tend to reduce the void spaces in the macrostructure, as the material, was constrained from overall swelling. The result in turn is likely to reduce the material's hydraulic conductivity.

Cui et al. (2008) presented an experimental investigation on unsaturated hydraulic conductivity determination of a compacted sand/bentonite mixture. Three infiltration tests were undertaken under either constant-volume conditions or free-swell conditions. In order to calculate the hydraulic conductivity, the total suction changes were monitored at different locations along the soil specimen. The results under constant volume conditions indicate that

when suction was decreasing (during infiltration), the hydraulic conductivity presented an initial decrease followed by an increase after a certain suction value. They explained this phenomenon by the fact that wetting under constant-volume condition reduced the volume of macro-pore family in the soil, thus decreasing the soil permeability and when the macropores disappeared, the suction became the only factor which drove the water flow and the hydraulic conductivity increased with further decrease in suction. This hydraulic conductivity corresponds to the equivalent value of a soil having a microstructure unchanged during wetting.

In order to consider the effects of hydration and microstructure evolution on water transport, a few models have been suggested in the literature. Xie et al. (2004) presented a hydro-mechanical model which included the microstructure swelling based on the diffuse double layer theory. According to their proposed model, total porosity is divided into interlayer pores and interparticle (macro) pores. The interlayer porosity is calculated via DDL theory with assumption of parallel arrangement of plates. In order to model the moisture flow, the intrinsic permeability variation was considered as a function of the interparticle or effective porosity. Hence the variations of the available porosity with chemical variations in the system were modelled using DDL theory. However, this model assumes a variation of the interlayer porosity in unsaturated condition based on a power function with respect to degree of saturation.

Kröhn, (2003) provided some commentary on the variety of conceptual models and how the flow and absorption rates may affect the micro-structure. Figure 2.10 presents the conceptual diagrams provided by Kröhn, (2003), on how the comparative flow and interlayer hydration rate may affect the absorbed water content in the bentonite. The interlayer space is the micropores where the water can be absorbed during the hydration and swelling process. In figure 2.10 a low hydration-to-flow concept is shown (left), whereby the pores in which flow can occur are only negligibly modified by the flow process. In fact, the rate of water exchange between the interlayer hydration is slow. On the other hand the interlayer space has swollen more quickly than the transport, restricting the pores available for flow (figure 2.10, right).

Kröhn, (2003) concluded that the conceptual very low hydration to flow ratio is in contradiction to experimental observations which show that uptake of liquid water cannot be significantly increased by applying hydraulic pressure (Pusch and Kasbohm, 2001). In other

words, hydration occurs as a much faster process than vapour diffusion during the re-saturation and re-saturation dynamics is predominantly controlled by the vapour supply and less by the hydration rate (Kröhn, 2003). However, the experimental evidence from large scale tests such as the Prototype Repository Project suggest that where water pressure is maintained high saturation occurs relatively quickly and where pressure is low saturation is not reached (Goudarzi and Johannesson, 2007), such differing responses cannot be described purely by moisture diffusion.

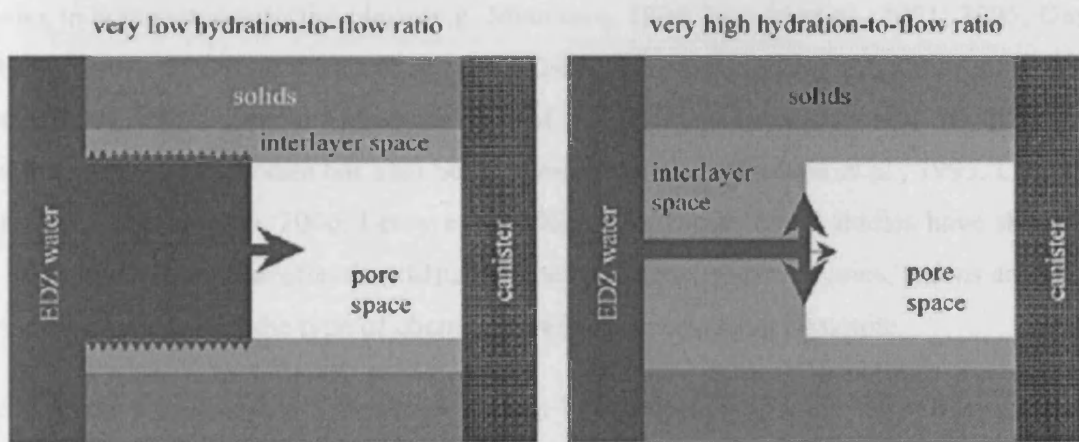


Figure 2.10 Effect of the hydration rate on the water distribution in the bentonite (Kröhn, 2003)

Vardon (2009) proposed a time dependent micro-structural modification to the unsaturated hydraulic conductivity of compacted bentonite. A first approximation of a time dependent material model for bentonite when swelling is restrained was presented. This model was tested against small scale controlled laboratory tests under non-isothermal conditions and also against a large-scale test. Comparable results were found in the short term to existing material models but significantly improved qualitative and quantitative results were found in the longer term.

2.7 Chemical diffusion in compacted bentonite

In order to predict the performance of the compacted clay buffer in high-level radioactive waste repository, the mechanisms by which chemicals migrate through bentonite pore water must be understood. The transport of chemical ions in low permeability clays and more

specifically in compacted expansive clays is dominated by the diffusion mechanism. The transport process is in fact, highly affected by the specific microstructure evolution and surface electrostatic forces of the clay minerals (Pusch and Yong, 2006). The diffusion of charged species in compacted bentonites compared to diffusion in free water is influenced by geometrical factors caused by the complex microstructure of the smectite clay (Leroy et al., 2006).

Several experimental investigations have been conducted to understand the diffusion of ionic species in compacted smectite clays (e.g. Muurinen, 1994; Kozaki et al., 2001; 2005; García-Gutiérrez et al., 2004; Muurinen et al., 1985; 2004; Van Loon et al., 2007; Sato, 2005; Glaus et al., 2007). The theoretical understanding of the effective mechanisms of the diffusion of ions in compacted bentonite has also been advanced (e.g. Lehtikoinen et al., 1995; Ochs et al. 2001; Bourg et al. 2003, 2006; Leroy et al. 2006). The experimental studies have shown that the diffusion rate and the effective diffusion coefficients of neutral species, anions and cations vary considerably with the type of chemical species in compacted bentonite.

A comprehensive analysis of literature data by Bourg et al. (2003) for the diffusion of tracer molecules in compacted bentonite has shown that only neutral and cationic species can diffuse in the interlayer water, diffuse layer and the free pore water. It has been found that due to the very limited space in the interlayer, the double layers overlap and the electric potential becomes considerably large leading to a complete exclusion of anions from the interlayer water (Pusch et al., 1990; Wersin et al., 2004). The interlayer water thus contains exclusively cations and the total concentration of the cations in the interlayer is constant and independent of the composition of the water in macropore space (Van Loon et al., 2007). Increasing the ionic strength of the free pore solution, decreases the exclusion effect because the double layers are compressed (Van Loon et al., 2007). These effects have an important impact on the diffusion of anions through such media (van Schaik and Kemper, 1966; Leroy et al., 2006). The diffusive behaviour of ions cannot be characterized by a single diffusion coefficient and porosity value, but is a complex function of the physico-chemical properties of the medium, the solute and the pore solution.

García-Gutiérrez et al. (2004) studied the diffusion properties of a Spanish bentonite (FEBEX bentonite) to chloride tracer $^{36}\text{Cl}^-$ compared with HTO (neutral and conservative tracer, tritiated water). Effective diffusion coefficients for $^{36}\text{Cl}^-$ and HTO were measured in through-

diffusion experiments. They reported that in FEBEX bentonite, the accessible porosity for HTO agrees very well with total porosity, which implies that all the pores in compacted bentonite are available for diffusion of neutral species. On the other hand, they found that the accessible porosity for chloride tracer is significantly smaller than total porosity, even at the lower densities, demonstrating a significant anionic exclusion. The accessible porosity for HTO is equal to the total porosity. Their results indicated that the accessible porosity for chloride is only a small fraction of total porosity (2–3 %) at a dry density of 1650 kg/m³. Figure 2.11 presents the experimental results of the effective diffusion coefficients of chloride and water tracer and the associated accessible porosity for diffusion in compacted FEBEX bentonite at different dry densities, reported by García-Gutiérrez et al. (2004).

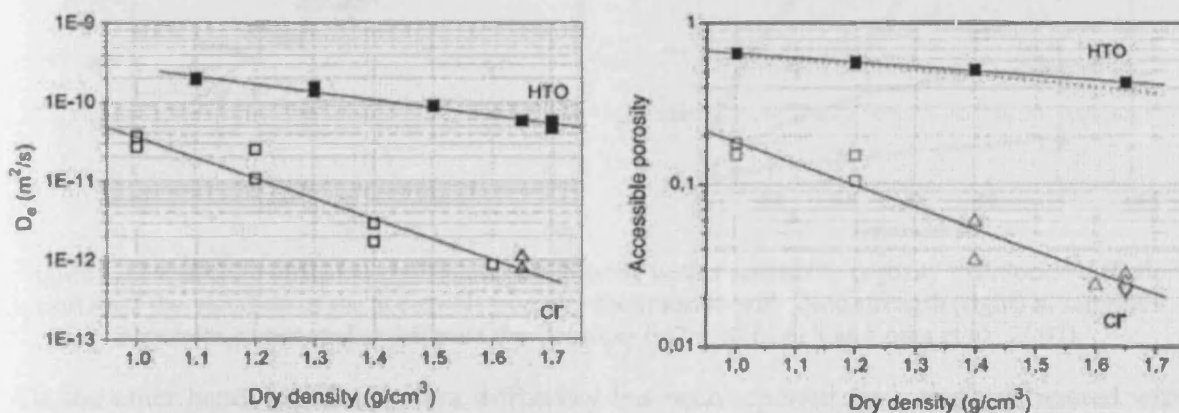


Figure 2.11 Effective diffusion coefficients of chloride and water tracer (left) and the associated accessible porosity for diffusion (right) in saturated FEBEX bentonite compacted at different dry densities (adopted from García-Gutiérrez et al., 2004).

The experimental diffusion study of Van Loon et al. (2007) on a compacted bentonite (70 % smectite) showed that the effective diffusion coefficient of chloride tracer (³⁶Cl) can be related to the diffusion-accessible porosity by an empirical power relationship. This observation is also in agreement with those reported by García-Gutiérrez et al. (2004). The relationship, provided by Van Loon et al. (2007), suggests that for prediction of the effective diffusion coefficient of Cl⁻ (and other monovalent anions), only its diffusion-accessible porosity has to be evaluated. Figure 2.12 shows the variation of the effective chloride diffusion and accessible porosity for chloride diffusion, reported by Van Loon et al. (2007). As an example the results indicate that for the studied bentonite, compacted at dry density equal to 1600 kg/m³, the maximum accessible porosity is approximately 0.09 (9.0 %) and the effective diffusion coefficient of chloride is in the range of 10⁻¹¹ m²/s. This diffusion

coefficient is approximately 100 times less than the tracer diffusion coefficient of chloride in water at 25 °C (Lasaga, 1998). The composition of the solution in contact with the surface also affects the anion exclusion. With increasing ionic strength in the solution, the charges on the surface are better shielded resulting in a weaker repulsion of the anions by the charged surface and thus leading to a lower exclusion effect (Van Loon et al., 2007).

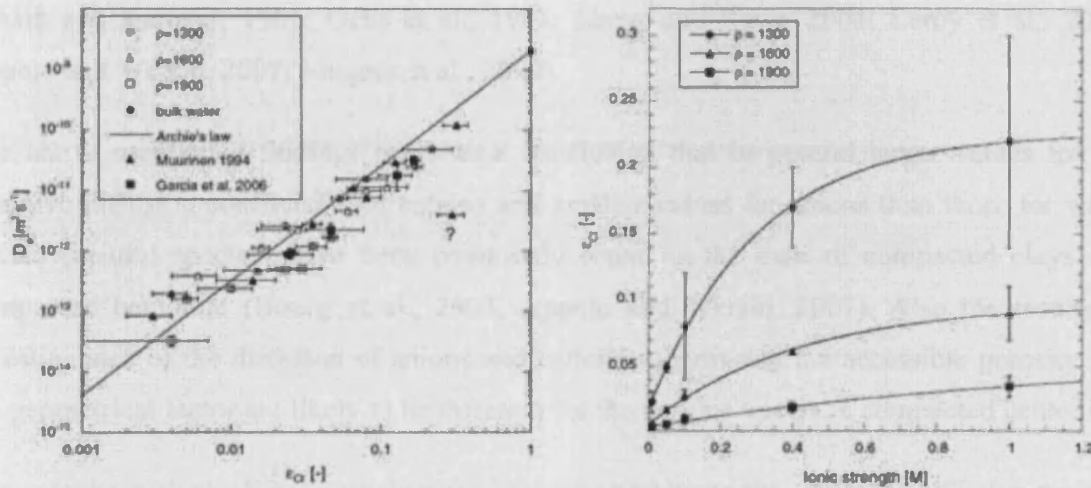


Figure 2.12 Effective diffusion coefficients of chloride versus accessible porosity to chloride diffusion (left) and the variation of the accessible porosity for chloride with ionic strength (right) in saturated bentonite compacted at different dry densities (adopted from Van Loon et al., 2007).

On the other hand, higher apparent diffusivity has been reported for cations, compared with the water tracer (e.g. Oscarson, 1994; Kozaki et al., 2005; Glaues et al., 2007; Melkior et al., 2009). Kozaki et al. (2001) reported the apparent diffusion coefficients of Na^+ ions in compacted Na-montmorillonite and in Na/Ca montmorillonite mixtures, determined by one dimensional, non-steady diffusion experiments at different dry densities. The results showed the apparent diffusion coefficients vary between approximately 1.0×10^{-10} to 2.0×10^{-11} m^2/s .

Glaus et al. (2007) experimentally studied the diffusion of sodium ($^{22}\text{Na}^+$) and strontium ($^{85}\text{Sr}^{2+}$) tracers in highly compacted Na-montmorillonite (dry density = 1950 kg/m^3). They reported that the diffusion of the tracer cations through the interlayer water is the dominant pathway in compacted swelling clays under the experimental conditions tested. They also showed that in highly compacted smectite clays, the diffusion of cations is related to their ion exchange and sorption properties. Comparing different experimental results of tracer diffusion coefficient of sodium with HTO diffusion coefficients in different compacted bentonite,

Melkior et al. (2009) reported that the ratio of the effective diffusion coefficients of $^{22}\text{Na}^+$ over HTO is greater than one and ranges between 1 and 8.

The increased diffusion of cations has been explained either by interlayer diffusion (Bourg, 2003; Bourg et al., 2006; Glaus et al., 2007), or by diffusion in the diffuse double layer (DDL) that surrounds the negatively charged clay surface and contains an excess of cations (Van Schaik and Kemper, 1966; Ochs et al., 1998; Leroy and Revil, 2004; Leroy et al., 2006; Appelo and Wersin, 2007; Jougnot et al., 2009).

The above mentioned findings result to a conclusion that in general larger values for the effective diffusion coefficients of cations and smaller values for anions than those for water tracers (neutral species) have been commonly found in the case of compacted clays and compacted bentonite (Bourg et al., 2003, Appelo and Wersin, 2007). Also the results of investigations of the diffusion of anions and cations suggest that the accessible porosity and the geometrical factor are likely to be different for the various tracers in compacted bentonite

Towards the realistic diffusion behaviour in compacted bentonite, different diffusion regimes under different porosity levels are required (e.g. Appelo et al., 2010). It requires the modelling of diffusion of ions under different rates. Since Coulombic forces act between all pairs of ions in an electrolyte solution, the diffusion of a charged ion in pore water is not entirely a random (i.e. independent) motion. In other words, when charged species are present in solution, the motion of one charged species will influence the transport of another and additional physical constraint is manifested globally due to the ion-pair forces. The macroscopic effect of the Coulombic forces between the ions is typically modelled by incorporation of the electrical field (Boudreau et al., 2004). Thus, the concentration and flux of one ion become linked to those of the other ions.

2.8 Diffusion under non-isothermal conditions

Due to the heat generation of the nuclear waste, large thermal gradients will arise in the engineered barrier system, i.e. the compacted bentonite buffer and the near field around the repository. Temperature affects the transport process directly through thermally induced diffusion. In addition to the direct influence of thermal diffusion, due to the temperature

dependency of coefficients and effective factors of transport mechanisms, it can indirectly affect the transport process under non-isothermal conditions.

It is well established that under non-isothermal conditions, a temperature gradient can induce mass flow due to thermal diffusion, i.e. the Soret-Ludwig effect or Soret effect (Ludwig, 1856; Soret, 1880). The Soret coefficient is defined as the ratio of the thermal diffusion coefficient to the molecular diffusion coefficient (K^{-1}).

Several studies have been conducted on the thermal diffusion in electrolyte solutions (e.g. Snowdon and Turner, 1960; Leaist and Hui, 1990; Engelhardt and Macdonald, 1997). However, few experimental investigations have been reported on the thermal diffusion in soils, especially in the case of compacted clays (Thornton and Seyfried, 1983; Rosanne et al., 2003, 2006).

At ambient temperature, the Soret coefficient has been reported in the order of 10^{-3} (K^{-1}) for binary solutions (Snowdon and Turner, 1960; Lerman, 1979; Lasaga, 1998). Both positive and negative values have been reported for mixed electrolytes (e.g. Leaist and Hui, 1990). The absolute values of the Soret coefficient are usually on the order of $10^{-2} \sim 10^{-3}$ (K^{-1}) for usual aqueous solutions or organic mixtures (Platten, 2006). It has been also found that the Soret coefficient is dependent on the concentration of the solution (Leaist and Hui, 1990; Engelhardt and Macdonald, 1997). Negative Soret coefficients have also been reported, but are usually small in magnitude (Leaist and Hui, 1990)

Thornton and Seyfried (1983) reported an average value of around 4×10^{-3} (K^{-1}) for multiple ionic water in sea sediments. However, their experimental results on the thermal diffusion in sediment-sea water system indicated the different values of the Soret coefficients for different ions in the range of 10^{-3} (K^{-1}). Rosanne et al. (2003, 2006) also reported an experimental comparison on thermal diffusion of NaCl solution in glass powder, mica and argillite clay. They found that the Soret coefficients for mica and glass powder are very close to the values reported for the Soret coefficient of NaCl in water. However, the values corresponding to the argillite clay was found to be five times larger than the value in free water, attributing to the electrostatic interaction with clay surfaces (Rosanne et al., 2006). The results of non isothermal diffusion experiment by Rosanne et al. (2003, 2006) show that the solute transfer

is enhanced by thermal diffusion and the Soret coefficients range between 5×10^{-3} and 1.3×10^{-2} (K^{-1}).

It is noted that in addition to the direct mass flux due to the thermal diffusion, temperature has an influence on the molecular diffusion and the effective diffusion coefficient. This phenomenon in aqueous systems has been well studied and established in the literature. In general, the self/tracer diffusion in pure solvent can be related to temperature using the Stokes-Einstein definition for self diffusion (e.g. Robinson and Stokes, 1959; Cussler, 1995). At variable temperature but fixed composition and pressure, self or tracer diffusion coefficient of ions in pure solution can be extrapolated from one to another temperature based on Stokes-Einstein relationship. The variation of diffusion coefficient through this relationship is more affected by the changes due to the viscosity dependency on temperature rather than due to the direct temperature variation (Cussler, 1995; Oelkers, 1996).

2.9 Experimental studies on the coupled thermal, hydraulic, chemical and mechanical behaviour of compacted bentonite

A number of experimental investigations have been reported on the coupled physical, chemical/geochemical and/or mechanical (i.e. THCM) behaviour and processes in compacted bentonite under repository conditions. The investigations have been conducted mostly at laboratory scale (e.g. Villar et al., 1996; Cuevas et al., 1997, 2002; Martín et al., 2000; ENRESA, 2000; ENRESA, 2006; Singh, 2007; Villar et al., 2008a; Villar et al., 2008b; Gómez-Espina and Villar, 2010; Fernandez and Villar, 2010) and some in mock-up and large scale under FEBEX project (e.g. ENRESA, 2000; 2006). Most of the experimental studies on THCM behaviour of compacted bentonite has been carried out as part of a major research study in the framework of FEBEX project (ENRESA, 2000, ENRESA, 2006). FEBEX project has aimed to study the transient state of the near field for a high level radioactive waste repository in crystalline rock according to the Spanish Reference Concept (ENRESA, 1995). In this disposal concept the canisters enclosing the conditioned waste are placed horizontally in drifts and surrounded by a clay barrier constructed of highly compacted bentonite blocks. The experimental work of the FEBEX project consisted of three main parts including an in situ test under natural conditions and at full scale (Grimsel, Switzerland); a

mock-up test at almost full scale (CIEMAT, Madrid); and a series of laboratory tests to complement the information from the two large-scale tests. Under FEBEX project, an extensive laboratory tests has been conducted to complement the information and obtain information on the thermal, hydraulic and geochemical processes in the bentonite buffer (ENRESA, 2000, ENRESA, 2006).

The results of these experiments have helped to improve the understanding of the behaviour of compacted bentonite under coupled THCM conditions and to identify the major processes affecting the hydro-geochemical behaviour of clay buffers under non-isothermal conditions of the repository. In addition, the results have been used for development and calibration of the computational tools for further applications in long term assessment analysis. In the following, a review on the recent laboratory tests conducted on coupled THCM processes on compacted bentonite is presented.

In order to investigate changes in pore water chemistry of compacted bentonite resulting from simultaneous heating and hydration, Villar et al. (1996) and Cuevas et al. (1997) carried out an experiment on FEBEX bentonite compacted at dry density of approximately 1620 kg/m^3 . The bentonite sample (diameter of 150 mm and height of 146 mm) was heated at the top at constant $100 \text{ }^\circ\text{C}$. At the bottom, deionized water was supplied for hydration. The test lasted for 2619 hours. They reported the distribution of the final water content and the geochemistry and pore water composition. A redistribution of salts was observed which was explained by the advection as water comes in, convection near the heater and diffusion due to concentration gradients. The results suggested that the electrostatic repulsion on clay surfaces seemed to reduce the mobility of sulphate ions with respect to chloride. The thermal gradient also affected the distribution of the exchangeable cations.

As part of the FEBEX project, Cuevas et al. (2002) carried out a thermo-hydraulic experiment on bentonite compacted at dry density of 1650 kg/m^3 . The main objective of this work was to simulate the transport behaviour of major soluble ions under the influence of opposing thermo-hydraulic gradients. The specimen was 0.025 m long and 0.05 m in diameter. Water was injected under a pressure of 1.1 MPa at the top of the cell. Two different thermal gradients were examined, in order to ascertain the effect of temperature in the observed processes. These include a high-temperature gradient, between 100 and $60 \text{ }^\circ\text{C}$ ($16 \text{ }^\circ\text{C/cm}$) to simulate regions closer to the container, and a low-temperature gradient, between 60 and 35

°C (10 °C/cm), to simulate zones near the host rock. The hydration processes was simulated by using two types of water, including granitic water to simulate the conditions of the outer part of the barrier and saline water, which simulates the situation in the internal part of the barrier where water is loaded with the ionic species dissolved during its inward movement. The experiments have been conducted for short periods of 10-16 days. The results of the experiment indicated that the advective transport of ions from the cold end toward the hot end during the initial stages of experiment controlled the behaviour of major dissolved ions. As a consequence, ionic concentrations were built up at the hot end. Chemicals were also reported to be transferred backward by diffusion mechanism from the hot end toward the cold end during the saturation phase. While chloride ions showed conservative behaviour, the remaining major soluble ions were influenced by precipitation-dissolution and ion exchange reactions. The short-distance/short-time scales of these experiments accelerated saturation and ion transport phenomena, which may have hidden the long-term alteration produced during the high temperature/low water content transient period near the heater.

Gómez-Espina and Villar (2010) conducted a thermo-hydraulic test on compacted MX-80 bentonite (dry density 1720 kg/m^3 with an initial water content of 16%). The experiment has been part of the Temperature Buffer Test (TBT) project, which is a full-scale test for HLW disposal that aims at improving the current understanding of the thermo-hydro-mechanical (THM) behaviour of buffers with a temperature around and above 100 °C during the water saturation transient. The test was performed in a cylindrical cell with internal diameter of 70 mm and sample length of 200 mm. The compacted bentonite sample was subjected to a simultaneous heating and hydration at opposite ends for a period of 496 days. A constant temperature was applied at the bottom and top of the specimen equal to 140 °C and at 30 °C, respectively. Deionised water was injected on top at relatively low pressure equal to 0.01 MPa. The water uptake and distribution of water content and dry density along the bentonite were conditioned by the thermal gradient. In terms of moisture transport, the results of Gómez-Espina and Villar (2010) indicated that water did not penetrate into the column beyond the area in which the temperature was higher than 100 °C. A convection area was found to be formed in the hydrated region where the liquid water and dissolved ions has transferred by advection towards the heater. As the water reached the area with high temperature, it evaporated which resulted in precipitation of minerals in the region close to the heater. The composition of the pore water along the column was shown to be affected by

advection, interlayer exchange and dissolution/precipitation processes. Thenardite (anhydrous sodium sulphate mineral), calcite and dolomite were the mineral phases controlling the concentration of the main ions in the pore water, in addition to halite near the heater. The cation content of the pore water was conditioned by the changes in the smectite interlayer, since exchangeable monovalent cations (especially sodium) were replaced by divalent cations (especially calcium), except in the coldest zone. In addition, near the heater the number of equivalent positions in the smectite interlayer decreased. The thermal and hydraulic treatment did not cause significant changes in the smectite or the other mineral phases content of the bentonite (Gómez–Espina and Villar, 2010).

Among the laboratory tests started in the framework of the FEBEX project and continued in the NF-PRO project, a series of experiments were performed under conditions in which compacted bentonite was subjected simultaneously to heating and hydration, in opposite directions and similar to the condition of the clay barrier in the repository. In particular, a series of long term laboratory experiments were conducted under heating and hydration conditions on a 600 mm (length) and 70 mm (diameter) cylindrical compacted FEBEX bentonite reported by Villar et al. (2007); Villar et al. (2008a); Villar et al. (2008b) and Fernández and Villar (2010). At the bottom part of the cells a constant temperature of 100 °C was maintained. On top of the cell temperature was controlled and fixed at room temperature (20–30 °C) using a circulation water tank. The granitic water was injected through the upper surface under a pressure of 1.2 MPa. Villar et al. (2008a) and Fernández and Villar (2010) reported the results of seven tests performed in the mentioned cells which included 0.5, 1, 2 and 7.6 years lasting experiments under the mentioned conditions. At the end of each test, the cell was disassembled and geochemistry of the bentonite and pore fluid composition was studied through a series of post-mortem geochemical laboratory analysis. The results of hydraulic and geochemical behaviour were reported by Villar et al. (2008b) and Fernández and Villar (2010). The results indicated that after 7.6 years, no significant mineralogical alteration of the montmorillonite was observed. However, as a consequence of the hydration and of the heating, two types of processes occurred along the bentonite column. In the coldest zones, the hydration of the bentonite diluted the bentonite-pore water and caused the dissolution of highly soluble accessory minerals, such as sulfates and carbonates. Chloride moved with the hydration water towards the hottest zone as a conservative anion by advection-diffusion affected by anion exclusion. The dissolution of sulfates and carbonates

with the hydration water caused changes to the composition of the exchangeable ions in the interlayer.

Singh (2007) studied the heat and mass movement in compacted MX-80 bentonite and Speswhite kaolin. Non-isothermal tests were carried out, with and without applied hydraulic gradients. The specimens were compacted to a dry density of 1600 kg/m^3 with different initial water contents providing specimens with the diameter of 100 mm and height of the 100 mm. The temperature at the bottom of the cell was maintained at $85 \text{ }^\circ\text{C}$ by a circular heater. At top of the specimen the temperature was controlled at $25 \text{ }^\circ\text{C}$ by circulating water from a water bath at constant temperature. Distilled water was injected at 600 kPa pressure. The temperature and relative humidity was monitored in-situ along the depth of the specimen. A series of post-mortem analysis was also conducted to obtain the variation of the pore fluid composition in the column. The results showed the gravimetric moisture content decreased near the hot end when the temperature gradient was applied due to moisture movement in vapour phase away from the hot region to the cold region. The amount of drying was found to be dependent on the initial moisture content. The dry sample had higher drying compared to the wet sample. The accumulation of ions including chloride, nitrate and sulphate near the cold end indicated that the liquid moisture moves towards the hot end from the colder region.

The FEBEX in situ test was performed in a gallery excavated in granite in the northern zone of the Grimsel underground laboratory operated by NAGRA in Switzerland. The test includes the heating system, the bentonite barrier and instrumentation, monitoring and control systems. The drift is 70.4 m long and 2.28 m in diameter. The test zone is located in the last 17.4 m of the drift where heaters, bentonite and instrumentation were installed. The test zone was sealed with a concrete plug. The main elements of the heating system are two heaters (1 and 2), separated horizontally by 1 m, which simulate full-sized canisters. Heaters are designed to maintain a maximum temperature of $100 \text{ }^\circ\text{C}$ at the steel liner/ bentonite interface. The in situ test began in February 1997 and the Heater 1 was switched-off in February 2002. Dismantling of heater 1 was performed from May to September 2002. A comprehensive post-mortem bentonite sampling and analysis program was designed to characterize solid and liquid phases, measure physical and chemical changes induced by the combined effect of heating and hydration; and test THM and THC models (ENRESA, 2006).

The experimental programmes and the achieved results reported have assisted to improve understanding of the major hydraulic and chemical transport and reactions in compacted bentonite under similar conditions to the compacted buffer in HLW repository conditions. They have provided valuable information about the major physical and chemical processes, and the response of the bentonite and the trends of variations in longer periods which have been adopted to validate or calibrate the computational models. However, the results of these studies all are limited to relatively short periods of time compared with the long term exposure of the buffer to thermo-hydro-geochemical effects.

2.10 Computational studies on the coupled thermal, hydraulic, chemical and mechanical behaviour of compacted bentonite

A number of coupled thermal, hydraulic, geochemical (and mechanical) computational simulation studies have been presented on the behaviour of compacted bentonite as the buffer candidate for the HLW disposal. The majority of these modelling studies have been based on the available experimentations on THCM behaviour of compacted bentonite and in order to calibrate and illustrate the capabilities of the models. However, the short- and long-term THCM behaviour of the compacted bentonite and the engineered barrier systems have also been the subject of several numerical modelling investigations. A review on some of the recent numerical modelling studies reported on the coupled THCM behaviour of compacted bentonite is presented below.

Under the FEBEX project, a coupled thermal, hydraulic, geochemical and mechanical model, *FADES-CORE-LE* was presented (ENRESA, 2000). The model is an extension to the existing model, *TRANQUI* (Xu et al., 1999). The chemical reactions assume local equilibrium approach and share an extensive thermodynamic database taken from the *EQ3/6* geochemical code. Chemical processes which can be modelled include homogeneous (e.g. speciation, acid-base and redox) and heterogeneous reactions (e.g. mineral dissolution and precipitation, adsorption, ion exchange, gas solution-exsolution). The model also considers radioactive decay processes. However, the model is limited to two-dimensional domains. In this model deformation variable is also coupled with moisture, heat and chemical flow equations. This model is able to handle various geochemical reactions. This model was specifically

developed to simulate small to large-scale experiments carried out as part of FEBEX project to assess the long-term behaviour of bentonite clay barriers in the deep nuclear waste repositories.

A numerical simulation of the coupled THCM behaviour of compacted bentonite was presented by Xie et al. (2006) based on the laboratory scale of simultaneous heating and hydration experiment reported by Cuevas et al. (1997). In this study, a two-phase and non-isothermal multi-species reactive transport model was developed and implemented in the object-oriented and process-oriented simulator *GeoSys/RockFlow*. Geochemical reactions were incorporated by coupling of *GeoSys/RockFlow* to the geochemistry code *PHREEQC2*. The reactive transport modelling included heat transport, two-phase flow, multicomponent transport and geochemical reactions in the liquid phase, i.e. ion exchange, mineral dissolution/precipitation under equilibrium reactions. The simulation results showed good agreement with those reported from experimental investigations. It was observed that during the experiment the highly soluble minerals like calcite, halite and gypsum strongly determined the pore water chemistry. In terms of moisture transfer, the model presented by Xie et al. (2006) incorporated the effects of interlayer/microscopic swelling under constrained condition on the flow of water based on the approach proposed by Xie et al. (2003). In this approach the effective permeability is modified via the swelling of the interlayer and microstructure based on a DDL calculation. In the simulations, it was shown that swelling significantly slows down the saturation process, because swelling reduces the porosity in the bentonite sample.

Seetharam (2003); Seetharam et al. (2006) and Cleall et al. (2007) presented a numerical simulation of coupled THCM behaviour of a small scale heating and hydration laboratory test on compacted FEBEX bentonite, reported by Cuevas et al. (2002). This was achieved via the application of a numerical model, *COMPASS*, which implements a fully coupled THCM formulation for unsaturated soils, including certain aspects of geochemical reactions by linking geochemical model *MINTEQA2* (Allison et al., 1991). The simulation consisted of a 25 mm compacted bentonite under a temperature gradient of 10 °C/cm. Granitic water was injected at the pressure of 1.2 MPa from the cold side similar to the conditions presented by Cuevas et al. (2002). The major concern on this numerical modelling has been on the capabilities of the model. The reactive transport of major ionic species in compacted bentonite

was simulated under thermo-hydraulic conditions of the experiment. In terms of heat and moisture transfer, good correlation was observed between the experimental and numerical modelling results. For all ions, the model showed a good qualitative and a reasonable quantitative agreement with respect to the experimental results. However, an overestimation of ion concentration at the hot end and underestimation at the hydration end for all the ions was observed. The model also predicted the final concentration of the exchange complex to be close to that of the initial values correlating well with the experimental observations. The precipitation/dissolution of trace minerals (calcite, dolomite, anhydrite and halite) under equilibrium condition has been considered in this study. The model presented, was not capable to simulate the chemical reactions under kinetically controlled condition. In this simulation an elastic model was assumed and acceptable trends in porosity variations was observed. Further applications of the developed numerical model and capabilities for simulation of coupled THCM behaviour were also presented by Seetharam et al. (2007).

Guimarães et al. (2007) presented a numerical simulation by coupling the reactive transport of chemicals with an existing THM model, developed by Olivella et al. (1994). Special attention has been given to phenomena likely to be encountered in clay barriers used as part of containment systems of nuclear waste. In the model, the total analytical concentrations (including precipitated minerals) are adopted as basic transport variables and chemical equilibrium is achieved by minimizing Gibbs free energy. As regards to precipitation/dissolution, both equilibrium and kinetic models are included. To evaluate the capabilities of the model, a simulation of a compacted bentonite under simultaneous hydration and heating was presented by Guimarães et al. (2007). The simulation was based on the experimental study presented by Cuevas et al. (1997) on simultaneous heating and hydration as presented previously. In addition, an example of application of the developed numerical model was also briefly described by Guimarães et al. (2006) which involved the simulation of a case of a large-scale in situ heating test of that simulates the conditions of a repository for high-level nuclear waste (ENRESA, 2000).

A numerical THC model of FEBEX in situ test was presented by Samper et al. (2008). THC predictions of the in situ test have been performed with *INVERSE-FADES-CORE* code. THC predicted concentrations systematically overestimated measured values near the heater and showed gradients sharper than those of measured data. They suggested that the discrepancy

could be overcome by considering bentonite swelling/shrinking and improving the estimate of water evaporation at heater-bentonite interface. Preliminary results from a coupled THCM model of a heating and hydration experiment on FEBEX bentonite indicated that geochemical results improve when changes in porosity caused by swelling are considered. The observations from the numerical simulation indicated that the spatial distribution of the chloride ions is the result of the combined effects due to the pore water evaporation near the heater, water condensation some distance away from heater, dilution due to inflow of granitic groundwater, advective displacement of the hydration front, and the solute diffusion which tends to dissipate solute gradients (Samper et al., 2008).

Yang et al., (2008) conducted a numerical simulation of coupled saturated/ unsaturated water flow, heat transfer and multi-component reactive solute transport to evaluate the long-term geochemical evolution in bentonite, concrete and clay formation for a potential geological radioactive waste repository. The model consisted of a bentonite buffer having a thickness of 0.75 m, a concrete sustainment (0.20 m in thickness) and the clay formation with a thickness of about 24 m. Simulations were carried out with a general-purpose multicomponent reactive transport code, *CORE2D V4* for a period of one million years. Changes in formation porosity caused by mineral dissolution/precipitation reactions were taken into account. The focus of this simulation was on evaluating the trends of long-term geochemical evolution in a potential repository due to interactions of pore water and solid phases. In terms of moisture transfer, the bentonite buffer becomes fully saturated in a short period of 20 years. The results of the numerical simulation indicated that dissolution of calcium silicate hydrate (C-S-H or $\text{CaO-SiO}_2\text{-H}_2\text{O}$) in concrete causes an increase in pH from neutral to up to 13 in bentonite buffer during the whole time period. After CSH minerals in the concrete are exhausted, pH starts to decrease in the whole system. In addition, mineral precipitation can reduce the pore space in the bentonite close to the bentonite–concrete interface due to diffusion of a hyper-alkaline plume from the concrete.

Arcos et al. (2008) presented a series of numerical simulations on the long-term geochemical evolution of bentonite and its pore water in the evolving geochemical environment due to climate change. The bentonite buffer in the KBS-3 underground nuclear waste repository concept designed by the Swedish Nuclear Fuel and Waste Management Co. (SKB) has been the subject of this study. The simulations were conducted by using *PHAST v.1.2* (Parkhurst et

al., 2004), which is the result of coupling a transport code, *HST3D*, and a geochemical code, *PHREEQC* (Parkhurst and Appelo, 1999). One simulation focused on the modelling of the thermal stage (i.e. 1000 years) whilst another two series of simulations were used to model the average interglacial period (i.e. 60,000 years). The influence of changes in climate has been tested using three different waters interacting with the bentonite: present-day groundwater, water derived from ice melting, and deep-seated brine. The model domain included a bentonite buffer barrier surrounding the copper canisters and the iron insert where spent nuclear fuel will be placed. The results from the simulations indicated that pore water chemistry is controlled by the equilibrium with the accessory minerals, especially carbonates. pH is buffered by precipitation/dissolution of calcite and dolomite, when present. The interaction of granitic groundwater with the bentonite blocks has minor effects on the chemical evolution of the pore water. In contrast, the intrusion of ice-melting water, which can be very dilute but alkaline (pH=9.6), modifies substantially the composition of pore water and bentonite. Due to the effect of a thermal gradient on the bentonite behaviour, the modelling results showed a redistribution of accessory minerals (anhydrite and silica) and cation exchange occupancy in accordance with what has been observed in large-scale experiments and natural analogues.

Computational modelling investigations have shown that temperature has a profound effect on hydraulic and chemical behaviour of compacted bentonite. In addition, although a very small percentage of commercially available bentonite consists of accessory minerals such as gypsum and calcite, these minerals have shown a considerable impact on the pore fluid composition under the heating and hydraulic conditions. In general, the results of the computational modelling for the re-saturation or long term performance of the compacted clay buffer indicate important developments in the capabilities of the models, although most of the modelling studies and developed models have some limitations in terms of the processes considered or the degree of coupling THCM behaviour.

2.11 Computational schemes and developments in modelling of the reactive transport of multicomponent chemicals

A variety of computational models and codes has been developed during the last three decades for simulating chemical transport in combination with biogeochemical reactions. The capabilities of the models for the reactive transport of chemicals have been advanced using the developments to the theory and computational aspects both in the area of transport processes and geochemical reactions. Seetharam (2003) presented a comprehensive review of developments in the reactive transport models by that time; hence it is not repeated here.

For any given reactive transport model, there are two main numerical strategies that require attention. Firstly, numerical schemes are required to solve the partial differential equations of transport processes and the non-linear algebraic or partial differential equations representing the equilibrium or kinetically controlled chemical reactions, respectively. Secondly, a method is required by which the governing equations for transport process and chemical reactions are coupled in an efficient manner. In this section, a review on the background and developments to methods for solving transport and reaction equations are presented.

Several methods have been proposed for solving the coupled transport and reaction equations, e.g. direct substitution approach (DSA); the mixed differential equation and algebraic equations (DAE), sequential iterative approach (SIA), sequentially non-iterative approach (SNIA) and sequentially partly-iterative approach (SPIA) (Samper et al., 2009). The main proposed and applied computational schemes for solving coupled transport and reaction governing equations can be categorised into (Steeffel and MacQuarrie, 1996):

- *Global implicit method, One-step or Direct Substitution Approach (DSA)*: in this method the governing equations including both transport and reaction terms are solved simultaneously which leads to a fully coupled system of equations. The chemical equations are substituted into the transport equations and it is solved applying the *Newton–Raphson method*.
- *Operator splitting technique*, where the calculation for transport and reaction equations is decoupled and the partial differential equation for chemical transport and chemical reactions are solved sequentially. The sequential approaches including *SIA*, *SNIA* and *SPIA* are among the proposed approaches in this category

In the *DSA* method, the non-linear chemical equations are directly substituted into the hydrological transport equations and the resulting sets of non-linear partial differential equations are solved simultaneously using the Newton-Raphson method (Saaltink et al., 2001).

In the case of sequential iterative approach (*SIA*), the transport equations are solved first, then using the results obtained from the transport step, values of chemical concentrations are corrected. This procedure is repeated for every iteration within a time step.

Sequential non-iterative approach (*SNIA*) is a special case of *SIA* where the chemical equations are solved only once per time-step, i.e., after the transport step has achieved converged results (Walter et al., 1994). A modified version of *SNIA* scheme, known as the *Strang splitting* method (Strang, 1968; Zysset and Stauffer, 1994) has also been proposed that involves centring the reaction step between two transport steps. In this method analysing time-step is divided into two equal steps, where transport equation is solved for the first half time-step. Then the equations for chemical reactions are calculated, followed by repeating the second half time-step transport calculation.

This has been suggested to improve the accuracy of *SNIA* method. Recently proposed, sequential partly iterative approach (*SPIA*) is an improved sequential technique (Samper et al. 2009). In this method after solving the transport equations, at a given time step, chemical calculations are performed only at the nodes not satisfying a prescribed partly iterative tolerance. In other words, iteration between transport and chemical equations is required only in nodes where there is a large mass transfer between the solid and liquid phases (Samper et al. 2009).

In the computational codes, presented for the modelling of reactive transport of multiple chemicals under variable saturation and temperature (and deformation) conditions, different schemes of solving the governing equations for the transport and chemical reactions have been adopted to utilize the advancements in geochemical modelling and in THM models. Table 2.1 presents a summary of the coupling schemes adopted for solving the transport and reaction formulations in some of the reactive transport models.

In general, the global implicit method provides more accurate results than operator splitting methods but it requires excessive CPU memory and CPU time (Yeh and Tripathy, 1989; Steefel and MacQuarrie, 1996; Saaltink et al., 2000; MacQuarrie and Mayer, 2005). In particular, in the case of two and three dimensional problems, using *DSA* and *DAE* approaches, the solution requires excessive CPU memory and CPU time (Yeh and Tripathy, 1989).

In a comparison study between different coupling schemes including *DSA*, *SIA* and *SNIA*, Steefel and MacQuarrie (1996) concluded that in the case of multiphase and multicomponent systems, using global implicit method becomes considerably difficult due to the size of the required matrix for coupling and enlargement of sets of non-linear equations which must be solved. Saaltink et al. (2001) also examined the efficiency and accuracy of *DSA* and *SIA*. They showed that *SIA* particularly gives problems for cases with high kinetic rates and cases with a high number of flushed pore volumes. On the other hand, the *DSA* computational behaviour is less affected by kinetics or large flushing rates than the *SIA*. Although *DSA* can be applied to solve all coupled reactive transport problems, the *SIA* is faster and requires less computer memory for large grids and it is computationally a more efficient approach (Steefel and MacQuarrie, 1996; Samper et al., 2009).

Steefel and MacQuarrie (1996) compared the results of simulations in simple cases using different sequential coupling methods. They reported that *SIA* sometimes gives the smallest error to CPU time ratio, although in other cases, *SNIA* is more efficient. However, the accuracy of *SNIA* is highly dependent on space and time discretisation and the type of chemical reactions. Xu et al. (1999) also employed *SNIA* in addition to *SIA* method and compared the accuracy and numerical performance of using several test cases. They demonstrated for a specific case that *SNIA* is more efficient and requires less CPU time. However, numerical dispersion was noticed and the accuracy also reduced. Therefore they concluded that there is no clear proof that *SNIA* is better than *SIA*, and it mainly depends on the choice of the chemical reactions and also on the time and space discretisation. Samper et al. (2009) showed that numerically *SNIA* is two to three times more efficient than *SIA*.

Table 2.1 Coupling schemes for transport and reaction models in some of the models/codes developed for reactive transport modelling

Model/Code	Reference	DSA	SIA	SNIA	Strang	SPIA
<i>PHREEQM</i>	Appelo and Willemssen (1987)			X		
<i>DYNAMIX</i>	Liu and Narasimhan (1989)			X		
<i>HYDROGEOCHEM</i>	Yeh and Tripathy (1991)		X			
<i>MST1D</i>	Engesgaard and Kipp (1992)		X			
<i>UNSATCHEM</i>	Šimůnek and Suarez (1994)		X			
<i>CRUNCH</i>	Steefel and Yabusaki (1995)	X	X			
<i>TOUGH2</i>	White (1995)	X				
<i>ARASE</i>	Grindrod and Takase(1996)	X				
<i>TBS</i>	Schäfer et al. (1998)		X			
<i>FEREACT</i>	Tebes-Stevens et al. (1998)		X			
<i>MIN3KIN</i>	Wernberg (1998)		X	X		
<i>TRANQUI</i>	Xu et al. (1999)		X	X		
<i>MINTRAN</i>	Walter et al. (1994)			X		
<i>DIAPHORE</i>	Le Gallo et al. (1998)			X		
<i>CHEMFRONTS</i>	Bäverman et al. (1999)	X				
<i>PHREEQC 2</i>	Appelo and Parkhaust (1999)			X		
<i>CORE 2D</i>	Samper et al. (2000)		X	X		
<i>PHT3D</i>	Prommer (2002)				X	
<i>COMPASS</i>	Seetharam (2003)		X	X		
<i>CORE 2D V4</i>	Samper et al. (2009)		X	X		X
<i>GeoSysBRNS</i>	Centler et al. (2010)			X		
<i>THOUGHREACT</i>	Xu et al. (2004)		X	X		

SNIA solutions are less accurate and exhibit more numerical dispersion than *SIA* solutions. *SNIA* errors increase with increasing Peclet and Courant numbers. Relative error ranges from 1.3 to 5 % on average, although it may reach locally very large values. The Peclet number also affects the magnitude of the differences, although its effect is much smaller than that of

the Courant number. In order to minimize the errors with *SNIA*, the time step should be limited to the values in which chemical species are not transported by advection faster than a single cell in one time step. This may restrict the simulation to the use of prohibitively small time steps. It should be mentioned that the sequential iteration approach (*SIA*), in theory, solves this problem. However, it has not been clearly demonstrated that this method provides a robust solution method for advective transports (MacQuarrie and Mayer, 2005).

The interest in the recent developed reactive transport models has been mainly on coupling transport of THM models with well established and advanced geochemical models such as *MINTEQA2* or *PHREEQC*. Some the recent models proposed as a linked transport and reaction models are as follows:

Prommer (2002) presented a computer code *PHT3D* for general reactive transport calculations, coupling *MODFLOW/MT3DMS* for transport and *PHREEQC version 2* for chemical reactions. The model uses a sequential non-iterative approach where the transport processes are calculated during a time step, an input file is written for *PHREEQC* for calculating reactions such as ion exchange and precipitation or dissolution of minerals, and these steps are repeated for subsequent time steps until finished.

Seetharam (2003) presented a coupled THCM model (*COMPASS*) in which the geochemical reactions are calculated via linking with geochemical equilibrium model (*MINTEQA2*) presented by Allison et al., (1991). This model is capable of modelling the reactive transport of multicomponent chemicals. Only equilibrium geochemical reaction can be calculated in this model. Apart from modelling the processes under coupled THCM framework, both *SIA* and *SNIA* have been adopted in this model. This capability can be used in the cases where uncertainty of the accuracy of *SIA* and *SNIA* exists; hence the modelling can be performed under both coupling schemes for comparison.

The reactive transport code, *HP1* was presented by Jacques and Šimůnek (2005) for modelling reactive transport and biogeochemical processes in variably-saturated porous media. *HP1* results from coupling the water and solute transport model *HYDRUS-1D* (Šimůnek et al., 2008) and *PHREEQC version 2* (Parkhurst and Appelo, 1999). *HP1* provides most of the features and capabilities of the *HYDRUS-1D* and *PHREEQC* programs into a single numerical simulator by using a sequential non-iterative coupling scheme. The *HP1* is

capable to model the transient water flow in variably-saturated media, transport of multiple components, mixed equilibrium/kinetic biogeochemical reactions, and heat transport. However, the capability of modelling the transport processes is limited to the one dimensional analyses. Wissmeier and Barry (2008) presented a one-dimensional flow and solute transport model in the unsaturated medium by implementing the moisture-based form of Richard's equation into the geochemical modelling framework *PHREEQC*. A second-order, cell-centred, explicit finite difference scheme was employed for the numerical solution of the partial differential equations of flow and transport. Geochemical reactions were coupled to transport processes by non-iterative sequential operator splitting. The scheme is currently limited to cases where changes in physical fluid properties and hydraulic flow characteristics due to geochemical reactions are negligible. The model has got all geochemical capabilities of *PHREEQC* including complex aqueous speciation, cation exchange, equilibrium phase dissolution and precipitation, formation of solid solutions, redox reactions, gas phase exchange, surface adsorption considering electrostatics and kinetic reactions.

Centler et al. (2010) provided a reactive transport code by coupling of *Biogeochemical Reaction Network Simulator (BRNS)* to the flow and transport simulator *GeoSys/RockFlow*. The *Biogeochemical Reaction Network Simulator (BRNS)* contains a solver for kinetically and thermodynamically constrained biogeochemical reactions, and *GeoSys/RockFlow*, a multidimensional finite element subsurface flow and transport simulator. The coupling scheme is based on an operator splitting scheme.

From the above review it can be seen that various coupling schemes have been suggested to solve the governing equations for chemical transport and reactions or to link transport and reaction models. These schemes have been successfully applied and verified in various models. It is noted that the computational performance and efficiencies of the various suggested coupling schemes are basically affected by the type of the transport problems and the degree of complexity in geochemical reactions.

2.12 Conclusions

This chapter presents a selected review on the hydraulic and chemical behaviour of compacted bentonite including the effects due to the microstructure evolution. Recent

developments in the experimentation and modelling studies of the coupled THCM behaviour of compacted bentonite under thermo-hydraulic conditions of the buffer in HLW repository were presented. Furthermore recent developed models of the reactive transport of chemicals in porous media and the computational aspects were considered.

The review indicated that the moisture and chemical transport processes in compacted bentonite are highly linked with the microstructure evolution of the smectite minerals in bentonite and the surface interaction. In terms of hydraulic behaviour, interaction of water with smectite minerals, as the major clay mineral component in compacted bentonite, has a profound effect on the saturation rate of the buffer. It has been well established that when water is adsorbed to the interlayer pore space of the smectite, the available pore space for water and chemical flow reduces significantly. However, quantitative evaluation of the amount and the rate of water exchange between immobile interlayer and mobile water/vapour especially under variable suction and temperature is key parameter for inclusion of this effect.

In terms of chemical diffusion in compacted bentonite, generally significant low rate of diffusion for anionic and high diffusion rate for cationic species has been found in experimental investigations. These have been suggested to be related to the microstructure and surface interaction. This effect requires the modelling of the diffusion under different effective diffusion coefficient combined with electrostatic balance of pore fluid.

Although, the effect of thermal diffusion, i.e. Soret-Ludwig effect, has been reported less important in geological media compared with the molecular diffusion, limited information is available on this effect and the quantitative evaluation in transport of chemicals in compacted bentonite. Under non-isothermal conditions, further developments and investigations of the diffusive behaviour of multicomponent chemicals, due to the effects of combined electrochemical and thermal diffusion potentials could provide a better and more confident understanding of the chemical processes under coupled THCM behaviour.

Available experimental results on coupled THCM behaviour of clay buffer under thermo-hydraulic conditions have been used in literature for developments of assessment of the capabilities of the computational models over the last few years. Various complexities have been identified in terms of geochemical and mineralogical behaviour of the clay buffer. A number of mineral reactions have been considered such as dissolution and precipitation of

minerals, ion-exchange and illitization and dissolution. Indeed, all models developed for studying reactive transport processes have some limitations.

The computational modelling of the reactive transport of multicomponent chemicals in porous media has advanced over three decades. Most of the models developed during last few years have adopted advancements in geochemical and transport modelling by combining separate models using various coupling schemes.

In conclusion, although there are numerous models available none are comprehensive enough to deal with all kinds of chemical transport problems. Especially, where nuclear waste repository modelling is considered there are only few models available that are capable of fully coupled THCM simulation on both three-dimensional and variably saturated conditions in addition to incorporating more comprehensive geochemical reactions acting over various time-scales. Moreover, these models have not yet been fully validated for all major applications. They are still in their developmental stages and are used only as research tools. Therefore, models, which give rigorous treatments to all aspects of coupling THCM framework in compacted bentonite, need further consideration.

2.13 References

- Allison, J.D., Brown, D.S., and Novo-Gradac, K.J. (1991). *MINTEQA2 User Manual version 3.0*. Environmental Research Laboratory, U.S. EPA.
- Arcos, D., Grandia, F., Domènech, C., Fernández, A.M., Villar, M.V., Muurinen, A., Carlsson, T., Sellin, P., and Hernán, P. (2008). Long-term geochemical evolution of the near field repository: Insights from reactive transport modelling and experimental evidences. *Journal of Contaminant Hydrology*, 102 (3-4), 196-209.
- Appelo, C.A.J., and Wersin, P. (2007). Multicomponent diffusion modeling in clay systems with application to the diffusion of tritium, iodide and sodium in Opalinus clay. *Environmental Science and Technology*, 41, 5002-5007.
- Appelo, C.A.J., Van Loon, L.R. and Wersin, P. (2010). Multicomponent diffusion of a suite of tracers (HTO, Cl, Br, I, Na, Sr, Cs) in a single sample of Opalinus Clay. *Geochimica et Cosmochimica Acta*, 74(4), 1201-1219.
- Barclay, L.M., and Thompson, D.W. (1969). Electron microscopy of sodium montmorillonite. *Nature*, 222-263.
- Bear, J. and Gilman, A. (1995). Migration of salts in the unsaturated zone caused by heating. *Letters in Mathematical Physics*, 19, 139-156.
- Birgersson, M., and Karnland, O. (2009). Ion equilibrium between montmorillonite interlayer space and an external solution-Consequences for diffusional transport. *Geochimica et Cosmochimica Acta*, 73, 1908-1923.
- Boudreau, B.P., Meysman, F.J.R. and Middelburg J.J. (2004). Multicomponent ionic diffusion in pore waters: Coulombic effects revisited. *Earth Planetary Science Letters*, 222, 653-666.
- Bourg, I.C., Bourg, A.C.M., and Sposito, G. (2003). Modeling diffusion and adsorption in compacted bentonite: a critical review. *Journal of Contaminant Hydrology*, 61, 293-302
- Bourg, I.C., Sposito, G., and Bourg, A.C.M. (2006). Tracer diffusion in compacted, water-saturated bentonite. *Clays and Clay Minerals*, 54 (3), 363-74.
- Bradbury, M.H., and Baeyens, B. (2003). Porewater chemistry in compacted re-saturated MX-80 bentonite. *Journal of Contaminant Hydrology*, 61, 329-338

- Centler, F., Shao, H., De Biase, C., Park, C-H., Regnier, P., Kolditz, O., and Thullner, M. (2010). GeoSysBRNS-A flexible multidimensional reactive transport model for simulating biogeochemical subsurface processes. *Computers and Geosciences*, 36, 397–405.
- Cleall, P.J., Seetharam, S.C., and Thomas, H.R. (2007). On the inclusion of some aspects of chemical behaviour of an unsaturated soil in thermo-hydro-chemical-mechanical models: II: Application and transport of soluble salts in compacted bentonite. *Journal of Engineering Mechanics, ASCE*, 133, 348-356.
- Cuevas, J., Villar, M.V., Fernández, A.M., Gómez, P., and Martín, P.L. (1997). Pore waters extracted from compacted bentonite subjected to simultaneous heating and hydration. *Applied Geochemistry*, 12, 473-481.
- Cuevas, J., Villar, M.V., Martín, M., Cobeña, J.C., and Leguey, S. (2002). Thermo-hydraulic gradients on bentonite: distribution of soluble salts, microstructure and modification of the hydraulic and mechanical behaviour. *Applied Clay Science*, 22, 25-38.
- Cui, Y.J., Loiseau, C., and Delage, P. (2002). Microstructure changes of a confined swelling soil due to suction controlled hydration. *Proceeding of the 3rd International Conference on Unsaturated Soils*, Recife, 593-598.
- Cui, Y.J., Tang, A.M., Loiseau, C., and Delage, P. (2008). Determining the unsaturated hydraulic conductivity of a compacted sand-bentonite mixture under constant-volume and free-swell conditions. *Physics and Chemistry of the Earth, Parts A/B/C*, 33 (Supplement 1), S462-S71.
- Cussler, E.L. (1997). *Diffusion-Mass Transfer in Fluid Systems*. University Press, Cambridge.
- Dixon, D.A., Gray, M.N., and Hnatiw, D.S.J. (1992). Critical gradients and pressures in dense swelling clays. *Canadian Geotechnical Journal*, 29, 1113-1119.
- Engersgaard, P. and Kipp, K.L. (1992). A geochemical transport model for redox-controlled movement of mineral fronts in groundwater flow systems: A case of nitrate removal by Oxidation of Pyrite. *Water Resources Research*, 28(10), 2829-2843.

ENRESA (2000). *Full-scale engineered barriers experiment for a deep geological repository for high-level radioactive waste in crystalline host rock, FEBEX project*. EUR 19147, Nuclear Science and Technology Series, European Communities, Luxembourg.

ENRESA (2006). *Full-Scale Engineered Barriers Experiment, Updated Final Report 1994-2004*. Technical Publication ENRESA 05-0/2006, Madrid.

Engelhardt, G.R., Lvov, S.N., and Macdonald, D.D. (1997). Importance of thermal diffusion in high temperature electrochemical cells. *Journal of Electroanalytical Chemistry*, 429, 193-201.

Fernández, A.M., and Villar, M.V. (2010). Geochemical behaviour of a bentonite barrier in the laboratory after up to 8 years of heating and hydration. *Applied Geochemistry*, 25, 809-824.

García-Gutiérrez, M., Cormenzana, J.L., Missana, T., and Mingarro, M. (2004). Diffusion coefficients and accessible porosity for HTO and ^{36}Cl in compacted FEBEX bentonite. *Applied Clay Science*, 26(1-4), 65-73.

Glaus, M.A., Baeyens, B., Bradbury, M.H., Jakob, A., Van Loon, L.R. and Yaroshchuk, A. (2007). Diffusion of ^{22}Na and ^{85}Sr in montmorillonite: evidence of interlayer diffusion being the dominant pathway at high compaction. *Environmental Science Technology*, 41, 478-485.

González Sánchez, F, Van Loon, L.R., Gimmi, T., Jakob, A., Glaus, M.A., and Diamond, L.W. (2008). Self-diffusion of water and its dependence on temperature and ionic strength in highly compacted montmorillonite, illite and kaolinite. *Applied Geochemistry*. 23(12), 3840-3851.

Gómez-Espina, R., and Villar, M.V. (2010). Geochemical and mineralogical changes in compacted MX-80 bentonite submitted to heat and water gradients. *Applied Clay Science*, 47(3-4), 400-408.

Goudarzi, R., and Johannesson, L-E. (2007). *Åspö Hard Rock Laboratory, Prototype Repository, Sensors data Report (Period 010917-070601)*. Report No 17, SKB, IPR-07-19, Stockholm.

Grim, R.E. (1962). *Applied Clay Mineralogy*. McGraw-Hill, New York.

Grindrod, P., and Takase, H. (1996), Reactive chemical transport within engineered barriers, *Journal of Contaminant Hydrology*, 21 (1-4), 283-96.

Guimarães, L.D.N., Gens, A., and Olivella, S. (2007). Coupled thermo-hydro-mechanical and chemical analysis of expansive clay subjected to heating and hydration. *Transport in Porous Media*, 66, 341-372

Homola, A.M., Israelachvili, J.N., Gee, M.L., and McGuiggak, P.M. (1989). Measurements of and relation between the adhesion and friction of 2 surfaces separated by molecularly thin liquid-films. *Journal of Tribology, ASME*, 111(4), 675-682.

Hueckel, T.A. (1992). Water-mineral interaction in hydromechanics of clay exposed to environmental loads: a mixture-theory approach. *Canadian Geotechnical Journal*, 29, 1071-1086.

Hueckel, T.A., Loret, B., and Gajo, A. (2002), Expansive clays as two-phase, deformable, reactive continua: Concepts and modeling options. *Proceedings of Chemo-Mechanical Coupling in Clays, From Nano-Scale to Engineering Applications*. Hueckel and Loret Di Maio (Edt.). Balkema Publisher, 105-20.

Ichikawa, Y., Kawamura, K., Nakano, M., Kitayama, K., and Kawamura, H. (1999). Unified molecular dynamics and homogenization analysis for bentonite behavior: Current results and future possibilities. *Engineering Geology*, 54, 21-31.

Jacques, D., and J. Šimůnek. 2005. *User manual of the Multicomponent Variably- Saturated Flow and Transport Model HP1*. Description, verification, and examples. Version 1.0. BLG-998 Rep. SCK · CEN, Mol, Belgium.

Jougnot, D., Revil, A., and Leroy, P. (2009). Diffusion of ionic tracers in the Callovo-Oxfordian clay-rock using the Donnan equilibrium model and the formation factor. *Geochimica et Cosmochimica Acta*, 73(10): 2712-2726.

Jullien, M., Raynall, J., Kohler, É. and Bildstein, O. (2005). Physicochemical reactivity in clay-rich materials: Tools for safety assessment. *Oil and Gas Science and Technology*, 60(1), 107-120.

Komine, H., and Ogata, N. (2004). Prediction swelling characteristics of bentonite. *Journal of Geotechnical and Geoenvironmental Engineering, ASCE*, 130(8), 818-829.

- Kozaki, T., Inada, K., Sato, S., and Ohashi, H. (2001). Diffusion mechanism of chloride ions in sodium montmorillonite. *Journal of Contaminant Hydrology*, 47, 159-170.
- Kozaki, T., Fujishima A., Saito, N., Sato, S. and Ohashi, H. (2005), Effects of dry density and exchangeable cations on the diffusion process of sodium ions in compacted montmorillonite, *Engineering Geology*, 81, 246-254.
- Kröhn, K-P. (2003). New conceptual models for the resaturation of bentonite. *Applied Clay Science*, 23, 25-33.
- Laird, D.A. (2006). Influence of layer charge on swelling of smectite. *Applied Clay Science*, 34, 74-87.
- Lasaga, A.C. (1998). *Kinetic Theory in the Earth Science*. Princeton Series in Geochemistry, Princeton University Press.
- Le Gallo, Y., Bildstein, O., and Brosse., E. (1998). Coupled reaction–flow modelling of diagenetic changes in reservoir permeability, porosity and mineral compositions. *Journal of Hydrology*. 209:366–388.
- Leaist, D.G., and Hui, L. (1990). Conductometric determination of the Soret coefficients of a ternary mixed electrolyte, Reversed thermal diffusion of sodium chloride in aqueous sodium hydroxide solutions. *Journal of Physical Chemistry*, 94, 447-451.
- Lehikoinen, J., Carlsson, T., Muurinen, A., Olin, M., and Salonen, P. (1995). *Evaluation of factors affecting diffusion in compacted bentonite*. In: Murphy, W.M., Knecht, K.A. (Eds.), Scientific Basis for Nuclear Waste Management XIX. Materials Research Society, Pittsburgh, PA, 675-682.
- Leoroy, P., Revil, A., and Coelho, D. (2006). Diffusion of ionic species in bentonite. *Journal of Colloid and Interface Science*, 296, 248–255.
- Likos, W.J. (2004), Measurement of crystalline swelling in expansive clay. *Geotechnical Testing Journal*, 27 (6), 1-7.
- Likos, W.J., and Lu, N. (2006). Pore-scale analysis of bulk volume change from crystalline swelling in Na⁺ and Ca²⁺ smectite. *Clays and Clay Minerals*, 54, 516-529.
- Likos, W.J., and Wayllace, A. (2010). Porosity evolution of free and confined bentonite during interlayer hydration, *Clays and Clay Minerals*, 58, 399-414.

- Liu, C.W., and Narasimhan, T.N., (1989). Redox-controlled multiple species reactive chemical transport I. Model development. *Water Resources Research*, 25(5), 869-882.
- Liu, J., Yamada, H., Kozaki, T., Sato, S., Ohashi, H. (2003). Effect of silica sand on activation energy for diffusion of sodium ions in montmorillonite and silica sand mixture. *Journal of Contaminant Hydrology*, 61, 85-93.
- Low, P.F., and Anderson, D.M. (1958). Osmotic pressure equations for determining thermodynamic properties of soil water. *Soil Science*, 86, 251-253.
- Ludwig, C. (1856). *Diffusion zwischen ungleich erwärmten orten gleich zusammengesetzter lösungen*. Sitz. Ber. Akad. Wiss. Wien Math-Naturw. Kl., 20.
- Ma, C., and Hueckel, T. (1993). Thermomechanical effects on adsorbed water in clays around a heat source. *International Journal for Numerical and Analytical Methods in Geomechanics*, 17, 175-196.
- MacQuarrie K.T.B. and Mayer, K.U. (2005). Reactive transport modeling in fractured rock: A state-of-the-science review. *Earth-Science Reviews*, 72, 189–227.
- Marcial, D., Delage, P., and Cui, Y.J. (2002). On the high stress compression of bentonite. *Canadian Geotechnical Journal*, 39, 812-20.
- Martín, M., Cuevas, J., and Leguey, S. (2000). Diffusion of soluble salts under a temperature gradient after the hydration of compacted bentonite. *Applied Clay Science*, 17, 55-70.
- Melkior, T., Gaucher, E.C., Brouard, C., Yahiaoui, S., Thoby, D., Clinard, Ch., Ferrage, E., Guyonnet, D., Tournassat, C., and Coelho, D. (2009). Na⁺ and HTO diffusion in compacted bentonite: Effect of surface chemistry and related texture. *Journal of Hydrology*, 370(1-4), 9-20.
- Mitchell, J.K. (1993). *Fundamentals of Soil Behaviour*. 2nd edition, John Wiley and Sons, New Jersey.
- Mitchell, J.K. and Soga, K. (2005). *Fundamentals of Soil Behaviour*. 3rd edition, John Wiley and Sons, New Jersey.
- Muurinen, A. (1994). *Diffusion of cations and anions in compacted sodium bentonite*. VTT Publications 168, Technical Research Centre of Finland, Espoo, Finland.

- Muurinen, A., Karnland, O., and Lehtikoinen, J. (2007). Effect of homogenization on the microstructure and exclusion of chloride in compacted bentonite *Physics and Chemistry of the Earth*, 32, 485-490.
- Nagra. (2002). *Project Opalinus Clay: Safety report. Demonstration of disposal feasibility for spent fuel, vitrified high-level waste and long lived intermediate-level waste (Entsorgungsnachweis)*. Nagra Technical Report NTB 02-05, Wettingen, Switzerland.
- Ochs, M., Lothenbach, B., Wanner, H., Sato, H., and Yui, M. (2001). An integrated sorption-diffusion model for the calculation of consistent distribution and diffusion coefficients in compacted bentonite. *Journal of Contaminant Hydrology*, 47, 283-296.
- Oelkers, E. (1996). *Physical and chemical properties of rocks and fluids for chemical mass transport calculations*. In *Reactive Transport in Porous Media, Reviews in Mineralogy*, 34, 130-191.
- Olivella, S., Carrera, J., Gens, A. and Alonso, E.E. (1994), Nonisothermal multiphase flow of brine and gas through saline media, *Transport Porous Media*, 15, 271-293.
- Oscarson, D.W. (1994). Surface diffusion: is it an important transport mechanism in compacted clays? *Clays and Clay Minerals*, 42, 534-543
- Parkhurst, D.L., and Appelo, C.A.J. (1999). *User's Guide to PHREEQC (version 2)*, U.S. Geological Survey, Water Resource Investigation Report, 99-4259.
- Posiva, (2006). *Petrology of Olkiluoto Aulis Kärki, Kivitieto Oy Seppo Paulamäki*, Geological Survey of Finland, POSIVA 2006-02
- Prommer, H., Barry, D.A., and Davis, G.B. (2002). Modelling of physical and reactive processes during biodegradation of a hydrocarbon plume under transient groundwater flow conditions. *Journal of Contaminant Hydrology*, 59, 113–131.
- Pusch, R. (1994). *Waste Disposal in Rock*. Developments in Geotechnical Engineering, 76. Elsevier.
- Pusch, R. (2001). *The microstructure of MX-80 clay with respect to its bulk physical properties under different environmental conditions*. Geodevelopment AB.
- Pusch, R. (2008). *Geological Storage of Highly Radioactive Waste*, Springer, New York.

Pusch, R., and Hökmark, H. (1990). Basic model of water- and gas-flow through smectite clay buffers. *Engineering Geology*, 28, 379-389.

Pusch, R., Karnland, O., and Hokmark, H. (1990). *GMM: a general microstructural model for qualitative and quantitative studies of smectite clays*, SKB, Technical Report, SKB-90-43, Stockholm.

Pusch, R., and Kasbohm, J. (2001). *Can the water content of highly compacted bentonite be increased by applying a high water pressure?*. SKB Technical Report, TR-01-33, Stockholm.

Pusch, R., and Yong, R.N. (2006). *Microstructure of Smectite Clays and Engineering Performance*. Taylor and Francis, New York..

Revil, A., and Leroy, P. (2004). Constitutive equations for ionic transport in porous shales. *Journal of Geophysical Research*, 109, B03208, 1-19.

Robinson, R.A., and Stokes, R.H. (1959). *Electrolyte Solutions*. Butterworth and Co. Ltd.

Rosanne, M., Paszkuta, M., Tevissen, E., and Adler, P.M. (2003). Thermodiffusion in compact clays. *Journal of Colloid Interface Science*, 267, 194-203.

Rosanne, M., Paszkuta, M., and Adler, P.M. (2006). Thermodiffusional transport of electrolytes in compact clays. *Journal of Colloid Interface Science*, 299, 797-805.

Salles, F., Beurroies, I., Bildstein, O., Jullien, M., Raynal, J., Denoyel, R., and Van Damme, H. (2008). A calorimetric study of mesoscopic swelling and hydration sequence in solid Na-montmorillonite. *Applied Clay Science*. 39(3-4), 186-201.

Salles, F., Douillard, J.-M., Denoyel, R., Bildstein, O., Jullien, M., Beurroies, I. and Van Damme, H. (2009). Hydration sequence of swelling clays: Evolutions of specific surface area and hydration energy, *Journal of Colloid and Interface Science*, 333(2), 510-522.

Saaltink, M.W., Carrera, J., Ayora, C. (2001). On the behavior of approaches to simulate reactive transport. *Journal of Contaminant Hydrology*, (48), 213-235.

Samper, J., Xu, T., and Yang, C. (2009). A sequential partly iterative approach for multicomponent reactive transport with CORE^{2D}. *Computers and Geosciences*, 13, 301-316.

Samper, J., Zheng, L., Montenegro, L., Fernández, A.M., and Rivas, P. (2008). Testing coupled thermo-hydro-chemical models of compacted bentonite after dismantling the FEBEX in situ test. *Applied Geochemistry*, 23(5), 1186-1201

- Sato, H. (2005). Effects of the orientation of smectite particles and ionic strength on diffusion and activation enthalpies of I⁻ and Cs⁺ ions in compacted smectite. *Applied Clay Science*, 29, 267-281
- Sato, H., and Suzuki, S. (2003). Fundamental study on the effect of an orientation of clay particles on diffusion pathway in compacted bentonite. *Applied Clay Science*, 23, 51-60
- Schäfer, D., Schäfer, W., and Kinzelbach, W. (1998). Simulation of reactive processes related to biodegradation in aquifers: 1. Structure of the three-dimensional reactive transport model. *Journal of Contaminant Hydrology*, 31, 167-186.
- Seetharam, S.C. (2003). *An investigation of the thermo/hydro/chemical/mechanical behaviour of unsaturated soils*. Ph.D. Thesis, Cardiff University, Wales, UK.
- Seetharam, S.C., Cleall, P.J., and Thomas, H.R. (2006). Modelling some aspects of ion migration in a compacted bentonitic clay. *Engineering Geology*, 85, 221-228.
- Seetharam, S.C., Thomas, H.R., and Cleall, P.J. (2007). Coupled thermo-hydro-chemical-mechanical model for unsaturated soils-Numerical algorithm. *International Journal of Numerical Methods in Engineering*, 70, 1480-1511.
- Šimůnek, J., van Genuchten, M.Th., and Šejna, M. (2008). *The HYDRUS-1D software package for simulating the one-dimensional movement of water, heat, and multiple solutes in variably-saturated media. Version 4.0*. HYDRUS Software Service 3. Department of Environmental Sciences, University of California, Riverside.
- Šimůnek, J., and Suarez, D.L. (1994). Two dimensional transport model for variably saturated porous media with major ion chemistry. *Water Resources Research*, 30(4), 1115-1133.
- Singh, R.M. (2007). *An experimental and numerical investigation of heat and mass movement in unsaturated clays*. PhD Thesis, Cardiff University, Wales, UK.
- SKB. (1999). *Processes in the repository evolution SKB*. Technical Report, TR-99-07. Stockholm, Sweden.
- Skipper, N.T., Refson, K., and McConnell, J.D.C. (1991). Computer simulation of interlayer water in 2:1 clays. *The Journal of Chemical Physics*, 94(11), 7434-7445.

- Snowdon, P.N., and Turner, J.C.R. (1960). The concentration dependence of the Soret effect. *Transaction Faraday Society*, 56, 1812-1819.
- Soret, Ch. (1880), Influence de la température sur la distribution des sels dans leurs solutions, *Acad. Sci., Paris*, 91(5), 289-291.
- Sposito, G. (1984). *The Surface Chemistry of Soils*. Oxford Press, New York.
- Steeffel, C.I., and MacQuarrie, K.T.B. (1996). *Approaches to modeling of reactive transport in porous media*. Reactive Transport in Porous Media, Reviews in Mineralogy, (34). Mineralogical Society of America, Washington, DC.
- Steeffel, C., Rutqvist, J. Tsang, C-F., Liu, H-H., Sonnenthal, E., Houseworth J., and Birkholzer, J. (2010) *Reactive transport and coupled THM processes in engineering barrier systems (EBS)*. Technical Report, LBNL-3901E, Lawrence Berkeley National Laboratory (LBNL).
- Steeffel, C.I., and Yabusaki, S.B. (1996). *OS3D/GIMRT, software for multicomponent-multidimensional reactive transport: user's manual and programmer's guide*. Report PNL-11166. Pacific Northwest National Laboratory, Richland, Washington.
- Strang, G. (1968). On the construction and comparison of difference schemes. *SIAM Journal of Numerical Analysis*, 5, 506-517.
- Suzuki, S., Prayongphan, S., Ichikawa, Y., and Chae, B.G. (2005). In situ observation of the swelling of bentonite aggregates in NaCl solution. *Applied Clay Science*, 29, 89-98.
- Tebes-Stevens, C., Valocchi, A.J., VanBriesen, J.M., and Rittmann, B.E. (1998). Multicomponent transport with coupled geochemical and microbiological reactions: Model description and example simulations. *Journal of Hydrology*, 209, 8-26.
- Thomas, H.R., Cleall, P.J., Chandler, N., Dixon, D., and Mitchell, H.P. (2003). Water infiltration into a large-scale in-situ experiment in an underground research laboratory. *Géotechnique*, 53(2), 207-224.
- Thomas, H.R., Cleall, P.J., Dixon, D.H., and Mitchell, P. (2009). The coupled thermal-hydraulic-mechanical behaviour of a large-scale in situ heating experiment. *Géotechnique*, 59, 401-413.

Thornton, E.C., and Seyfried, W.E. (1983). Thermodiffusional transport in pelagic clay: implications for nuclear waste disposal in geological media. *Science*, 220, 1156-1158.

Tong F.G., Jing, L., and Zimmerman, R.W. (2009). *An effective thermal conductivity model of geological porous media for coupled thermo-hydro-mechanical systems with multiphase flow*. *International Journal of Rock and Mining Science*, 46, 1358-1369.

Tripathy, S., Sridharan, A., and Schanz, T. (2004). Swelling pressures of compacted bentonites from diffuse double layer theory. *Canadian Geotechnical Journal*, 41, 437-450

van Olphen, H. (1977). *An Introduction to Clay Colloid Chemistry*, John Wiley & Sons, New York.

van Schaik, J.C., and Kemper, W.D. (1966). Chloride diffusion in clay water systems. *Soil Science Society of America Proceeding*. 30, 22-25.

Van Loon, L.R., Glaus, M.A., and Müller, W. (2007). Anion exclusion effects in compacted bentonite: Towards a better understanding of anion diffusion. *Applied Geochemistry*, 22, 2536-2552.

Vardon, P.J. (2009). *A three-dimensional numerical investigation of the therm-hydro-mechanical behaviour of a large-scale prototype repository*. Ph.D. Thesis, Cardiff University, Wales, UK.

Villar, M.V., Cuevas, J., and Martín, P.L. (1996). Effects of heat/water flow interaction on compacted bentonite: preliminary results. *Engineering Geology*, 41, 257-267.

Villar, M.V., Fernández, A.M., Martín, P.L., Barcala, J.M., Gómez-Espina, R., and Rivas, P. (2008b). *Effect of Heating/Hydration on Compacted Bentonite: Tests in 60 cm Long Cells*. Publishing House CIEMAT. Madrid. ISBN: 978-84-7834-597-4.

Villar, M.V., and Lloret, A. (2004). Influence of temperature on the hydro-mechanical behaviour of a compacted bentonite. *Applied Clay Science*, 26, 337-50.

Villar, M.V., Sánchez, M., and Gens, A. (2008a). Behaviour of a bentonite barrier in the laboratory: experimental results up to 8 years and numerical simulation. *Physics and Chemistry of the Earth*, 33, S476-S485.

- Walter, A.L., Frind, E.O., Blowes, D.W., Ptacek, C.J. and Molson, J.W. (1994). Modelling of multicomponent reactive transport in groundwater: Model development and evaluation. *Water Resources Research*, 30(11), 3137-3148.
- Wernberg, T. (1998). Multicomponent groundwater transport with chemical equilibrium and kinetics: model development and evaluation. *Hydrological Sciences*, 43(2), 299-317.
- Wersin, P., Curti, E., and Appelo, C. A. J. (2004). Modelling bentonite-water interaction at high solid/liquid ratios: swelling and diffuse double layer effects. *Applied Clay Science*, 26, 249-257.
- Wersin, P., Johnson, L. H., and McKinley, I.G. (2007). Performance of the bentonite barrier at temperatures beyond 100 °C: A critical review. *Physics and Chemistry of the Earth, Parts A/B/C*, 32, 780-788.
- White, S.P. (1995). Multiphase nonisothermal transport of systems of reacting chemicals. *Water Resources Research*, 31(7), 1761-1772.
- Wissmeier, L., and Barry, D.A., 2008. Reactive transport in unsaturated soil: comprehensive modelling of the dynamic spatial and temporal mass balance of water and chemical components. *Advances in Water Resources*, 31 (5), 858-875.
- Xie, M., Agus, S., Schanz, T., and Kolditz, O. (2004). An upscaling method and numerical modelling of swelling/shrinking processes in compacted bentonite /sand mixtures." *International Journal of Numerical and Analytical Methods in Geomechanics*, 28, 1479-1502.
- Xie, M., Bauer, S., Kolditz, O., Nowak, T., and Shao, H. (2006). Numerical simulation of reactive processes in an experiment with partially saturated bentonite, *Journal of Contaminant Hydrology*, 83, 122-47.
- Xu, T., Samper, J., Ayora, C., Manzano, M., and Emilio, C. (1999). Modeling of non-isothermal multi-component reactive transport in field scale porous media flow systems. *Journal of Hydrology*, 214, 144-164.
- Yang, C., Samper, J., and Montenegro, L. (2008). A coupled non-isothermal reactive transport model for long-term geochemical evolution of a HLW repository in clay. *Environmental Geology*, 53(8), 1627-1638.

Yeh, G.T., and Tripathi, V.S. (1989). A critical evaluation of recent developments in hydrogeochemical transport models of reactive multichemical components. *Water Resources Research*, 25(1), 93-108.

Yong, R.N. (1999). Overview of modeling of clay microstructure and interactions for prediction of waste isolation barrier performance. *Engineering Geology*, 54, 83-91.

Yong, R.N. (2003). Influence of microstructural features on water, ion diffusion and transport in clay soils. *Applied Clay Science*, 23, 3-13.

Yong, R.N., Pusch, R., and Nakano, M. (2010). *Containment of High-Level Radioactive and Hazardous Solid Wastes with Clay Barriers*. Spon Press, New York.

Yong, R.N., and Warkentin, B.P. (1975). *Soil Properties and Behaviour*, Elsevier, Amsterdam.

Zhang, F., and Low, P.F. (1995). Effect on monovalent, exchangeable cations and electrolytes on the retention between swelling pressure and interlayer distance in montmorillonite. *Journal of Colloid and Interface Science*, 173, 34-41.

Zysset, A., Stauffer, F. and Dracos, T. (1994). Modelling of chemically reactive groundwater transport. *Water Resource Research*, (30), 2217-2228.

Chapter 3

Theoretical Formulation

3.1 Introduction

This chapter describes the theoretical formulation for thermal, hydraulic, chemical and mechanical behaviour of porous media. The main objective is to present the developments in the context of this dissertation to the formulation of hydro-geochemical behaviour of unsaturated soils. Since the primary variables of the model influence each other (i.e. are coupled), it is useful to present in reasonable detail the governing equations for all thermal, hydraulic, chemical and mechanical behaviours.

The governing equations for coupled moisture, air, temperature, and deformation behaviour have already been covered in detail elsewhere (Ramesh, 1996; Thomas and He, 1998; Cleall, 1998; Mitchell, 2002; Melhuish, 2004; Vardon, 2009). The formulation of the reactive transport of multicomponent chemical transport was also presented by Seetharam (2003), where the effects of geochemical reactions were included via a sink/source term in the governing chemical transport equation using a geochemical equilibrium model, linked to the transport model.

General aspects of the theoretical formulation are presented in section 3.2 including the basic assumptions and the primary variables. The governing equation describing the moisture transfer is developed in section 3.3 based upon the principle of conservation of mass and treating moisture flow as a two phase flow process. The effect of the presence of dissolved chemicals on the flow of moisture, i.e. osmotic potential effects, is included in the governing equation for moisture transport. Air transfer is considered in section 3.4 considering air to be a binary mixture of dry air and water vapour. Total air content is considered as sum of the bulk air and the dissolved air in water phase. The governing equation of heat transfer is presented in section 3.5 based on the conservation of energy and identifying conduction, convection and latent heat of evaporation as the main mechanisms of transfer.

The governing equations for the reactive transport of multicomponent chemicals are explained in section 3.6. The principle of mass conservation law is applied to the transport equation of multicomponent chemicals. The general flux of each chemical component includes advective, dispersive and diffusive fluxes. Both molecular and thermal diffusion potentials are considered in the diffusive flux. In addition, developments to the chemical transport model via inclusion of the overall charge conservation, i.e. the electro-neutrality

condition, is included in the governing equation. A theoretical approach is adopted for evaluation of the thermal diffusion coefficient or the Soret coefficient.

The homogenous and heterogeneous geochemical reactions are considered as a sink/source term in the governing equation. The geochemical reactions are calculated utilising an advanced geochemical model, PHREEQC *version 2*, adopted to solve mass action equations.

The governing equation for deformation is derived from considerations of stress equilibrium. The general formulation for mechanical behaviour is detailed in section 3.7. Finally, a summary of the formulation of flow and deformation and the developments made in this chapter is presented in section 3.8.

3.2 Theoretical formulation-General aspects

Soil porous medium is considered to be a three-phase system, consisting of a solid skeleton, pore water and pore air. The pore water consists of the components of dissolved chemicals and dissolved air. The pore air is made up of dry air and water vapour. In the following, formulation the flow of moisture, air and heat energy in a deformable porous media are considered. Moisture is considered as the total water in the form of liquid and vapour. The transfer of water and vapour is considered utilising the principle of conservation of mass, as is the transfer of pore air. The pore air is considered as binary mixture of dry air and water vapour. The dissolved chemical concentration is expressed as a vector of any number of chemical species in the system in which the concentration of each species is treated as a primary variable in this model.

The governing equations are expressed in terms of five primary variables; namely

- Pore water pressure (u_l)
- Pore air pressure (u_a)
- Temperature (T)
- Dissolved chemical concentrations, e.g. for component i^{th} (c_d^i) where i can be 1 to nc components

- Displacement (\mathbf{u})

The behaviour of all these variables is included within coupled thermo-hydro-chemo-mechanical (THCM) formulation.

The driving mechanism of liquid water is considered as the total water potential or suction. Heat transfer is governed by the conservation of energy, taking into account conduction, convection and the latent heat of vapourisation, with radiation assumed to be negligible. Advection, dispersion and diffusion are considered as the major mechanisms for chemical transport. The mechanical behaviour is governed by an appropriate constitutive relationship, e.g. an elasto-plastic relationship for a slightly swelling soil, via consideration of stress equilibrium. All of the governing equations are then developed in a three-dimensional form.

3.3 Moisture flow

Transfer of moisture in unsaturated soils can be described as a two phase flow process, comprising water transport as liquid and vapour. The volumetric water content, θ , is defined as the sum of these phases:

$$\theta = \theta_l + \theta_v \quad (3.1)$$

where θ_l is the volumetric liquid content and θ_v is the volumetric vapour content .

Based on the principle of thermodynamic equilibrium, the volumetric liquid water and water vapour (equivalent amount of liquid precipitated) are in equilibrium at any point (de Vries, 1958) giving:

$$\theta_v = \frac{n - \theta_l}{\rho_l} \rho_v \quad (3.2)$$

where n is the porosity, ρ_l is the density of liquid water and ρ_v is the density of water vapour.

The law of conservation of mass can be considered separately in liquid and vapour phases in order to derive the general mass conservation for moisture transport.

The law of mass conservation dictates that the time derivative of the liquid water content is equal to the gradient of the liquid flux. Mathematically this can be expressed as:

$$\frac{\partial}{\partial t}(\rho_l \theta_l \delta V) = -\delta V \nabla \cdot (\rho_l \mathbf{v}_l) - \delta V \rho_l E_{ss} \quad (3.3)$$

where t is time, ∇ is the gradient operator and δV is the incremental volume. \mathbf{v}_l is the velocity of liquid, E_{ss} is a sink/source term representing vaporisation and condensation.

Similarly for the vapour phase, the law of conservation of mass dictates that the time derivative of the vapour content is equal to the gradient of the vapour flux as:

$$\frac{\partial}{\partial t}(\rho_v \theta_v \delta V) = -\delta V \nabla \cdot (\rho_l \mathbf{v}_v) - \delta V \nabla \cdot (\rho_v \mathbf{v}_a) + \delta V \rho_l E_{ss} \quad (3.4)$$

where \mathbf{v}_v is the velocity of vapour and \mathbf{v}_a is the velocity of pore air.

The volumetric air content, θ_a , can be expressed considering porosity and volumetric water content as:

$$\theta_a = n - \theta_l \quad (3.5)$$

Substituting equations (3.2) and (3.5) into equation (3.4), the law of conservation of mass for liquid vapour flow may now be expressed in terms of porosity and volumetric air content:

$$\frac{\partial}{\partial t}(\rho_v \theta_a \delta V) = -\rho_l \delta V \nabla \cdot \mathbf{v}_v - \delta V \nabla \cdot (\rho_v \mathbf{v}_a) + \rho_l \delta V E_{ss} \quad (3.6)$$

Summing the equations of conservation of mass for liquid and vapour flow, i.e., equations (3.3) and (3.6), gives the general equation of conservation of mass for moisture:

$$\rho_l \frac{\partial}{\partial t}(\theta_l \delta V) + \frac{\partial}{\partial t}(\rho_v \theta_a \delta V) = -\rho_l \delta V \nabla \cdot \mathbf{v}_l - \delta V \nabla \cdot (\rho_l \mathbf{v}_v) - \delta V \nabla \cdot (\rho_v \mathbf{v}_a) \quad (3.7)$$

The volumetric liquid may be expressed in terms of porosity and degree of saturation, giving;

$$\theta_l = n S_l \quad (3.8)$$

Where S_l is degree of saturation of pore water.

Similarly, the volumetric air contents can be expressed in terms of porosity and degree of saturation, as:

$$\theta_a = n S_a = n(1 - S_l) \quad (3.9)$$

where S_a is the degree of saturation of pore air.

The term ∂V , the incremental volume, is a summation of the void volume and solid volume. Hence it can be shown that:

$$\delta V = (1 + e)\delta V_s \quad (3.10)$$

where δV_s is the increment volume of the solids and e stands for the void ratio of soil.

Substituting equations (3.8), (3.9) and (3.10) into equation (3.7) gives:

$$\begin{aligned} \rho_l \frac{\partial}{\partial t} [nS_l(1+e)\delta V_s] + \frac{\partial}{\partial t} [\rho_v n(1-S_l)(1+e)]\delta V_s = \\ -\rho_l(1+e)\delta V_s \nabla \cdot \mathbf{v}_l - \rho_l(1+e)\delta V_s \nabla \cdot \mathbf{v}_v - (1+e)\delta V_s \nabla \cdot (\rho_v \mathbf{v}_a) \end{aligned} \quad (3.11)$$

Since the volume of the soil (solid) is assumed to remain constant, the term ∂V_s can be eliminated from equation (3.11). Moreover, the porosity can be related to the void ratio as:

$$n = \frac{e}{(1+e)} \quad (3.12)$$

Substituting porosity from equation (3.12) and eliminating the volume of solid in equation (3.11), the general mass conservation equation for moisture becomes:

$$\rho_l \frac{\partial(eS_l)}{\partial t} + \frac{\partial[\rho_v e(1-S_l)]}{\partial t} = -\rho_l(1+e)\nabla \cdot \mathbf{v}_l - \rho_l(1+e)\nabla \cdot \mathbf{v}_v - (1+e)\nabla \cdot (\rho_v \mathbf{v}_a) \quad (3.13)$$

According to equation (3.13), the total moisture flux includes the components of liquid flux, vapour flux due to vapour pressure gradients, and vapour flux arising from the bulk flow of vapour due to movement of pore air. The flow mechanisms and flow laws that govern them are discussed below.

3.3.1 Mechanism of liquid water flow

Liquid flow in unsaturated soils can be formulated using Darcy's equation replacing the hydraulic gradient with total water potential gradient (Yong and Warkenting, 1975; Lu and Likos). Hence, the velocity of liquid water can be expressed in Darcy's equation for unsaturated flow as:

$$\mathbf{v}_l = -k_l \nabla \psi \quad (3.14)$$

where k_l is unsaturated hydraulic conductivity and ψ is the total water potential.

The total water potential is defined as the energy with which water or liquid is held in a soil and it might include the components of matric, osmotic, thermal, electrical and gravitational potentials (Yong and Warkenting, 1975). In this study the total soil-water potential components are considered as the sum of the effects related to the components of matric, osmotic and gravitational potentials. The flow of liquid water due to electrical potential is not considered in this study. The total soil-water potential, ψ , can therefore be expressed as the sum of its components, given by:

$$\psi = \psi_m + \psi_\pi + \psi_g \quad (3.15)$$

where ψ_m stands for matric potential, ψ_π is osmotic potential and ψ_g is gravitational potential.

Matric potential can be described as the result of the combined effects of capillary and adsorptive potentials within the soil matrix (Philip, 1977; Derjaguin et al., 1987; Tuller et al., 1999; Baker and Frydman, 2009). Dominant mechanisms for these effects include (Or and Wraith, 2001):

- Capillarity caused by liquid-gas and liquid-solid-gas interface interacting within the irregular geometry of soil pores.
- Adhesion of water molecules to solid surfaces due to short-range London van der Waals forces and extension of these effects by cohesion through H bonds formed in the liquid.
- Ion hydration and binding of water in diffuse layers

The term matric suction or tension is commonly used instead of matric potential mainly because it is more convenient or intuitive to work with positive terms than negative values (Or and Wraith, 2001). The absolute value of the total matric potential can be assumed to be equal to the difference of water pressure and air pressure according to Sheng et al. (2008), and Baker and Frydman (2009) which is equivalent to the definition of matric suction (s). Fredlund and Rahardjo (1993) has defined a macroscopic definition for matric suction as the

difference between pore air pressure and pore liquid pressure. Accordingly matric suction is mathematically expressed as:

$$\psi_m = -s = u_l - u_a \quad (3.16)$$

Edlefsen and Anderson (1943) stated that in moist conditions where the effects of adsorptive forces on the free energy of soil system are negligible, the capillary potential is synonymous with free energy of the soil-water system. In this condition, the changes in free energy with temperature are caused by the variation of the surface tension of water with temperature (Edlefsen and Anderson, 1943; Fredlund and Rahardjo, 1993). Edlefsen and Anderson (1943) expressed that the surface energy is solely a function of temperature. Temperature dependency of surface tension of pure water (ξ) was given by Edlefsen and Anderson (1943) and Grant and Salehzadeh (1996) as:

$$\xi = a' + b'T \quad (3.17)$$

where a' is equal to $0.11766 \text{ (N.m}^{-1}\text{)}$ and b' is $0.0001535 \text{ (N.m}^{-1}\text{K}^{-1}\text{)}$ for pure water.

Phillip and de Vries (1957) stated that the change of soil-water potential is attributed to temperature impact on interfacial tension of pure water. Thus, for unsaturated soils, suction is dependent on the surface energy, which is in turn dependent on the absolute temperature. Therefore, suction at any moisture content and temperature can be obtained by the following relationship;

$$s = \frac{\xi}{\xi_r} s_r \quad (3.18)$$

where s_r and ξ_r are the suction and the surface energy at the reference temperature T_r , respectively. ξ is the surface energy at the actual temperature T .

It is noted that the application of the mentioned expression for dependency of suction to temperature is theoretically limited to the capillary component of matric soil-water potential or capillary suction. In the case of compacted clays, Romero et al. (2001) stated that simple dependency of suction on temperature based on surface tension can not solely explain the variation of suction with temperature of a compacted clay (Boom clay). It was suggested that at higher moisture values, the inter-aggregate porosity region presents a dominant capillary storage mechanism containing bulk water. At this level of suction or saturation, temperature

induced changes are mostly related to the changes in interfacial tension, thermal expansion of entrapped air, releasing air entrapped water. At low water contents, the majority of water is contained in the intra-aggregate porosity via adsorption storage mechanism of quasi-immobile water. The latter mechanism is therefore dependent on clay microstructure and pore fluid chemistry and temperature influence on chemical induced water adsorption potential (Zhang et al., 1993; Romero et al. 2001). The temperature dependency of soil-water potential or suction for compacted swelling clays will be discussed further in chapter 6.

The presence of dissolved solutes in soil water system can decrease the potential energy of water and the vapour pressure relative to the reference state (pure water) (Or and Wraith, 2001). All inorganic salts and many large organic molecules are osmotically active. Osmotically active solutes lower the potential energy of water in an *ideal membrane* (Or and Wraith, 2001). An ideal membrane completely restricts the passage of ions while *non-ideal membranes* do not restrict the passage of all the solutes present in the solvent as it passes the membrane. A non-ideal membrane's performance is reflected by osmotic efficiency or reflection coefficient.

Clays can act as a semi-permeable membrane, defined as the ability of a material to prevent the passage of a solute without affecting the passage of the solvent (Mitchell, 1993). The osmotic potential can be represented as a function of the chemical concentration, temperature, activity coefficient and osmotic efficiency or reflection coefficient as (e.g. Mitchell, 1993; Wu and Cheing, 1995):

$$\psi_{\pi} = -RT\omega_{\pi} \sum_{i=1}^{nc} \gamma_i c_d^i \quad (3.19)$$

where, R is universal gas constant, γ_i is the activity coefficient of the i^{th} chemical species in aqueous. In this equation the unit for chemical concentration is mol/l, and nc represents the total number of chemical components. ω_{π} denotes the osmotic efficiency coefficient or reflection coefficient of the soil. γ_i is the activity coefficient of the i^{th} chemical component.

For ideal membranes which restrict the passage of all charged solutes, ω_{π} is equal to 1; for porous media without membrane properties (e.g. sand), it is equal to zero. The value of osmotic efficiency depends on the clay properties, i.e. surface charge, exchangeable cation, porosity or density, mean pore water concentration, and temperature (Kharaka and Berry,

1973; Fritz, 1986). Mitchell (1993) reported the significance of osmotically driven water flow relative to hydraulically driven water flow in heavily over-consolidated clays and clay shale, where the void ratio is low and the hydraulic conductivity is also very low.

Gravitational potential is determined solely by the elevation of a point to some arbitrary reference point. When expressed as energy per unit weight, the gravitational potential is simply the vertical distance from a reference level to the point of interest (Or and Wraith, 2001) and it is given as:

$$\psi_g = \rho_l g z \quad (3.20)$$

where z is the elevation from the reference level and g is the gravitational constant.

In the case of compacted smectite clay soils, the organisation of the pore spaces and water in the system is an essential issue for studying the soil-water interaction and mechanism. For smectite type of expansive clays, mechanisms of water sorption and retention in the interlayer pores results from the adsorption term of matric potential. Beyond the interlayer water adsorption the effective mechanism in water uptake and retention stems from interactions described by the osmotic potential (Yong, 1999). The water adsorption in smectite clays is followed by developing air-water interface due the capillary term of matric potential. When the pore water exists as capillary water at relatively high degrees of saturation, the capillary effect is dominant in matric potential. When the pore water exists as adsorbed water films in the soil, the adsorptive mechanism becomes dominant in the matric potential (Romero and Vautat, 2002; Delage, 2002; Sheng et al., 2008; Baker and Frydman, 2009).

Fredlund and Raharadjo (1993) have shown that only the water pressure (u_l) potential should be used as the driving potential for the liquid water instead of matric potential, which includes the effects of both water and air pressure. In fact, the variation of the moisture due to the air pressure is reflected in the liquid transport through the dependency of soil water retention on matric suction. Following Fredlund and Raharadjo (1993) and by incorporating the gradient of total potential in terms of total water head, comprising water pressure head, osmotic head and gravitational head, the velocity of the liquid flux can be given as:

$$\mathbf{v}_l = -k_l \left(\frac{\nabla u_l}{\rho_l g} + \frac{\nabla \psi_\pi}{\rho_l g} + \nabla z \right) \quad (3.21)$$

The gradients of osmotic head can be presented as the head due to the dissolved chemical concentration gradients and temperature gradient:

$$\nabla \psi_{\pi} = \frac{\partial \psi_{\pi}}{\partial c_d^i} \nabla c_d^i + \frac{\partial \psi_{\pi}}{\partial T} \nabla T \quad (3.22)$$

Considering the dependency of activity coefficient on chemical concentration, the derivative of osmotic potential with respect to chemical concentration can be given as:

$$\frac{\partial \psi_{\pi}}{\partial c_d^i} = -RT \omega_{\pi} \gamma_i \left(1 + \frac{\partial \ln \gamma_i}{\partial \ln c_d^i} \right) \quad (3.23)$$

Variation of the activity coefficient in the range of normal temperature is almost negligible; therefore the derivative of osmotic potential with respect to temperature is obtained as:

$$\frac{\partial \psi_{\pi}}{\partial T} = R \omega_{\pi} \sum_{i=1}^{nc} \gamma_i c_d^i \quad (3.24)$$

Substituting the expanded forms of matric, osmotic and gravimetric potentials and the derivative of osmotic potential with respect to chemical concentration and temperature from equations (3.23) and (3.24), into equation (3.14), the general equation for flux of liquid in terms of primary variable is obtained as:

$$\mathbf{v}_l = -k_l \left[\frac{\nabla u_l}{\rho_l g} - \frac{RT \omega_{\pi}}{\rho_l g} \sum_{i=1}^{nc} \gamma_i \left(1 + \frac{\partial \ln \gamma_i}{\partial \ln c_d^i} \right) \nabla c_d^i - \left(\frac{R \omega_{\pi}}{\rho_l g} \sum_{i=1}^{nc} \gamma_i c_d^i \right) \nabla T + \nabla z \right] \quad (3.25)$$

In general, the hydraulic conductivity is influenced by a number of factors such as soil fabric, pore fluid characteristics, particle size and particle distribution, void ratio, and mineralogical composition (Yong and Warkentin, 1975; Mitchell, 1933). Degree of saturation and turbulence of flow are also known to affect the hydraulic conductivity. However, the turbulence of flow may be neglected, as flow is slow in clays.

Unsaturated hydraulic conductivity has been often expressed as a power function of the saturated conductivity, given as:

$$k_l = k_{sat} (S_l)^{\alpha} \quad (3.26)$$

where k_{sat} is the saturated hydraulic conductivity and α , is the power number.

The saturated hydraulic conductivity is itself a function of intrinsic hydraulic conductivity, K_I and viscosity of flowing fluid, μ_l as (Mitchell, 1993):

$$k_{sat} = \frac{K_I}{\mu_l} \quad (3.27)$$

Temperature variation influences the absolute viscosity. Kaye and Laby (1973) presented a relationship between the dynamic viscosity of liquid water and the absolute temperature valid in the range $273 < T < 373$ (K):

$$\mu_l = 661.2(T - 229)^{-1.562} \times 10^{-3} \pm 0.5\% \text{ (N.s.m}^{-2}\text{)} \quad (3.28)$$

3.3.2 Mechanisms of water vapour flow

As explained earlier, vapour transfer occurs as a result of two main mechanisms, namely; diffusive and pressure flows. The bulk air is considered to be a binary mixture of water vapour and dry air (Pollock, 1986) and is dealt with via a generalised Darcy's law, following the approach of a number of researchers (Carman, 1956; Alonso et al., 1988). Diffusive flow is described by the theory proposed by Philip and de Vries (1957), for diffusive vapour flow in unsaturated soil.

For small scale problems, Fredlund and Rahardjo, (1993) found that the elevation gradient or gravitational potential has a negligible effect on air transfer. Therefore, the pressure gradient is usually considered to be the only driving potential for air transfer. The rate of flow of air in unsaturated soil can be defined incorporating Darcy's law as:

$$\mathbf{v}_a = -k_a \nabla u_a \quad (3.29)$$

where k_a is the unsaturated conductivity of pore air. The unsaturated conductivity of gases in soil is a function of the pore air properties and volume/mass of soil. As the properties of air are generally assumed to be constant during the flow process, the volume/mass properties control the air conductivity (Olson, 1963). In this study the volume/mass properties chosen are void ratio and degree of pore air saturation; given as:

$$k_a = k_a(e, S_a) \quad (3.30)$$

$$\nabla \rho_0 = \frac{\partial \rho_0}{\partial T} \nabla T \quad (3.40)$$

Since the relative humidity due to matric potential is dependent on both temperature and matric potential, i.e. suction; the gradient of h_m may be expressed as:

$$\nabla h_m = \frac{\partial h_m}{\partial s} \nabla u_a - \frac{\partial h_m}{\partial s} \nabla u_l + \frac{\partial h_m}{\partial T} \nabla T \quad (3.41)$$

Similarly, the relative humidity due to osmotic potential is dependent on both temperature and dissolved chemical concentration. Therefore, the gradient of h_π is expressed as:

$$\nabla h_\pi = \sum_{i=1}^{nc} \frac{\partial h_\pi}{\partial c_d^i} \nabla c_d^i + \frac{\partial h_\pi}{\partial T} \nabla T \quad (3.42)$$

Substituting the components of the gradient of water vapour density in equation (3.39) with equations (3.40), (3.41) and (3.42), yields:

$$\nabla \rho_v = \left\{ \begin{array}{l} h_m h_\pi \left[\frac{\partial \rho_0}{\partial T} \nabla T \right] + \rho_0 h_\pi \left[\frac{\partial h_m}{\partial s} \nabla u_a - \frac{\partial h_m}{\partial s} \nabla u_l + \frac{\partial h_m}{\partial T} \nabla T \right] \\ + \rho_0 h_m \left[\sum_{i=1}^{nc} \frac{\partial h_\pi}{\partial c_d^i} \nabla c_d^i + \frac{\partial h_\pi}{\partial T} \nabla T \right] \end{array} \right\} \quad (3.43)$$

Grouping similar terms, gives:

$$\nabla \rho_v = \left\{ \begin{array}{l} \left[-\rho_0 h_\pi \frac{\partial h_m}{\partial s} \right] \nabla u_l + \left[\rho_0 h_\pi \frac{\partial h_m}{\partial s} \right] \nabla u_a \\ + \left[h_m h_\pi \frac{\partial \rho_0}{\partial T} + \rho_0 h_\pi \frac{\partial h_m}{\partial T} + \rho_0 h_m \frac{\partial h_\pi}{\partial T} \right] \nabla T + \sum_{i=1}^{nc} \left[\rho_0 h_m \frac{\partial h_\pi}{\partial c_d^i} \right] \nabla c_d^i \end{array} \right\} \quad (3.44)$$

Similarly, the temporal derivative of water vapour density can be given as:

$$\frac{\partial \rho_v}{\partial t} = \left\{ \begin{array}{l} \left[-\rho_0 h_\pi \frac{\partial h_m}{\partial s} \right] \frac{\partial u_l}{\partial t} + \left[\rho_0 h_\pi \frac{\partial h_m}{\partial s} \right] \frac{\partial u_a}{\partial t} \\ + \left[h_m h_\pi \frac{\partial \rho_0}{\partial T} + \rho_0 h_\pi \frac{\partial h_m}{\partial T} + \rho_0 h_m \frac{\partial h_\pi}{\partial T} \right] \frac{\partial T}{\partial t} + \sum_{i=1}^{nc} \left[\rho_0 h_m \frac{\partial h_\pi}{\partial c_d^i} \right] \frac{\partial c_d^i}{\partial t} \end{array} \right\} \quad (3.45)$$

The velocity of water vapour is obtained by substitution of the gradient of water vapour density from equation (3.44) into equation (3.31):

$$\mathbf{v}_v = \left\{ \begin{array}{l} \left[\frac{D_{atms} v_v \tau_v \theta_a}{\rho_l} \rho_0 h_\pi \frac{\partial h_m}{\partial s} \right] \nabla u_l - \left[\frac{D_{atms} v_v \tau_v \theta_a}{\rho_l} \rho_0 h_\pi \frac{\partial h_m}{\partial s} \right] \nabla u_a \\ - \left[\frac{D_{atms} v_v \tau_v \theta_a}{\rho_l} \left(h_m h_\pi \frac{\partial \rho_0}{\partial T} + \rho_0 h_m \frac{\partial h_\pi}{\partial T} + \rho_0 h_\pi \frac{\partial h_m}{\partial T} \right) \right] \nabla T \\ - \sum_{i=1}^{nc} \frac{D_{atms} v_v \tau_v \theta_a}{\rho_l} \rho_0 h_m \frac{\partial h_\pi}{\partial c_d^i} \nabla c_d^i \end{array} \right\} \quad (3.46)$$

Experimental work carried out by Philip and de Vries (1957) suggested that the theory defined in equation (3.46) was not fully valid at increased temperature gradients. They proposed two refinements to the thermal gradient term. Firstly a flow area factor, f , was included to achieve a reduction of the vapour flow as the available flow area decreased at higher moisture contents. Secondly a microscopic pore temperature gradient factor $\frac{(\nabla T)_a}{\nabla T}$, was introduced, which is the ratio of the average temperature gradient in the air filled pores to the overall temperature gradient. This factor takes into account the microscopic effect of heat flow paths being shared between sections of solid and fluid paths, giving rise to microscopic temperature gradients in the fluid filled pores, which may be much higher than the macroscopic temperature gradients across the sample as a whole. Including these two amendments into equation (3.46) yields:

$$\mathbf{v}_v = \left\{ \begin{array}{l} \left[\frac{D_{atms} v_v \tau_v \theta_a}{\rho_l} \rho_0 h_\pi \frac{\partial h_m}{\partial s} \right] \nabla u_l - \left[\frac{D_{atms} v_v \tau_v \theta_a}{\rho_l} \rho_0 h_\pi \frac{\partial h_m}{\partial s} \right] \nabla u_a \\ - \left[\frac{D_{atms} v_v}{\rho_l} f \frac{(\nabla T)_a}{\nabla T} \left(h_m h_\pi \frac{\partial \rho_0}{\partial T} + \rho_0 h_m \frac{\partial h_\pi}{\partial T} + \rho_0 h_\pi \frac{\partial h_m}{\partial T} \right) \right] \nabla T \\ - \sum_{i=1}^{nc} \frac{D_{atms} v_v \tau_v \theta_a}{\rho_l} \rho_0 h_m \frac{\partial h_\pi}{\partial c_d^i} \nabla c_d^i \end{array} \right\} \quad (3.47)$$

Preece (1975) proposed an expression to evaluate the microscopic pore temperature gradient factor, based on a proposed geometrical method (de Vries, 1966). This expression was developed for a sand soil as:

$$\frac{(\nabla T)_a}{\nabla T} = \frac{1}{3} \left[\frac{2}{1 + BG_v} + \frac{1}{1 + B(1 - 2G_v)} \right] \quad (3.48)$$

where,

$$B = \frac{(\lambda_a + \lambda_v)}{\lambda_l} - 1 \quad (3.49)$$

and;

$$G_v = \begin{cases} 0.3333 - 0.325 \times \left(\frac{n - \theta_l}{n} \right) & 0.09 < \theta_l < n \\ 0.0033 + 11.11 \times \left(0.33 - 0.325 \frac{n - 0.09}{n} \right) \theta_l & 0 < \theta_l < 0.09 \end{cases} \quad (3.50)$$

λ_a is the thermal conductivity of pore air, λ_l is the thermal conductivity of pore liquid and λ_v is the thermal conductivity of pore vapour, which can be defined as:

$$\lambda_v = D_{atms} v_v h L \frac{\partial \rho_0}{\partial t} \quad (3.51)$$

where L is the latent heat of vaporisation.

Campbell (1985) represented an expression to evaluate the microscopic temperature gradient factor for clay soils as a function of volumetric water content and clay fraction (f_c) (Wu and Cheing, 1995):

$$\frac{(\nabla T)_a}{\nabla T} = 9.5 + 6.0\theta_l - 8.5 \exp\left\{-\left[(1 - 2.6f_c^{-0.5})\theta_l\right]^4\right\} \quad (3.52)$$

Ewen and Thomas (1989) suggested two alterations to the extended vapour velocity equation proposed by Philip and de Vries (1957). They suggested that the vapour flow area factor should be presented in both temperature and moisture gradients terms. They also suggested that the form of flow area factor needs to be modified and considered to be equal to the porosity. Adopting these suggestions in the present work, vapour velocity can be written as:

$$\mathbf{v}_v = \left\{ \begin{aligned} & \left[\frac{D_{atms} v_v \tau_v \theta_a}{\rho_l} \rho_0 h_\pi \frac{\partial h_m}{\partial s} \right] \nabla u_l - \left[\frac{D_{atms} v_v \tau_v \theta_a}{\rho_l} \rho_0 h_\pi \frac{\partial h_m}{\partial s} \right] \nabla u_a \\ & - \left[\frac{D_{atms} v_v}{\rho_l} f \frac{(\nabla T)_a}{\nabla T} \left(h_m h_\pi \frac{\partial \rho_0}{\partial T} + \rho_0 h_m \frac{\partial h_\pi}{\partial T} + \rho_0 h_\pi \frac{\partial h_m}{\partial T} \right) \right] \nabla T \\ & - \sum_{i=1}^{nc} \frac{D_{atms} v_v \tau_v \theta_a}{\rho_l} \rho_0 h_m \frac{\partial h_\pi}{\partial c_d^i} \nabla c_d^i \end{aligned} \right\} \quad (3.53)$$

An experimental and numerical study conducted by Singh (2007) into vapour flow in high-density clays under temperature and hydraulic gradients. It was proposed by Singh (2007) that

additional modification factors are required to the vapour flow factors. Including the proposed empirical correction factors suggested by Singh (2007), the equation can then be expressed as:

$$\mathbf{v}_v = \left\{ \begin{array}{l} \left[\eta_2 \frac{D_{atms} v_v n}{\rho_l} \rho_0 h_x \frac{\partial h_m}{\partial s} \right] \nabla u_l + \left[-\eta_2 \frac{D_{atms} v_v n}{\rho_l} \rho_0 h_x \frac{\partial h_m}{\partial s} \right] \nabla u_a \\ + \left[-\eta_1 \frac{D_{atms} v_v n}{\rho_l} \frac{(\nabla T)_a}{\nabla T} \left(h_m h_x \frac{\partial \rho_0}{\partial T} + \rho_0 h_m \frac{\partial h_x}{\partial T} + \rho_0 h_x \frac{\partial h_m}{\partial T} \right) \right] \nabla T \\ + \sum_{i=1}^{nc} -\eta_2 \frac{D_{atms} v_v n}{\rho_l} \rho_0 h_m \frac{\partial h_x}{\partial c_d^i} \nabla c_d^i \end{array} \right\} \quad (3.54)$$

where η_1 and η_2 are material dependent factors. For MX-80 bentonite these were initially predicted to be 0.17 and 0.60 respectively. However, it was concluded by Singh (2007) that both further experimental and numerical work is required to characterise the behaviour of high-density clays. The form of the vapour flow factor, especially, may need to be re-evaluated as a consequence of such work. It is acknowledged that the application of this approach requires further research and development when considering the movement of vapour in cohesive soils, especially in compacted swelling clays.

3.3.3 Governing differential equation for moisture flow

The components of flow for the liquid and vapour were defined in the previous sections. The governing equations for flow are now included in the equation of mass conservation for moisture flow, i.e. equation (3.13) and expanded in terms of its primary variables.

The first two terms of equation (3.11) can be expanded, which leads to the following expression:

$$\begin{aligned} e(\rho_l - \rho_v) \frac{\partial S_l}{\partial t} + e(1 - S_l) \frac{\partial \rho_v}{\partial t} + [\rho_l S_l + \rho_v (1 - S_l)] \frac{\partial e}{\partial t} = \\ - \rho_l (1 + e) \nabla \cdot \mathbf{v}_l - \rho_l (1 + e) \nabla \cdot \mathbf{v}_v - (1 + e) \nabla \cdot (\rho_v \mathbf{v}_a) \end{aligned} \quad (3.55)$$

Dividing equation by $(1 + e)$ and replacing $e/(1 + e)$ by n yields:

$$\begin{aligned} n(\rho_l - \rho_v) \frac{\partial S_l}{\partial t} + n(1 - S_l) \frac{\partial \rho_v}{\partial t} + [\rho_l S_l + \rho_v (1 - S_l)] \frac{\partial e}{(1 + e) \partial t} = \\ - \rho_l \nabla \cdot \mathbf{v}_l - \rho_l \nabla \cdot \mathbf{v}_v - \nabla \cdot (\rho_v \mathbf{v}_a) \end{aligned} \quad (3.56)$$

Considering the third term, it can be shown that:

$$\frac{\partial e}{(1+e)\partial t} = \frac{\partial \varepsilon_v}{\partial t} \quad (3.57)$$

where ε_v is the volumetric strain which by definition is the rate of change of void ratio with respect to initial volume. Substituting this term into equation (3.56) gives:

$$\begin{aligned} n(\rho_l - \rho_v) \frac{\partial S_l}{\partial t} + n(1 - S_l) \frac{\partial \rho_v}{\partial t} + [\rho_l S_l + \rho_v (1 - S_l)] \frac{\partial \varepsilon_v}{\partial t} = \\ - \rho_l \nabla \cdot \mathbf{v}_l - \rho_l \nabla \cdot \mathbf{v}_v - \nabla \cdot (\rho_v \mathbf{v}_a) \end{aligned} \quad (3.58)$$

Matyas and Radhakrishna (1968) proposed that the degree of liquid saturation is a function of the initial void ratio, the initial degree of liquid saturation, and the stress parameters, namely; net stress, deviatoric stress, and suction. However, Alonso et al. (1988) found the influence of stress on the degree of saturation to be relatively insignificant. The absolute value of total matric potential can be assumed to be equal to the difference of water pressure and air pressure, i.e. matric suction according to Sheng et al. (2008) and Baker and Frydman (2009). Experimental study of Thyagaraj and Rao (2010) has shown that the osmotic suction affects the water content/void ratio of compacted clays during the wetting path and its role therefore might become important in determination of matric suction from the soil water characteristic curve. However, the osmotic effects are neglected in soil water characteristic behaviour in this formulation. In other words, it is assumed that the osmotic potential might only affect the rate of moisture transport, not the equilibrium condition of water. It is noted that the effects of gravitational potentials is ignored due to the negligible effects in compacted fine soils on the variation of degree of saturation with total suction.

If the initial void ratio of a soil sample is controlled and the sample is remained confined the variation of degree of saturation can be expressed as a function of total suction, i.e.:

$$S_l = S_l(s) \quad (3.59)$$

Based on equation (3.18), matric suction is also dependent on temperature. Therefore, temporal derivative of the degree of saturation can be expressed in terms of partial derivatives with respect to the primary variables as:

$$\frac{\partial S_l}{\partial t} = \frac{\partial S_l}{\partial s} \frac{\partial u_a}{\partial t} - \frac{\partial S_l}{\partial s} \frac{\partial u_l}{\partial t} + \left(\frac{\partial S_l}{\partial s} \frac{\partial s}{\partial T} \right) \frac{\partial T}{\partial t} \quad (3.60)$$

The first term in the left side of equation (3.58) can be expressed, with appropriate substitution from equation (3.60), as:

$$n(\rho_l - \rho_v) \frac{\partial S_l}{\partial t} = \left\{ -n(\rho_l - \rho_v) \frac{\partial S_l}{\partial s} \frac{\partial u_l}{\partial t} + n(\rho_l - \rho_v) \left(\frac{\partial S_l}{\partial s} \frac{\partial s}{\partial T} \right) \frac{\partial T}{\partial t} + n(\rho_l - \rho_v) \frac{\partial S_l}{\partial s} \frac{\partial u_a}{\partial t} \right\} \quad (3.61)$$

With substitution from equation (3.45) the second term of the left side of equation (3.58) can also be expressed as:

$$n(1 - S_l) \frac{\partial \rho_v}{\partial t} = \left\{ n(1 - S_l) \left[-\rho_0 h_x \frac{\partial h_m}{\partial s} \right] \frac{\partial u_l}{\partial t} + n(1 - S_l) \left[h_m h_x \frac{\partial \rho_0}{\partial T} + \rho_0 h_x \frac{\partial h_m}{\partial T} + \rho_0 h_m \frac{\partial h_x}{\partial T} \right] \frac{\partial T}{\partial t} \right. \\ \left. + n(1 - S_l) \left[\rho_0 h_x \frac{\partial h_m}{\partial s} \right] \frac{\partial u_a}{\partial t} + n(1 - S_l) \sum_{i=1}^{nc} \rho_0 h_m \frac{\partial h_x}{\partial c_d^i} \frac{\partial c_d^i}{\partial t} \right\} \quad (3.62)$$

It can be shown that:

$$\frac{\partial \varepsilon_v}{\partial t} = (1 + e) \frac{\partial n}{\partial t} = \mathbf{m}^T \frac{\partial \varepsilon}{\partial t} = \mathbf{m}^T \mathbf{P} \frac{\partial \mathbf{u}}{\partial t} \quad (3.63)$$

where ε_v is the volumetric strain and ε is the strain vector. The strain matrix \mathbf{P} and the differential operator \mathbf{m}^T will be defined in section 3.7. The third term of equation can therefore be expressed as:

$$[\rho_l S_l + \rho_v (1 - S_l)] \frac{\partial \varepsilon_v}{\partial t} = [\rho_l S_l + \rho_v (1 - S_l)] \mathbf{m}^T \mathbf{P} \frac{\partial \mathbf{u}}{\partial t} \quad (3.64)$$

Substituting \mathbf{v}_l , \mathbf{v}_a and \mathbf{v}_v from equations (3.25), (3.29) and (3.46), respectively into the right side of the governing equation for moisture transport, with some re-arrangements of similar items, the right side of equation (3.55) can be presented as:

$$\begin{aligned}
& -\rho_l \nabla \mathbf{v}_l - \rho_v \nabla \mathbf{v}_v - \nabla \rho_v \mathbf{v}_a = \\
& -\nabla \cdot \left\{ \begin{aligned} & \left[-\frac{k_l}{g} + D_{a\text{ims}} \nu_v n \rho_0 h_\pi \frac{\partial h_m}{\partial s} \right] \nabla u_l + \left[-\rho_v k_a - D_{a\text{ims}} \nu_v n \rho_0 h_\pi \frac{\partial h_m}{\partial s} \right] \nabla u_a \\ & + \left[-D_{a\text{ims}} \nu_v n \frac{(\nabla T)_a}{\nabla T} \left(h_m h_\pi \frac{\partial \rho_0}{\partial T} + \rho_0 h_m \frac{\partial h_\pi}{\partial T} + \rho_0 h_\pi \frac{\partial h_m}{\partial T} \right) + \sum_{i=1}^{nc} \frac{k_l R \omega_\pi}{g} \gamma_i c_d^i \right] \nabla T \\ & + \sum_{i=1}^{nc} \left[\frac{k_l R T \omega_\pi}{g} \gamma_i \left(1 + \frac{\partial \ln \gamma_i}{\partial \ln c_d^i} \right) - D_{a\text{ims}} \nu_v n \rho_0 h_m \frac{\partial h_\pi}{\partial c_d^i} \right] \nabla c_d^i - \rho_l k_l \nabla z \end{aligned} \right\} \quad (3.65)
\end{aligned}$$

Finally, the governing equation of moisture flow can be represented in a simplified form as:

$$\begin{aligned}
& C_{ll} \frac{\partial u_l}{\partial t} + C_{lT} \frac{\partial T}{\partial t} + C_{la} \frac{\partial u_a}{\partial t} + \sum_{i=1}^{nc} C_{lc_d^i} \frac{\partial c_d^i}{\partial t} + C_{lu} \frac{\partial \mathbf{u}}{\partial t} \\
& = \nabla \cdot [K_{ll} \nabla u_l] + \nabla \cdot [K_{lT} \nabla T] + \nabla \cdot [K_{la} \nabla u_a] + \nabla \cdot \left[\sum_{i=1}^{nc} K_{lc_d^i} \nabla c_d^i \right] + J_l \quad (3.66)
\end{aligned}$$

where:

$$C_{ll} = -n(\rho_l - \rho_v) \frac{\partial S_l}{\partial s} - n(1 - S_l) \rho_0 h_\pi \frac{\partial h_m}{\partial s} \quad (3.67)$$

$$C_{lT} = n(\rho_l - \rho_v) \frac{\partial S_l}{\partial T} + n(1 - S_l) \left(h_m h_\pi \frac{\partial \rho_0}{\partial T} + \rho_0 h_\pi \frac{\partial h_m}{\partial T} + \rho_0 h_m \frac{\partial h_\pi}{\partial T} \right) \quad (3.68)$$

$$C_{la} = n(\rho_l - \rho_v) \frac{\partial S_l}{\partial s} + n(1 - S_l) \rho_0 h_\pi \frac{\partial h_m}{\partial s} \quad (3.69)$$

$$C_{lc_d^i} = n(1 - S_l) \rho_0 h_m \frac{\partial h_\pi}{\partial c_d^i} \quad (3.70)$$

$$C_{lu} = [S_l \rho_l + (1 - S_l) \rho_v] \mathbf{m}^T \mathbf{P} \quad (3.71)$$

$$K_{ll} = \frac{k_l}{g} - D_{a\text{ims}} \nu_v n \rho_0 h_\pi \frac{\partial h_m}{\partial s} \quad (3.72)$$

$$K_{lT} = D_{a\text{ims}} \nu_v n \frac{(\nabla T)_a}{\nabla T} \left(h_m h_\pi \frac{\partial \rho_0}{\partial T} + \rho_0 h_m \frac{\partial h_\pi}{\partial T} + \rho_0 h_\pi \frac{\partial h_m}{\partial T} \right) - \sum_{i=1}^{nc} \frac{k_l R \omega_\pi}{g} \gamma_i c_d^i \quad (3.73)$$

$$K_{la} = \rho_v k_a + D_{a\text{ims}} \nu_v n \rho_0 h_\pi \frac{\partial h_m}{\partial s} \quad (3.74)$$

$$K_{k_d} = -\frac{k_l RT \omega_\pi}{g} \gamma_i \left(1 + \frac{\partial \ln \gamma_i}{\partial \ln c_d^i} \right) + D_{atms} v_v n \rho_0 h_m \frac{\partial h_\pi}{\partial c_d^i} \quad (3.75)$$

$$J_i = \nabla \cdot (-\rho_i k_i \nabla z) \quad (3.76)$$

3.4 Dry air transfer

Dry air can be considered to consist of two forms in unsaturated soil, i.e. bulk air and dissolved air, (Rodebush and Busswell, 1958). The gradient of air pressure drives the transfer of bulk air. The bulk air flow can be determined by the use of Darcy's law. The flow of dissolved air is also considered as advective flow within the pore liquid. Henry's law is used to define the proportion of dry air contained in the pore liquid.

The general law of conservation of mass dictates that the temporal derivative of the dry air content is equal to the spatial derivative of the dry air flux. Mathematically this can be expressed as:

$$\frac{\partial}{\partial t} [(\theta_a + H_s \theta_l) \rho_{da} \delta V] = -\delta V \nabla \cdot [\rho_{da} (\mathbf{v}_a + H_s \mathbf{v}_l)] \quad (3.77)$$

where H_s is Henry's volumetric coefficient of solubility and ρ_{da} is the density of dry air.

Substituting equations (3.5) and (3.10) into equation (3.77) yields the mass conservation equation in terms of degree of saturation, porosity and void ratio:

$$\frac{\partial}{\partial t} [(S_a + H_s S_l) \rho_{da} n(1+e) \delta V_s] = -(1+e) \delta V_s \nabla \cdot [\rho_{da} (\mathbf{v}_a + H_s \mathbf{v}_l)] \quad (3.78)$$

As stated previously, since δV_s is constant, this term can be eliminated from equation (3.78).

Substituting $n(1+e) = e$ and $S_a = 1 - S_l$, yields:

$$\frac{\partial}{\partial t} [(1 - S_l + H_s S_l) \rho_{da} e] = -(1+e) \nabla \cdot [\rho_{da} (\mathbf{v}_a + H_s \mathbf{v}_l)] \quad (3.79)$$

Expanding the first term of equation (3.79) gives:

$$\begin{aligned} \frac{\partial}{\partial t} [(1 - S_l + H_s S_l) \rho_{da} e] = \\ \rho_{da} (1 - S_l + H_s S_l) \frac{\partial e}{\partial t} + e(1 - S_l + H_s S_l) \frac{\partial \rho_{da}}{\partial t} - e \rho_{da} \frac{\partial S_l}{\partial t} + e \rho_{da} H_s \frac{\partial S_l}{\partial t} \end{aligned} \quad (3.80)$$

Grouping similar terms yields:

$$\begin{aligned} \frac{\partial}{\partial t} (1 - S_l + H_s S_l) \rho_{da} e = \\ \rho_{da} (1 - S_l + H_s S_l) \frac{\partial e}{\partial t} + e (1 - S_l + H_s S_l) \frac{\partial \rho_{da}}{\partial t} + e \rho_{da} (H_s - 1) \frac{\partial S_l}{\partial t} \end{aligned} \quad (3.81)$$

Substituting equation (3.12) into equation (3.81) and dividing the resultant equation by $(1+e)$ whilst replacing $e/(1+e)$ by n yields:

$$\begin{aligned} \rho_{da} \frac{(1 - S_l + H_s S_l)}{(1 + e)} \frac{\partial e}{\partial t} + n (1 - S_l + H_s S_l) \frac{\partial \rho_{da}}{\partial t} + n \rho_{da} (H_s - 1) \frac{\partial S_l}{\partial t} = \\ - \nabla \cdot [\rho_{da} (\mathbf{v}_s + H_s \mathbf{v}_l)] \end{aligned} \quad (3.82)$$

Substituting equations (3.57) and (3.63) into equation (3.82) yields:

$$\begin{aligned} \rho_{da} (1 - S_l + H_s S_l) \mathbf{m}^T \mathbf{P} \frac{\partial \mathbf{u}}{\partial t} + n (1 - S_l + H_s S_l) \frac{\partial \rho_{da}}{\partial t} + n \rho_{da} (H_s - 1) \frac{\partial S_l}{\partial t} = \\ - \nabla \cdot [\rho_{da} (\mathbf{v}_s + H_s \mathbf{v}_l)] \end{aligned} \quad (3.83)$$

Following the approach proposed by Thomas and Samson (1995), the density of dry air, i.e. ρ_{da} , is determined. As stated previously, the air phase in soils is considered to be a mixture of dry air and water vapour. It has been found that the behaviour of this mixture obeys the laws of a mixture of ideal gases to a sufficient degree of accuracy (Geraminegad and Saxena, 1986). The partial pressures of dry air and vapour can be expressed as:

$$u_{da} = \rho_{da} R_{da} T \quad (3.84)$$

and,

$$u_v = \rho_v R_v T \quad (3.85)$$

where R_v and R_{da} are the specific gas constants of vapour and dry air respectively.

Partial pressure of air can be given by applying Dalton's law of partial pressures:

$$u_a = u_{da} + u_v \quad (3.86)$$

To determine the dry air density, equations (3.85) and (3.86) are substituted into equation (3.84) that yields:

$$\rho_{da} = \frac{u_a}{R_{da} T} - \frac{\rho_v R_v}{R_{da}} \quad (3.87)$$

The partial derivative of equation (3.87) with respect to time can be expressed as follows:

$$\frac{\partial \rho_{da}}{\partial t} = \frac{1}{R_{da} T} \frac{\partial u_a}{\partial t} - \frac{\rho_a}{T^2} \frac{\partial T}{\partial t} - \frac{R_v}{R_{da}} \frac{\partial \rho_v}{\partial t} \quad (3.88)$$

It is noted that the last differential term can be obtained from equation (3.45).

Substituting for the time derivative terms of degree of saturation from equation (3.60) and density of dry air from equation (3.87), velocity of pore liquid and pore air from equations (3.25) and (3.29), respectively leads to the governing equation for air transfer in terms of primary variables. The governing equation for air transfer is therefore given as:

$$\begin{aligned} C_{al} \frac{\partial u_l}{\partial t} + C_{aT} \frac{\partial T}{\partial t} + C_{aa} \frac{\partial u_a}{\partial t} + \sum_{i=1}^{nc} C_{ac_d} \frac{\partial c_d^i}{\partial t} + C_{au} \frac{\partial \mathbf{u}}{\partial t} \\ = \nabla \cdot [K_{al} \nabla u_l] + \nabla \cdot [K_{aT} \nabla T] + \nabla \cdot [K_{aa} \nabla u_a] + \nabla \cdot \left[\sum_{i=1}^{nc} K_{ac_d} \nabla c_d^i \right] + J_a \end{aligned} \quad (3.89)$$

where;

$$C_{al} = -n \rho_{da} (H_s - 1) \frac{\partial S_l}{\partial s} + n (S_a + H_s S_l) \frac{R_v}{R_{da}} \left(\rho_0 h_\pi \frac{\partial h_m}{\partial s} \right) \quad (3.90)$$

$$\begin{aligned} C_{aT} = -n \rho_{da} (H_s - 1) \frac{\partial S_l}{\partial s} \\ + n (S_a + H_s S_l) \left[\frac{\rho_a}{T} - \frac{R_v}{R_{da}} \left(\rho_0 h_\pi \frac{\partial h_m}{\partial s} + \rho_0 h_m \frac{\partial h_\pi}{\partial s} + h_m h_\pi \frac{\partial \rho_0}{\partial s} \right) \right] \end{aligned} \quad (3.91)$$

$$C_{aa} = n \rho_{da} (H_s - 1) \frac{\partial S_l}{\partial s} + n (S_a + H_s S_l) \left(\frac{1}{R_{da} T} - \frac{R_v}{R_{da}} \rho_0 h_\pi \frac{\partial h_m}{\partial s} \right) \quad (3.92)$$

$$C_{ac_d} = n (S_a + H_s S_l) \left(-\frac{R_v}{R_{da}} \rho_0 h_m \frac{\partial h_\pi}{\partial s} \right) \quad (3.93)$$

$$C_{au} = [S_l \rho_l + (1 - S_l) \rho_v] \mathbf{m}^T \mathbf{P} \quad (3.94)$$

$$K_{al} = \frac{\rho_{da} H_s}{\gamma_l} k_l \quad (3.95)$$

$$K_{aT} = -\rho_{da} H_s \frac{R\omega_\pi}{\gamma_l} \sum_{i=1}^{nc} \gamma_i c_d^i \quad (3.96)$$

$$K_{aa} = \rho_{da} k_a - \frac{\rho_{da} H_s}{\gamma_l} k_l \quad (3.97)$$

$$K_{ac_d} = -\rho_{da} H_s \frac{R\omega_\pi}{\gamma_l} \gamma_i c_d^i \left(1 + \frac{\partial \ln \gamma_i}{\partial \ln c_d^i} \right) \quad (3.98)$$

$$J_a = \nabla \cdot (-\rho_{da} H_s k_l \nabla z) \quad (3.99)$$

3.5 Heat transfer

Heat transfer is widely regarded to occur via three mechanisms namely conduction, convection and radiation (Jakob, 1949). Heat transfer is also found to occur due to chemical concentration gradients, i.e. Dufour effect which has not been found to be of significance in soils (Mitchell, 1993). Therefore, Dufour effect is ignored in this study. The heat transfer due to radiation mechanism is also ignored, as its influence is assumed to be negligible. The effect of latent heat of vaporisation is included.

The law of conservation of energy is applied to form the general equation of heat transfer. The law of conservation of energy for heat flow dictates that the temporal derivative of the heat content, Ω , is equal to the spatial derivative of the heat flux, Q . This may be expressed as:

$$\frac{\partial(\Omega \delta V)}{\partial t} = -\nabla \cdot (\delta V Q) \quad (3.100)$$

The heat content of unsaturated soil per unit volume, i.e. Ω , is assumed to be the sum of soil heat storage capacity (H_c) and the contribution resulting from the latent heat of vaporisation (L). It therefore can be defined as:

$$\Omega = H_c (T - T_r) + LnS_a \rho_v \quad (3.101)$$

where T_r denotes the reference absolute temperature. L is the latent heat of vaporisation.

Following the approach presented by Ewen and Thomas (1989) the heat capacity of unsaturated soil, H_c , at reference absolute temperature, T_r , may be defined as:

$$H_c = (1-n)C_{ps}\rho_s + n(C_{pl}S_l\rho_l + C_{pv}S_a\rho_v + C_{pda}S_a\rho_{da}) \quad (3.102)$$

where C_{ps} , C_{pl} , C_{pv} , and C_{pda} are the specific heat capacities of solid particles, liquid, vapour, and dry air respectively and ρ_s is the density of solid particles.

Following Thomas and He (1995), three modes of heat transfer are considered: thermal conduction obeying Fourier's law, convection of heat associated with liquid and vapour flow, and latent heat flow. The heat flux per unit area, Q , is determined therefore as:

$$Q = -\lambda_r \nabla T + L(\mathbf{v}_v \rho_l + \mathbf{v}_a \rho_v) + (C_{pl} \mathbf{v}_l \rho_l + C_{pv} \mathbf{v}_v \rho_l + C_{pv} \mathbf{v}_a \rho_v + C_{pda} \mathbf{v}_a \rho_{da})(T - T_r) \quad (3.103)$$

where λ_T is the coefficient of thermal conductivity of unsaturated soil. The coefficient of thermal conductivity of unsaturated soil has been found to be a function of degree of saturation, following Thomas and King (1991) it can be given as:

$$\lambda_T = \lambda_T(S_l) \quad (3.104)$$

The first term in equation (3.103) reflects the transfer of heat due to conduction. The second term reflects latent heat flow with vapour movement. Heat convection is considered in the third term comprising components of movements due to liquid phase, vapour phase associated with a vapour pressure gradient, vapour phase associated with the bulk flow of air, and the air phase. Substituting heat content, Ω , from equation (3.102) and heat flux, Q from equation (3.103) into equation (3.100) yields:

$$\begin{aligned} \frac{\partial}{\partial t} [(H_c(T - T_r) + LnS_a\rho_v)\delta V] = \\ -\nabla \cdot \left\{ \left[-\lambda_T \nabla T + L(\mathbf{v}_v \rho_l + \mathbf{v}_a \rho_v) + \right. \right. \\ \left. \left. (C_{pl} \mathbf{v}_l \rho_l + C_{pv} \mathbf{v}_v \rho_l + C_{pv} \mathbf{v}_a \rho_v + C_{pda} \mathbf{v}_a \rho_{da})(T - T_r) \right] \delta V \right\} \end{aligned} \quad (3.105)$$

Substituting equation (3.10) into equation (3.105), and cancelling the term δV , yields:

$$\begin{aligned} \frac{\partial}{\partial t} [H_c(T - T_r)(1 + e)] + \frac{\partial}{\partial t} [LnS_a\rho_v(1 + e)] = \\ -\nabla \cdot \left\{ \left[-\lambda_T \nabla T + L(\mathbf{v}_v \rho_l + \mathbf{v}_a \rho_v) + \right. \right. \\ \left. \left. (C_{pl} \mathbf{v}_l \rho_l + C_{pv} \mathbf{v}_v \rho_l + C_{pv} \mathbf{v}_a \rho_v + C_{pda} \mathbf{v}_a \rho_{da})(T - T_r) \right] (1 + e) \right\} \end{aligned} \quad (3.106)$$

The first term of the left hand side of equation (3.106) can be expanded further which yields:

$$\frac{\partial}{\partial t} [H_c(T - T_r)(1 + e)] = H_c(1 + e) \frac{\partial T}{\partial t} + (T - T_r) \frac{\partial}{\partial t} [H_c(1 + e)] \quad (3.107)$$

Considering the second term of equation (3.107) with substitution from equation (3.102) and rearranging the terms gives:

$$\begin{aligned} \frac{\partial}{\partial t} [H_c(T - T_r)(1 + e)] = + H_c(1 + e) \frac{\partial T}{\partial t} + \\ (T - T_r) \frac{\partial}{\partial t} [C_{ps} \rho_s + n(-C_{ps} \rho_s + C_{pl} S_l \rho_l + C_{pv} S_a \rho_v + C_{pda} S_a \rho_{da})] \end{aligned} \quad (3.108)$$

Expanding equation (3.108) further and substituting $n(l + e) = e$ yields:

$$\begin{aligned} \frac{\partial}{\partial t} [H_c(T - T_r)(1 + e)] &= +H_c(1 + e) \frac{\partial T}{\partial t} + \\ &+ (T - T_r) \frac{\partial}{\partial t} \left[C_{ps} \rho_s \frac{\partial e}{\partial t} + n \left(-C_{ps} \rho_s + C_{pl} S_l \rho_l + C_{pv} S_a \rho_v + C_{pda} S_a \rho_{da} \right) \frac{\partial e}{\partial t} \right] \\ &+ e \left(C_{pl} \rho_l \frac{\partial S_l}{\partial t} - C_{pv} \rho_v \frac{\partial S_l}{\partial t} + C_{pv} (1 - S_l) \frac{\partial \rho_v}{\partial t} \right) \\ &+ e \left(C_{pda} (1 - S_l) \frac{\partial \rho_{da}}{\partial t} - C_{pda} \rho_{da} \frac{\partial S_l}{\partial t} \right) \end{aligned} \quad (3.109)$$

Noting that $\frac{\partial e}{\partial t} = (1 + e)^2 \frac{\partial n}{\partial t}$ and rearranging similar items, equation (3.109) becomes:

$$\begin{aligned} \frac{\partial}{\partial t} [H_c(T - T_r)(1 + e)] &= H_c(1 + e) \frac{\partial T}{\partial t} \\ &+ (T - T_r) \left[C_{ps} \rho_s (1 + e)^2 \frac{\partial n}{\partial t} \right. \\ &+ \left(-C_{ps} \rho_s + C_{pl} S_l \rho_l + C_{pv} S_a \rho_v + C_{pda} S_a \rho_{da} \right) (1 + e)^2 \frac{\partial n}{\partial t} \\ &+ e \left(C_{pl} \rho_l - C_{pv} \rho_v - C_{pda} \rho_{da} \right) \frac{\partial S_l}{\partial t} \\ &\left. + e C_{pv} (1 - S_l) \frac{\partial \rho_v}{\partial t} + e C_{pda} (1 - S_l) \frac{\partial \rho_{da}}{\partial t} \right] \end{aligned} \quad (3.110)$$

Considering the second term of equation (3.106), and substituting $n(1 + e) = e$ yields:

$$\frac{\partial}{\partial t} [Ln S_a \rho_v (1 + e)] = \frac{\partial}{\partial t} [Le S_a \rho_v] \quad (3.111)$$

Expanding equation (3.111) yields:

$$\frac{\partial}{\partial t} [Ln S_a \rho_v (1 + e)] = L(1 - S_l) e \frac{\partial \rho_v}{\partial t} - Le \rho_v \frac{\partial S_l}{\partial t} + L(1 - S_l) \rho_v \frac{\partial e}{\partial t} \quad (3.112)$$

Substituting equation (3.57) and (3.63) into the last term of equation (3.112) and rearrangement of the like terms yields:

$$\frac{\partial}{\partial t} [Ln S_a \rho_v (1 + e)] = L(1 - S_l) e \frac{\partial \rho_v}{\partial t} - Le \rho_v \frac{\partial S_l}{\partial t} + L(1 - S_l) \rho_v (1 + e)^2 \frac{\partial n}{\partial t} \quad (3.113)$$

Substituting equations (3.110), and (3.113) into equation (3.106) yields the governing equation for heat flow as:

$$\begin{aligned}
& (T - T_r) \left[\begin{aligned} & C_{ps} \rho_s (1+e)^2 \frac{\partial n}{\partial t} \\ & + (-C_{ps} \rho_s + C_{pl} S_l \rho_l + C_{pv} S_a \rho_v + C_{pda} S_a \rho_{da}) (1+e)^2 \frac{\partial n}{\partial t} + \\ & e(C_{pl} \rho_l - C_{pv} \rho_v - C_{pda} \rho_{da}) \frac{\partial S_l}{\partial t} + e C_{pv} (1 - S_l) \frac{\partial \rho_v}{\partial t} \\ & + e C_{pda} (1 - S_l) \frac{\partial \rho_{da}}{\partial t} \end{aligned} \right] \quad (3.114) \\
& + H_c (1+e) \frac{\partial T}{\partial t} + L(1 - S_l) e \frac{\partial \rho_v}{\partial t} - L e \rho_v \frac{\partial S_l}{\partial t} + L(1 - S_l) \rho_v (1+e)^2 \frac{\partial n}{\partial t} = \\
& - \nabla \cdot \left[\begin{aligned} & -\lambda_T \nabla T + L(\mathbf{v}_v \rho_l + \mathbf{v}_a \rho_v) \\ & + (C_{pl} \mathbf{v}_l \rho_l + C_{pv} \mathbf{v}_v \rho_l + C_{pv} \mathbf{v}_a \rho_v + C_{pda} \mathbf{v}_a \rho_{da}) (T - T_r) \end{aligned} \right] (1+e)
\end{aligned}$$

Dividing equation by $(1+e)$ and substituting $e/(1+e)=n$, yields:

$$\begin{aligned}
& (T - T_r) \left[\begin{aligned} & C_{ps} \rho_s (1+e) \frac{\partial n}{\partial t} \\ & + (-C_{ps} \rho_s + C_{pl} S_l \rho_l + C_{pv} S_a \rho_v + C_{pda} S_a \rho_{da}) (1+e) \frac{\partial n}{\partial t} \\ & + n(C_{pl} \rho_l - C_{pv} \rho_v - C_{pda} \rho_{da}) \frac{\partial S_l}{\partial t} + n C_{pv} (1 - S_l) \frac{\partial \rho_v}{\partial t} \\ & + n C_{pda} (1 - S_l) \frac{\partial \rho_{da}}{\partial t} \end{aligned} \right] \quad (3.115) \\
& + H_c \frac{\partial T}{\partial t} + L(1 - S_l) n \frac{\partial \rho_v}{\partial t} - L n \rho_v \frac{\partial S_l}{\partial t} + L(1 - S_l) \rho_v (1+e) \frac{\partial n}{\partial t} = \\
& - \nabla \cdot \left[\begin{aligned} & -\lambda_T \nabla T + L(\mathbf{v}_v \rho_l + \mathbf{v}_a \rho_v) \\ & + (C_{pl} \mathbf{v}_l \rho_l + C_{pv} \mathbf{v}_v \rho_l + C_{pv} \mathbf{v}_a \rho_v + C_{pda} \mathbf{v}_a \rho_{da}) (T - T_r) \end{aligned} \right]
\end{aligned}$$

Substituting the temporal derivatives of porosity from equation (3.63), degree of saturation from (3.60), vapour density from equation (3.35), dry air density from equation (3.87) into the left hand side of equation (3.115) and equations (3.25), (2.29) and (3.45) for the velocity terms of liquid, air and vapour, respectively, yields;

$$\begin{aligned}
& C_{Tl} \frac{\partial u_l}{\partial t} + C_{Tl} \frac{\partial T}{\partial t} + C_{Ta} \frac{\partial u_a}{\partial t} + \sum_{i=1}^{nc} C_{Tc_d} \frac{\partial c_d^i}{\partial t} + C_{Tu} \frac{\partial \mathbf{u}}{\partial t} \quad (3.116) \\
& = \nabla \cdot [K_{Tl} \nabla u_l] + \nabla \cdot [K_{Tl} \nabla T] + \nabla \cdot [K_{Ta} \nabla u_a] + \nabla \cdot \left[\sum_{i=1}^{nc} K_{Tc_d} \nabla c_d^i \right] + J_T
\end{aligned}$$

where;

$$C_{Tl} = \left[\begin{array}{l} (T - T_r) \left\{ \begin{array}{l} -n(C_{pl}\rho_l - C_{pv}\rho_v - C_{pda}\rho_{da}) \frac{\partial S_l}{\partial s} - nC_{pv}(1 - S_l)\rho_0 h_\pi \frac{\partial h_m}{\partial s} \\ + nC_{pda}(1 - S_l) \frac{R_v}{R_{da}} \rho_0 h_\pi \frac{\partial h_m}{\partial s} \end{array} \right\} \\ -L(1 - S_l)n\rho_0 h_\pi \frac{\partial h_m}{\partial s} + Ln\rho_v \frac{\partial S_l}{\partial s} \end{array} \right] \quad (3.117)$$

$$C_{Tl} = \left[\begin{array}{l} (T - T_r) \left\{ \begin{array}{l} n(C_{pl}\rho_l - C_{pv}\rho_v - C_{pda}\rho_{da}) \frac{\partial S_l}{\partial s} \\ + nC_{pv}(1 - S_l) \left[\rho_0 h_\pi \frac{\partial h_m}{\partial s} + \rho_0 h_m \frac{\partial h_\pi}{\partial s} + h_m h_\pi \frac{\partial \rho_0}{\partial s} \right] \\ + nC_{pda}(1 - S_l) \frac{\rho_a}{T} \end{array} \right\} \\ -nC_{pda}(1 - S_l) \frac{R_v}{R_{da}} \left[\rho_0 h_\pi \frac{\partial h_m}{\partial s} + \rho_0 h_m \frac{\partial h_\pi}{\partial s} + h_m h_\pi \frac{\partial \rho_0}{\partial s} \right] \\ + H_c + L(1 - S_l)n \left[\rho_0 h_\pi \frac{\partial h_m}{\partial s} + \rho_0 h_m \frac{\partial h_\pi}{\partial s} + h_m h_\pi \frac{\partial \rho_0}{\partial s} \right] - Ln\rho_v \frac{\partial S_l}{\partial s} \end{array} \right] \quad (3.118)$$

$$C_{Ta} = \left[\begin{array}{l} (T - T_r) \left\{ \begin{array}{l} n(C_{pl}\rho_l - C_{pv}\rho_v - C_{pda}\rho_{da}) \frac{\partial S_l}{\partial s} + nC_{pv}(1 - S_l)\rho_0 h_\pi \frac{\partial h_m}{\partial s} \\ + nC_{pda}(1 - S_l) \frac{1}{R_{da}T} - nC_{pda}(1 - S_l) \frac{R_v}{R_{da}} \rho_0 h_\pi \frac{\partial h_m}{\partial s} \end{array} \right\} \\ + L(1 - S_l)n\rho_0 h_\pi \frac{\partial h_m}{\partial s} - Ln\rho_v \frac{\partial S_l}{\partial s} \end{array} \right] \quad (3.119)$$

$$C_{Tc_d} = \left[\left\{ (T - T_r) \left\{ nC_{pv}(1 - S_l) - nC_{pda}(1 - S_l) \frac{R_v}{R_{da}} \right\} + L(1 - S_l)n \right\} \rho_0 h_m \frac{\partial h_\pi}{\partial c_d^i} \right] \quad (3.120)$$

$$C_{Tu} = \left[(T - T_r)(C_{pl}S_l\rho_l + C_{pv}S_a\rho_v + C_{pda}S_a\rho_{da}) + L(1 - S_l)\rho_v \right] \mathbf{m}^T \mathbf{P} \quad (3.121)$$

$$K_{Tl} = \left[\begin{array}{l} -L\rho_l \frac{D_{atms}v_v\tau_v\theta_a}{\rho_l} \rho_0 h_\pi \frac{\partial h_m}{\partial s} - (T - T_r)C_{pv}\rho_l \frac{D_{atms}v_v\tau_v\theta_a}{\rho_l} \rho_0 h_\pi \frac{\partial h_m}{\partial s} \\ + (T - T_r)C_{pl}\rho_l \frac{k_l}{\rho_l g} \end{array} \right] \quad (3.122)$$

$$K_{TT} = \left[\begin{array}{l} \lambda_T + L\rho_l \frac{D_{atms} v_v \tau_v \theta_a}{\rho_l} f \frac{(\nabla T)_a}{\nabla T} \left(h_m h_\pi \frac{\partial \rho_0}{\partial T} + \rho_0 h_m \frac{\partial h_\pi}{\partial T} + \rho_0 h_\pi \frac{\partial h_m}{\partial T} \right) \\ -(T - T_r) C_{pl} \rho_l \frac{k_l R \omega_\pi}{\rho_l g} \sum_{i=1}^{nc} \gamma_i c_d^i \\ + (T - T_r) C_{pv} \rho_l \frac{D_{atms} v_v \tau_v \theta_a}{\rho_l} f \frac{(\nabla T)_a}{\nabla T} \left(h_m h_\pi \frac{\partial \rho_0}{\partial T} + \rho_0 h_m \frac{\partial h_\pi}{\partial T} + \rho_0 h_\pi \frac{\partial h_m}{\partial T} \right) \end{array} \right] \quad (3.123)$$

$$K_{Ta} = \left[\begin{array}{l} L\rho_l \frac{D_{atms} v_v \tau_v \theta_a}{\rho_l} \rho_0 h_\pi \frac{\partial h_m}{\partial s} \\ + \left\{ C_{pv} \rho_v k_a + C_{pda} \rho_{da} k_a + C_{pv} \rho_l \frac{D_{atms} v_v \tau_v \theta_a}{\rho_l} \rho_0 h_\pi \frac{\partial h_m}{\partial s} - C_{pl} \rho_l \frac{k_l}{\rho_l g} \right\} (T - T_r) \\ + L\rho_v k_a \end{array} \right] \quad (3.124)$$

$$K_{Tc_d} = \left[\begin{array}{l} -(T - T_r) C_{pl} \rho_l \frac{k_l R T \omega_\pi}{\rho_l g} \gamma_i \left(1 + \frac{\partial \ln \gamma_i}{\partial \ln c_d^i} \right) + L\rho_l \frac{D_{atms} v_v \tau_v \theta_a}{\rho_l} \rho_0 h_m \frac{\partial h_\pi}{\partial c_d^i} \\ + (T - T_r) C_{pv} \rho_l \frac{D_{atms} v_v \tau_v \theta_a}{\rho_l} \rho_0 h_m \frac{\partial h_\pi}{\partial c_d^i} \end{array} \right] \quad (3.125)$$

$$J_T = (T - T_r) C_{pl} \rho_l \nabla \cdot (k_l \nabla z) \quad (3.126)$$

3.6 Reactive transport of multicomponent chemicals

The combined effect of all the, hydrological, physical and geochemical processes on multicomponent chemical transport must satisfy the principles of conservation of mass and the principle of conservation of charge (e.g. Lasaga, 1979; Lichtner, 1995). The governing equation for reactive transport of multicomponent chemicals is formulated from the principles of mass balance and charge conservation. The reactive transport of multicomponent chemicals is described in terms of a set of chemical components with the stoichiometries of species that appear in the fluid. Since terminology of chemical species or species may be repeatedly used when the mechanisms or the processes are described, the distinction between species and component is critical. Species and phases exist as real entities that can be observed in nature, whereas components are simply mathematical tools for describing composition (Bethke, 1996).

The law of mass conservation for every chemical component describes the transport of a dissolved chemical component and the associated chemical reactions. The chemical reactions, in fact, accounts for the rate of gain or loss of chemical component due to homogenous and heterogeneous geochemical reactions (Lichtner, 1995). Following Lichtner (1995) and Seetharam (2003), the law of conservation of mass for the i^{th} chemical component can be written in a general form for unsaturated porous media as:

$$\frac{\partial}{\partial t} (\theta_i c_d^i \delta V) + \frac{\partial}{\partial t} (\theta_i s_i \delta V) = -\delta V \nabla \cdot \mathbf{J}_i \quad (3.127)$$

\mathbf{J}_i is the total chemical flux that represents the major hydraulic and physical processes affecting the transport of chemical in porous media, s_i denotes a geochemical sink/source term in mass conservation equation which stands for the amount of i^{th} chemical component which is produced or depleted due to geochemical reactions. The geochemical sink/source term in the governing chemical transport equation is evaluated using geochemical model PHREEQC version 2 which is coupled with the transport model. The geochemical sink/source term is the resultant of the homogenous and heterogeneous geochemical reactions in the system.

One of the fundamental properties of an aqueous solution is that it is electrically neutral on macroscopic scale (Lichtner, 1996; Bethke, 1996). The general form of charge conservation can be obtained by multiplying the mass conservation equation by the charge of i^{th} component and summing over all components (Lichtner, 1996). Accordingly, if equation (3.127) is

multiplied by the associate charge of the component for every component and followed by summing over all components, the general charge conservation is obtained:

$$\delta V \sum_{i=1}^{nc} \left(\frac{\partial}{\partial t} \theta_i F z_i c'_d \right) + \delta V \sum_{i=1}^{nc} \frac{\partial}{\partial t} (\theta_i F z_i s_i) + \delta V \sum_{i=1}^{nc} \nabla \cdot F z_i \mathbf{J}_i = 0 \quad (3.128)$$

where z_i is the charge of i^{th} species and F is the Faraday constant.

The electro-neutrality in principle is associated with two separate physical requirements, if the charge is assumed to be conserved over geochemical reactions, i.e. $\sum_{i=1}^{nc} \frac{\partial}{\partial t} (\theta_i F z_i s_i) = 0$. These two conditions related to the physical processes, i.e. non-reactive transport, may be given as (e.g. Lasaga, 1979; Boudreau et al., 2004):

1. The total charge should be conserved, i.e. *no net charge condition*, given as:

$$\sum_{i=1}^{nc} \frac{\partial}{\partial t} (\theta_i F z_i c'_d \delta V) = 0 \quad (3.129)$$

2. No electrical current should run through the solution, i.e. *no current condition*, given as:

$$\sum_{i=1}^{nc} \nabla \cdot (F z_i \mathbf{J}_i) = 0 \quad (3.130)$$

The major mechanisms for the physical processes, i.e. non-reactive transport, comprise the processes of advection, dispersion and diffusion in general. The mechanisms of transport of chemicals and the governing equations are discussed in the following section.

3.6.1 Transport processes and mechanisms

The chemical flux of i^{th} component in general consists of contributions from advective, diffusive and dispersive transport mechanisms (Bear and Verruijt, 1987; Lasaga, 1998), given as:

$$\mathbf{J}_i = \mathbf{J}_i^{\text{Adv}} + \mathbf{J}_i^{\text{Diff}} + \mathbf{J}_i^{\text{Disp}} \quad (3.131)$$

where, $\mathbf{J}_i^{\text{Adv}}$, $\mathbf{J}_i^{\text{Diff}}$ and $\mathbf{J}_i^{\text{Disp}}$ stand for advective, diffusive and dispersive flux, respectively.

Each of the effective transport mechanisms are discussed separately as follows:

3.6.1.1 Advection

Advection describes the movement of solutes carried by the water flow and can be defined by a convective flux component. In fact it involves simply the spatial translation of dissolved chemical species at the rate of movement of the bulk fluid (Steefel, 2007). The rate of transport via advection is the average linear velocity defined in equation (3.25), in the direction of flow. The advective flux may be given as (e.g. Bear and Verruijt, 1987; Lasaga, 1998; Seetharam, 2003; Steefel, 2007):

$$\mathbf{J}_i^{\text{Adv}} = c_d^i \mathbf{v}_1 \quad (3.132)$$

where \mathbf{v}_1 represents the velocity of liquid water which is calculated using equation (3.25).

In order to consider the osmosis effects on the advective flux, it has been suggested to reduce the advective flux by a reduction factor as a function of osmotic efficiency (e.g. Malusis and Shackelford, 2002; Manassero and Dominijanni, 2003) as:

$$\mathbf{J}_i^{\text{Adv}} = (1 - \omega_\pi) c_d^i \mathbf{v}_1 \quad (3.133)$$

where ω_π is the osmotic efficiency coefficient. In an ideal membrane, no chemicals can move with liquid which is reflected properly with this equation.

3.6.1.2 Diffusion

The process of diffusion is the spreading of the solute molecules through the fluid by virtue of their kinetic motion, even when the fluid is at rest (Crank, 1975). The forces driving the diffusion of an aqueous species under isothermal condition, within a solvent reference frame, are stemmed from both chemical potential and electrical potential gradients, i.e. the electrochemical potential gradient (Miller, 1966; Lasaga, 1979, Oelker, 1996, Cussler, 1997). It is also well established that under non-isothermal conditions, a temperature gradient can also induce mass flow due to thermal diffusion, i.e. Soret-Ludwig effect or Soret effect (e.g. Lasaga, 1998; Platten, 2006).

The diffusion process in clays and more specifically in compacted swelling clays is highly affected by the specific microstructure evolution and surface electrostatic forces of the clay minerals (e.g. Jougnot et al., 2009; Oscarson, 1994; Pusch and Yong, 2006; Van Loon, 2007; Appelo and Wesin, 2007). As a result, the diffusion rate of an ionic species may vary with the type of moving ion in the system which consequence a macroscopic electrical field in pore fluid. This requires the modelling of diffusion process under coupled chemical and electrical potential effects to maintain the balance in the electroneutrality of pore fluid. Under non-isothermal conditions and in multiple ionic systems, the diffusion flux has to be obtained due to electrochemical and thermal diffusion i.e. Soret effect, potentials.

In order to incorporate the electro-neutrality condition in both molecular and thermal diffusion explicitly, the general derivation of diffusion flux in aqueous system under coupled chemical, electrical and thermal potentials is revisited in this section. The derivation follows a similar to that approach proposed by Lasaga (1979) for multicomponent diffusion under isothermal condition and adopted by various researchers (e.g. Lichtner, 1995; Oelkers, 1996; Boudrau et al., 2004; Appelo and Wersin, 2007). However, thermal diffusion is included as an additional component of the diffusion flux in the approach proposed.

Lasaga (1998) presented the total diffusive flux of a chemical component due to the coupled electrochemical and thermal potentials based on the irreversible thermodynamics:

$$\mathbf{J}_i^{\text{Diff}} = -L_{ii} [\nabla\mu_i + Fz_i\nabla\Phi] - L_{iq} \frac{\nabla T}{T} \quad (3.134)$$

where, the first term of the equation represents the diffusion flux due to the chemical and electrical potentials and the second term represents the thermal diffusion, where, L_{ii} stands for the phenomenological transport coefficient due to electrochemical potential and L_{iq} represents the phenomenological coefficient of thermally induced chemical diffusion for the i^{th} chemical component. μ_i represents the chemical potential and z_i is the charge of the i^{th} chemical component, respectively. F denotes the Faraday's constant, Φ refers to the electrical potential of the solution and T is the absolute temperature.

The chemical potential of a chemical species in a non-ideal solution is a function of chemical concentration, activity coefficient and temperature, expressed as (e.g. Lasaga 1979; Oelker, 1996):

$$\mu_i = \mu_i^0 + RT \ln(\gamma_i c_d^i) \quad (3.135)$$

where, μ_i^0 denotes the chemical potential at reference state. R is the gas constant. γ_i is the activity coefficient of the i^{th} chemical component; which accounts for the non-ideality of the aqueous solution, i.e. aqueous concentration effects. The activity coefficient decreases with increasing ionic strength up to 0.1mol/kg and it is always lower than the concentration, because charged ions reduce the activity of each other in solution through interactions (Merkel et al., 2005).

Following Lasaga (1998) and Balluffi et al. (2005), if the spatial derivative of the gradient of chemical potential, i.e., $\nabla\mu$, is replaced by its derivatives with respect to chemical concentration and temperature, the diffusion flux can be given as:

$$\mathbf{J}_i^{\text{Diff}} = \underbrace{-L_{ii} \left[\frac{\partial \mu_i}{\partial c_d^i} \nabla c_d^i + Fz_i \nabla \Phi \right]}_{\text{Electrochemical diffusion}} - \underbrace{\frac{L_{ii}}{T} \left[T \frac{\partial \mu_i}{\partial T} + \frac{L_{iq}}{L_{ii}} \right]}_{\text{Thermal diffusion}} \nabla T \quad (3.136)$$

The term inside the second bracket in the coefficient for thermal diffusion is known as the heat of transport (Q^*).

The heat of transport is mathematically a combination of the derivative of chemical potential with respect to temperature and the ratio of thermally induced diffusion off-diagonal phenomenological coefficient to the on-diagonal diffusion coefficients (Balluffi et al., 2005) as:

$$Q_i^* = T \frac{\partial \mu_i}{\partial T} + \frac{L_{iq}}{L_{ii}} \quad (3.137)$$

The heat of transport corresponds to the energy state of the diffusing ions in the regions with different temperatures which directly corresponds to the entropy of transport (Agar et al., 1989; Balluffi et al., 2005).

The phenomenological coefficients of diffusion for each component L_{ii} , can be approximated from their respective tracer diffusion coefficient in water (Lasaga, 1979; Oelkers, 1996) as:

$$L_{ii} = \frac{D_i^0 c_d^i}{RT} \quad (3.138)$$

where D_i^0 refers to the tracer diffusion coefficient of the subscripted component in pure water.

Substituting the phenomenological coefficient using equation (3.138), following Lasaga (1979), and the heat of transport, defined by Ballufi et al. (2005) from equation (3.137) into equation (3.136), the diffusion flux is represented as:

$$\mathbf{J}_i^{\text{Diff}} = -\frac{D_i^0 c_d^i}{RT} \frac{\partial \mu_i}{\partial c_d^i} \nabla c_d^i - \frac{D_i^0 c_d^i F z_i}{RT} \nabla \Phi - \frac{D_i^0 c_d^i Q_i^*}{RT^2} \nabla T \quad (3.139)$$

Under isothermal conditions, the diffusive flux is limited to the first and second terms which is identical to the diffusive flux for multicomponent chemicals presented by several researchers (e.g. Lasaga, 1979; Boudrau et al., 2004; Appelo and Wersin, 2007). The third term represents the effects of including thermal diffusion in a multi-ionic system.

Overall electroneutrality requires that *no electrical current*, should run through the solution (after Lasaga, 1979), i.e., equation (3.128). Incorporating the *no electrical current* condition,

i.e. $\sum_{j=1}^{nc} z_j \mathbf{J}_j = 0$, yields:

$$\sum_{j=1}^{nc} z_j D_j^0 c_d^j \frac{1}{RT} \frac{\partial \mu_j}{\partial c_d^j} \nabla c_d^j + \sum_{j=1}^{nc} z_j^2 D_j^0 c_d^j \frac{F}{RT} \nabla \Phi + \sum_{j=1}^{nc} z_j D_j^0 c_d^j \frac{Q_j^*}{RT^2} \nabla T = 0 \quad (3.140)$$

The gradient of electrical potential can therefore be determined explicitly from equation (3.140) as:

$$\nabla \Phi = -\frac{RT}{F} \left[\frac{\sum_{j=1}^{nc} z_j D_j^0 c_d^j \frac{1}{RT} \frac{\partial \mu_j}{\partial c_d^j} \nabla c_d^j + \sum_{j=1}^{nc} z_j D_j^0 c_d^j \left(\frac{Q_j^*}{RT^2} \right) \nabla T}{\sum_{j=1}^{nc} z_j^2 D_j^0 c_d^j} \right] \quad (3.141)$$

Note that the derivative of chemical potential with respect to chemical concentration is given as (Oelkers, 1996):

$$\frac{\partial \mu_i}{\partial c_d^i} = \frac{RT}{c_d^i} \left(1 + \frac{\partial \ln \gamma_i}{\partial \ln c_d^i} \right) \quad (3.142)$$

Substituting the electrical potential from equation (3.141), following the approach proposed by Lasaga (1979) for derivation under isothermal conditions; and the derivative of chemical potential with respect to chemical concentration from equation (3.142) into the diffusion flux, the expanded form of diffusion flux equation is obtained as:

$$\mathbf{J}_i^{\text{Diff}} = \begin{bmatrix} -D_i^0 \left(1 + \frac{\partial \ln \gamma_i}{\partial \ln c_d^i} \right) \nabla c_d^i + \frac{z_i D_i^0 c_d^i}{\sum_{k=1}^{nc} z_k^2 D_k^0 c_d^k} \sum_{j=1}^{nc} z_j D_j^0 \left(1 + \frac{\partial \ln \gamma_j}{\partial \ln c_d^j} \right) \nabla c_d^j \\ -D_i^0 c_d^i \frac{Q_i^*}{RT^2} \nabla T + \frac{z_i D_i^0 c_d^i}{\sum_{k=1}^{nc} z_k^2 D_k^0 c_d^k} \sum_{j=1}^{nc} z_j D_j^0 c_d^j \frac{Q_j^*}{RT^2} \nabla T \end{bmatrix} \quad (3.143)$$

Equation (3.143) represents the diffusion process comprising two compartments of chemical (molecular) diffusion and thermally induced mass diffusion considering the effects related to the electrical potential sourcing from different diffusion coefficients. Accordingly the degree of the coupling of the ions diffusion depends on the relative concentration gradient which yields to a component or species dependant diffusion coefficient both for molecular and thermal diffusion. The diffusive flux can be expressed in a simplified form as:

$$\mathbf{J}_i^{\text{Diff}} = \sum_{j=1}^{nc} D_{ij}^0 \nabla c_j + D_i^T \nabla T \quad (3.144)$$

where the molecular diffusion coefficient and thermal diffusion coefficients can be represented as follows:

$$D_{ij}^0 = -\delta_{ij} D_i^0 \left(1 + \frac{\partial \ln \gamma_i}{\partial \ln c_d^i} \right) + \frac{z_i D_i^0 c_d^i}{\sum_{k=1}^{nc} z_k^2 D_k^0 c_d^k} z_j D_j^0 \left(1 + \frac{\partial \ln \gamma_j}{\partial \ln c_d^j} \right) \quad (3.145)$$

$$D_i^T = -D_i^0 c_d^i \frac{Q_i^*}{RT^2} + \frac{z_i D_i^0 c_i}{\sum_{k=1}^{nc} z_k^2 D_k^0 c_d^k} \sum_{j=1}^{nc} z_j D_j^0 c_d^j \frac{Q_j^*}{RT^2} \quad (3.146)$$

where δ_{ij} is the Kronecker's delta function which it is equal to 1 when $i=j$ and equal to 0 when $i \neq j$.

The degree of coupling of thermal diffusion with the overall mass diffusion is determined by the heat of transport. The heat of transport and the Soret coefficient are related to each other.

The heat of transport for a single ion in a dilute solution (Q_i^{*0} for the i^{th} component) is related to the Soret coefficient, S^T (Agar et al., 1989; Newman, 1991; Rosanne et al., 2006). This relationship can be given as:

$$Q_i^{*0} = RT^2 S_i^T \quad (3.147)$$

In a concentrated solution, the heat of transport can be related to the Soret coefficient, by considering the thermodynamic correction factor, i.e. $\left(1 + \frac{\partial \ln \gamma_i}{\partial \ln c_d^i}\right)$ which reflects the non-ideality effects in the concentrated solution. The relationship between heat of transport and the Soret coefficient for a single charged ion yields (e.g. Snowdon and Turner, 1960; Leaist and Hui, 1990):

$$\frac{Q_i^*}{RT^2} = S_i^T \left(1 + \frac{\partial \ln \gamma_i}{\partial \ln c_d^i}\right) \quad (3.148)$$

Replacing the heat of transport in equation (3.146) with equation (3.148) gives:

$$D_i^T = D_i^0 c_d^i S_i^T \left(1 + \frac{\partial \ln \gamma_i}{\partial \ln c_d^i}\right) - \frac{z_i D_i^0 c_i}{\sum_{k=1}^{nc} z_k^2 D_k^0 c_d^k} \sum_{j=1}^{nc} z_j D_j^0 c_d^j S_j^T \left(1 + \frac{\partial \ln \gamma_j}{\partial \ln c_d^j}\right) \quad (3.149)$$

As mentioned in chapter 2, few experimental studies have been reported on thermal diffusion in clays. In the absence of sufficient experimental data, a theoretical approach is adopted and suggested here for approximation of the Soret coefficient which can be incorporated in the diffusion flux equation in order to study the overall effects of thermal diffusion.

In an effort to provide a theoretical interpretation for the heat of transport, Agar et al. (1989) proposed a hydrodynamic theory for the heat of transport. The similarity between the heat sink and source surrounding a moving particle and the existence of the electrical charge sink and source in a dipolar molecule led Agar et al. (1989) to suggest that the moving particles are surrounded by *thermal dipole moments*. Based on a hydrodynamic approach, Agar et al. (1989) provided a theoretical formulation for standard heat of transport of ions in infinite dilute electrolyte solution at temperature 25 °C. They have shown that standard heat of transport can be related to the structure and dynamics of the solution through the velocity field induced by the ionic motion and the entropy density of the solvent around the ion. The

theoretical approach suggested analogies between the heat of transport and dielectric properties of the solutions. According to the theoretical approach proposed by Agar et al. (1989), the heat of transport of i^{th} component at reference temperature, i.e. 25 °C, and in a dilute solution can be obtained as a function of ion tracer diffusion and its valence. The simplified form may be given as:

$$Q_i^{*0} = Az_i^2 D_i^0 \quad (3.150)$$

where A is a constant value depending on the hydrodynamic boundary condition. Agar et al., (1989) have calculated A equal to 2.48×10^{12} and 2.20×10^{12} for two different hydrodynamic boundary conditions.

The heat of transport in equation (3.147) can be substituted by its theoretical approximation from equation (3.150) and the Soret coefficient for a single charged ion in a dilute solution is obtained as:

$$S_i^T = \frac{Az_i^2 D_i^0}{RT^2} \quad (3.151)$$

This theoretical approach can be incorporated in the diffusive flux in equation (3.143), in the absence of experimental data on the Soret coefficient in multiple ionic systems.

The diffusive flux in porous media is generally modified by replacement of the tracer diffusion coefficient in water with the effective diffusion coefficient in porous medium (Lasaga, 1998). The effective diffusion coefficient in porous material is calculated by incorporating some modification factors to the tracer diffusion coefficient in water which accounts for medium geometry and liquid content (Hu and Wang, 2003). The value of the effective tracer diffusion coefficient can be given as (Hu and Wang, 2003; Van Brakel and Heertjes, 1974) as:

$$D_i = nS_i \tau \delta D_i^0 \quad (3.152)$$

where, τ is the tortuosity factor and δ stand for constrictivity coefficient.

Constrictivity in general term has been used to describe a decrease in the apparent diffusion coefficient of tracer caused by pore-size variability (Van Brakel and Heertjes, 1974). In the case of compacted swelling clays, it evidently reflects in some way the properties of water

molecules that are vicinal to the basal surface bounding interlayer (Bourg et al., 2006). The constrictively can be contributed to the two components of geometrical constrictively, due to the pore space topography and an electrostatic constrictively which accounts for the electrostatic interaction between charge surface minerals and ionic species, i.e. diffuse double layer effects, (Sato et al., 1995; Jougnot et al., 2009). The latter effect also reflects the membrane behaviour of clay, i.e., osmosis behaviour. Complex effects due to the physico-chemical properties of the porous medium, the solute and the pore solution control the diffusive behaviour of anions and cations in clay (Van Loon et al., 2007). These effects result in a preferential flow path for different ions, i.e., different diffusion coefficient for different ions as discussed in chapter 2.

A general species dependant tortuosity factor, τ_i is considered in this formulation which reflects the effects of tortuous path and constrictivity together. The later will be discussed and expanded in chapter 6 for the case of compacted smectite clays. The tracer diffusion coefficient is therefore presented as:

$$D_i = nS_i \tau_i D_i^0 \quad (3.153)$$

The temperature dependence of the free solution diffusion coefficient can be expressed using the Stokes-Einstein relationship as (Robinson and Stokes, 1959; Lerman, 1988; Cussler, 1995):

$$(D_i^0)_T = (D_i^0)_{T_r} \frac{T_r}{T} \frac{(\eta)_{T_r}}{(\eta)_T} \quad (3.154)$$

where η stands for the viscosity of solvent. The variation of diffusion coefficient through this relationship is more affected by the changes due to the viscosity dependency on temperature rather than due to the direct temperature effect.

It is noted that the activity coefficient of the ions is calculated using Davis equation in diffusion module. The Davies equation for activity coefficient is valid for ionic strength ranging between 0.1 and 0.7 mol/l (Langmuir, 1997), given as:

$$\log \gamma_i = -A' z_i^2 \left(\frac{\sqrt{I}}{1 + \sqrt{I}} - 0.3I \right) \quad (3.155)$$

where, A' is a temperature dependent parameter and I stands for ionic strength (i.e.

$$I = 0.5 \sum_{i=1}^{nc} 0.001 c_d^i z_i^2).$$

3.6.1.3 Dispersion

Due to the irregular shapes of grains and pores, local fluid velocities inside individual pores deviate from the average pore velocity and leading to a mixing process that is macroscopically similar to mixing caused by the diffusive transport (Steefel, 2008). The term mechanical dispersion is often used to describe mixing and spreading of solute due to the heterogeneity of the microscopic velocities in the motion of the fluid in terms of averaged and measurable quantities (Bear and Verruijt, 1987). This process is caused by three microscopic processes occurring in the pore channels (Mangold and Tsang, 1991; Oelkers, 1996):

- Mixing within individual pore channels due to differences in velocity of the molecules between those in the middle of the channel and those subject to dragging forces along the pore walls (i.e. friction between mineral grains and fluids leads to relatively slower flow rates along grain boundaries).
- Mixing caused by differences in pore channel sizes and hence velocities along the flow path (i.e. the velocity of solutes flowing in a porous medium varies according to flow path).
- Differences caused by the branching of flow channel paths in the solid matrix (tortuosity) (i.e. at each pore space juncture there is both a mixing and a splitting of the flow streams).

These three mixing processes cause spreading the solute both in the direction of the flow, termed longitudinal dispersion, and in directions perpendicular to the flow, called transverse dispersion. This can be represented by (Bear and Verruijt, 1987):

$$\mathbf{J}_i^{\text{Disp}} = n S_l \mathbf{D}_m \nabla c_d^i \quad (3.156)$$

where, \mathbf{D}_m is the coefficient of mechanical dispersion and is considered to be a function of the average velocity (Pickens and Gillham, 1980).

$$\mathbf{D}_m = \frac{\alpha_T |\nu| \delta_{mn}}{nS_l} + (\alpha_L - \alpha_T) \frac{\nu_p \nu_q}{nS_l |\nu|} \quad (3.157)$$

where $|\nu|$ is the absolute average velocity of advection flow, α_L and α_T are longitudinal and transversal dispersivity parameters, respectively. δ_{mn} denotes the Kronecker delta. ν_p and ν_q are the velocities of water in different spatial directions (e.g. x and y)

The chemicals are carried with the liquid flow; therefore the effects of osmosis are also applied to the dispersion. In other word, in an ideal membrane, the osmosis effects prevent the migration of chemicals with liquid water transfer. If the osmotic effects are also included similar to the adaptation in equation (3.133); in the case of three dimensional transports, \mathbf{D}_m yields to a square matrix (3×3):

$$\mathbf{D}_m = (1 - \omega_x) \frac{1}{nS_l} \begin{bmatrix} \alpha_T |\nu| + (\alpha_L - \alpha_T) \frac{\nu_x^2}{|\nu|} & (\alpha_L - \alpha_T) \frac{\nu_x \nu_y}{|\nu|} & (\alpha_L - \alpha_T) \frac{\nu_x \nu_z}{|\nu|} \\ (\alpha_L - \alpha_T) \frac{\nu_y \nu_x}{|\nu|} & \alpha_T |\nu| + (\alpha_L - \alpha_T) \frac{\nu_y^2}{|\nu|} & (\alpha_L - \alpha_T) \frac{\nu_y \nu_z}{|\nu|} \\ (\alpha_L - \alpha_T) \frac{\nu_z \nu_x}{|\nu|} & (\alpha_L - \alpha_T) \frac{\nu_z \nu_y}{|\nu|} & \alpha_T |\nu| + (\alpha_L - \alpha_T) \frac{\nu_z^2}{|\nu|} \end{bmatrix} \quad (3.158)$$

3.6.2 Geochemical reactions

In order to calculate the geochemical reactions, i.e. the sink/source term in the mass conservation equation, an advanced geochemical model, PHREEQC *version 2*, (Parkhurst and Appelo, 1999) was linked to the chemical transport model. A sequential approach was incorporated for coupling the transport model and the geochemical model which will be discussed in detail in the following chapter. In this coupling approach chemical transport equations are solved first. Then the achieved converged value for each node is transferred to the geochemical code. The values of chemical concentration and geochemical parameters are then updated via the geochemical modelling. The procedure is repeated for all subsequent time-steps.

PHREEQC *version 2* is a computer program designed to perform low-temperature aqueous geochemical calculations. The chemical reactions in and between aqueous, mineral and gas phases can be modelled using this model. PHREEQC *version 2* is capable to model both equilibrium controlled and kinetically controlled geochemical reactions. The solid-solution reactions, surface-complexation, and ion-exchange reactions can be modelled too.

In general, PHREEQC is based on an ion-association aqueous model and has capabilities for speciation, saturation-index and batch-reaction. Non-equilibrium reactions can also be modelled, including aqueous-phase mixing, user-specified changes in the elemental totals of the system, kinetically controlled solid-liquid heterogeneous reactions, and to a limited extend kinetically controlled aqueous homogeneous reactions. Kinetic reactions can be model with user-defined rate expressions. Rate expressions written in the *Basic* language are included in the input file, and the program uses the *Basic* interpreter to calculate the rate of reactions.

Modelling the reactions in equilibrium with fixed-volume or fixed-pressure gas phases has been provided in PHREEQC; as well as modelling formation or dissolution of ideal, multicomponent or nonideal, binary solid solutions. The generalized two-layer model of Dzombak and Morel (1990), a model with an explicitly calculated diffuse layer (Borkovec and Westall, 1983), and a non-electrostatic model (Davis and Kent, 1990) have been incorporated for modelling surface-complexation reactions. Surface complexation constants for two of the databases distributed with the program (*phreeqc.dat* and *wateq4f.dat*) are taken from Dzombak and Morel (1990); surface complexation constants for the other database distributed with the program (*minteq.dat*) are taken from MINTEQA2 (Allison et al., 1990). Ion-exchange reactions are modelled with the Gaines-Thomas convention and equilibrium constants derived from Appelo and Postma (1993) are included in two of the databases distributed with the program (*phreeqc.dat* and *wateq4f.dat*).

The activity coefficient of ions can be calculated by different equations including Davies equation and extended Debye-Hückel equation (valid up to 0.7 mol/l). For high ionic concentrations (up to 6 mol/l), PHREEQC *version 2.12* included an implementation of the Pitzer specific-interaction activity coefficient formulation which can be simply used though "*pitzer.dat*" database.

Any number of solution compositions, gas phases, or pure-phase, solid-solution, exchange, or surface-complexation assemblages can be defined in PHREEQC. Batch reactions allow any combination of solution (or mixture of solutions), gas phase, and assemblages to be brought together, any irreversible reactions are added, and the resulting system is brought to equilibrium. If kinetic reactions are defined, then the kinetic reactions are integrated with an automatic time-stepping algorithm and system equilibrium is calculated after each time step.

Detailed information about the theoretical and numerical formulations of the geochemical model can be found in Parkhurst and Appelo (1999).

The geochemical features which have been so far linked and verified (presented in chapter 5) include:

- Equilibrium reactions, tested for precipitation/dissolution of minerals
- Kinetically controlled, reactions tested for precipitation/dissolution of minerals
- Ion exchange process, tested under equilibrium conditions

The surface complexation features of PHREEQC such as the calculation of the diffuse double layer are not linked explicitly with transport module. However, this feature can be used to calculate the distribution of chemicals in DDL space.

Mineral precipitation and dissolution during the reactive transport can change the water and chemical flow properties as the variation of the mineral volume during precipitation/dissolution can change the available porosity for the flow processes. Porosity feed back from geochemical model has been also implemented in the computational code. The volumes of solid minerals which can be accumulated or dissipated after precipitation/dissolution calculation are likely to change the flow parameters. The porosity is modified after geochemical calculation and its modified value is sent back to the hydraulic and chemical transport modules, which modify the transport characteristics such as hydraulic permeability or diffusion coefficient of chemicals.

Following Steefel and Lasaga, (1994) and Sonnenthal et al. (2003), the permeability variation caused by a change in porosity can be simplified form of the Kozeny-Carmen equation; therefore:

$$k_l = k_{sat} \left(\frac{n}{n_0} \right)^3 \quad (3.159)$$

where, k_{sat} and n_0 are the saturated permeability and its associate porosity.

The computational aspects of porosity feed back will be discussed more in the following chapter.

3.6.3 Implementation of mass and charge conservation laws

The total flux of each component due to the transport mechanism including advection, diffusion and dispersion can be replaced from equations (3.133), (3.144) and (3.156), respectively into the mass conservation, equation (3.127), giving:

$$\begin{aligned} \frac{\partial}{\partial t} (\theta_l c_d^i \delta V) + \frac{\partial}{\partial t} (\theta_l s_i \delta V) = & -\nabla \cdot [(1 - \omega_\pi) c_d^i \mathbf{v}_l \delta V] - \nabla \cdot (n S_l \mathbf{D}_m \nabla c_d^i \delta V) \\ & - \nabla \cdot \left(\sum_{j=1}^{nc} n S_l \tau_i D_{ij}^0 \nabla c_j \delta V \right) - \nabla \cdot (n S_l \tau_i D_i^T \nabla T \delta V) \end{aligned} \quad (3.160)$$

In addition to the conservation of mass, the overall charge must be conserved as stated in equation (3.128). This includes employing *no-charge* and *no-current* conditions explicitly along with the mass conservation equation for non-reactive transport and for all components. In addition, the electro-neutrality must be maintained during geochemical reactions. The geochemical reaction model, PHREEQC *version 2*; considers the charge conservation in the reactions by adjusting the concentration pH in the solution. When specified, a charge-balance equation is used in initial solution calculations to adjust the pH or the activity of a master species (and consequently the total concentration of an element or element valence state) to produce electro-neutrality in the solution (Parkhurst and Appelo, 1999).

So far, the *no-current condition* has been applied explicitly to drive the electrical potential in diffusive flux. The advective and dispersive fluxes were not considered in that equation because all ions move with same rate or speed by advection and dispersion. Mathematically, this is also obtained by integration over *no-charge condition*, i.e. $\sum_{j=1}^{nc} \frac{\partial}{\partial t} (n S_l F z_j c_d^j \delta V) = 0$.

Lasaga (1979) and Boudreau et al. (2004) have shown that if overall charge conservation equation is employed explicitly in combination with the *nc* conservation equations for mass,

an over determined system of equations is obtained. To prevent this, Lasaga, (1979) proposed that one of the concentrations and its derivatives needs to be eliminated from all the model equations in order to obtain both conditions explicitly. Hence, a particular dependent ion and its concentration is eliminated from the model and its actual concentration is calculated by knowing the concentration of the remained $nc-1$ components through the charge conservation equation (Lasaga 1981; Boudreau et al. 2004). In other words, the mass conservation is solved for $nc-1$ components where the diffusive flux will no longer contain the mutual dependant concentration effects. The concentration of the dependant component is then simply calculated by means of the no-charge constraint. Lasaga, (1979) interpreted that one of the concentrations and its derivatives need to be eliminated from all the model equations in order to obtain a solution to a multicomponent ionic diffusion problem. This later procedure is not, however, a mathematical or physical necessity. It is instead one possible route to solve the new set of equations (Boudreau et al. 2004).

Accordingly, a particular *dependent ion* is eliminated from mass conservation and its actual concentration is calculated by knowing the concentration of the remained $nc-1$ components through the *no-charge condition*. If the first component is arbitrarily considered as *dependant ion*, its concentration can be calculated according to the charge conservation equation.

$$z_1 c_d^1 = - \sum_{j=2}^{nc} z_j c_d^j \quad (3.161)$$

Substituting the concentration of the first component from equation (3.161) and its derivative into equations (3.145) and (3.149), the molecular diffusion coefficient and thermal diffusion coefficient for all components, except the *dependent component* i.e., *first component* is obtained as:

$$D_{ij}^0 = \left\{ \begin{array}{l} -\delta_{ij} D_i^0 \left(1 + \frac{\partial \ln \gamma_i}{\partial \ln c_d^i} \right) \\ + \frac{z_i D_i^0 c_d^i}{\sum_{k=2}^{nc} (z_k D_k^0 - z_1 D_1^0) z_k c_d^k} z_j \left[D_j^0 \left(1 + \frac{\partial \ln \gamma_j}{\partial \ln c_d^j} \right) - D_1^0 \left(1 + \frac{\partial \ln \gamma_1}{\partial \ln c_d^1} \right) \right] \end{array} \right\} \quad (3.162)$$

$$D_i^T = \left\{ \begin{array}{l} -D_i^0 c_d^i S_i^T \left(1 + \frac{\partial \ln \gamma_i}{\partial \ln c_d^i} \right) + \\ + \frac{z_i D_i^0 c_d^i}{\sum_{k=2}^{nc} (z_k D_k^0 - z_1 D_1^0) z_k c_d^k} \sum_{j=2}^{nc} \left[D_j^0 S_j^T \left(1 + \frac{\partial \ln \gamma_j}{\partial \ln c_d^j} \right) - D_1^0 S_1^T \left(1 + \frac{\partial \ln \gamma_1}{\partial \ln c_d^1} \right) \right] z_j c_d^j \end{array} \right\} \quad (3.163)$$

Diffusion flux for component 2 to nc does no longer contain the concentration of the first component and its derivatives. Note that this flux is applied for $nc-1$ component. Hence, one can now solve a reduced set of $nc-1$ differential equations to obtain the $nc-1$ principal concentrations. The concentration of dependent component is then simply calculated by means of charge conservation, i.e. *no-charge constraint*.

Bethke (1996) stated that the electroneutrality condition is almost always used to set the bulk concentration of the species in abundant concentration for which the greatest analytic uncertainty exists. In practice, this component is generally selected as chloride (Cl) because most commercial labs, unless instructed otherwise, report a chloride concentration calculated by a rough charge balance rather than a value resulting from direct analysis.

3.6.4 Governing equations for chemical reactive transport

To form the governing equation for the reactive transport of chemicals, the general mass conservation presented in equation (3.160) is expanded as follows:

Substituting ∂V from equation (3.10) in (3.160) yields:

$$\begin{aligned} \frac{\partial}{\partial t} [nS_i c_d^i (1+e) \delta V_s] + \frac{\partial}{\partial t} [nS_i s_i (1+e) \delta V_s] &= -\nabla \cdot [(1-\omega_\pi) c_d^i \mathbf{v}_i (1+e) \delta V_s] \\ -\nabla \cdot [nS_i \mathbf{D}_m \nabla c_d^i (1+e) \delta V_s] - \nabla \cdot \left[\sum_{j=2}^{nc} nS_i \tau_i D_{ij}^0 \nabla c_j (1+e) \delta V_s \right] & \\ -\nabla \cdot [nS_i \tau_i D_i^T \nabla T (1+e) \delta V_s] & \end{aligned} \quad (3.164)$$

Since the volume of the soil (solid) is assumed to remain constant, the term ∂V_s can be eliminated from equation (3.164). Moreover, by definition, it is known that $n = e/(1+e)$. Making these two changes to equation (3.164) yields:

$$\begin{aligned} \frac{\partial(eS_i c_d^i)}{(1+e)\partial t} + \frac{\partial(eS_i s)}{(1+e)\partial t} = & -\nabla \cdot [(1-\omega_\pi)c_d^i \mathbf{v}_1] - \nabla \cdot [nS_i \mathbf{D}_m \nabla c_d^i] \\ & - \nabla \cdot \left[\sum_{j=1}^{nc} nS_i \tau_i D_{ij}^0 \nabla c_j \right] - \nabla \cdot [nS_i \tau_i D_i^T \nabla T] \end{aligned} \quad (3.165)$$

The first term on the left-hand side of equation (3.165) can be represented as:

$$\frac{\partial(eS_i c_d^i)}{(1+e)\partial t} = nS_i \frac{\partial c_d^i}{\partial t} + nc_d^i \frac{\partial S_i}{\partial t} + S_i c_d^i \frac{\partial e}{(1+e)\partial t} \quad (3.166)$$

Substituting for the second and third terms for the time derivatives in the above equation from equations (3.60), (3.57) and (3.63) will yield:

$$\begin{aligned} \frac{\partial(eS_i c_d^i)}{(1+e)\partial t} = & nS_i \frac{\partial c_d^i}{\partial t} - nc_d^i \frac{\partial S_i}{\partial s} \frac{\partial u_i}{\partial t} + nc_d^i \frac{\partial S_i}{\partial s} \frac{\partial s}{\partial T} \frac{\partial T}{\partial t} \\ & + nc_d^i \frac{\partial S_i}{\partial s} \frac{\partial u_a}{\partial t} + S_i c_d^i \mathbf{m}^T \mathbf{P} \frac{\partial \mathbf{u}}{\partial t} \end{aligned} \quad (3.167)$$

Substitution of velocity of water with the components from equation (3.25); mass conservation equation for i^{th} component yields:

$$\begin{aligned} nS_i \frac{\partial c_d^i}{\partial t} + nS_i \frac{\partial s_i}{\partial t} - nc_d^i \frac{\partial S_i}{\partial s} \frac{\partial u_i}{\partial t} + nc_d^i \frac{\partial S_i}{\partial s} \frac{\partial s}{\partial T} \frac{\partial T}{\partial t} \\ + nc_d^i \frac{\partial S_i}{\partial s} \frac{\partial u_a}{\partial t} + S_i c_d^i \mathbf{m}^T \mathbf{P} \frac{\partial \mathbf{u}}{\partial t} = \end{aligned} \left\{ \begin{aligned} & -(1-\omega_\pi)c_d^i \frac{k_l}{\rho_l g} \nabla u_i + (1-\omega_\pi)c_d^i k_l \frac{R\omega_\pi}{\rho_l g} \sum_{j=1}^{nc} \gamma_j c_d^j \nabla T \\ & + (1-\omega_\pi)c_d^i k_l \frac{RT\omega_\pi}{\rho_l g} \sum_{j=1}^{nc} \gamma_j \left(1 + \frac{\partial \ln \gamma_j}{\partial \ln c_d^j} \right) \nabla c_d^j \\ & - (1-\omega_\pi)c_d^i k_l \nabla z + \sum_{j=1}^{nc} (nS_i \delta_{ij} \mathbf{D}_m + nS_i \tau_i D_{ij}^0) \nabla c_j + nS_i \tau_i D_i^T \nabla T \end{aligned} \right\} \quad (3.168)$$

Note that the above equation is applied for the 2^{nd} to nc^{th} chemical components.

Grouping the similar items, with some rearrangement, the governing equation for the reactive transport of multicomponent chemicals in terms of primary variables will yield for the i^{th} chemical ($i=2$ to nc):

$$\begin{aligned}
& C_{c_d l} \frac{\partial u_l}{\partial t} + C_{c_d T} \frac{\partial T}{\partial t} + C_{c_d a} \frac{\partial u_a}{\partial t} + C_{c_d c_d} \frac{\partial c_d^i}{\partial t} + C_{c_d s} \frac{\partial s_i}{\partial t} + C_{c_d u} \frac{\partial \mathbf{u}}{\partial t} \\
& = \nabla \cdot [K_{c_d l} \nabla u_l] + \nabla \cdot [K_{c_d T} \nabla T] + \nabla \cdot \left[\sum_{i=1}^{nc} K_{c_d c_d} \nabla c_d^i \right] + J_{c_d}
\end{aligned} \tag{3.169}$$

where;

$$C_{c_d l} = -nc_d^i \frac{\partial S_l}{\partial s} \tag{3.170}$$

$$C_{c_d T} = nc_d^i \frac{\partial S_l}{\partial s} \frac{\partial s}{\partial T} \tag{3.171}$$

$$C_{c_d a} = nc_d^i \frac{\partial S_l}{\partial s} \tag{3.172}$$

$$C_{c_d c_d} = nS_l \tag{3.173}$$

$$C_{c_d s} = nS_l \tag{3.174}$$

$$C_{c_d u} = S_l c_d^i \mathbf{m}^T \mathbf{P} \tag{3.175}$$

$$K_{c_d l} = -(1 - \omega_\pi) c_d^i \frac{k_l}{\rho_l g} \tag{3.176}$$

$$K_{c_d T} = (1 - \omega_\pi) c_d^i k_l \frac{R \omega_\pi}{\rho_l g} \sum_{j=1}^{nc} (\gamma_j c_d^j) + nS_l \tau_i D_i^T \tag{3.177}$$

$$K_{c_d c_d} = (1 - \omega_\pi) c_d^i k_l \frac{RT \omega_\pi}{\rho_l g} \gamma_j \left(1 + \frac{\partial \ln \gamma_j}{\partial \ln c_d^j} \right) + \delta_{ij} nS_l \mathbf{D}_m + nS_l \tau_i D_{ij}^0 \tag{3.178}$$

$$J_{c_d} = -(1 - \omega_\pi) c_d^i k_l \nabla z \tag{3.179}$$

If charge is conserved in the reaction sink/source terms separately, the charge conservation is applied for the 1st chemical component from equation (3.129) which yields:

$$\begin{aligned}
& \sum_{j=1}^{nc} nS_l z_j \frac{\partial c_d^j}{\partial t} - \sum_{j=1}^{nc} z_j n c_d^j \frac{\partial S_l}{\partial s} \frac{\partial u_l}{\partial t} + \sum_{j=1}^{nc} z_j n c_d^j \frac{\partial S_l}{\partial s} \frac{\partial s}{\partial T} \frac{\partial T}{\partial t} \\
& + \sum_{j=1}^{nc} z_j n c_d^j \frac{\partial S_l}{\partial s} \frac{\partial u_a}{\partial t} + \sum_{j=1}^{nc} z_j S_l c_d^j \mathbf{m}^T \mathbf{P} \frac{\partial \mathbf{u}}{\partial t} = 0
\end{aligned} \tag{3.180}$$

Similarly, incorporating the sink/source term for the first component, the governing equation is obtained in terms of primary variables as:

$$C_{c_d l} \frac{\partial u_l}{\partial t} + C_{c_d T} \frac{\partial T}{\partial t} + C_{c_d a} \frac{\partial u_a}{\partial t} + \sum_{j=1}^{nc} C_{c_d c_d} \frac{\partial c_d^j}{\partial t} + C_{c_d s} \frac{\partial s}{\partial t} + C_{c_d \mathbf{u}} \frac{\partial \mathbf{u}}{\partial t} = 0 \tag{3.181}$$

where;

$$C_{c_d l} = - \sum_{j=1}^{nc} z_j n c_d^j \frac{\partial S_l}{\partial s} \tag{3.182}$$

$$C_{c_d T} = \sum_{j=1}^{nc} z_j n c_d^j \frac{\partial S_l}{\partial s} \frac{\partial s}{\partial T} \tag{3.183}$$

$$C_{c_d a} = \sum_{j=1}^{nc} z_j n c_d^j \frac{\partial S_l}{\partial s} \tag{3.184}$$

$$C_{c_d c_d} = n S_l z_j \tag{3.185}$$

$$C_{c_d s} = n S_l \tag{3.186}$$

$$C_{c_d \mathbf{u}} = \sum_{j=1}^{nc} z_j S_l c_d^j \mathbf{m}^T \mathbf{P} \tag{3.187}$$

3.7 Deformation behaviour

This section presents the theoretical background of deformation behaviour in the model. Since the deformation behaviour is not under detailed investigation in this thesis, only the general framework of mechanical/deformation model is provided for the sake of completeness. The majority of the formulation for deformation behaviour has been previously presented by Thomas and He, 1998; Cleall, 1998; Mitchell, 2002; Melhuish, 2004 and Vardon, 2009, based on an elasto-plastic constitutive model, i.e., BBM developed by Alonso et al. (1990).

In this model, deformation is assumed to occur due to stress, suction and temperature. Any deformation due to osmosis effects is not dealt with in this work. It has been stated that the stress state of soil in relation to volume change behaviour can be described by two independent stress-state parameters (Fredlund and Rahardjo, 1993). The BBM uses this assumption and uses two independent stress-state variables, net stress and suction. Alonso et al. (1990) proposed an elasto-plastic work hardening constitutive model using net mean stress and suction as the relevant stress variables. The net mean stress was defined as:

$$\sigma'' = \sigma - u_a \quad (3.188)$$

where σ'' represents the net stress and σ is the total stress. In this work a tension positive sign convention is adopted for stress, but the pore pressures, u_l , and u_a are defined as positive in compression.

For an element of soil with unit length and a cross sectional area of $dx dy dz$ under a system of three-dimensional stresses and body forces, the stress equilibrium equation in an incremental form can be represented as:

$$\mathbf{P} d\sigma'' + \mathbf{P} m du_a + d\mathbf{b} = 0 \quad (3.189)$$

where \mathbf{b} is the vector of body forces and \mathbf{P} represents the strain matrix given as:

$$\mathbf{P} = \begin{bmatrix} \frac{\partial}{\partial x} & 0 & 0 & \frac{\partial}{\partial z} & 0 & \frac{\partial}{\partial y} \\ 0 & \frac{\partial}{\partial z} & 0 & \frac{\partial}{\partial x} & \frac{\partial}{\partial y} & 0 \\ 0 & 0 & \frac{\partial}{\partial y} & 0 & \frac{\partial}{\partial z} & \frac{\partial}{\partial x} \end{bmatrix} \quad (3.190)$$

For a three dimensional analysis, the vector \mathbf{m}^T is defined as:

$$\mathbf{m}^T = [1 \ 1 \ 1 \ 0 \ 0 \ 0] \quad (3.191)$$

To form a constitutive elasto-plastic model a series of relationships are required. These are defined below (Britto and Gunn, 1987; Owen and Hinton, 1980):

- *constitutive elastic relationship*
- *yield function*, defining the yield surface in stress space
- *flow rule*, defining the direction and magnitude of strains produced during yielding
- *hardening law*, defining the relationship between plastic strain and material hardening

These requirements are discussed briefly as follows.

3.7.1 Constitutive elastic relationship

For a soil exhibiting elasto-plastic behaviour, during any increment of stress, the change of strain $d\boldsymbol{\varepsilon}$ is assumed to be divided into elastic and plastic components (Owen and Hinton, 1980). The incremental strain can be expressed as:

$$d\boldsymbol{\varepsilon} = d\boldsymbol{\varepsilon}^e + d\boldsymbol{\varepsilon}^p \quad (3.192)$$

where $d\boldsymbol{\varepsilon}^e$ is the incremental elastic component of strain, and $d\boldsymbol{\varepsilon}^p$ is the incremental plastic component of strain.

Thomas and He (1995), based on the proposed approach by Wang (1953), stated that the incremental elastic strain may be written as:

$$d\boldsymbol{\varepsilon}^e = d\boldsymbol{\varepsilon}_p^e + d\boldsymbol{\varepsilon}_s^e + d\boldsymbol{\varepsilon}_T^e \quad (3.193)$$

where $\boldsymbol{\varepsilon}$ is the strain vector, and the subscripts p , s , and T , represent the components due to change in stress, suction, and temperature respectively.

Based on generalised Hooke's law, the *constitutive elastic relationship*, i.e. stress-strain relationship can be described as follows:

$$d\boldsymbol{\sigma}^n = \mathbf{D}d\boldsymbol{\varepsilon}_p^e = \mathbf{D}(d\boldsymbol{\varepsilon} - d\boldsymbol{\varepsilon}_s^e - d\boldsymbol{\varepsilon}_T^e - d\boldsymbol{\varepsilon}^p) \quad (3.194)$$

where \mathbf{D} represents the elasticity matrix.

It is assumed that the elastic deformation of partially saturated soil is due to changes in the net stress and the suction under isothermal conditions, (Alonso et al., 1990). Suction changes are also assumed that only produce volumetric strain. The elastic volumetric strain components due to suction and temperature changes can be presented as (Thomas and He, 1995):

$$d\varepsilon_p^e = -\frac{\kappa_s}{v} \frac{ds}{(s + p_{atms})} = A_s ds \quad (3.195)$$

$$d\varepsilon_T^e = \left(\frac{\alpha_T}{v_0} dT + A_s \frac{\partial s}{\partial T} dT \right) = \left(A_T + A_s \frac{\partial s}{\partial T} \right) dT \quad (3.196)$$

Where v is the specific volume, κ_s represents the slope of the specific volume-suction (v - s) curve, in the elastic region, and p_{atms} , is the atmospheric pressure added to avoid infinite values of strain as suction approaches zero. α_T stands for the coefficient of thermal expansion, and v_0 is the initial specific volume. The relationships were presented in simplified forms using parameters A_s and A_T .

3.7.2 Yield function

The *yield criteria* function determines where stress starts to yield. Alonso et al. (1990) proposed the use of two yield functions, the loading-collapse (LC) curve and the suction-increase (SI) curve. The LC curve indicates that yielding occurs when pre-consolidation stress reaches a critical stress value, p_0 . The SI curve indicates that yield occurs when suction reaches a critical value, s_0 . These two yield functions can be mathematically represented as:

$$F_1(p, q, s, p_0^*) = q^2 - M^2 (p + p_s)(p_0 - p) = 0 \quad (3.197)$$

$$F_2(s, s_0) = s - s_0 = 0 \quad (3.198)$$

where q is the deviatoric stress, M is the slope of the critical state line, p_0 is the pre-consolidation stress, p_s is related to the suction effect on the cohesion of the soil and s_0 is the previously attained maximum value of suction.

Alonso et al. (1990) proposed the following equation, which defines the set of yield p_0 values for the associated suction values:

$$\left(\frac{p_0}{p_c} \right) = \left(\frac{p_0^*}{p_c} \right)^{\left(\frac{\lambda(0) - \kappa}{\lambda(s) - \kappa} \right)} \quad (3.199)$$

where p_0^* is the pre-consolidation stress of saturated soil, p_c is the reference stress, $\lambda(s)$ is the stiffness parameter for changes in net mean stress for virgin states of the soil and $\lambda(0)$ is the stiffness parameter for changes in net mean stress for virgin states of saturated soil.

Alonso et al. (1990) proposed an asymptotic expression for the prediction of the virgin soil stiffness parameter, $\lambda(s)$, as:

$$\lambda(s) = \lambda(0) \left[(1 - r) \exp(-\beta s) + r \right] \quad (3.200)$$

where β is a parameter controlling the rate of increase of soil stiffness with suction, and the parameter r controls the maximum stiffness of the soil.

3.7.3 Flow rule

As yield occurs, the plastic strain increment is related to the stress gradient by definition of a flow rule. This theoretical assumption is termed the *flow rule* as it governs the plastic flow after yielding. Therefore, flow rules are required to define the magnitude of plastic strains produced when the material is yielding. Alonso et al. (1990) proposed two types of flow rules. An associated plastic flow rule for the SI surfaces and a non-associated flow rule for the LC yield surface.

Thomas and He (1998) proposed the use of these functions as plastic potentials. The plastic potential for LC yield surface Q_1 , as defined by non-associated flow rule is:

$$Q_1 = \alpha_q q^2 - M^2 (p + p_s) (p_0 - p) \quad (3.201)$$

The plastic potential for SI yield surface Q_2 , as defined by associated flow rule is:

$$Q_2 = s - s_0 \quad (3.202)$$

Assuming that the elastic strain increment is zero, α_q was defined by Alonso et al. (1990) as:

$$\alpha_q = \frac{M(M-9)(M-3)}{6(6-M)} \left(1 - \frac{\kappa}{\lambda(0)}\right)^{-1} \quad (3.203)$$

It is assumed that the strain increment is proportional to the stress gradient of the plastic potentials which yields:

$$d\varepsilon^p = \chi_1 \frac{dQ_1}{d\sigma^n} + \chi_2 \frac{dQ_2}{ds} \quad (3.204)$$

where χ_1 and χ_2 are plastic multipliers which are determined through plastic consistency conditions (Alonso et al., 1990).

Accordingly, the plastic strain increments associated with yield surface F_1 is,

$$d\varepsilon_p^p = \chi_1 \frac{dQ_1}{dp} = \chi_1 M^2 (2p + p_s - p_0) \quad (3.205)$$

$$d\varepsilon_q^p = \chi_1 \frac{dQ_1}{dq} = \chi_1 2\alpha_q q \quad (3.206)$$

Where α_q is a constant derived from K_0 , the 'at rest' stress state, where there is no lateral deformation as defined by (Alonso et al., 1990).

The plastic strain increment associated with yield surface F_2 can be given as:

$$d\varepsilon_s^p = \chi_2 \frac{dQ_2}{ds} = \chi_2 \quad (3.207)$$

From the above discussions, the total plastic strain increment is considered as a sum of plastic strain increments due to stress changes and suction changes.

3.7.4 Hardening law

After yielding, the stress level at which further plastic deformation occurs is dependent on the current degree of plastic straining. Josa et al. (1987) found there was a coupling between the hardening of the two yield surfaces. The yield surfaces are controlled by the hardening parameters p_0^* and s_0 , and they depend on the plastic volumetric strain increment $d\varepsilon_v^p$ as:

$$d\varepsilon_v^p = d\varepsilon_{vp}^p + d\varepsilon_{vs}^p \quad (3.208)$$

The two hardening laws for the yield surfaces F_1 and F_2 are, respectively (Alonso et al., 1990):

$$\frac{dp_0^*}{p_0^*} = \frac{v}{\lambda(0) - \kappa} d\varepsilon_v^p \quad (3.209)$$

$$\frac{ds_0}{s_0} = \frac{v}{\lambda_s - \kappa_s} d\varepsilon_v^p \quad (3.210)$$

where λ_s is the stiffness parameter for changes in suction for suction virgin soil states.

3.7.5 Governing equation for deformation

As shown in section 3.7.1, the elastic stress-strain relationship can be related by the use of elastic incremental constitutive matrix \mathbf{D} . This elastic stiffness matrix is used to predict the change in stress produced as a result of changes in volumetric strain. However, if this stiffness matrix was adopted whilst plastic deformation was occurring it would over-predict the change in stress. Therefore the stiffness matrix \mathbf{D} must be modified taking account of the plastic strain produced due to an application of load. The complete elasto-plastic incremental stress-strain relation may now be formulated, after Owen and Hinton (1980):

$$d\sigma^n = \mathbf{D}_{ep} d\varepsilon_p^e \quad (3.211)$$

Mitchell (2002) defined the matrix \mathbf{D}_{ep} as:

$$\mathbf{D}_{ep} = \mathbf{D} - \frac{\mathbf{D} \frac{\partial Q_1}{\partial \sigma^n} \frac{\partial F_1}{\partial \sigma^n} \mathbf{D}}{\mathbf{A}_p + \left(\frac{\partial Q_1}{\partial \sigma^n} \right)^T \mathbf{D} \frac{\partial F_1}{\partial \sigma^n}} \quad (3.212)$$

where \mathbf{A}_p is the plastic modulus defined as:

$$\mathbf{A}_p = M^2 (p + p_s) \frac{\lambda(0) - \kappa}{\lambda(s) - \kappa} p_0 \frac{v}{\lambda(0) - \kappa} \left[M^2 (2p + p_s - p_0) \right] \quad (3.213)$$

The stress-strain relationship expressed in equation (3.211) may now be given as:

$$d\sigma^n = \mathbf{D}_{ep} (d\varepsilon - d\varepsilon_s^e - d\varepsilon_T^e - d\varepsilon_s^p) \quad (3.214)$$

Substitution of equations (3.195) and (3.196) into equation (3.214) gives:

$$d\sigma'' = \mathbf{D}_{ep} (d\varepsilon - A_s ds - (A_T + A_s \frac{dS_l}{dT})dT - d\varepsilon_s^p) \quad (3.215)$$

The stress equilibrium equation (3.189) can be rewritten with substitution from equation (3.215) as:

$$P \left[\mathbf{D}_{ep} \left(P^T du + A_s du_l - \left(A_T + A_s \frac{ds}{dT} \right) dT - A_s du_a - d\varepsilon_s^p \right) \right] + Pmdu_a + db = 0 \quad (3.216)$$

The governing differential equation for this approach can then be written as:

$$C_{ul} du_l + C_{uT} dT + C_{ua} du_a + C_{uu} du - \mathbf{PD}_{ep} d\varepsilon_s^p + d\mathbf{b} = 0 \quad (3.217)$$

where;

$$C_{ul} = \mathbf{PD}_{ep} A_s \quad (3.218)$$

$$C_{uT} = \mathbf{PD}_{ep} \left(-A_T - A_s \frac{ds}{dT} \right) \quad (3.219)$$

$$C_{ua} = -\mathbf{PD}_{ep} A_s + \mathbf{mP} \quad (3.220)$$

$$C_{uu} = -\mathbf{PD}_{ep} \mathbf{P}^T \quad (3.221)$$

3.8 Summary

This chapter presented the theoretical formulation for the thermo/hydro/chemical/mechanical behaviour. The governing equations for moisture, air and heat transfer have been modified to incorporate osmotic effects. Seetharam (2003) presented the effects of osmosis only on liquid water transport and implicitly in the formulation while in the presented work; the osmotic potential is calculated explicitly both in liquid water and vapour flow equation. Neglecting included osmotic effect, the governing equations for the moisture and dry air transport are identical to those proposed earlier (Ramesh, 1996; Thomas and He, 1998; Cleall, 1998; Mitchell, 2002; Seetharam, 2003; Vardon, 2009). In terms of heat transport, osmosis effects were included for the sake of completeness as it affects the formulation of fluid flux. In the case of compacted swelling clay, further modifications to the flow properties and constitutive equation will be provided in chapter 7 where in particular, a model for approximation of the interlayer hydrate water is provided and the effects on flow behaviour will be expanded more.

The main contribution of this chapter is in the development of the reactive transport of multicomponent chemicals. Charge conservation law was explicitly included in the derivation of formulation. The diffusive flux was modified in order to include the effect of electrochemical diffusion potential, developing due to migration of chemical with different rate of diffusion as it is expected in compacted clays. The formulation of multicomponent chemical diffusion proposed by Seetharam (2003) is based on Fick's law of diffusion in which the overall neutrality condition is not satisfied when ions migrate with different diffusion coefficients. In the formulation of the general diffusive flux presented in this chapter, the derivation forces for diffusion are derived from combined electrical and chemical potential rather than from the chemical concentration potential.

In addition, the effects of thermal diffusion, i.e. Soret effect, was considered in an explicit form which is combined with diffusion due to the electrochemical potential. A theoretical approach for the Soret coefficient was adopted that can be applied in the absence of sufficient experimental data. The individual requirements of overall charge conservation were included in the formulation. Provided in this chapter, a general formulation for multi-chemical reactive transport was presented where the advective flux, molecular and thermal diffusive flux and dispersive flux have been considered as the main hydro/chemical potentials. The effects of interlayer hydrate water and osmosis on tracer diffusion coefficient of ions in compacted

clays were considered in a general tortuosity factor which can be different for different ions. The later will be discussed more in chapter 6 for the case of compacted smectite clays.

Another highlight of the chemical governing equation is the coupling an advanced geochemical model, PHREEQC *version 2*, in order to calculate the sink/source reaction term, which represents the chemical reactions. PHREEQC *version 2* has advantages over the geochemical model, MINTEQA2 utilised by Seetharam (2003). The capability of modelling kinetically controlled reactions, the implemented Pitzer's equation for calculating activity coefficient of ions in high ionic concentration solutions, and the availability of various databases in the package are among the highlights of this model in the framework of the modelling geochemical processes in compacted clays. The theoretical basis for the geochemical reactions has not been covered in this chapter as the proposed model utilises an existing geochemical model, PHREEQC *version 2*, for this purpose. Details information about the theoretical and numerical formulation of PHREEQC *version 2* has been provided by Parkhurst and Appelo (1999).

The effects of mineral precipitation/dissolution on flow parameter were implemented as a porosity modification feed-back from the geochemical model. In other words, flow parameters such as hydraulic conductivity, is modified due to variation in porosity with mineral precipitation or dissolution.

Finally, the theoretical formulation for deformation proposed by Thomas and He (1998) based on Alonso's model has been briefly covered.

3.9 References

Allison, J.D., Brown, D.S. and Novo-Gradac, K.J. (1991). *MINTEQA2 user manual version 3.0*. Environmental Research Laboratory, US EPA.

Alonso, E.E., Gens, A., and Josa, A. (1990). A constitutive model for partially saturated soils. *Géotechnique*, 40(3), 405-430.

Agar, J.N., Mou, C.Y., and Lin, J. (1989). Single-ion heat of transport in electrolyte solutions, A hydrodynamic theory. *Journal of Physical Chemistry*, 93, 2079-2082.

Alonso, E.E., Battle, F., Gens, A., and Lloret, A. (1988). Consolidation analysis of partially saturated soils- Application to earth dam construction. *Numerical Methods in Geomechanics*, 1303-1308.

Appelo, C.A.J., and Postma, D. (1993). *Geochemistry, Groundwater and Pollution*. A.A. Balkema, Rotterdam.

Appelo, C.A.J., and Wersin, P. (2007). Multicomponent diffusion modeling in clay systems with application to the diffusion of tritium, iodide and sodium in Opalinus clay. *Environmental Science and Technology*, 41, 5002-5007.

Baker, R., and Frydman, S. (2009). Unsaturated soil mechanics-Critical review of physical foundations. *Engineering Geology*, 106, 26-39.

Balluffi, R.W., Allen, S.M., and Carter, W.C. (2005). *Kinetics of Materials*. (ed. Kemper, R. A.), John Wiley and Sons Inc.

Bear, J. and Verruijt, A. (1987). *Modeling Groundwater Flow and Pollution*. D. Redel Pub. Co., Dordrecht.

Bethke, C.M. (1996). *Geochemical Reaction Modeling: Concepts and Applications*. Oxford University Press.

Borkovec, M., and Westall, J. (1983). Solution of the Poisson-Boltzmann equation for surface excesses of ions in the diffuse layer at the oxide-electrolyte interface. *Journal of Electroanalytical Chemistry*, 150, 325-337.

Boudreau, B.P., Meysman, F.J.R. and Middelburg, J.J. (2004). Multicomponent ionic diffusion in pore waters: Coulombic effects revisited. *Earth Planetary Science Letters*, 222, 653-666.

- Bourg, I.C., Sposito, G., and Bourg, A.C.M. (2006). Tracer diffusion in compacted, water-saturated bentonite. *Clays and Clay Minerals*, 54 (3), 363-74.
- Britto, A.M., and Gunn, M.G. (1987). *Critical State Soil Mechanics via Finite Elements*. Ellis Horwood Ltd.
- Campbell, G.S. 1985. *Soil physics with BASIC*. Elsevier, New York.
- Carman, P.C. (1956). *Flow of gases through porous media*. Butterworths Scientific Publications, London.
- Cleall, P.J. (1998). *An investigation of the thermo/hydraulic/mechanical behaviour of unsaturated soils, including expansive clays*, Ph.D. Thesis. Cardiff University, Wales, U.K.
- Crank, J. (1975). *The Mathematics of Diffusion*. 2nd ed., Clarendon, Oxford.
- Cussler, E.L. (1997). *Diffusion-Mass Transfer in Fluid Systems*. University Press, Cambridge, 2nd Edition.
- Davis, J.A., and Kent, D.B. (1990). Surface complexation modeling in aqueous geochemistry. In Hochella, M.F., and White, A.F., (eds.), *Mineral-Water Interface Geochemistry: Washington D.C., Mineralogical Society of America, Reviews in Mineralogy*, 23,177-260.
- de Vries, D.A. (1958). Simultaneous transfer of heat and moisture in porous media. *Transaction American Geophysical Union*, 39(5), 909-916.
- de Vries, D.A. (1966). *Physics of Plant Environment*. 2nd Edition, North Holland Publishing Company, 215-235.
- Delage, P. (2002). State of-the-art-report: experimental unsaturated soil mechanics. 3rd *International Conference on Unsaturated Soils*, Recife, Brazil.
- Derjaguin, B.V., Churaev, N.V., and Muller, V.M. (1987). *Surface Forces*. Plenum, New York.
- Dzombak, D.A., and Morel, F.M.M. (1990). *Surface Complexation Modeling-Hydrous Ferric Oxide*. New York, John Wiley.
- Edelfsen, N.E., and Andersen, A.B.C. (1943). Thermodynamics of soil moisture. *Hilgardia*, 15(2), 31-298.

- Ewen, J., and Thomas, H.R. (1989). Heating unsaturated medium sand, *Géotechnique*, 39(3), 455-470.
- Fredlund, D.G., and Rahardjo, H. (1993). *Soil Mechanics for Unsaturated Soils*. John Wiley, New York.
- Fritz, S.J. (1986). Ideality of clay membranes in osmotic processes: A review. *Clays and Clay Minerals*, 34(2), 214-223.
- Grant, S.A., and Salehzadeh, A. (1996). Calculations of temperature effects on wetting coefficients of porous solids and their capillary pressure functions. *Water Resource Research*, 32, 261-79.
- Geraminegrad, M., and Saxena, S. (1986). *Finite Elements in Plasticity: Theory and Practice*. Pineridge Press Ltd., Swansea.
- Hu, Q.H., and Wang, J.S.Y. (2003). Aqueous-phase diffusion in unsaturated geological media: A review. *Critical Reviews in Environmental Science and Technology*, 33(3), 275-297
- Jakob, M. (1949). *Heat Transfer: Vol 1*. Wiley.
- Josa, A., Alonso, E.E., Lloret, A., and Gens, A. (1987). Stress-strain behaviour of partially saturated soils. In *Proceedings of the 9th European Conference on Soil Mechanics and Foundation Engineering, Dublin, 2*, 561-564.
- Jougnot, D., Revil, A., and Leroy, P. (2009). Diffusion of ionic tracers in the Callovo-Oxfordian clay-rock using the Donnan equilibrium model and the formation factor. *Geochimica et Cosmochimica Acta*, 73(10): 2712-2726.
- Kaye, G.W.C., and Laby, T.M. (1973). *Tables of Physical and Chemical Constants*. 14th Edition, Harlow, Longman.
- Kharaka, Y.K., and Berry, F.A.F. (1973). Simultaneous flow of water and solutes through geological membranes—I. Experimental investigation. *Geochimica et Cosmochimica Acta*, 37(12), 2577-2603.
- Langmuir, D. (1997). *Aqueous Environmental Geochemistry*. Prentice Hall.
- Lasaga, A.C. (1979). The treatment of multicomponent diffusion and ion pairs in diagenetic fluxes. *American Journal of Science*, 279, 324-346.

- Lasaga, A.C. (1981). Reply-diffusion of seawater ions: significance and consequences of cross coupling effects: further comments and clarifications. *American Journal of Science*, 281, 981-988.
- Lasaga, A.C. (1998). *Kinetic Theory in the Earth Science*. Princeton Series in Geochemistry, Princeton University Press.
- Leaist, D.G., and Hui, L. (1990). Conductometric determination of the Soret coefficients of a ternary mixed electrolyte-Reversed thermal diffusion of sodium chloride in aqueous sodium hydroxide solutions. *Journal of Physical Chemistry*, 94, 447-451.
- Lerman, A. (1979). *Geochemical Processes, Water and Sediment Environments*. Wiley, New York.
- Lichtner, P.C. (1995). Principles and practice of reactive transport modelling. *Material Research Society Symposium Proceeding*, 353, 117-130.
- Lichtner, P.C. (1996). Continuum formulation of multicomponent multiphase reactive transport. *In Reactive Transport in Porous Media: Reviews in Mineralogy*, 34, 1-81.
- Malusis MA, Shackelford C.D. (2002). Theory for reactive solute transport through clay membrane barriers. *Journal of Contaminant Hydrology*, 59,291–316.
- Manassero, M., and Dominijanni, A. (2003). Modelling the osmosis effect on solute migration through porous media. *Géotechnique*, 53, 481–92.
- Mangold, D.C., and Tsang, C.F. (1991). A summary of subsurface hydrological and hydrochemical models. *Review of Geophysics*, 29(1), 51-79.
- Mayhew, Y.R., and Rogers, G.F.C. (1976). *Thermodynamic and Transport Properties of Fluids*. 2nd Edition, Blackwell, Oxford.
- Melhuish, T.A. (2004). *An investigation of the three-dimensional thermo/hydro/mechanical behaviour of large scale in-situ experiments*. PhD Thesis, Cardiff University, Cardiff.
- Merkel, B.J., Planer-Friedrich, B. and Nordstrom, D.K. (2005). *Groundwater Geochemistry: A Practical Guide to Modeling of Natural and Contaminated Aquatic Systems*, Springer.
- Miller, D.G. (1966). Application of irreversible thermodynamics to electrolyte solutions. I determination of ionic transport coefficients I_{ij} for isothermal vector transport processes in binary systems. *Journal of Physical Chemistry*, 70, 2693-2659.

- Mitchell, J.K. (1993). *Fundamentals of Soil Behaviour*. John Wiley, New York.
- Mitchell, H.P. (2002). *An investigation into the thermo/hydro/mechanical interactions involved in high level nuclear waste disposal*. PhD Thesis, University of Wales, Cardiff.
- Newman, J. (1991). *Electrochemical Systems*. Prentice-Hal., New Jersey, 2nd Edition.
- Olson, R.E. (1963). Effective stress theory of compaction. *Proceedings of the American Society of Civil Engineering*, 81, 27-44.
- Oelkers, E. (1996). *Physical and chemical properties of rocks and fluids for chemical mass transport calculations*. In *Reactive Transport in Porous Media, Reviews in Mineralogy*, 34, 130-191.
- Or, D., and Wraith, J.M. (2001). *Soil Water Content and Potential*. In: Warrick A. (ed.), *Soil Physics Companion*. CRC Press, Boca Raton, FL.
- Oscarson, D.W. (1994). Surface diffusion: Is it an important transport mechanism in compacted clays? *Clays and Clay Minerals*, 42, 534-543.
- Owen, D.R.J., and Hinton, E. (1980). *Finite Elements in Plasticity: Theory and Practice*. Pineridge Press Ltd., Swansea.
- Parkhurst, D.L., and Appelo, C.A.J. (1999). *User's Guide to PHREEQC (version 2)*, U.S. Geological Survey, Water Resource Investigation Report, 99-4259.
- Partington, J.R. (1949). *Advanced Treatise on Physical Chemistry*, Volume 1, Longmans, London.
- Philip, J.R. (1977). Unitary approach to capillary condensation and adsorption. *Journal of Chemical Physics*, 66, 5069-75.
- Philip, J.R., and de Vries, D.A. (1957). Moisture movement in porous materials under temperature gradients. *Transaction American Geophysical Union*, 38(2), 222-232.
- Pickens, J.F. and Gilham, R.W. (1980). Finite element analysis of solute transport under hysteresis unsaturated flow conditions. *Water Resource Research*, 16, 1071-1078.
- Platten, J.K. (2006). The Soret effect: A review of recent experimental results. *Journal of Applied Mechanics*, 73, 5-15.

- Pollock, D.W. (1986). Simulation of fluid flow and energy transport processes associated with high-level radio active waste disposal in unsaturated alluvium, *Water Resources Research*, 22(5), 765-775.
- Preece, R.J. (1975). *The measurement and calculation of physical properties of cable bedding sands. Part 2; specific thermal capacity, thermal conductivity and temperature ratio across 'air' filled pores*, C.E.G.B. Laboratory Note No. RD/L/N 231/74.
- Pusch, R. (1998). Microstructural evolution of buffer clay. In *Proceedings of workshop on microstructural modelling of natural and artificially prepared clay soils with special emphasis on the use of clays for waste isolation*, Lund, 31-38.
- Pusch, R. and Yong, R.N. (2006). *Microstructure of Smectite Clays and Engineering Performance*. Taylor and Francis, New York.
- Ramesh, A.D. (1996). *Modelling the thermo/hydraulic/mechanical behaviour of unsaturated soil using an elasto-plastic constitutive relationship*, Ph.D thesis. University of Wales Cardiff.
- Robinson, R.A., and Stokes, R.H. (1959). *Electrolyte Solutions*. Butterworth and Co. Ltd.
- Rodebush, W.H., and Buswell, A.M. (1958). *Properties of Water Substances*. Highway Resources Board Special Report, No. 40.
- Romero, E., Gens, A., and Lloret, A. (2001). Temperature effects on the hydraulic behaviour of an unsaturated clay. *Geotechnical and Geological Engineering*, 19, 311-32.
- Romero, E.M., and Vaunat, J. (2000). Retention curves of deformable clays. In Tarantino, M. (ed.), *Conference on Experimental Evidence and Theoretical Approach in Unsaturated Soils*, Balkema, Rotterdam, 91-106.
- Rosanne, M., Paszkuta, M., and Adler, P.M. (2006). Thermodiffusional transport of electrolytes in compact clays. *Journal of Colloid Interface Science*, 299, 797-805.
- Sato, H., Yui, M. and Yoshikawa, H. (1995). Diffusion behavior for Se and Zr in sodium-bentonite. *Material Research Society Symposium Proceeding*, 353, 269-276.
- Seetharam, S.C. (2003). *An investigation of the thermo/hydro/chemical/mechanical behaviour of unsaturated soils*. Ph.D. Thesis, Cardiff University, Wales, UK.

- Sheng D., Gens, A., Fredlund, D.G., and Sloan, S.W. (2008). Unsaturated soils: From constitutive modelling to numerical algorithms. *Computers and Geotechnics*, 35 810-24.
- Singh, R.M. (2007). *An experimental and numerical investigation of heat and mass movement in unsaturated clays*. PhD Thesis, Cardiff University, Wales, UK.
- Snowdon, P.N., and Turner, J.C.R. (1960). The concentration dependence of the Soret effect. *Transaction Faraday Society*, 56, 1812-1819.
- Sonnenthal, E., Spycher, N. and Xu, T. (2003). Linking reaction, transport, and hydrological parameters in unsaturated fractured rock: TOUGHREACT implementation and application. *In Proceedings TOUGH Symposium 2003, Lawrence Berkeley National Laboratory, Berkeley, California*, (<http://escholarship.org/uc/item/37f0d52p>).
- Steeffel, C.I. (2008). *Geochemical kinetics and transport*. In Kinetics of Water-Rock Interaction Brantley, S.L., Kubicki, J.D., and White, A.F.(ed.) Springer, 545-589.
- Steeffel, C.I. and Lasaga, A.C. (1994). A coupled model for transport of multiple chemical species and kinetic precipitation/dissolution reactions with application to reactive flow in single phase hydrothermal systems. *American Journal of Science*, 294, 529-592.
- Thomas, H.R., Cleall, P.J., Chandler, N., Dixon, D., and Mitchell, H.P. (2003). Water infiltration into a large-scale in-situ experiment in an underground research laboratory. *Géotechnique*, 53(2), 207-224.
- Thomas, H.R., and He, Y. (1995). Analysis of coupled heat, moisture and air transfer in a deformable unsaturated soil. *Géotechnique*, 45(4), 677-689.
- Thomas, H.R., and He, Y. (1998). Modelling the behaviour of unsaturated soil using an elasto plastic constitutive relationship. *Géotechnique*, 48, 589-603.
- Thomas, H.R., and King, S.D. (1991). Coupled temperature/capillary potential variations in unsaturated soil. *Journal of Engineering Mechanics, ASCE*, 117, 2475-2491.
- Thomas, H.R., and Samson, M.R. (1995). A fully coupled analysis of heat, moisture and air transfer in unsaturated soil. *Journal of Engineering Mechanics, ASCE*, 12(3), 392-405.
- Thyagaraj, T. and Rao, M.S. (2010). Influence of osmotic suction on the soil-water characteristic curves of compacted expansive clay. *Journal of Geotechnical and Geoenvironmental Engineering, ASCE*, 136(12), 1695-1702.

- Tuller, M., Or, D., and Dudley, L.M. (1999). Adsorption and capillary condensation in porous media: liquid retention and interfacial configurations in angular pores. *Water Resources Research*, 35, 1949-64.
- Van Brakel J. and Heertjes P.M. (1974). Analysis of diffusion in macroporous media in terms of a porosity, a tortuosity, and a constrictivity factor. *International Journal of Heat and Mass Transfer*, 17, 1093-1103.
- Van Loon, L.R., Glaus, M.A., and Müller, W. (2007). Anion exclusion effects in compacted bentonite: Towards a better understanding of anion diffusion. *Applied Geochemistry*, 22, 2536-2552.
- Vardon, P.J. (2009). *A three-dimensional numerical investigation of the therm-hydro-mechanical behaviour of a large-scale prototype repository*. Ph.D. Thesis, Cardiff University, Wales, UK.
- Wang, C. (1953). *Applied Elasticity*. McGraw-Hill Book Co.
- Wu, G., and Chieng, S.T. (1995). Modelling multicomponent reactive chemical transport in non isothermal unsaturated saturated soils, Part 1-Mathematical model development. *Transactions of the ASAE*, 38(3), 817-826.
- Yong, R.N. (1999). Soil suction and soil-water potentials in swelling clays in engineered clay barriers. *Engineering Geology*, 54, 3-13.
- Yong, R.N., and Warkentin, B.P. (1975). *Soil Properties and Behaviour*. Elsevier, Amsterdam.
- Zhang, F., Zhang, Z.Z., Low, P.F. and Roth, C.B. (1993). The effect of temperature on the swelling of montmorillonite. *Clay Minerals*, 28, 25-31.

Chapter 4

Numerical Formulation

4.1 Introduction

The numerical formulation of the solution of the governing differential equations representing heat, moisture, air, multicomponent reactive chemical and deformation behaviour is presented in this chapter. A finite element method is employed to spatially discretise the equations while a finite difference algorithm is used to achieve temporal discretisation. The numerical formulation concerning chemical reaction equations is briefly reviewed as the geochemical model, PHRREQC version 2 (Parkhurst and Appelo, 1999), is directly implemented without any modification to its numerical formulation. The sequential non-iterative approach adopted for solving the coupled chemical transport and reactions are also presented.

The numerical formulation concerning coupled heat, moisture, air and deformation has already been dealt with in detail by Ramesh (1996); Cleall (1998), Seetharam (2003) and Vardon (2009). The numerical formulation of the chemical transport equation has been specifically addressed by Hashm (1999) and Seethram (2003). Seethram (2003) presented the general numerical formulation for the multicomponent reactive chemical transport governing equations. In this chapter the numerical formulation for the multicomponent reactive chemical transport equations and the derivation will be presented in details. For the sake of completeness the final matrix form of heat, moisture, air and deformation is included.

Section 4.2 deals with the spatial discretisation of flow and deformation variables. In this section, the use of the Galerkin weighted residual method is presented to discretise the flow and deformation variables. Sections 4.3 deals with the general representation of the matrix form of the governing equations the temporal discretisation of the governing equations. A forward finite difference mid-interval time-stepping algorithm is used to achieve temporal discretisation. Section 4.4 provides the details of scheme adopted for coupling chemical transport equation with the geochemical model. The computational aspects of the coupling method are provided in this section. Finally, section 4.5 presents the overall summary of the above work.

4.2 Spatial discretisation

In the study presented here, the *Galerkin weighted residual method* is employed for the spatial discretisation (Zienkiewicz and Taylor, 1989). This method is widely recognised as a general numerical technique, for the solution of partial differential equation systems subject to appropriate boundary and initial conditions (Hinton and Owen, 1977). This method has been also found to be effective for the type of coupled formulations discussed in previous chapter (e.g. Thomas and He, 1995; Thomas and He, 1998; Seetharam et al., 2007; Seetharam et al., 2010).

Since the use of the finite element method to spatially discretise governing differential equations has been broadly described in literature (e.g. Zienkiewicz and Taylor, 1989), the spatial discretisation of the governing equations is introduced here in an abbreviated form.

Based on the Galerkin weighted residual method, the primary unknowns and their spatial derivatives can be approximated using shape functions. For an element with n_{node} nodes, this yields:

$$\omega \approx \hat{\omega} = \sum_{s=1}^{n_{node}} N_s \hat{\omega}_s \quad (4.1)$$

$$\nabla \hat{\omega} = \sum_{s=1}^{n_{node}} (\nabla N_s) \hat{\omega}_s \quad (4.2)$$

where ω represents any of the primary variables including u_l , T , u_a , c_d^i and \mathbf{u} . N_s is the shape function, the subscript, s , characterises nodal points, the symbol, $\hat{\cdot}$, indicates an approximation form.

4.2.1 Spatial discretisation for chemical flow

The derivation of the chemical flow differential equation is presented below. The numerical formulation is derived for a single chemical component. The procedure for any number of components remains the same as this one, and is hence not repeated for “ n ” number of chemicals.

The governing differential equation for an arbitrary chemical component can be presented in terms of the approximate functions as:

$$\begin{aligned}
& -C_{c_d l} \frac{\partial \hat{u}_l}{\partial t} - C_{c_d T} \frac{\partial \hat{T}}{\partial t} - C_{c_d a} \frac{\partial \hat{u}_a}{\partial t} - C_{c_d c_d} \frac{\partial \hat{c}_d^i}{\partial t} - C_{c_d s} \frac{\partial s_i}{\partial t} - C_{c_d u} \frac{\partial \hat{\mathbf{u}}}{\partial t} \\
& + \nabla \cdot [K_{c_d l} \nabla \hat{u}_l] + \nabla \cdot [K_{c_d T} \nabla \hat{T}] + \nabla \cdot [K_{c_d a} \nabla \hat{u}_a] + \nabla \cdot \left[\sum_{j=1}^{nc} K_{c_d c_d} \nabla \hat{c}_d^j \right] + J_{c_d} = R_\Omega
\end{aligned} \tag{4.3}$$

where R_Ω is the residual error.

In the Galerkin weighted residual approach, this residual over the entire element domain Ω^e is attempted to be minimised using the shape functions N_r as weighting coefficients as:

$$\int_{\Omega^e} N_r R_\Omega d\Omega^e = 0 \tag{4.4}$$

Replacing the residual error in equation (4.4) from equation (4.3) yields:

$$\int_{\Omega^e} N_r \left[-C_{c_d l} \frac{\partial \hat{u}_l}{\partial t} - C_{c_d T} \frac{\partial \hat{T}}{\partial t} - C_{c_d a} \frac{\partial \hat{u}_a}{\partial t} - C_{c_d c_d} \frac{\partial \hat{c}_d^i}{\partial t} - C_{c_d s} \frac{\partial s_i}{\partial t} - C_{c_d u} \frac{\partial \hat{\mathbf{u}}}{\partial t} + \nabla \cdot [K_{c_d l} \nabla \hat{u}_l] + \nabla \cdot [K_{c_d T} \nabla \hat{T}] + \nabla \cdot [K_{c_d a} \nabla \hat{u}_a] + \nabla \cdot \left[\sum_{j=1}^{nc} K_{c_d c_d} \nabla \hat{c}_d^j \right] + J_{c_d} \right] d\Omega^e = 0 \tag{4.5}$$

Employing integration by parts, the weak form of equation (4.5) may be obtained. For example the seventh term can be expressed as:

$$\int_{\Omega^e} N_r \nabla \cdot (K_{c_d l} \nabla \hat{u}_l) d\Omega^e = \int_{\Omega^e} \nabla \cdot (N_r K_{c_d l} \nabla \hat{u}_l) d\Omega^e - \int_{\Omega^e} K_{c_d l} \nabla \hat{u}_l \nabla N_r d\Omega^e \tag{4.6}$$

Also the term, J_{c_d} , can be expressed, with an appropriate substitution from equation (3.179) as:

$$\int_{\Omega^e} N_r \nabla J_{c_d} d\Omega^e = \int_{\Omega^e} \nabla \cdot (N_r c_d^i k_l \nabla z) d\Omega^e - \int_{\Omega^e} c_d^i k_l \nabla z \nabla N_r d\Omega^e \tag{4.7}$$

In a similar manner, by repeating the above process, the rest of the flux terms can be reduced, and substituting the reduced form in equation (4.5) will yield:

$$\int_{\Omega^e} \left[\begin{aligned} & + \nabla \cdot (N_r K_{c_d l} \nabla \hat{u}_l) - K_{c_d l} \nabla \hat{u}_l \nabla N_r + \nabla \cdot (N_r K_{c_d T} \nabla \hat{T}) - K_{c_d T} \nabla \hat{T} \nabla N_r \\ & + \nabla \cdot (N_r K_{c_d a} \nabla \hat{u}_a) - K_{c_d a} \nabla \hat{u}_a \nabla N_r + \nabla \cdot \left(\sum_{i=1}^{nc} N_r K_{c_d c_d} \nabla \hat{c}_d^i \right) \\ & - \sum_{j=1}^{nc} K_{c_d c_d} \nabla \hat{c}_d^j \nabla N_r + \nabla \cdot (N_r c_d^i k_l \nabla z) - c_d^i k_l \nabla z \nabla N_r \\ & + N_r \left[-C_{c_d l} \frac{\partial \hat{u}_l}{\partial t} - C_{c_d T} \frac{\partial \hat{T}}{\partial t} - C_{c_d a} \frac{\partial \hat{u}_a}{\partial t} - C_{c_d c_d} \frac{\partial \hat{c}_d^i}{\partial t} - C_{c_d s} \frac{\partial s_i}{\partial t} - C_{c_d u} \frac{\partial \hat{u}}{\partial t} \right] \end{aligned} \right] d\Omega^e = 0 \quad (4.8)$$

The *Gauss-Green Divergence Theorem* (e.g. Zienkiewicz and Morgan, 1982), is used to relate surface integrals to boundary integrals. This implementation reduces the second order terms to first order terms. Surface integrals are therefore introduced which cancel each other on adjacent elements, leaving only a contribution on the boundaries of the domain. Application of the divergence formula in (4.8) yields:

$$\int_{\Omega^e} \left[\begin{aligned} & - K_{c_d l} \nabla \hat{u}_l \nabla N_r - K_{c_d T} \nabla \hat{T} \nabla N_r - K_{c_d a} \nabla \hat{u}_a \nabla N_r - \sum_{j=1}^{nc} K_{c_d c_d} \nabla \hat{c}_d^j \nabla N_r - c_d k_l \nabla z \nabla N_r \\ & + N_r \left[-C_{c_d l} \frac{\partial \hat{u}_l}{\partial t} - C_{c_d T} \frac{\partial \hat{T}}{\partial t} - C_{c_d a} \frac{\partial \hat{u}_a}{\partial t} - C_{c_d c_d} \frac{\partial \hat{c}_d^i}{\partial t} - C_{c_d s} \frac{\partial s_i}{\partial t} - C_{c_d u} \frac{\partial \hat{u}}{\partial t} \right] \end{aligned} \right] d\Omega^e \quad (4.9)$$

$$+ \int_{\Gamma^e} N_r \left[K_{c_d l} \nabla \hat{u}_l + K_{c_d T} \nabla \hat{T} + K_{c_d a} \nabla \hat{u}_a + \sum_{j=1}^{nc} K_{c_d c_d} \nabla \hat{c}_d^j + c_d^i k_l \nabla z \right] n d\Gamma^e$$

where Γ^e is the element boundary surface and n is the direction cosine normal to the surface.

If expressions for the derivatives of primary variables are introduced to equation (4.9) and expanded, it becomes:

$$\begin{aligned} & \int_{\Omega^e} [K_{c_d l} \nabla \mathbf{N}^T \nabla \mathbf{N}] d\Omega^e \mathbf{u}_{ls} + \int_{\Omega^e} [K_{c_d T} \nabla \mathbf{N}^T \nabla \mathbf{N}] d\Omega^e \mathbf{T}_s + \int_{\Omega^e} [K_{c_d a} \nabla \mathbf{N}^T \nabla \mathbf{N}] d\Omega^e \mathbf{u}_{as} \\ & + \sum_{j=1}^{nc} \int_{\Omega^e} [K_{c_d c_d} \nabla \mathbf{N}^T \nabla \mathbf{N}] d\Omega^e \mathbf{c}_{ds}^j + \int_{\Omega^e} [C_{c_d l} \mathbf{N}^T \mathbf{N}] d\Omega^e \frac{\partial \mathbf{u}_{ls}}{\partial t} + \int_{\Omega^e} [C_{c_d T} \mathbf{N}^T \mathbf{N}] d\Omega^e \frac{\partial \mathbf{T}_s}{\partial t} \\ & + \int_{\Omega^e} [C_{c_d a} \mathbf{N}^T \mathbf{N}] d\Omega^e \frac{\partial \mathbf{u}_{as}}{\partial t} + \int_{\Omega^e} [C_{c_d c_d} \mathbf{N}^T \mathbf{N}] d\Omega^e \frac{\partial \mathbf{c}_{ds}^i}{\partial t} + \int_{\Omega^e} [C_{c_d s} \mathbf{N}^T \mathbf{N}] d\Omega^e \frac{\partial s_s^i}{\partial t} \\ & \int_{\Omega^e} [C_{c_d u} \mathbf{N}^T \mathbf{N}] d\Omega^e \frac{\partial \hat{u}}{\partial t} + \int_{\Omega^e} [c_d k_l \nabla \mathbf{N}^T \nabla z] d\Omega^e + \int_{\Gamma^e} N_r [f_{c_d}] n d\Gamma^e = 0 \end{aligned} \quad (4.10)$$

where f_{c_d} represents the approximate chemical solute flux normal to the boundary surface and \mathbf{N} is the shape function matrix. \mathbf{u}_{ls} , \mathbf{T}_s , \mathbf{u}_{as} , \mathbf{c}_{ds} and \mathbf{u}_s represents pore water pressure,

temperature, pore air pressure, dissolved chemical concentration and deformation vectors, respectively.

Equation (4.10) can be rewritten in a concise matrix notation as:

$$\begin{aligned} & \mathbf{C}_{c_d l} \frac{\partial \mathbf{u}_l}{\partial t} + \mathbf{C}_{c_d T} \frac{\partial T_s}{\partial t} + \mathbf{C}_{c_d a} \frac{\partial \mathbf{u}_a}{\partial t} + \mathbf{C}_{c_d c_d} \frac{\partial \mathbf{c}_{d s}^i}{\partial t} + \mathbf{C}_{c_d u} \frac{\partial \mathbf{u}}{\partial t} \\ & + \mathbf{K}_{c_d l} \mathbf{u}_l + \mathbf{K}_{c_d T} T_s + \mathbf{K}_{c_d a} \mathbf{u}_a + \sum_{j=1}^{nc} \mathbf{K}_{c_d c_d} \mathbf{c}_{d s}^j = \mathbf{f}_{c_d}^i \end{aligned} \quad (4.11)$$

where;

$$\mathbf{C}_{c_d l} = \sum_{e=1}^m \int [C_{c_d l} \mathbf{N}^T \mathbf{N}] d\Omega^e \quad (4.12)$$

$$\mathbf{C}_{c_d T} = \sum_{e=1}^m \int [C_{c_d T} \mathbf{N}^T \mathbf{N}] d\Omega^e \quad (4.13)$$

$$\mathbf{C}_{c_d a} = \sum_{e=1}^m \int [C_{c_d a} \mathbf{N}^T \mathbf{N}] d\Omega^e \quad (4.14)$$

$$\mathbf{C}_{c_d c_d} = \sum_{e=1}^m \int [C_{c_d c_d} \mathbf{N}^T \mathbf{N}] d\Omega^e \quad (4.15)$$

$$\mathbf{C}_{c_d u} = \sum_{e=1}^m \int [C_{c_d u} \mathbf{N}^T \mathbf{N}] d\Omega^e \quad (4.16)$$

$$\mathbf{K}_{c_d l} = \sum_{e=1}^m \int [K_{c_d l} \nabla \mathbf{N}^T \nabla \mathbf{N}] d\Omega^e \quad (4.17)$$

$$\mathbf{K}_{c_d T} = \sum_{e=1}^m \int [K_{c_d T} \nabla \mathbf{N}^T \nabla \mathbf{N}] d\Omega^e \quad (4.18)$$

$$\mathbf{K}_{c_d a} = \sum_{e=1}^m \int [K_{c_d a} \nabla \mathbf{N}^T \nabla \mathbf{N}] d\Omega^e \quad (4.19)$$

$$\mathbf{K}_{c_d c_d} = \sum_{e=1}^m \int [K_{c_d c_d} \nabla \mathbf{N}^T \nabla \mathbf{N}] d\Omega^e \quad (4.20)$$

$$\mathbf{f}_{c_d} = \sum_{e=1}^m \int [c_d k_l \nabla \mathbf{N}^T \nabla z] d\Omega^e + a_{ss} - \sum_{e=1}^m \int \mathbf{N}^T [f_{c_d}] d\Gamma^e \quad (4.21)$$

where, a_{ss} is the sink/source term for each chemical component.

$$\mathbf{a}_{ss} = \sum_{e=1}^m \int [C_{c_d s} \mathbf{N}^T \mathbf{N} \frac{\partial s_s}{\partial t}] d\Omega^e \quad (4.22)$$

The above formulation can be repeated for any number of chemical components.

4.2.2 Spatial discretisation for moisture, heat and air transfer-deformation

The above formulation may be repeated for the moisture flow variable (u_l) which yields:

$$\begin{aligned} & \mathbf{C}_{ll} \frac{\partial \mathbf{u}_l}{\partial t} + \mathbf{C}_{lT} \frac{\partial \mathbf{T}_s}{\partial t} + \mathbf{C}_{la} \frac{\partial \mathbf{u}_a}{\partial t} + \mathbf{C}_{lc_d} \frac{\partial \mathbf{c}_{ds}^l}{\partial t} + \mathbf{C}_{lu} \frac{\partial \mathbf{u}}{\partial t} \\ & + \mathbf{K}_{ll} \mathbf{u}_l + \mathbf{K}_{lT} \mathbf{T}_s + \mathbf{K}_{la} \mathbf{u}_a + \sum_{j=1}^{nc} \mathbf{K}_{lc_d}^j \mathbf{c}_{ds}^j = \mathbf{f}_l \end{aligned} \quad (4.23)$$

where;

$$\mathbf{C}_{ll} = \sum_{e=1}^m \int [C_{ll} \mathbf{N}^T \mathbf{N}] d\Omega^e \quad (4.24)$$

$$\mathbf{C}_{lT} = \sum_{e=1}^m \int [C_{lT} \mathbf{N}^T \mathbf{N}] d\Omega^e \quad (4.25)$$

$$\mathbf{C}_{la} = \sum_{e=1}^m \int [C_{la} \mathbf{N}^T \mathbf{N}] d\Omega^e \quad (4.26)$$

$$\mathbf{C}_{lc_d} = \sum_{e=1}^m \int [C_{lc_d} \mathbf{N}^T \mathbf{N}] d\Omega^e \quad (4.27)$$

$$\mathbf{C}_{lu} = \sum_{e=1}^m \int [C_{lu} \mathbf{N}^T \mathbf{N}] d\Omega^e \quad (4.28)$$

$$\mathbf{K}_{ll} = \sum_{e=1}^m \int [K_{ll} \nabla \mathbf{N}^T \nabla \mathbf{N}] d\Omega^e \quad (4.29)$$

$$\mathbf{K}_{lT} = \sum_{e=1}^m \int [K_{lT} \nabla \mathbf{N}^T \nabla \mathbf{N}] d\Omega^e \quad (4.30)$$

$$\mathbf{K}_{la} = \sum_{e=1}^m \int [K_{la} \nabla \mathbf{N}^T \nabla \mathbf{N}] d\Omega^e \quad (4.31)$$

$$\mathbf{K}_{lc_d} = \sum_{e=1}^m \int [K_{lc_d} \nabla \mathbf{N}^T \nabla \mathbf{N}] d\Omega^e \quad (4.32)$$

$$\mathbf{f}_l = \sum_{e=1}^m \int [k_l \rho_l \nabla \mathbf{N}^T \nabla z] d\Omega^e - \sum_{e=1}^m \int_{\Gamma^e} \mathbf{N}^T [f_l] d\Gamma^e \quad (4.33)$$

where, f_l , represent the total moisture flux comprising liquid and vapour components.

Similarly, the above formulation can be repeated for the heat transfer (T) producing:

$$\begin{aligned}
& \mathbf{C}_{Tl} \frac{\partial \mathbf{u}_l}{\partial t} + \mathbf{C}_{TT} \frac{\partial T_s}{\partial t} + \mathbf{C}_{Ta} \frac{\partial \mathbf{u}_{as}}{\partial t} + \mathbf{C}_{Tc_d} \frac{\partial \mathbf{c}_{ds}^i}{\partial t} + \mathbf{C}_{Tu} \frac{\partial \mathbf{u}}{\partial t} \\
& + \mathbf{K}_{Tl} \mathbf{u}_l + \mathbf{K}_{TT} T_s + \mathbf{K}_{Ta} \mathbf{u}_{as} + \sum_{j=1}^{nc} \mathbf{K}_{Tc_d} \mathbf{c}_{ds}^j = \mathbf{f}_T
\end{aligned} \tag{4.34}$$

where;

$$\mathbf{C}_{Tl} = \sum_{e=1}^m \int [C_{lT} \mathbf{N}^T \mathbf{N}] d\Omega^e \tag{4.35}$$

$$\mathbf{C}_{TT} = \sum_{e=1}^m \int [C_{TT} \mathbf{N}^T \mathbf{N}] d\Omega^e \tag{4.36}$$

$$\mathbf{C}_{Ta} = \sum_{e=1}^m \int [C_{Ta} \mathbf{N}^T \mathbf{N}] d\Omega^e \tag{4.37}$$

$$\mathbf{C}_{Tc_d} = \sum_{e=1}^m \int [C_{Tc_d} \mathbf{N}^T \mathbf{N}] d\Omega^e \tag{4.38}$$

$$\mathbf{C}_{Tu} = \sum_{e=1}^m \int [C_{Tu} \mathbf{N}^T \mathbf{N}] d\Omega^e \tag{4.39}$$

$$\mathbf{K}_{Tl} = \sum_{e=1}^m \int [K_{lT} \nabla \mathbf{N}^T \nabla \mathbf{N}] d\Omega^e \tag{4.40}$$

$$\mathbf{K}_{TT} = \sum_{e=1}^m \int [K_{TT} \nabla \mathbf{N}^T \nabla \mathbf{N}] d\Omega^e \tag{4.41}$$

$$\mathbf{K}_{Ta} = \sum_{e=1}^m \int [K_{Ta} \nabla \mathbf{N}^T \nabla \mathbf{N}] d\Omega^e \tag{4.42}$$

$$\mathbf{K}_{Tc_d} = \sum_{e=1}^m \int [K_{Tc_d} \nabla \mathbf{N}^T \nabla \mathbf{N}] d\Omega^e \tag{4.43}$$

$$\mathbf{f}_T = \sum_{e=1}^m \int [C_{pl} \rho_l k_l \nabla \mathbf{N}^T \nabla z] d\Omega^e - \sum_{e=1}^m \int \mathbf{N}^T [f_T] d\Gamma^e \tag{4.44}$$

where, f_T , represent the total heat flux.

The numerical formulation for the air flow variable (u_a) can be obtained similarly as:

$$\begin{aligned}
& \mathbf{C}_{al} \frac{\partial \mathbf{u}_l}{\partial t} + \mathbf{C}_{aT} \frac{\partial T_s}{\partial t} + \mathbf{C}_{aa} \frac{\partial \mathbf{u}_{as}}{\partial t} + \mathbf{C}_{ac_d} \frac{\partial \mathbf{c}_{ds}^i}{\partial t} + \mathbf{C}_{au} \frac{\partial \mathbf{u}}{\partial t} \\
& + \mathbf{K}_{al} \mathbf{u}_l + \mathbf{K}_{aT} T_s + \mathbf{K}_{aa} \mathbf{u}_{as} + \sum_{j=1}^{nc} \mathbf{K}_{ac_d} \mathbf{c}_{ds}^j = \mathbf{f}_a
\end{aligned} \tag{4.45}$$

where;

$$\mathbf{C}_{\mathbf{a}\mathbf{l}} = \sum_{e=1}^m \int [C_{aT} \mathbf{N}^T \mathbf{N}] d\Omega^e \quad (4.46)$$

$$\mathbf{C}_{\mathbf{a}\mathbf{T}} = \sum_{e=1}^m \int [C_{aT} \mathbf{N}^T \mathbf{N}] d\Omega^e \quad (4.47)$$

$$\mathbf{C}_{\mathbf{a}\mathbf{a}} = \sum_{e=1}^m \int [C_{aa} \mathbf{N}^T \mathbf{N}] d\Omega^e \quad (4.48)$$

$$\mathbf{C}_{\mathbf{a}\mathbf{c}_d} = \sum_{e=1}^m \int [C_{ac_d} \mathbf{N}^T \mathbf{N}] d\Omega^e \quad (4.49)$$

$$\mathbf{C}_{\mathbf{a}\mathbf{u}} = \sum_{e=1}^m \int [C_{au} \mathbf{N}^T \mathbf{N}] d\Omega^e \quad (4.50)$$

$$\mathbf{K}_{\mathbf{a}\mathbf{l}} = \sum_{e=1}^m \int [K_{al} \nabla \mathbf{N}^T \nabla \mathbf{N}] d\Omega^e \quad (4.51)$$

$$\mathbf{K}_{\mathbf{a}\mathbf{T}} = \sum_{e=1}^m \int [K_{aT} \nabla \mathbf{N}^T \nabla \mathbf{N}] d\Omega^e \quad (4.52)$$

$$\mathbf{K}_{\mathbf{a}\mathbf{a}} = \sum_{e=1}^m \int [K_{aa} \nabla \mathbf{N}^T \nabla \mathbf{N}] d\Omega^e \quad (4.53)$$

$$\mathbf{K}_{\mathbf{a}\mathbf{c}_d} = \sum_{e=1}^m \int [K_{ac_d} \nabla \mathbf{N}^T \nabla \mathbf{N}] d\Omega^e \quad (4.54)$$

$$\mathbf{f}_{\mathbf{a}} = \sum_{e=1}^m \int [k_l \rho_{da} \nabla \mathbf{N}^T \nabla z] d\Omega^e - \sum_{e=1}^m \int \mathbf{N}^T [f_a] d\Gamma^e \quad (4.55)$$

where, f_a , represent the total air flux.

The formulation for deformation variables can be presented as:

$$\mathbf{C}_{\mathbf{u}\mathbf{l}} \frac{\partial \mathbf{u}_{\mathbf{l}s}}{\partial t} + \mathbf{C}_{\mathbf{u}\mathbf{T}} \frac{\partial \mathbf{T}_s}{\partial t} + \mathbf{C}_{\mathbf{u}\mathbf{a}} \frac{\partial \mathbf{u}_{\mathbf{a}s}}{\partial t} + \mathbf{C}_{\mathbf{u}\mathbf{u}} \frac{\partial \mathbf{u}}{\partial t} = \mathbf{f}_{\mathbf{u}} \quad (4.56)$$

where;

$$\mathbf{C}_{\mathbf{u}\mathbf{l}} = \sum_{e=1}^m \int [\mathbf{B} (\mathbf{D}_{\mathbf{ep}} A_s) \mathbf{N}] \nabla t d\Omega^e \quad (4.57)$$

$$\mathbf{C}_{\mathbf{u}\mathbf{T}} = \sum_{e=1}^m \int [\mathbf{B} \mathbf{D}_{\mathbf{ep}} \left(-A_T - A_s \frac{dS_r}{dt} \right) \mathbf{N}] \nabla t d\Omega^e \quad (4.58)$$

$$\mathbf{C}_{\mathbf{u}\mathbf{a}} = \sum_{e=1}^m \int [\mathbf{B} (\mathbf{D}_{\mathbf{ep}} A_s - \mathbf{m}) \mathbf{N}] \nabla t d\Omega^e \quad (4.59)$$

$$\mathbf{C}_{uu} = \sum_{e=1}^m \int_{\Omega^e} \mathbf{B} \mathbf{D}_{ep} \mathbf{B}^T \nabla t d\Omega^e \quad (4.60)$$

$$\mathbf{f}_u = \sum_{e=1}^m \left[\int_{\Omega^e} [\mathbf{B} \mathbf{D}_{ep} \varepsilon_s^p] d\Omega^e + \int_{\Omega^e} \mathbf{N}^T d\mathbf{b} d\Omega^e + \int_{\Gamma^e} \mathbf{N}^T \hat{\underline{T}}_r d\Gamma^e \right] \quad (4.61)$$

4.3 Temporal discretisation

To determine the values of the primary variables over time an implicit mid-interval forward-difference time-stepping algorithm was employed. This has been found as a suitable solution for highly non-linear class of equations such as the current application problem (Thomas et al., 1998).

The spatially discretised equations for heat, moisture, air, multicomponent reactive chemical and deformation can be combined in a matrix form. The matrix equation can conveniently be expressed as:

$$\mathbf{A} \phi + \mathbf{B} \frac{\partial \phi}{\partial t} + \mathbf{C} = \{0\} \quad (4.62)$$

where \mathbf{A} , \mathbf{B} and \mathbf{C} are the matrices of coefficients and ϕ is the vector of variables. The expanded form of matrix presentation is given in figure (4.1).

As reported earlier, the spatially discretised equations are time discretised by the application of an implicit mid-interval forward difference time-stepping algorithm. This algorithm can be expressed as:

$$\mathbf{A}^{\phi_l} \left[(1 - \Theta) \phi^{n+1} + \Theta \phi^n \right] + \mathbf{B}^{\phi_l} \left[\frac{\phi^{n+1} - \phi^n}{\Delta t} \right] + \mathbf{C}^{\phi_l} = \{0\} \quad (4.63)$$

where Θ represents an integration constant varying from 1 for *implicit time integration* scheme; 0.5 for *Crank-Nicholson* scheme and 0 for *explicit time integration* scheme. The superscript l represents the level at which the matrices \mathbf{A} , \mathbf{B} and \mathbf{C} are evaluated. This level is given by:

$$\phi_l = \mathcal{G}(n+1) + (1 - \mathcal{G})(n) \quad (4.64)$$

where \mathcal{G} is a constant which defines the level at which the matrices are evaluated. For *fully implicit mid-interval forward difference time-stepping algorithm* the constants Θ and \mathcal{G} take the values of 1 and 0.5 respectively.

Applying equation (4.64), into equation (4.63), yields:

$$\mathbf{A}^{n+1/2} \phi^{n+1} + \mathbf{B}^{n+1/2} \left[\frac{\phi^{n+1} - \phi^n}{\Delta t} \right] + \mathbf{C}^{n+1/2} = \{0\} \quad (4.65)$$

Rearranging equation (4.65) gives:

$$\phi^{n+1} = \left[\mathbf{A}^{n+1/2} + \frac{\mathbf{B}^{n+1/2}}{\Delta t} \right]^{-1} \left[\frac{\mathbf{B}^{n+1/2} \phi^n}{\Delta t} - \mathbf{C}^{n+1/2} \right] \quad (4.66)$$

Since equation (4.66) can not be solved directly, as each calculation of ϕ^{n+1} requires the determination of the coefficient at the mid-interval; an iterative solution procedure is necessary. In the current work a *predictor-corrector algorithm* is used. This method can be described by the following steps;

- i. A first estimate, named the *predictor*, is produced by evaluating matrices **A**, **B** and **C** at time n .
- ii. The predictor and previous time step values are then used to evaluate matrices **A**, **B** and **C** at time $n + \frac{1}{2}$. This produces an estimate called the *corrector*.
- iii. For the elasto-plastic algorithm only, a check for yielding is then required. If the developed strain rate is greater than a specified tolerance, plastic strain will be produced and hardening parameters will be developed.
- iv. Either of the following conditions may then be used to check for convergence;

$$\left| \phi_{iC}^{n+1} - \phi_{(i-1)C}^{n+1} \right| \langle \mathbf{TL}_{abs} \quad (4.67)$$

$$\left| \frac{\phi_{iC}^{n+1} - \phi_{(i-1)C}^{n+1}}{\phi_{(i-1)C}^{n+1}} \right| \langle \mathbf{TL}_{rel} \quad (4.68)$$

where i is the iteration level, C denotes that the corrector value has been used. \mathbf{TL}_{abs} and \mathbf{TL}_{rel} are the matrices of absolute and relative tolerances for each variable. The stress equilibrium

is also checked to ensure the residual force is within a tolerance value. The residual force, ζ , can be calculated from stress equilibrium as, (Owen and Hinton, 1980);

$$\int_{\Omega} \mathbf{B}^T \Delta \sigma d\Omega - \Delta F = \zeta \quad (4.69)$$

where ΔF is the increment of applied force. If the variables do not converge, or the residual is too large, the algorithm returns to step ii where the corrector then becomes the new predictor.

- v. Once convergence has been reached and the residual force is below the tolerance, the algorithm moves onto the next time step and starts again from step 1. This process is repeated for all time steps.

$$\begin{bmatrix} \mathbf{K}_{ll} & \mathbf{K}_{lT} & \mathbf{K}_{la} & \mathbf{K}_{lc_d^1} & \mathbf{K}_{lc_d^2} & \dots & \mathbf{K}_{lc_d^{nc}} & \mathbf{0} \\ \mathbf{K}_{Tl} & \mathbf{K}_{TT} & \mathbf{K}_{Ta} & \mathbf{K}_{Tc_d^1} & \mathbf{K}_{Tc_d^2} & \dots & \mathbf{K}_{Tc_d^{nc}} & \mathbf{0} \\ \mathbf{K}_{al} & \mathbf{K}_{aT} & \mathbf{K}_{aa} & \mathbf{K}_{ac_d^1} & \mathbf{K}_{ac_d^2} & \dots & \mathbf{K}_{ac_d^{nc}} & \mathbf{0} \\ \mathbf{0} & \mathbf{0} & \mathbf{0} & \mathbf{0} & \mathbf{0} & \dots & \mathbf{0} & \mathbf{0} \\ \mathbf{K}_{c_d^2 l} & \mathbf{K}_{c_d^2 T} & \mathbf{K}_{c_d^2 a} & \mathbf{K}_{c_d^2 c_d^1} & \mathbf{K}_{c_d^2 c_d^2} & \dots & \mathbf{K}_{c_d^2 c_d^{nc}} & \mathbf{0} \\ \dots & \dots \\ \mathbf{K}_{c_d^{nc} l} & \mathbf{K}_{c_d^{nc} T} & \mathbf{K}_{c_d^{nc} a} & \mathbf{K}_{c_d^{nc} c_d^1} & \mathbf{K}_{c_d^{nc} c_d^2} & \dots & \mathbf{K}_{c_d^{nc} c_d^{nc}} & \mathbf{0} \\ \mathbf{0} & \mathbf{0} & \mathbf{0} & \mathbf{0} & \mathbf{0} & \dots & \mathbf{0} & \mathbf{0} \end{bmatrix} \times \begin{bmatrix} \mathbf{u}_{ls} \\ \mathbf{T}_s \\ \mathbf{u}_{as} \\ \mathbf{c}_{ds}^1 \\ \mathbf{c}_{ds}^2 \\ \dots \\ \mathbf{c}_{ds}^{nc} \\ \mathbf{u}_s \end{bmatrix} + \begin{bmatrix} \mathbf{C}_{ll} & \mathbf{C}_{lT} & \mathbf{C}_{la} & \mathbf{C}_{lc_d^1} & \mathbf{C}_{lc_d^2} & \dots & \mathbf{C}_{lc_d^{nc}} & \mathbf{C}_{lu} \\ \mathbf{C}_{Tl} & \mathbf{C}_{TT} & \mathbf{C}_{Ta} & \mathbf{C}_{Tc_d^1} & \mathbf{C}_{Tc_d^2} & \dots & \mathbf{C}_{Tc_d^{nc}} & \mathbf{C}_{Tu} \\ \mathbf{C}_{al} & \mathbf{C}_{aT} & \mathbf{C}_{aa} & \mathbf{C}_{ac_d^1} & \mathbf{C}_{ac_d^2} & \dots & \mathbf{C}_{ac_d^{nc}} & \mathbf{C}_{au} \\ \mathbf{C}_{c_d^1 l} & \mathbf{C}_{c_d^1 T} & \mathbf{C}_{c_d^1 a} & \mathbf{C}_{c_d^1 c_d^1} & \mathbf{C}_{c_d^1 c_d^2} & \dots & \mathbf{C}_{c_d^1 c_d^{nc}} & \mathbf{C}_{c_d^1 u} \\ \mathbf{C}_{c_d^2 l} & \mathbf{C}_{c_d^2 T} & \mathbf{C}_{c_d^2 a} & \mathbf{C}_{c_d^2 c_d^1} & \mathbf{C}_{c_d^2 c_d^2} & \dots & \mathbf{C}_{c_d^2 c_d^{nc}} & \mathbf{C}_{c_d^2 u} \\ \dots & \dots \\ \mathbf{C}_{c_d^{nc} l} & \mathbf{C}_{c_d^{nc} T} & \mathbf{C}_{c_d^{nc} a} & \mathbf{C}_{c_d^{nc} c_d^1} & \mathbf{C}_{c_d^{nc} c_d^2} & \dots & \mathbf{C}_{c_d^{nc} c_d^{nc}} & \mathbf{C}_{c_d^{nc} u} \\ \mathbf{C}_{ul} & \mathbf{C}_{uT} & \mathbf{C}_{ua} & \mathbf{C}_{uc_d^1} & \mathbf{C}_{uc_d^2} & \dots & \mathbf{C}_{uc_d^{nc}} & \mathbf{C}_{uu} \end{bmatrix} \times \begin{bmatrix} \dot{\mathbf{u}}_{ls} \\ \dot{\mathbf{T}}_s \\ \dot{\mathbf{u}}_{as} \\ \dot{\mathbf{c}}_{ds}^1 \\ \dot{\mathbf{c}}_{ds}^2 \\ \dots \\ \dot{\mathbf{c}}_{ds}^{nc} \\ \dot{\mathbf{u}}_s \end{bmatrix} + \begin{bmatrix} \mathbf{f}_l \\ \mathbf{f}_T \\ \mathbf{f}_a \\ \mathbf{f}_{c_d^1} \\ \mathbf{f}_{c_d^2} \\ \dots \\ \mathbf{f}_{c_d^{nc}} \\ \mathbf{f}_u \end{bmatrix} = \begin{bmatrix} \mathbf{0} \\ \mathbf{0} \\ \mathbf{0} \\ \mathbf{0} \\ \mathbf{0} \\ \dots \\ \mathbf{0} \\ \mathbf{0} \end{bmatrix}$$

Figure 4.1 Matrix presentation of the numerical formulations; the terms $\dot{\mathbf{u}}_{ls}$, $\dot{\mathbf{u}}_{as}$, $\dot{\mathbf{T}}_s$, $\dot{\mathbf{c}}_d$ and $\dot{\mathbf{u}}$ represent the time differentials of pore water pressure, pore air pressure, temperature, chemical concentrations and deformation variables respectively.

The amount of corrector iterations required is dependent on the size of the time step used. In order to provide an efficient solution algorithm a variable time-stepping scheme is applied. If

the number of iterations exceeds a specified maximum the time step size is decreased by a multiplier factor. However, if the number of iterations is lower than a specified minimum then the time step size is increased by a factor. This leads to an efficient solution algorithm.

This model has been incorporated into a computer code COMPASS, the *COde for Modelling Partially Saturated Soils*, which has been incrementally developed at the *Geoenvironmental Research Centre (GRC)*, Cardiff University (e.g. Thomas et al., 1998).

4.4 Coupling between the transport and chemical reaction model

In this section the method implemented for coupling the chemical transport equations in transport module, i.e. COMPASS, with the geochemical reaction module, i.e. PHREEQC *version 2* is presented. As reported in chapter 2, the sequential methods, in particular the sequential iterative approach (SIA) and the sequential non-iterative approach (SNIA) have been proposed and applied successfully for the coupling transport and chemical equations in various models/codes. Seetharam (2003) implemented both the sequential iterative and the sequential non-iterative approach for coupling COMPASS chemical transport module with geochemical reaction model, MINTEQA2 (Allison et al., 1992). The coupling schemes implemented in COMPASS-MINTEQA2 have been successfully tested and applied for the modelling reactive transport of multicomponent chemicals under coupled THCM conditions by Seetharam et al. (2007), Cleall et al. (2007) and Seetharam et al. (2010).

In this study, a sequential non-iterative approach (SNIA) is used for coupling chemical transport equations solved by COMPASS and the geochemical reactions which are calculated by PHREEQC *version 2*. In this approach, the chemical equations are solved only once during a time step. In other words, after transport equations have achieved convergence, concentrations of chemicals are modified using the geochemical model PHREEQC. Then the corrected values of dissolved chemical concentrations are introduced again into the transport module for the next step of analysis. Mathematically, the first step of calculations under the SNIA coupling scheme, which includes transport process can be represented as (Steeffel and MacQuarrie, 1996):

$$\frac{(c_d^i)^{Transport} - (c_d^i)^n}{\Delta t} = L(J_{c_d^i})^n \quad (4.70)$$

where L is the spatial operators applying to the fluxes. In this stage the results of dissolved chemical concentrations for previous time step, n is applied in the transport equation to obtain the new values of dissolved chemical concentrations associate with the transport processes. This step is followed by solving reaction equations as:

$$\frac{(c_d^i)^{n+1} - (c_d^i)^{Transport}}{\Delta t} = R_i^{n+1} \quad (4.71)$$

where R symbolises the rate expression for the associated geochemical reactions.

COMPASS has been written in *FORTTRAN*, while PHREEQC is *C* based program. The two models were linked together using a *Cross-linked* subroutine written in *C* language. In the *Cross-linked* subroutine, the results of transport process calculated by COMPASS are collected first using *pointer* variables which assist with an efficient and secure data exchange. Then the main subroutine of PHREEQC program is called and input data required for geochemical analysis is exchanged. Then PHREEQC calculates the equilibrium or kinetically controlled chemical reactions which provide the modified concentration of all dissolved chemicals. The outputs are exchanged again in *Cross-linked* subroutine and sent back to interface module of COMPASS. The COMPASS-PHREEQC linked model works based on a single compiler program. Figure (4.2) presents the coupling approach and modular data exchange between COMPASS and PHREEQC. It is noted that the time-step of the current transport analysis is transferred to PHREEQC which is applied for calculating kinetically controlled reactions.

In order to accelerate computation, provision is made to impose a relative tolerance level check for dissolved chemical concentration and temperature, i.e. defined in figure (4.2) as $diff1 = (c_d^i)^{transport} - (c_d^i)^n$ and $diff2 = (T)^{transport} - (T)^n$, respectively. In other words, if the concentrations of chemicals and the temperature do not vary more than a specific amount during time steps n and $n+1$, then the program skips the geochemical analysis.

A feed back between mineral precipitation/dissolution (geochemical model), total mineral volume and eventually porosity has been provided under the coupling scheme. The amount of

mineral precipitate volumes as part of solid phase is updated from the results of geochemical analysis. As the result of changes in the mineral volume, the porosity varies and the flow parameters including hydraulic conductivity and tortuosity factor for chemical diffusion are changed. The resultant concentrations of minerals calculated from equilibrium precipitation/dissolution reactions or kinetically controlled reactions are used to calculate the total amount of volume related to the precipitation/dissolution process during each time-step. The mineral volume for each node is updated after geochemical reaction step and sent back to the transport module. Then porosity is modified for each integration point in an element where the hydro/chemical flow properties such hydraulic conductivity or diffusion coefficient is evaluated in the model.

The numerical formulation concerning reactive chemical equations is not dealt within this work as the geochemical model, PHREEQC *version 2* (Parkhurst and Appelo, 1999), is directly used without any modification to its numerical formulation. However, it is worthwhile to review the numerical method implemented in PHREEQC. The geochemical model PHREEQC employs two different numerical solutions depending on the type of reaction. Those can be summarised as follows (Parkhurst and Appelo, 1999):

A modified *Newton-Raphson method* is employed for solving non-linear algebraic equations for chemical reactions under equilibrium condition. The solution technique assigns initial values to the master unknowns and then uses a modification of the Newton-Raphson method iteratively to revise the values of the master unknowns until a solution to the equations has been found within specified tolerances.

PHREEQC solves the differential equations for kinetically controlled reaction using a *Runge-Kutta algorithm* by Fehlberg (1969), which integrates the rate of reactions over time. The scheme includes a Runge-Kutta method with lower order to derive an error estimate with up to six intermediate evaluations of the derivative. The error estimate is compared with a user-defined error tolerance to automatically decrease or increase the integration time interval to maintain the errors within the given tolerance. Furthermore, if the rates in the first three Runge-Kutta evaluations differ by less than the tolerance, the final rate is calculated directly and checked once more against the required tolerance.

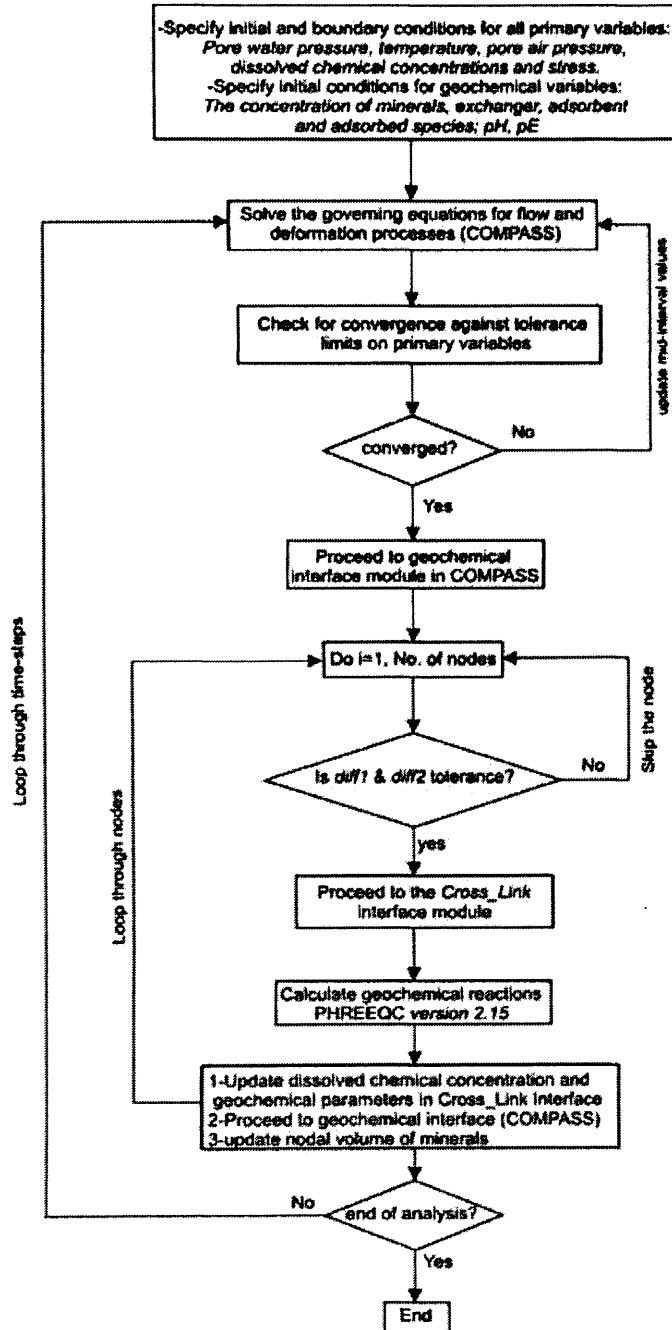


Figure 4.2 The sequential non-iterative approach (SNIA) used for coupling COMPASS and PHREEQC

4.5 Summary

A numerical solution of the coupled flow and deformation formulation given in Chapter 3 has been presented. Spatial discretisation of the five governing differential equations has been achieved using a finite element method, whilst an implicit forward difference, mid-interval time stepping algorithm has been employed to achieve temporal discretisation. The chemical transport module of the flow and deformation model has been coupled to the geochemical model, PHREEQC *version 2*, with minor modifications to the latter code, via sequential non-iterative coupling techniques. The implementation of the coupling techniques has been described. In addition, the algorithm of porosity modification feed back from geochemical analysis has been explained in this chapter. The model has been incorporated into an existing computer code COMPASS which has been developed at the Geoenvironmental Research Centre, Cardiff University.

4.6 References

Allison, J.D., Brown, D.S., and Novo-Gradac, K.J. (1991). *MINTEQA2 User Manual version 3.0*. Environmental Research Laboratory, U.S. EPA.

Cleall, P.J. (1998). *An investigation of the thermo/hydraulic/mechanical behaviour of unsaturated soils, including expansive clays*, Ph.D. Thesis. Cardiff University, Wales, U.K.

Cleall, P.J., Seetharam, S.C., and Thomas, H.R. (2007). On the inclusion of some aspects of chemical behaviour of an unsaturated soil in thermo-hydro-chemical-mechanical models: I Model development. *Journal of Engineering Mechanics, ASCE*, 133, 338-347.

Fehlberg, E. (1969). Klassische Runge-Kutta-Formeln fünfter und siebenter Ordnung mit Schrittweiten-Kontrolle. *Computing*, 4, 93-106.

Hashm, A.A. (1999). *A study of the transport of a selection of heavy metals in unsaturated soils*. Ph.D thesis. University of Wales, Cardiff, UK.

Hinton, E., and Owen, D.R.J. (1977). *Finite Element Programming, Computational Mathematics and Applications*. Academic Press, London.

Owen, D.R.J., and Hinton, E. (1980). *Finite Elements in Plasticity: Theory and Practice*. Pineridge Press Ltd., Swansea.

Parkhurst, D.L., and Appelo, C.A.J. (1999). *User's Guide to PHREEQC (version 2)*, U.S. Geological Survey, Water Resource Investigation Report, 99-4259.

Ramesh, A.D. (1996). *Modelling the thermo/hydraulic/mechanical behaviour of unsaturated soil using an elasto-plastic constitutive relationship*. Ph.D. Thesis. University of Wales, UK.

Seetharam, S.C. (2003). *An investigation of the thermo/hydro/chemical/mechanical behaviour of unsaturated soils*. Ph.D. Thesis, Cardiff University, Wales, UK.

Seetharam, S.C., Thomas, H.R., and Cleall, P.J. (2007). Coupled thermo-hydro-chemical-mechanical model for unsaturated soils-Numerical algorithm. *International Journal of Numerical Methods in Engineering*, 70, 1480-1511.

Seetharam, S.C., Thomas, H.R., and Vardon, P.J. (2010). Non-isothermal multi-component reactive transport model for unsaturated soils. *International Journal of Geomechanics, ASCE*, doi.org/10.1061/(ASCE)GM.1943-5622.0000018.

Steeffel, C.I., MacQuarrie, K.T.B. (1996). *Approaches to modeling of reactive transport in porous media*, Reactive. Transport in Porous Media, Reviews in Mineralogy, (34). Mineralogical Society of America, Washington, DC.

Thomas, H.R., and He, Y. (1995). Analysis of coupled heat, moisture and air transfer in a deformable unsaturated soil. *Géotechnique*, 45(4), 677-689.

Thomas, H.R., and He, Y. (1998). Modelling the behaviour of unsaturated soil using an elasto plastic constitutive relationship. *Géotechnique*, 48, 589-603.

Thomas, H.R., Rees, S.W., Sloper, N.J. (1998). Three-dimensional heat, moisture and air transfer in unsaturated soils. *International Journal of Numerical and Analytical Methods in Geomechanics*, 22(2), 75-95.

Vardon, P.J. (2009). *A three-dimensional numerical investigation of the therm-hydro-mechanical behaviour of a large-scale prototype repository*. Ph.D. Thesis, Cardiff University, Wales, UK.

Zienkiewicz, O.C., and Morgan, K. (1982). *Finite Elements and Approximation*. John Wiley and Sons.

Zienkiewicz, O.C., and Taylor, R.L. (1989). *The Finite Element Method*. McGraw Hill, 4th edition.

Chapter 5

Verification and Validation

5.1 Introduction

In this chapter a description of the verification and validation tests carried out as part of the research is presented. Verification and validation tests are obviously essential steps before application of the model for predictive purposes. It is noted that verifications tests are carried out to explore whether the solution algorithm of the model is correct, whilst validations are carried out to examine the value of the underlying conceptual model. The developments to the theoretical formulation of hydraulic and chemical behaviour, presented in chapter 3 and their implementation in the numerical model are examined via the series of verification and validation tests reported in the chapter.

The numerical model has already been examined for a number of test cases involving coupled moisture, air, heat and deformation (e.g. King, 1994; Sansom, 1995 and Cleall, 1998). In addition, developments to COMPASS model presented by Thomas and He (1995); Thomas and Sansom, 1995; Thomas and He (1998), Thomas et al. (1998) and Cleall (1998) was also re-verified and tested by Mitchell (2002) for coupled thermal, hydraulic and mechanical behaviour. In terms of reactive transport of chemicals, the verification of the chemical transport module of the model has been examined by Seetharam (2003). A comprehensive series of verifications of the chemical transport in COMPASS model was performed by Seetharam (2003). In addition, the coupling between the chemical transport model, i.e. COMPASS and the geochemical reaction model, i.e. MINTEQA2 (Allison et al. 1991), was also verified by Seetharam (2003) and Cleall et al. (2007) for different geochemical features included in the model.

Section 5.2 will present the verification and validation tests carried out on the inclusion of osmosis phenomenon on moisture transport in the model. Two verifications are presented with regards to moisture flow due to chemo-osmosis. First a verification test is presented under saturated conditions where a chemical gradient in the system causing a gradient of water pressure. The results are compared with the results of an analytical solution at steady-state. Another series of verifications are also performed under unsaturated conditions. Comparison is made against experimental data. The focus of the simulation is to examine the model for the approach adopted for the inclusion of the osmotic effects on vapour movement.

In terms of chemical behaviour, section 5.3 presents the verifications of the advances included in the chemical transport model. Two verifications are presented in order to check the theoretical components included in the governing equation for the reactive transport of multicomponent chemicals under isothermal condition. The results of the model for multicomponent chemical diffusion are first presented via an example of pure diffusion in a binary ionic solution, i.e. a solution containing two ionic species. In the second verification, results of the modelling pure diffusion in a mixed electrolyte system under isothermal conditions are examined via a similar simulation, reported by Lichtner (1995) and Appelo (2007). The verification of the model in terms of thermal effects on the diffusion process, i.e. Soret effect, in multiple ionic species is also presented and the validity of the theoretical approach proposed for the calculation of the Soret coefficient are also examined. In the third verification, the diffusion model for multicomponent chemicals due to temperature gradients, i.e. Soret effect, is examined via a series of experimental results reported by Leaist and Hui (1990). Simulations have been performed using the values for the Soret coefficients reported by Leaist and Hui (1990). In addition, similar series of simulations are repeated using the theoretical approach adopted for determination of the Soret coefficient.

The coupling between chemical transport model, COMPASS and chemical reaction model, PHREEQC version 2, is examined for the geochemical features presented in section 5.4. The results of the simulations using the developed model, i.e. COMPASS-PHREEQC, are verified against several well established verification examples, used in other codes or via analytical solutions. In general, the coupled set of governing equations describing multicomponent transport and chemical reactions are not amenable to analytical solutions except in the simplest cases. In this section the developed coupled reactive chemical transport model is examined for the geochemical reaction features including precipitation and dissolution reactions under equilibrium condition, precipitation and dissolution under kinetically controlled condition and equilibrium ion exchange reaction. The verifications of the coupling of binary solution transport and dissolution/precipitation of mineral reactions are presented first. These include the mineral precipitation reaction under equilibrium and kinetically controlled conditions. The results of numerical model are compared with the results of analytical solutions. A verification of multicomponent chemical transport coupled with multiple mineral precipitation/dissolution reactions is also presented where the results are compared with the result of a well established verification test used in several reactive

transport codes. Finally a verification test on the multicomponent ionic transport coupled with ionic exchange process is given and the results of numerical model are compared with a similar simulation using the reactive transport model, PHREEQC version 2.

The approach adopted for considering porosity modification feed-back from geochemical reaction modelling and the effects on hydro/chemical transport properties are also demonstrated. The results of a preliminary simulation of the effects of coupling porosity and mineral reactions are presented, acknowledging the fact that further usage of this coupling requires more verification/validation. The numerical simulation test is designed to demonstrate the effect of mineral precipitation/dissolution reaction on chemical diffusion. Section 5.5 presents then results of the above mentioned simulations.

Finally section 5.6 provides a summary and conclusions from the above work.

5.2 Osmotic potential effects on moisture transport

This section presents the verification result of chemo-osmosis potential component included in the governing equation for moisture flow. According to the formulation proposed for moisture transfer, a gradient in the osmotically active ions in aqueous phase of the soil can cause a flow of liquid water and vapour in the system.

5.2.1 Osmotic potential under saturated conditions (Test I)

5.2.1.1 Introduction

This simulation considered a two dimensional (2D) soil domain (0.10×0.10 m). The soil initially contained no chemicals but subjected to a solution with some amount of Na^+ and Cl^- dissolved ions. The soil was assumed as a fully saturated system. Specific boundary conditions were designed which simplify the analytical solution for verification of the osmosis phenomenon. The chemical concentrations at boundaries were assumed as fixed values which provide constant concentration gradients over the domain at steady-state condition. Due to the gradient of chemical concentration in the domain, a gradient of water pressure is established in order to balance the osmosis potential over the domain. At steady-state conditions, the developed pressure and the gradients of water pressure can be analytically calculated for the above mentioned case. A series of simulations were performed assuming different values for osmotic efficiency under the boundary conditions presented above.

5.2.1.2 Numerical model conditions

Applying above mentioned conditions, a series of simulations were performed using the approach adopted for osmosis induced water transport. A two-dimensional finite elements domain was discretised to 100 equally sized 4-noded quadrilateral elements. A constant time-step of 3600 seconds was considered. The simulation was carried out under coupled thermal, hydraulic and chemical behaviour and under isothermal conditions. The system considered was initially saturated and the water pressure and chemical concentrations were initially set as zero in the domain. The water pressure was also considered fixed at one boundary condition while the other side was considered as impermeable boundary for water flow. The pore water

in the domain was assumed to contain two dissolved ionic species, Na^+ and Cl^- , and the concentrations of chemicals at boundaries were considered as fixed values, providing constant chemical gradients in the domain at steady state. The chemical transport was considered under non-reactive conditions, therefore no chemical reactions occurred in the domain during the analysis. A schematic of the initial and boundary conditions of the domain is shown in figure 5.1.

<i>Boundary condition:</i> $u_l = 0 \text{ Pa}$, $T = 293 \text{ K}$ $c_d(\text{Na}^+) = 0 \text{ mol/m}^3$ $c_d(\text{Cl}^-) = 0 \text{ mol/m}^3$	<i>Initial condition:</i> $u_l = 0 \text{ Pa}$ $T = 293 \text{ K}$ $c_d(\text{Na}^+) = 0 \text{ mol/m}^3$ $c_d(\text{Cl}^-) = 0 \text{ mol/m}^3$	<i>Boundary condition:</i> $\partial u_l / \partial x = 0$ $T = 293 \text{ K}$ $c_d(\text{Na}^+) = 10 \text{ mol/m}^3$ $c_d(\text{Cl}^-) = 10 \text{ mol/m}^3$
---	--	--

Figure 5.1 Schematic of the initial and boundary conditions (Test I)

The simulation was performed assuming three different values for the osmotic efficiency including values of $\omega_\pi = 0.1, 0.5$ and 0.9 . Other required parameters used in the simulation are also presented in table 5.1.

Table 5.1 Material parameters (Test I)

<i>Material parameter</i>	<i>Relationship/value</i>
Porosity:	$n = 0.6$
Saturated hydraulic conductivity:	$K_{sat} = 3.9 \times 10^{-12} \text{ m/s}$
Chemical tracer diffusion coefficient in water: (Lasaga, 1998)	$D_{\text{Na}^+}^0 = D_{\text{Cl}^-}^0 = 13 \times 10^{-10} \text{ m}^2/\text{s}$

5.2.1.3 Results and discussion

Figure 5.2 presents the profiles of water pressures and dissolved chemical concentrations at steady-state for three different osmotic efficiencies including $0.1, 0.5$ and 0.9 . The results of the numerical model show that at equilibrium condition, a constant gradient of water pressure is established, which is reduced as the osmotic efficiency decreases. From the simulation results, the value of gradient of water pressure is obtained as $\nabla u_l = 48.7 \times 10^4 \omega_\pi$.

According to the formulation developed in chapter 3, the flow of liquid water due to pressure and osmotic potential under isothermal conditions can be given as:

$$v_l = \frac{-k_l}{\rho_l g} \nabla u_l + \frac{k_l RT \omega_\pi}{\rho_l g} \sum_{i=1}^{nc} \gamma_i \left(1 + \frac{\partial \ln \gamma_i}{\partial \ln c_d^i} \right) \nabla c_d^i \quad (5.1)$$

This equation is a simplified form of the velocity of liquid presented in chapter 3, i.e. equation (3.25) if the gravitational potential is neglected.

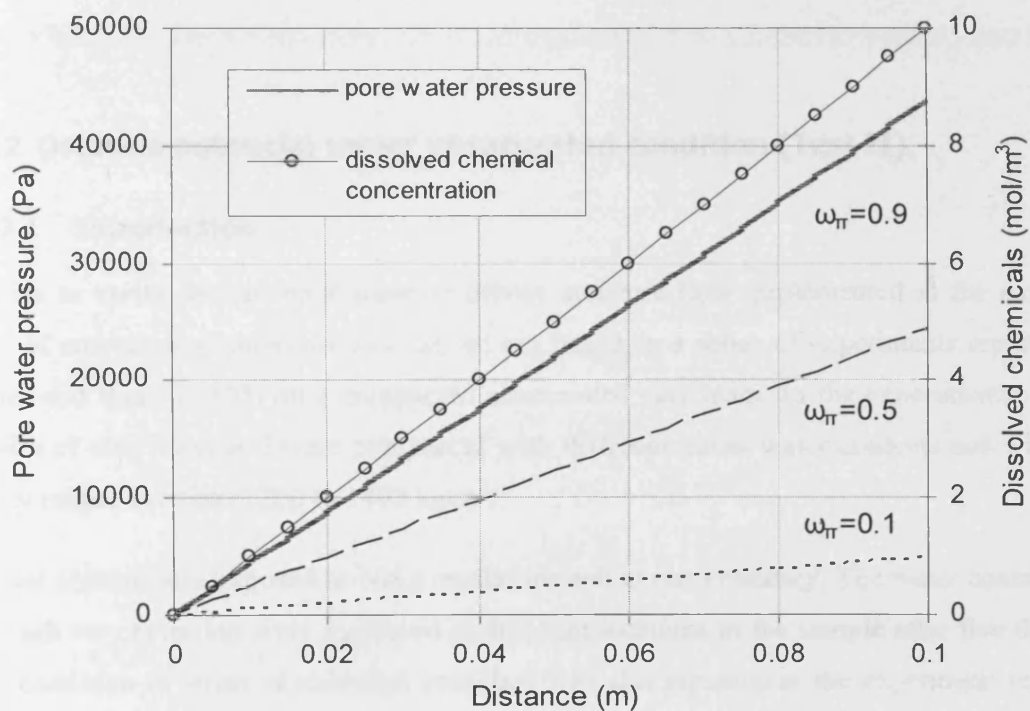


Figure 5.2 Profiles of pore water pressure and chemical distributions at steady-state for Test I

For the specific impermeable boundary condition for the water flow, presented in figure 5.1, the velocity of liquids becomes zero at steady-state condition. Therefore, at steady-state, if the activity coefficients of chemicals are assumed as 1, i.e. ideal solution, equation (5.1) yields:

$$\nabla u_l = RT \omega_\pi \sum_{i=1}^{nc} \nabla c_d^i \quad (5.2)$$

Therefore, knowing the concentration gradients of chemicals in the system, the gradients of water pressure can be calculated analytically over the domain at steady-state. For the test conditions, the gradient of pore water pressure can be given as:

$$\nabla u_l = 8.31 \times 293 \times \omega_\pi \times \left(\frac{10+10}{0.1} \right) = 48.7 \times 10^4 \omega_\pi \text{ (Pa.m}^{-1}\text{)} \quad (5.3)$$

The results of the analytical solution and numerical simulations give a same value for the gradient of pore water pressure, providing verification for the osmosis phenomena adopted in the model under the specified conditions.

5.2.2 Osmosis potential under unsaturated condition (Test II)

5.2.2.1 Introduction

In order to verify the chemical-osmosis driven moisture flow implemented in the model, a series of numerical simulations was carried out based on a series of experiments reported by Scotter and Raats (1970) on a compacted unsaturated clay loam. In the experimental study, samples of clay loam soil were compacted with different initial water contents and with dry density ranges between 1200 to 1400 kg/m³.

The soil column was exposed to NaCl crystalline salt at one boundary. The water content and NaCl salt concentration were measured at different locations in the sample after five days. A same condition in terms of chemical boundary was also repeated in the experiment reported by Scotter and Raats (1970) with initially 8.4 % water content and the variation of the water content was reported after 4, 5, 8 and 16 days.

The experimental results demonstrated that the moisture profile varies in the soil caused by the osmotic potential due to salt presence at the boundary. The experiment reported by Scotter and Raats (1970) was simulated in order to validate the osmotic potential effects on moisture transport and in particular on vapour movement. Scotter and Raats (1970) reported the results for four different initial water contents; therefore the simulation results will be reported for different initial water contents.

5.2.2.2 Numerical model conditions

The domain consists of a two dimensional horizontal soil domain (16×3.15 cm) width. The analysis domain is discretised into 200 equally sized 2D elements. In order to prevent numerical oscillation and to achieve a better convergence due to the high concentration gradients, 8-node quadrilateral elements were used in the simulation. The variable time-step scheme implemented in COMPASS was employed which allowed the time-step increase or decrease by a multiplier factor depending on the convergence. The value of 3600 seconds was considered as the maximum allowed time-step based on trials with different values. The simulations were performed using non-reactive transport of chemicals model, therefore no coupling was made with geochemical model.

The soil initially contained no chemicals including sodium and chloride dissolved ions. At the boundary soil was exposed to concentrated ions which were reasonable to assume a fixed concentration for the dissolved sodium and chloride ions. This concentration was considered as the corresponding values of sodium and chloride concentrations in equilibrium with 1 mol/l NaCl salt, i.e. saturated salt solution (Scotter and Raats, 1970). Both boundary sides were assumed as impermeable to moisture flow. A schematic of the initial and boundary conditions used in the simulations is shown in figure 5.3.

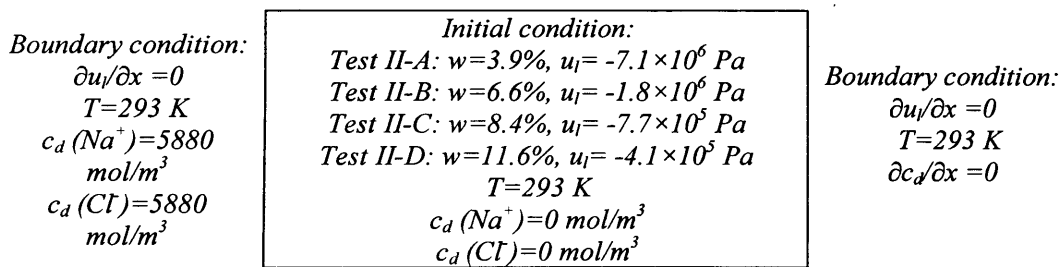


Figure 5.3 Schematic of the initial and boundary conditions (Test II)

The material parameters, required in the analysis were adopted from Scotter and Raats (1970), except for hydraulic conductivity which was not reported there. The van Genuchten equation for the soil water characteristic curve (van Genuchten, 1980) was used to establish the suction-water content relationship. The best fitted equation and the required parameter for van Genuchten's model, was obtained based on the experimental data provided by Scotter and Raats (1970). The initial values of pore water pressure were extracted from the soil water characteristics for different initial water contents in the experiment. The osmosis efficiency

was considered as zero as there was no exact value, reported in the experiment and the primary concern in the simulations has been on osmosis induced vapour transfer. Therefore, the analysis of liquid water movement was not affected by the osmosis potential and only vapour has been transferred due to the osmosis in the system.

A parametric study was performed on *Test II-C* to extract the best value for saturated hydraulic conductivity based on the hydraulic conductivity relationship of van Genuchten-Mualem model (van Genuchten 1980). The vapour flux considered was based on the relationship proposed by Phillip and de Vries (1957) using equation (3.47). It is noted that no modification factor was used for the vapour flux equation. In terms of chemical diffusion, different tracer diffusion coefficients in water for Na^+ and Cl^- ions were used and the simulation was considered under coupled electrochemical diffusion potentials. The material parameters and values used in the simulations are presented in table 5.2.

Table 5.2 Material parameters (Test II)

<i>Material parameter</i>	<i>Relationship/value</i>
Porosity:	$n=0.3$
Water content-suction relationship:	$\theta_l = \theta_r + (\theta_s - \theta_r) \left[1 + \alpha s^\beta \right]^{-\left(\frac{1-\beta}{\beta}\right)}$ $\theta_r=0.02, \theta_s=0.3, \alpha=0.22, \beta=1.42$
Unsaturated hydraulic conductivity relationship:	$k_l = k_{sat} \left(\frac{\theta - \theta_r}{\theta_s - \theta_r} \right)^{0.5} \left\{ 1 - \left[1 - \left(\frac{\theta - \theta_r}{\theta_s - \theta_r} \right)^{1/m} \right]^m \right\}^2$ $\theta_r=0.02, \theta_s=0.3, m=0.296, k_{sat}=2.5 \times 10^{-9} \text{ m/s}$
Chemical tracer diffusion coefficient in water (Lasaga, 1998):	$D_{\text{Na}^+}^0 = 2.03 \times 10^{-9} \text{ m}^2/\text{s}$ $D_{\text{Cl}^-}^0 = 1.33 \times 10^{-9} \text{ m}^2/\text{s}$
Tortuosity factor for chemical diffusion (Millington and Quirk, 1961):	$\tau = \frac{\theta^{7/3}}{n^2}$

5.2.2.3 Results and discussion

Figure 5.4 presents the profiles of saturation degree in the domain after five days of analysis for the simulations with different initial water contents (lines). The results of the experimental

work reported by Scotter and Raats (1970) have been also presented in this figure for comparison (symbols). A good correlation in the profiles of the degree of saturation between the results of numerical simulation and experimental data is observed. As it is anticipated from osmosis phenomenon, moisture and dominantly water vapour tend to migrate from the soil domain towards the boundary due to the high concentration of dissolved chemicals at boundary. The consequence is an increase in the degree of saturation in the salt boundary regions as observed in figure 5.3. Both numerical model and experimental results indicate that the drying region in the domain is limited mostly to about 3 to 6 cm distance from the salt boundary.

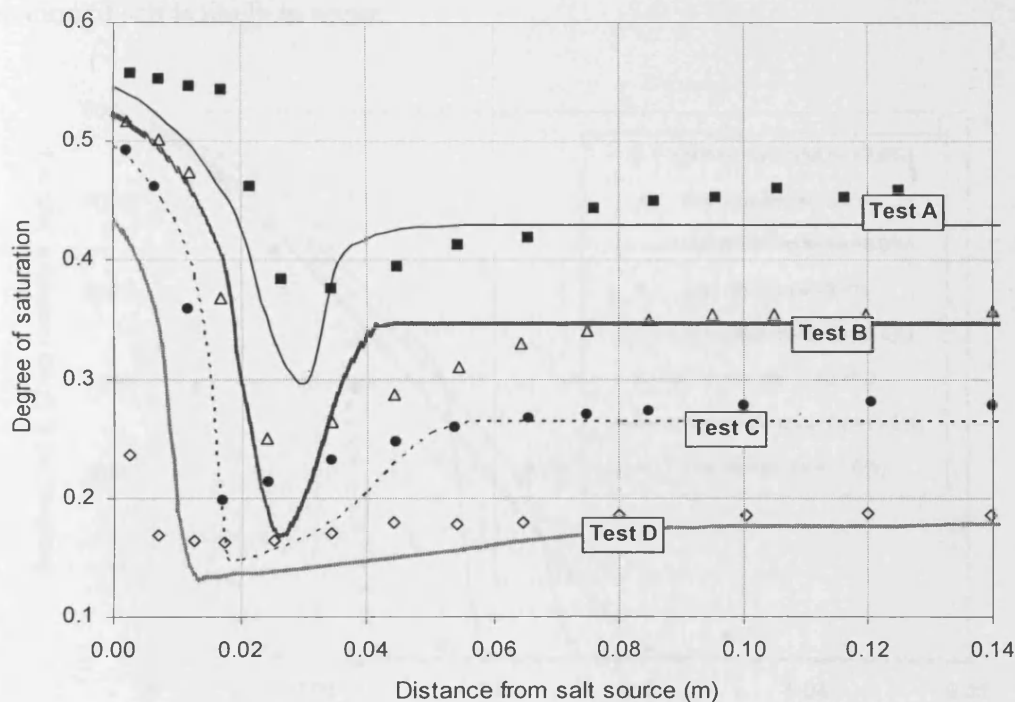


Figure 5.4 Profiles of the degree of saturation in the domain considering different initial water contents. Lines represent the results of the numerical model and symbols show the experimental results reported by Scotter and Raats (1970)

In comparison between the numerical model results and experimental data, the numerical model resulted larger decrease in the moisture content in the drying regions. As reported earlier, no modification factors were used for the components of vapour flux equation proposed by Phillip and de Vries (1957). The higher drying can be related to the vapour flux equation used in the simulation.

Figure 5.5 also shows the profiles of distribution of dissolved chemicals in the first five centimetres of the domain close to the salt boundary, after five days of test. The results of the numerical simulations are shown by the lines and symbols represent the experimental results reported by Scotter and Raats (1970). In analysis with higher initial water contents, i.e. *Test II-D*, a good agreement the numerical results and experimental data is observed. The results of the numerical model show higher values for the dissolved chemicals in the cases with lower initial water contents. However, the general trend demonstrates similar qualitative trend observed in the experiment, especially in prediction of the region affected by the diffusion. However, the discrepancies are greater with lowering the initial water content which can be related to the fact that no chemical reaction was considered in the simulation whilst the precipitation of salt is likely to occur.

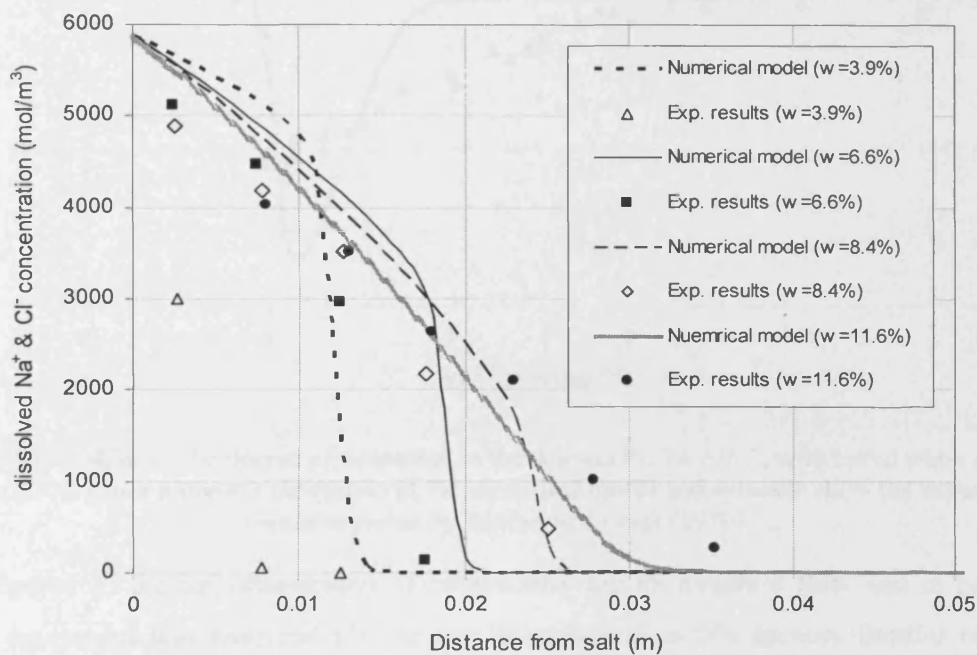


Figure 5.5 Profiles of the dissolved chemical concentrations in the first 5 cm of the domain considering different initial water contents.

As mentioned earlier, Scotter and Raats (1970) repeated the experiment for the sample with initial water content of 8.4 % and reported the results of degree of saturation for the periods of 4, 5, 8 and 16 days. The numerical simulations on *Test II-C*, i.e. with initial water content of 8.4%, are also repeated and the results for the mentioned periods are collected. Following Scotter and Raats (1970), the results of moisture profile are provided as a function of distance

divided by square root of time ($xt^{-0.5}$). The results of the second series of simulations and the experimental data are shown in figure 5.6. The results of the model follows the same pattern as with the experimental data, although higher drying is observed due to the high rate of vapour flux. Figure 5.6 also presents the results of simulation.

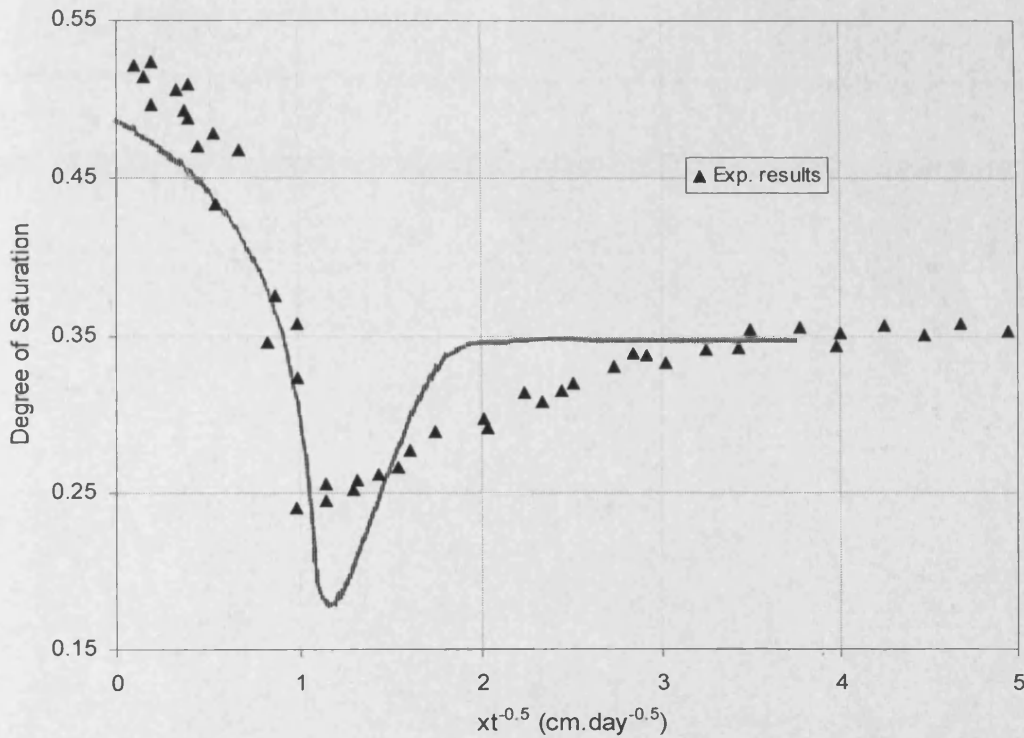


Figure 5.6 Profiles of the degree of saturation in the domain for *Test II-C*, with initial water content equal to 8.4%. Lines represent the results of the numerical model and symbols show the experimental results reported by Scotter and Raats (1970)

The accuracy of the implementation of osmotically driven moisture flow and in particular vapour movement was explored via the results presented in this section. Similar reduction factor such as that proposed for modification of the vapour flux in Phillip and de Vries equation can be used to the osmotically driven vapour component in the vapour flux equation used in this simulation.

5.3 Verification of Multicomponent Chemicals Transport

In this section the verifications of the non-reactive transport model for multicomponent chemicals are presented. The first two tests deal with the diffusion model adopted for multicomponent chemicals under coupled electrochemical potentials and isothermal conditions. The third example provides a verification test for the approach used for diffusion of multicomponent chemicals under coupled electrochemical and thermal potentials. The multicomponent diffusion model is verified in binary and ternary electrolyte solutions under coupled electrochemical and thermal potentials. First, the charge conservation or electro-neutrality condition in the model is checked during thermal diffusion in binary and ternary electrolyte solutions using the experimentally determined thermal diffusion coefficients, i.e. the Soret coefficients. Secondly, the theoretical approach adopted for the approximation of the Soret coefficient is validated. In this test, theoretical approach proposed for approximation of the Soret coefficient in chapter 3, is examined against, a series of experimental data. All verifications are performed in electrolyte solutions.

5.3.1 Diffusion of binary electrolyte solutions under electrochemical potential (Test III)

5.3.1.1 Introduction

The multicomponent diffusion model is verified in this simulation for binary electrolyte solutions. A binary electrolyte solution contains an ion pair including a cationic and an anionic chemical species. In the case of binary solutions, the multicomponent diffusion formulation due to the electrochemical potential can be simplified and expressed via Fick's law of diffusion, using a modified diffusion coefficient (Cussler, 1997). Therefore in this case, the multicomponent diffusion model is verified against modelling the problem using Fick's law of diffusion.

The general diffusion flux due to electrochemical potential presented in equation (3.143) can be simplified for the case of binary solutions. The equation can be reduced to a problem of diffusion under the second Fick's diffusion law.

The general diffusive flux due to electrochemical potential (under isothermal condition), presented in equation (3.143) for an ionic species can be given as:

$$\mathbf{J}_i^{\text{Diff}} = \left[-D_i^0 \left(1 + \frac{\partial \ln \gamma_i}{\partial \ln c_d^i} \right) \nabla c_d^i + \frac{z_i D_i^0 c_d^i}{\sum_{k=1}^{nc} z_k^2 D_k^0 c_d^k} \sum_{j=1}^{nc} z_j D_j^0 \left(1 + \frac{\partial \ln \gamma_j}{\partial \ln c_d^j} \right) \nabla c_d^j \right] \quad (5.4)$$

For a binary ionic solution and if the effect of thermodynamic correction factor, i.e. $1 + \frac{\partial \ln \gamma_i}{\partial \ln c_d^i}$, is ignored, the diffusive flux for the cationic (component 1 in this simulation)

and anionic species (component 2 in this simulation) become:

$$\mathbf{J}_1^{\text{Diff}} = -D_1^0 \nabla c_d^1 + \frac{z_1 D_1^0 c_d^1}{z_1^2 D_1^0 c_d^1 + z_2^2 D_2^0 c_d^2} \left[z_1 D_1^0 \nabla c_d^1 + z_2 D_2^0 \nabla c_d^2 \right] \quad (5.5)$$

$$\mathbf{J}_2^{\text{Diff}} = -D_2^0 \nabla c_d^2 + \frac{z_2 D_2^0 c_d^2}{z_1^2 D_1^0 c_d^1 + z_2^2 D_2^0 c_d^2} \left[z_1 D_1^0 \nabla c_d^1 + z_2 D_2^0 \nabla c_d^2 \right] \quad (5.6)$$

Based on equations (3.129) and (3.161), the charge conservation dictates that at any point in the solution:

$$\sum_{i=1}^{nc} z_i c_d^i = 0 \quad (5.7)$$

For a binary solution, e.g. NaCl or CaSO_4^{2-} , the equation (5.7) reduces to:

$$z_1 c_d^1 = -z_2 c_d^2 \quad (5.8)$$

The spatial differential form of the equation (5.8) also yields:

$$z_1 \nabla c_d^1 = -z_2 \nabla c_d^2 \quad (5.9)$$

Replacing the conditions presented in equations (5.8) and (5.9) into the diffusion fluxes yield a simplified form as:

$$\mathbf{J}_1^{\text{Diff}} = \mathbf{J}_2^{\text{Diff}} = -\frac{(z_1 - z_2) D_1^0 D_2^0}{z_1 D_1^0 - z_2 D_2^0} \nabla c_d^1 \quad (5.10)$$

For a binary solution containing single ionic species, e.g. NaCl where $z_1 + z_2 = 0$, the equations (5.10) yield a further simplified form:

$$\mathbf{J}_1^{\text{Diff}} = \mathbf{J}_2^{\text{Diff}} = -\frac{2D_1^0 D_2^0}{D_1^0 + D_2^0} \nabla c_d^1 \quad (5.11)$$

The flux equation is in fact, in the form of diffusion flux based on Fick's first diffusion law which is solely based on concentration gradients. The only difference is in the diffusion coefficient which is modified using a *harmonic mean* of the diffusion coefficients of the ion pairs in the binary solution. A similar derivation of the diffusion in a binary solution has been also presented by Cussler (1997) and Jungnickel et al. (2004).

If the diffusion process of the binary solution is modelled via the multicomponent diffusion formulation, the same results shall be generated with modelling via Fick's diffusion approach considering the harmonic mean of the diffusion coefficients of the ion pairs. This condition is examined to verify the approach adopted for multicomponent diffusion approach in the case of binary solutions.

5.3.1.2 Numerical model conditions

A series of numerical simulations on the diffusion of binary solutions are performed. The numerical model developed here for the diffusion of multicomponent is examined against the Fick's diffusion model implemented in COMPASS. The implementation of the Fick's law of diffusion in the model was extensively verified with different examples and against analytical solutions and other numerical models by Seetharam (2003), providing confidence in the application of the model for the purpose of comparison.

Two different binary solutions were used in the simulation comprising NaCl and HCl electrolyte solutions. The domain consisted of an electrolyte tube (0.1×0.1 m) containing NaCl or HCl which was exposed to same electrolyte solution but with different concentration at one boundary side. The domain initially contained no electrolyte solution including NaCl or HCl. At one boundary, a fixed concentration of NaCl or HCl was considered and at the other boundary, an impermeable condition was assumed. Figure 5.7 provides a schematic representation of the initial and boundary conditions of the electrolyte tube.

The 2D domain was discretised into 100 equally sized 4-noded quadrilateral elements. The system considered was saturated and the porosity was set as one. The water pressure and temperature were fixed during the analysis in the whole domain; therefore the transport flux

occurred purely by isothermal diffusion. The simulations were performed under coupled THC behaviour in the model. A fixed time-step of 3600 seconds was used for all simulations.

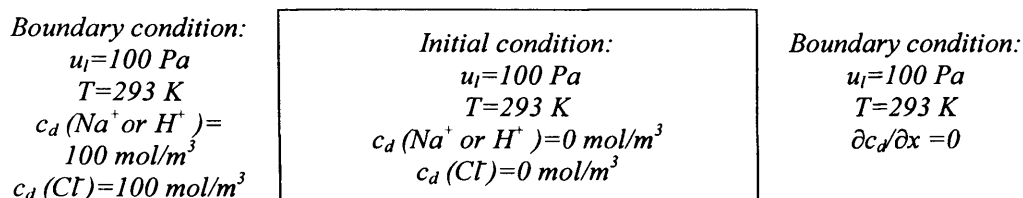


Figure 5.7 Schematic of the initial and boundary conditions (Test III)

Different tracer diffusion coefficients in water (D^0) were considered for the involving chemical components in the simulation based on multicomponent approach whilst in the modelling based on Fick's law of diffusion a harmonic mean was applied according to equation (5.11). The diffusion coefficient of Na^+ , Cl^- , and H^+ in water were considered as 13.3×10^{-10} , 20.3×10^{-10} , and $93.1 \times 10^{-10} \text{ m}^2/\text{s}$, respectively (Lasaga 1998).

Calculation of the harmonic mean of the tracer diffusion coefficient gives the value of 16.1×10^{-10} and $33.3 \times 10^{-10} \text{ m}^2/\text{s}$ for NaCl and HCl, respectively.

5.3.1.3 Results and discussion

Due to the higher concentration of the electrolyte solution at the boundary, ions diffuse into the tube. In the case of simulation under the multicomponent diffusion model, ions migrate from the boundary with different rates due to the difference in the diffusion coefficients used in the simulation data and the general conservation of charge adopted in the formulation provides a coupling between chemical and electrical diffusion potentials.

In the case of simulations based on the Fick's law of diffusion, ion pairs diffuse with the same rate of diffusion considering that same diffusion coefficients for the latter analysis were used as the harmonic mean between the diffusion coefficients of the ionic pairs.

Figure 5.8 shows the simulation results of the chemical concentration patterns of Na^+ or Cl^- ions, i.e. NaCl binary solution at different times of analysis according to the multicomponent diffusion approach and based on the Fick's law of diffusion. In figure 5.9, the modelling results of the profile for H^+ or Cl^- ions, i.e. HCl binary solution at different times of analysis is also presented. The symbols represent the results of simulation based on multicomponent diffusion approach and lines give the results based on the Fick's law of diffusion.

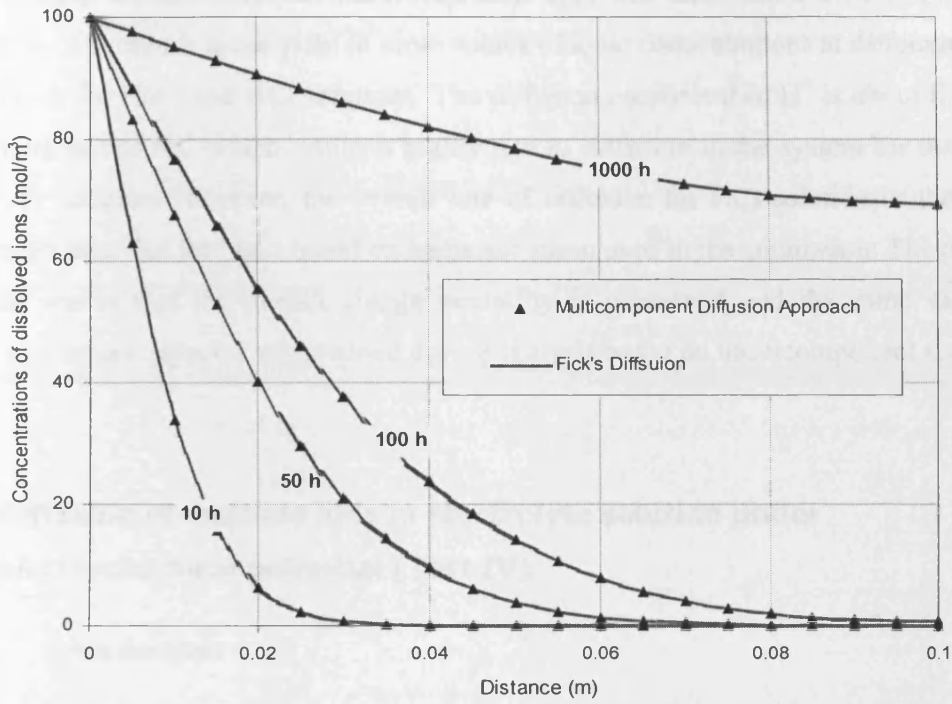


Figure 5.8 Profiles of the concentrations of Na^+ and Cl^- ions in the domain.

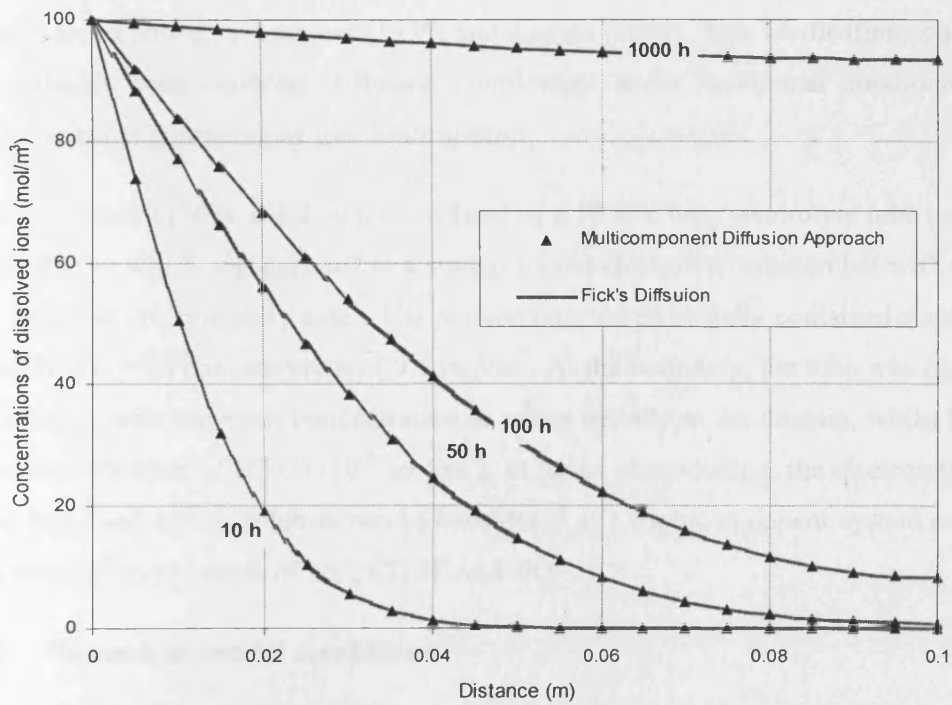


Figure 5.9 Profiles of the concentrations of H^+ and Cl^- ions in the domain.

The modelling results based on multicomponent approach and Fick's diffusion with the assumption of harmonic mean yield to same values of ionic concentrations at different time of analysis both for NaCl and HCl solutions. The diffusion coefficient of H^+ is about five times greater than that of Na^+ which results a higher rate of diffusion in the system for the case of HCl binary solution. However, the overall rate of diffusion for HCl solution is about three times higher than that for NaCl based on harmonic mean used in the simulation. The results of modelling shows that the overall charge neutrality is conserved and the same values for anionic and cationic species are obtained during analysis based on multicomponent approach.

5.3.2 Diffusion of multiple ions in electrolyte solution under electrochemical potential (Test IV)

5.3.2.1 Introduction

In this example, the theoretical and numerical model adopted for multicomponent chemical transport under electrochemical diffusion potential is examined in the case of an electrolyte solution containing multiple ionic species. This example was adopted from a similar verification test reported by Lichtner (1995) and Appelo (2007). This verification consisted of a pure diffusion with different diffusion coefficients under isothermal conditions in an electrolyte solution consisting of four ionic species.

Following Lichtner (1995), the domain consisted of a 10 mm long electrolyte tube containing NaCl and HNO_3 , which was exposed to a similar mixed electrolyte solution but with different concentrations at one boundary side. The domain considered initially contained a solution of NaCl and HNO_3 with concentration of 0.1 mol/m^3 . At the boundary, the tube was exposed to a NaCl solution with the same concentration as exists initially in the domain, whilst having a different concentration of HNO_3 (10^{-3} mol/m^3). In terms of modelling, the electrolyte system of mixed NaCl and HNO_3 solution can be considered as a multicomponent system consisting of four chemical components of Na^+ , Cl^- , H^+ and NO_3^- .

5.3.2.2 Numerical model conditions

The domain was discretised into 100 equally sized 4-noded quadrilateral elements. The system was saturated and the porosity was considered as one (pure aqueous system). A fixed

time-step of 3600 seconds was used for all simulations. The transport flux is purely diffusive and the tracer diffusion coefficient (D^0), of Na^+ , Cl^- , H^+ and NO_3^- were considered as 13.3×10^{-10} , 20.3×10^{-10} , 93.1×10^{-10} and $19.0 \times 10^{-10} \text{ m}^2/\text{s}$, respectively based on Lasaga (1998). The water pressure and temperature were fixed during the analysis in the whole domain; therefore the transport flux is purely isothermal diffusive.

The boundary condition at one side was considered as fixed with the concentration of the four components. At the other side, an impermeable boundary condition was assumed in the model. The simulations were performed under coupled THC behaviour in the model. Figure 5.9 provides a schematic representation of the initial and boundary conditions of the electrolyte tube.

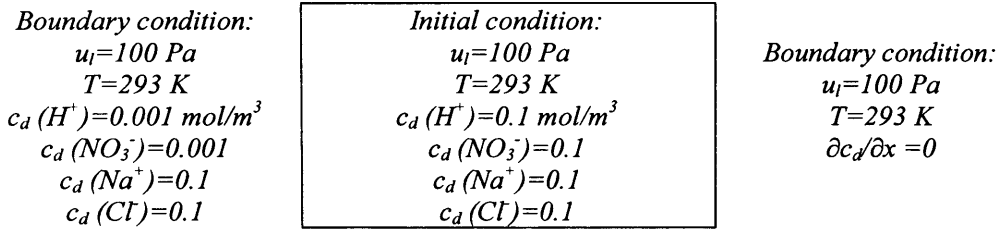


Figure 5.9 Schematic of the initial and boundary conditions (Test IV)

5.3.2.3 Results and discussion

Due to the higher concentration of HNO_3 in the tube, H^+ and NO_3^- ions diffuse from the tube to the outer boundary. Figure 5.10 shows the modelling results of the chemical concentrations profiles of H^+ and NO_3^- ions at different times of analysis according to the multicomponent diffusion adopted in the model. The diffusion coefficient of H^+ is about five times greater than that of NO_3^- . Therefore, after some time the domain contains higher concentration of NO_3^- than H^+ ions.

In order to maintain the overall charge neutrality of the solution, the Na^+ and Cl^- ions diffuse through the system and their concentration varies in the column despite the fact that initially there is no concentration gradient for Na^+ and Cl^- ions. Figure 5.11 shows the variation of the dissolved concentrations of Na^+ and Cl^- ions in the domain at different time of analysis.

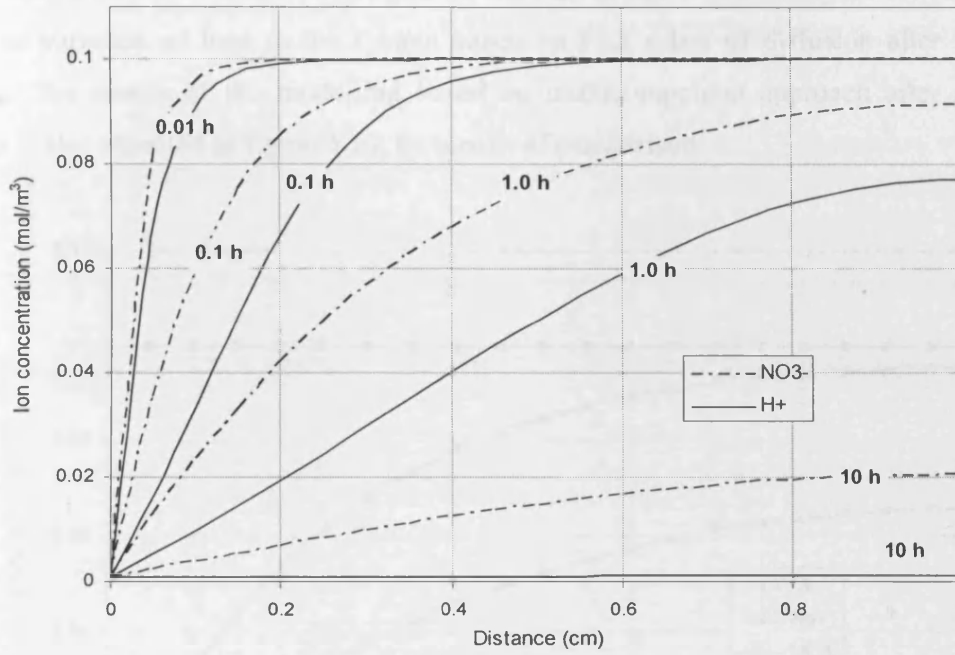


Figure 5.10 Concentration patterns of NO_3^- and H^+ at different times

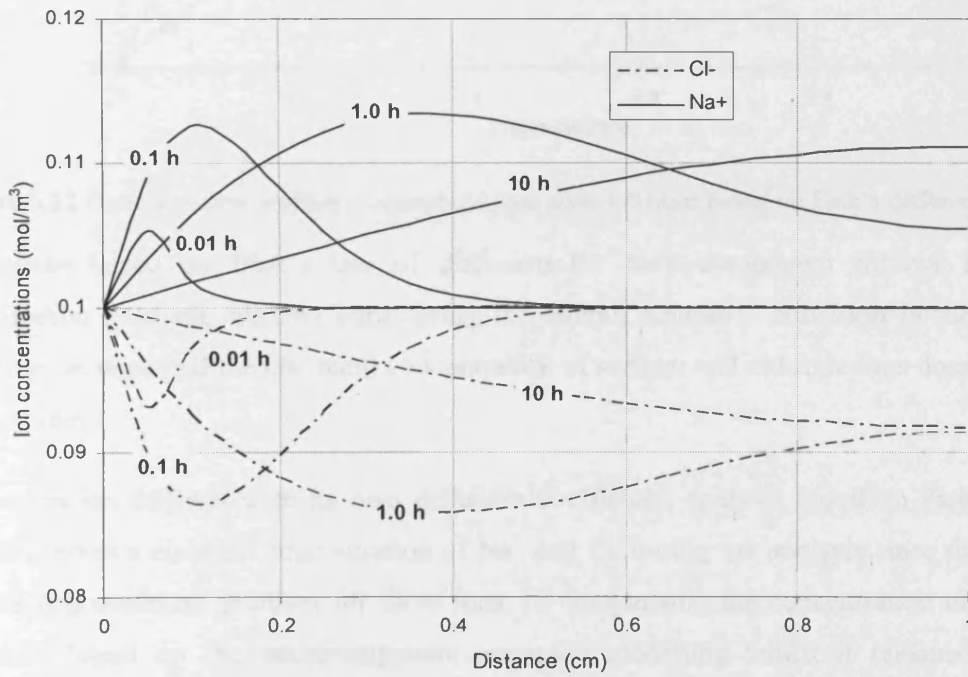


Figure 5.11 Concentration patterns of Cl^- and Na^+ at different times

In order to demonstrate the difference between modelling the example via the multicomponent approach and Fick's law, the simulation is repeated via Fick's diffusion

model using different diffusion coefficient for the ions as stated before. Figure 5.12 shows the results of variation of ions in the system based on Fick's law of diffusion after one hour analysis. The results of the modelling based on multicomponent approach after one hour analysis is also repeated in figure 5.13, by means of comparison.

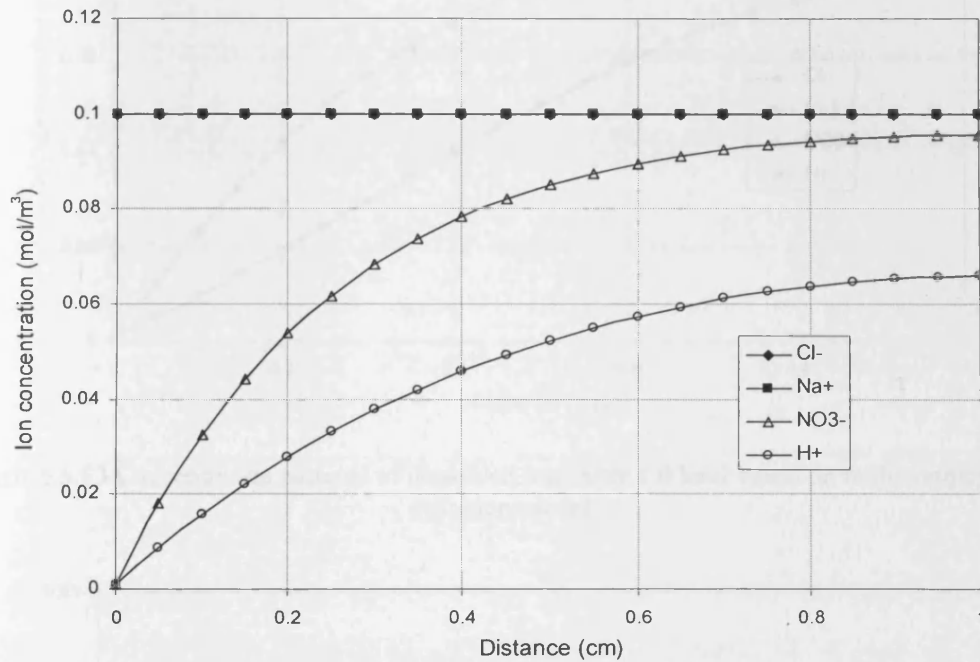


Figure 5.12 Concentration profiles of dissolved ions after 1.0 hour based on Fick's diffusion model

The results based on Fick's law of diffusion for each component follows its actual concentration gradient, without considering the overall neutrality condition in the domain. Therefore, as expected the chemical concentration of sodium and chloride ions does not vary in the system.

When each ion diffuses with its own diffusion coefficient, analysis based on Fick's law of diffusion, gives a constant concentration of Na^+ and Cl^- during the analysis since there is not absolute concentration gradient for these ions. In comparison, the concentration of Na^+ and Cl^- varies based on the multicomponent approach modelling whilst it remains constant according to the modelling based on Fick's law. Figure 5.14 shows the variation of total charge along the domain based on multicomponent approach and Fick's law of diffusion assuming different diffusion coefficients for chemicals after one hour of simulation.

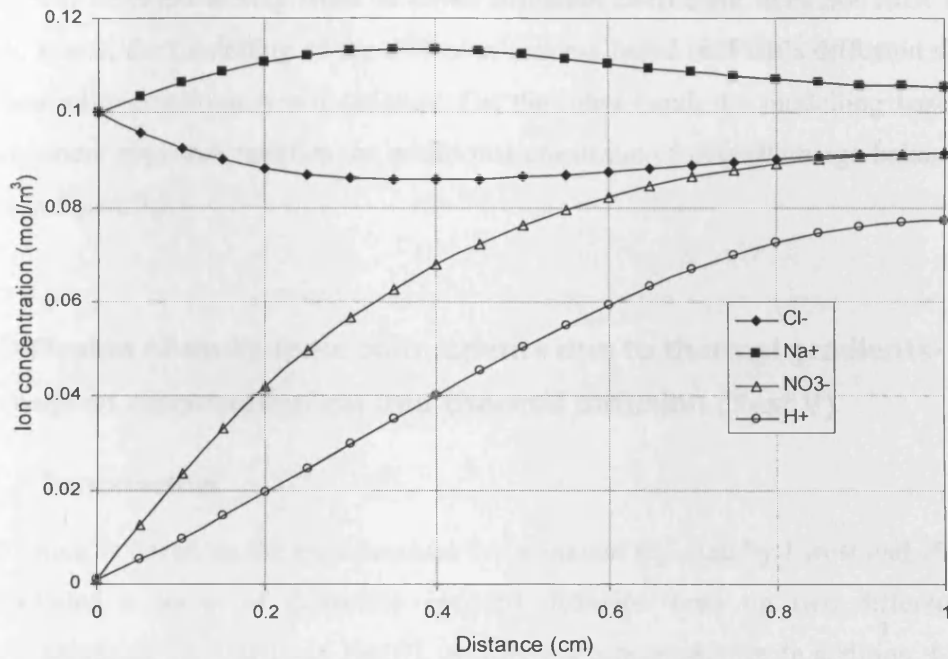


Figure 5.13 Concentration patterns of dissolved ions after 1.0 hour based on multicomponent diffusion model

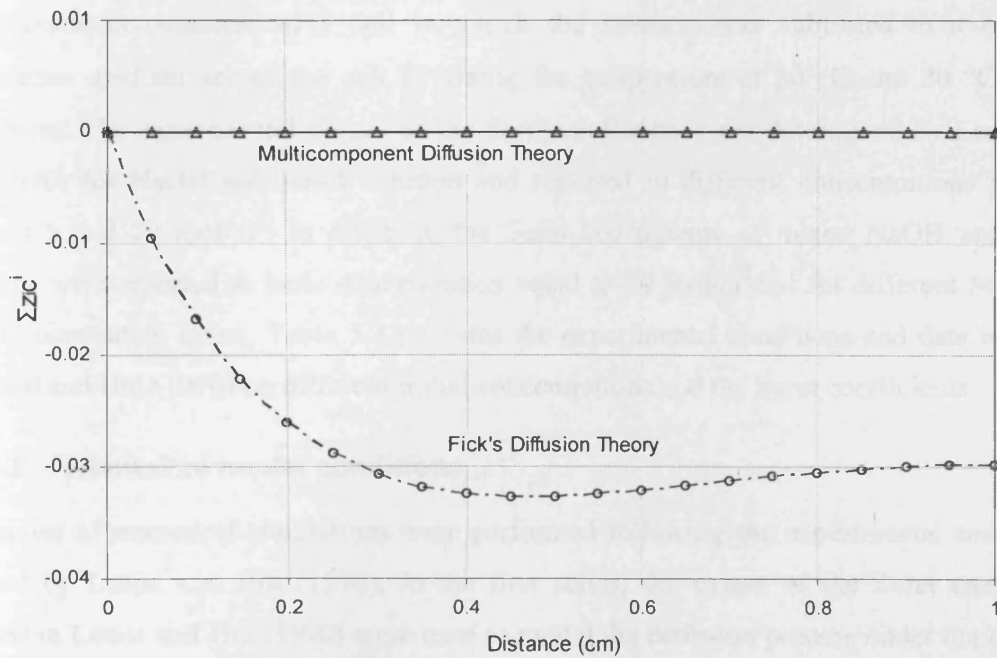


Figure 5.14 Charge conservation along the domain for the analysis results after 1 hour

The electrical potential arising from different diffusion coefficient does not exist in Fick's approach; hence, the modelling of the diffusion process based on Fick's diffusion shows the overall neutrality condition is not satisfied. On the other hand, the modelling based on the multicomponent approach satisfies the additional constraint of overall charge balance as it is observed in figure 5.14.

5.3.3 Diffusion of multi-ionic components due to thermal gradients-coupled electrochemical and thermal diffusion (Test V)

5.3.3.1 Introduction

The simulation is based on the experimental investigation reported by Leaist and Hui (1990) which included a series of thermally induced diffusion tests on two different binary electrolyte solutions, i.e. NaCl and NaOH, at different concentrations. In addition, Leaist and Hui (1990) conducted another series of experiments on mixed NaCl-NaOH solutions, i.e. ternary solutions, in a range of concentrations, providing the second series of tests.

The experiment consisted of a cell in which the solution was subjected to a constant temperature gradient across the cell by fixing the temperature at 30 °C and 20 °C at the boundaries. The experimental values of the Soret coefficient were determined by Leaist and Hui (1990) for NaOH and NaCl solution and reported in different concentrations ranging between 5 and 20 mol/m³. In addition, the Soret coefficients of mixed NaOH and NaCl solutions were reported at ionic concentration equal to 20 mol/m³ and for different NaOH to NaCl concentration ratios. Table 5.3 provides the experimental conditions and data reported by Leaist and Hui (1990) on different initial concentrations and the Soret coefficients.

5.3.3.1 Numerical model conditions

Two series of numerical simulations were performed following the experimental conditions reported by Leaist and Hui (1990). In the first series, the values of the Soret coefficient reported in Leaist and Hui (1990) were used to model the diffusion process under the thermal gradient and under the different conditions presented in table 5.3. In the simulations ionic components of Na⁺, Cl⁻ and OH⁻ were considered as the dissolved chemicals in the system.

The values presented for the Soret coefficient reported by Leaist and Hui (1990) were used from the values in table 5.3 in association with each initial concentration. It is noted that Leaist and Hui (1990) reported the Soret coefficients as a single value for the involving species, i.e. NaOH or NaCl. For ternary solutions, the simulations were carried out considering four components including Na^+ , Cl^- for NaCl species and again Na^+ and OH^- for NaOH species. The reason for repeating Na^+ in the simulations of ternary solutions is that, the Soret coefficients have been reported for species, rather than the components and therefore, information provided by Leaist and Hui (1990) on the Soret coefficients applies to the ionic species not the ion pairs. Therefore, it was assumed that the Soret coefficients of the ion pairs for each species are identical in the analysis, e.g.: $S_{\text{NaOH}}^T = S_{\text{Na}^+}^T = S_{\text{OH}^-}^T$ or $S_{\text{NaCl}}^T = S_{\text{Na}^+}^T = S_{\text{Cl}^-}^T$

Table 5.3 Initial conditions of different tests and average experimentally determined Soret coefficients reported by Leaist and Hui (1990)

<i>Test</i>	<i>Initial concentration</i> <i>(mol/m³)</i>		<i>Experimentally determined</i> <i>Soret coefficients (1/K)</i>	
	<i>NaOH</i>	<i>NaCl</i>	<i>S^T(NaOH)</i>	<i>S^T(NaCl)</i>
<i>Test V-a</i>	5	0	14.3×10^{-3}	-
	10	0	14.1×10^{-3}	-
	15	0	11.7×10^{-3}	-
	20	0	11.7×10^{-3}	-
<i>Test V-b</i>	0	5	-	1.9×10^{-3}
	0	10	-	1.8×10^{-3}
	0	15	-	1.6×10^{-3}
	0	20	-	1.3×10^{-3}
<i>Test V-c</i>	15	5	14.7×10^{-3}	-5.4×10^{-3}
<i>Test V-d</i>	10	10	16.6×10^{-3}	-4.4×10^{-3}
<i>Test V-e</i>	5	15	17.5×10^{-3}	-1.1×10^{-3}

In the second series of analysis, the theoretical approach adopted for calculating the Soret coefficient based on Agar et al. (1989) was applied in the numerical simulation instead of the experimentally determined values used in the first series of simulation. Similar conditions applied in the first series were used in the second series. The second series of simulation provided a validation test for the theoretical approach for determination of the Soret coefficient in comparison with the results in the first series. The values of the Soret coefficient were calculated based on the tracer diffusion coefficient of each component using equation (3.151).

The studied 2D domain is 1 cm long which was discretised into 100 equally sized 4-noded quadrilateral elements. The temperature was fixed at 20 and 30 °C at the boundaries and the initial temperature was 25 °C. The system considered is saturated and porosity was assumed equal to one. The water pressure was constant along the domain during the analysis, providing a purely diffusive flux. Figure (5.15) presents schematics of the initial and boundary conditions for different simulations performed on binary and ternary solution.

Different diffusion coefficients were considered for the various chemical components. The simulation was carried out with variable time-steps and continued to reach steady-state conditions for the dissolved chemical concentrations. The tracer diffusion coefficients (D^0) of Na^+ , Cl^- , OH^- were considered equal to 13.3×10^{-10} , 20.3×10^{-10} , $52.7 \times 10^{-10} \text{ m}^2/\text{s}$, respectively based on Lasaga (1998). Since different diffusion coefficients are used in the simulation, the overall charge must be conserved during the analysis, according to the formulation of diffusion developed earlier, providing a verification test on diffusion under non-isothermal conditions.

5.3.3.3 Results and discussion

Figure 5.16 and Figure 5.17 shows the simulation results of concentration variation of ions at steady state for binary solution containing different initial concentrations of NaOH and NaCl, respectively, i.e. Case V-a and V-b in figure 5.15. The lines represent the results based on the theoretical approach for the Soret coefficient and the symbols show the simulation results based on the experimentally determined Soret coefficient values reported by Leaist and Hui (1990).

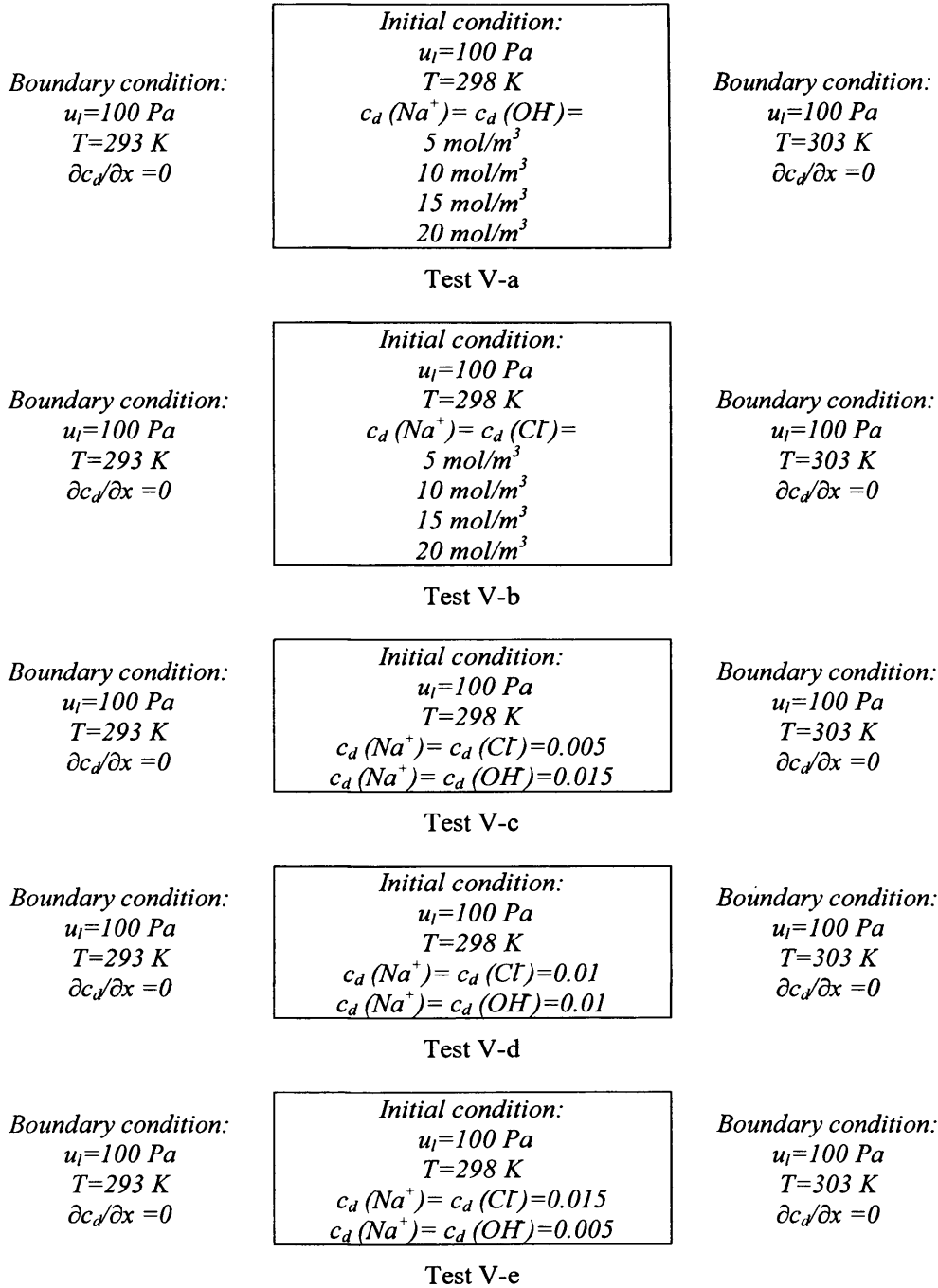


Figure 5.15 Schematic of the initial and boundary conditions (Test V)

The results indicate that ion pairs in each binary solution migrate with the same rate under coupled thermal potential, sourcing from boundary condition and electrochemical potential arising from the application of different diffusion coefficients. The simulation results also show a good match between the theoretical approach adopted for thermal diffusion and the experimental values reported by Leaist and Hui (1990).

Figure 5.17, 5.18 and 5.19 shows the simulation results of concentration of Cl^- and OH^- ions at steady state for mixed solutions of NaOH and NaCl at two different ratios of concentrations of NaOH over NaCl, i.e. case III, IV and V in figure 5.15. The symbols show the results based on the experimentally determined values for the Soret coefficient reported by Leaist and Hui (1990). The lines represent the results based on the theoretical approach for Soret coefficient, i.e. equation (3.151).

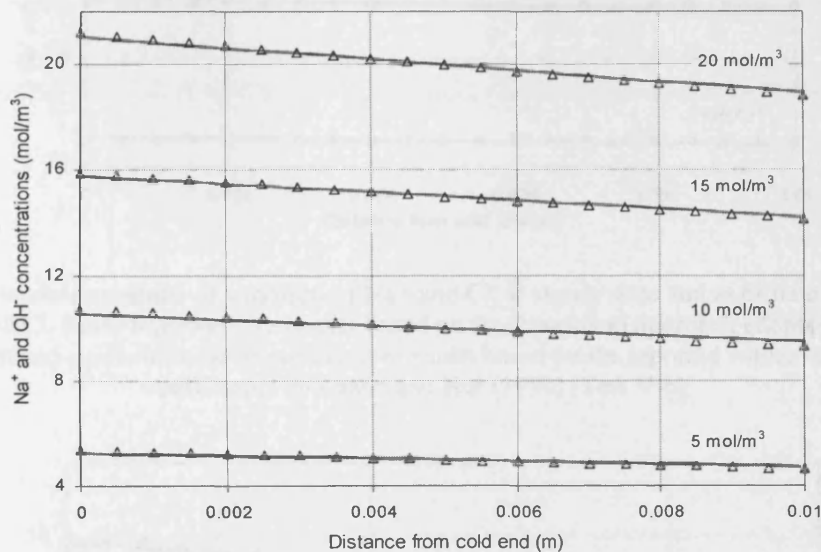


Figure 5.16 Simulation results of variation of Na^+ and OH^- at steady state and at different initial binary solutions of NaOH. Lines represent the results based on the theoretical approach adopted for the Soret coefficient and symbols show the simulation results based on the reported values of the Soret coefficients by Leaist and Hui (1990) (Test V-a)

The results show a good correlation between simulation based on the adopted approach and on the experimentally determined values for the Soret coefficient in the case of OH^- ions. However, in the case of ternary solutions, Leaist and Hui (1990) reported negative values for the Soret coefficient for NaCl. This implies that in the ternary solutions, chloride ions tend to move toward hot side in contrast with the general trend observed in binary solutions. Such a trend in the distribution of chloride is not observed in the results of simulation using the theoretical approach adopted for thermal diffusion effects. However, the coupling of the chemical and electrical potential effects reduces the rate of chloride migration away from heat source. The model results for all simulations conserve the overall charge during the analysis and at steady state, verifying the charge conservation in the transport equation for multicomponent chemicals under coupled electrochemical and thermal diffusion potentials.

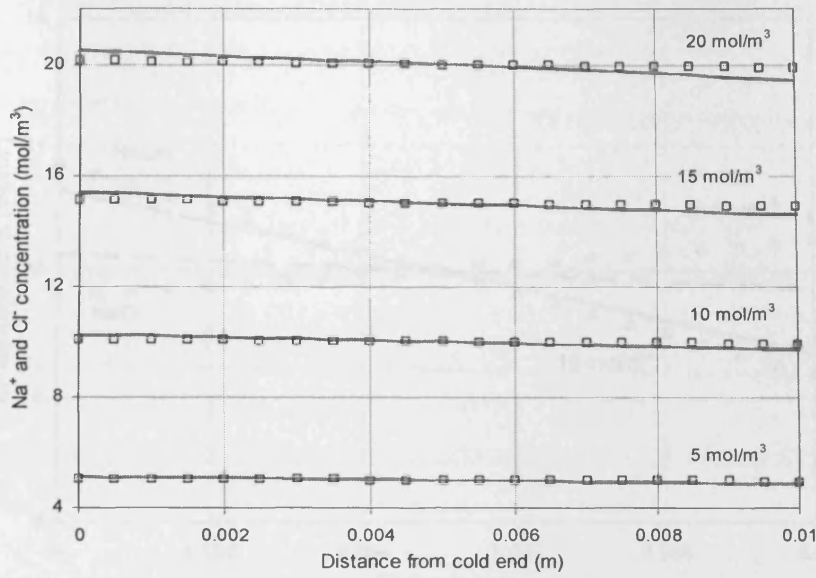


Figure 5.17 Simulation results of variation of Na⁺ and Cl⁻ at steady state and at different initial binary solutions of NaCl. Lines represent the results based on the theoretical approach adopted for the Soret coefficient and symbols show the simulation results based on the reported values of the Soret coefficients by Leaist and Hui (1990) (Test V-b)

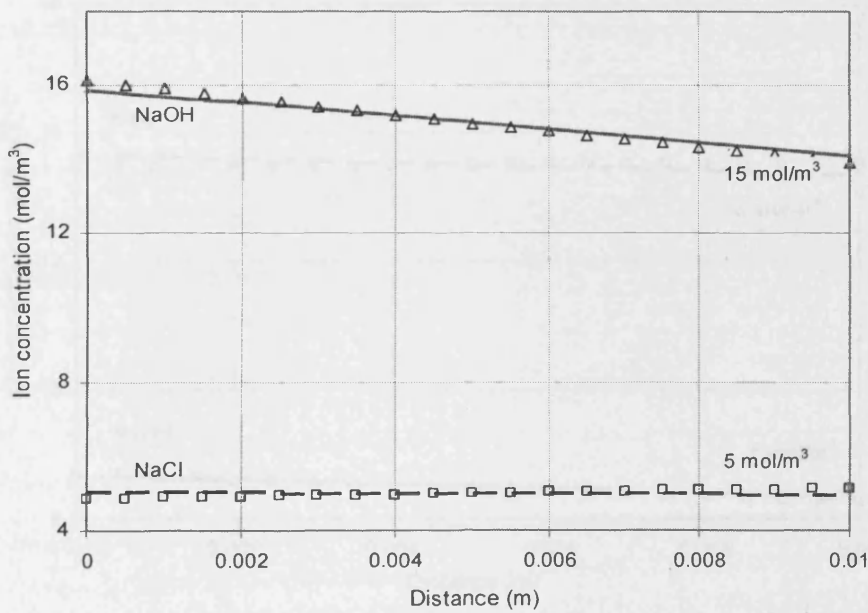


Figure 5.18 Simulation results of concentration profiles of ions at steady state for ternary mixed NaCl and NaOH solution at NaOH/NaCl molarity ratio of 3, based on the theoretical approach adopted for the Soret coefficient (lines) and based on the values for the Soret coefficients (Test V-c)

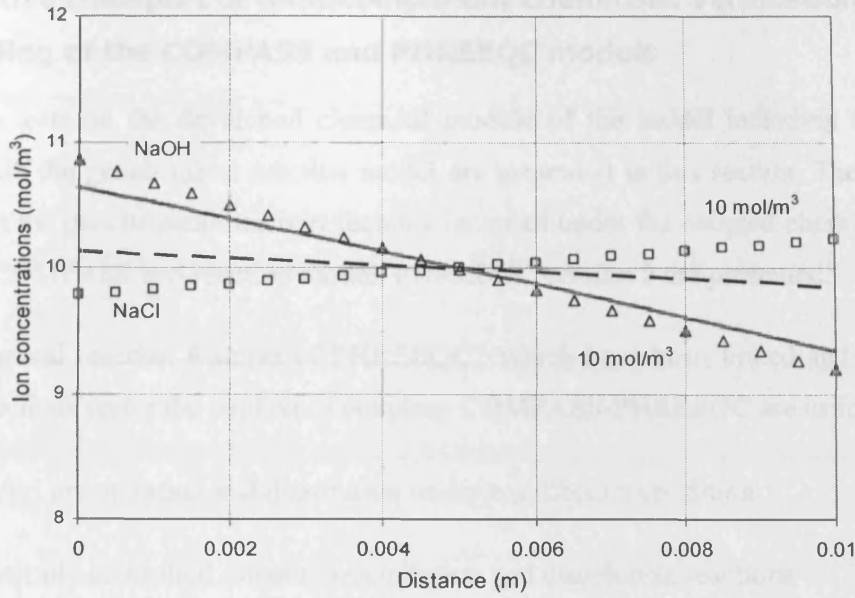


Figure 5.19 Simulation results of concentration profiles of ions at steady state for ternary mixed NaCl and NaOH solution at NaOH/NaCl molarity ratio of 1, based on the theoretical approach adopted for the Soret coefficient (lines) and based on the values for the Soret coefficients (Test V-d)

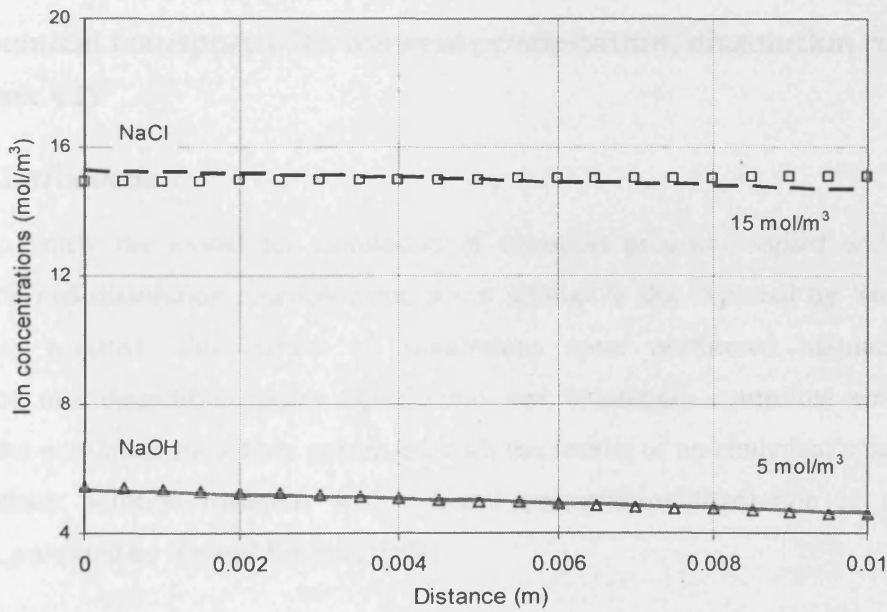


Figure 5.20 Simulation results of concentration profiles of ions at steady state for ternary mixed NaCl and NaOH solution at NaOH/NaCl molarity ratio of 1/3, based on the theoretical approach adopted for the Soret coefficient (lines) and based on the values for the Soret coefficients (Test V-e)

5.4 Reactive transport of multicomponent chemicals: verification of the coupling of the COMPASS and PHREEQC models

Verification tests on the developed chemical module of the model including the coupling transport with the geochemical reaction model are presented in this section. The verification examples on the geochemical reaction features included under the coupled chemical transport model, i.e. COMPASS and reaction model, PHREEQC version 2 are presented.

The geochemical reaction features of PHREEQC2 which have been linked and tested in the following sections under the context of coupling COMPASS-PHREEQC are as follows:

- Mineral precipitation and dissolution under equilibrium condition
- Kinetically controlled mineral precipitation and dissolution reactions
- Ion exchange process under equilibrium condition.

5.4.1 Chemical transport with mineral precipitation/dissolution reaction (Test VI)

5.4.1.1 Introduction

In order to verify the model for simulation of transport process coupled with a mineral precipitation and dissolution reaction front, a test similar to that reported by Xu and Pruess (1998) was adopted. Two series of simulations were performed assuming mineral precipitation and dissolution under equilibrium and kinetically controlled reactions. The results of the numerical model are compared with the results of an analytical solution for the case of binary solution transport with mineral precipitation/dissolution in the specific conditions, provided by Xu and Pruess (1998).

The studying system corresponds to one-dimensional transport of two hypothetical species A and B which originate from the dissolution of a mineral phase AB_s (i.e., $AB_s = A^+ + B^-$). This verification series is similar to those performed by Xu and Pruess (1998). Two series of numerical simulations were performed. First the reactive transport of a binary solution with equilibrium mineral precipitation/dissolution was studied. The results are compared with the

the results of an analytical solution provided by Xu and Pruess (1998). The second simulation deals with the transport of the same binary solution with kinetically controlled mineral reactions. Xu and Pruess (1998) provided an analytical solution for the problem under steady-state conditions. The results at steady-state will be compared with the results of the analytical solution. Finally, the results of simulations with different rates of mineral precipitation/dissolution reaction are compared with simulation under equilibrium condition.

5.4.1.2 Numerical model conditions

The system was considered as 1 m of saturated medium under a steady flow of a solution from one boundary containing same concentration of chemical B^+ as it in the domain, but with a different concentration of component A^+ compared with the corresponding value of the initial state. The domain was discretised into 100 equally 4-noded quadrilateral elements. A variable time-step was considered for the simulation which allows the time-step to be increased or decreased depending on convergence. The maximum allowable time-step was 3600 seconds. Temperature is fixed in the domain; therefore the modelling is performed under isothermal condition. The porosity and pore velocity of the study domain was considered as 0.4 and 0.1 m/day. A fixed pore water pressure was designed in the boundary to provide the required constant pore velocity.

The domain initially contained same concentrations of A^+ and B^- components. At the boundary, the concentrations of A^+ and B^- were considered to be different. The concentrations of ionic chemicals were considered relatively low, therefore, the ionic activity can be assumed equal to the concentration and the activity modification factor can be ignored in calculations. Figure 5.21 shows a schematic of the initial and boundary conditions used in the verification.

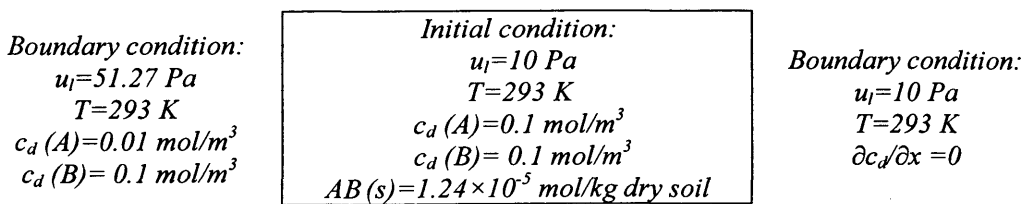


Figure 5.21 Schematic of the initial and boundary conditions (Test VI)

Physical and chemical parameters required for the modelling are summarised in table (5.5).

Following Xu and Pruess (1998), a first-order kinetic rate of reaction, i.e. r_{AB} , is considered for the simulations based on kinetically controlled condition based on Lasaga (1994).

$$r_{AB} = k\sigma\left(1 - \frac{c_d^A c_d^B}{K_{eq}}\right) \quad (5.12)$$

where k represent the kinetic rate constant, σ is the specific surface area and K_{eq} is the equilibrium constant of the reaction.

Table 5.5 Material parameters (Test VI)

<i>Material parameter</i>	<i>Relationship/value</i>
Porosity:	$n = 0.4$
Degree of saturation	$S_l = 1.0$
Pore water velocity:	$V_l = v_l/n = 0.1 \text{ m/day} = 1.157 \times 10^{-6} \text{ m/s}$
Hydraulic conductivity:	$k_f = 1.1 \times 10^{-4} \text{ m/s}$
Diffusion coefficient of chemicals:	$D_i = 0 \text{ m}^2/\text{s}$
Dispersivity coefficient (Longitudinal)	$\alpha_L = 0.02 \text{ m}$
Equilibrium constant of reaction at 25 °C $AB(s) = A^+ + B^-$	$\log K_{eq} = -8.0$

5.4.1.3 Analytical solution under equilibrium condition

Xu and Pruess (1998) provided an analytical solution for the specified problem under equilibrium condition. The solution is repeated here for the sake of completeness. Under the specified conditions, the governing equation for transport of ionic components A and B due to the advective-dispersive flux based on a simplified form of equation (3.127) can be given as:

$$\frac{\partial c_d^A}{\partial t} = -V_l \frac{\partial c_d^A}{\partial x} + D \frac{\partial^2 c_d^A}{\partial x^2} + r_{AB} \quad (5.13)$$

$$\frac{\partial c_d^B}{\partial t} = -V_l \frac{\partial c_d^B}{\partial x} + D \frac{\partial^2 c_d^B}{\partial x^2} + r_{AB} \quad (5.14)$$

where V_l is the pore velocity defined as:

$$V_l = \frac{\mathbf{v}_l}{n} \quad (5.15)$$

where \mathbf{v}_l is the Darcy's liquid flux, defined in equation (3.25).

Subtracting equation (5.13) from equation (5.14) removes the sink/source term, i.e. r_{AB} . If the difference between the concentrations of A and B components is assumed as ψ , i.e. $\psi = c_d^B - c_d^A$, it can be written:

$$\frac{\partial \psi}{\partial t} = -V_l \frac{\partial \psi}{\partial x} + D \frac{\partial^2 \psi}{\partial x^2} \quad (5.16)$$

The equation (5.16) demonstrates a governing differential equation of conservative advective-dispersive flow for parameter ψ . The analytical solution for equation (5.16), proposed by van Genuchten and Alvez (1982) are as follows:

$$\psi(x,t) = \psi_0 \left\{ \begin{array}{l} \frac{1}{2} \operatorname{erfc} \left(\frac{x - V_l t}{2\sqrt{Dt}} \right) + \sqrt{\frac{V_l^2 t}{\pi D}} \exp \left(-\frac{(x - V_l t)^2}{4Dt} \right) \\ - \frac{1}{2} \left(1 - \frac{V_l x}{D} + \frac{V_l^2 x}{D} \right) \exp \left(\frac{V_l x}{D} \right) \operatorname{erfc} \left(\frac{x - V_l t}{2\sqrt{Dt}} \right) \end{array} \right\} \quad (5.17)$$

where, $\psi_0 = (c_d^B)_{x=0} - (c_d^A)_{x=0}$

The difference between concentrations of A and B can be calculated using equation (5.17). Under equilibrium condition and for the specified range of concentrations, the mineral AB is in equilibrium with dissolved chemicals A and B. Therefore it can be given:

$$K_{eq} = c_d^B c_d^A \quad (5.18)$$

Eventually the concentration of chemical component A can be calculated as:

$$c_d^A = \frac{\sqrt{\psi^2 + 4K_{eq}} - \psi}{2} \quad (5.19)$$

If concentration of component A is known from equation (5.17), the concentration of component B can be calculated either from equation (5.18) or from $c_d^B = \psi + c_d^A$

5.4.1.4 Analytical solution under kinetically controlled steady-state condition

Xu and Pruess (1998) also provided an analytical solution for the specified problem under kinetically controlled condition at steady-state. The solution was provided for advective transport of binary solution with mineral precipitation/dissolution. Under the specified

conditions, the governing equation for transport of ionic components of A and B due to the advective flux based on simplified form of equation (3.127) can be given as:

$$-V_l \frac{dc_d^A}{dx} + r_{AB} = 0 \quad (5.20)$$

$$-V_l \frac{dc_d^B}{dx} + r_{AB} = 0 \quad (5.21)$$

Similar to the analytical solution under equilibrium condition, if the equations (5.20) and (5.21) are subtracted from each other, they yield:

$$-V_l \frac{d(c_d^B - c_d^A)}{dx} = 0 \quad (5.22)$$

This equation indicates that the difference between concentrations of component A and B remains constant which is equivalent to the difference at boundary, i.e.

$$\psi_0 = (c_d^B)_{x=0} - (c_d^A)_{x=0}.$$

Therefore, the rate of mineral reaction can be re-written based on one of the component concentrations as:

$$r_{AB} = k\sigma \left[1 - \frac{c_d^B (c_d^B - \psi_0)}{K_{eq}} \right] \quad (5.23)$$

The equation (5.21) is then simplified as:

$$-V_l \frac{dc_d^B}{dx} + k\sigma \left[1 - \frac{c_d^B (c_d^B - \psi_0)}{K_{eq}} \right] = 0 \quad (5.24)$$

The solution for the above equation can be given as (Xu and Pruess, 1998):

$$c_d^B = \frac{\lambda_1 - \lambda_2 \beta_0 \exp\left(-\frac{x}{d_e}\right)}{1 - \beta_0 \exp\left(-\frac{x}{d_e}\right)} \quad (5.25)$$

where

$$\beta_0 = \frac{(c_d^B)_{x=0} - \lambda_1}{(c_d^B)_{x=0} - \lambda_2} \quad (5.26)$$

$$d_e = \frac{V_l K_{eq}}{k\sigma(\lambda_1 - \lambda_2)} \quad (5.27)$$

and values of λ_1 and λ_2 are the roots of the following second-order polynomial equation:

$$\lambda^2 - \psi_0 \lambda - K_{eq} = 0 \quad (5.28)$$

5.4.1.5 Results and discussion

Figure 5.22 shows the variation of concentration of chemicals A and B in the domain calculated using numerical model and analytical solution under equilibrium condition for mineral precipitation. The results are presented for five days analysis and indicate a match between the numerical model and analytical solution.

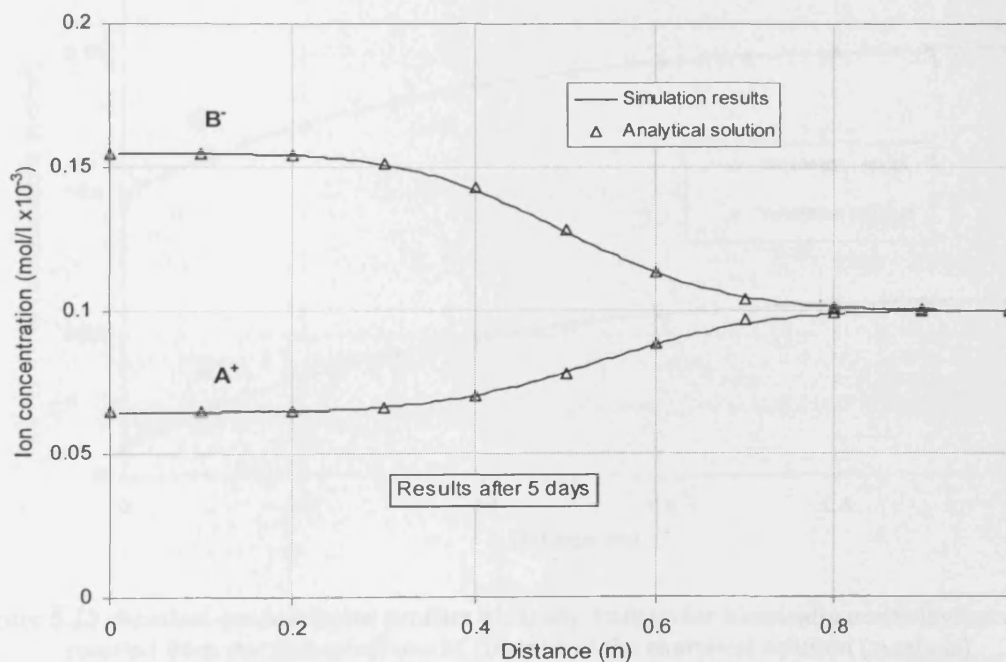


Figure 5.22 Concentration patterns of dissolved ions after 5 days under mineral equilibrium condition, resulted from numerical model (lines) and analytical solution (symbols)

The concentration of component A at the boundary is lower than in the solution. Accordingly and in order to maintain the equilibrium between mineral and dissolved components, some

mineral has been dissolved in to the system which has increased the concentration of component B from the initial level. Therefore, after some time, the re-equilibrated system, contains an unequal solution in terms of ionic components A and B . However, the equilibrium condition between the mineral content and dissolved chemicals always remains based on the defined equilibrium constant, i.e. 10^{-8} .

As reported previously, the same simulation was repeated considering the mineral reaction under kinetic condition according to the relationship defined in equation (5.12). Note that in the simulation based on kinetically controlled condition, dispersion coefficient was set to zero, providing a pure advective flow. The kinetic rate constant is assumed as $2 \times 10^{-10} \text{ mol.s}^{-1} \cdot \text{m}^{-2}$ and the specific surface area was considered equal to $1.0 \text{ m}^2/\text{l}$.

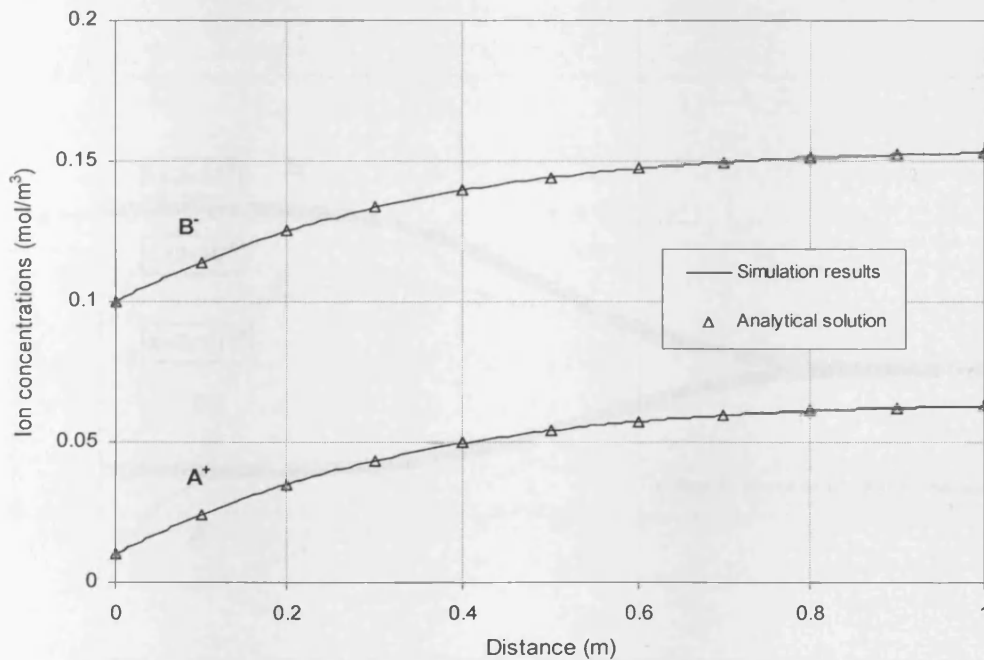


Figure 5.23 chemical concentration profiles at steady-state under kinetically controlled condition resulted from the numerical model (lines) and the analytical solution (symbols)

Figure 5.23 shows the concentration patterns of dissolved chemicals A and B in the domain, calculated by the numerical modelling and analytical solution under kinetically controlled condition for mineral precipitation/dissolution. The results are presented at steady-state in order to compare with the results of the analytical solution. The numerical model and analytical solution provide same results and agree well with each other. The results indicate

that at steady-state, the concentrations of the dissolved chemicals at the boundary have changed to the concentration of the flushing solution through precipitation of the AB mineral in the domain.

A series of numerical simulations was also performed under different kinetic reaction rates. Different values for the reaction rate constants were assumed including 2×10^{-8} , 2×10^{-9} and $2 \times 10^{-10} \text{ mol s}^{-1} \text{ m}^{-2}$, similar to the modelling examples reported by Xu and Pruess (1998). The results are also compared with those under equilibrium condition. In this series of analysis dispersion coefficient was assumed equal to 0.02, providing an advective-dispersive flow regime in the domain. In these simulations the major aims have been to demonstrate the difference in the reactive transport behaviour of the model under equilibrium and kinetic mineral reaction.

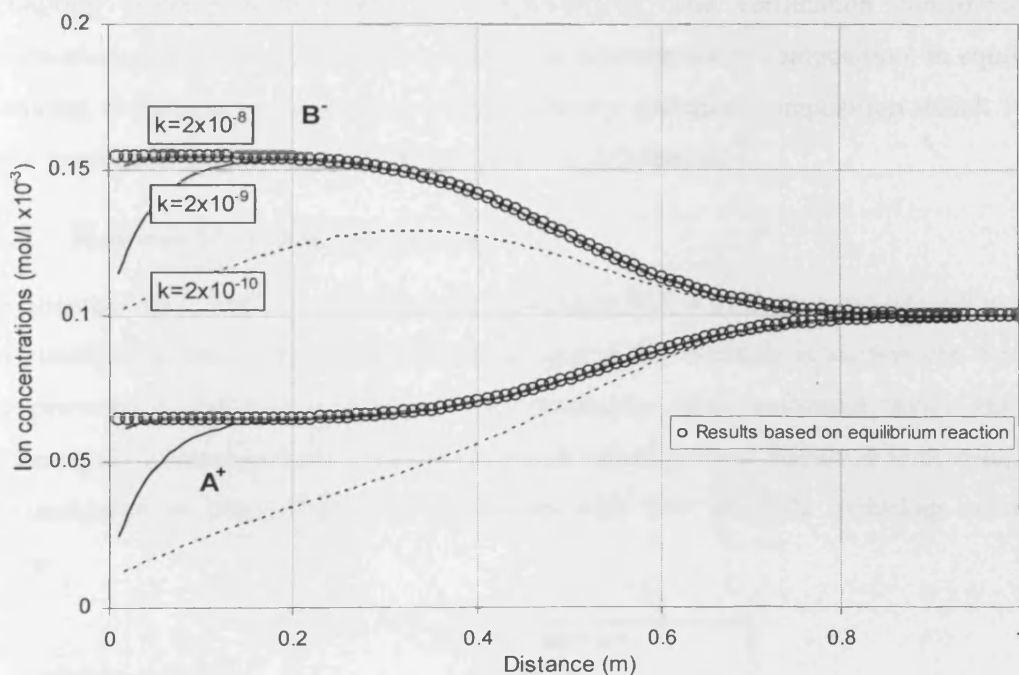


Figure 5.24 chemical concentration profiles after five days of numerical analysis resulted different under kinetically controlled condition resulted (lines) and under equilibrium condition (symbols)

Figure 5.24 shows the results of simulations in terms of dissolved chemical concentrations under kinetic with different rates and equilibrium after five days. As it is expected, with increasing the reaction rate, the concentration profile tends to a similar profile resulted under

equilibrium precipitation and dissolution reaction at same time (symbols). The results are in agreement with the results of a similar simulation reported by Xu and Pruess (1998).

5.4.2 Chemical Transport with multiple Precipitation/Dissolution Front (Test VII)

5.4.2.1 Introduction

This simulation aims to verify the ability of the developed model for simulation of the reactive transport of multicomponent chemicals with precipitation and dissolution. The verification test was first formulated by Engesgaard and Kipp (1992) and has been also used by Prommer (2002) for verification of PHT3D code and Cleall et al. (2007) for verification of the coupling between COMPASS and MINTEQA2. The verification considered is a hypothetical example of a 2D domain in which an aqueous water composition, in equilibrium with calcite, is flushed by a solution with a different chemical composition which leads to multiple precipitation/dissolution fronts of calcite and dolomite.

5.4.2.2 Numerical model conditions

A two dimensional 0.5 m long column was considered with a uniform mesh of 0.01 m long 4-noded quadrilateral elements. A constant time-step of 200 seconds is used in the simulation which provided a good convergence. The simulation was performed under isothermal conditions and equilibrium controlled geochemical reaction. Four dissolved ionic components were considered in the model, in equilibrium with two minerals including calcite and dolomite.

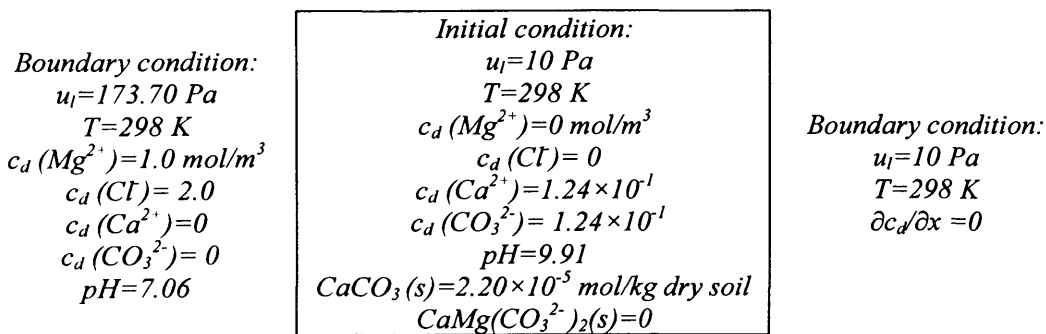


Figure 5.25 Schematic of the initial and boundary conditions (Test VII)

At one boundary, fixed concentrations of dissolved ions are assumed while at the other end, impermeable chemical boundary condition is assumed. A fixed pore water pressure at each boundary is assumed, providing a constant pore water velocity. Figure 5.25 presents a schematic of the initial and thermal, hydraulic and chemical conditions considered in this simulation. The system considered is saturated and porosity was assumed as 0.32. The bulk density is 1800 kg/m^3 . Pore velocity and dispersivity coefficient are $9.37 \times 10^{-6} \text{ m/s}$ and 0.002 m , respectively. Table 1 presents the required physical and chemical properties.

Table 5.6 Material parameters (Test VII)

<i>Material parameter</i>	<i>Relationship/value</i>
Porosity:	$n = 0.32$
Pore water velocity:	$V_l = v_l/n = 9.37 \times 10^{-6} \text{ m/s}$
Hydraulic conductivity:	$k_l = 1.1 \times 10^{-4} \text{ m/s}$
Diffusion coefficient of chemicals:	$D_i = 0 \text{ m}^2/\text{s}$
Dispersivity coefficient (Longitudinal)	$\alpha_L = 0.0067 \text{ m}$
Equilibrium constant of reactions at $25 \text{ }^\circ\text{C}$:	
$\text{CaCO}_3(\text{s}) = \text{Ca}^{2+} + \text{CO}_3^{2-}$	$\log K_{eq} = -8.47$
$\text{CaMg}(\text{CO}_3)_2(\text{s}) = \text{Ca}^{2+} + \text{Mg}^{2+} + 2\text{CO}_3^{2-}$	$\log K_{eq} = -17.7$

5.4.2.3 Results and discussion

Figure 5.26 shows the dissolved chemical distribution in the domain after 21000 seconds of simulation. The time was selected to compare the results with same simulation, reported by Engesgaard and Kipp, 1992. The numerical model results for calcite and dolomite mineral concentrations are also presented in figure 5.27. The results of the modelling reported by Engesgaard and Kipp (1992) are also provided in each figure for comparison.

Higher concentration of Mg^{2+} ions and lower Ca^{2+} ions migrate from the boundary to the domain. In order to maintain the equilibrium between dissolved chemicals and minerals, calcite is dissolved into the pore fluid, providing more calcium ions whilst dolomite

precipitated in the domain. As a result, the concentration of calcium ions varies in the region, affected by dissolution of calcite and precipitation of dolomite.

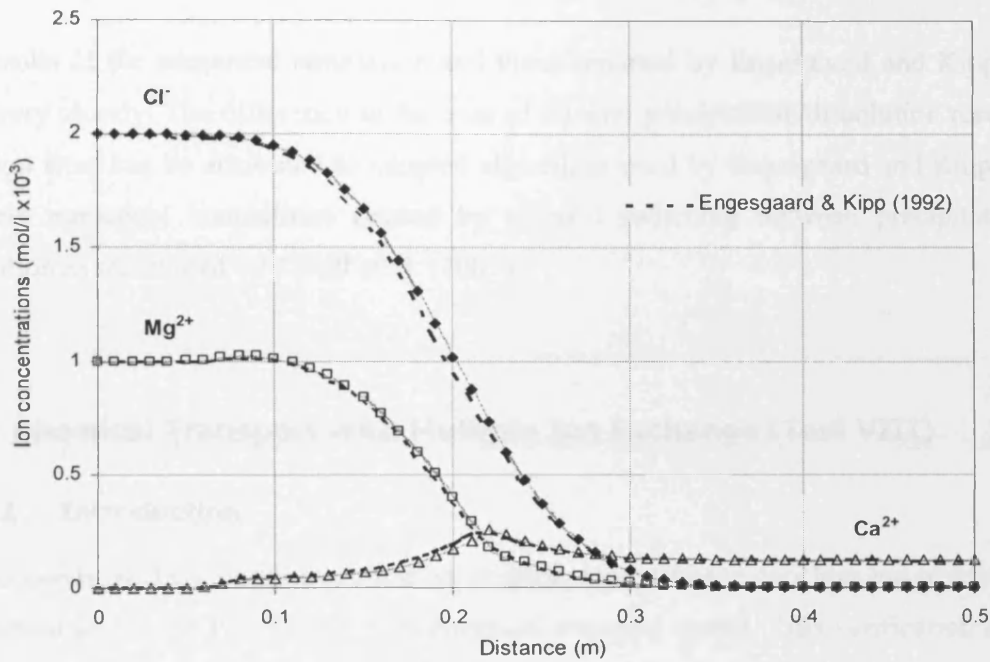


Figure 5.26 Concentration profiles of dissolved chemical components after 21,000 seconds of analysis

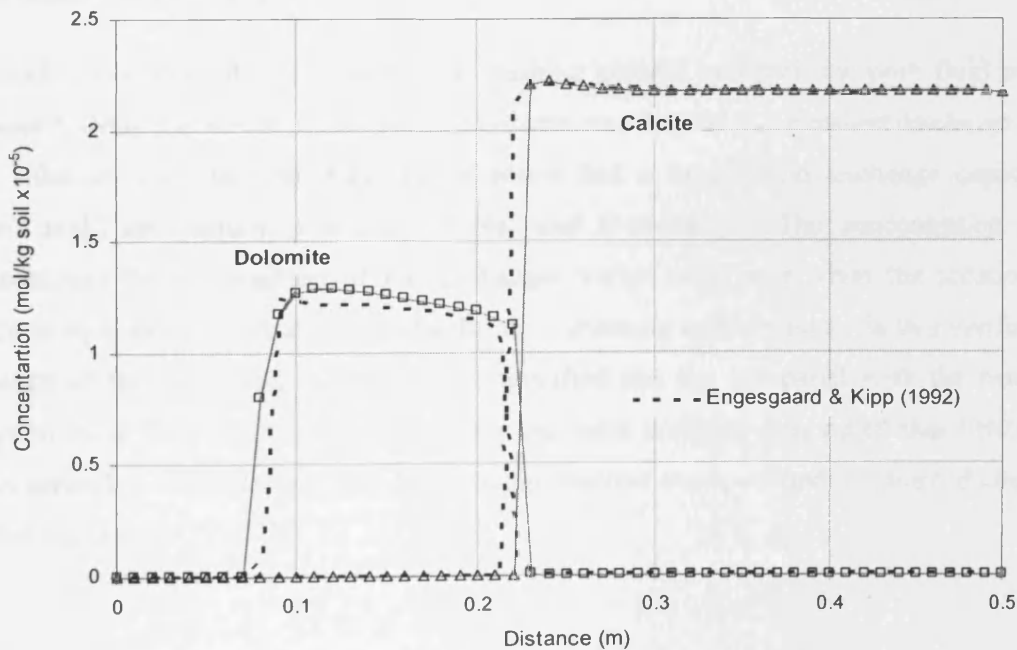


Figure 5.27 Calcite and Dolomite concentration profiles at 21,000 second

In the area close to boundary, further flushing of the dissolved ions with water, has resulted in dissolution of both minerals. Therefore, both minerals were dissolved completely in the approximately 8 cm away from the boundary.

The results of the numerical simulation and those reported by Engesgaard and Kipp (1992) agree very closely. The difference in the case of mineral precipitation/dissolution results near the sharp front can be attributed to adopted algorithms used by Engesgaard and Kipp (1992), to avoid numerical instabilities caused by mineral switching between precipitation and dissolution as mentioned by Cleall et al. (2007).

5.4.3 Chemical Transport with Multiple Ion Exchange (Test VIII)

5.4.3.1 Introduction

This section provides a verification test on coupling ion exchange geochemical reaction under equilibrium feature of PHREEQC with chemical transport model. This verification has been used in PHREEQM (Nienhuis et al., 1991) and also in PHREEQC *version 2* by Parkhurst and Appelo (1999) as example simulations. This example has been also used by Prommer (2002) for verification of PHT3D code.

The simulation consisted of a hypothetical flushing column in which the pore fluid initially contained NaNO_3 and KNO_3 solutions. The column was flushed at a constant discharge with a CaCl_2 solution from the boundary. The medium had a total cation exchange capacity of 1.1×10^{-3} mol/l and initially consisted of Na- and K-exchanger. The concentration of the chemicals and the composition of the exchanger varied with time when the solution was brought to equilibrium with the flushed solution containing calcium ions. In this verification, the results of the numerical model for the specified test are compared with the results of simulation using PHREEQC version 2.15 for the same problem. It is noted that PHREEQC has the capability of modelling one dimensional reactive transport under saturated condition as stated in chapter 3.

5.4.3.2 Numerical model conditions

The analysing domain length is 0.08 m with porosity of 1.0, discretised into 40 elements consisting 4-noded quadrilateral elements. A constant time-step of 90 seconds was considered for the simulation. The simulation was performed under isothermal condition. Five ionic components were considered in the model including Ca^{2+} , Cl^- , K^+ , Na^+ and NO_3^- . The exchanger components are considered as Na-, K- and Ca-X, where X is the exchanger body.

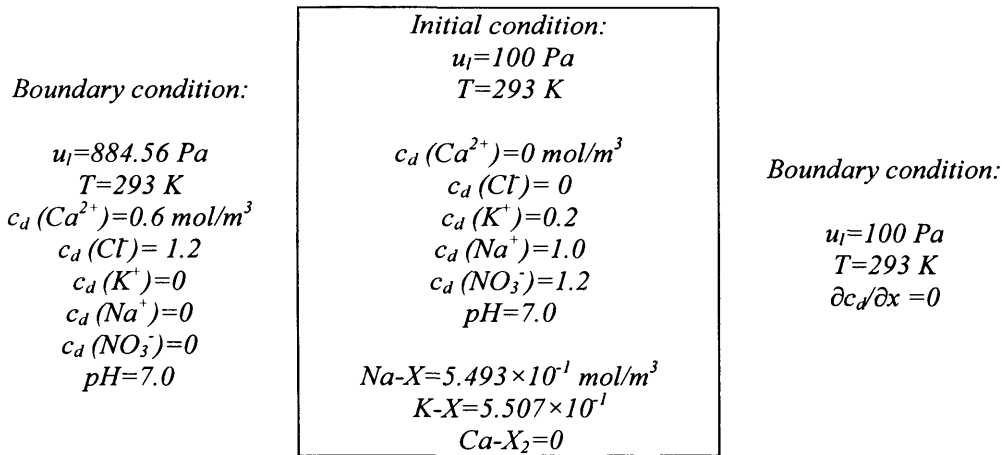


Figure 5.28 Schematic of the initial and boundary conditions (Test VIII)

Table 5.7 Material parameters (Test VIII)

Material parameter	Relationship/value
Porosity:	$n = 1.0$
Pore water velocity:	$V_l = v_l/n = 1.0 \text{ m/day} = 1.157 \times 10^{-5} \text{ m/s}$
Hydraulic conductivity: m/s	$k_l = 1.157 \times 10^{-5}$
Diffusion coefficient of chemicals: m^2/s	$D_i = 0$
Dispersivity coefficient (Longitudinal) m	$\alpha_L = 0.002$
Equilibrium constant of reactions at 25 °C	
$\text{Na-X} = \text{Na}^+ + \text{X}$	$\log K_{eq} = 0.0$
$\text{K-X} = \text{K}^+ + \text{X}$	$\log K_{eq} = 0.7$
$\text{Ca-X}_2 = \text{Ca}^{2+} + 2\text{X}$	$\log K_{eq} = 0.8$

At one boundary, fixed concentrations of dissolved ions are assumed while at the other end, impermeable boundary condition is assumed. A fixed pore water pressure at each boundary is assumed, providing a constant pore water velocity. Figure 5.28 presents a schematic of the initial and thermal, hydraulic and chemical conditions of the model. Pore velocity and dispersivity are considered as 1 m/day and 0.002 m, respectively. Table 5.7 presents the parameters used in the simulation.

5.4.3.3 Results and discussion

Figure 5.29 presents the analysed break through curves of different chemical ions in the solution at different pore volumes compared with the results of modelling using PHREECQ2 (example 11 in the user manual, Parkhurst and Appelo, 1999). Pore volume is defined as the volume of water that completely fills all of the void space in a given volume of porous matrix. The pore volume is defined as $PV = V_i t / L$ where L is the domain length, t is time and V_i is the pore water velocity defined in table 5.7.

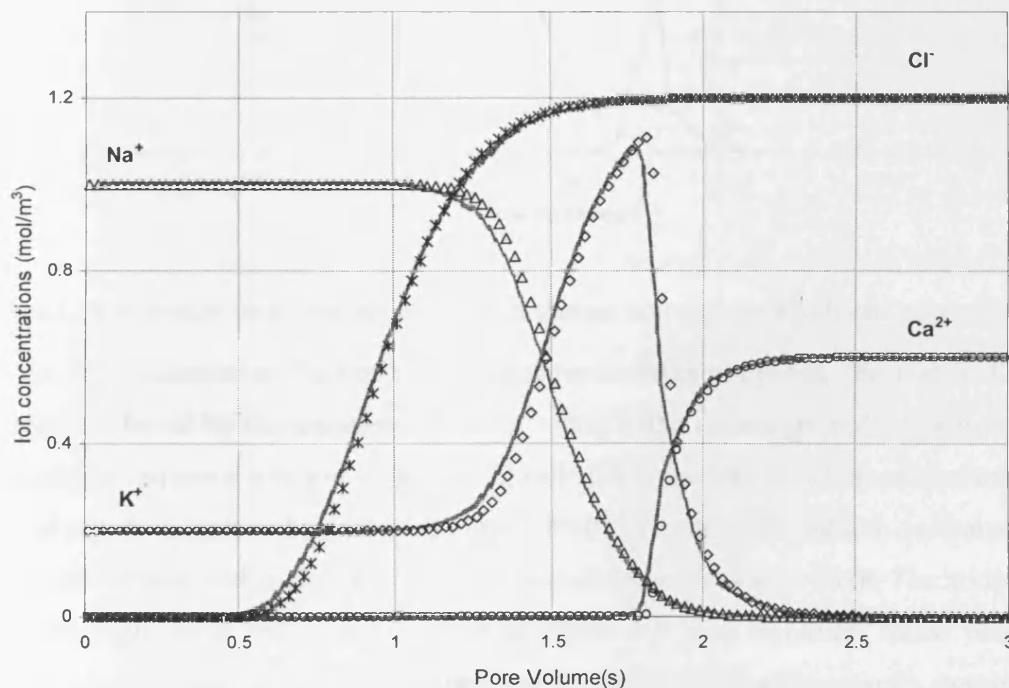


Figure 5.29 Discharge of the dissolved chemical concentrations at different pore volumes at the boundary calculated by the numerical model (solid lines) and by PHREEQC version 2.15 (symbols)

Since the results of simulation in the manual of PHREEQC have been presented as a function of pore volume, similar presentation of distribution of chemicals was selected. The results show a close agreement between the two models. Figure 5.30 also presents the variation of exchanger composition at different pore volumes.

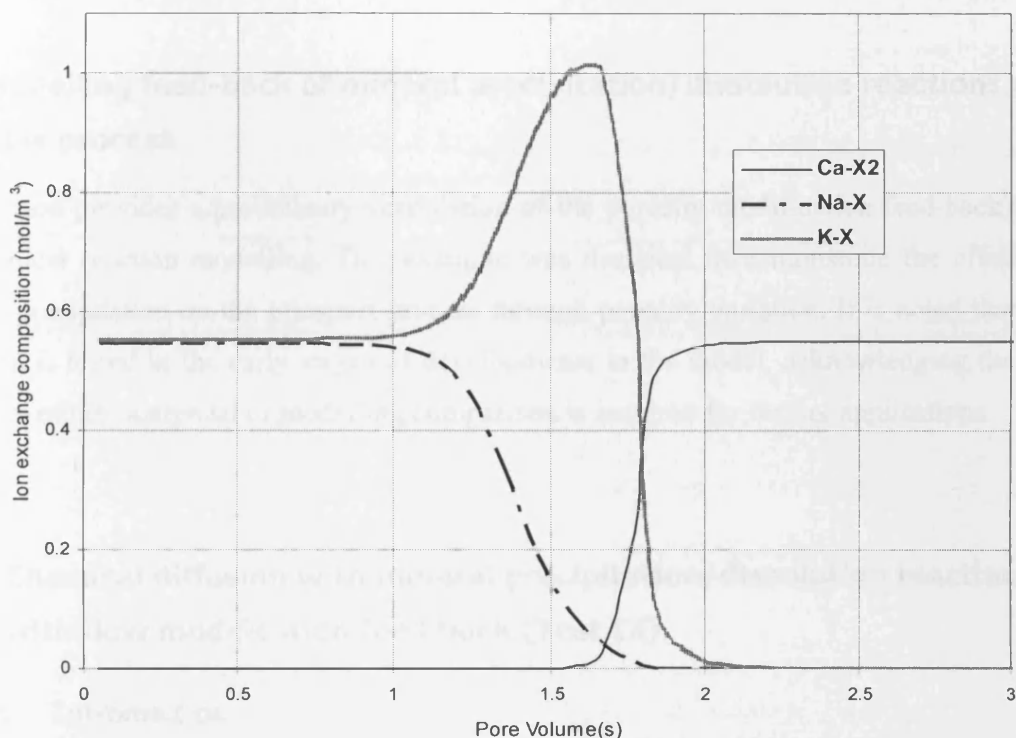


Figure 5.30 Numerical model prediction of the exchanger composition at different pore volumes

When the inlet solution is flushed to the aqueous-exchanger system, the composition of exchanger is affected by the replacement of Ca^{2+} ions in the exchanger and consequently the concentration of aqueous solution changes. Chloride is a conservative solute and arrives in the effluent at about 0.5 pore volume. The sodium initially present in the column exchanges with the incoming calcium and is eluted as long as the exchanger contains sodium. The midpoint of the breakthrough curve for sodium occurs at about 1.5 pore volumes. Since potassium exchanges more strongly than sodium (larger $\log K_{eq}$ in the exchange reactions), potassium is released after sodium. Finally, when all potassium has been released, the concentration of calcium increases to a steady-state value equal to the concentration in the infilling solution.

The simulation results are closely correlated with the results calculated by PHREEQC that has been well verified for one dimensional reactive transport in saturated systems. This allows demonstrating the correctness of the implementation of the approach adopted for reactive transport under equilibrium ion exchange reaction over the particular bench-mark.

5.5 Modelling feed-back of mineral precipitation/dissolution reactions on flow process

This section provides a preliminary verification of the porosity modification feed-back from geochemical reaction modelling. This example was designed to demonstrate the effects of mineral precipitation on the transport process through porosity variation. It is noted that this inclusion is tested in the early stages of developments in the model, acknowledging the fact that more robust analytical or modelling comparison is required for further applications

5.5.1 Chemical diffusion with mineral precipitation/dissolution reaction with flow modification feed back (Test IX)

5.5.1.1 Introduction

This simulation was designed to demonstrate the effects of porosity modification due to mineral precipitation on the diffusion of a binary solution. In the simulation, a saturated low porosity porous medium was considered which initially contains no dissolved chemicals and minerals. The domain was exposed to a super-saturated binary solution at one boundary. The diffusion process is coupled with mineral precipitation. Diffusion of the binary solution through the domain was investigated numerically under the porosity feed back implemented algorithm and without this effect. The feed-back between mineral precipitation volume and porosity affects the tortuosity of chemical diffusion which changes the diffusion pattern of chemicals.

5.5.1.2 Numerical model conditions

The analysing domain length considered is 2D (0.1×0.1 m) with porosity of 0.05. The domain was discretised into 100 equally sized elements consisting 4-noded quadrilateral elements. A

variable time-step was used, allowing the variation of time-step depending on convergence. The simulation was performed under isothermal and saturated conditions. Therefore, water pressure and temperature were fixed during the analysis. These assumptions lead to pure isothermal diffusion flow in the domain.

Two ionic components were considered in the model including, hypothetically A^+ and B^- in equilibrium with AB mineral. At one boundary, fixed concentrations of dissolved ions are assumed while at the other end, an impermeable boundary condition is assumed. The solution at one boundary is considered as super-saturated solution. Figure 5.31 presents a schematic of the initial and thermal, hydraulic and chemical conditions of the model.

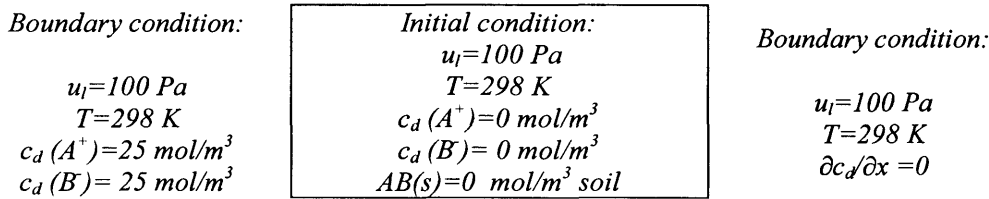


Figure 5.31 Schematic of the initial and boundary conditions (Test IX)

Table 5.8 presents the physical and chemical parameters used for simulation.

Table 5.8 Material parameters (Test VIII)

<i>Material parameter</i>	<i>Relationship/value</i>
Porosity:	$n = 0.05$
Degree of saturation:	$S_l = 1.0$
Hydraulic conductivity: m/s	$K_{sat} = 1.0 \times 10^{-13}$
Tracer diffusion coefficient of chemicals in water: m^2/s	$D^0(A^+) = D^0(B^-) = 10 \times 10^{-10}$
Equilibrium constant of reactions at 25 °C $AB(s) = A^+ + B^-$	$\log K_{eq} = -4.64$
Molar volume of $AB(s)$ m^3/mol	$V_m = 7.5 \times 10^{-13}$

The tortuosity factor for chemical diffusion is considered via a modified equation, proposed by Millington and Quirk (1961). As a first approximation, the effect of mineral precipitate volume on tortuosity is included as an additional term to the original tortuosity factor proposed by Millington and Quirk (1961) as:

$$\tau = \left(1 - \frac{n_{\text{mineral}}}{n}\right) \frac{(nS_l)^{7/3}}{n^2} \quad (5.29)$$

where, n_{mineral} is the ratio of mineral volume over the soil volume, which is calculated from geochemical interface module in the model.

5.5.1.3 Results and discussions

Figure 5.32 shows the transient profiles of the dissolved chemical in the domain, resulted from modelling with and without considering porosity feed-back modification. The results indicate that porosity modification from mineral precipitation hinders the diffusion front compared with the simulation without considering porosity feed back.

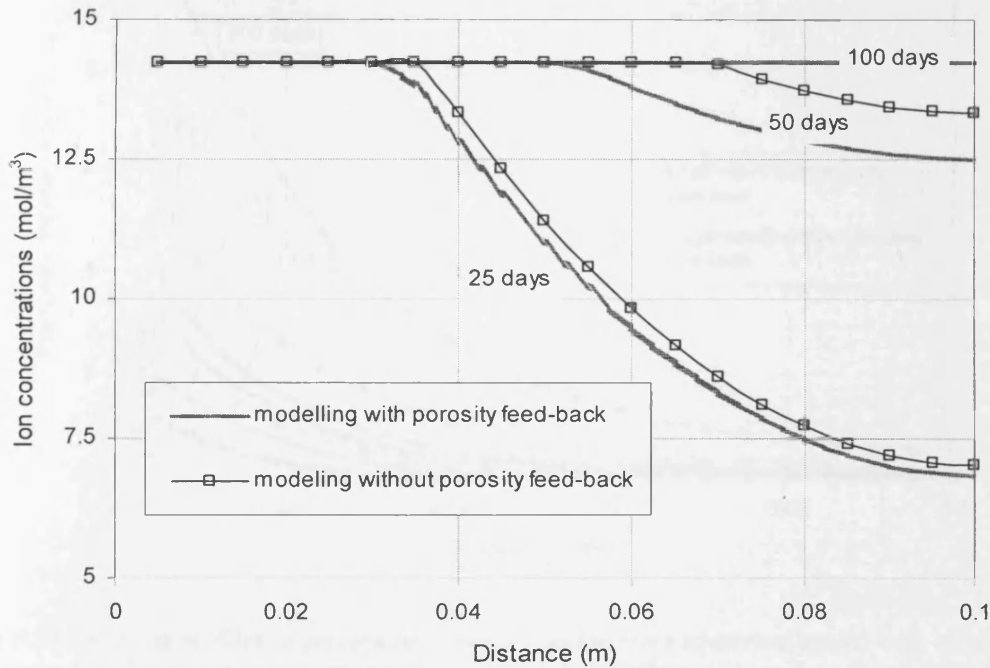


Figure 5.32 Transient profiles of dissolved chemical components resulted from numerical model with considering porosity feed back from geochemistry (lines) and the modelling without the effect (symbols)

Due to the equilibrium condition assumed for mineral precipitation, the dissolved chemicals were in equilibrium with the precipitate mineral. Therefore, the concentration of dissolved chemicals did not increase from the associated value with equilibrium reaction condition. In other words, extra amount of dissolved chemicals have been precipitated in the system.

Figure 5.33 presents the results of mineral profiles at different time with and without considering porosity feed back. The results show that the additional dissolved chemical has to be precipitated and accumulated in the domain. As a result of porosity feed-back algorithm implemented in the model, lower amount of minerals has been precipitated in the simulation with considering this effect especially in longer times. This is due to the effective diffusion coefficient decrease as a result of porosity reduction with mineral precipitation and therefore the amount of dissolved chemicals which diffuse to the system is reduced. This observation is more highlighted in longer simulation times.

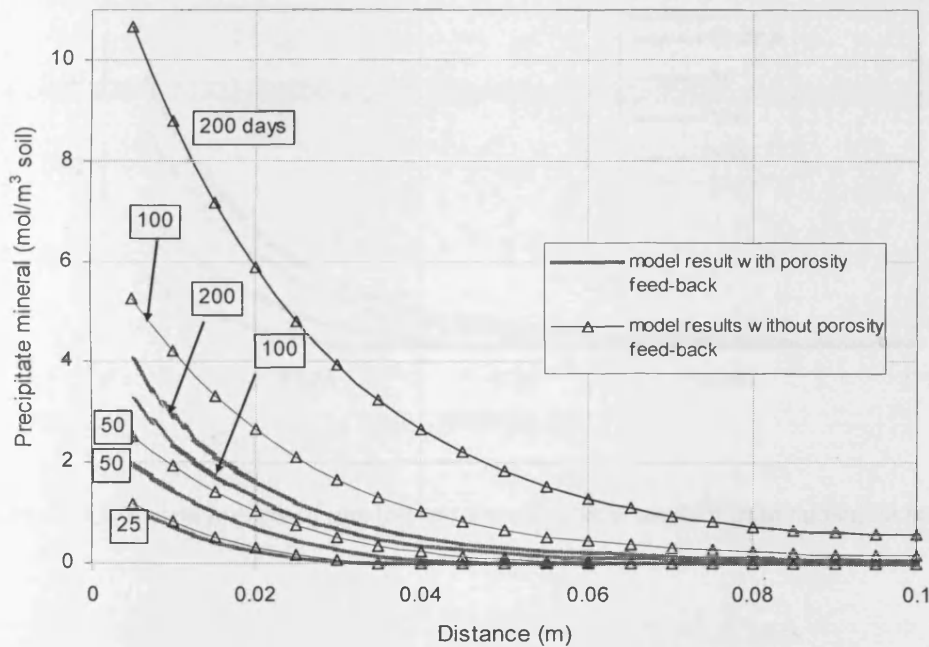


Figure 5.33 Transient profiles of precipitate mineral resulted from numerical model with considering porosity feed back from geochemistry (lines) and the modelling without the effect (symbols)

As a consequence of mineral precipitation, the available porosity has decreased due to the accumulated mineral. It affects implicitly the tortuosity factor and reduces the rate of migration of chemicals. The reduction of porosity also prevents further mineral precipitation as a result of lower migration rate of dissolved chemicals. Figure 5.34 shows the transient volume of mineral, precipitated in the domain. A comparison is provided with the available initial porosity.

The simulations presented in this section aimed to demonstrate the effects of porosity variation with geochemical mineral reactions. Indeed, the implementation requires further exploration and application; nevertheless, preliminary investigation presented, indicate a coupling scheme between porosity and geochemistry has been build in the model.

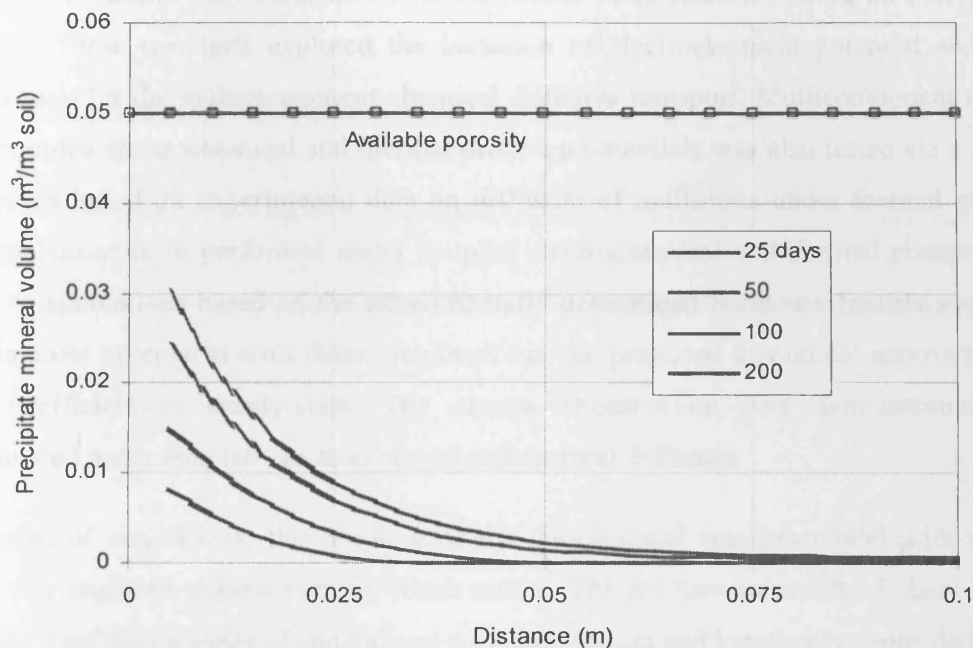


Figure 5.34 Transient profiles of precipitate mineral volume resulted from numerical model

5.6 Conclusions

This chapter presents the verification and validation tests carried out on the theoretical developments of the numerical model for the following cases:

Two verifications were presented on the coupling moisture transfer with chemical transport due to osmosis phenomenon. In the first example, the simulation results related to the osmotic potential effect on water transport were compared with the results of an analytical solution at steady state. The results match with those calculated from the analytical solution. In the second example vapour transport induced by osmotic potential, was explored against a series of experimental results. The results are in good agreement compared with the results of the

experiments, demonstrating the implementation of osmotically driven vapour flux in the model.

Two simulations were presented on multicomponent transport under electrochemical diffusion potential. The first example dealt with diffusion of ionic species in electrolyte solution. The results were compared with the results of calculations based on Fick's law of diffusion. These two tests explored the inclusion of electrochemical potential and charge conservation for the multicomponent chemical diffusive transport. Multicomponent transport under coupled electrochemical and thermal diffusion potentials was also tested via a series of simulations based on experimental data on diffusion of multi-ions under thermal gradients. The simulations were performed under coupled electrochemical and thermal potentials. The results of simulations based on the experimentally determined Soret coefficients were found to be in close agreement with those simulated via the proposed theoretical approach for the Soret coefficient at steady-state. The charge conservation was demonstrated to be implemented under coupled electrochemical and thermal diffusion.

In a series of simulations, the coupling of the geochemical reaction model with transport model was explored against various bench marks. The reactive transport of chemicals was examined first with a series of simulations with equilibrium and kinetically controlled mineral reactions. The transport of binary solution with precipitation/ dissolution of a mineral reaction was first presented and tested using an alternative analytical solution. The verification was followed by an example of multicomponent transport and multiple equilibrium precipitation/dissolution reactions. The results of the latter simulation were compared with the results of an alternative reactive transport model reported in the literature which showed good correlation between the results of the two models. Verification on multicomponent chemical transport and multiple ion exchange reaction was provided. The results were compared with the results of similar simulation using well established example of PHREEQC version 2. A close correlation between the results of the developed model and the results of PHREEQC was found. In addition, a preliminary simulation example was presented to demonstrate the effect of coupling between mineral reaction and porosity variation and the effects on chemical transport.

This chapter demonstrated that the developments in the formulation of hydro-chemical transport have been successfully implemented in the model and the coupling between the

transport model, COMPASS and the reaction model PHREEQC has been achieved under the conditions and scopes of the studied bench mark tests. Within this chapter the confidence was built in the theoretical approach and numerical implementation, via as series of verification exercise, for further applications and exploration the developments provided in the model.

5.7 References

- Agar, J.N., Mou, C.Y., and Lin, J. (1989). Single-ion heat of transport in electrolyte solutions, A hydrodynamic theory. *Journal of Physical Chemistry*, 93, 2079-2082.
- Allison, J.D., Brown, D.S., and Novo-Gradac, K.J. (1991). *MINTEQA2 user manual version 3.0*. Environmental Research Laboratory, U.S. EPA.
- Appelo, C.A.J. (2007). Multicomponent diffusion in clays. *Water Pollution in Natural Porous Media Proceeding*, Instituto Geológico de España, Madrid, 3-13.
- Cleall, P.J. (1998). *An investigation of the thermo/hydraulic/mechanical behaviour of unsaturated soils, including expansive clays*. Ph.D. Thesis, Cardiff University, Wales, UK.
- Cleall, P.J., Seetharam, S.C., and Thomas, H.R. (2007). On the inclusion of some aspects of chemical behaviour of an unsaturated soil in thermo-hydro-chemical-mechanical models: I Model development. *Journal of Engineering Mechanics, ASCE*, 133, 338-347.
- Cussler, E.L. (1997). *Diffusion-Mass Transfer in Fluid Systems*. University Press, Cambridge.
- Engesgaard, P., and Kipp, K.L. (1992). A geochemical transport model for redox-controlled movement of mineral fronts in groundwater flow systems: A case of nitrate removal by oxidation of pyrite. *Water Resource Research*, 28(10), 2829-2843.
- Jungnickel, C., Smith, D. and Fityus, S. (2004). Coupled multi-ion electrodiffusion analysis for clay soils. *Canadian Geotechnical Journal*, 41, 287-298.
- King, S.D. (1994). *A potential based model of coupled heat and moisture transfer in unsaturated soil*. Ph.D. Thesis, University of Wales, Cardiff, U.K.
- Lasaga, A.C. (1998). *Kinetic Theory in the Earth Science*. Princeton Series in Geochemistry, Princeton University Press.
- Leaist, D.G., and Hui, L. (1990). Conductometric determination of the Soret coefficients of a ternary mixed electrolyte-Reversed thermal diffusion of sodium chloride in aqueous sodium hydroxide solutions. *Journal of Physical Chemistry*, 94, 447-451.
- Lichtner, P.C. (1995). Principles and practice of reactive transport modelling. *Material Research Society Symposium Proceeding*, 353, 117-130.

- Millington, R.J., and Quirk, J.M. (1961). Permeability of porous solids. *Transaction Faraday Society*, 57, 1200–1207.
- Mitchell, H.P. (2002). *An investigation into the thermo/hydro/mechanical interactions involved in high level nuclear waste disposal*. PhD Thesis, University of Wales, Cardiff.
- Nienhuis, P., Appelo, C.A.T., and Willemsen, A. (1991). *Program PHREEQM, Modified from PHREEQE for use in mixing cell flow tube*. The Netherlands, Amsterdam Free University.
- Parkhurst, D.L., and Appelo, C.A.J. (1999). *User's guide to PHREEQC (version 2)*, U.S. Geological Survey, Water Resource Investigation Report, 99-4259.
- Philip, J.R., and de Vries, D.A. (1957). Moisture movements in porous materials under temperature gradients. *Transactions American Geophysical Union*, 38(2), 222-232.
- Prommer, H. (2002). *A reactive multicomponent transport model for saturated porous media. PHT3D user's manual, version 1.0*. University of Edinburgh, Edinburgh.
- Sansom, M.R. (1995). *A fully coupled numerical analysis of mass, air and heat transfer in unsaturated soil*. PhD Thesis, University of Wales, Cardiff, UK.
- Scotter, D.R., and Raats, P.A. (1970). Movement of salt and water near crystalline salt in relatively dry soil. *Soil Science*, 100 (1), 170-178.
- Seetharam, S.C. (2003). *An investigation of the thermo/hydro/chemical/mechanical behaviour of unsaturated soils*. Ph.D. Thesis, Cardiff University, Wales, UK.
- Thomas, H.R., and He, Y. (1995). Analysis of coupled heat, moisture and air transfer in a deformable soil. *Géotechnique*, 45(4), 677-689.
- Thomas, H.R., and He, Y. (1998). Modelling the behaviour of unsaturated soil using an elasto-plastic constitutive relationship. *Géotechnique*, 48(5), 589-603.
- Thomas, H.R., He, Y., and Onofrei, C. (1998). An examination of the validation of a model of the hydro/thermo/mechanical behaviour of engineered clay barriers. *International Journal of Numerical and Analytical Methods in Geomechanics*, 22, 49-71.
- Thomas, H.R., and Samson, M.R. (1995). A fully coupled analysis of heat, moisture and air transfer in unsaturated soil, *Journal of Engineering Mechanics, ASCE*, 12(3), 392-405.

van Genuchten, M.Th. (1980). A closed-form equation for predicting the hydraulic conductivity of unsaturated soils. *Soil Science Society of America Journal*, 44, 892-898.

Vardon, P.J. (2009). *A three-dimensional numerical investigation of the therm-hydro-mechanical behaviour of a large-scale prototype repository*. Ph.D. Thesis, Cardiff University, Wales, UK.

Xu, T., and Pruess, K. (1998). *Coupled modeling of non-isothermal multiphase flow, solute transport and reactive chemistry in porous and fractured media: 1. Model development and validation*. Lawrence Berkeley National Laboratory Report, LBNL-42050, Berkeley, California.

Chapter 6

Simulation of the Reactive Transport of Chemicals under Coupled THC Conditions

6.1 Introduction

This chapter presents a series of numerical simulations of the reactive transport of chemicals under coupled thermal, hydraulic, chemical framework. The numerical investigation has been conducted on hydro-geochemical behaviour of compacted clay under simultaneous heating and hydration. In particular, combined effects due to the electrochemical and thermal diffusion potentials on transport of ionic species in compacted clays are investigated in the simulation series presented in this chapter.

The simulations aimed to test the numerical model behaviour under coupled THC conditions and more importantly to investigate the coupled electrochemical and thermal diffusion potentials effects on the distribution of chemicals in a clay system. As reported in chapter 2, it has been well established that under non-isothermal conditions, a temperature gradient can induce mass flow due to thermal diffusion, i.e. Soret effect. Thermal diffusion behaviour could be more complicated due to coupling with electrochemical diffusion potential in multi-ionic systems. Therefore, in the modelling of the transport of multicomponent ionic chemicals, the electrochemical diffusion potential needs to be coupled with thermal diffusion in order to obtain an overall understanding of the combined effects as described in the theoretical formulation of multicomponent chemical transport presented in chapter 3.

Although the contribution of thermally induced diffusion in diffusive transport is reported to be small in geological materials compared to diffusion due to chemical potential (Lasaga, 1998), consideration of the effect is required for the analysis of mass transport, especially in cases where long term impacts are considered, e.g. compacted clays as the candidate buffer in nuclear waste disposal concept. The effects of thermal diffusion on the reactive transport were studied in the simulations based on the theoretical approach adopted for calculating the Soret coefficient.

The behaviour of the developed model for the reactive transport of a multicomponent chemical model under THC conditions was investigated via a simulation of the phenomena in unsaturated compacted clay. The simulation considers a 0.1 m long unsaturated compacted clay, subjected to heating from one side and hydration with distilled water from the other side. It is noted that this simulation was adopted from a similar modelling example given by Cleall et al. (2007).

6.2 Model domain and conditions

The simulations considered, consist of a two dimensional clay domain (0.1 m long and 0.01 m wide). The soil is initially unsaturated and deionised water at pressure of 1.5 MPa was injected at one boundary side (hydration side). A temperature gradient was applied across the length of the domain by fixing the temperature at 25 °C at the hydration end and at 40 °C at the opposite end. The hot side is assumed to be impermeable to flow.

The clay initial moisture condition was considered similar to the initial condition of a swelling clay, i.e. FEBEX bentonite, compacted at dry density of approximately 1700-1800 kg/m³, (e.g. ENRESA, 2000). The initial porosity of the clay was considered as 0.35. The system was initially unsaturated with a degree of saturation equal to 65%. Based on the water retention relationship, given by ENRESA (2000), the initial pore water pressure of the 65 % degree of saturation is obtained equal to approximately -100 MPa.

With regards to the chemical conditions, the pore water was hypothetically considered as binary chemical system, containing two dissolved ionic species, i.e. Ca²⁺ and SO₄²⁻, in equilibrium with the anhydrite mineral. Anhydrite mineral reaction has been reported as one of the precipitation/dissolution reactions in bentonite under HLW repository condition (ENRESA, 2000). The reaction can be presented as:



Figure (6.1) provides a schematic diagram of the THC initial and boundary conditions of the domain.

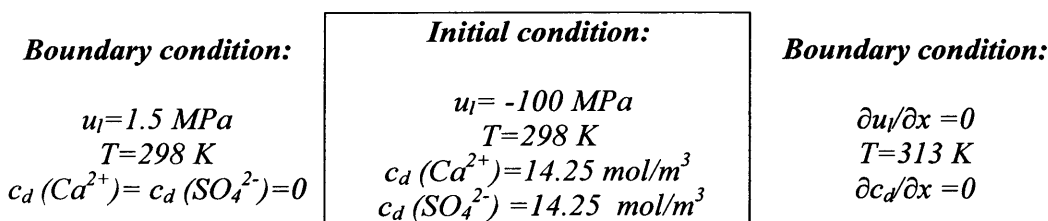


Figure 6.1 Schematic of the initial and boundary conditions

The domain was discretised into 100 equally sized 4-noded quadrilateral elements. The numerical simulation was performed under THC framework for a period of 200 days considering a variable time-step. An initial time-step of 360 seconds was considered which was allowed to vary depending on the convergence rate. The maximum time-step was allowed

to increase to 360,000 seconds. The maximum time-step was found as a suitable value with regards to the rate of convergence for this simulation based on several trials.

6.3 Material parameters and relationships

The required parameters and relationship for modelling the thermal and hydraulic behaviour including thermal conductivity relationships, water retention relationship, and unsaturated hydraulic conductivity relationship were adopted from ENRESA (2000).

The material constants such as density of water, density of solid, specific heat capacity of solid, liquid and vapour, latent heat of vaporisation have been obtained based on Mayhew and Rogers (1976) and ENRESA (2000). All the material relationships and parameters are summarised in table 6.1.

Table 6.1 Material constants used in the numerical modelling

<i>Constants</i>	<i>Values</i>
Density of liquid, ρ_l at 25 °C (kg m^{-3})	1000
Density of solid, ρ_s (kg m^{-3})	2700
Specific heat capacity of soil solids C_{ps} ($\text{J kg}^{-1} \text{K}^{-1}$) (Martin et. al, 1998)	870
Specific heat capacity of soil water, C_{pl} ($\text{J kg}^{-1} \text{K}^{-1}$) (Mayhew and Rogers, 1976)	4180
Specific heat capacity of soil vapour, C_{pv} ($\text{J kg}^{-1} \text{K}^{-1}$) (Mayhew and Rogers, 1976)	1870
Latent heat of vaporisation, L (J kg^{-1}) (Mayhew and Rogers, 1976)	2.4×10^6
Specific gas constant for water vapour, R ($\text{J kg}^{-1} \text{K}^{-1}$) (Mayhew and Rogers, 1976)	461.5

The thermal conductivity of the compacted bentonite was adopted from the relationship given by ENRESA (2000) as:

$$\lambda = A_2 + \frac{A_1 - A_2}{1 + \exp\left(\frac{S_l - x_0}{d_x}\right)} \quad (6.1)$$

where λ is the thermal conductivity in W/m.K, S_l is the degree of saturation, A_1 is the value of λ associated with $S_r = 0$, A_2 is the value of λ for $S_r = 1$, x_0 is the degree of saturation for which the thermal conductivity is the average value between the extreme values, and d_x is a parameter. The values of these fitting parameters are as follows (ENRESA, 2000):

$$A_1 = 0.57 \pm 0.02; A_2 = 1.28 \pm 0.03; x_0 = 0.65 \pm 0.01; d_x = 0.100 \pm 0.016$$

The van Genuchten expression (van Genuchten, 1980) was used for describing suction-degree of saturation relationship based on ENRESA (2000) for compacted bentonite, given as:

$$S_l = S_{l_0} + (S_{l_{\max}} - S_{l_0}) \left[1 + \left(\frac{s}{p_0} \right)^{1-\alpha} \right]^{-\alpha} \quad (6.2)$$

where, S_{l_0} and $S_{l_{\max}}$ are the residual and maximum degree of saturation and p_0 (MPa) and α are material constants.

The parameters for van Genuchten's moisture relationship have been given also in ENRESA (2000), given as:

$$p_0 = 14.5; \lambda = 0.17; S_{l_0} = 0.0; S_{l_{\max}} = 1.00$$

The unsaturated hydraulic conductivity of compacted bentonite is often expressed by means of a power law for the relative permeability (ENRESA, 2000) as:

$$k_l = k_{sat} (S_l)^n \quad (6.3)$$

Corresponding saturated hydraulic conductivity in this simulation study was considered as 1.0×10^{-13} m/s and n equal to 3.

The vapour flux was considered based on the Phillip and de Vries (1958) equation as presented in equation (3.53) in the theoretical formulation.

With regards to the chemical transport modelling, different tracer diffusion coefficients were considered for the chemical components involved in the model. The tracer diffusion coefficients of Ca^{2+} and SO_4^{2-} in water were considered equal to 7.9×10^{-10} and 10.6×10^{-10} m^2/s , respectively (Lasaga, 1998).

At variable temperature but fixed composition and pressure, self or tracer diffusion coefficient of ions in pure solution can be extrapolated from one to another temperature based on Stokes-Einstein relationship (Cussler, 1997). Similar approach was used to calculate the variation of tracer diffusion coefficients with temperature, given as:

$$(D_i^0)_T = (D_i^0)_{T_0} \frac{\eta_{T_0}}{\eta_T} \frac{T}{T_0} \quad (6.4)$$

where η represents the viscosity of solvent, i.e. water in this case. T_0 is the reference temperature.

The tortuosity factor for chemical transport is calculated based on the relationship proposed by Millington and Quirk (1961) for unsaturated porous medium defined as

$$\tau = \frac{(\theta_l)^{7/3}}{n^2} \quad (6.5)$$

where θ_l represents the volumetric water content and n is porosity.

As mentioned in chapter 2, it is well known that in a highly compacted bentonite, the accessible porosities for anions are generally not equal to the total porosity due to the anion exclusion phenomenon, caused by negatively charged clay surfaces. As a result, only a small fraction of the total pore volume is available for anionic transport. However, for cations and neutral species it can be assumed that the entire pore volume is available for transport. As formulated in chapter 3, i.e. equation (3.153), one way of incorporating variability in the accessible porosity for different ions is proposed here by introducing an additional term, the correction factor for accessibility κ , which can be different for anionic and cationic species in compacted bentonite. This modification can be represented as:

$$\tau = \kappa_i \frac{(\theta_l)^{7/3}}{n^2} \quad (6.6)$$

where the superscript i indicates the i^{th} chemical component.

Based on the effective diffusion coefficient relationship, given in equation (6.6), the variation in the magnitude of effective diffusion coefficients for different ionic species in multiple ionic systems of the clay pore fluid, is related to i): the difference in the tracer diffusion coefficient of different ionic species and ii): the difference in the tortuosity factor for anionic and cationic species in compacted clays.

Accordingly, two series of simulation were performed where once κ was assumed as 1.0 for both anionic and cationic component. This simulation represents the condition where the variations in the diffusion coefficients of anionic and cationic species originated from their different tracer diffusion coefficient in water. In the second simulation κ was assumed as 0.1 for anionic component and equal to 1.0 for cationic component. The difference in the diffusion coefficient for ionic species is therefore derived from their different tracer diffusion coefficients in water and different tortuosity factors. The latter assumption gives higher values for the effective tracer diffusion of ions than that expected in compacted clays but it assists with demonstrating the contribution of thermal diffusion in the formulation developed for chemical transport under non-isothermal conditions.

The thermal diffusion coefficient, i.e. the Soret coefficient, was calculated using the theoretical approach presented in chapter 3. The values of the Soret coefficients in dilute electrolyte solution were calculated using the approach proposed by Agar et al. (1989) based on equation (3.151). This equation is repeated here as:

$$S_i^T = \frac{Az_i^2 D_i^0}{RT^2} \quad (6.7)$$

where A is a constant value depending on the hydrodynamic boundary condition (i.e. 2.48×10^{12} and 2.20×10^{12} for two different hydrodynamic boundary conditions, based on Agar et al., 1989). Here an average value of the two hydrodynamic boundary conditions was used for parameter A due to the uncertainty in the condition in soils. However, the variations in A are found to not be very influential on the overall magnitude of the Soret coefficient.

In order to investigate the effects related to the thermal diffusion contribution on the ion migration, in each series of simulations, the analysis was performed once considering the thermal diffusion effect applying the theoretical approximation for the Soret coefficient. The

same analysis was repeated without considering Soret effect in the diffusion flux assuming $S_i^T = 0$.

With regards to the geochemical reaction parameters, the equilibrium constant of the anhydrite mineral precipitation/dissolution reaction was adopted from the database of PHREEQC version 2.15 (*minteq.dat* data base, Parkhurst and Appelo, 1999). Therefore, the equilibrium constant of the reaction ($\log K_{eq}$) and the enthalpy difference of the reaction (ΔH^0) (at reference temperature, 25 °C) were considered equal to -4.637 and -3.769 kcal, respectively.

6.4 Numerical simulation results

The results of the numerical simulation in terms of the temperature, degree of saturation, dissolved chemicals and anhydrite mineral content are presented in this section.

6.4.1 Temperature and moisture distribution

Figure (6.2) shows transient profiles of temperature in the domain. Steady-state temperature profile is achieved across the domain within a few hours. Achieving the final steady state of the temperature profile is coupled to the moisture fields, and it is affected, in particular, by the dependence of the thermal conductivity on the degree of saturation.

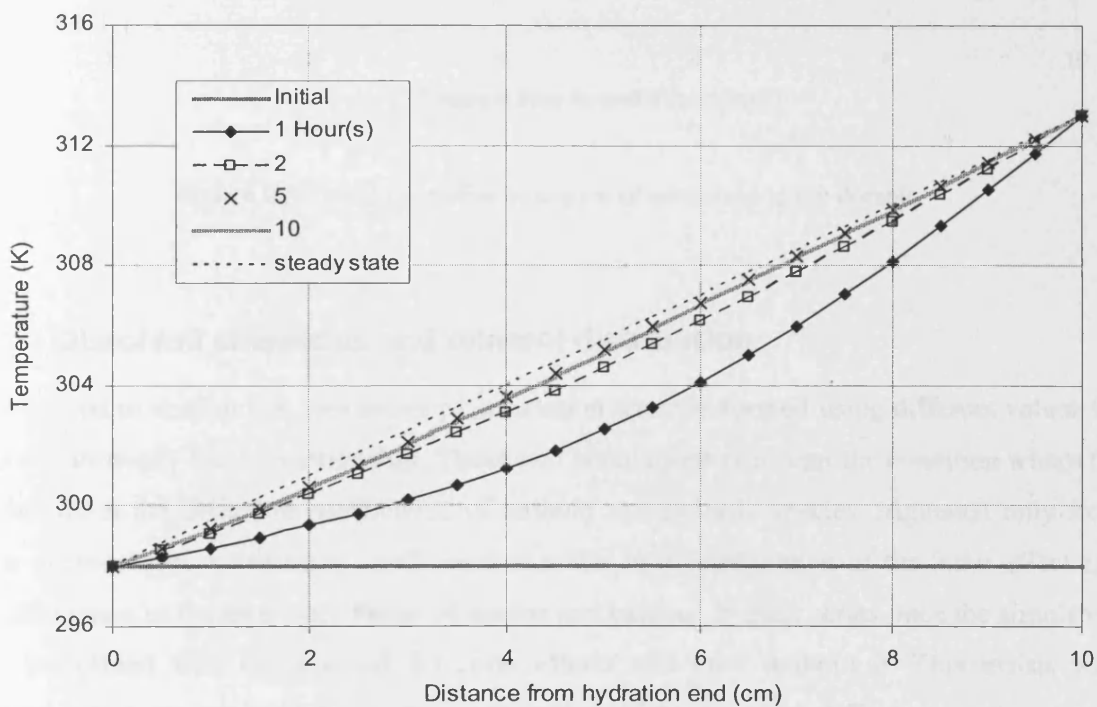


Figure 6.2 Transient profile of temperature in the domain

Figure (6.3) provides the results of moisture profiles at different times of analysis. During the initial stages, up to approximately 2 days, the moisture content of the soil is reduced at the hot end due to vapour flow away from the heater. After 2 days, the model predicts that the resaturation front has reached the hot end and the moisture content gradually increases in the whole domain. The resaturation of the whole domain is completed after 50 days.

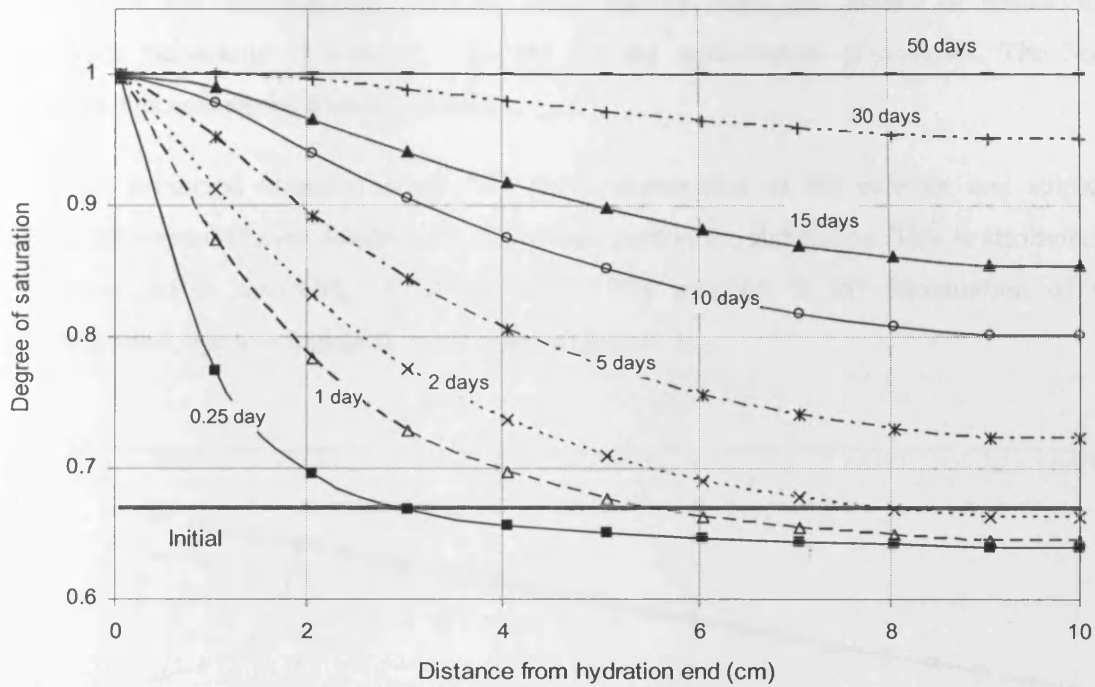


Figure 6.3 Transient profile of degree of saturation in the domain

6.4.2 Dissolved chemicals and mineral distribution

As reported in section 6.3, two series of simulation were performed using different values for κ in the tortuosity factor relationship. These two simulations represent the condition where the variations in the diffusion coefficients of anionic and cationic species originated only from their different tracer diffusion coefficients in water or a combination of the latter effect and the difference in the tortuosity factor of anions and cations. In each series once the simulation was performed with the thermal diffusion effects and once without it. This assists with understanding the magnitude of the contribution of the thermal diffusion on the overall distribution of dissolved ions and mineral.

6.4.2.1 Analysis results with $\kappa=1$ for both anionic and cationic components

Figure (6.4) shows the results of transient profile of the dissolved ion concentrations for the first series of analysis in which κ is assumed as 1.0 in the effective diffusion coefficients of

both calcium and sulphate ions. Figure (6.5) also presents the pattern of dissolution-precipitation behaviour of anhydrite mineral for the same series of analysis. The Soret coefficient was considered in this simulation.

The model predicted identical results for the concentration of the calcium and sulphate although different diffusion coefficients have been used in the simulation. This is attributed to the overall charge neutrality condition which was adopted in the formulation of the multicomponent reactive transport, presented in chapter 3.

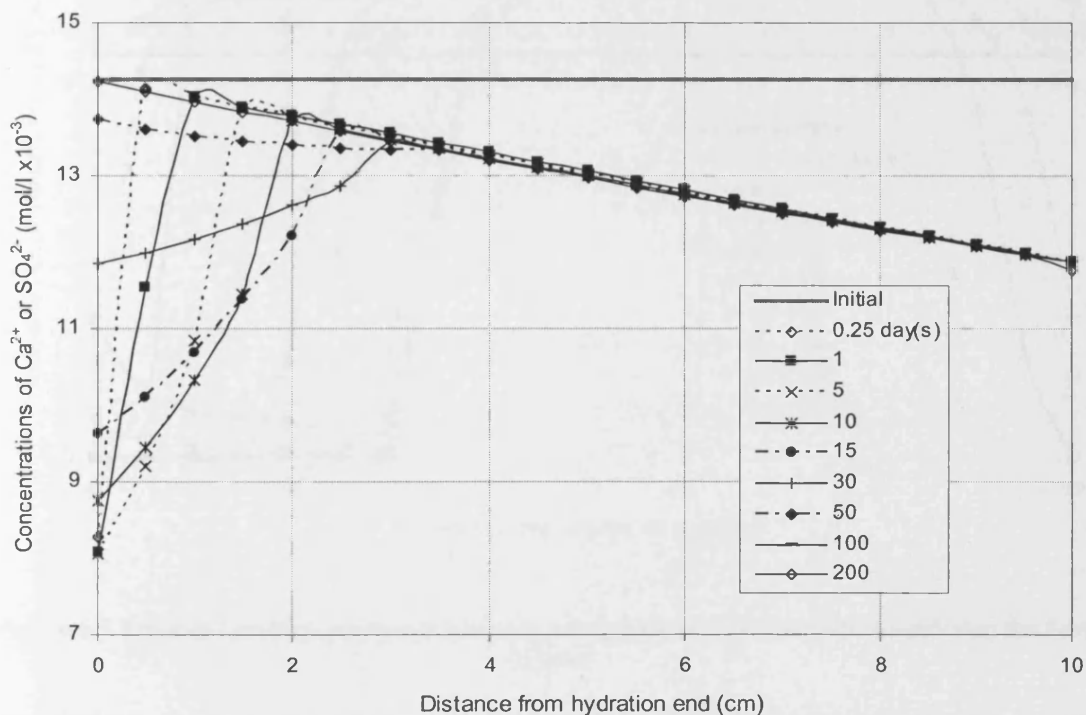


Figure 6.4 Transient profiles of the dissolved ion concentrations ($\kappa=1.0$ and with considering the Soret effect)

During the initial stages, the model predicts reduction in the dissolved ion concentrations and anhydrite mineral concentration near the hydration end. The decrease in the dissolved ion concentrations is due to the advective flow toward the hot end which leads to the dissolution of the anhydrite mineral, to maintain the equilibrium condition between solid and aqueous phases. Temperature variation in the domain affects the equilibrium condition between anhydrite mineral phase and dissolved ions which is controlled mathematically by the equilibrium constant in the mass action law of the reaction.

The drop in the dissolved calcium concentration at hot end can be attributed to the precipitation of mineral caused mainly by the temperature. Due to the migration of dissolved ions to the hot end, the amount of precipitate anhydrite increases towards the hot end in the regions beyond the dissolution front up to about 30 days.

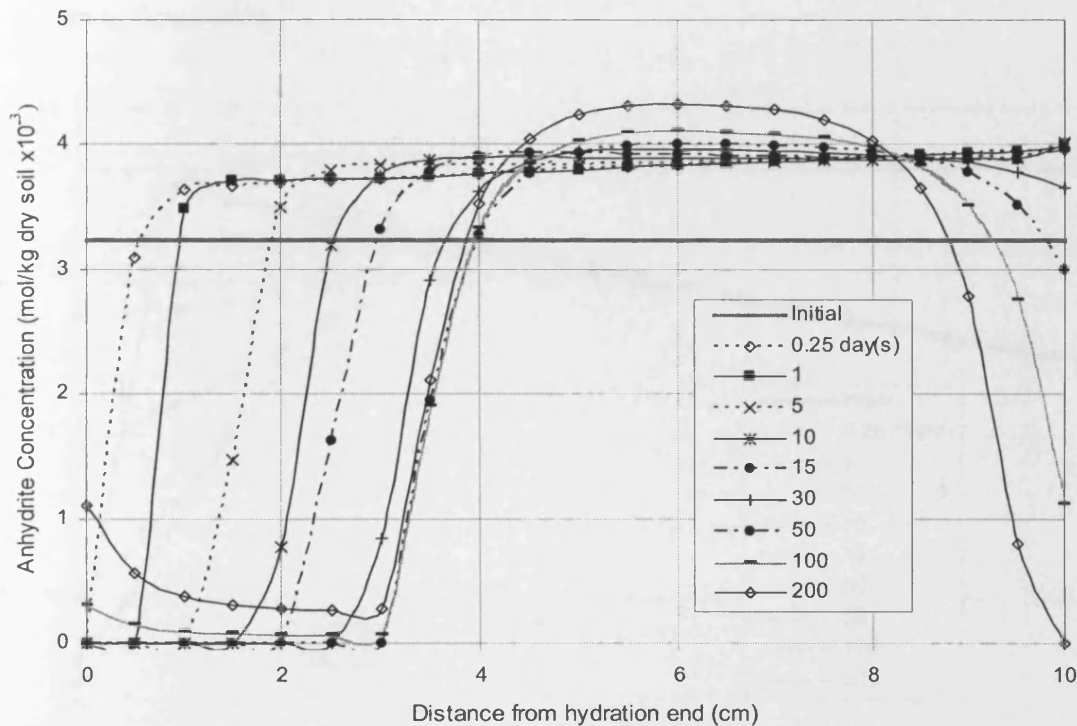


Figure 6.5 Transient profiles of the anhydrite concentration ($\kappa=1.0$ and with considering the Soret effect)

After 30 days, the system is almost saturated and the dissolved ions tend to move towards lower concentrations in the hot end. Thermal diffusion effect push the ions from hot end to the cold side which consequences in reduction in the rate of mineral precipitation at the hot region. The ion migration induced by temperature can further enhance dissolution of anhydrite in the hot region and toward the cold end to maintain the equilibrium between dissolved ion concentration and mineral content. After 50 days, the system is saturated and the concentration of anhydrite reduces near the hot end and is dissolved after 200 days which results in the release of higher amount of dissolved ions to the pore.

As mentioned earlier, a similar simulation was repeated without considering the effects of the thermal diffusion in the simulation, i.e. $S^T=0$, to investigate the importance and the magnitude of the effect on the transient distribution of dissolved ions and mineral phase, Figure (6.6) demonstrates the results of the transient profile of the dissolved ion concentrations neglecting the effects related to the thermal diffusion. The profiles of the anhydrite mineral distribution are shown in figure (6.7).

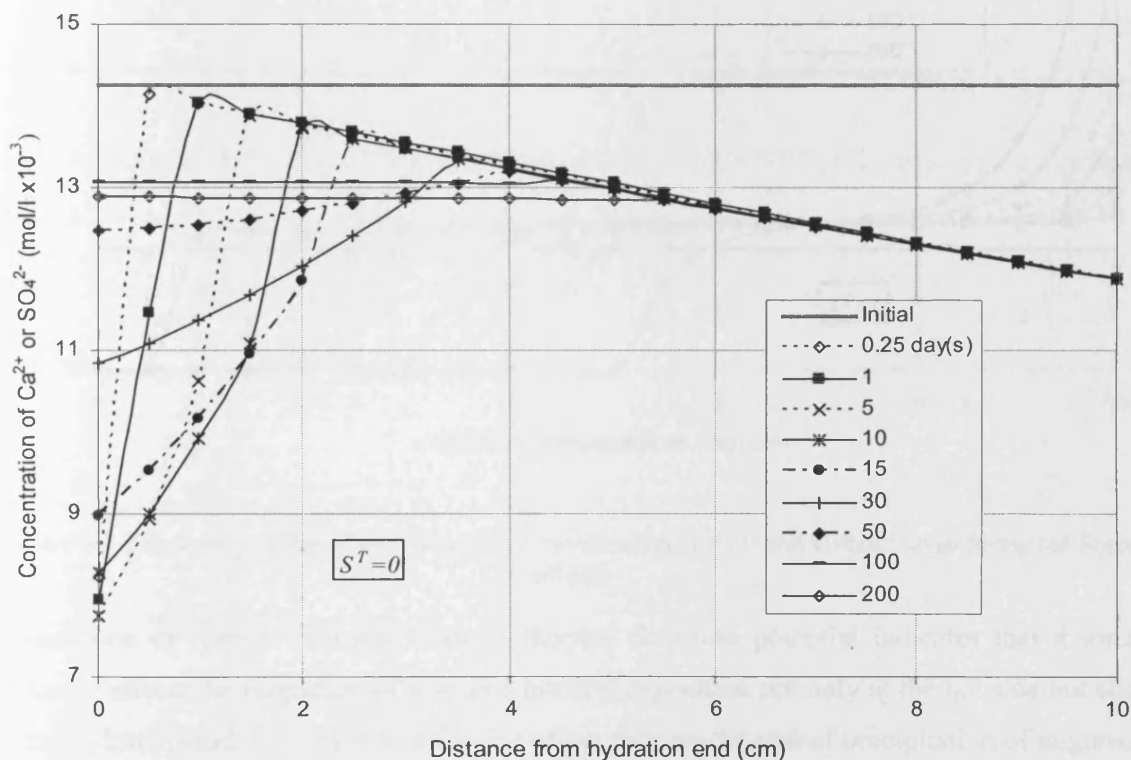


Figure 6.6 Transient profiles of the dissolved ion concentrations ($\kappa=1.0$ and without considering the Soret effect)

In the early stages of resaturation, the results demonstrate a similar distribution pattern for dissolved chemicals and anhydrite precipitated compared with the previous results. The similar trends for the dissolved chemicals and the dissolution front at the hydration end are attributed to the advective nature of the transport of ions for up to 15 days of analysis.

After about 50 days the entire amount of available anhydrite mineral is dissolved in the aqueous phase in the region close to the hydration side and the dissolved ions start to diffuse due to the concentration gradient towards the hot end with a lower dissolved concentration.

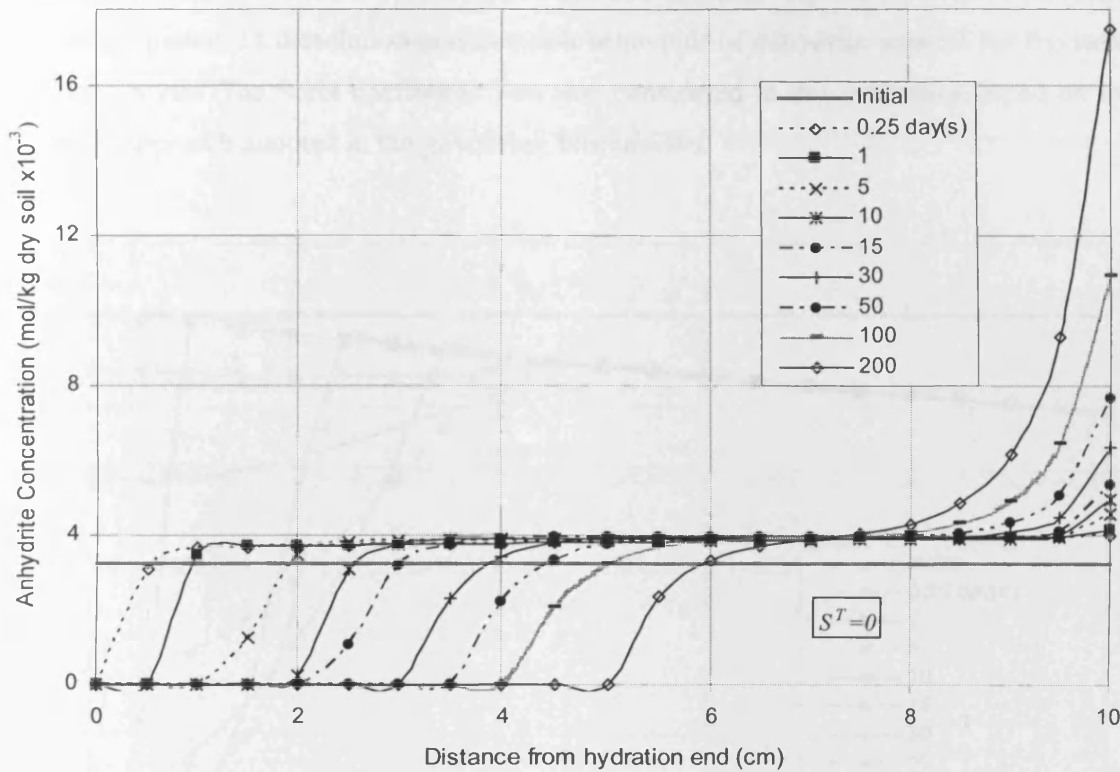


Figure 6.7 Transient profiles of the anhydrite concentration ($\kappa=1.0$ and without considering the Soret effect)

Comparison of results with and without thermal diffusion potential indicates that thermal diffusion affects the migration of ions and mineral deposition not only at the hot side but also in the hydration end. The thermal diffusion effect reduces the rate of precipitation of migrated dissolved ions to the hot region and enhances the migration of dissolved ions towards the hydration end. The ion migration induced by temperature can further enhance dissolution of anhydrite in the hot region and ion migration towards the cold end to maintain the equilibrium between dissolved ion concentration and mineral content.

6.4.2.2 Analysis results with κ equal to 0.1 for anionic and equal to 1.0 for cationic component

Figure (6.8) shows the results of transient profile of the dissolved ion concentrations for the second series of analysis which different κ values were used in the tortuosity coefficient

relationship, equal to 0.1 and 1.0 for sulphate and calcium ions, respectively. Figure (6.9) also presents the pattern of dissolution-precipitation behaviour of anhydrite mineral for the same series of analysis. The Soret coefficient was also considered in this simulation based on the theoretical approach adopted in the governing formulation.

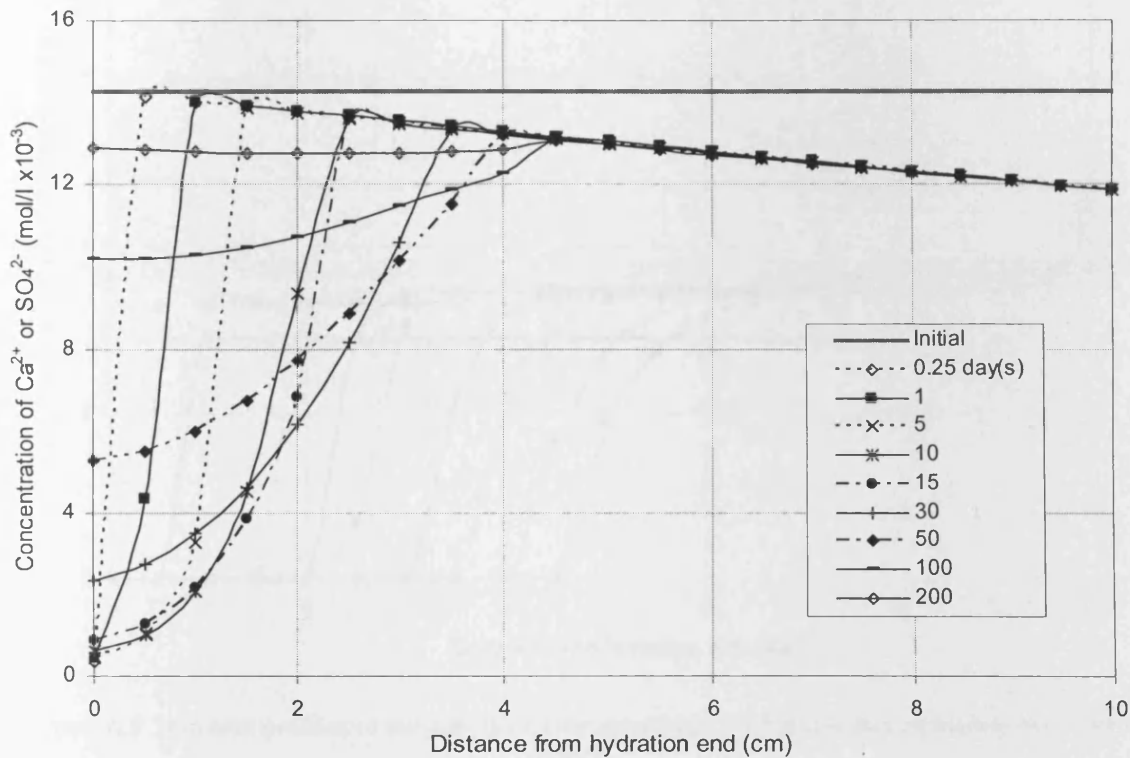


Figure 6.8 Transient profiles of the dissolved ion concentrations ($\kappa=0.1$ and with considering the Soret effect)

The model predicted identical results for the concentrations of the calcium and sulphate although the effective diffusion coefficient of calcium used in the simulation is about 10 time greater than that for sulphate ions. This is attributed to the overall charge neutrality condition under coupled electrochemical and thermal diffusion potentials, adopted in the formulation of the multicomponent reactive transport.

Similar to the previous simulation series, during the initial stages, the model predicted a reduction in the dissolved ion concentrations and anhydrite mineral concentration near the hydration end. This is due to the advective flow toward the hot end. Similarly, the drop in the dissolved chemical concentrations at the hot end can be attributed to the precipitation of the

mineral caused by the higher temperature and decreasing moisture content due to vapour flow.

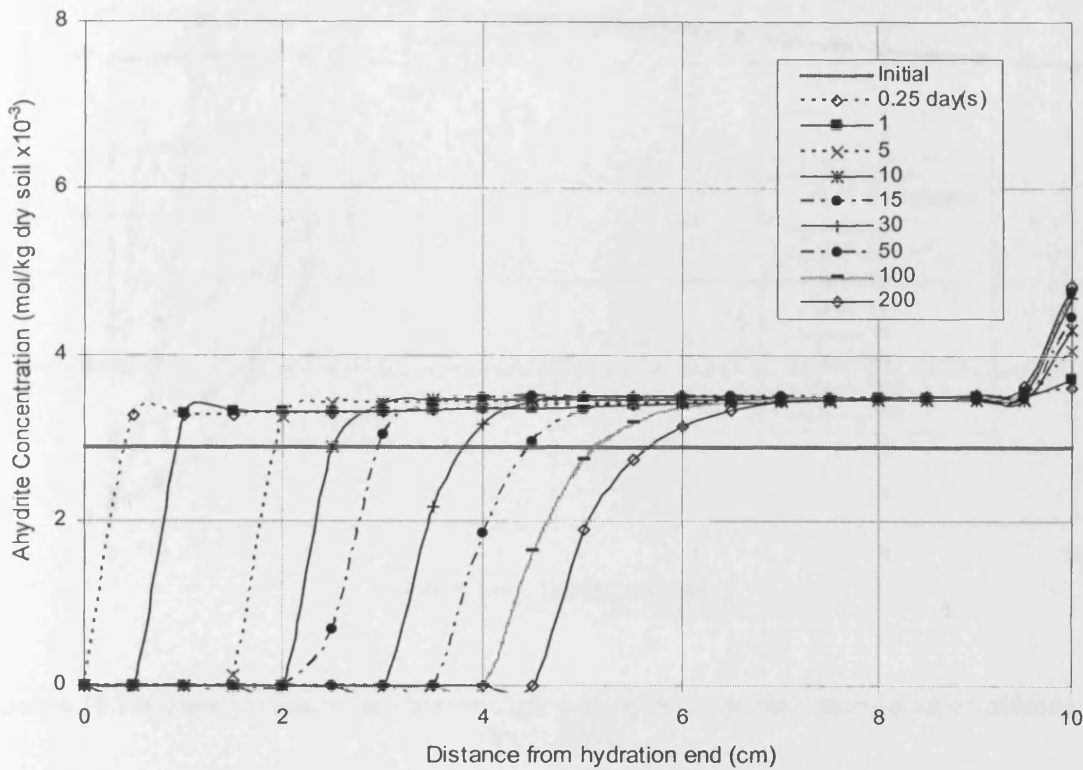


Figure 6.9 Transient profiles of the anhydrite concentration $\kappa = 0.1$ and with considering the Soret effect)

In order to demonstrate the magnitude of the thermal diffusion effects, the simulation is repeated but without considering thermal diffusion effects, i.e. $S_T = 0$. Figure 6.10 presents the profile of dissolved ions distribution in the domain resulted from the modelling without considering the Soret effects. Figure 6.11 also shows the transient profile of the distribution of precipitate anhydrite mineral for the analysis.

The results of the distribution of the dissolved chemicals with and without the Soret effects are almost identical for the second series of analysis. However, the distribution of the anhydrite mineral in the domain has been affected by the thermal diffusion. In the early stages of resaturation, up to about 15 days, the distribution pattern is similar to that presented in figure 6.9.

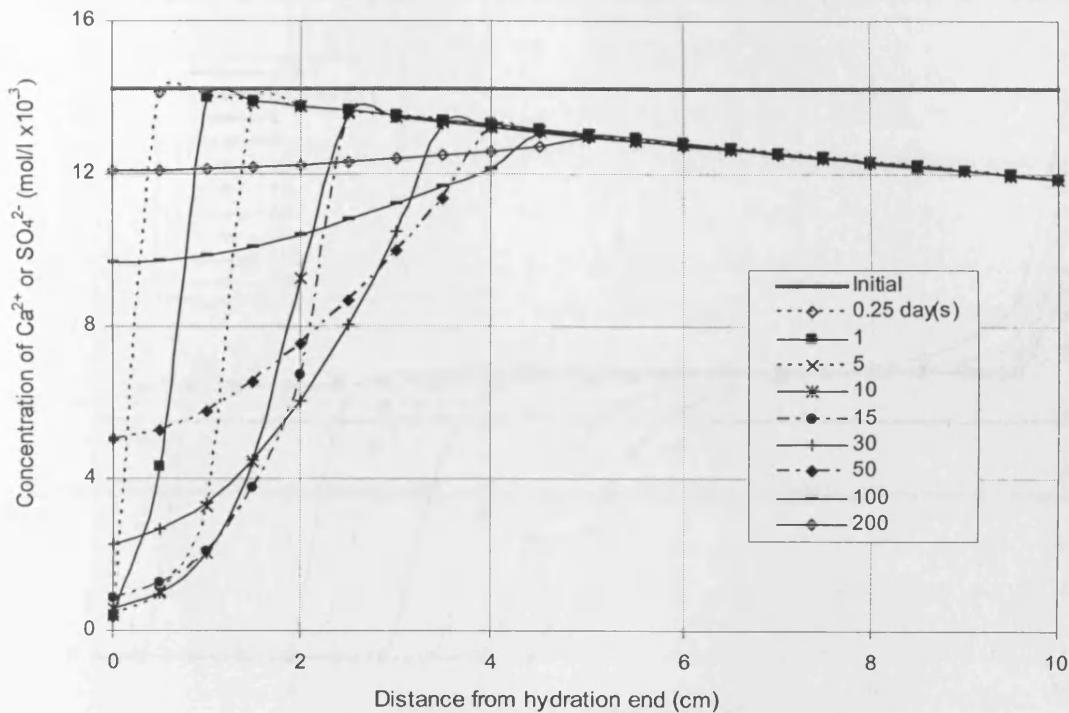


Figure 6.10 Transient profiles of the dissolved ion concentrations ($\kappa=0.1$ and without considering the Soret effect)

After 30 days, when the system became almost saturated and the dissolved ions tended to move towards lower concentrations. Thermal diffusion effects decrease the rate of precipitation of migrated dissolved ions at vicinity of the hot region and the subsequent increase in the precipitate amount of mineral near the heater.

Comparison of results with and without Soret effects shows that the effects of thermal diffusion are highlighted at the hot end where the amount of precipitate is less than the amount obtained from the analysis without considering thermal diffusion effects after 200 days of analysis.

The results of the modelling with and without thermal diffusion effects indicate that the effects of thermal diffusion are highlighted at the hot end where thermal diffusion decreases the amount of precipitate minerals in this region. Indeed, the overall impact of thermal diffusion depends on the effective diffusion coefficient in the system.

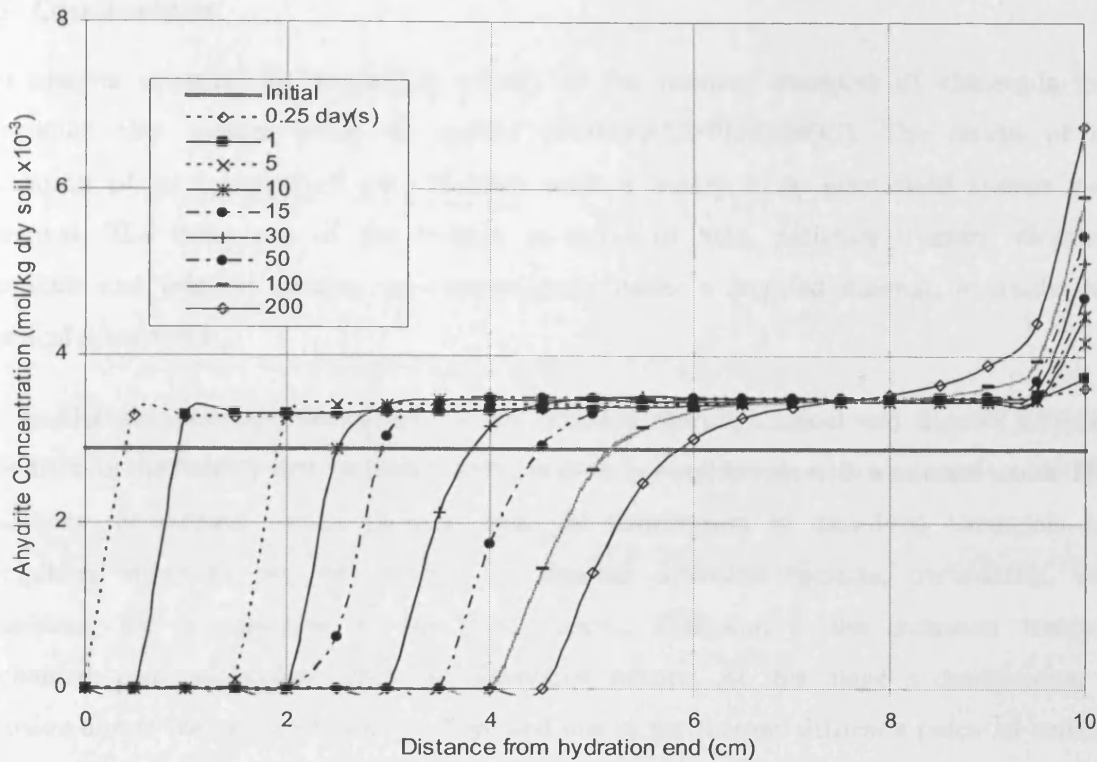


Figure 6.9 Transient profiles of the anhydrite concentration ($\kappa=0.1$ and without considering the Soret effect)

In comparison between the results of the first and second simulations, where the average effective diffusion coefficients of the ions are greater in the first series, it is observed that thermal diffusion effect has considerable impacts in the dissolved chemicals and mineral distribution in the system. In the case of highly compacted bentonite, the second analysis condition would be more towards the realistic condition in terms of the effective rate of diffusion. In clay deposits, such as Boom clay where the diffusion coefficients for HTO has been reported in the range of 10^{-10} m²/s (Aertsens et al. 2004), the first simulation assumptions from the effective diffusion coefficients are close to the reported values. Therefore, the contribution of the thermal diffusion might be an important aspect in this type of clays as the host formation of the HLW disposal system.

6.5 Conclusions

This chapter presents the modelling results of the reactive transport of chemicals in a compacted clay system using the model (COMPASS-PHREEQC). The results of the simulation of an unsaturated clay domain with a binary ionic pore fluid system were presented. The behaviour of the system in terms of heat, moisture transfer, dissolved chemicals and mineral content was investigated under a coupled thermal, hydraulic and chemical framework.

The results demonstrated the effects of the coupled electrochemical and thermal diffusion potentials on the behaviour of a binary ionic system in equilibrium with a mineral under THC conditions. Modelling results showed that the distribution of dissolved chemicals and precipitated minerals can be affected by thermal diffusion impacts, particularly, after completing the re-saturation of the clay system. Diffusion is the dominant transport mechanism after saturation when no advection occurs. At this stage a combination of diffusion due to the concentration gradient and due to the thermal diffusion potential controls the transport of chemicals. The simulation results demonstrate the charge conservation condition implemented in the theoretical formulation under advective-diffusive flow regime.

The simulation examples showed that the contribution of the Soret effect in the overall process of reactive diffusion could change the distribution of minerals in the boundary regions, especially close to the heat source where a high degree of precipitation of minerals is expected. Variation in the amount of precipitate mineral induces changes to the available porosity for hydraulic processes and aqueous chemical reaction which could be an important issue for example in the case of compacted clay buffer in nuclear waste disposal repositories where minerals would be likely precipitated in the vicinity of heater.

As mentioned in chapter 2, there is limited information available on the effects of the thermal diffusion, especially in multiple ionic systems and in clays. The theoretical approach adopted for this effect in the formulation of the model and an example simulation presented, can potentially be utilised for the assessment of the effect. It is acknowledged that some simplifications have been made in the simulation work, and hence it is anticipated that improved solutions can be achieved by including more complexities into the model.

6.6 References

- Aertsens, M., Wemaere, I., and Wouters, L. (2004). Spatial variability of transport parameters in the Boom Clay. *Applied Clay Science*, 26, 37-45.
- Agar, J.N., Mou, C.Y., and Lin, J. (1989). Single-ion heat of transport in electrolyte solutions. A hydrodynamic theory. *Journal of Physical Chemistry*, 93, 2079-2082.
- Cleall, P.J., Seetharam, S.C., and Thomas, H.R. (2007). On the inclusion of some aspects of chemical behaviour of an unsaturated soil in thermo-hydro-chemical-mechanical models: II Application and transport of soluble salts in compacted bentonite. *Journal of Engineering Mechanics, ASCE*, 133, 348-356.
- Cussler, E.L. (1997). *Diffusion-Mass Transfer in Fluid Systems*. University Press, Cambridge.
- ENRESA, (2000). *Full-scale engineered barriers experiment for a deep geological repository for high-level radioactive waste in crystalline host rock, FEBEX project*. EUR 19147, Nuclear Science and Technology Series, European Communities, Luxembourg.
- Lasaga, A.C. (1998). *Kinetic Theory in the Earth Science*. Princeton Series in Geochemistry, Princeton University Press.
- Mayhew, Y.R., and Rogers, G.F.C. (1976). *Thermodynamic and Transport Properties of Fluids*. 2nd edition, Oxford: Blackwell.
- Millington, R.J., and Quirk, J.M. (1961). Permeability of porous solids. *Transaction Faraday Society*, 57, 1200–1207.
- Parkhurst, D.L., and Appelo, C.A.J. (1999). *User's guide to PHREEQC (version 2)*, U.S. Geological Survey, Water Resource Investigation Report, 99-4259.
- Philip, J.R., and de Vries, D.A. (1957). Moisture movements in porous materials under temperature gradients. *Transactions American Geophysical Union*, 38(2), 222-232.
- van Genuchten, M.Th. (1980). A closed-form equation for predicting the hydraulic conductivity of unsaturated soils. *Soil Science Society of America Journal*, 44, 892-898.

Chapter 7

Transport Processes in Compacted Swelling Clays-Microstructural Effects

7.1 Introduction

As reported in chapter 2, it has been found that water molecules in the interlayer pore space of swelling clays (between individual layers or lamellas of mineral units) have different physical properties, e.g. density and viscosity, from those in free water. This fraction of the pore water is widely regarded as immobile water or adsorbed component in solid phase. The fraction the interlayer water to the intralayer/interparticle water is significantly greater in compacted smectite clays compared with that in non-swelling or low-swelling clays, as discussed in chapter 2.

The microstructural evolution of the clay and the physical state of pore water can effectively control the hydraulic, chemical and mechanical behaviour of compacted smectite (Pusch and Yong, 2006). Since the major fraction of the pore water in compacted bentonite is located in the interlayer or micropores, an accurate estimation of the amount of this water fraction is an important issue for modelling the hydro-geochemical behaviour of compacted swelling clays. An evaluation of the quantity of the interlayer water is therefore required first. Secondly, the physical contribution of the interlayer water hydration or dehydration in the formulation of the water and chemical transport model, is required to incorporate an important aspect of the physical behaviour of compacted swelling clays.

In this chapter, a model for calculating the interlayer (and intralayer/interparticle) water fraction in compacted smectite clays, e.g. bentonite is presented. The model is theoretically based on a thermodynamic modelling framework. In this approach, the interlayer hydration and dehydration is treated as a geochemical reaction and aimed to provide a link between the geochemical microstructural features of the smectite minerals, and the macroscopic properties and behaviour.

Section 7.2 presents the theoretical background and formulation of the geochemical solid solution model of smectite hydration/dehydration. The model is based on the thermodynamic approach proposed by Ransom and Helgeson, (1994) in which the problem of hydration-dehydration of smectite is addressed as a solid solution reaction with water molecules. The solid solution model of hydration/dehydration can be applied in variable temperature and relative humidity conditions. The temperature and suction dependency of the model proposed for hydration/dehydration of smectite is discussed in section 7.3. In section 7.4, the

hydration/dehydration model is extended to calculate the interlayer water content of compacted smectite clays. The theoretical model of hydration/dehydration is applied to derive an approach in order to evaluate the amount of interlayer water in smectite clay as a variable function of suction, temperature and the interlayer cation.

Section 7.5 presents the results of model application in the case of compacted and saturated Na-smectite clay (MX-80 bentonite). The parameters required for the solid solution model of hydration/dehydration proposed by Ransom and Helgeson (1994) is investigated and modified in the case of the mentioned smectite. This required re-visiting the derivation of the model parameters, discussed in detail in this section. The variation of the interlayer water content with temperature and suction, based on the model is also presented and discussed. Since there is no alternative model or exact experimental data on the variation of interlayer water content with temperature or suction, the results are qualitatively compared.

Section 7.6 deals with the inclusion of the interlayer hydrate water effects on the hydraulic behaviour of confined compacted smectite clays, using the solid solution model of hydration/dehydration. The interlayer water adsorption effect on water transport is implicitly included via modification of the hydraulic conductivity. The background of the hypothesis is explained in this section followed by a modified equation for unsaturated hydraulic conductivity as an initial approximation of the interlayer water variation impact.

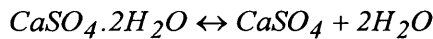
In section 7.7, the proposed hydraulic conductivity equation, modified by the interlayer hydration/dehydration impacts is investigated against experimental studies of moisture transport in compacted bentonite (FEBEX bentonite) under isothermal and non-isothermal conditions. The simulations of moisture transfer are based on a series of experimental investigations on the compacted FEBEX bentonite reported by Villar et al. (2005). Two series of simulations are reported under isothermal condition and under thermal gradients and using the modified hydraulic conductivity with interlayer water effect and without this effect. The results are compared with the experimental results in terms of relative humidity variations in the system.

A conclusion of the chapter is presented in section 7.8.

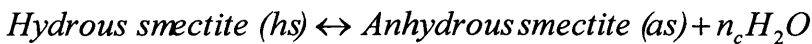
7.2 A geochemical solid-solution model for the hydration/dehydration of smectite

The hydration and dehydration process consists of sequential adsorption/desorption of one, two and three layers of water molecules to and from the interlayer pore space between the mineral lamellas in smectite rich clay. The process is driven primarily by the energy associated with, initially the hydration of mineral surfaces and consequently with hydration of exchangeable interlayer (e.g., Iwata et al., 1995; Likos, 2004).

The process of hydration and dehydration of smectite consists of addition or loss of interlayer water in 2:1 silicate sheet of the mineral. During the hydration/dehydration process, the composition and crystalline structure of the mineral layers remains unchanged. As a result, the process of hydration/dehydration can be regarded as a reversible heterogeneous geochemical reaction between a symbolic hydrous and its homologous anhydrous counterparts similar to the hydration/dehydration of a solid solution (e.g. Tardy, 1990; Ransom and Helgeson, 1994; Vidal and Dubacq, 2009). In other words, smectite solid phase can be considered as a regular solid solution of hydrous and anhydrous components that differ only by some moles of water molecules presented in the interlayer pores. This case is similar to the hydration/dehydration of gypsum where two molecules of hydrated water remain attached to the structural formula (Tardy, 1990):

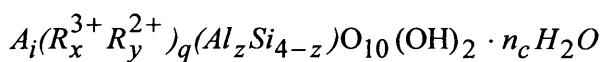


Following a similar hypothesis, Ransom and Helgeson (1994) addressed the problem of the hydration/dehydration of smectite as a geochemical process of solid solution reaction with water molecules. In terms of hydrous and anhydrous smectite components, this can be represented as:



where n_c represents the number of moles of H_2O involved in the reaction.

The structural formula for one mole of a hydrous smectite solid solution can be expressed as (Ransom and Helgeson, 1994):



where A is a proxy for the interlayer cation, R represents the interlayer cations and the subscripts i , x , y , and z designate the number of moles of the respective cations per $O_{10}(OH)_2$, which is the half unit cell of structural formula. q is the number of occupied octahedral sites per mole of the mineral.

In the hydration/dehydration model proposed by Ransom and Helgeson (1994), the number of water moles per smectite half formula unit, i.e. $O_{10}(OH)_2$, is assumed to be independent of the interlayer cations. In addition, the surface area of same smectite remains constant when the interlayer cation is exchanged with different cations.

The law of mass action for the hydration/dehydration reaction of smectite according to the solid solution model ($hs \leftrightarrow as + n_c H_2O$) can be written as:

$$K_{eq} = \frac{a_{as} (a_{H_2O})^{n_c}}{a_{hs}} \quad (7.1)$$

Where K_{eq} represents the equilibrium constant of the reaction and a_{H_2O} refers to the activity of adsorbed water. a_{as} and a_{hs} denotes the activity of the anhydrous and hydrous components of the smectite solid solution, respectively.

Expressing the activities in terms of product of molar fraction and the activity coefficients gives:

$$a_{as} = \lambda_{as} X_{as} \quad (7.2)$$

$$a_{hs} = \lambda_{hs} X_{hs} \quad (7.3)$$

where X_{as} and X_{hs} represents the mole fractions of anhydrous and hydrous smectite, respectively. λ_{as} and λ_{hs} is the activity coefficient of anhydrous and hydrous smectite.

For a binary solid solution, the mole fraction of anhydrous and hydrous phase is defined as (Ransom and Helgeson, 1994):

$$X_{hs} = 1 - X_{as} = \frac{m_{hs}}{m_{as} + m_{hs}} \quad (7.4)$$

where m_{as} and m_{hs} stand for the number of moles of anhydrous and hydrous smectite.

The logarithmic form of mass law can therefore be written as a function of mole fractions and activity coefficients of the reaction components as:

$$\log K_{eq} = \log\left(\frac{1-X_{hs}}{X_{hs}}\right) + \log\left(\frac{\lambda_{as}}{\lambda_{hs}}\right) + n_c \log a_{H_2O} \quad (7.5)$$

Based on the experimental data, Ransom and Helgeson (1994) stated that the solid solution reaction of homologous hydrous and anhydrous smectite components at constant temperature (25 °C) and pressure (1 bar) are consistent with the regular solid solution theory. Therefore it can be given:

$$\log \lambda_{as} = \frac{W_s}{2.303RT} (1-X_{as})^2 \quad (7.6)$$

$$\log \lambda_{hs} = \frac{W_s}{2.303RT} (1-X_{hs})^2 \quad (7.7)$$

where W_s denotes the Margules parameter for a binary regular solid solution of hydrous and anhydrous smectite components. The Margules parameter is independent of pressure and temperature. R refers to gas constant and T is temperature (K).

Defining a parameter as:

$$\Phi \equiv \log\left(\frac{1-X_{hs}}{X_{hs}}\right) + n_c \log a_{H_2O} \quad (7.8)$$

A relationship between the equilibrium constant and parameter Φ is established (Ransom and Helgeson, 1994):

$$\Phi = -\frac{W_s}{2.303RT} (2X_{hs} - 1) + \log K_{eq} \quad (7.9)$$

Knowing the data related to the activity of water and the molar fraction of hydrous smectite, the values of Φ can be interpreted using equation (7.8). If the number of moles of water adsorbed or released per mole of hydrous smectite, i.e. n_c , is known, it is also possible to establish a linear relationship between Φ and $(2X_{hs}-1)$ which gives the values of Margules parameter and the equilibrium constant of the reaction.

Hence, the equation (7.5) can be re-written as:

$$\log K_{eq} = \log\left(\frac{1 - X_{hs}}{X_{hs}}\right) + \frac{W_s}{2.303RT}(2X_{hs} - 1) + n_c \log a_{H_2O} \quad (7.10)$$

According to the equation (7.10), the amount of molar fraction of hydrous member of the solid solution reaction can be calculated at any temperature and activity of water, if the equilibrium constant and Margules parameter of the solid solution reaction are known.

Ransom and Helgeson (1994) calculated the number of water moles per $O_{10}(OH)_2$ (i.e. n_c) of a fully hydrated smectite (i.e., $X_{hs}=1$) based on the analysis of the reported XRD results. They concluded that the basal spacing between dioctahedral aluminous layers extends from 10 Å to 15.7 Å in a fully hydrated smectite. They reported the moles number of interlayer water per $O_{10}(OH)_2$ (n_c) of fully hydrated smectite as 4.5 which corresponds to the basal spacing of 15.7 Å. This amount of water corresponds to two layers of water in the interlayer space (Cuadros, 1997).

Although basal spacing between the dioctahedral layers of smectite may differ with the exchangeable cations, Cuadros (1997) reported that the maximum number of water moles per half formula unit considering two layers of water is approximately 4.5 for smectite exchanged with Na, Ba, Li, Ca, Mg, and Sr cations but the behaviour of K and Cs-smectite is different.

Base on the experimental data on the water-vapour pressure isotherm studies on Na and Ca smectite, Ransom and Helgeson (1994) calculated the equilibrium constant and Margules parameter of the solid solution model for Na- and Ca-smectite solid solutions assuming that fully hydrous smectite contains two mono layers of water or 4.5 moles of water in the interlayer space.

In the formulation of the solid solution model for hydration/dehydration, the natural variations in the hydration/dehydration behaviour of smectite exchanged with different exchangeable cations is considered through the dependency of Margules parameter (W_s) and the values of Gibbs free energy of the reaction on the interlayer cation. Ransom and Helgeson, (1994) also provided theoretically the values of Margules parameters and standard Gibbs free energy of the hydration/dehydration reaction at standard pressure of 1 bar and temperature 25 °C for different homo-ionic smectite solid solutions with different interlayer cations. The later calculations for different homo-ionic smectites were adopted based on the thermodynamic parameters obtained of hydration/dehydration of Na- and Ca-smectite and by assuming that

the contribution of 2:1 silicate layer in the standard molal Gibbs free energy of the hydration/dehydration reaction is negligible and it mainly represents the hydration of the interlayer cation.

Table (7.1) provides the values of Margules parameters, Standard change of Gibbs free energy, $\log K_{eq}$ of various homo-ionic smectite solid solutions at 25 °C and 1 bar. It is noted that the parameters are consistent with hydration/dehydration with two layers of water in the interlayer space and the corresponding molar value of 4.5 per $O_{10}(OH)_2$.

Table 7.1 Calculated Margules parameters (W_s), Standard change of Gibbs free energy (ΔG_r^0), $\log K_{eq}$ and standard change in enthalpy (ΔH_r^0) of various homo-ionic smectite solid solutions at 25 °C and 1 bar in accordance to the hydration-dehydration reaction (adopted from Ransom and Helgeson, 1994;1995)

<i>Parameters</i>	W_s (kcal/mol)	ΔG_r^0 (kcal/mol)	$\log K_{eq}$ (at 25 °C)	ΔH_r^0 (kcal/mol)
<i>Na-smectite</i>	-3.254	1.047	-0.767	5.81
<i>K-smectite</i>	-3.289	0.207	-0.151	4.974
<i>NH₄-smectite</i>	-3.293	0.129	-0.095	4.896
<i>Rb-smectite</i>	-3.300	-0.052	0.038	4.714
<i>Cs-smectite</i>	-3.314	-0.374	0.274	4.392
<i>Mg-smectite</i>	-2.806	5.842	-4.28	10.609
<i>Ca-smectite</i>	-2.883	4.926	-3.61	9.639
<i>Sr-smectite</i>	-2.909	4.620	-3.39	9.387
<i>Ba-smectite</i>	-2.948	4.160	-3.05	8.962

Using the parameters given in table (7.1), the mole fraction of hydrous homo ionic smectite for a given temperature and activity of water, i.e. relative humidity, can be calculated by equation (7.10).

7.3 Suction and temperature dependency of the hydration/dehydration model

The mole fraction of hydrous smectite is controlled by the parameters of the solid solution model presented in equation (7.10) including:

- Activity of water ($\log a_{H_2O}$)
- Temperature (T)
- Equilibrium constant of the reaction ($\log K_{eq}$)
- Margules parameter (W_s).

The activity of water can be related to the relative humidity and soil water potential (suction) in the system as:

$$\log a_{H_2O} \cong \log \left(\frac{P_{H_2O}}{P_{H_2O}^0} \right) = -\frac{v_w}{2.303RT} s \quad (7.11)$$

where s is suction and v_w is the molar volume of water. P_{H_2O} and $P_{H_2O}^0$ are the partial pressures of water in soil and in a pure solution under identical conditions, respectively. R is gas constant.

Based on equation (7.11), activity of water can be related to the suction and temperature. Consequently, the amount of the partial molar of hydrated smectite can also be determined at a given suction and temperature from equation (7.10).

The equilibrium constant of the reaction varies also with temperature (Ransom and Helgeson, 1995). The temperature dependency of the equilibrium constant of the reaction can be also expressed as a function of standard enthalpy of reaction (ΔH_r^0) and the standard change of heat capacity of the reaction at constant pressure, (ΔC_p^0), (Langmuir, 1997). Accordingly, the variation of the equilibrium constant of the reaction can be represented as (Langmuir, 1997):

$$\frac{\partial \log K_{eq}}{\partial T} = \frac{\Delta H_{r,T}^0}{2.303RT^2} - \frac{\Delta C_p^0}{2.303RT^2} + \frac{\Delta C_p^0}{2.303RT} \quad (7.12)$$

Integrating the equation (7.12), the equilibrium constant at any temperature can be therefore calculated from its value at reference temperature, the standard values of enthalpy at reference temperature given by Ransom and Helgeson (1994 and 1995) for different homo-ionic smectite (i.e. table 7.1) and the heat capacity of the reaction as:

$$\log K_{eq} = (\log K_{eq})_{T_r} + \frac{\Delta H_{r,T_r}^0}{2.303R} \left(\frac{1}{T_r} - \frac{1}{T} \right) + \frac{\Delta C_p^0}{2.303R} \left(\frac{T}{T_r} - 1 \right) + \frac{\Delta C_p^0}{2.303R} \ln \left(\frac{T}{T_r} \right) \quad (7.13)$$

The values of standard heat capacity of hydration/dehydration reaction at different temperatures and pressures were calculated by Ransom and Helgeson, (1995) for a binary solid-solution of smectite. The reported values of ΔC_p^0 by Ransom and Helgeson (1995) for smectite solid solution at different temperatures ranging from 25 to 300 °C show that the variation of ΔC_p^0 is almost negligible in temperature ranges between 25-150 °C, hence it can be approximated as a constant value in that range of temperature considered in the scope of this research ($\Delta C_p^0 \approx 69.13 \text{ cal/mol}$).

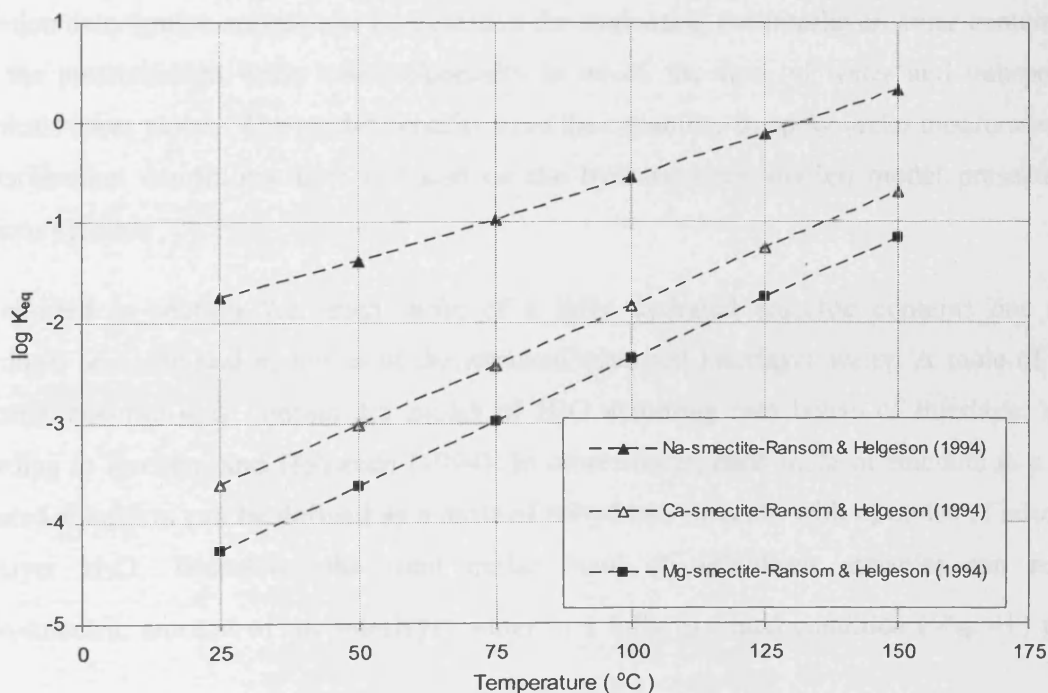


Figure 7.1 Variation of the logarithm of equilibrium constant of the hydration/dehydration reactions with temperature for different homo-ionic smectite solid solutions

Figure 7.1 presents the variation of the logarithm of equilibrium constant for different homo-ionic smectite solid solutions, using the reported values of $\log K_{eq}$ at standard state by Ransom and Helgeson (1994; 1995).

As discussed in this section, the presented model of hydration/dehydration provides a theoretical framework to calculate the amount of the mole fraction of the hydrous homo-ionic smectite and its variation with the primary variables of suction and temperature. In the following section the solid solution model is applied to calculate the interlayer water content in compacted smectite clay.

7.4 Evaluation of the interlayer water content in compacted smectite clays

In this section, a formulation for evaluating the amount of interlayer water based on the mole fraction of hydrous smectite is derived. In fact, this section explains the way that the hydration/dehydration model can be extended for evaluating the interlayer water content and then the meso/macro water content/porosity in which the flow of water and transport of chemicals takes places. The model benefits from the capability to apply under unsaturated and non-isothermal conditions as it is based on the hydration/dehydration model presented in previous section.

As reported in section 7.2, each mole of a fully hydrated smectite contains one mole anhydrous smectite and n_c moles of the attached/adsorbed interlayer water. A mole of fully hydrated smectite may contain 4.5 moles of H₂O assuming two layers of interlayer water according to Ransom and Helgeson (1994). In other words, each mole of smectite in a fully hydrated condition can be defined as a mole of anhydrous smectite with n_c moles of adsorbed interlayer H₂O. Therefore, the total molar mass of anhydrous smectite can adsorb V_I^{IL} volumetric amount of the interlayer water in a fully hydrated condition ($X_{hs} = 1$) given as:

$$V_I^{IL} = m_{as} n_c v_{il} \quad (7.14)$$

where m_{as} is the total molar mass of anhydrous smectite in soil, and v_{il} is the molar volume of interlayer water which is about $17.22 \text{ cm}^3/\text{mol}$ given by Ransom and Helgeson, (1995) at 25°C . It is noted that the interlayer molar volume of water is lower than the corresponding average values for bulk water (i.e. $18.0 \text{ cm}^3/\text{mol}$) as stated Ransom and Helgeson (1994).

The total molar mass of anhydrous smectite (m_{as}) can then be approximated by dividing the total mass of dry smectite (i.e. anhydrous smectite) to the molar mass of dry smectite m_{sm} .

$$m_{as} = \frac{M_{dry}^{sm}}{m_{sm}} \quad (7.15)$$

where M_{dry}^{sm} is the total mass of dry smectite at macro scale.

The total mass of the dry smectite, i.e., anhydrous component, in macro scale can be calculated knowing the partial dry density of smectite and the total volume of the soil as:

$$M_{dry}^{sm} = \rho_d^{sm} V_T \quad (7.16)$$

where ρ_d^{sm} represents the partial bulk dry density of smectite. V_T is the total volume of the dry smectite.

By replacement of the amount of the total mass of dry smectite with equation (7.16), the total molar mass of smectite is given as:

$$m_{as} = \frac{\rho_d^{sm}}{m_{sm}} V_T \quad (7.17)$$

Therefore the total volume of interlayer water in fully hydrated condition (i.e., $X_{hs} = 1$) yields:

$$V_l^{IL} = \frac{\rho_d^{sm}}{m_{sm}} n_c v_{il} V_T \quad (7.18)$$

In partially hydrated conditions (or at any molar fraction of hydrous smectite, $X_{hs} \leq 1$), total volume of the interlayer water can therefore be calculated as:

$$V_l^{IL} = X_{hs} \frac{\rho_d^{sm}}{m_{sm}} n_c v_{il} V_T \quad (7.19)$$

The volumetric content of the interlayer water θ_i^{IL} can further be given as a function of dry density and the molar fraction of hydrous smectite as:

$$\theta_i^{IL} = X_{hs} \frac{n_c V_{il}}{m_{sm}} \rho_d^{sm} \quad (7.20)$$

The interlayer space is always saturated with water and the adsorption/desorption of water/vapour due to the variation in suction or temperature is manifested through the expansion or contraction of basal spacing (Hueckel et al., 2002), i.e. $\theta_i^{IL} = n_{IL}$.

The volume fraction of the interlayer water in compacted smectite, f_{IL} , then is calculated as:

$$f_{IL} = \frac{\theta_i^{IL}}{\theta_i} = \frac{n_{IL}}{nS_i} \quad (7.21)$$

In general, the smectite clays may contain some impurities or non-smectite solid portion such as quartz, feldspar, and clay minerals such as kaolinite, and illite. The partial dry density of smectite of clay can be calculated, knowing the mass fraction of smectite in clay and bulk dry density of the clay as (Idemitsu et al., 1996; Liu et al., 2003; Bourg, 2004):

$$\rho_d^{sm} = X_{sm} \rho_d \left[1 - \frac{(1 - X_{sm}) \rho_d}{\rho_{im}} \right]^{-1} \quad (7.22)$$

where X_{sm} is the mass fraction of smectite in clay and ρ_d represents the bulk dry density of the clay. ρ_s denotes the density of non-smectite minerals or impurities. Here the density of non-smectite minerals or other impurities is assumed similar to that of smectite (i.e. $\rho_{im} = \rho_{sm} \approx 2840 \text{ kg/m}^3$) according to Bourg et al. (2006).

For a given homo-ionic smectite (smectite with single ion type in the interlayer) with a specific dry density and a partial smectite percentage, equation (7.20) gives the volumetric content of the interlayer water, in accordance with the molar fraction of hydrous smectite which itself can be calculated using equation (7.10) as a function of relative humidity (or suction) and temperature.

In this section a model was proposed for quantification of the interlayer water content in compacted smectite clays. The developed model utilises a geochemical reaction concept for interlayer hydration/dehydration. In the proposed model the molar fraction of hydrous

smectite and consequently the amount of interlayer water can be calculated mainly as a function of suction, temperature, dry density and smectite content and the type of interlayer. It is noted that the developed model provides the volumetric amount of water to the two or three monolayers of H₂O which are adsorbed into the interlayer space. This is not necessarily the same as the water content of clay, as the water content includes contributions from pore and surface adsorbed water (Ransom and Helgeson, 1995).

The developed model is applied and validated in the following sections and the outcomes will be discussed.

7.5 Application and adaptation of the model for compacted Na-smectite clay

In this section, the results of the application of the developed mode, described in previous sections, for compacted homo-ionic Na-smectite clay are presented. The model has been applied also for compacted MX-80 bentonite. The proposed model for hydration/dehydration is re-visited to validate and adopt it of the case of MX-80 compacted bentonite.

7.5.1 Interlayer porosity of saturated compacted Na-smectite

In a fully saturated condition, i.e., when the activity of water or relative humidity reaches to one, the mole fraction of hydrous Na-smectite (X_{hs}) at 25 °C is obtained equal to 0.62 using equation (7.10) in accordance with the reported values of -0.767 and -3.254 kcal/mol for log K_{eq} and W_s , respectively, presented in table 7.1 (Ransom and Helgeson, 1994). It is assumed that maximum two monolayers of water are adsorbed in the interlayer space (Ransom and Helgeson, 1994). Using the average value of mass density of montmorillonite (i.e. $\rho_{sm} = 2840$ kg/m³), the volumetric content of interlayer water or interlayer porosity as a function of dry density can be obtained based on equation (7.20) as:

$$\theta_1^{IL} = n_{IL} = 0.62 \frac{4.5 \times 17.22}{378.787} \rho_d^{sm} = 0.13 \rho_d^{sm} \quad (7.23)$$

Liu and Lin (2005) suggested that the applied basal spacing of 15.7 Å for fully hydrated Na-smectite in the solid-solution model of Ransom and Helgeson (1994) needs to be revised to

$\sim 19 \text{ \AA}$ which corresponds to three layers of water in the interlayer space. They calculated the number of moles of water released by the dehydration of fully hydrous smectite equal to 7.16 corresponding to three layers of water. They reported the equilibrium constant and Margules parameter of hydration/dehydration reaction of Na-smectite solid solution considering three layers of interlayer water ($n_c = 7.16$). They found that the $\log K_{eq}$ yields to -1.76 at 25 °C considering three layers of adsorbed water for Na-smectite and Margules parameter was found close to the calculated value by Ransom and Helgeson (1994), i.e., $W_s = -3.14 \text{ kcal/mol}$.

If three layers of hydrated water, i.e. $n_c = 7.16$, is considered in the thermodynamic solid solution model of hydration/dehydration based on Liu and Lin (2005) and by applying the values of -1.76 and -3.14 kcal/mol for $\log K_{eq}$ and W_s , respectively, the mole fraction of hydrous component of smectite solid solution is obtained equal to 0.79 (Liu and Li, 2005). Consequently from equation (7.20), the interlayer volumetric water content of a fully smectite clay yields to:

$$\theta_i^{IL} = n_{IL} = 0.79 \frac{7.16 \times 17.22}{378.787} \rho_d^{sm} = 0.26 \rho_d^{sm} \quad (7.24)$$

The fraction of interlayer water in compacted smectite clays has been estimated by some researchers under saturated and isothermal conditions. Kozaki et al. (2001) calculated the fraction of interlayer porosity in compacted saturated smectite as a function of internal specific surface area (i.e., the specific area of the basal surface bounding to the interlayer), the interlayer water thickness and gravimetric water content from the equation:

$$n_{IL} = \frac{A_s^{int} \cdot d_{IL} \cdot \rho_w}{2 \cdot w} \quad (7.25)$$

where A_s^{int} is the internal specific surface area which is calculated as the difference between total specific surface area and external specific surface area which are measured using the EGME and BET experimental methods, respectively ($A_s^{int} = A_{EGME} - A_{BET}$). w is the gravimetric water content and ρ_w denotes the specific mass of water. d_{IL} represents the average thickness of interlayer water observed by X-ray diffraction analysis (XRD) which is equal to:

$$d_{IL} = d_{basal \text{ spacing}} - d_{smectite \text{ sheet}} \quad (7.26)$$

The XRD results of Kozaki et al. (1998) on a Na-smectite (purified Kunipia-F bentonite with more than 95% sodium montmorillonite) compacted to different dry densities indicated that only three layers of hydrate water can be adsorbed in the interlayer space in the range of smectite dry densities from 980 to 1270 kg/m³ and only two layers of interlayer water at dry densities ranging between 1570-1800 kg/m³. The presence of both 2- and 3-layer hydrate water was observed in smectite dry densities between 1370 and 1470 kg/m³ (Bourg et al., 2006). Based on these observations, Kozaki et al. (2001) calculated the interlayer fraction of pore water assuming that there are only three layers of water in the interlayer space at dry densities of 700 up to 1300 kg/m³ and only two layers of interlayer water from 1400 to 1800 kg/m³.

Bourg et al. (2006) also calculated the interlayer water porosity in saturated compacted Na-smectite assuming that at some ranges of dry densities only 3-layers or 2-layers of hydrate water exist in the interlayer space whilst in a transition state of dry densities both 2-layers and 3-layers of hydrates water co-exist in the interlayer space. They modified the Kozaki et al., (2001) approach to calculate interlayer porosity, given as:

$$n_{IL} = \frac{A_s^{int.}}{2} \left(\frac{\xi_{2-layer}}{d_{2-layers}} + \frac{1-\xi_{2-layer}}{d_{3-layers}} \right)^{-1} \rho_d^{sm} \quad (7.27)$$

where $d_{2-layer}$ and $d_{3-layer}$ are the thicknesses of 2- and 3-layer hydrates water, respectively. The volume fraction of the 2-layer hydrate water in the total interlayer water is expressed by $\xi_{2-layer}$ parameter. This parameter is defined as equal to 0 for the smectite partial dry densities between 980-1270 kg/m³ and equal to 1 for the partial dry densities from 1570 to 1760 kg/m³. At dry densities from 1270 to 1570 kg/m³, Bourg et al. (2006) assumed a linear increase for this parameter which starts from 0 at dry density equal to 1270 kg/m³ and 1 at dry density of 1570 kg/m³.

Figure (7.2) shows the variation of the interlayer porosity of saturated Na-smectite with dry density for pure smectite clay calculated based on the developed model assuming 2 layers of hydrate water. In addition, the results of calculation assuming 3-layers of hydrated water based on the parameters suggested by Liu and Lin (2005) for solid solution model are also presented. The values of interlayer porosity for a Na-smectite calculated and reported by

Kozaki et al. (2001) and calculated values based on the equation proposed by Bourg et al. (2006) are also given by means of comparison.

The results show that the values calculated using the solid solution model considering two layers of hydrate water are lower than those reported by Kozaki et al. (2001) and calculated using the equation proposed by Bourg et al. (2006) at all dry densities. The values calculated using solid solution model considering 3 layers of water are greater than those reported by Kozaki et al. (2001) and calculated using the equation proposed by Bourg et al. (2006) at dry densities greater than 1350-1400 kg/m³ while it is lower in lower dry densities. The results indicate that, in the case of compacted Na-smectite, solid solution model parameters reported by Ransom and Helgeson (1994) or Liu and Lin (2005) might require to be revisited and modified since those parameters have been extracted based on vapour adsorption on powder samples. In addition, the theoretical approximation based on the distance between the sheets and internal specific surface area assumes parallel orientation between the lamellas and ignores the effects of stacking of the lamellas to form particles in compacted smectite.

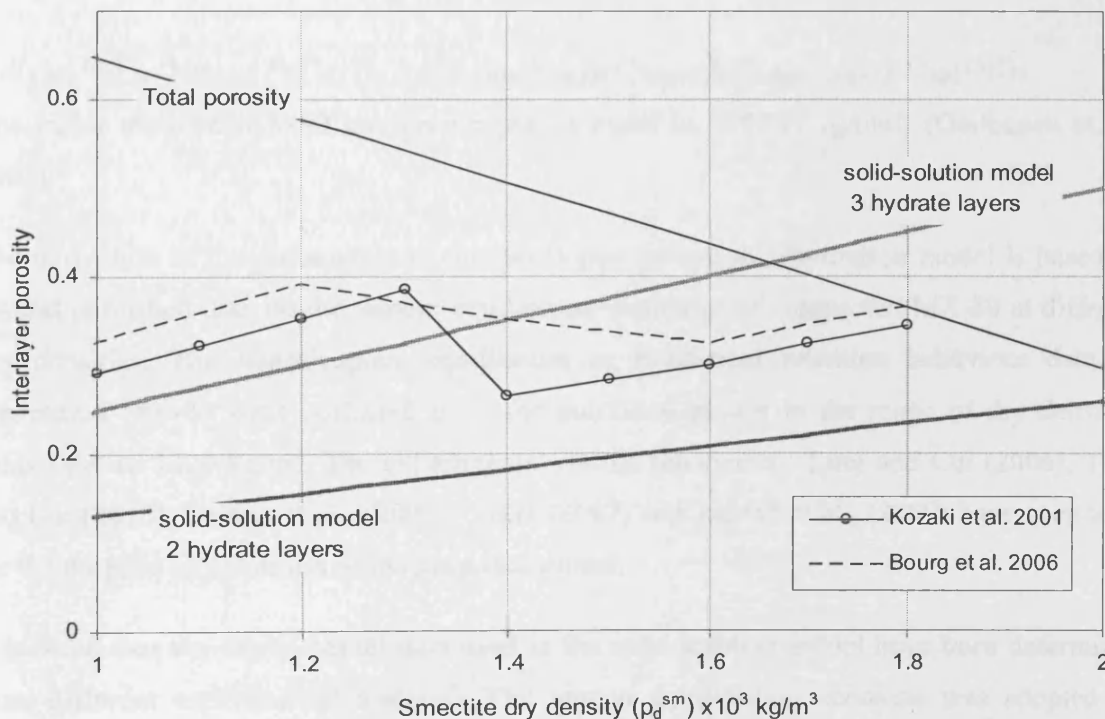
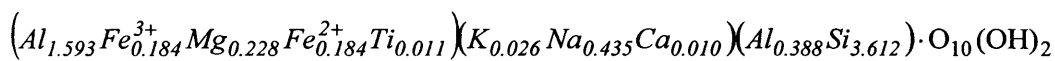


Figure 7.2 Variation of the interlayer porosity with dry density for Na-smectite

7.5.2 Application and adaptation of the solid solution model for compacted MX-80 bentonite

The development of the solid solution model for hydration/dehydration is based on the vapour equilibrium tests on powder smectite and this approach has not been adopted for the case of compacted smectite clays. In order to validate and adopt the solid solution model, in this section, the required thermodynamics parameters of the solid solution model of hydration/dehydration proposed by Ransom and Helgeson (1994) is derived for the case of compacted bentonite. The validity of the solid solution model is explored and improved for the case of compacted bentonite.

MX-80 bentonite is considered as the bench mark for the analyses as it has been the subject of several studies on water retention behaviour. The MX-80 bentonite consists mainly of montmorillonite (65-90%) and the major exchangeable cation is sodium (Villar, 2007). Accordingly the MX-80 is considered as a homo ionic Na-smectite with about 22.5 percents other minerals and impurities. The structural formula for MX-80 smectite has been given as (Gailhanou et al., 2007):



The molar mass of MX-80 has been reported equal to 378.787 (g/mol) (Gailhanou et al., 2007).

The derivation of the parameters of the developed hydration/dehydration model is based on several published data on the vapour equilibrium isotherms of compacted MX-80 at different dry densities. The water/vapour equilibrium or isothermal retention behaviour data on compacted MX-80 were collected from the published results in the range of dry densities from 1400 to 1800 kg/m³. The experimental results reported by Tang and Cui (2006), Tang and Cui (2010), Delage et al., (2006), Villar (2007) and Jacinto et al., (2009) have been used for the purpose of validation of the proposed model.

It is noted that the experimental data used in the solid solution model have been determined from different experimental methods. The vapour equilibrium technique was adopted by Delage et al. (2006) to obtain water retention behaviour of compacted MX-80 at dry density 1700 kg/m³ in a confined condition. Tang and Cui (2005; 2010) reported the water retention

of compacted MX-80 at dry density 1650 and 1820 kg/m³. Villar (2007) reported the retention behaviour of compacted MX-80 at dry density 1300 and 1600 kg/m³ using cell method in which the swelling constrained system is exposed to different relative vapour pressures. In addition the water retention behaviour of compacted MX-80 at dry density 1600 kg/m³ was also presented by Villar (2007) using two other different methods. More recently Jacinto et al., (2009) reported the water/vapour adsorption of compacted MX-80 at dry density of 1600 and 1700 kg/m³ under confined condition and at different temperatures.

Figure (7.3) presents the vapour isothermal retention behaviour of compacted MX-80 at different dry densities at ambient temperature reported in the above mentioned studies. The results are presented in terms of water content (m_w/m_s) versus activity of water (a_{H_2O}). In the graph trends of the data variations have been shown to illustrate the differences.

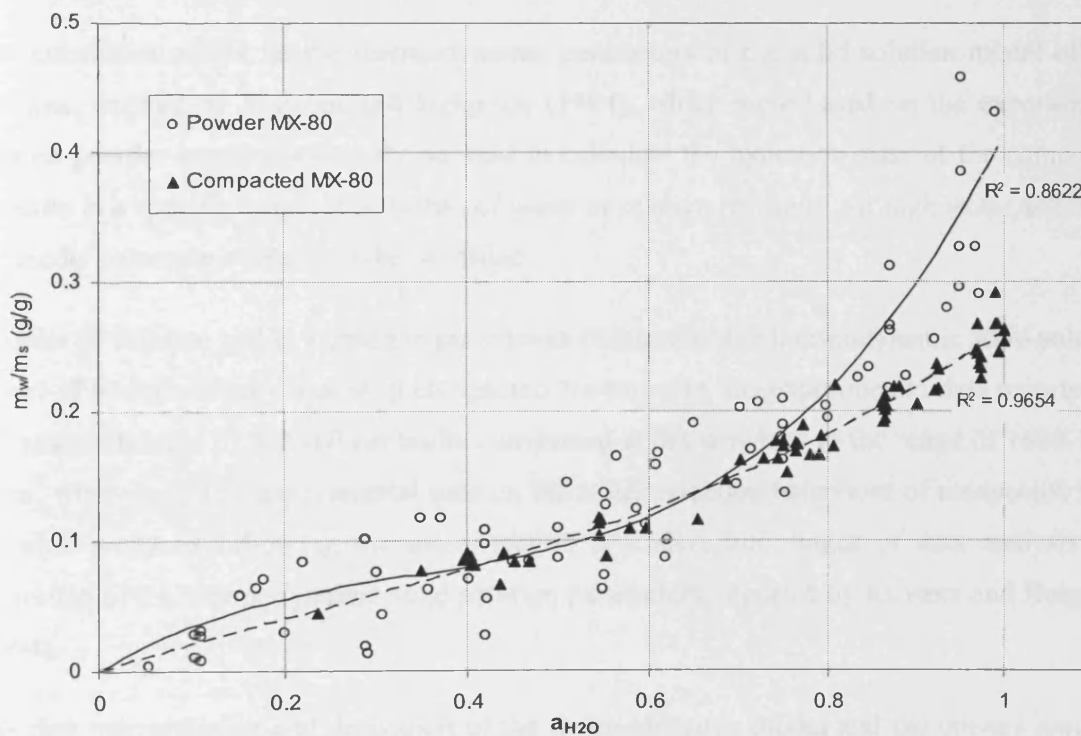


Figure 7.3 Vapour adsorption behaviour in compacted and powder MX-80 reported in the literature. Lines represent the best fitted trend to demonstrate the variation trend

In order to compare the water retention behaviour of MX-80 in compacted form with the powder behaviour, available data on the water retention behaviour of powder MX-80 or Na-Wyoming smectite were also gathered. The results reported by Keren and Shainberg (1975);

Delage et al. (2008), Montes et al. (2003) and Mooney et al. (1952) are also plotted in figure (7.3). Note that Ransom and Helgeson (1994), derived the required solid solution parameters based on the vapour adsorption isotherms, reported by Keren and Shainberg (1975). Indeed, the effects of laboratory methods or errors on the comparison between the reported data have been neglected.

The comparison between the behaviour of compacted and powder samples indicates small difference in the retention behaviour of water compacted samples and powder samples at relative humidity less than about 70-80 %. However, at greater water activity or relative humidity, the behaviour of the compacted samples is different from the powder as powder samples have higher water content compared with the compacted samples. Similar results on the behaviour of compacted and powder samples has been reported in Delage et al. (2005) and Tang and Cui (2010).

One conclusion might be the thermodynamic parameters of the solid solution model of Na-smectite, derived by Ransom and Helgeson (1994), which were based on the experimental data on powder samples, can only be used to calculate the hydration state of the compacted smectite in a specific range of activities of water or relative humidity. At high water activities, the model parameters require to be modified.

In order to validate and evaluate the parameters required of the thermodynamic solid solution model of hydration/dehydration in compacted Na-smectite, the experimental data reported on the water retention of MX-80 bentonite compacted at dry densities in the range of 1600-1800 kg/m³ were used. The experimental data on the water retention behaviour of compacted MX-80 was analysed following the interpretation procedure and stages of data analysis and derivation of the thermodynamic solid solution parameters, reported by Ransom and Helgeson (1994).

The data interpretation and derivation of the thermodynamic model and parameters required the following steps:

1. The amount of adsorbed mass of water in the interlayer space and the equivalent mole of H₂O molecules adsorbed into the interlayer were calculated knowing the amount of total

water at any relative humidity values and the amount of adsorbed water in kaolinite clay at the same relative humidity as suggested by Ransom and Helgeson (1994), using:

$$m_{IL} = (g_s - 2g_k) \frac{M_s}{M_w} \quad (7.28)$$

where m_{IL} represents the molar content of the interlayer H₂O per mole of smectite. g_s and g_k are the total mass of water adsorbed in smectite and kaolinite, respectively measured during water-vapour isothermal test. M_s and M_w stands for the molecular weight of water and smectite.

An exponential regression on the vapour adsorption data of kaolinite, reported by Johansen and Dunning (1959) was used to calculate the amount of moles of water in the interlayer at given relative humidity related to the experimental data reported for the water adsorption behaviour in compacted MX-80

2. The next step was to define the amount of hydrous fraction of smectite (X_{hs}) by knowing the moles of interlayer water and the number of water layers in the interlayer. Villar (2007) reported the basal spacing of compacted MX-80 bentonite at dry densities 1300 and 1600 kg/m³ and at different values of relative humidity. The results indicate that the measured basal spacing of samples does not exceed about 15.55 and 15.99 Å, at low suction values, i.e. 1.3 MPa. The basal spacing of samples is reduced slightly with increasing in the suction values in the range of 1.3 to 19.9 MPa and remains almost in the equivalent thickness corresponding to two monolayers of adsorbed water. It is only dropped to about 12.7 Å which is equivalent to the thickness of one mono layer water in the interlayer space at relatively high suction value of 127.2 MPa. Therefore, in the range of dry densities studied here (i.e., 1600-1800 kg/m³) we assume that no more than two layers of hydrated water exist in the interlayer space which is equivalent to 4.5 water moles in fully hydrated smectite same as the value used by Ransom and Helgeson (1994). Knowing the moles of interlayer water in water-vapour vapour isotherm behaviour, the mole fraction of hydrous component of smectite solid solution assuming two monolayers of interlayer water at fully hydrated state can be given as:

$$X_{hs} = \frac{m_{IL}}{4.5} \quad (7.29)$$

3. The parameter Φ was calculated using equation (7.8) and the variation of this parameter with $2X_{hs}-1$ was produced.
4. Based on equation (7.9), if the best linear variation of parameter Φ versus $(2X_{hs}-1)$ is produced, the Margules parameter and $\log K_{eq}$ of the solid solution reaction of hydration/dehydration can be obtained from the slope of the linear relationship Φ versus $(2X_{hs}-1)$ to obtain the slope of the trend line, i.e. $W_s/2.30RT$ and interception point, i.e. $\log K_{eq}$.

The values of parameter Φ were calculated knowing the activity of water and X_{hs} and plotted versus $(2X_{hs}-1)$ in figure (7.4).

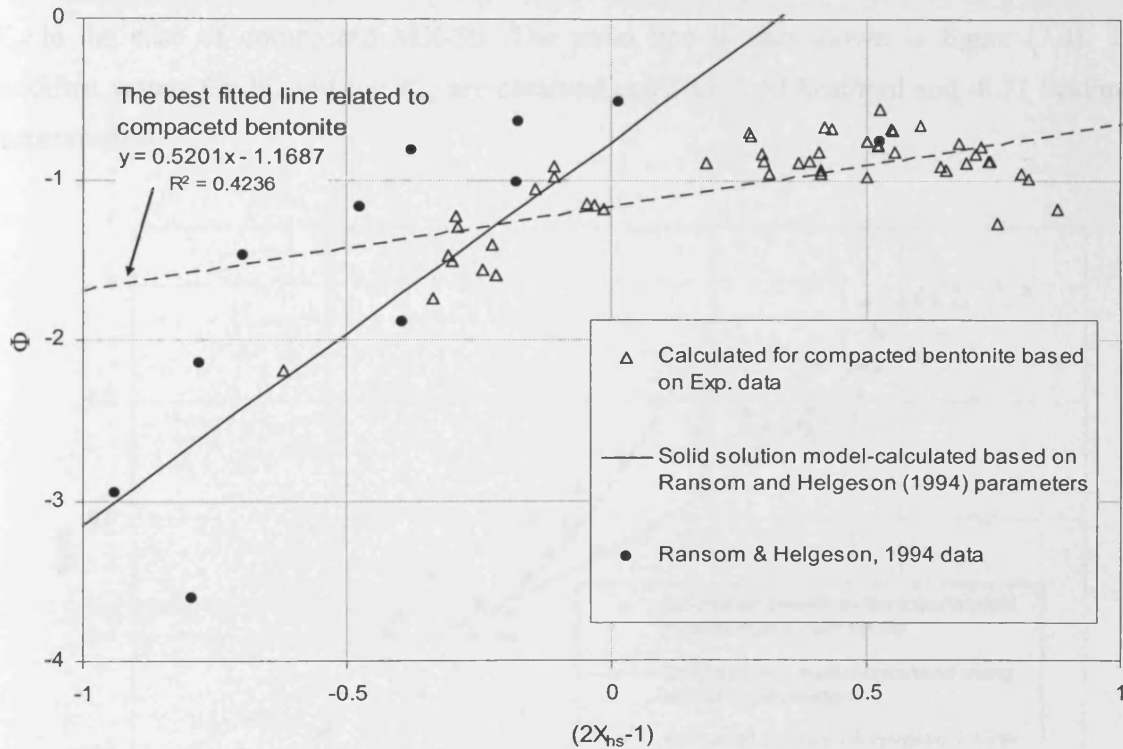


Figure 7.4 Using the linear relationship of Φ versus $(2X_{hs}-1)$ to obtain the slope $W_s/2.30RT$ and intercept $\log K_{eq}$

The linear relationship between Φ and $(2X_{hs}-1)$ as proposed by Ransom and Helgeson (1994) is also presented in figure (7.4) which was calculated based on equation (7.9) and using the Margules parameter and $\log K_{eq}$ reported by Ransom and Helgeson (1994) for Na-smectite (refer to table 7.1). Figure (7.4) also shows the data related to the variation of Φ versus $(2X_{hs}-$

1) which was used by Ransom and Helgeson (1994) to interpolate the best fitted linear relationship of Φ versus $(2X_{hs}-1)$.

The results show that the values of Φ calculated using original parameters of W_s and $\log K_{eq}$ are fitted better within the region where the hydrous fraction of smectite solid solution is lower than 0.5 ($X_{hs}=0.5$) in the experimental data. However for higher hydration states the discrepancy is considerable. This might be due to the fact that in Ransom and Helgeson work which is based on Keren and Shainberg (1975) experiment on powder Na-Wyoming, only one calculated Φ is available which the corresponding hydrous fraction is greater than 0.5 ($X_{hs}>0.5$). Therefore, the interpolation does not include the all ranges of X_{hs} values. Following Ransom and Helgeson (1994), a trend line was interpolated on the results of Φ versus $(2X_{hs}-1)$ in order to generate the parameters of the solid solution model, i.e. W_s and $\log K_{eq}$ in the case of compacted MX-80. The trend line is also shown in figure (7.4). The modified values for W_s and $\log K_{eq}$ are obtained equal to -1.17 kcal/mol and -0.71 kcal/mol, respectively.

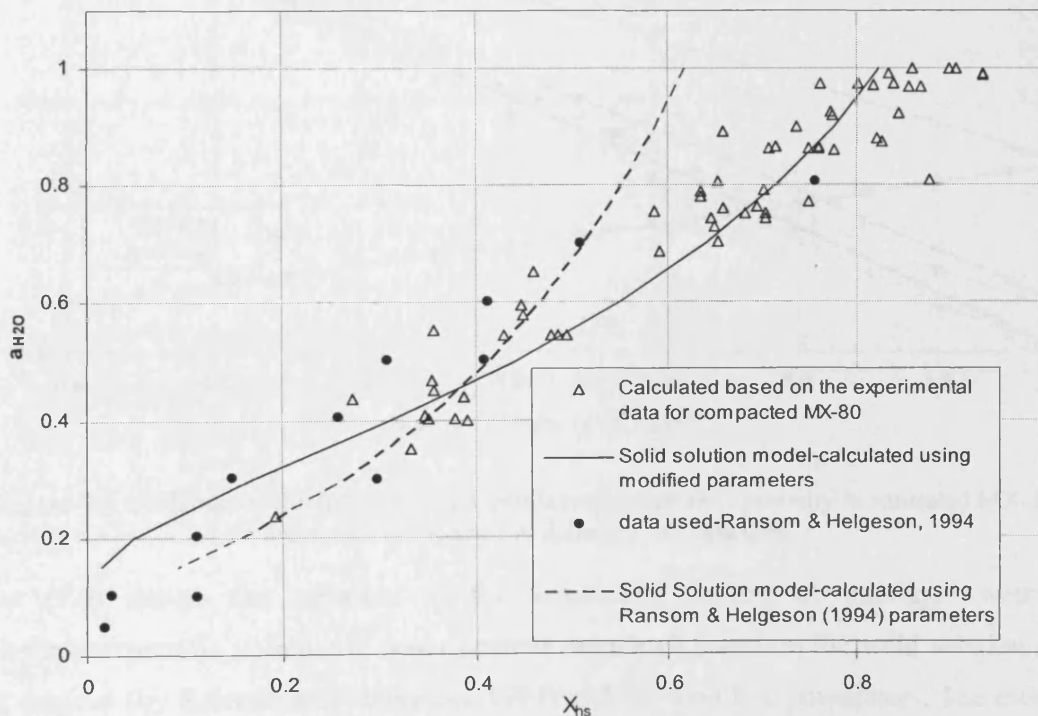


Figure 7.5 Water activity versus mol fraction of hydrous smectite (X_{hs})

The results of the X_{hs} calculated values based on equation (7.9) incorporating the modified W_s and $\log K_{eq}$ are represented in figure (7.5) with the experimental data. The calculated values based on original Ransom and Helgeson parameters are also presented in the figure along with the experimental data used by Ransom and Helgeson (1994). At high water activities, the modified model presents a better correlation with data whilst at low activities of water the original Ransom and Helgeson parameters provide a closer match with the experimental data. The modified parameters of W_s and $\log K_{eq}$ were applied in the solid solution model of hydration/dehydration using equation (7.10) and the volumetric amount of interlayer water of saturated compacted MX-80 at different dry densities were obtained using equation (7.20).

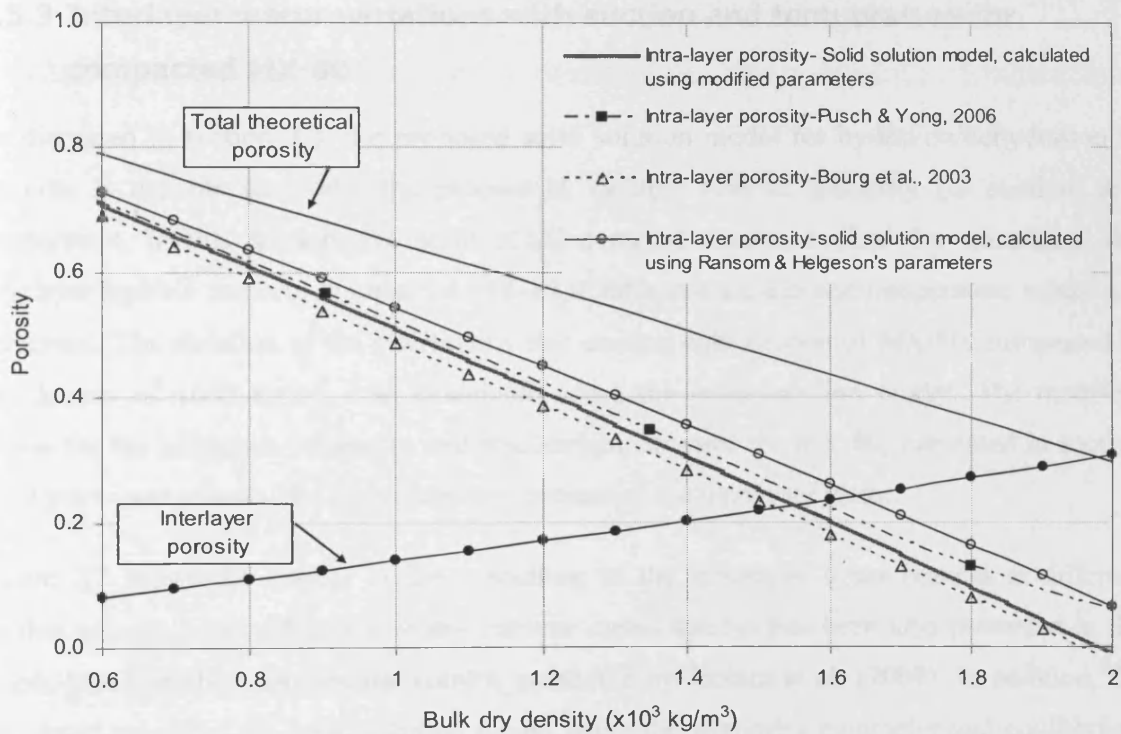


Figure 7.6 Variation of the interlayer and intralayer/interparticle porosity in saturated MX-80 bentonite compacted at different dry densities.

Figure (7.6) shows the variation of the volumetric content of interlayer water and intralayer/interparticle volumetric water content calculated based on the solid solution model using original (by Ransom and Helgeson, 1994) and the modified parameters. The estimated results of the intralayer/interparticle porosity calculated by Bourg et al. (2003) were also presented. They estimated that the interlayer porosity of compacted sodium smectite, considering two layers of hydrates water in the interlayer space is roughly equal

to $n_{IL} = 0.16 \rho_d$. In addition, the variation of the intralayer/interparticle porosity of MX-80 bentonite, reported by Pusch and Yong (2006) have also been shown in the graph.

The results indicate that the calculated values using solid solution model are closely match with those calculated or reported by Bourg et al. (2003) and Pusch and Yong (2006). However, the solid solution model using the original parameters resulted greater values while using the modified parameter are in close agreement with the results of Bourg et al. (2003) and Pusch and Yong (2006).

7.5.3 Interlayer water variations with suction and temperature for compacted MX-80

As discussed in section 7.3, the proposed solid solution model for hydration/dehydration of smectite is capable to model the process at variable relative humidity (or suction) and temperature. In this section, the solid solution model results, applied for calculating the interlayer hydrate water of compacted MX-80 at different suction and temperature values are presented. The variation of the interlayer water content with suction of MX-80, compacted at dry density of 1600 kg/m^3 , was calculated using the solid solution model. The modified values for the Margules parameter and equilibrium constant for MX-80, presented in section 7.5.2 were used to calculate the volumetric content of the interlayer water.

Figure 7.7 shows the results of the modelling of the interlayer water content at different suction values. Total volumetric water content versus suction has been also presented in the graph, based on the experimental results, presented by Jacinto et al. (2009). In addition, the calculated values of the solid solution model using the Margules parameter and equilibrium constant of Na-smectite, proposed by Ransom and Helgeson (1994) was also presented in this figure.

The results show that the interlayer volumetric water content has decreased with increasing suction as the total water content decreases. However the major variation of the interlayer water content occurred in the range of suction values between 1.1×10^7 and 1.1×10^8 Pa using the modified parameters in the solid solution model. The amount of the interlayer water content reaches to a constant value in suction values less than 1.1×10^7 Pa, while the total

amount of interlayer water tends to increase with lowering suction. This indicates that at the mentioned suction value, the interlayer porosity has reached to the maximum saturation and the rest of water exists in the intralayer/interparticle porosity.

The overall trend of variation the amount of interlayer volumetric water content with suction is qualitatively in agreement with the conceptual hydration or water uptake of compacted smectite clays presented by Salles et al. (2009) as discussed in chapter 2. Four major regions can be identified in the graph following the concept of hydration sequences proposed by Salles et al. (2009).

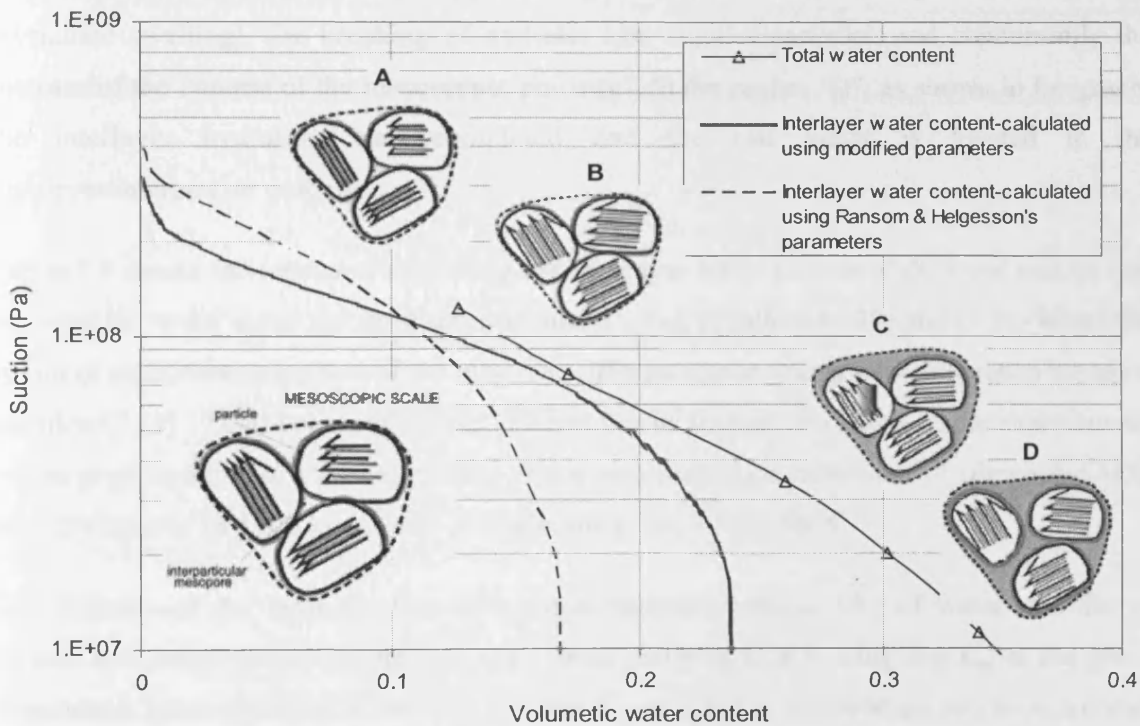


Figure 7.7 Variation of the interlayer and total volumetric water content with suction for MX-80 bentonite compacted at dry densities of 1600 kg/m^3 .

In the region "A", with high suction values, as explained by Salles et al. (2009), the majority of water is likely located in the vicinity of surfaces of the platelets rather than the interlayer space in meso-scale. However, it is difficult to make a conclusion, since there was not experimental data in those ranges of suction. Salles et al. (2009) explained that "*for relative humidity higher than 10%, water enters in the interlayer space hydrating the cations and partially the internal surfaces and simultaneously, water fills completely the mesoscopic*

porosity". The amount of the interlayer water in this region is very low based on the solid solution model using modified parameter, because the solid solution model is based on the concept of complete hydration or dehydration of two layers of hydrate water. However, there might be one monolayer of water remaining even at high suction values.

Between regions "B", and "C", water uptake to the interlayer space was initiated which became almost complete in suction values around 1.1×10^7 Pa. This behaviour is in qualitative agreement with the results reported by Salles et al. (2009). They stated that "at 54% relative humidity, the mesoscopic porosity for Na-montmorillonites is filled. The next step is the further filling of the interlayer space, producing an increase of the interlayer distance (called crystalline swelling), the breaking of particles into smaller particles, and concurrently the increase of the volume of the mesoscopic porosity". In the region "D", as shown in the graph, the interlayer hydration was completed and the rest water is located in the intralayer/interparticle porosity.

Figure 7.8 shows the results of modelling the interlayer water content at different suction and temperature values using the solid solution model using equations (7.10) and (7.20) where the values of equilibrium constant of the model at different temperatures were calculated based on equation (7.13). Total volumetric water content versus suction, are based on the experimental results presented by Jacinto et al. (2009) on the water retention behaviour of compacted MX-80 at dry density of 1600 kg/m^3 and at temperatures 20, 40 and 80 °C.

The variation of the mole fraction of hydrous smectite with activity of water at different suction and temperatures can be calculated from equation (7.10) using $\log K_{eq}$ at the given temperature. As mentioned in section 7.3, $\log K_{eq}$ at a given temperature can be calculated from $\log K_{eq}$ at reference temperature and the values for heat of enthalpy and heat capacity of the reaction, reported by Ransom and Helgeson (1995).

It is observed in figure 7.8 that the values of the interlayer volumetric water content reduced with increasing temperature. Even at relatively low suctions, where the amount of interlayer water content tends to a threshold value, increasing temperature reduces the interlayer water content. In other words, temperature variation induces a water mass exchange between interlayer and intralayer/interparticle space.

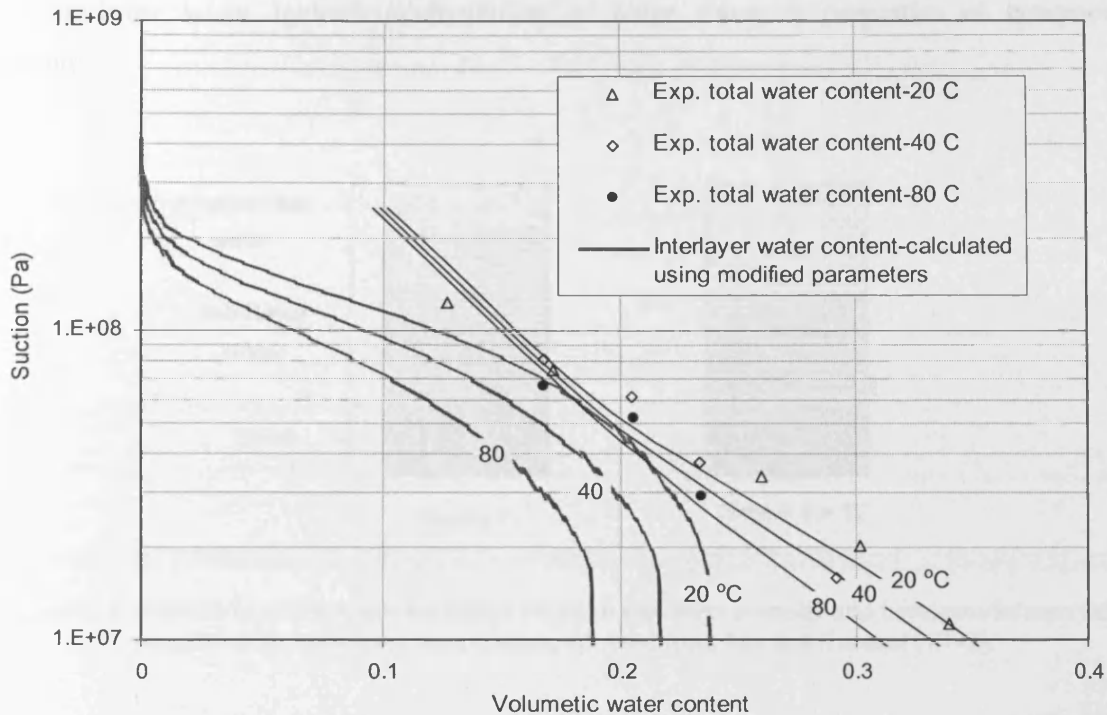


Figure 7.8 Variation of the interlayer and total volumetric water content with suction and temperature for MX-80 bentonite compacted at dry densities of 1600 kg/m^3 .

In fact during heating, the adsorbed water (i.e. interlayer water) may degenerate into bulk water in macro pores that permits the cluster to be contracted and consequences the stack to be collapsed (Derjaguin et al., 1986). According to Ma and Hueckel, (1992), temperature increase results an inter-constituent mass exchange between the adsorbed water in the interlayer pores and the bulk water whose physical properties are similar to the free water. This statement is in agreement with the theoretical calculations based on the solid solution model. This behaviour in saturated condition is illustrated in figure 7.9. As an application, this suggest that in compacted bentonite buffer, in the region close to the heater, the liquid moisture can be exchanged between the adsorbed interlayer phase to free water phase in which dissolved ions exists. As a result, the available space for ions to move is increased.

As presented in previous sections, the developed model for hydration/dehydration and interlayer water content/porosity evolution can be used in variable suction and temperature conditions such as the condition in HLW disposal conditions. The developed model provides a geochemical approach to link between microstructure and pore water/porosity evolution. In following section, the model is extended and applied to include microstructure effects due to

the interlayer water hydration/dehydration in water transport properties of compacted bentonite.

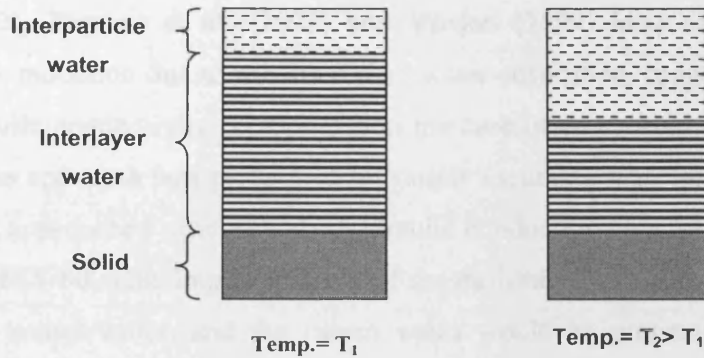


Figure 7.9 Illustration of the water exchange between interlayer porosity and intralayer/interparticle porosity with increasing temperature, adopted from Ma and Hueckel (1992).

7.6 Proposed approach for representing the interlayer water effects on water transport model (an example application of the model)

The developed model for calculating the interlayer water content in compacted smectite clays has potential applications in the modelling of hydraulic, chemical and mechanical behaviour of expansive smectite rich clay. In this section, and as an example application, the effects of the interlayer hydration/dehydration are introduced in simulating the liquid water transport via a modified hydraulic conductivity approach.

7.6.1 Background of the hypothesis

The flow of water in unsaturated clays is controlled mainly by the available porosity for flow of water, i.e. free porosity, and the degree of saturation of the free porosity (e.g. Fredlund and Rahardjo, 1993; Thomas et al., 2003; Thomas et al., 2009). These two factors represent, in total, the amount of volumetric content of the free water in soil. Regarding the water flow in confined compacted swelling clays and in particular compacted smectite clays, Pusch et al. (1990) stated that a proportion of the water that is held in the soil may be absorbed into the

micro-structure and unavailable for flow. If this material is restrained from expanding then the swelling particle would reduce the size of the macro-pores where flow can easily occur (Pusch, 1998).

Mitchell (2002), Thomas et al. (2003) and Vardon (2009) have adopted the concept of macropore size reduction due to the micropore water adsorption, suggested by Pusch (1998), into the hydraulic conductivity relationship in the case of compacted bentonite. As the first assessment, this approach was performed by simply assuming that, for a particular geometry, as the material approached saturation the hydraulic conductivity tends to zero for a compacted bentonite, i.e. MX-80. This implies that all of the moisture in the soil, at this state, would be considered as bound water, and the macro voids would be progressively eliminated. The amount of adsorbed water assumed by Mitchell (2002) and Thomas et al. (2003) was in fact based on Pusch et al. (1990), who estimated that for a sodium montmorillonite of dry density 1730 kg/m^3 , 94 % of the water present in the clay would be bound to the microstructure. It was found that this approach has greatly improved the correlation of the numerical modelling results with the experimentally measured results based on a series of simulations (e.g. Thomas et al., 2003). The approach adopted initially, to assess the validity of the hypothesis was simply to modify the hydraulic conductivity variation to accommodate this effect.

In the modified hydraulic conductivity relationship suggested by Thomas et al. (2003), it was assumed that the transition of water between macro-porosity and micro-porosity happens instantaneously. In other words, the hydration process was considered as a process with a much faster rate than the advective flow of water occurs in the system.

The adsorption of water to the micropores can be a time-dependent process as it has been suggested by Tang and Cui (2005) suggested that this could take a number of months. According to the kinetic nature of water adsorption process, Vardon (2009) proposed a conceptual transient model for water adsorption into the interlayer and adopted this model to modify the hydraulic conductivity. A modified form of the hydraulic conductivity relationship has been proposed by Vardon (2009) for high density swelling clays where the micro-structure changes over time in response to change in degree of saturation. The modified hydraulic conductivity relationship was used in a simulation of non-isothermal moisture transfer in a small scale experiment. Improvements in absolute values and perhaps more

importantly, the temporal gradients, especially at the later stages were reported using the modified hydraulic conductivity relationship.

The amount of water which is adsorbed to the interlayer space or micropores has been approximated in the study presented by Mitchell (2002), Thomas et al. (2003) and Vardon (2009) and there is a real uncertainty about the amount of interlayer water and its variation with suction or temperature. The solid solution model proposed for hydration and dehydration provides a unique platform, to the knowledge of the author, for calculating the equilibrium amount of water which is exchanged between the inter-layer porosity (micropores) and intralayer/interparticle (macropores). In addition, a kinetically controlled formulation can easily be adopted to include the rate of water exchange between two levels of porosities, if the kinetics parameters of water/vapour adsorption to the interlayer are known.

In the following section, a similar approach for modification of hydraulic conductivity due to the interlayer water adsorption proposed by Mitchell (2002), Thomas et al. (2003) and Vardon (2009) is adopted where the equilibrium amount of interlayer water is calculated by the solid-solution model. It is fully recognised that this represents a first attempt only at simulating this behaviour. It is noted that it is assumed that the interlayer hydration/dehydration occurs instantaneously. In other words, the process is studied under equilibrium condition, acknowledging the fact that the process might require to be considered as a kinetically controlled reaction in a more realistic framework.

7.6.2 Modified hydraulic conductivity relationship

Based on the preceding discussion in section 7.6.1 a conceptual model to include the effects of hydration/dehydration of the interlayer on liquid water transport properties of confined swelling clay is presented in this section. It is assumed that the water that is available for flow is only contained within the intralayer/interparticle porosity. In addition, it is assumed that the water transfer between the interlayer and intralayer/interparticle is an instantaneous process. Therefore, it is assumed that the amount of interlayer water is always in equilibrium with total suction and temperature in system.

The basic hydraulic conductivity relationship that has been modified is based upon the approach for MX-80 by Börgesson and Hernelind (1999) as:

$$k_l = k_{sat} (S_l)^\alpha \quad (7.30)$$

where k_l is the unsaturated hydraulic conductivity, k_{sat} is the saturated hydraulic conductivity, S_l is the degree of saturation and α is a parameter usually between 3 and 10 which has been calibrated to 3 for compacted MX-80 and FEBEX bentonite by Börgesson and Hernelind (1999) and Villar et al. (2005), respectively.

Mitchell (2002) defined a relationship for the change in hydraulic conductivity, as a first approximation, based upon a fixed absorbed proportion, taken as 94% for a particular case study, and the assumption that the volume of water absorbed would be equal to the volume of macro-pore reduction, given as:

$$k_l = k_{sat} (S_l)^\alpha (1 - 0.94S_l) \quad (7.31)$$

Vardon (2009) extended this relationship including a time-variant absorbed/free water ratio. The proposed relationship yields:

$$k_l = k_{sat} (S_l)^\alpha (1 - \omega_{abs} S_l) \quad (7.32)$$

where ω_{abs} is the proportion of pore-water absorbed, allowing for time-dependent processes in the absorption of pore-water into the micro-pores.

If the amount of interlayer adsorbed water is calculated using the developed model of hydration/dehydration using equations (7.10), (7.13) and (7.20) which varies with suction and temperature, equation (7.32) can be adopted as:

$$k_l = k_{sat} (S_l)^\alpha (1 - f_{IL}) \quad (7.33)$$

where f_{IL} is equal to the ratio of interlayer volumetric water content (θ_l^{IL}) to the total volumetric water content (θ_l):

$$f_{IL} = \frac{\theta_l^{IL}}{\theta_l} \quad (7.34)$$

It is acknowledged that the modified hydraulic conductivity proposed here might be contradictory with conventional understanding and observations in experimental studies that hydraulic conductivity increases with degree of saturation, and eventually reaches to the saturated hydraulic conductivity. As reported in chapter 2, the results of unsaturated hydraulic conductivity determination in a compacted sand-bentonite by Cui et al. (2008), indicated that under constant-volume conditions when suction was decreasing (during infiltration), the hydraulic conductivity presented an initial decrease followed by an increase after a certain suction which is not in agreement with the traditional understanding about the unsaturated hydraulic conductivity variation. Cui et al. (2008) stated that wetting under constant-volume condition reduced the volume of macro-pore family in the soil, thus decreasing the soil permeability. When the macropores were disappeared, the suction became the only factor which drove the water flow and the hydraulic conductivity increased with further decrease in suction. Mechanisms that occur in different scales of pore size variation and the way these affect the water transport are not fully understood in the literature. The modified relationship proposed here is the initial step to include the effects of the interlayer swelling on decreasing the rate of water flow in confined conditions.

Figure (7.10) presents an example of the variation of hydraulic conductivity with degree of saturation for compacted MX-80 at dry density of 1600 kg/m^3 , calculated using the original relationship proposed by Börgesson and Hernelind (1999) and using the modified relationship presented in equation (7.40).

As it is seen in this figure, with increasing the degree of saturation, hydraulic conductivity is increased both in the relationship proposed by Börgesson and Hernelind (1999) and the modified relationship presented in equation (7.33). However, the rate of increase in the hydraulic conductivity with saturation is much lower in the case of the modified hydraulic conductivity compared with the relationship proposed by Börgesson and Hernelind (1999). This is due to the fact that with increasing degree of saturation, the interlayer water increases and tends toward the maximum value at saturated condition. As a result it reduces the hydraulic conductivity. At low saturation degrees, the hydraulic conductivity is mainly controlled by the power function of the degree of saturation (S_r^α) and the two models yielded same results.

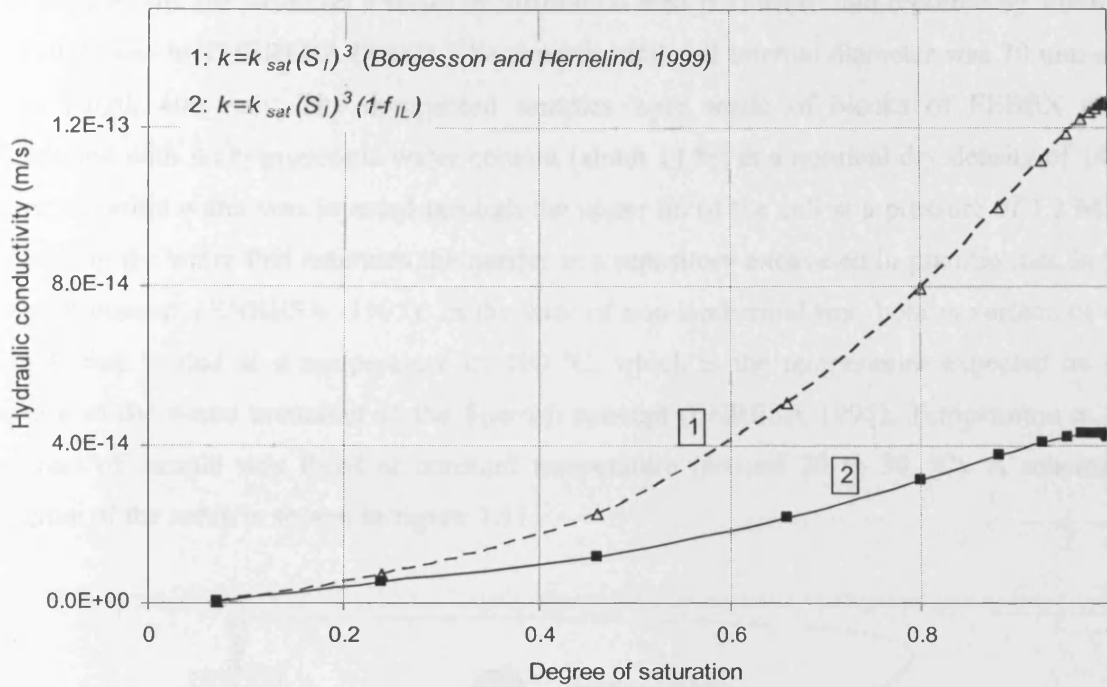


Figure 7.10 Variation of hydraulic conductivity of compacted MX-80 bentonite calculated using the relationship proposed by Børgesson and Hernelind (1999) and using the modified relationship considering interlayer water effects

7.7 Simulation of isothermal and non-isothermal transfer of moisture in compacted smectite clay (FEBEX bentonite)

A series of numerical simulation of small scale laboratory tests on moisture transfer in compacted FEBEX bentonite has been undertaken to validate the proposed modification to the hydraulic conductivity relationship due to the interlayer hydration/dehydration. Two series of numerical simulation results are presented which include the hydraulic behaviour of a 400 mm long cylindrical compacted FEBEX bentonite with a diameter of 70 mm. In the first test, the moisture transfer in compacted clay has been investigated on a sample exposed to the infiltration of water under isothermal condition. In the second simulation, same compacted soil has been under the effects a simultaneous heating and hydration condition. In this test, water was injected from one boundary whilst the soil was exposed to a constant temperature gradient by fixing the temperature at boundaries.

The simulations are based on a series of infiltration tests performed and reported by Villar et al. (2005) and in THERESA (2007). The experimental cell internal diameter was 70 mm and inner length 400 mm. The compacted samples were made of blocks of FEBEX clay, compacted with its hygroscopic water content (about 14 %) at a nominal dry density of 1650 kg/m³. Granitic water was injected through the upper lid of the cell at a pressure of 1.2 MPa, simulating the water that saturates the barrier in a repository excavated in granitic rock in the Spanish concept (ENRESA, 1995). In the case of non-isothermal test, bottom surface of the sample was heated at a temperature of 100 °C, which is the temperature expected on the surface of the waste container in the Spanish concept (ENRESA 1995). Temperature at the top part of sample was fixed at constant temperature (around 20 to 30 °C). A schematic diagram of the setup is shown in figure 7.11.

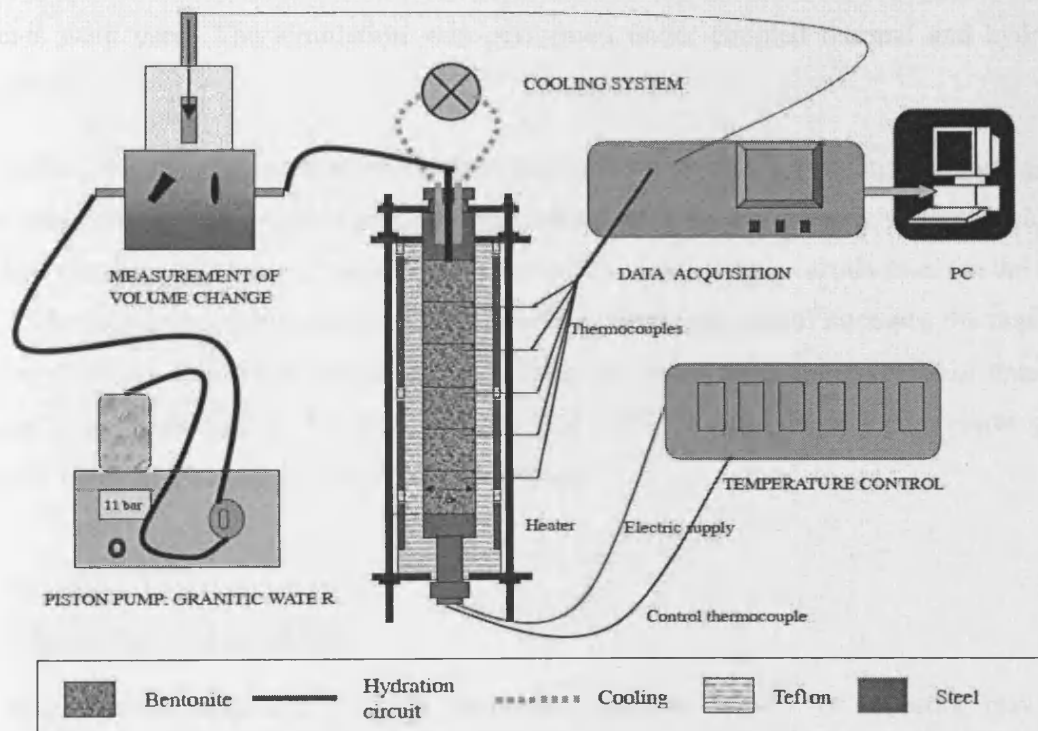


Figure 7.11 Schematic of infiltration experimental set (Villar et al., 2005)

The samples were hydrated from the top end and in the case of the non-isothermal test it was heated from the bottom. Temperature and relative humidity were measured. These sensors were located at 100, 200 and 300 mm away from the heater or hydration boundaries. The results of sensor measurements for up to 30,000 hours were reported by Villar et al. (2005)

which are used for validation of the numerical model and the approach adopted for modelling the effects of interlayer hydration/dehydration on moisture transport.

7.7.1 Model domain and time-step

As shown in figure 7.11 the bentonite cell is of 400 mm height and 70 mm diameter. The simulation was performed under two-dimensional framework using an axi-symmetric analysis, as the domain is symmetrical about the vertical axis. The domain was discretised into 300 unequally sized, 4-noded axi-symmetric elements. A denser mesh was used in the heating boundary region in order to prevent numerical instability and improve the convergence. The first 200 mm in the heating side (bottom) of the sample was discretised into equally sized 1 mm elements. For the rest of the domain, i.e. 200 mm, equally sized 2 mm elements were used. The simulation was performed under coupled thermal and hydraulic framework.

A variable time-step was used, allowing the variation of time-step depending on convergence. Under this scheme, if the convergence criteria are satisfied for the primary variables within a specified numbers of attempts, time-step is allowed to increase by a certain rate. On the other hand, if the primary variables are not converged in a certain number of attempts, the time-step is reduced for the following time of analysis. The maximum time-step and rate of time-step increase was considered as 500,000 seconds and 1.05, yielding more stable convergence based on different trial values used in the simulation.

7.7.2 Material parameters

The clay studied here, i.e. FEBEX bentonite, consists mainly of smectite clay, i.e. montmorillonite 90-92 weight percentage (Fernández et al. 2004). The specific gravity is 2.70 ± 0.04 . The liquid limit of the bentonite is $102 \pm 4\%$ and the plastic limit is $53 \pm 3\%$. The total specific surface area has been determined as $725 \pm 47 \text{ m}^2/\text{g}$. The external specific surface area, determined by N_2 adsorption, is $62 \text{ m}^2/\text{g}$ (ENRESA, 2000; Fernández et al., 2004). The FEBEX bentonite has a high cation exchange capacity, i.e. $\text{CEC} \approx 1000 \text{ meq/kg}$ of dry soil, (ENRESA, 2000; Fernández et al., 2004). The total exchangeable cation (CEC) of the FEBEX

bentonite varies from 96 to 102 meq/100 gr solid. The major exchangeable cations are: Ca^{2+} , Mg^{2+} , Na^+ and K^+ equal to 35-42, 31-32, 24-27 and 2-3 meq/100 g dry soil, respectively (Villar, 2007).

The thermal conductivity of the compacted FEBEX bentonite was adopted from the relationship given by ENRESA (2000). The van Genuchten expression was used for describing moisture retention relationship based on the relationship and parameters provided in ENRESA (2000) for compacted FEBEX bentonite. According to experimental results presented by ENRESA, (2000), the saturated permeability to deionised water (k_{sat} , m/s) of samples of untreated FEBEX bentonite compacted at different dry densities is exponentially related to dry density. Corresponding saturated hydraulic conductivity of the dry density in this simulation study is 3.5×10^{-14} m/s.

The material constants such as density of water, density of solid, specific heat capacity of solid, liquid and vapour, latent heat of vaporisation, Henry's constant and specific gas constant for gas vapour are presented in table 8.8. These constants have been obtained based on Mayhew and Rogers (1976) and ENRESA (2000). All the material relationships and parameters are summarised in table 7.2.

The unsaturated hydraulic conductivity of compacted bentonite is expressed by means of a power law for the relative permeability (ENRESA, 2000). Incorporating the modification due to the interlayer hydrate water, presented in previous section, the general unsaturated hydraulic conductivity of compacted bentonite can be expressed as:

$$k_l = (1 - f_{IL})k_{sat}(S_l)^n \quad (7.35)$$

where f_{IL} is the interlayer water volumetric portion and n is a parameter, given as 3 for this experiment (Villar et al., 2005).

In the case of simulation considering the effects of interlayer water, the amount of interlayer water porosity and subsequently f_{IL} , was calculated using the hydration/dehydration model. The parameters required for the solid-solution model were adopted from those reported by Ransom and Helgesson (1994) including the equilibrium constants and the Margules parameters for the interlayer cations of FEBEX smectite.

The theoretical solid solution model proposed by Ransom and Helgeson (1994) has been developed for smectites with homogenous interlayer cations, e.g. Na-smectite or Ca-smectite. In addition, Ransom and Helgeson (1994) also extended the formulation for smectite with binary mixed ionic layers, e.g. Na/Ca-smectite. However, the application is not as technically feasible as in the range of applications considered in this study, since it includes difficulties and uncertainties regarding the calculations of mixed layer smectite. Instead, the mixed layer smectite is here considered as a parallel system, composed of a several different uniform-layer smectite with a percentage of contribution to the hydration/dehydration process by their percentage weight in CEC.

Table 7.2 Material parameters/relationships

<i>Parameters/relationship</i>	
<i>Thermal conductivity:</i>	
$\lambda = A_2 + (A_1 - A_2) \left[1 + \exp\left(\frac{S_l - x_0}{d_x}\right) \right]^{-1} \quad (W/m.K)$	
$A_1 = 0.57 \pm 0.02, A_2 = 1.28 \pm 0.03, x_0 = 0.65 \pm 0.01, d_x = 0.100 \pm 0.016$	
<i>Water retention:</i>	
$S_l = S_{l0} + (S_{lmax} - S_{l0}) \left[1 + \left(\frac{s}{p_0}\right)^{1-\alpha} \right]^{-\alpha}$	
$p_0 = 30, \lambda = 0.32, S_{l0} = 0.10, S_{lmax} = 1.00$	
<i>Hydraulic conductivity: (m/s)</i>	
$k_l = (1 - f_{IL}) k_{sat} (S_l)^n, \log k_{sat} = -2.96 \rho_d - 8.57, n=3$	
<i>Density of liquid: $\rho_l = 1000$ (kg m⁻³)</i>	
<i>Density of solid: $\rho_s = 2700$ (kg m⁻³)</i>	
<i>Porosity: $n = 0.40$</i>	
<i>Specific heat capacity of soil solids:</i>	$C_{ps} = 870 \quad (J \text{ kg}^{-1} \text{ K}^{-1})$
<i>Specific heat capacity of soil water:</i>	$C_{pl} = 4180 \quad (J \text{ kg}^{-1} \text{ K}^{-1})$
<i>Specific heat capacity of soil vapour:</i>	$C_{pv} = 1870 \quad (J \text{ kg}^{-1} \text{ K}^{-1})$

In the case of FEBEX bentonite, the mixed Ca/Mg/Na/K system of this clay is considered as a composition of homo-ionic Ca-, Mg-, Na- and K- smectites. The fraction of each of these uniform smectites is obtained knowing their cation exchange ratio to the total CEC. This yield to approximately 38.5, 31.5, 25.5 and 2.5 percents of Ca-, Mg-, Na- and K-smectite, respectively, based on the average values of cation exchange composition reported by Villar (2007). The parameters of W_s and $\log K_{eq}$ reported by Ransom and Helgeson (1994, 1995), (refer to table 7.1) were incorporated in the solid solution modelling of hydration/dehydration of FEBEX. The contribution of K-smectite is neglected because of the relatively small ratio.

The correction factors to the vapour fluxes of the Phillip and de Vries model were applied following the suggestions of Melhuish (2004) and Singh (2007) as discussed in chapter 3. The temperature induced vapour flux was modified by a factor of 0.25 and isothermal vapour flux by a 0.7 factor. These values were found to yield appropriate amounts of drying. It is noted that it is difficult to separate the moisture flow into the constitutive vapour and liquid phases and that the calibration of the vapour law will impact the prediction of the hydraulic conductivity. The calibration of η_1 and η_2 is close to the values found experimentally by Sing (2007) for a compacted sample of MX-80 bentonite ($\eta_1=0.16$ and $\eta_2=0.6$). It is noted that η_2 is of less importance due to the lower magnitude of the differential.

7.7.3 Initial and boundary conditions

In all of the simulation cases the initial and boundary conditions are as shown on figure 7.12. The initial conditions are uniform with a temperature of 25 °C (measured) and a pore-water pressure of approximately -90 MPa, corresponding value to the initial degree of saturation equal to 58.6% based on the moisture retention relationship. It is assumed that the temperature is in equilibrium with the laboratory conditions and is equal to 298 K.

Referring to the heating/hydration cell used in the experimental work, at the radial boundary a heat flux is required to be considered in the model representing the heat loss from the cell. Theoretically this heat loss is equal to 2.3 W/m²/K, calculated from the PTFE casing and foam insulation, both 15 mm thick and having thermal conductivities of 0.25 and 0.4W/m/K respectively (Villar et al., 2008). A lower value of heat flux, i.e. 1.78 W/m²/K, was used in simulation compared with the theoretically calculated value to give better correlation for

temperature distribution with those reported in the experiment. This can be explained that in the experimental cell, a layer of air trapped in radial boundary of the sample, may have provided an extra isolation layer. In addition, the radial boundary is prescribed as being hydraulically and chemically impermeable.

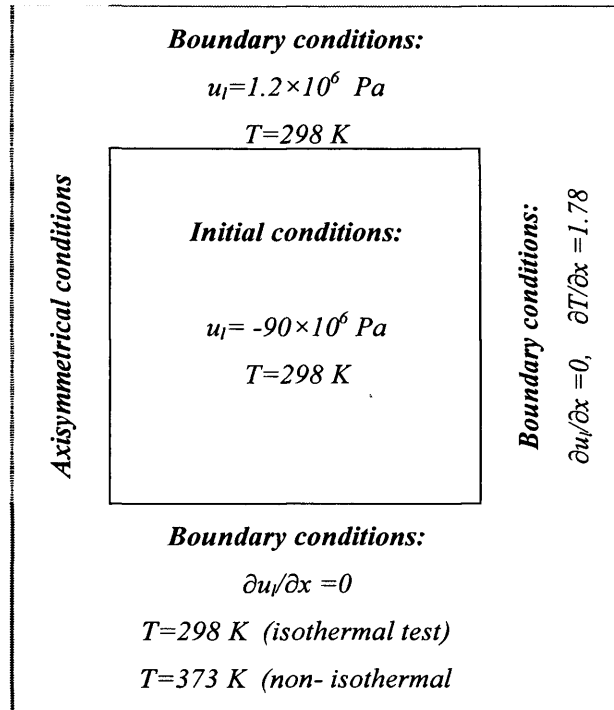


Figure 7.12 Schematic of the initial and boundary conditions for TH simulation of heating and hydration test

In the case of simulation under non-isothermal condition, at the base of the sample the temperature is fixed at 100 °C and is also impermeable. At the top end atmospheric temperature was maintained (and recorded) and a pore-water pressure of 1.2 MPa applied after 65 hours and impermeable before (Villar et al., 2005; THERESA, 2007), as the boundary conditions to reflect these conditions that were applied.

Two series of analyses have been undertaken for both isothermal and non-isothermal infiltration. The hydraulic conductivity relationship once was applied with considering interlayer water correction factor, i.e. $k_l = (1 - f_{IL})k_{sat}(S_l)^n$ and once without considering this effect, i.e. $k_l = k_{sat}(S_l)^n$. The results for each test are compared with the experimental results, reported by Villar et al. (2005).

7.7.4 Simulation results of the isothermal infiltration test

Figure 7.13 shows the results of a simulation of the infiltration experiment under isothermal condition using the modified relationship for the unsaturated hydraulic conductivity by interlayer hydrate water, i.e. $k_l = (1 - f_{IL})k_{sat}(S_l)^n$. Figure 7.14 presents the results using the relationship for the unsaturated hydraulic conductivity without considering interlayer hydrate water effect, i.e. $k_l = k_{sat}(S_l)^n$. The temporal variations of the relative humidity in 100, 200, and 300 mm distance from the heater (bottom) of the cell, resulted from the numerical simulation and measured in the sensors during the experiment, have been presented in both graphs.

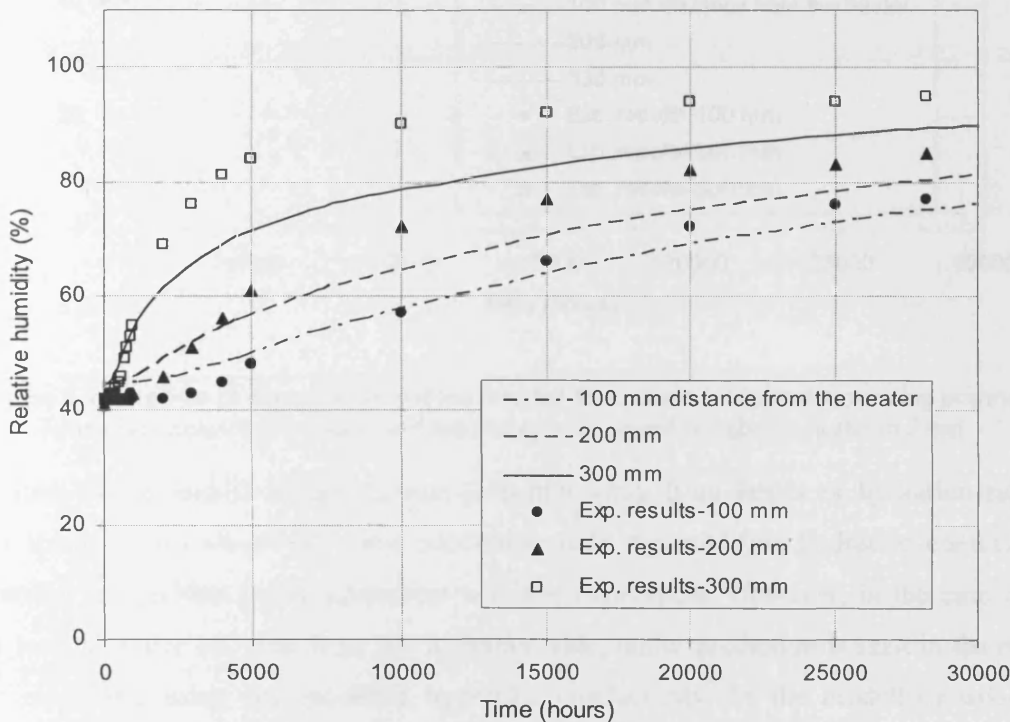


Figure 7.13 Profiles of degree of saturation resulted from numerical simulation using modified hydraulic conductivity relationship (lines) and laboratory experiment (symbols)-isothermal test

The comparison between the results of these two analyses shows that the simulation using modified hydraulic conductivity based on the proposed approach decreased the rate of hydration front. In the bottom boundary (300 mm from the injection water side or 100 mm from the heater), modelling with the original hydraulic conductivity over-predicted the relative humidity in comparison with the measured data. However, the results of the

numerical modelling using the modified hydraulic conductivity are in good quantitative agreement with the experimental results at this point in the sample.

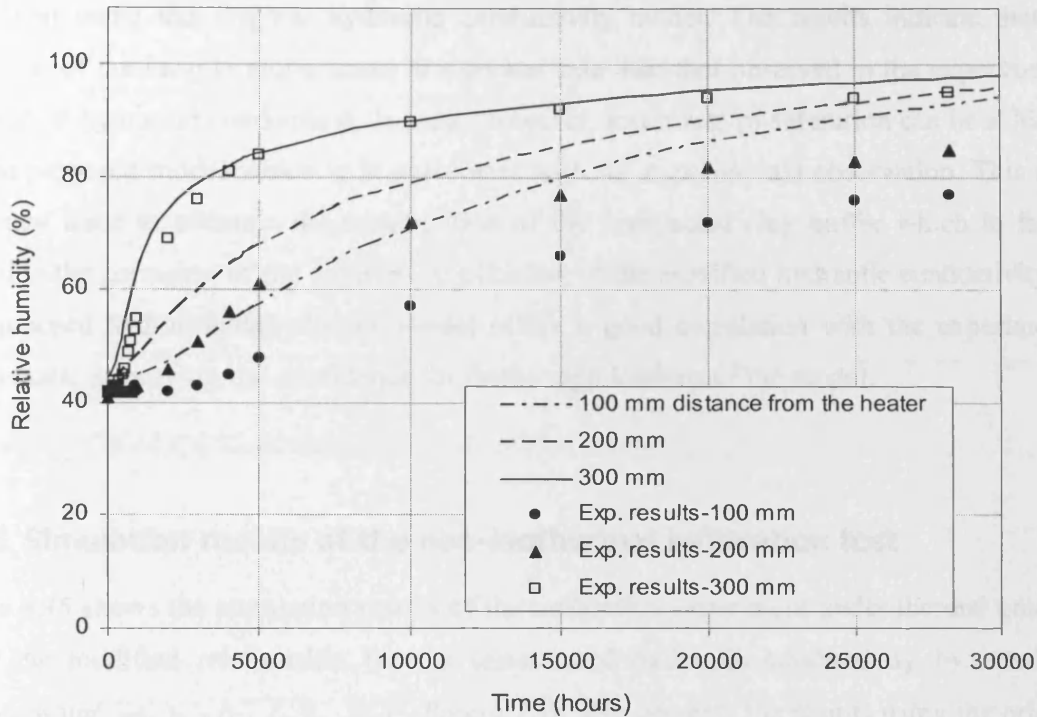


Figure 7.14 Profiles of degree of saturation resulted from numerical simulation using original hydraulic conductivity (lines) and laboratory experiment (symbols)-isothermal test

In the case of the middle sample sensor (200 mm away from heater or hydration side), a similar trend is also observed where modelling with the modified hydraulic conductivity relationship has yielded better agreement with the experiment. However, in the case of the sensor located at the 100 mm from the hydration side, under-prediction is seen in the results of the modelling using the modified hydraulic conductivity. In the modelling using the modified hydraulic conductivity, with increasing the degree of saturation, the fraction of the volume of the soil occupied by the interlayer hydrate water to the total water volume is increased which results to the decline of the rate of saturation and water movement. This mechanism has reduced the overall saturation rate of the sample in comparison with the modelling using the original hydraulic conductivity.

At the bottom end and the middle of the sample, i.e. 100 mm and 200 mm distance from the water injection point, the rate of water from the simulation using the original hydraulic

conductivity is greater than the results of the modelling with the modified hydraulic conductivity. The results of simulation with the modified hydraulic conductivity have shown a closer agreement with the experimental results compared with those obtained from the simulation using the original hydraulic conductivity model. The results indicate that the saturation of the sample might occur at a greater rate than that observed in the experiment if the original hydraulic conductivity is used. However, lower rate of saturation can be achieved via the proposed model which is in agreement with the experimental observation. This is an important issue to estimate the re-saturation of the compacted clay buffer which in fact is related to the corrosion of the canister. Application of the modified hydraulic conductivity via the proposed hydration/dehydration model offers a good correlation with the experimental bench mark, improving the confidence for further applications of the model.

7.7.5 Simulation results of the non-isothermal infiltration test

Figure 7.15 shows the simulation results of the infiltration experiment under thermal gradient using the modified relationship for the unsaturated hydraulic conductivity by interlayer hydrate water, i.e. $k_l = (1 - f_{IL})k_{sat}(S_l)^n$. Figure 7.16 also presents the results using the original relationship for the unsaturated hydraulic conductivity without considering interlayer hydrate water effect, i.e. $k_l = k_{sat}(S_l)^n$. The temporal variations of the relative humidity in 100, 200, and 300 mm distance from the heater (bottom) of the cell, resulted from the numerical simulation and measured in the sensors during the experiment have been presented in both graphs.

The results of modelling using the modified hydraulic conductivity are qualitatively and to some extent quantitatively in good agreement with the experimental results compared with the simulation results using the original hydraulic conductivity. Especially close to the heater, i.e. sensor 3, modelling using the original hydraulic conductivity has highly over-predicted the relative humidity (and moisture content). In the other two locations, i.e. sensors 1 and 2, it is also observed that the original hydraulic conductivity has predicted higher relative humidity than those resulted from the modified relationship. At the hydration side the original hydraulic conductivity relationship and the modified relationship with fixed hydraulic conductivity at saturation, seem to maintain a good fit with the experimental results.

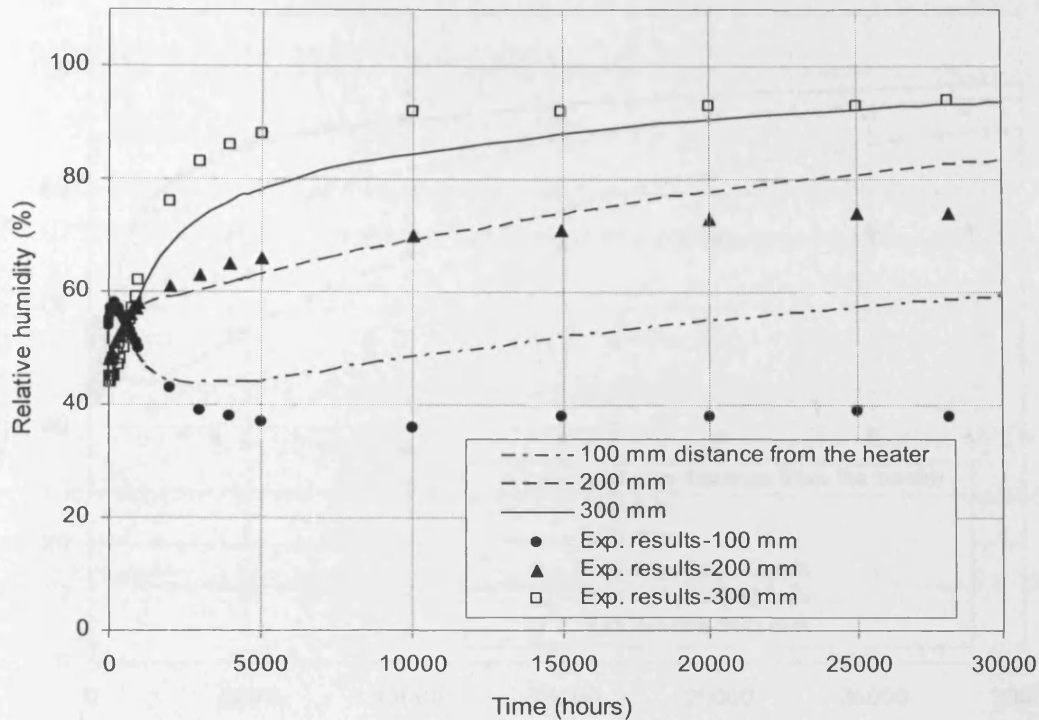


Figure 7.15 Profiles of degree of saturation resulted from numerical simulation using modified hydraulic conductivity (lines) and laboratory experiment (symbols)-non-isothermal test

Similar to the non-isothermal case, variation of the interlayer water has reduced the rate of water migration towards the heater in the modelling with the modified hydraulic conductivity. Importantly the gradients of the relative humidity (and moisture content) with respect to time at the end of the analysis are much improved using the modified hydraulic conductivity which gives more confidence to long term predictive simulations. In fact the modelling results of the isothermal condition using the modified hydraulic conductivity relationship seem to simulate the quantitative and qualitative results well with the important aspect for long term analyses, where the overall saturation of the sample is of the prediction interest.

In the example simulations presented on hydraulic and thermo-hydraulic behaviour of compacted bentonite, the microstructure effects due to the interlayer hydration/dehydration was investigated via the proposed model and the modified unsaturated hydraulic conductivity. As an attempt for coupling between microstructure evolution and macroscopic behaviour, the developed model showed a very good correlation with experimental results.

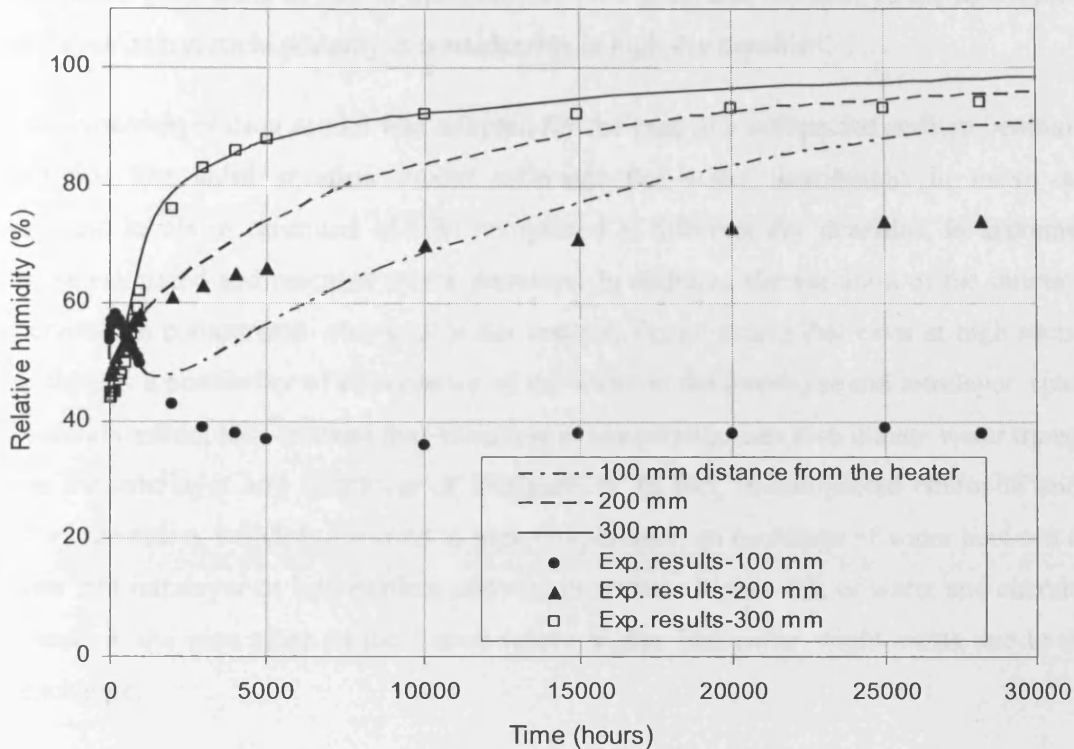


Figure 7.16 Profiles of degree of saturation resulted from numerical simulation using original hydraulic conductivity (lines) and laboratory experiment (symbols)-non-isothermal test

7.8 Conclusions

This chapter presents an approach for modelling the hydration/dehydration process and evaluating the pore water physical evolution in compacted smectite clays based on a geochemical solid solution concept. Utilising the model proposed in this section, the amount of interlayer adsorbed water can be calculated based on a thermodynamic solid solution approach. In addition, the developed model is capable of estimating the interlayer water content variation for a given bentonite at different suctions and temperatures.

The model presented for hydration/dehydration of smectite provides a flexible computing platform for evaluation the interlayer and inter/intra-aggregate porosity or pore water under the variable conditions of suction and temperature. This can help to model the hydraulic and chemical transport processes in compacted swelling clay where the water physical properties

differ in micro pore scale to that in meso/macro pore scale and the ratio of the interlayer to the intralayer/interparticle porosity is considerable at high dry densities.

The hydration/dehydration model was adopted for the case of a compacted sodium bentonite, i.e. MX-80. The solid solution model estimates the water distribution in micro and meso/macro levels in saturated MX-80 compacted at different dry densities, in agreement with those estimated and reported in the literature. In addition, the variation of the interlayer water content in comparison with total water content, demonstrates that even at high suction values, there is a possibility of coexistence of the water in the interlayer and intralayer space. Solid solution model also showed that variation in temperature can also induce water transfer between the interlayer and intralayer or interparticle. In fact, in compacted bentonite under repository condition, which is exposed to high temperature, an exchange of water between the interlayer and intralayer or interparticle porosity provides a higher risk of water and chemical movements in the area close to the heater where higher free water might exist due to this mass exchange.

The microstructure evolution through the interlayer hydration and swelling under confined condition has the potential to delay the re-saturation of the buffer material. This process may change the time when the canister may begin to corrode, which is significant for performance assessment. A modified form of the hydraulic conductivity relationship has been proposed for materials where the micro-structure changes in response to changes in suction and temperature. This is of relevance for high density swelling clays that are proposed to be used in waste isolation. Modification to the existing concept of the modified unsaturated hydraulic conductivity relationships is presented which allows the inclusion of the solid solution model for hydration/dehydration of smectite to be used to calculate the corresponding values of the interlayer porosity.

Two series of small scale experiments on moisture transfer in compacted bentonite under isothermal condition and under thermal gradient have been utilised to compare the modified unsaturated hydraulic conductivity relationship against a standard relationship. The results of the modelling using the modified relationship indicate improvements against the 'standard' relationship. In particular, the behaviour of the highly compacted bentonite in the long term is improved, i.e. the gradients of saturation were improved which may in turn yield significantly

improved long term predictions. This gives increased confidence in longer term predictions made using numerical simulation.

7.9 References

- Bourg, I.C., Bourg, A.C.M., and Sposito, G. (2003). Modeling diffusion and adsorption in compacted bentonite: a critical review. *Journal of Contaminant Hydrology*, 61, 293-302.
- Bourg, I.C. (2004). Tracer diffusion of water and inorganic ions in compacted saturated *sodium bentonite*, PhD Thesis, University of California, Berkeley, USA.
- Bourg, I.C., Sposito, G., and Bourg, A.C.M. (2006). Tracer diffusion in compacted, water-saturated bentonite. *Clays and Clay Minerals*, 54 (3), 363-74.
- Börjesson, L., and Hernelind, J. (1999). *Preliminary modelling of the water saturation phase of the buffer and backfill materials*, SKB, IPR-00-11, Stockholm.
- Cuadros, J. (1997). Interlayer cation effects on the hydration state of smectite. *American Journal of Science*, 297, 829-41.
- Cui, Y.J., Tang, A.M., Loiseau, C., and Delage, P. (2008). Determining the unsaturated hydraulic conductivity of a compacted sand-bentonite mixture under constant-volume and free-swell conditions. *Physics and Chemistry of the Earth, Parts A/B/C*, 33 (Supplement 1), S462-S71.
- Cui, Y.J., Yahia-Aissa, M., and Delage, P. (2002). A model for the volume change behavior of heavily compacted swelling clays. *Engineering Geology*, 64, 233-250.
- Delage, P., Marcial, D., Cui, Y.J., and Ruiz, X. (2006). Ageing effects in a compacted bentonite: a microstructure approach. *Géotechnique*, 56(5), 291-304.
- Derjaguin, B.V., Churaev, N.V., and Muller, V.M. (1987). *Surface Forces*. Plenum, New York.
- ENRESA. (1995). *Almacenamiento Geológico Profundo de Residuos Radiactivos de Alta Actividad (AGP), Diseños Conceptuales Genéricos*. Technical Publication ENRESA 11/95, Madrid.
- ENRESA. (2000). *Full-scale engineered barriers experiment for a deep geological repository for high-level radioactive waste in crystalline host rock, FEBEX project*. EUR 19147, Nuclear Science and Technology Series, European Communities, Luxembourg.

- Fernández, A.M., Baeyens, B., Bradbury, M., and Rivas, P. (2004). Analysis of the pore water chemical composition of a Spanish compacted bentonite used in an engineered barrier. *Physics and Chemistry of the Earth*, 29, 105-118.
- Fredlund, D.G., and Rahardjo, H. (1993). *Soil Mechanics for Unsaturated Soils*. John Wiley and Sons Inc., New York.
- Gailhanou, H., van Miltenburg, J.C., Rogez J., Olives, J., Amouric, M., Gaucher, E.C., and Blanc, P. (2007). Thermodynamic properties of anhydrous smectite MX-80, illite IMt-2 and mixed-layer illite-smectite ISCz-1 as determined by calorimetric methods. Part I: Heat capacities, heat contents and entropies. *Geochimica et Cosmochimica Acta*, 71, 5463-5473.
- Hueckel, T.A., Loret, B., and Gajo, A. (2002), Expansive clays as two-phase, deformable, reactive continua: Concepts and modeling options, *In Chemo-Mechanical Coupling in Clays; From Nano-Scale to Engineering Applications*, Balkema Publisher, 105-20.
- Iwata, S., Tabuchi, T., and Warkentin, B.P. (1995). *Soil-Water Interactions: Mechanisms and Applications*, 2nd edition, Marcel Dekker, New York.
- Jacinto, A.C., Villar, M.V., Gómez-Espina, R., and Ledesma, A. (2009). Adaptation of the van Genuchten expression to the effects of temperature and density for compacted bentonites. *Applied Clay Science*, 42, 575-82.
- Johansen, R.T., and Dunning, H.N. (1959). Water-vapor adsorption on clays. *Clays and Clay Minerals*, 23, 249-258.
- Keren, R., and Shainberg, I. (1975). Water vapour isotherms and heat of immersion Na/Ca-montmorillonite systems I: Homoionic clay. *Clays and Clay Minerals*, 23, 193-200.
- Kozaki, T., Fujishima, A., Sato, S., and Ohashi, H. (1998). Self-diffusion of sodium ions in compacted sodium montmorillonite. *Nuclear Technology*, 121, 63-69.
- Kozaki, T., Saito, N., Fujishima, A., Sato, S., and Ohashi, H. (2001). Diffusion mechanism of chloride ions in sodium montmorillonite. *Journal of Contaminant Hydrology*, 47, 159-70.
- Langmuir, D. (1997). *Aqueous Environmental Geochemistry*. Prentice Hall.
- Likos, W.J. (2004). Measurement of crystalline swelling in expansive clay. *Geotechnical Testing Journal*, 27 (6), 1-7.

- Liu, C.W., and Lin, W.S. (2005). A smectite dehydration model in a shallow sedimentary basin: model development. *Clays and Clay Minerals*, 53 (1), 55-70.
- Liu, J., Yamada, H., Kozaki, T., Sato, S., and Ohashi, H., (2003). Effect of silica sand on activation energy for diffusion of sodium ions in montmorillonite and silica sand mixture. *Journal of Contaminant Hydrology*, 61, 85-93.
- Ma, C., and Hueckel, T. (1992). Stress and pore pressure in saturated clay subjected to heat from radioactive waste: a numerical simulation. *Canadian Geotechnical Journal*, 29, 1087-1094.
- Mayhew, Y.R., and Rogers, G.F.C. (1976). *Thermodynamic and Transport Properties of Fluids*. 2nd edition, Oxford: Blackwell.
- Melhuish, T.A. (2004). *An investigation of the three-dimensional thermo/hydro/ mechanical behaviour of large scale in-situ experiments*. PhD Thesis, Cardiff University.
- Mitchell, H.P. (2002). *An investigation into the thermo/hydro/mechanical interactions involved in high level nuclear waste disposal*. PhD Thesis, University of Wales, Cardiff.
- Montes-H, H., Duplay, J., Martinez, Gerauda, L, and Rousset-Tourniera, B.(2003).Influence of interlayer cations on the water sorption and swelling–shrinkage of MX80 bentonite. *Applied Clay Science*, 23, 309-321.
- Mooney, R.W., Keenan, A.C., and Wood, L.A. (1952). Adsorption of water vapour by montmorillonite, II: effect of exchangeable ions and lattice swelling as measured by x-ray diffraction. *Journal of American Chemical Society*, 74, 1371-1374.
- Philip, J.R., and de Vries, D.A. (1957). Moisture movements in porous materials under temperature gradients. *Transactions American Geophysical Union*, 38(2), 222-232.
- Pusch, R. (1998). Microstructural evolution of buffer clay. *Proceedings of workshop on microstructural modelling of natural and artificially prepared clay soils with special emphasis on the use of clays for waste isolation*. Lund, 31-38.
- Pusch, R., Karnland, O., and Hokmark, H. (1990). *GMM: a general microstructural model for qualitative and quantitative studies of smectite clays*, SKB, Technical Report, SKB-90-43, Stockholm.

Pusch, R., and Yong, R.N. (2006). *Microstructure of Smectite Clays and Engineering Performance*. Taylor and Francis, New York.

Ransom, B., and Helgeson, H.C. (1994). A chemical and thermodynamic model of aluminous dioctahedral 2:1 layer clay minerals in diagenetic processes: Regular solution representation of interlayer dehydration in smectite, *American Journal of Science*, 294, 449-484.

Ransom, B., and Helgeson, H.C. (1995). A chemical and thermodynamic model of aluminous dioctahedral 2:1 layer clay minerals in diagenetic processes: Dehydration of dioctahedral aluminous smectites as a function of temperature and depth in sedimentary ', *American Journal of Science*, 295, 245-281.

Salles, F., Douillard, J.-M., Denoyel, R., Bildstein, O., Jullien, M., Beurroies, I. and Van Damme, H. (2009). Hydration sequence of swelling clays: Evolutions of specific surface area and hydration energy, *Journal of Colloid and Interface Science*, 333(2), 510-522.

Singh, R.M. (2007). *An experimental and numerical investigation of heat and mass movement in unsaturated clays*. PhD Thesis, Cardiff University, Wales, UK.

Tang, A.M., and Cui, Y.J. (2005). Controlling suction by the vapour equilibrium technique at different temperatures and its application in determining the water retention properties of MX-80 clay. *Canadian Geotechnical Journal*, 42, 287-96.

Tang, A.M., and Cui, Y.J. (2010). Effects of mineralogy on thermo-hydro-mechanical parameters of MX80 bentonite. *Journal of Rock Mechanics and Geotechnical Engineering*, 2 (1), 91-96.

Tardy, Y. (1990). Gibbs free energy of formation of hydrated and dehydrated clay minerals. *2nd International Symposium on Geochemistry of the Earth's Surface and of Mineral Formation*. Aix en Provence, France, 255-258.

Thomas, H.R., Cleall, P.J., Chandler, N., Dixon, D., and Mitchell, H.P. (2003). Water infiltration into a large-scale in-situ experiment in an underground research laboratory. *Géotechnique*, 53(2), 207-224.

Thomas, H.R., Cleall, P.J., Dixon, D., and Mitchell, H.P. (2009). The coupled thermal-hydraulic-mechanical behaviour of a large-scale in situ heating experiment. *Géotechnique*, 59(4), 401-413.

van Genuchten, M.Th. (1980). A closed-form equation for predicting the hydraulic conductivity of unsaturated soils. *Soil Science Society of America Journal*, 44, 892-898.

Vardon, P.J. (2009). *A three-dimensional numerical investigation of the therm-hydro-mechanical behaviour of a large-scale prototype repository*. Ph.D. Thesis, Cardiff University, Wales, UK.

Vidal, O., and Dubacq, B. (2009). Thermodynamic modelling of clay dehydration, stability and compositional evolution with temperature, pressure and H₂O activity. *Geochimica et Cosmochimica Acta*, 73(21), 6544-6564.

Villar, M.V. (2007). Water retention of two natural compacted bentonites. *Clays and Clay Minerals*, 55(3), 311-322.

Villar, M.V., Martín, P.L., and Barcala, J.M. (2005). *Infiltration tests at isothermal conditions and under thermal gradient*. CIEMAT, Technical Report CIEMAT/DMA /M2140/1/05, Madrid.

Chapter 8

Numerical Simulation of the Coupled Thermal, Hydraulic and Chemical Behaviour of Compacted Bentonite

8.1 Introduction

This chapter presents the results of the simulation of a heating and hydration experiment carried out by CIEMAT, Spain, on compacted FEBEX bentonite clay as part of a major research study in the framework of FEBEX project (ENRESA, 1998; ENRESA, 2000, ENRESA, 2006). The simulation presented in this chapter aimed to investigate the thermal, hydraulic and geochemical behaviour of compacted bentonite subjected to simultaneous heating and hydration condition, representing the boundary conditions of the buffer material in the geological disposal of HLW. In addition, this simulation exercise will be used to test and validate the model for complex and coupled behaviour which is achieved by comparing the results of the heating and hydration experiments with those obtained from the numerical simulation.

The simulation of the heating and hydration is based on a series of experiments, reported by Villar et al. (2007); Villar et al. (2008a); Villar et al. (2008b) and Fernández and Villar (2010). In these experimental investigations, the FEBEX bentonite samples, compacted at dry density of 1660 kg/m^3 , were hydrated from the top while a thermal gradient was applied sourcing from the bottom of the cell. A large scale and laterally gas- and water-tight experimental cell with an inner length of 600 mm and internal diameter of 70 mm has been used to conduct the experiment for different periods of time ranging from 0.5 to 7.6 years. At the bottom part of the cells a constant temperature of $100 \text{ }^\circ\text{C}$ was set. This temperature is expected at the surface of the waste container in the Spanish disposal concept (ENRESA, 1995). On top of the cell, temperature was controlled and fixed at room temperature (around $20\text{-}30 \text{ }^\circ\text{C}$) using a circulation water tank. The water was injected through the upper surface under a pressure of 1.2 MPa. The injected solution was granitic water with 0.2 % salinity, simulating the water that is likely saturate the barrier in a repository excavated in granitic rock under the Spanish repository concept (ENRESA, 1995). Figure 8.1 shows a schematic diagram of the experimental setup.

Seven experimental tests were conducted in the mentioned cells which included 0.5, 1, 2 and 7.6 years lasting experiments under the mentioned conditions. Temperature in different positions along the bentonite column and water intake were measured and monitored during the tests. At the end of the thermo-hydraulic treatment for each test, the cell was disassembled and the clay columns extracted, weighed and sub-sampled. The experiments were followed by

post-mortem geochemical experimental analyses. The results of temperature, moisture, dry density and pore fluid chemistry have been reported by Villar et al. (2008b) for the longest test in detail. The results of the geochemistry for all test durations were also given and discussed by Fernández and Villar (2010) which will be used to compare the numerical simulation results in this chapter.

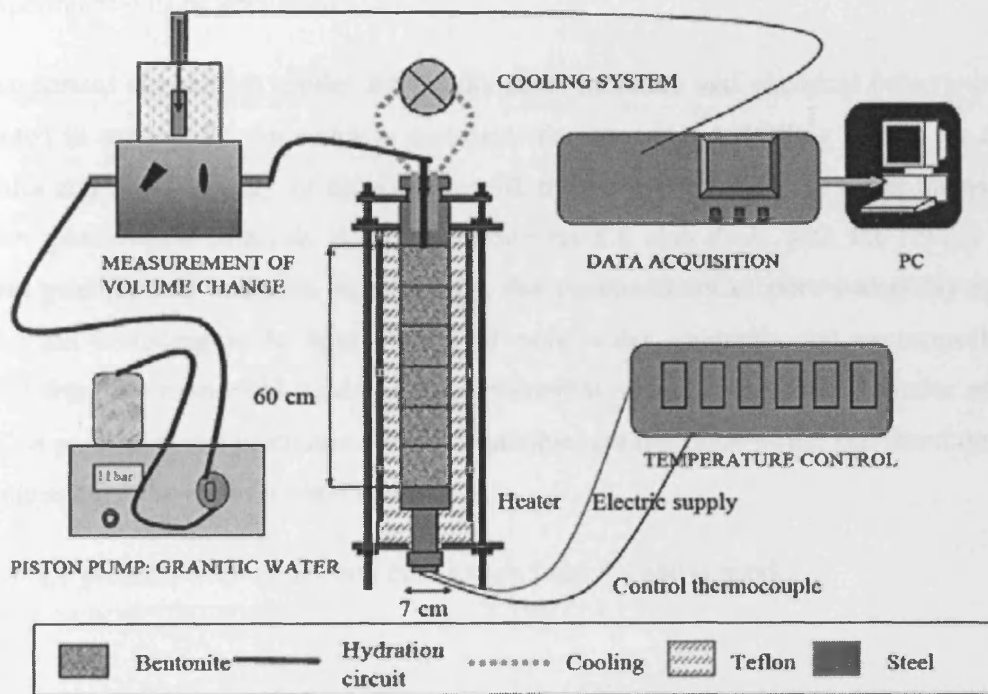


Figure 8.1 Schematic of heating/hydration experimental set on compacted FEBEX bentonite (Villar et al., 2008b)

In section 8.2, some mineralogical and chemical characteristics of the FEBEX bentonite material used in the experiment are discussed. In addition, in order to obtain the initial pore water composition of the compacted FEBEX bentonite and the validity of the geochemical parameter used in the simulation, a geochemical analysis was performed using PHREEQC. This section also presents the result of the geochemical modelling and the evaluation of the initial composition of the pore water and geochemical parameters required for the coupled modelling.

Section 8.3 discusses the results of the post-mortem chemical analysis of the heating and hydration experiments, reported by Fernández and Villar (2010). The hydro-geochemical

post-mortem results are presented which will be used to check the numerical simulations and also to assist with the explanation the complex behaviour of the system.

Section 8.4 presents the numerical simulation of the mentioned large cell heating and hydration experiment. In this section, the assumptions, material parameters and relationships, initial conditions, boundary conditions and the material constants that were used to simulate the experiment will be presented.

The numerical simulation results for temperature, moisture and chemical behaviour will be presented in section 8.5. In order to compare the numerical modelling results for chemical variables and geochemistry of the system with those reported from the experiments, a post-mortem geochemical analysis is required. Section 8.6 also deals with the results of post-mortem geochemical analysis. Accordingly, the geochemistry of pore water-clay system in the domain including ionic composition of pore water, minerals and exchangeable ions, resulted from the numerical model and experimental data provided by Fernández and Villar (2010) is presented and discussed. Where available, comparisons of the simulated results will be made against the experimental results.

Section 8.6 presents a summary and conclusion from the above work.

8.2 FEBEX bentonite and the pore water chemistry

The detailed mineralogical, physical and chemical properties of FEBEX bentonite have been extensively studied and can be found in the literature (e.g. ENRESA, 2000; Fernández et al., 2001; Fernández et al., 2004). The FEBEX bentonite, used in the heating and hydration experiment consists, mainly of smectite clay, i.e. montmorillonite (90-92 wt. %). It also contains numerous accessory minerals (Fernández et al. 2004). Some accessory minerals, such as carbonates, chlorides and sulphates, have been identified in FEBEX bentonite which might influence on the chemistry evolution of the pore water (Fernández et al. 2004). Table 8.1 presents a summary of the mineral composition of typical FEBEX bentonite.

The specific gravity of the FEBEX bentonite has been reported as 2.70 ± 0.04 . The liquid limit of the bentonite is $102 \pm 4\%$ and the plastic limit is $53 \pm 3\%$. The hygroscopic water

content in equilibrium with the laboratory atmosphere is $13.7 \pm 1.3\%$. The total specific surface area has been determined as $725 \pm 47 \text{ m}^2/\text{g}$. The external specific surface area, determined by N_2 adsorption, is $62 \text{ m}^2/\text{g}$ (ENRESA, 2000; Fernández et al., 2001; Fernández et al., 2004).

Table 8.1 Major main and accessory mineral contents of FEBEX bentonite (Fernández et al., 2004)

<i>Main minerals wt %</i>		<i>Accessory minerals wt %</i>	
<i>Smectite</i>	<i>92±3</i>	<i>Organic matter (as CO₂)</i>	<i>0.35±0.05</i>
<i>Quartz</i>	<i>2±1</i>	<i>Carbonates (calcite, dolomite)</i>	<i>0.60±0.13</i>
<i>Plagioclase</i>	<i>2±1</i>	<i>Soluble sulphates (gypsum)</i>	<i>0.14±0.01</i>
<i>Cristobalite</i>	<i>2±1</i>	<i>Low soluble sulphates (barite, celestite)</i>	<i>0.12±0.05</i>
		<i>Chlorides (halite)</i>	<i>0.13±0.02</i>

The FEBEX bentonite has a high cation exchange capacity, i.e. $\text{CEC} \approx 1000 \text{ meq/kg}$ of dry soil, (ENRESA, 2000). Table 8.2 shows the exchangeable cation composition of FEBEX bentonite. Based on the average values of the exchangeable cations shown in table 8.2, the FEBEX bentonite can be represented as a Ca/Mg/Na smectite.

Table 8.2 Average values of cation exchange complex composition of the FEBEX bentonite

<i>cation exchangeable</i> <i>(meq/kg soil)</i>	<i>ENRESA,</i> <i>(2000)</i>	<i>Fernández et al.</i> <i>(2001)</i>	<i>Fernández et al.</i> <i>(2004)</i>
<i>Ca²⁺</i>	<i>420</i>	<i>346.2</i>	<i>331.0</i>
<i>Mg²⁺</i>	<i>320</i>	<i>340.1</i>	<i>331.5</i>
<i>Na⁺</i>	<i>250</i>	<i>311.8</i>	<i>269.5</i>
<i>K⁺</i>	<i>25</i>	<i>19.4</i>	<i>22.9</i>
<i>Sr²⁺</i>	<i>0</i>	<i>0</i>	<i>4.3</i>
<i>CEC</i>	<i>1002</i>	<i>1020</i>	<i>959.2</i>

The initial gravimetric water content of the bentonite sample for the previously-referred heating and hydration experiment is approximately 14%. At such low water content, it is difficult to extract the pore water even by the squeezing technique (Fernández et al. 2001).

Hence, there is no experimental information available as regards the initial conditions of the pore water chemistry of bentonite in this range of compaction. An alternative solution is to simulate the pore water chemistry using a geochemical model knowing necessary material parameters such as selectivity coefficients and mineral composition and by using realistic and available thermodynamic constants. Employing geochemical modelling, the pore water composition of the FEBEX bentonite at different dry densities has been investigated and reported in the literature (e.g. ENRESA 1998; ENRESA 2000; Fernández et al., 2001; Fernández et al., 2004; Seetharam, 2003; Cleall et al., 2007).

The pore water chemistry of FEBEX bentonite compacted at dry density of 1650 kg/m^3 was modelled using PHREEQC version 2.17, in order to obtain the composition of the initial pore water, mineral and exchangeable ions which were applied in the numerical model. This also assisted with validating the geochemical parameters used in the numerical model. This was a necessary step to establish a sound geochemical modelling approach before proceeding with any coupled modelling.

Geochemical modelling of pore water of FEBEX bentonite was conducted at two different solid/water ratios including:

- Solid/water ratio of 100/14, ($w = 14 \%$), representing the initial condition of the compacted bentonite
- Solid/water ratio of 1/4 ($w = 400 \%$), the water content at which the experimental post-mortem chemical analyses were conducted (Fernández and Villar, 2010). The results associated with this water content represent the reference condition of the post-mortem geochemical results for comparison or further discussions.

The geochemical analysis for evaluating the initial/reference pore water composition of the FEBEX bentonite was performed using PHREEQC version 2. Following ENRESA (2000) and Fernández et al. (2001), the geochemical processes that have been considered for the geochemical modelling of the initial pore water in this study can be given as:

- Dissolution-precipitation of minerals including calcite, halite and gypsum

- Ion exchange reactions including sodium, calcium, magnesium and potassium exchangeable ions
- Equilibrium with atmospheric CO₂ partial pressure i.e. $P_{CO_2} \approx 10^{-3.5}$

It was also assumed that the clay mineral is thermodynamically stable at pH values between 7 and 11 (Fernández et al., 2001).

The steps which were followed in the geochemical modelling of the initial pore water composition can be described as:

1. Definition of the initial condition: including the amounts of the mentioned soluble minerals of bentonite, and the content of exchangeable cations of the smectite. The initial values were adopted from those used for a similar simulation by Fernández et al. (2001). Table 8.3 presents the initial values of accessory mineral and exchangeable cations in the model.
2. Determination of the thermodynamics of mineral reactions and selectivity coefficients for the exchange reactions. The values of selectivity coefficients for exchange reaction reported by Fernández et al. (2001) were employed. For mineral reactions the data-base of *phreeqc.dat* of PHREEQC version 2.17 (Parkhurst and Appelo, 1999) was used. A summary of the equilibrium constants for the ion exchange reactions is presented in table 8.4. The thermodynamics parameters of mineral reaction are also given in table 8.5.
3. Equilibration of the whole system with pure water with pH 7.72.

The results of geochemical modelling the pore water composition of the FEBEX bentonite in equilibrium with distilled water are presented in table 8.6 at two gravimetric water contents of 0.14 and 4. The results of a similar modelling by Fernández et al. (2001) corresponding to the water content of 0.14 is also presented for comparison. In the case of initial pore-water chemistry of bentonite with the water content of 4, the aqueous extract results reported by Fernández et al. (2004) and Fernández and Villar (2010) are also provided by means of comparison.

Table 8.3 Average values of accessory minerals and cation exchange complex of the FEBEX bentonite adopted in pore water geochemical analysis from Fernández et al. (2001)

<i>Mineral/Exchangeable</i>	<i>Amount (mol/kg dry soil)</i>
<i>Calcite</i>	<i>0.060</i>
<i>Gypsum</i>	<i>0.010</i>
<i>Halite</i>	<i>0.022</i>
<i>Ca-X₂</i>	<i>0.171</i>
<i>Mg- X₂</i>	<i>0.167</i>
<i>Na-X</i>	<i>0.304</i>
<i>K-X</i>	<i>0.019</i>

Table 8.4 Equilibrium constants of ion exchange reactions for the FEBEX bentonite adopted from Fernández et al. (2001)

<i>Cation exchange reactions</i>	<i>Log K_{eq} at 25 °C</i>
<i>Na-X=Na⁺ + X</i>	<i>0.0</i>
<i>Ca-X₂=Ca²⁺ + 2X</i>	<i>0.774</i>
<i>Mg-X₂=Mg²⁺ + 2X</i>	<i>0.655</i>
<i>K-X=K⁺ + X</i>	<i>0.878</i>

Table 8.5 Thermodynamic parameters used for dissolution/precipitation of minerals adopted from *phreeqc.dat* data-base of PHREEQC version 2 (Perkhurst and Appelo, 1999)

<i>Mineral reactions</i>	<i>Thermodynamic data</i>	
	<i>Log K_{eq} at 25 °C</i>	<i>ΔH_r⁰ (kcal)</i>
<i>Anhydrite</i> <i>CaSO₄=Ca²⁺ + SO₄²⁻</i>	<i>-4.360</i>	<i>-1.710</i>
<i>Gypsum</i> <i>CaSO₄·2H₂O=Ca²⁺ + SO₄²⁻ + 2H₂O</i>	<i>-4.580</i>	<i>-0.109</i>
<i>Halite</i> <i>NaCl=Na⁺ + Cl⁻</i>	<i>1.582</i>	<i>0.918</i>
<i>Calcite</i> <i>CaCO₃=Ca²⁺ + CO₃²⁻</i>	<i>-8.480</i>	<i>-2.297</i>

The results show that the initial concentration of ions at a water content of 14 % is different from those resulted for at water content of 400 % equal to 1/4 aqueous extract results, with the exception of chloride ion that the total molar mass of chloride per unit weight of the soil remains constant. It has also been found experimentally that unlike other ions which might be influenced by precipitation-dissolution and ion exchange reactions, the chloride ions vary linearly as a function of the solid/liquid ratio (ENRESA, 2000; Fernández et al., 2001).

A close agreement can be seen between the results this study and those reported by Fernández et al. (2001). From the results presented in table 8.6, it can be observed that the modelled results agree very closely with the experimental results of aqueous extraction, with the exception of magnesium. This could be attributed to the modelling assumption where only carbonate mineral was considered in the precipitation/dissolution reaction whilst FEBEX bentonite contains both calcite and dolomite. Nevertheless, there is a general agreement between the modelled and experimental results.

Table 8.6 The results of geochemical analysis of pore fluid composition for the FEBEX bentonite at two solid/water ratios

<i>FEBEX Bentonite pore water composition</i>	<i>soil/water ratio=100/14 water content=14%</i>		<i>soil/water ratio=1/4 water content=400%</i>	
	<i>PHREEQC This study</i>	<i>PHREEQC by Fernández et al. (2001)</i>	<i>PHREEQC This study</i>	<i>Experimental results Fernández et al. (2001)</i>
<i>Cl⁻ (mol/l)</i>	1.58×10^{-1}	1.59×10^{-1}	5.56×10^{-3}	4.95×10^{-3}
<i>SO₄²⁻ (mol/l)</i>	3.47×10^{-2}	3.27×10^{-2}	2.57×10^{-3}	2.45×10^{-3}
<i>HCO₃⁻ (mol/l)</i>	4.32×10^{-4}	4.09×10^{-4}	2.27×10^{-3}	2.96×10^{-3}
<i>Ca²⁺ (mol/l)</i>	2.23×10^{-2}	2.29×10^{-2}	1.83×10^{-4}	1.25×10^{-4}
<i>Mg²⁺ (mol/l)</i>	2.70×10^{-2}	2.34×10^{-2}	2.16×10^{-4}	1.37×10^{-4}
<i>Na⁺ (mol/l)</i>	1.29×10^{-1}	1.30×10^{-1}	1.21×10^{-2}	1.25×10^{-2}
<i>K⁺ (mol/l)</i>	1.11×10^{-3}	1.68×10^{-3}	1.08×10^{-4}	1.83×10^{-4}
<i>pH</i>	7.73	7.72	8.60	8.73

The results of the geochemical analysis of pore fluid at water content equal to 0.14 have been used as the initial geochemical condition of the compacted bentonite in the numerical

simulation in terms of the initial conditions for major dissolved chemicals, ion exchange and mineral composition. In addition, the results of the pore fluid composition analysis at soil/water ratio equal to 1/4 have been used as the reference composition when the results of post-mortem model are compared with the experimental results.

8.3 Hydro-geochemical results of the heating and hydration experiments

As reported in section 8.1, at the end of the thermo-hydraulic treatment for each heating and hydration test, reported by Villar et al. (2008 a,b), the cell was disassembled and the clay column extracted, weighed and sub-sampled. Once the bentonite column was extracted, it was sawn into 24 cylindrical sections of 25 mm in thickness and post-mortem geochemical analyses were conducted on each section (Fernández and Villar, 2010). The appearance of the compacted bentonite sample upon extraction is presented in figure 8.2.

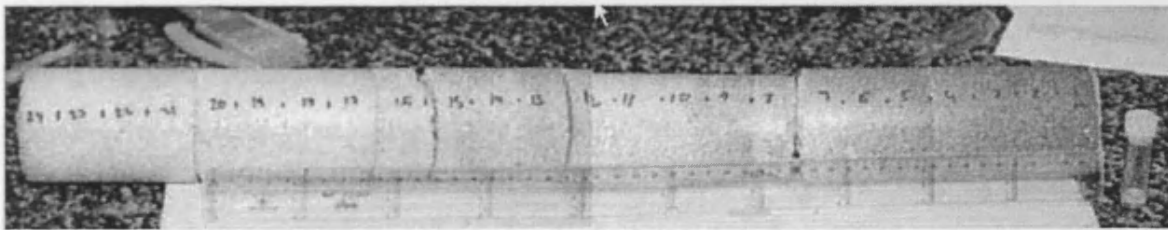


Figure 8.2 Appearance of the bentonite column after two years of heating and hydration upon extraction and establishment of the 24 sampling sections (adopted from Fernández and Villar, 2010)

8.3.1 Experimental methodologies of post-mortem analyses

The experimental investigations and methodologies described below were applied to determine the geochemical and mineralogical properties of the FEBEX bentonite in each of the sections at the end of the heating and hydration tests.

In terms of mineralogical analysis, XRD (X-Ray Diffraction), SEM (Scanning Electron Microscopy) and FTIR (Fourier transform Infrared) tests were conducted. X-Ray diffraction patterns were obtained on random powders and in oriented aggregates in order to identify the mineralogical phases in the bentonite samples. Scanning electron microscope examinations were used to define the microstructure of the minerals, the possible alteration products and the

accessory minerals. FTIR spectra can serve as a fingerprint for mineral identification and provides information about mineral structure, degree of regularity within the structure, nature of isomorphic constituents (e.g. the nature of the octahedral cations in clay minerals), distinction of molecular water from constitutional hydroxyl, and presence of both crystalline and non crystalline impurities (Fernández and Villar, 2010).

The pore water of the bentonite was obtained by two different techniques, squeezing and aqueous extract tests. The soluble elements were determined in aqueous extract solutions. In the aqueous extract technique, the subsamples were crushed without previous drying, and placed in contact with deionised, degassed water at a solid to liquid ratio of 1:4, shaken end-over-end and allowed to react for two days under atmospheric conditions. After phase separation by centrifugation the supernatant solutions were filtered through syringe filter and analysed.

The pore water of the most hydrated sections of some of the tests was obtained and reported by the squeezing technique (Cuevas et al., 1997; Fernández, 2004). In this method, a squeezer was designed to compress the sample uniaxially by means of an automatic hydraulic ram operating downwards, the squeezed water being expelled through a system of filters into vacuum vials at the top and bottom of the cell. Once the water extraction was completed, the water sample was collected, avoiding any contact with the atmosphere, weighed, filtered and it was analysed.

8.3.2 Experimental results of post-mortem analyses

The distribution of water content along the bentonite column at the end of the heating and hydration tests reported by Villar et al. (2008a) is shown in figure 8.3. This figure also shows the variation of the dry densities measured along the bentonite column at the end of the tests.

In terms of moisture variations in the cell, a significant gradient can be observed even in the longest test. The results show that the water content increased within the closest 20 cm from the hydration surface in the 6-month test, and within 40 cm in the 12- and 24- month tests. In the 7.6-year test the increase of water content took place all over the column except in the 10 cm closest to the heater (Villar et al., 2008a). The dry density decreases from the heater

towards the hydration surface following an approximately linear trend. The dry density varied in the domain caused by the different swelling of the bentonite, since the most hydrated sections have swollen more (Villar et al., 2008a, b). After 6 months, the closest 18 cm to the heater experienced a desiccation that is not recovered after 24 months; hence in this area, the water content remained below the initial value, being close to 6% in the vicinity of the heater. In the areas affected by hydration, the densities decreased below the initial value (nominal 1650 kg/cm^3) due to the expansion caused by saturation. On the contrary, near the heater, the dry density increased, due to the shrinkage caused by desiccation (Villar et al., 2008a).

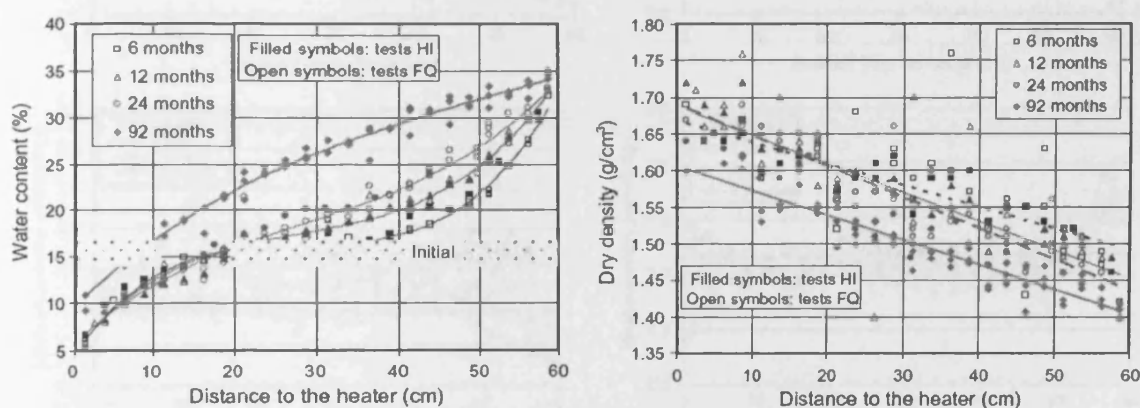


Figure 8.3 Final water content and dry densities along the bentonite columns of the different tests performed at 0.5-, 1-, 2- and 7.6 years (Villar et al., 2007, 2008a,b). FQ and HI: Tests for hydro-mechanical and geochemical post-mortem analyses, respectively.

With regards, to the mineralogical studies, Fernández and Villar (2010) reported that the mineral phases observed in the XRD results were similar to those of the untreated sample. The observations performed with the SEM technique in samples taken at different positions along the bentonite columns from the different tests indicated different accessory minerals (chlorides, sulfates and carbonates) seemed to have formed at different positions along the bentonite columns, depending on the duration of the tests and the extension of the hydration front. No obvious change was observed by FTIR analyses in the FEBEX bentonite samples after the 7.6-a heating and hydration test.

Figure 8.4 presents the concentrations of major soluble ions measured in aqueous extracts, i.e. obtained by mixing soil and deionised water in a 1/4 ratio, and reported by Fernández and Villar, (2010). In general, the aqueous extracts showed that there were changes in

concentration along the bentonite columns in all the tests, as reflected by their electrical conductivity, which clearly increased towards the heater (Fernández and Villar, 2010).

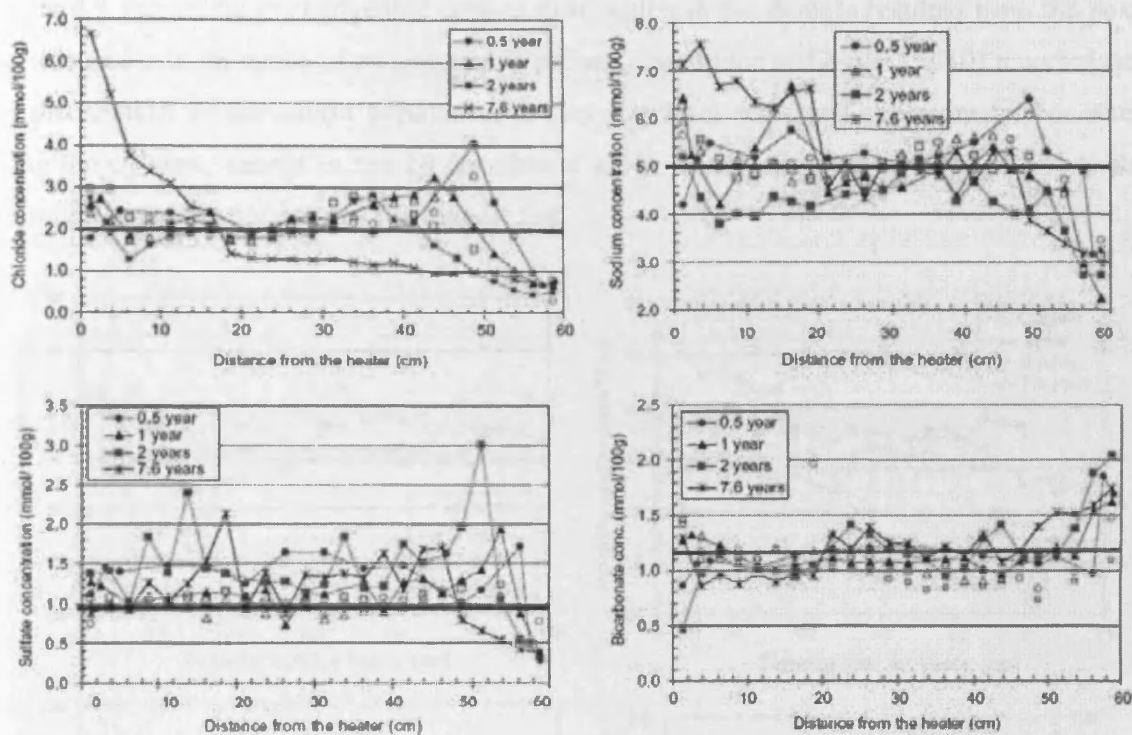


Figure 8.4 Concentration of ions obtained from 1:4 aqueous extracts (in mmol/100 g dried clay) of samples taken at different positions along the bentonite columns from different duration tests (thick lines: reference values) (Fernández and Villar, 2010).

It is observed in figure 8.4 that the maximum chloride content along the bentonite column varied as a function of the test duration. Chloride was almost removed from the more hydrated 40 cm of bentonite, whereas its concentration showed a sharp gradient in the 20 cm closest to the heater, reaching 7 mmol/100 g at the bottom of the cell. The main counter ion that followed the chloride movement in all the tests was sodium, decreasing close to the hydration source and increasing towards hotter zones, especially in the longest test. Sulfate was leached at the hydration source and moved more slowly than chloride ions. Bicarbonate concentrations showed a different behaviour in the wet and hot zones. Close to the hydration surface there was a clear increase in bicarbonate concentrations in all the tests. In the rest of the bentonite column, there were slight changes in the concentration of bicarbonate with a general tendency to decrease. Fernández and Villar (2010) also reported that in all of the tests, there has been an increase in the soluble Mg^{2+} , Na^+ , K^+ and Ca^{2+} concentrations close to the

heater, whereas the K^+ content also increased near the hydration source, decreasing the Na^+ content.

Figure 8.5 shows the exchangeable cations distribution in the domain resulted from the post-mortem analysis. In terms of exchangeable cations, Fernández and Villar (2010) reported that the distribution of the cation population at clay interlayer remained approximately constant along the column, except in the 20 cm closest to the heater and in the 14 cm closest to the hydration source in the case of the longest test.

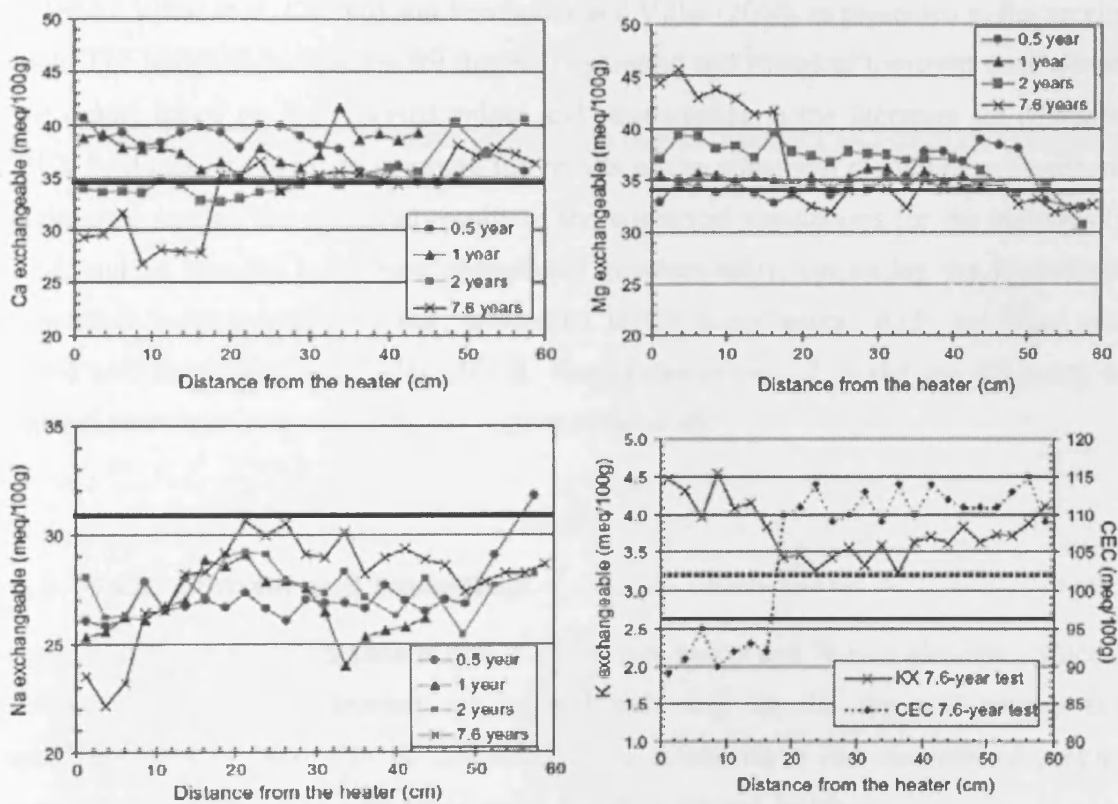


Figure 8.5 Distribution of the cation exchange population along the bentonite columns at different periods of time (Fernández and Villar, 2010).

The Ca^{2+} exchange population was reported higher in the vicinity of the hydration surface and clearly decreased close to the heater zone. The exchangeable Mg^{2+} concentration decreased close to the hydration source and increased significantly in the 15 cm closest to the heater. The exchangeable Na^+ tended to decrease along the whole bentonite column, but this tendency was particularly apparent close to the hydration surface and especially in the 20 cm closest to the heater (where exchangeable Mg^{2+} and K^+ concentrations increased, and

exchangeable Ca^{2+} also decreased). In the case of K^+ exchange population; although there was a slight increase along the entire bentonite column, this tendency was more prominent towards the heater and close to the hydration surface.

8.4 Numerical simulation of the heating/hydration test

This section deals with the numerical simulation of the coupled thermal, hydraulic and chemical behaviour of the heating and hydration tests on compacted FEBEX bentonite reported by Villar et al. (2008b) and Fernández and Villar (2010) as presented in the previous section. The required parameters for thermal, hydraulic and chemical transport were adopted in the model based on the reported values and relationships in the literature for compacted FEBEX bentonite. In order to compare the results of the numerical modelling with reported experimental results, the chemical results of the numerical simulations for the periods of 6, 12, 24, and 92 months have been re-analysed geochemically, simulating the post-mortem geochemical batch equilibrium test, conducted in the experimental study by Villar et al. (2008b) and Fernández and Villar (2010). Finally the results of model are discussed and compared with those reported from the experimental study.

8.4.1 Model domain and time-step

As shown in figure 8.1 the bentonite cell is of 600 mm height and 70 mm diameter. Since the hydration water and the heating are applied uniformly on the top and bottom faces respectively, this problem can be construed to be effectively a one-dimensional problem. However the modelling was performed under two-dimensional problem.

The domain was discretised into 500 unequally sized, 4-noded axi-symmetric elements. An axi-symmetric analysis was used, as the domain is symmetrical about the vertical axis. A denser mesh was used in the heating and hydration boundary regions in order to prevent numerical instability and improve the convergence. The first 200 mm in the heating side (bottom) and the hydration side (top) of the sample was discretised into equally sized 1 mm elements. For the rest of the domain, i.e. 200 mm in the middle, equally sized 2 mm sized elements were used.

A variable time-step was used, allowing the variation of time-step depending on convergence. Under this scheme, if the convergence criteria are satisfied for the primary variables within a specified numbers of iterations, time-step is allowed to increase by a specified rate. On the other hand, if the primary variables are not converged in a certain number of attempts, the time-step is reduced for the following time of analysis. The maximum time-step and increase rate of time-step were considered as 500000 seconds and 1.05, respectively. These values provided a better convergence rate compared with some other trial values.

The simulation was performed under coupled thermal, hydraulic and chemical framework. It is noted that the mechanical and deformation behaviour was not considered in the model. However the effects of variation in the available porosity for the flow of water and chemicals due to the hydration or heating were partly considered through the implicit modification of the hydraulic conductivity with interlayer hydration/dehydration effects, as discussed in chapter 7.

As it can be observed in the experimental results of dry density variation, reported by Villar et al. (2008a) and Villar et al. (2008b) shown in figure 8.3, dry density changed from the initial value of around 1650 kg/m^3 to the a maximum range of $1700\text{-}1750 \text{ kg/m}^3$ in the area close to the heater and to a minimum of approximately $1400\text{-}1450 \text{ kg/m}^3$. This indicates that the total porosity could theoretically be reduced to 0.35 in the vicinity of heater and increased to 0.47 in the hydration zone from the initial values of approximately 0.39. The effect of porosity variation in the heater zone is small. However, in the hydration side, since the cell was constrained for swelling the increase in the porosity is supposed to reduce the intralayer/interparticle porosity (macropores) which was considered implicitly in the hydraulic transport. Therefore the contribution of the mechanical/deformation modelling effects are likely to be less effective in comparison with direct effects of thermal, hydraulic and chemicals effects, acknowledging the fact that towards understanding the swelling pressure development in the system and more accurate justifications of the coupled processes, mechanical behaviour is also an important element of the model.

8.4.2 Material parameters and relationships for modelling of thermal and hydraulic processes

The material parameters and relationships for thermal and hydraulic simulation are similar to those presented in section 7.7.2 of chapter 7. For sake of completeness these parameters are presented in details here.

The material constants such as density of water, density of solid, specific heat capacity of solid, liquid and vapour, latent heat of vaporisation, Henry's constant and specific gas constant for gas vapour are presented in table 8.7. These constants have been obtained based on Mayhew and Rogers (1976) and ENRESA (2000).

Table 8.7 Material constants used in the numerical modelling

<i>Constants</i>	<i>Values</i>
<i>Density of liquid, ρ_l at 25 °C (kg m⁻³)</i>	1000
<i>Density of solid, ρ_s (kg m⁻³) (Martin et al., 1998),</i>	2700
<i>Porosity, n</i>	0.40
<i>Specific heat capacity of soil solids C_{ps} (J kg⁻¹ K⁻¹) (Martin et. al, 1998)</i>	870
<i>Specific heat capacity of soil water, C_{pl} (J kg⁻¹ K⁻¹) (Mayhew and Rogers, 1976)</i>	4180
<i>Specific heat capacity of soil vapour, C_{pv} (J kg⁻¹ K⁻¹) (Mayhew and Rogers, 1976)</i>	1870
<i>Latent heat of vaporisation, L (J kg⁻¹) (Mayhew and Rogers, 1976)</i>	2.4×10^6
<i>Specific gas constant for water vapour, R (J kg⁻¹ K⁻¹) (Mayhew and Rogers, 1976)</i>	461.5

The thermal conductivity of the compacted FEBEX bentonite was adopted from the relationship given by ENRESA (2000) as:

$$\lambda = A_2 + \frac{A_1 - A_2}{1 + \exp\left(\frac{S_l - x_0}{d_x}\right)} \quad (8.1)$$

where λ is the thermal conductivity in W/m.K, S_l is the degree of saturation, A_1 is the value of λ for $S_r = 0$, A_2 is the value of λ for $S_r = 1$, x_0 is the degree of saturation for which the thermal conductivity is the average value between the extreme values, and d_x is a parameter. The values of these fitting parameters, based on the experimental evidence, are as follows (ENRESA, 2000):

$$A_1 = 0.57 \pm 0.02; A_2 = 1.28 \pm 0.03; x_0 = 0.65 \pm 0.01; d_x = 0.100 \pm 0.016$$

The van Genuchten expression was used for describing the moisture retention relationship based on the relationship and parameters provided in ENRESA (2000) for compacted FEBEX bentonite. The parameters for van Genuchten's moisture relationship (van Genuchten, 1980) have been given also in ENRESA (2000) for a range of initial dry densities. The general form of the degree of saturation-suction relationship for compacted FEBEX bentonite used in the simulation is given as:

$$S_l = S_{l0} + (S_{lmax} - S_{l0}) \left[1 + \left(\frac{s}{p_0} \right)^{\frac{1}{1-\alpha}} \right]^{-\alpha} \quad (8.2)$$

where, S_{l0} and S_{lmax} are the residual and maximum degree of saturation and p_0 (MPa) and α are material constants. These parameters depend on the initial dry density of the soil.

For the experiment under consideration, the average dry density of the bentonite clay is approximately 1650 kg/m^3 in the in-placed condition (Villar et al. 2008b; Fernández and Villar, 2010). Corresponding to this dry density the fitting parameters for the above equation are as follows (ENRESA, 2000):

$$p_0 = 30; \lambda = 0.32; S_{l0} = 0.10; S_{lmax} = 1.00$$

According to experimental results presented by ENRESA, (2000), the saturated permeability to deionised water (k_{sat} , m/s) of samples of untreated FEBEX bentonite compacted at different dry densities is exponentially related to dry density (ρ_d , g/cm^3). An empirical relationship for

saturated hydraulic conductivity has been proposed as a function of dry density for compacted FEBEX bentonite as:

$$\log k_{sat} = -2.96\rho_d - 8.57 \quad (8.3)$$

This relationship is valid for the dry densities range between 1470 and 1840 kg/m³ (Villar et al., 2008b). Corresponding saturated hydraulic conductivity of the dry density in this simulation study is 3.5×10^{-14} m/s.

The unsaturated hydraulic conductivity of compacted bentonite is often expressed by means of a power law for the relative permeability (ENRESA, 2000). Incorporating the modification due to the interlayer hydrate water, presented in chapter 7, the general unsaturated hydraulic conductivity of compacted bentonite can be expressed as:

$$k_l = (1 - f_{IL})k_{sat}(S_l)^n \quad (8.4)$$

where f_{IL} is the interlayer water volumetric portion and n is a constant which has been given as 3 for this experiment (Villar et al., 2008a).

Table 8.8 Parameter used in the hydration/dehydration model for the FEBEX bentonite in order to calculate interlayer hydrate water content or equivalent porosity

<i>Parameters</i>	<i>Ca-smectite</i>	<i>Mg-smectite</i>	<i>Na-smectite</i>
<i>Percentage %</i>	37	34	29
W_s (kcal/mol)	-2883	-2806	-3254
$\log K_{eq}$ at 25 °C	-3.61	-4.28	-0.767
ΔH_r^0 (kcal/mol)	9630	10609	5810

In order to calculate the amount of interlayer water porosity and subsequently f_{IL} , the hydration/dehydration model presented in chapter 7 was employed. Using this model, the amount of interlayer water porosity can be calculated knowing the suction and temperature. To apply the hydration/dehydration model for calculating interlayer porosity, the smectite clay portion of FEBEX bentonite, i.e. 92% of total solid, was considered as a complex of Ca-, Mg- and Na-smectite with percentage of each ion, as it was presented in table 8.2. For the sake of completeness the required parameters for each smectite component were adopted from

those reported by Ransom and Helgeson (1994) in the interlayer hydration model. A summary of parameters used in the modelling of hydrate water amount is given in table 8.8.

8.4.3 Material parameters and relationships for modelling of the reactive transport of chemicals

As stated in chapter 3 the effective diffusion coefficients for chemical diffusion in the formulation are obtained knowing the water tracer diffusion coefficients of each species and the tortuosity factors. According to equation (3.153), the relationship applied for determination of the effective tracer diffusion coefficients in the model is:

$$D_i^{eff} = nS_i\tau_i D_i^0 \quad (8.5)$$

where τ_i is the tortuosity factor for the i^{th} component. S_i represents the degree of saturation and n is porosity. D_i^0 is tracer diffusion coefficient in water for the i^{th} component.

The values of tracer diffusion coefficients of ions in water at 25 °C are shown in table 8.9 according to the values reported by Lasaga (1998).

Table 8.9 Tracer diffusion coefficients of the ionic species involved in the simulation

<i>Chemical component</i>	<i>D⁰_i (m²/s)</i>
	<i>Lasaga (1998)</i>
<i>Cl⁻</i>	<i>2.03 × 10⁻⁹</i>
<i>SO₄²⁻</i>	<i>1.07 × 10⁻⁹</i>
<i>HCO₃⁻</i>	<i>1.18 × 10⁻⁹</i>
<i>Ca²⁺</i>	<i>0.79 × 10⁻⁹</i>
<i>Mg²⁺</i>	<i>0.70 × 10⁻⁹</i>
<i>Na⁺</i>	<i>1.33 × 10⁻⁹</i>
<i>K⁺</i>	<i>1.96 × 10⁻⁹</i>

At variable temperature but fixed composition and pressure, self or tracer diffusion coefficient of ions in pure solution can be extrapolated from one to another temperature based on the

Stokes-Einstein relationship (Cussler, 1997). Similar approach was used to calculate the variation of tracer diffusion coefficients with temperature, given in equation (3.154):

$$\left(D_i^0\right)_T = \left(D_i^0\right)_{T_0} \frac{\eta_{T_0}}{\eta_T} \frac{T}{T_0} \quad (8.6)$$

where η represents the viscosity of solvent, i.e. water in this case. T_0 is the reference temperature.

The effect of porosity and moisture content on diffusion coefficient was considered using a similar relationship proposed by Revil and Jougnot (2008) for unsaturated diffusion coefficients of ions in porous media. As reported in chapter 2, different effective porosities for diffusion of anionic and cationic species should be considered in the case of compacted smectite clays, representing the effects related to the interlayer hydrate water and diffuse double layer development in the system. Accordingly, the tortuosity factor proposed by Revil and Jougnot (2008) was modified and the porosity was replaced by the effective porosity. The modified relationship used in this simulation can be given as:

$$\tau_i = \left(n_{eff}^i\right)^{n-1} \left(S_i - S_i^c\right)^{m-1} \quad (8.7)$$

where n_{eff} is the effective porosity for diffusion of ionic species. S_i^c is the percolation threshold for degree of saturation, suggested by Revil and Jougnot (2008). m and n are constants. In this study the values of S_i^c , m and n are considered equal to 0, 2.5 and 2.75, respectively.

As discussed in chapter 2, the values of effective porosity for anions diffusion can be approximated from:

$$n_{eff} = n - n_{IL} - n_{DDL} \quad (8.8)$$

where n is the total porosity, n_{IL} represents the interlayer porosity and n_{DDL} is the porosity associated with developed diffusion layer.

The interlayer porosity was calculated by the hydration/dehydration model proposed in chapter 7. The model gives the amount of the interlayer porosity at saturated state and ambient temperature equal to about 0.27. The effective porosity for chloride diffusion has been given in the range of 0.02-0.03 for FEBEX bentonite compacted at dry density of 1650

kg/m^3 and at saturated state (García-Gutiérrez et al., 2004). DDL porosity was approximated as a constant value of 0.105 for the anionic species to produce the effective porosity using equation 8.8 in the range of 0.02-0.03 at saturated state, i.e., $n_{eff} = 0.4 - 0.27 - 0.105 = 0.025$. Including the above tortuosity factor and volumetric water content using the above equations, the corresponding value for the effective diffusion coefficient for chloride in FEBEX bentonite compacted at dry density of 1650 kg/m^3 and at saturated condition is obtained equal to $1.27 \times 10^{-12} \text{ m}^2/\text{s}$ which is close to the experimentally determined value of approximately $1.1 \times 10^{-12} \text{ m}^2/\text{s}$ reported by García-Gutiérrez et al. (2004). For all anionic species same tortuosity factor was applied.

The effective porosity of cations was assumed as the effective porosity for water tracer HTO diffusion, given as total porosity in compacted bentonite soils (García-Gutiérrez et al., 2004; Mekior et al. 2009). In the simulation presented here, the effective porosity for cations was considered as the total porosity. However it is noted that higher diffusion rate for cations than HTO has been also reported due to the interlayer diffusion or surface diffusion, as discussed in chapter 2.

Applying total porosity to the tortuosity factor equation for cations, the effective diffusion coefficient for cations is obtained in the range of 6.32×10^{-11} to $1.56 \times 10^{-10} \text{ m}^2/\text{s}$. These values are also in agreement with the values reported for HTO effective diffusion coefficient equal to $5.8 \times 10^{-11} \text{ m}^2/\text{s}$, for compacted saturated FEBEX bentonite at dry density of 1650 kg/m^3 (García-Gutiérrez et al., 2004).

Regarding the geochemical reactions, similar assumptions made for the evaluation of the initial pore water composition of the FEBEX bentonite, presented in section 8.2, were considered in the simulation of reactive transport of chemicals. Only in the case of calcite reactions, dissolution and precipitation of calcite was considered under kinetically controlled condition to model the more realistic behaviour as a time-dependent geochemical process. The geochemical parameters required are the thermodynamic constants for all the reactions. The thermodynamics constant of mineral reactions including equilibrium constant and enthalpy at reference state are adopted from the *phreeqc.dat* data-base implemented in PHREEQC package (Perkhurst and Appelo, 1999). The values of equilibrium constant of ion

exchange reactions for FEBEX bentonite, reported by Fernández et al. (2001) were used. The required equilibrium constants of ion exchange reactions can be found in table 8.4.

Table 8.5 also presents the thermodynamics parameters of mineral reactions. The kinetic parameters are also required for calculating the rate of calcite dissolution-precipitation. The relationship for kinetic rate of calcite dissolution/reaction proposed by Plummer et al. (1978) will be used. The kinetic rate equation of calcite reaction and the required parameters of the model proposed by Plummer et al. (1978) have been included in *phreeqc.dat* data-base in PHREEQC and will be used in the simulation. Table 8.10 presents the kinetic data for calcite reaction used in the simulation.

Table 8.10 Kinetics parameter used for modelling calcite reaction adopted from *phreeqc.dat* data-base of PHREEQC version 2 (Perkhurst and Appelo, 1999)

<i>Kinetic reactions</i>	<i>Kinetic data</i>
$CaCO_3 = Ca^{2+} + CO_3^{2-}$	
Rate of reaction (R):	
$R = k \left(\frac{A}{V} \right)^\alpha (1 - \Omega)^n$	$\left(\frac{A}{V} \right) = 5.0 \text{ cm}^2 \text{ l}^{-1}, \alpha = 0.6, n = 2/3$
$k = k_1 a_{H^+} + k_2 a_{H_2CO_3^*} + k_3 a_{H_2O}$	$\log k_1 = 0.198 - \frac{444}{T} \quad \log k_2 = 2.840 - \frac{2177}{T}$
$\Omega = \frac{IAP}{K_{eq}}$	$\log k_3 = -5.86 - \frac{317}{T} \quad \text{if } T \leq 298$
K_{eq} : Equilibrium constant from table 8.5	$\log k_3 = -1.10 - \frac{1737}{T} \quad \text{if } T > 298$
IAP : Ion Activity Product	
$H_2CO_3^* = CO_{2(aq)} + H_2CO_3$	

8.4.4 Initial and boundary conditions

The bentonite cell is initially set to be in equilibrium with the laboratory conditions (14% gravimetric water content) (Villar et al., 2008). This amount corresponds to an initial degree of saturation (S_i) equal to 58.6% (based on $n=0.4$) and corresponds to suction value of 90.0 MPa based on the moisture retention relationship, i.e. equation 8.2. It is assumed that the temperature is in equilibrium with the laboratory conditions and is equal to 298 K.

Based on the geochemical analysis of pore water chemistry presented in section 8.2, the initial conditions for the primary dissolved chemical components are presented in table 8.11. Accordingly, the pore fluid contained 7 dissolved components which were involved in the transport and reaction processes.

Table 8.11 Initial dissolved chemical concentration and inflow water composition

<i>Chemical component</i>	<i>Initial pore water</i>	<i>Inflow granitic water</i>
<i>Cl⁻ (mol/m³)</i>	<i>158</i>	<i>0.369</i>
<i>SO₄²⁻</i>	<i>34.7</i>	<i>0.150</i>
<i>HCO₃⁻</i>	<i>0.432</i>	<i>2.593</i>
<i>Ca²⁺</i>	<i>22.2</i>	<i>1.00</i>
<i>Mg²⁺</i>	<i>27.1</i>	<i>0.387</i>
<i>Na⁺</i>	<i>129.9</i>	<i>0.461</i>
<i>K⁺</i>	<i>1.11</i>	<i>0.026</i>
<i>pH</i>	<i>7.73</i>	<i>8.72</i>

Chloride component was considered as the dependent component in the transport processes associated with total charge conservation as explained in chapter 3. It is noted that pH was considered only in the geochemical calculation and the transport of H⁺ ions was ignored in the simulation. The pore water dissolved chemicals are in equilibrium with the initially presented mineral and ion exchange complexes. Based on geochemical modelling the initial composition of the minerals and exchange complex including Na-X, K-X, Mg-X₂ and CaX₂ are presented in table 8.12.

In the experiment, the hydration water (granitic) was applied uniformly at the top face at a pressure of 1.2 MPa and at the same time a hot water circulation tank maintained the temperature at the top face at 298 K. The bottom face was impermeable to moisture flow and was maintained at a uniform temperature of 373 K by a heater. Therefore, fixed type boundary conditions were applied at both the top and bottom faces of the domain. The boundary conditions for the chemical components were also considered as fixed boundary condition. Therefore only the composition of ions in the incoming granitic water has to be specified in the model which will then calculate the chemical flux related to the moisture flux. The composition of the granitic water is also presented in table 8.11.

Table 8.12 Initial quantities of minerals and exchangeable ions in FEBEX bentonite

<i>Initial minerals and cation exchangeables</i>	<i>mol/kg dry soil</i>
<i>Calcite</i>	<i>0.060</i>
<i>Gypsum</i>	<i>0.0054</i>
<i>Halite</i>	<i>0.0</i>
<i>Anhydrite</i>	<i>0.0</i>
Ca^{2+} (<i>Ca-X₂</i>)	17.15×10^{-2}
Mg^{2+} (<i>Mg-X₂</i>)	16.7×10^{-2}
Na^+ (<i>Na-X</i>)	30.4×10^{-2}
K^+ (<i>K-X</i>)	1.90×10^{-2}

Referring to the heating/hydration cell used in the experimental work, at the radial boundary a heat flux is required to be considered in the model representing the heat loss from the cell. Theoretically this heat loss is equal to $2.3 \text{ W/m}^2/\text{K}$, calculated from the PTFE casing and foam insulation, both 15 mm thick and having thermal conductivities of 0.25 and 0.4 W/m/K respectively (Villar et al. 2008b).

Similar to the coupled TH simulations presented in chapter 7 on compacted FEBEX in a similar cell, a lower value of heat flux, i.e. $1.78 \text{ W/m}^2/\text{K}$, was used in simulation compared with the theoretically calculated value to give better correlation for temperature distribution with those reported in the experiment. This can be explained that in the experimental cell, a layer of air trapped in radial boundary of the sample, may have provided an extra isolation layer. In addition, the radial boundary is prescribed as being hydraulically and chemically impermeable.

A schematic of the initial and boundary conditions used in the simulations is shown in figure 8.5.

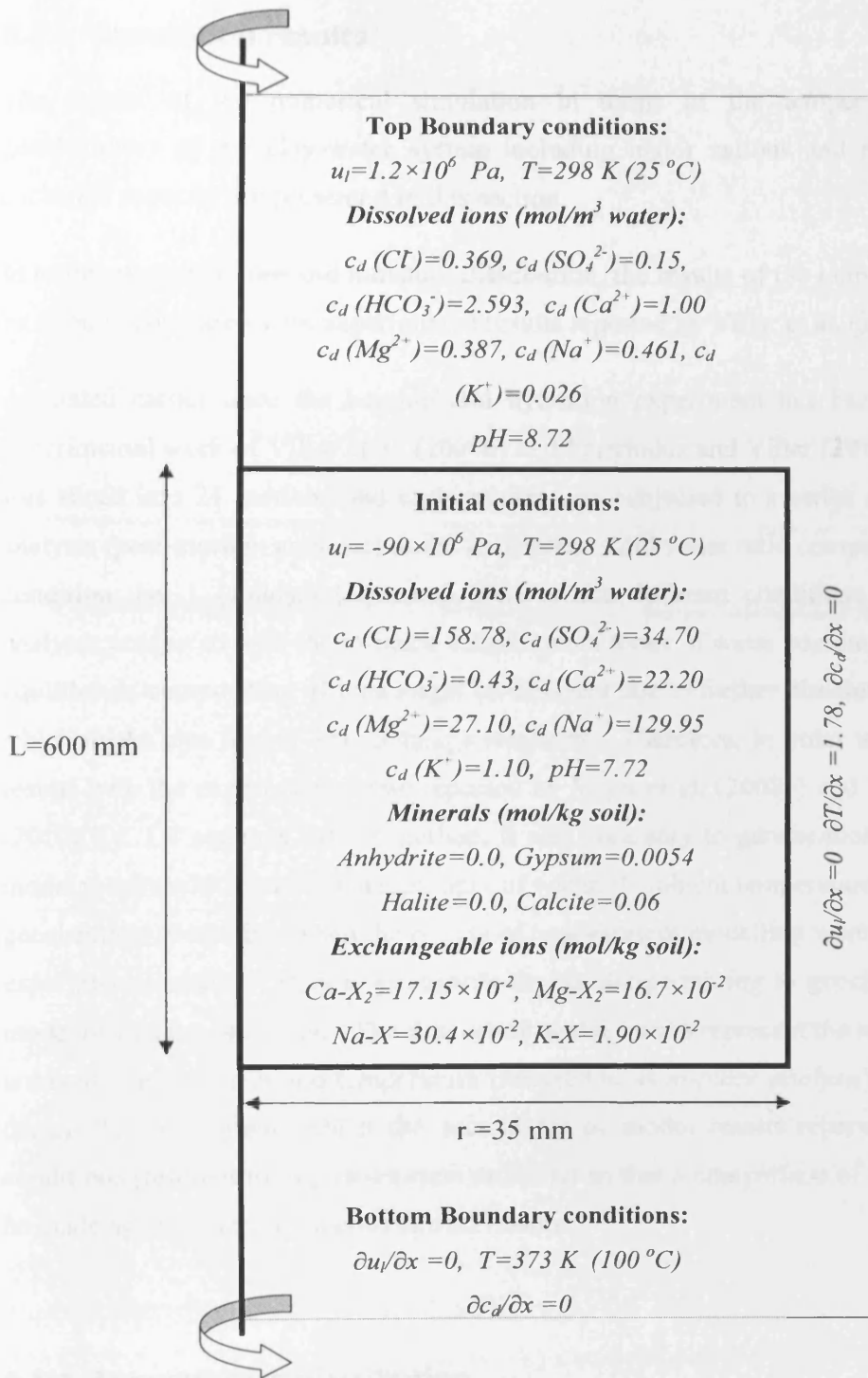


Figure 8.6 Schematic of the initial and boundary conditions for THC simulation of heating and hydration test

8.5 Simulation results

The results of the numerical simulation in terms of the temperature, moisture and geochemistry of the clay-water system including major cations and anions, minerals and exchange capacity are presented in this section.

In terms of temperature and moisture distribution, the results of the numerical modelling will be directly compared with experimental results reported by Villar et al. (2008b).

As stated earlier once the heating and hydration experiment has been completed, in the experimental work of Villar et al. (2008b) and Fernández and Villar (2010), the bentonite cell was sliced into 24 sections and each section was subjected to a series of pore water extract analysis (post-mortem analysis) under a different solid/water ratio compared with the in-place condition, i.e. 1(solid):4 (aqueous). Due to the different conditions in the post-mortem analyses compared with the in-place conditions in terms of water content and temperature, the equilibrium composition of ions might be different due to further dissolution of trace minerals which might also trigger ion exchange reactions. Therefore, in order to compare the model results with the experimental data reported by Villar et al. (2008b) and Fernández and Villar (2010), i.e. 1:4 aqueous extract method, it was necessary to geochemically re-equilibrate the model results with the additional amount of water at ambient temperature with a series of post geochemical modelling. Then the results of post-mortem modelling were comparable with the experimental results. Hence, as regards the results pertaining to geochemistry, two sets of model results are presented. The first set of model results represent the in-place conditions, in terms of water content and temperature (referred to as *in-place analysis*) in the bentonite cell during the experiment, whilst the second set of model results represent the post-mortem conditions (referred to as *post-mortem analysis*) so that a comparison of the model results can be made against the 1:4 aqueous extract results.

8.5.1 Temperature distribution

Figure 8.7 presents the transient simulated results of temperature distribution in the bentonite cell and those reported by Villar et al.(2008b) for the periods of 6, 12, 24 and 92 months. The numerical results correlated well with the experimental results. The temperature distribution

in the domain remains at steady-state condition for the periods of 6, 12, 24 and 92 months. The curvature in temperature profile is related to radial boundary flux due to heat loss from the cell.

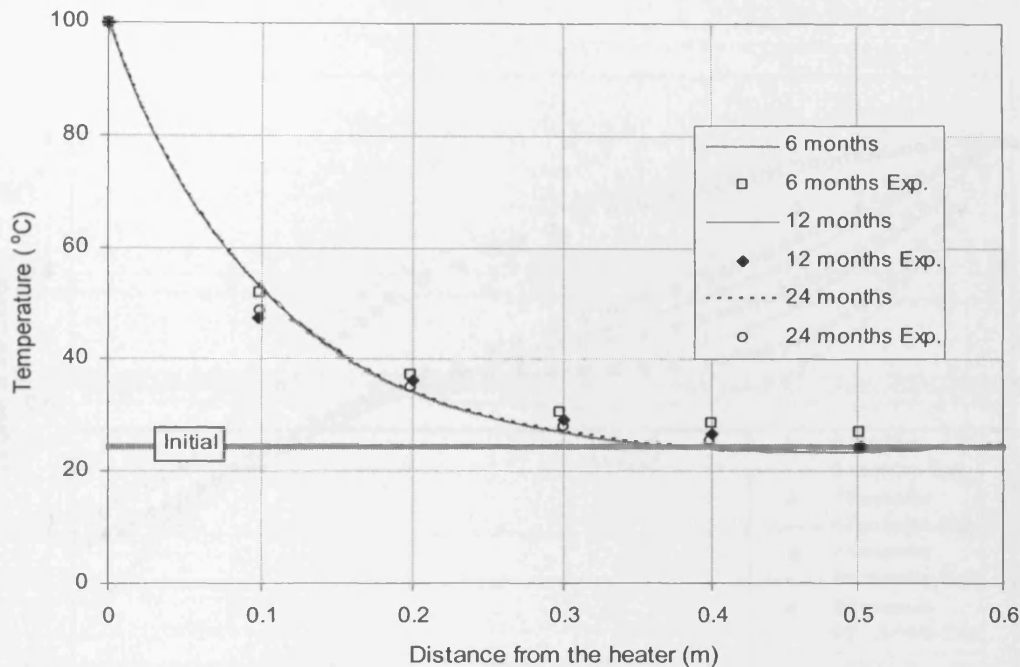


Figure 8.7 Profiles of temperature resulting from numerical simulation (lines) and the laboratory experiment (symbols)

8.5.2 Moisture distribution

The transient profile for the degree of saturation is presented in figure 8.8 where the results of the numerical simulation and experiment are also compared. The results are presented for 6, 12, 24 and 92 months analysis. Villar et al. (2008b) presented both the profiles of moisture content and dry density in the domain sections for the mentioned period of times. Their results were used to extract the degree of saturation in the domain and plotted in figure 8.5. It is noted that the coupled modelling in this study has been performed under THC framework and deformation behaviour is not considered.

Comparison between experimental and numerical modelling results shows that the model results follow very closely the experimental observations for degree of saturation. However,

the numerical model over-predicted drying in the hot boundary region for the first three periods of simulation. In the hydration side, model predicted slightly higher degree of saturation up to 24 months but it is correlated well with the experimental results for the period of 92 months analysis.

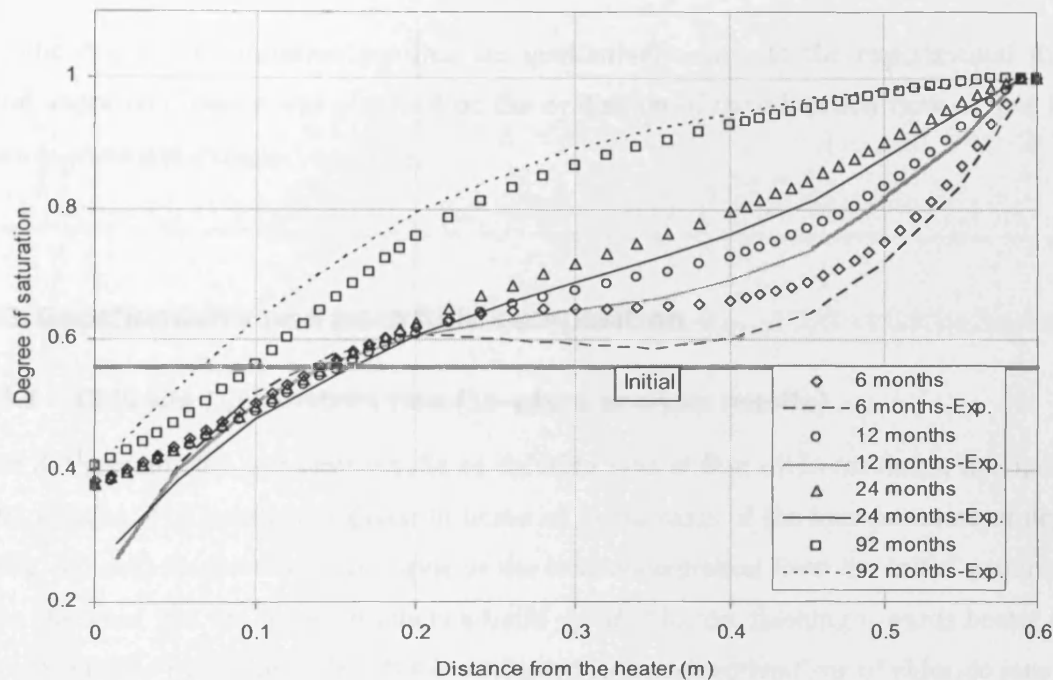


Figure 8.8 Profiles of degree of saturation resulting from numerical simulation (symbols) and laboratory experiment (lines)

Higher drying in the model predictions in the heater region can be related to the parameters used in the vapour transport model, i.e. Phillip and de Vries (1957), which generally yields higher vapour flux due to temperature gradient. It is noted that two correction factors to the vapour fluxes of Phillip and de Vries model were applied following suggestions of the experimental and numerical study of Singh (2007) as discussed in chapter 3. The temperature induced vapour flux has been reduced by a factor of 0.25 and isothermal vapour flux by a 0.7 factor. These values have been obtained based on the coupled thermal and hydraulic analysis on same compacted FEBEX bentonite presented in chapter 7.

The rate of hydration due to the injecting fluid is gradually reduced and well correlated with the results of experimental hydration front for the duration of 92 months. This is mainly due

to the application of the interlayer hydrate modification factor, i.e. $(1-f_{IL})$ in the effective hydraulic conductivity relationship, i.e. equation (8.4). With increasing degree of saturation, hydraulic conductivity increases by a power function. At the same time, interlayer hydration reduced the hydraulic conductivity as the interlayer water ratio approaches higher values through $(1-f_{IL})$ parameter.

Since the degree of saturation profiles are qualitatively close to the experimental data in general, more confidence was obtained on the evaluation of the advection flow of ions in the system in chemical transport analysis.

8.5.3 Geochemistry and pore fluid composition

8.5.3.1 Chloride (Cl⁻) distribution (In-place analysis results)

Figure 8.9 presents the transient results of chloride ions at four different times, i.e. 6, 12, 24 and 92 months. The results are given in terms of molar mass of the ions per mass of dry soil (mol/kg dry soil) to show the variations of the ion concentration from the initial condition. It can be observed that the model predicts a build up of chloride, flushing towards heater in the areas close to the hydration side. This is attributed to the advective flow of chloride ions from the hydration side which also results in accumulation of chloride ions in the first 200 mm close to the hydration side. The front peak in chloride profile is extended towards the middle of the domain with time.

Moreover, due to the increase in temperature in the areas close to the heater, liquid water is suggested to be transferred toward the heater due to the hydraulic potential. The water has carried the available chloride in the domain towards the heater. At the same time, moisture transfer can also take place simultaneously from the hot end towards the cold end in the form of water vapour. The chloride ions carried by liquid flow remained at the hot end, as vapour cannot carry chemicals with it.

The process of simultaneous water and vapour movement in the areas close to the heater has resulted in higher amount of chloride, precipitated by the heater while the chloride content was reduced from the initial amount in the area of approximately 80 to 300 mm away from the heater.

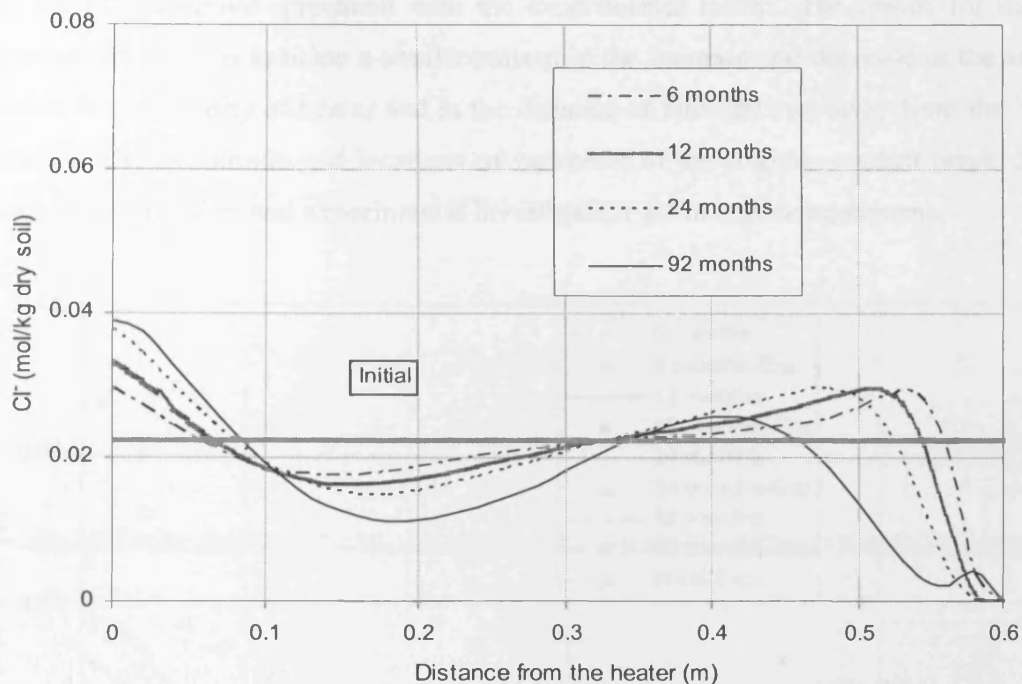


Figure 8.9 Profiles of chloride contents resulting from the numerical simulation at different times

8.5.3.2 Chloride (Cl⁻) distribution (Post-mortem simulation results)

Figure 8.10 presents a comparison of post-mortem analysis results against the experimental results, reported by Fernández and Villar (2010) for the dissolved chloride ion concentrations at different time intervals. The results of the numerical model are presented with lines and the symbols represent the experimental reported values.

As chloride behaves as a conservative anion, the chloride distribution in the domain has not been affected by geochemical reaction during post-mortem analysis. The chloride profile related to the in-place and post-mortem analysis, yielded exactly same values as expected.

From figure 8.10, it can be seen that there is a good qualitative correlation between the experimental and model results for the period of 6, 12 and 24 months. The magnitude accumulation peaks of chloride in the area of hydration side are also close to the experimental results for the periods of 6, 12 and 24 months. In the second half of the domain which was more affected by temperature increase (refer to figure 8.7), the results for the 6, 12 and 24

months are in qualitative agreement with the experimental results. The results for the first three periods of analysis indicate a similar pattern in the increase and decrease of the amount of chloride in the vicinity of heater and in the distance of 100-200 mm away from the heater, respectively. The magnitude and locations of variations of the chloride content resulted from the numerical simulation and experimental investigation are in a close agreement.

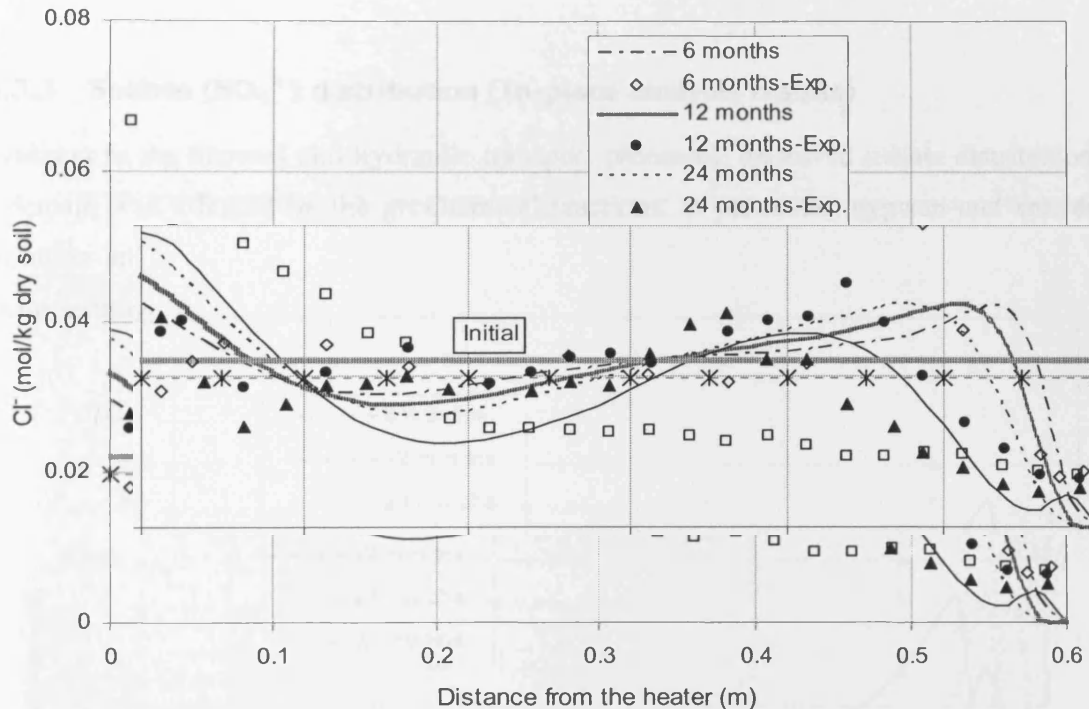


Figure 8.10 Profiles of chloride contents at different times, resulting from the post-mortem analysis (lines) and experimental results (symbols) reported by Fernández and Villar (2010)

The results of model for the 92 months test show a higher amount of chloride in the area of 100-300 mm in the vicinity of the hydration side compared with the experimental results. For the periods of 92 months, numerical model also shows continues increase in the amount of accumulated chloride by the heater. However, the model predicted a lower amount of chloride close to the heater. The experimental results show that chloride was almost removed from the more hydrated 400 mm of bentonite, whereas its concentration showed a sharp gradient in the 200 cm closest to the heater.

The maximum value of chloride content reaches approximately 0.07 mol/kg, at the hot end of the experiment whilst the numerical model yields 0.04 mol/kg for 92 months time. The

experimental results indicate that the flow of chloride has more been regulated due to the combination of chloride diffusion in the first 200 mm towards the heater and chloride advection in the vicinity of heater. However, model result shows that after 92 months part of the chloride have been diffused toward the hydration boundary due to the concentration gradient.

8.5.3.3 Sulfate (SO_4^{2-}) distribution (In-place analysis results)

In addition to the thermal and hydraulic transport processes, dissolved sulfate distribution in the domain was affected by the geochemical reactions, in particular, gypsum and anhydrite dissolution and precipitation. Figure 8.11 presents the distribution profile of sulfate in the domain resulted from the numerical analysis.

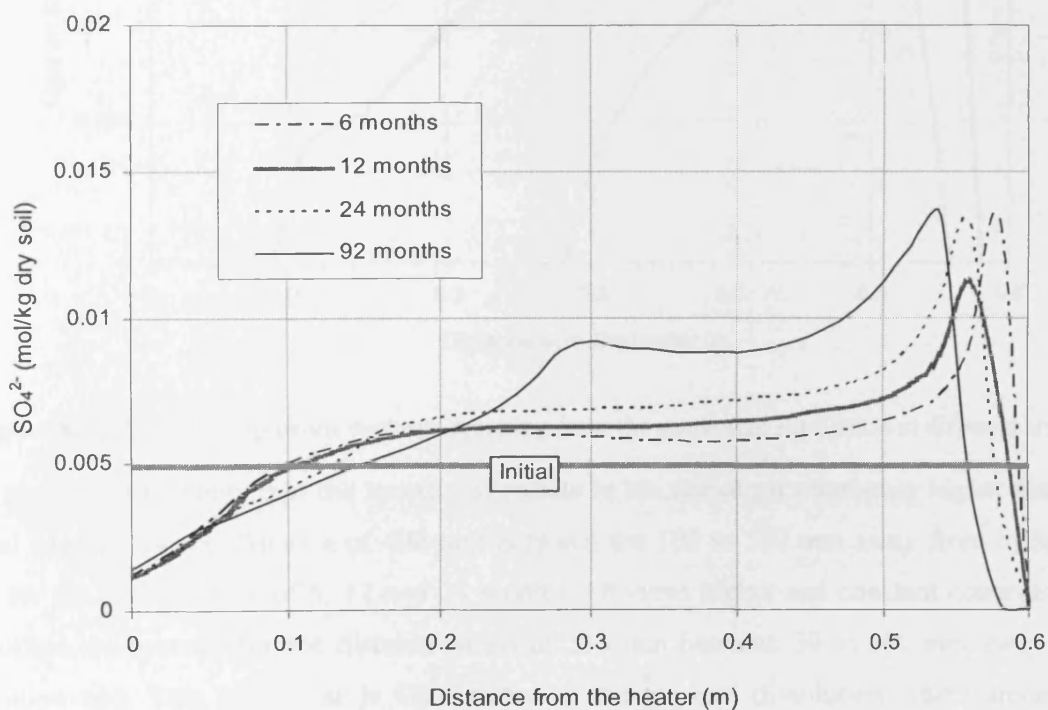


Figure 8.11 Profiles of the dissolved sulfate contents resulting from the numerical simulation at different times

The sulfate behaviour was affected by the equilibrium reactions with anhydrite and gypsum minerals. The domain initially contained some gypsum but no anhydrite (table 8.12).

Therefore, when the concentration of sulfate reduced by advancing hydration, gypsum was dissolved which was controlled by the amount of the dissolved sulfate in the area affected by hydraulic process. The results of gypsum distribution in the domain, i.e. figure 8.12, also indicate that almost all gypsum was dissolved in 50 mm distance from hydration boundary. The peak of leached sulfate in the hydration side is also located in the same region where gypsum has been dissolved.

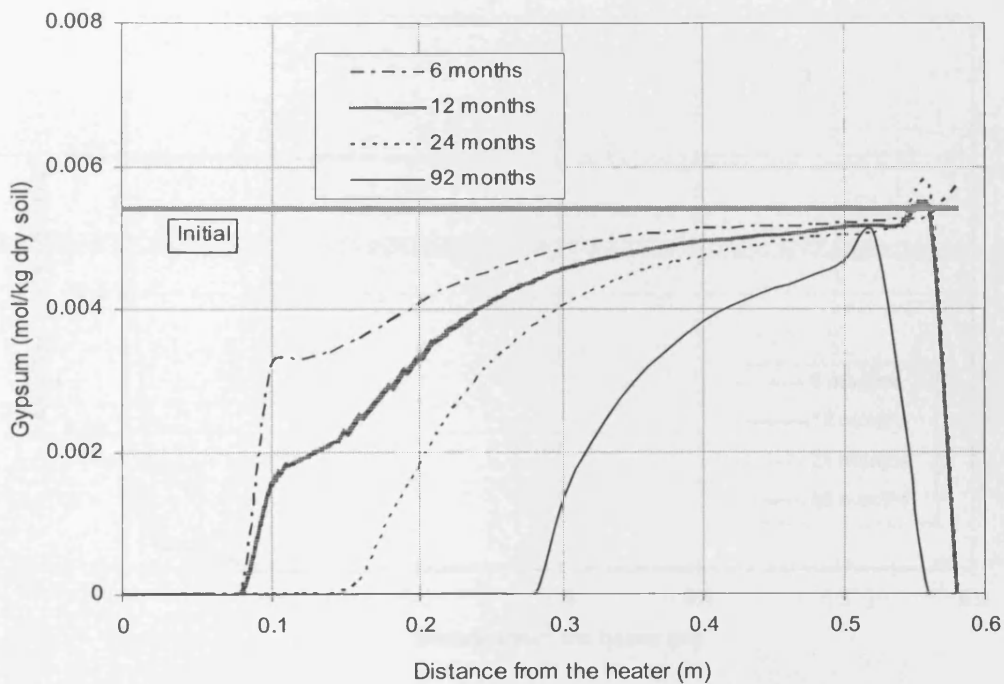


Figure 8.12 Profiles of gypsum contents resulting from the numerical simulation at different times

The model results show that the amount of sulfate in the domain is constantly higher than the initial amount for the distance of 400 mm between the 100 to 500 mm away from hydration side for the time periods of 6, 12 and 24 months. Obvious higher and constant concentration of sulfate is observed for the distance of about 250 mm between 50 to 300 mm away from hydration end. This behaviour is also related to the gypsum dissolution where amount of gypsum has decreased according to the results presented in figure 8.12. Due to the equilibrium mineral condition, the amount of dissolved sulfate has increased and remained constant in the mentioned area.

The amount of sulfate shows a decrease in the areas close to the heater. This is believed due to the precipitation of anhydrite as it can be seen in figure 8.13. The equilibrium constant of mineral reactions for gypsum and anhydrite are very close whilst their enthalpies of reaction are different, leading to a different behaviour of these two minerals at the regions with higher temperature. The distribution of the dissolved sulfate at hot end is believed to be attributed to the precipitation of anhydrite due to the higher temperature.

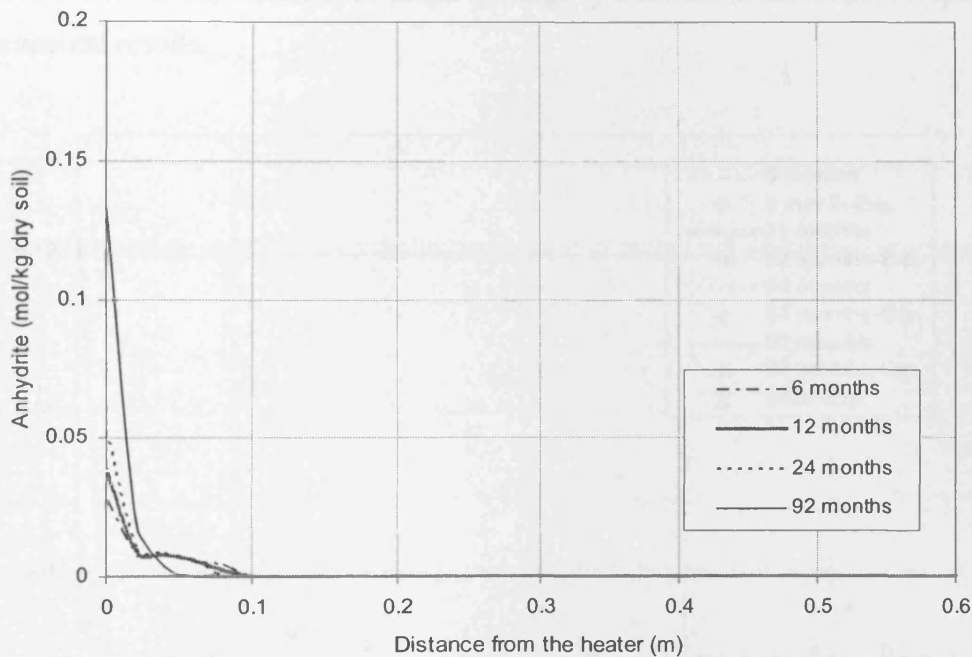


Figure 8.13 Profiles of anhydrite contents resulting from the numerical simulation at different times

The results, presented in figure 8.13, indicate that anhydrite has been precipitated in the vicinity of heater in a considerable amount. The amount of precipitated anhydrite has reached to about 0.125 mol/kg soil for the period of 92 months by the heater. On the other hand, the system initially contained 5.43×10^{-3} (mol/kg) gypsum. Also from figure 8.11 it can be seen that gypsum was dissolved in the hydration side due to the reduction of dissolved chemicals of calcium and sulfate in this region. In the model, gypsum behaviour was considered in instantaneous equilibrium with dissolved calcium and sulfate. Therefore gypsum was dissolved into the system to provide the balance between mineral phase and dissolved calcium and sulfate which were flushed towards the heater.

8.5.3.4 Sulfate (SO_4^{2-}) distribution (Post-mortem simulation results)

Figure 8.14 presents a comparison between post-mortem model results and the experimental results for the dissolved sulfate ion concentration at different time intervals. From this figure it can be seen that there is a reasonable qualitative agreement in terms of distribution pattern between the model and experimental results for all time intervals. In the area of hydration, numerical model predicted the precipitated magnitude of sulfate close to those reported in the experiment. However the locations of peaks are slightly different in the model compared with the experimental results.

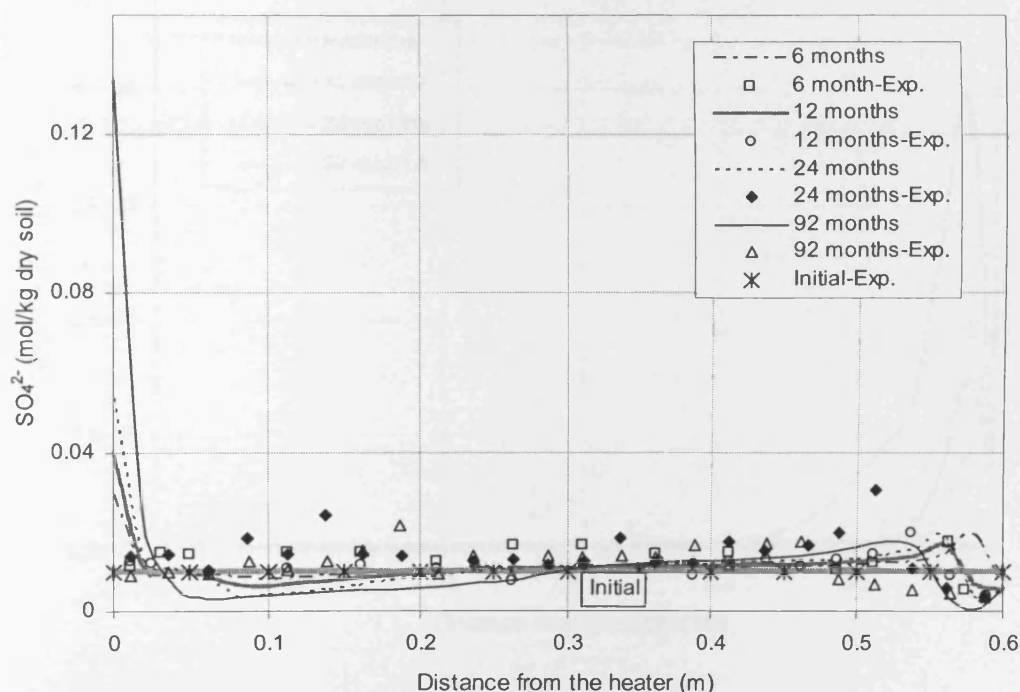


Figure 8.14 Profiles of dissolved sulfate contents at different times, resulted from the post-mortem simulation (lines) and experimental results (symbols) reported by Fernández and Villar (2010)

As stated by Fernández and Villar (2010) gypsum is more stable at ambient conditions, the transition of gypsum to anhydrite being above 43–57 °C and anhydrite seemed to have precipitated close to the heater, decreasing the sulfate concentration in this zone. The model shows also an over-prediction at the hot end and an under-prediction in the area close to the hot end, affected by the coupled thermally induced liquid-vapour movement. It is suggested that the over-prediction at the hot end is due to the high amount of anhydrite precipitation in the in-place numerical modelling results (refer to figure 8.13).

8.5.3.5 Bicarbonate (HCO_3^-) distribution (In-place analysis results)

Figure 8.15 shows the results of numerical simulation for the dissolved bicarbonate at different times in the domain. The concentration of bicarbonate has been increased close to the hydration side due to the higher concentration at the boundary. The concentration peaks are located about 58 mm from the hydration side with considerable increases with time. Higher amount of bicarbonate than the initial values was injected by the water at this boundary and accumulated in a limited region close to the boundary.

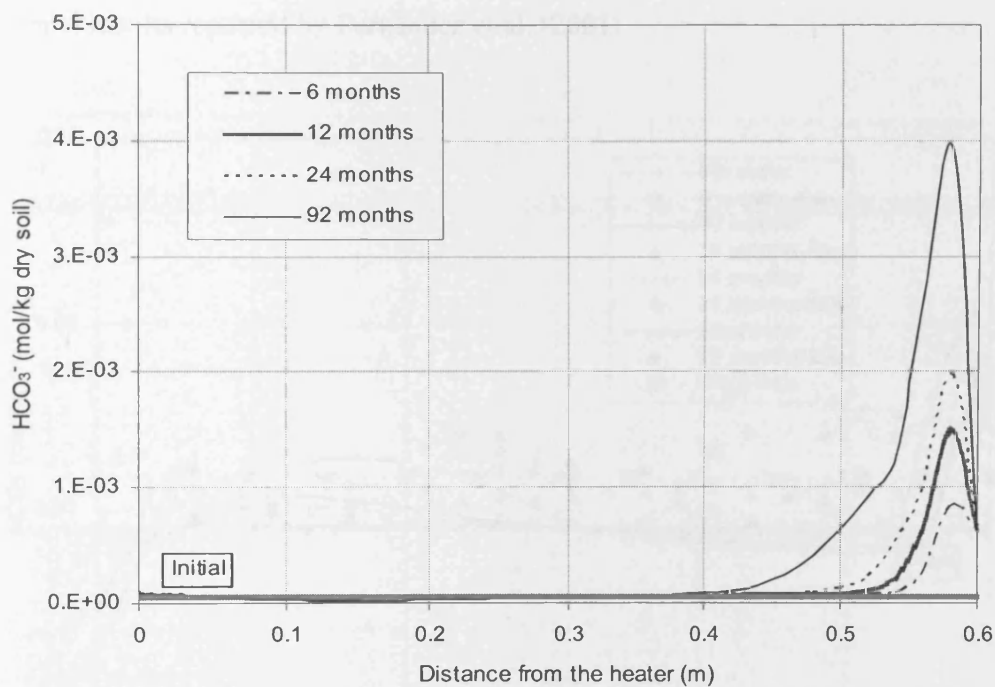


Figure 8.15 Profiles of the bicarbonate contents resulting from the numerical simulation at different times

Due to the considerable low rate of precipitation/dissolution of calcite, the initial amount of calcite was not changed for different periods of analysis. The XRD analysis reported by Villar et al. (2008b) also showed that in the 92 months test, a slight decrease in the calcite content with respect to the original bentonite was detected in all the powder samples after the test. Therefore, the behaviour of bicarbonate was not affected by calcite reactions.

8.5.3.6 Bicarbonate (HCO_3^-) distribution (Post-mortem simulation results)

Figure 8.16 presents a comparison of post-mortem model results against the experimental results for the dissolved bicarbonate ion concentration at different time intervals. There is a close agreement between the model results and experimental data in terms of distribution pattern for all time intervals. It is noted that there is a small difference in the initial values of bicarbonate used in the simulation and those reported by Fernández and Villar (2010). This is because in the simulation, the initial values for the model were adopted from those calculated from geochemical modelling, presented in table 8.6, where it is slightly different from the experimental results reported by Fernández et al. (2001).

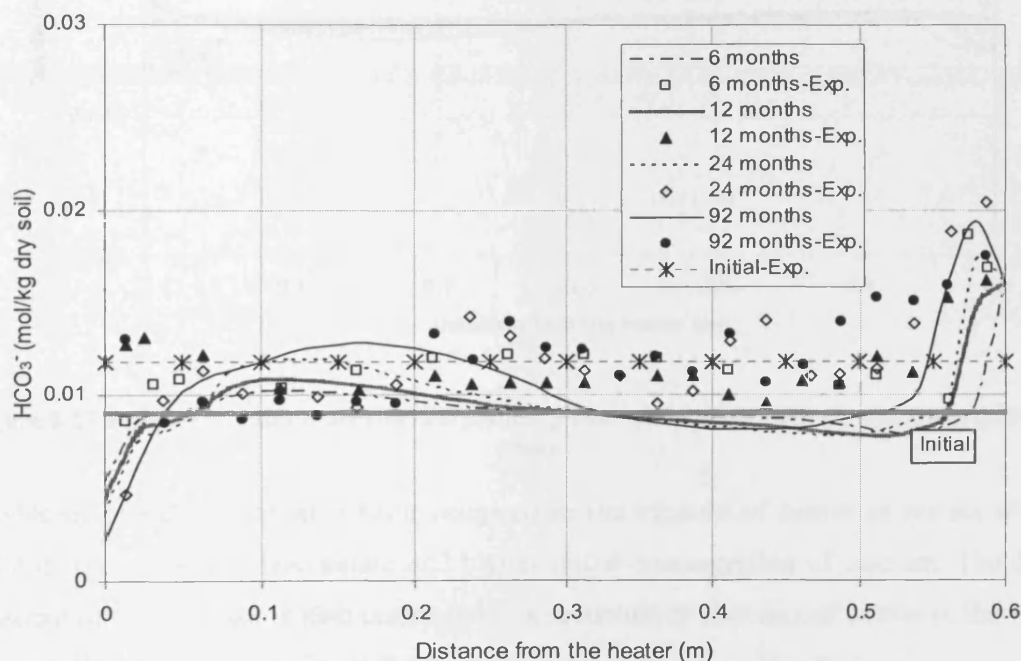


Figure 8.16 Profiles of dissolved bicarbonate contents at different times, resulting from the post-mortem simulation (lines) and experimental results (symbols) reported by Fernández and Villar (2010)

The concentration of bicarbonate shows an increase in the hydration side both in the numerical model prediction and in the experimental results in the 6, 12, 24 and 92 months tests. This is believed to be related to the dissolution of calcite in the vicinity of water injection site. The results of numerical model for calcite distribution are presented in figure 8.17, which demonstrate that, the amount of calcite in this area has been reduced from the initial condition. The results presented in figure 8.17, show calcite dissolution occurs in a

region of about 100 mm close to the hydration side. This is because in this region lower amount of calcium and high amount of bicarbonate existed initially before post-mortem analyses. As the results, calcite is dissolved to maintain the equilibrium condition.

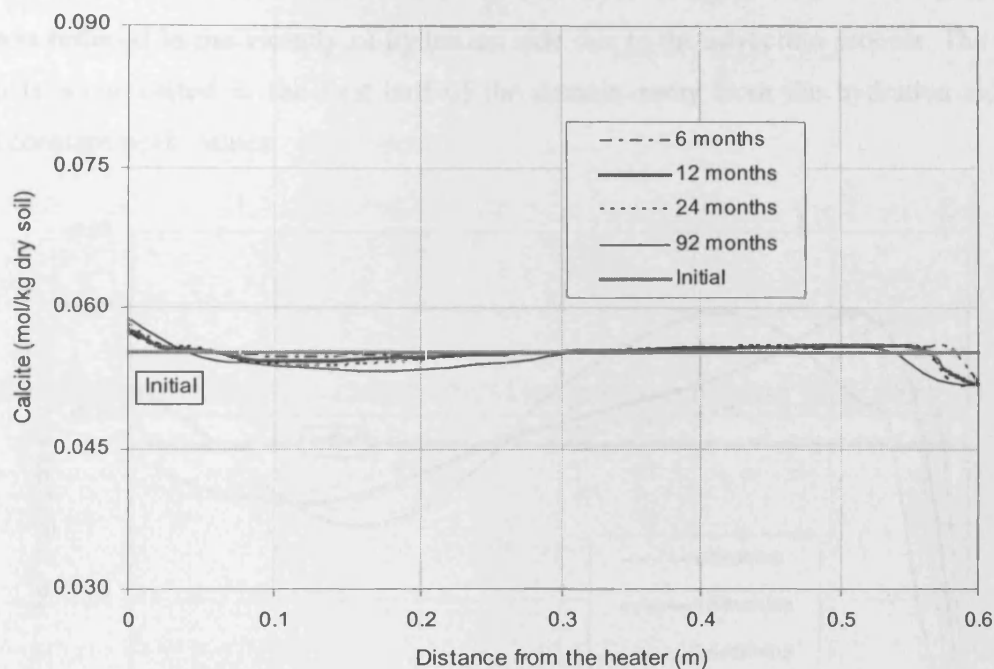


Figure 8.17 Profiles of calcite distribution resulting from the post-mortem simulation at different times

Precipitation of calcite has also been occurred in the vicinity of heater as results of lower initial concentrations of bicarbonate and higher initial concentration of calcium. The drop in the amount of bicarbonate is also correlated to a reduction in the amount calcite in the vicinity of heater as it can be seen in figure 8.17.

Similar explanation about the behaviour of bicarbonate and calcite in the experimental results has been given by Fernández and Villar (2010). This idea can also explain the fact that in the regions about 50 to 300 mm from the heater, that the amount of calcite has been reduced due to dissolution according to figure 8.17, and consequently the amount of bicarbonate has been increased in all time intervals. This is the area which is affected by the simultaneous water and vapour transfer due to higher temperature.

8.5.3.7 Sodium (Na^+) distribution (In-place analysis results)

Figure 8.18 presents the results of numerical simulation for dissolved sodium at different times in the domain. It can be seen that the trends for sodium concentration variations follow a similar pattern as observed in the case of chloride (refer to figure 8.9). The concentration of sodium is reduced in the vicinity of hydration side due to the advection process. The flushed sodium is accumulated in the first half of the domain away from the hydration side, with almost constant peak values.

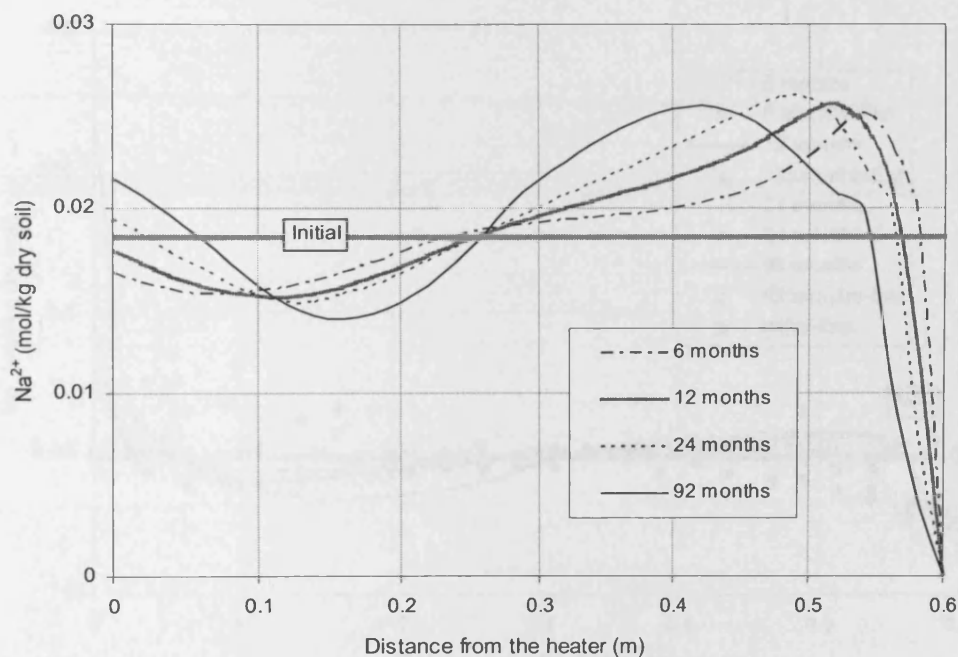


Figure 8.18 Profiles of the dissolved sodium contents resulting from the numerical simulation at different times

The accumulated sodium ions, flushed by water has been transferred by water and through diffusion further toward the heater, providing an area with greater amount of sodium than the initial ranges between 50 mm to 350 mm away from the hydration source.

In the area which is affected by temperature, simultaneous water and vapour flow due to temperature gradient affects the behaviour of sodium similar to chloride. In addition, ion exchange reactions also affect the available sodium in the system, as will be discussed in section (8.5.4).

8.5.3.8 Sodium (Na^+) distribution (Post-mortem simulation results)

Figure 8.19 presents a comparison of post-mortem model results against the experimental results for the dissolved sodium in the domain at different times. The general trend for distribution of sodium ions is in agreement with those from experimental results for all time intervals. However, in the vicinity of heater higher concentrations of sodium were predicted by the model which can be related to the higher drying exhibited in the periods of 6, 12, 24 months at this region predicted by the numerical model.

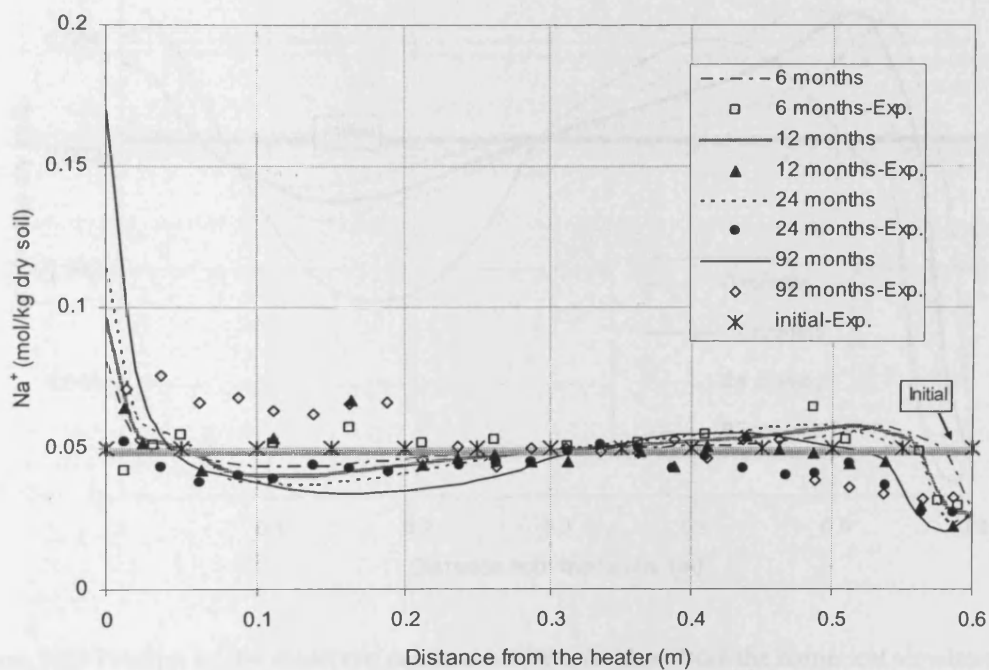


Figure 8.19 Profiles of the dissolved sodium contents at different times, resulting from the post-mortem simulation (lines) and experimental results (symbols) reported by Fernández and Villar (2010)

The transport processes of sodium ions have only been affected by the ion exchange reaction as sodium ions were not involved in any mineral precipitation and dissolution reactions. Part of the high accumulation of sodium ions in the vicinity of heater can be related to the ion exchange process as will be discussed in section (8.5.4).

8.5.3.9 Calcium (Ca^{2+}) distribution (In-place analysis results)

Figure 8.20 presents the profiles of the calcium ion distribution in the domain resulted from the numerical simulation at different times. The concentration of calcium was reduced in the vicinity of hydration side due to the advection process and the flushed sodium in this region was accumulated in the first 300 mm from the water injection side.

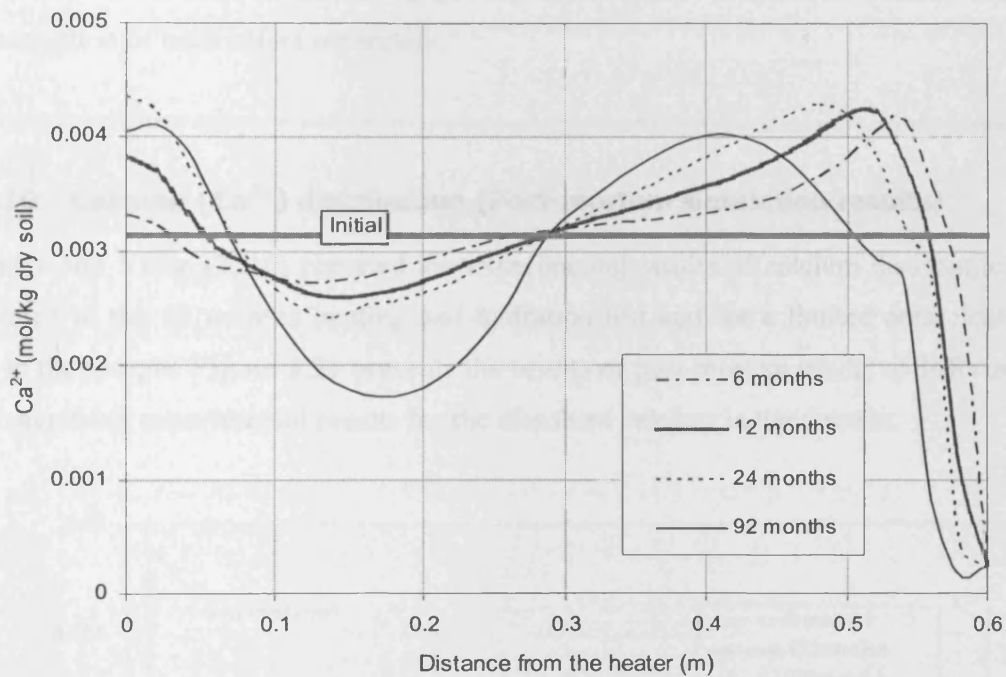


Figure 8.20 Profiles of the dissolved calcium contents resulted from the numerical simulation at different times

The concentration of calcium was also increased close to the heater and reduced in the area between about 50 to 300 mm from the heater. This behaviour is affected by temperature and simultaneous water and vapour flow.

Dissolved calcium has been involved in four geochemical processes which have affected the calcium behaviour. These geochemical reactions included anhydrite, gypsum and calcite reactions and ion exchange. Since calcite dissolution was considered as a kinetically controlled reaction and no sign of calcite variation was observed (as discussed previously), therefore it is believed that only gypsum and anhydrite dissolution-precipitations has been affected on the behaviour of calcium among all mineral reactions.

It is noted that the variations in the amount dissolved calcium and Ca^{2+} exchangeable in the interlayer affect the trend of each other. The latter will be discussed in section 8.5.4.

Dissolution of anhydrite due to high temperature and precipitation of anhydrite in the vicinity of heater might have controlled and regulated the amount of accumulated calcium simultaneously with the transport processes. In fact, the behaviour of calcium was controlled by advection-diffusion processes and geochemical reactions which makes difficult to explain the contribution of each effect separately.

8.5.3.10 Calcium (Ca^{2+}) distribution (Post-mortem simulation results)

Fernández and Villar (2010) reported the experimental results of calcium distribution in the cell related to the 92 months heating and hydration test and for a limited area close to the heater in the sample. Figure 8.21 presents the results of post-mortem model at different times and the available experimental results for the dissolved calcium in the domain.

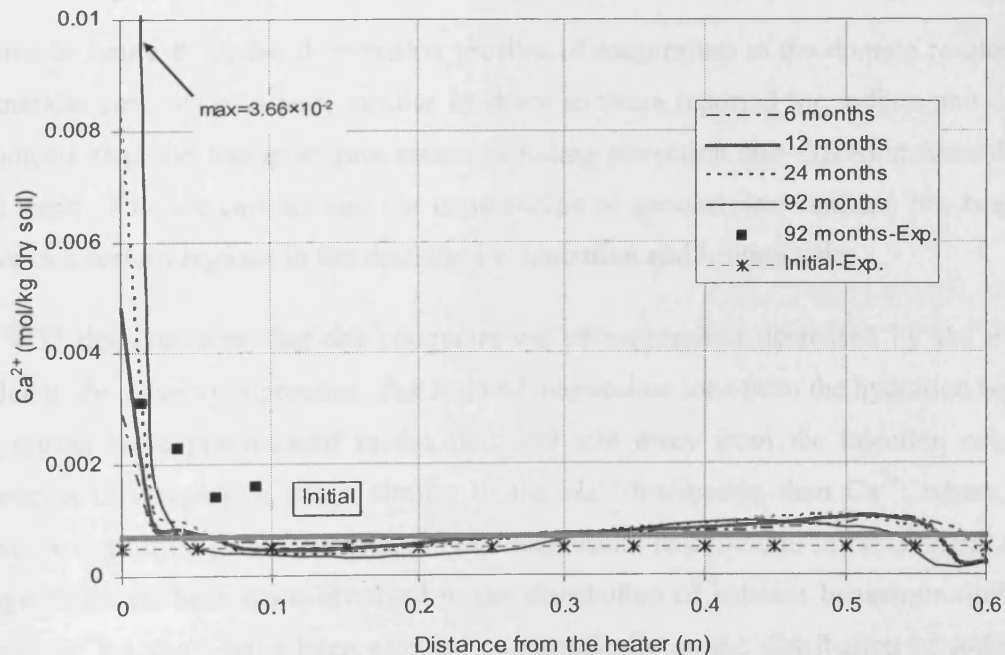


Figure 8.21 Profiles of the dissolved calcium contents at different times, resulting from the post-mortem simulation (lines) and experimental results (symbols) reported by Fernández and Villar (2010) for the 92 months test

No other information was reported for the rest of the durations for calcium, magnesium and potassium in the system. Therefore very limited data are available to validate the results of the numerical simulation.

The numerical simulation predicted a similar pattern as observed for sodium. The amount of calcium was reduced close to the hydration from the initial amount. The calcium ions were accumulated in the first half of the domain in hydration side for all time intervals which is related to the advection mechanism.

In the hot side, the model shows that high amount of calcium has been precipitated close to the heater. This trend is in qualitative agreement with the experimental result, although higher values are observed from the results of simulation. This could be related to the high amount of anhydrite in the model, precipitated close to the hot end. However it is acknowledged that justification requires more experimental data and analysis.

8.5.3.11 Magnesium (Mg^{2+}) distribution (In-place analysis results)

As shown in figure 8.22, the distribution profiles of magnesium in the domain resulted from the numerical simulation is very similar in shape to those reported for sodium and calcium. This indicate that the transport processes, including advection and diffusion controlled the general trend of major cations and the contribution of geochemical reaction has been more effective in a certain regions in the domain, i.e. hydration and heating sides.

Figure 8.22 demonstrates that the concentration of magnesium decreased by the injecting water due to the advection process. The leached magnesium ions from the hydration boundary in this region were precipitated in the first 250 mm away from the injection point. The behaviour in this region is more similar to the Na^+ distribution than Ca^{2+} , where almost constant concentration peaks are seen in both magnesium and sodium. In fact mineral and ion exchange reactions have been involved in the distribution of calcium behaviour whilst only ion exchange reactions have been affected geochemically on the distribution of sodium and magnesium.

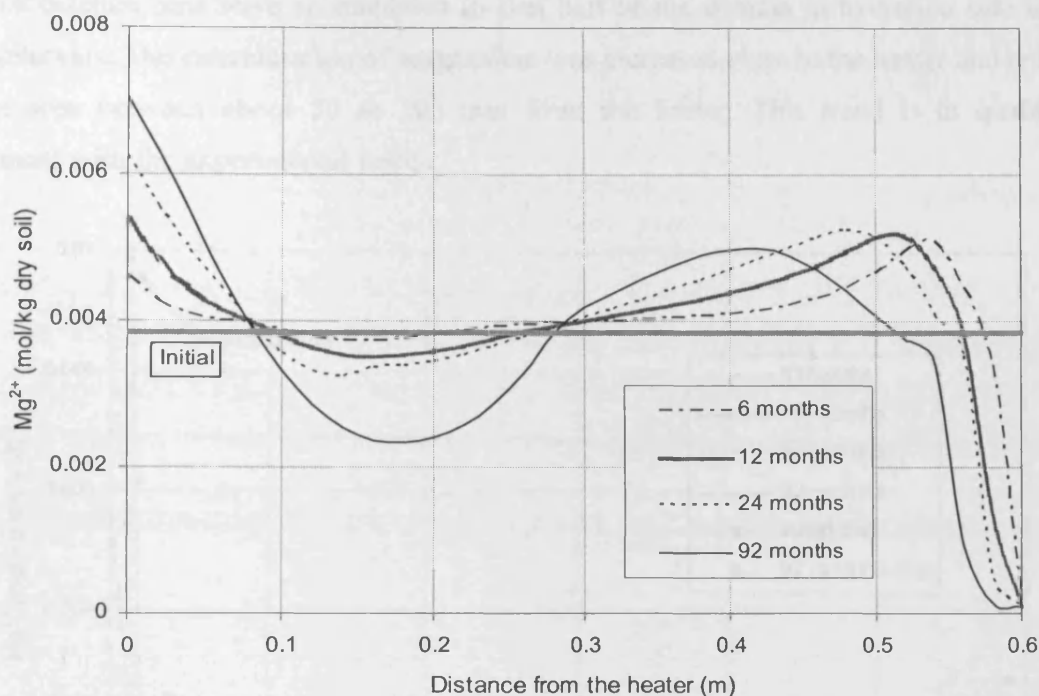


Figure 8.22 Profiles of the magnesium contents resulting from the numerical simulation at different times

Since dissolution/precipitation of dolomite was not considered in this numerical simulation, there is some uncertainty about the fate of magnesium in the domain. However it is suggested that transport processes had a greater contribution to the distribution of magnesium.

8.5.3.12 Magnesium (Mg^{2+}) distribution (Post-mortem simulation results)

The available experimental results reported by Fernández and Villar (2010) for magnesium distribution is also limited for the duration of 92 months test and only for a limited regions closed to the heater similar to the calcium case. Therefore this limited data is used to check the results of the numerical simulation. Figure 8.23 shows the results of post-mortem model at different times and the available experimental results for the dissolved magnesium in the domain.

The numerical simulation predicted a similar pattern as observed for sodium and calcium. The amount of magnesium was reduced close to the hydration from the initial amount. The

leached calcium ions were accumulated in first half of the domain in hydration side for all time intervals. The concentration of magnesium was increased close to the heater and reduced in the area between about 50 to 300 mm from the heater. This trend is in qualitative agreement with the experimental result.

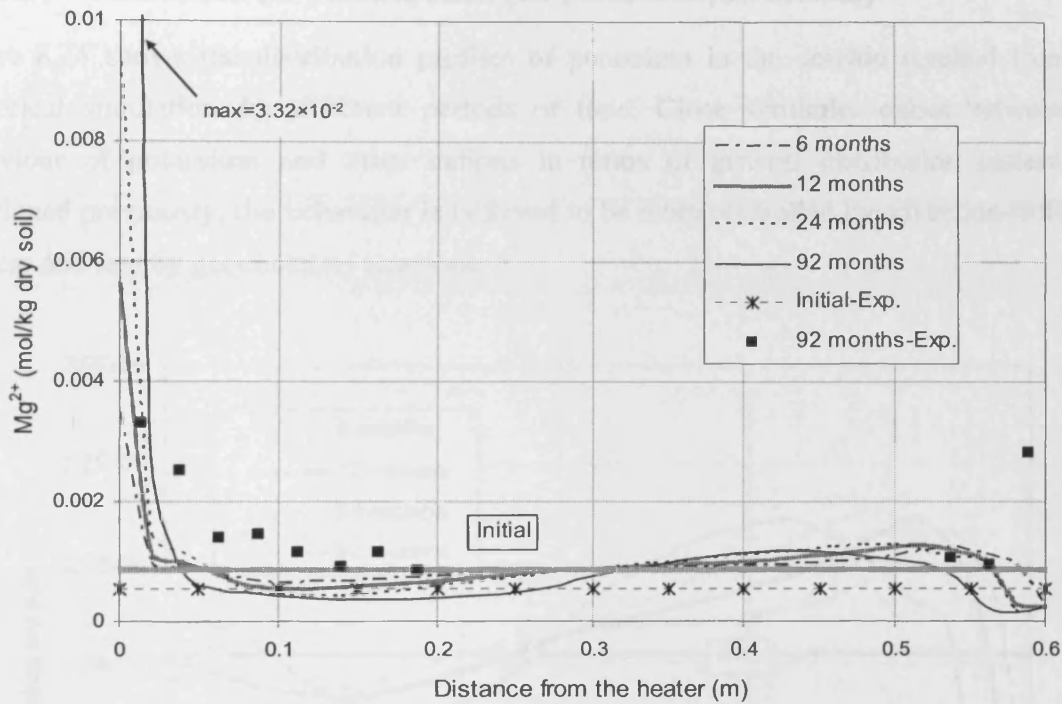


Figure 8.23 Profiles of the dissolved magnesium contents at different times, resulting from the post-mortem simulation (lines) and experimental results (symbols) reported by Fernández and Villar (2010) for the 92 months test

Fernández and Villar (2010) stated that the magnesium increase in the experimental results can be a consequence of different processes influenced by temperature (near the heater) and the advance of the water front along the bentonite column. They reported the effective geochemical reactions on magnesium behaviour as: precipitation of calcite closed to the hottest zones; dolomite dissolution simultaneously enhanced by the temperature, calcite precipitation, and dissolution of sulphate; and the release of Mg^{2+} from the interlayer of smectite in the coolest zone due to calcite and sulphate (gypsum) dissolution. It is noted that dolomite reaction was not considered in the simulation mainly because the initial amount was not reported in the literature clearly (e.g. whilst it was required in the geochemical modelling of the initial pore fluid composition). The absence of dolomite in the reactions applied in the

numerical simulation, has limited the contribution of different geochemical mechanisms to the ion exchange reaction. This will be discussed in the ion exchangeable section.

8.5.3.13 Potassium (K^+) distribution (In-place analysis results)

Figure 8.24 shows the distribution profiles of potassium in the domain resulted from the numerical simulation for different periods of time. Close similarity exists between the behaviour of potassium and other cations in terms of general distribution pattern. As mentioned previously, the behaviour is believed to be more controlled by advection-diffusion process and less by geochemical reactions.

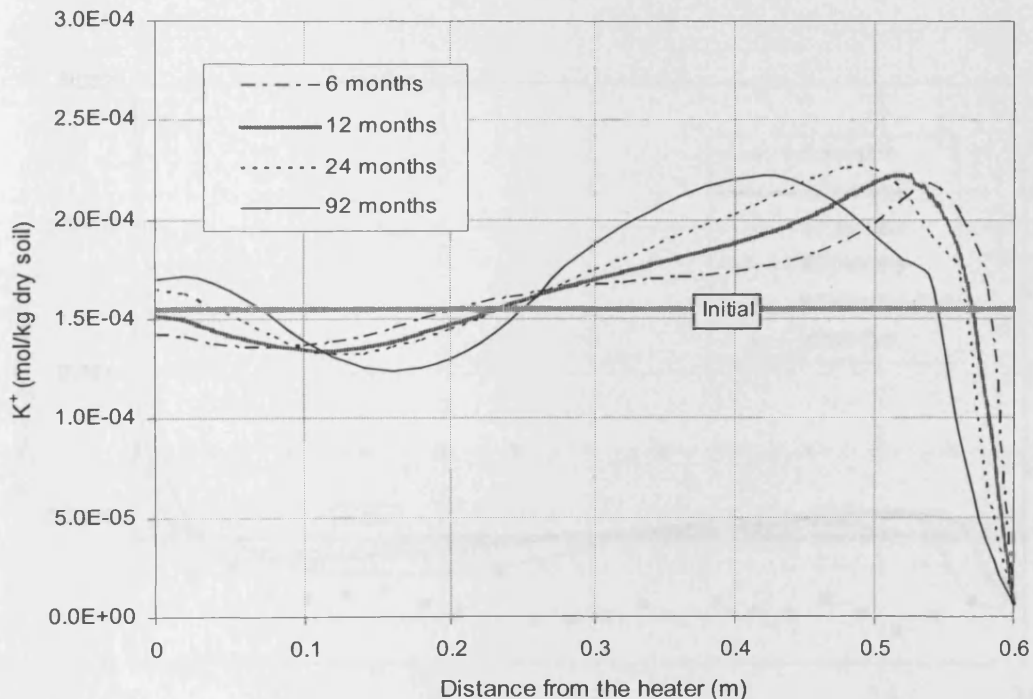


Figure 8.24 Profiles of potassium contents resulting from the numerical simulation at different times

From this figure it can be seen that the concentration of potassium has decreased close the injecting water due to the advection process. The flushed ions in this region were precipitated in the region between 50 to 350 mm away from the injection point. The behaviour in this region is more similar to the Na^+ and Mg^{2+} in terms of distribution pattern where almost constant concentration peaks are seen in all three cations. Only ion exchange reactions have

been affected geochemically on the distribution of potassium similar to those reported for sodium and magnesium.

8.5.3.14 Potassium (K^+) distribution (Post-mortem simulation results)

Figure 8.25 compares the results of post-mortem model at different times and the available experimental results for the dissolved potassium in the domain. The available experimental results reported by Fernández and Villar (2010) for magnesium distribution is limited to the duration of 92 months. Fernández and Villar (2010) reported that for all tests, there was an increase in the soluble Mg^{2+} , Na^+ , K^+ and Ca^{2+} concentrations close to the heater, whereas the K^+ content decreased near the hydration source and Na^+ decreased in that region.

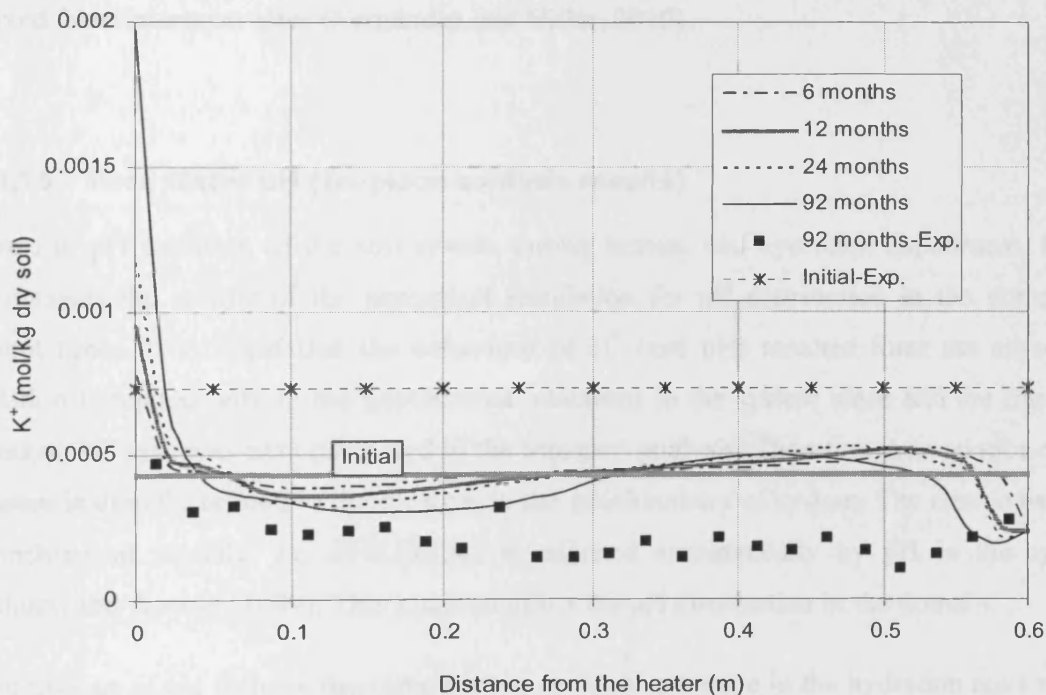


Figure 8.25 Profiles of the dissolved potassium contents at different times, resulting from the post-mortem simulation (lines) and experimental results (symbols) reported by Fernández and Villar (2010) for the 92 months test

The numerical simulation predicted a similar pattern as observed for other cations. The results of the numerical simulation show that the amount of potassium was reduced close to the hydration from the initial amount in a limited area. The potassium ions leached by water

advection were added in the region in first half of the domain in hydration side for all time intervals. Close to the hot boundary, high amount of potassium was precipitated due to water-vapour advection process in the 300 mm distance for the heater, similar to the behaviour of other cations

The geochemical modelling conducted for the assessment of the initial pore water composition, resulted in a lower amount of potassium initially in the domain for the solid/water ratio of 1/4 compared with that reported in the experiment by Fernández et al. (2001). In addition, numerical simulation results show small variations of potassium in the domain from the initial condition, except for a limited area in the vicinity of heater. However as Fernández and Villar (2010) reported, the determination of K^+ exchangeable has been conducted using $CsNO_3$ method where the K^+ content in all the samples (even in the reference one) might be overestimated due to the high affinity of Cs^{2+} for displacing more K^+ than expected from interlayer sites (Fernández and Villar, 2010).

8.5.3.15 Pore water pH (In-place analysis results)

In terms of pH variation of the soil system during heating and hydration experiment, figure 8.26 presents the results of the numerical simulation for pH distribution in the domain at different times. It is noted that the behaviour of H^+ (and pH) resulted from the numerical simulation is related only to the geochemical reactions in the system since and the transport process of H^+ ions was not considered in the transport analysis. Therefore the variation of pH in system is directly related to the changes in the geochemistry of system. The charge balance in geochemical module, i.e. PHREEQC, is adjusted automatically by pH in the system (Parkhurst and Appelo, 1999). This also can affect the pH distribution in the domain.

The behaviour of pH follows the same pattern as the bicarbonate in the hydration zone where high amount of bicarbonate were accumulated (refer to figure 8.15). Figure 8.26 also shows that pH variations exhibited a decrease from the initial state in the region of 200 to approximately 500 mm away from hydration side. This trend is more highlighted for the 92 months analysis. The decrease of pH in this region can be related to the dissolution of gypsum and increase in sulfate content in this region. A general increase in pH values is observed in

the area of 100 mm close to the heater side which can be related to the precipitation of anhydrite where the gypsum content was reduced.

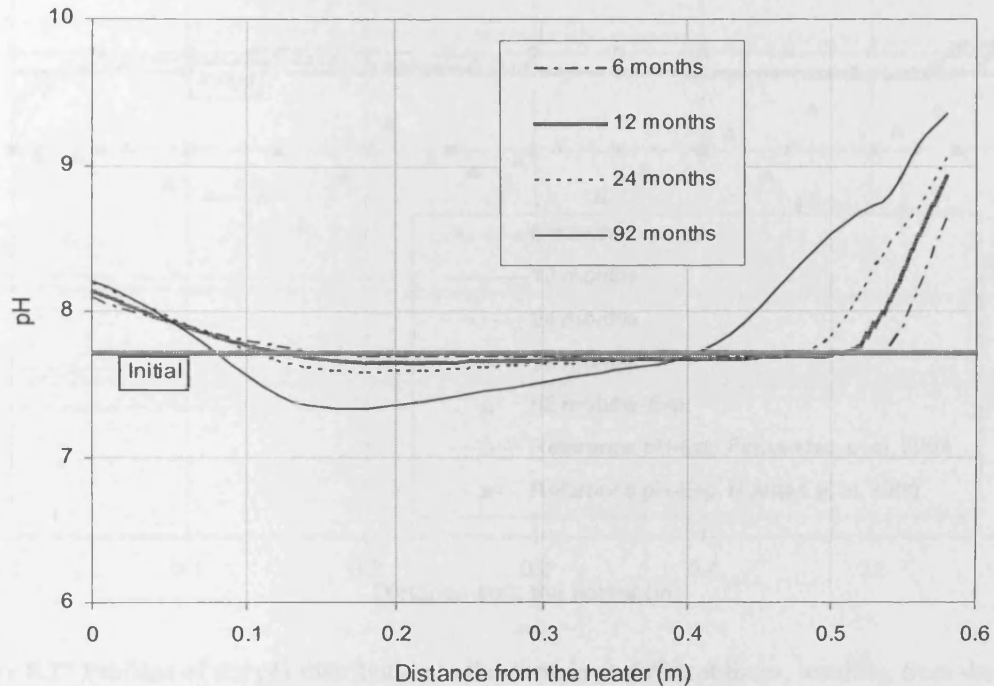


Figure 8.26 Profiles of pH distribution in the domain resulting from the numerical simulation at different times

8.5.3.16 Pore water pH (Post-mortem simulation results)

The experimental results have been only reported for the period of 92 months. These experimental results are compared with the experimental results. Figure 8.27 presents a comparison of post-mortem model results against the experimental results for the dissolved sodium in the domain at different times.

The model results follow same pattern as the bicarbonate variation as shown in figure 8.16. The pH of the system increased in the hydration side and decreased in the hot bottom similar to the pattern of bicarbonate presented in figure 8.11. The latter is in qualitative agreement with the trend observed in the experiment and reported by Fernández and Villar (2010). It is also noted that the lowering pH in the heater side can be related to the precipitation of calcite. Similarly calcite dissolution has controlled the pH increase in the hydration side.

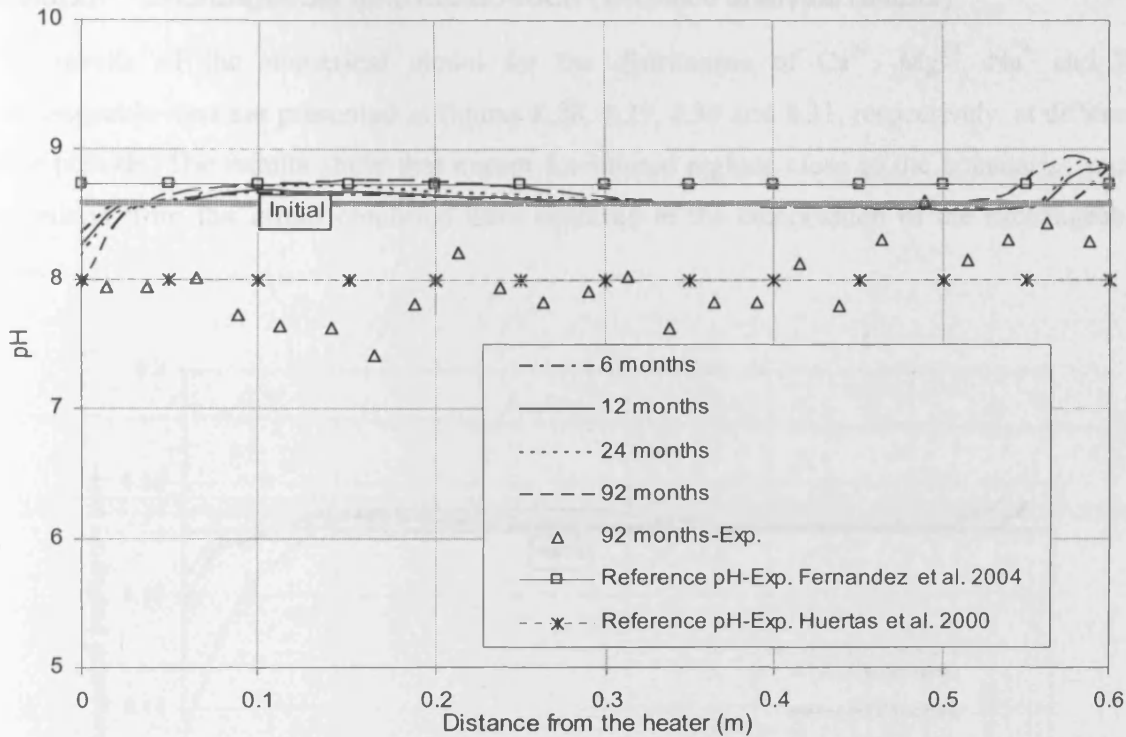


Figure 8.27 Profiles of the pH distribution in the domain at different times, resulting from the post-mortem simulation (lines) and the experimental results (symbols) reported by Fernández and Villar (2010) for the 92 months heating and hydration test

The values of pH reported by Fernández and Villar (2010) for the 92 months experiment are generally lower than the pH values resulted from the numerical simulation. This is because of the difference in the initial pH value of the soil in the numerical simulation and in the experiment reported by Fernández and Villar (2010). The initial pH value calculated from the geochemical pore water simulation, presented in table 8.6 was used as the reference value for the numerical simulation results. As stated in section 8.2, the reference value of pH of the soil at solid/water ratio of $\frac{1}{4}$ (i.e. pH=8.60) is in close agreement with the experimental value reported by Fernández et al. (2004) for the same water/solid ratio (i.e. pH=8.73). However, the pH of the FEBEX bentonite at the same solid/water ratio reported by ENRESA (2000) (i.e. pH=7.93) is different from the value given by Fernández (2004). The variation of the pH after 92 month heating and hydration is closer to the value of pH reported by ENRESA (2000). The difference can be related to variations of the FEBEX material and its constituents used in ENRESA (2000) and Fernández et al. (2004).

8.5.3.17 Exchangeable ions distribution (In-place analysis results)

The results of the numerical model for the distribution of Ca^{2+} , Mg^{2+} , Na^+ and K^+ exchangeable ions are presented in figures 8.28, 8.29, 8.30 and 8.31, respectively, at different time periods. The results show that except for limited regions close to the boundaries small variations from the initial condition have occurred in the composition of the exchangeable ions.

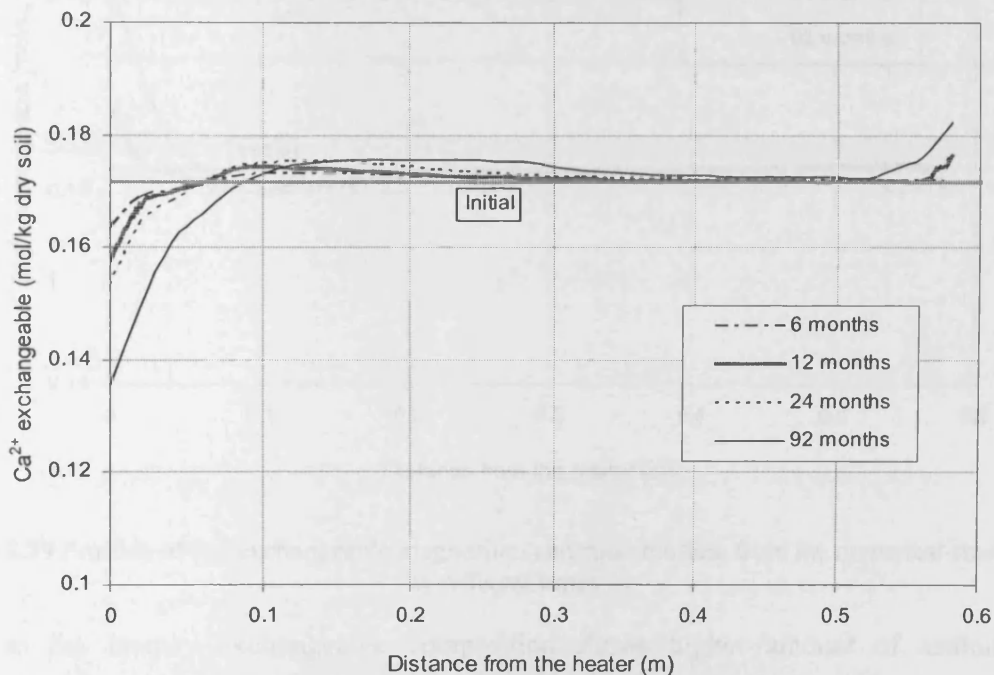


Figure 8.28 Profiles of the exchangeable calcium contents resulting from the numerical simulation at different times

Close to the hydration boundary greater amount of Ca^{2+} exchangeable ions and lower amount Na^+ exchangeable ions are observed. The values for magnesium and potassium varied also slightly in this region. As shown in figure 8.12, dissolution of gypsum in this region has resulted in higher amount of calcium ions which has replaced sodium ions in the interlayer. In other words, sodium ions are released into the system and calcium ions are replaced on to the vacant sodium sites leading to an increase in Ca^{2+} exchangeable concentration.

With regards to K^+ and Mg^{2+} exchangeable concentrations, they remain nearly constant over the range of solid to liquid ratios as these ions are not greatly influenced by dissolution/precipitation process unlike sodium and calcium whose concentrations depends on

the solubility of halite, calcite, gypsum and anhydrite (Fernández et al., 2000; ENRESA, 2000).

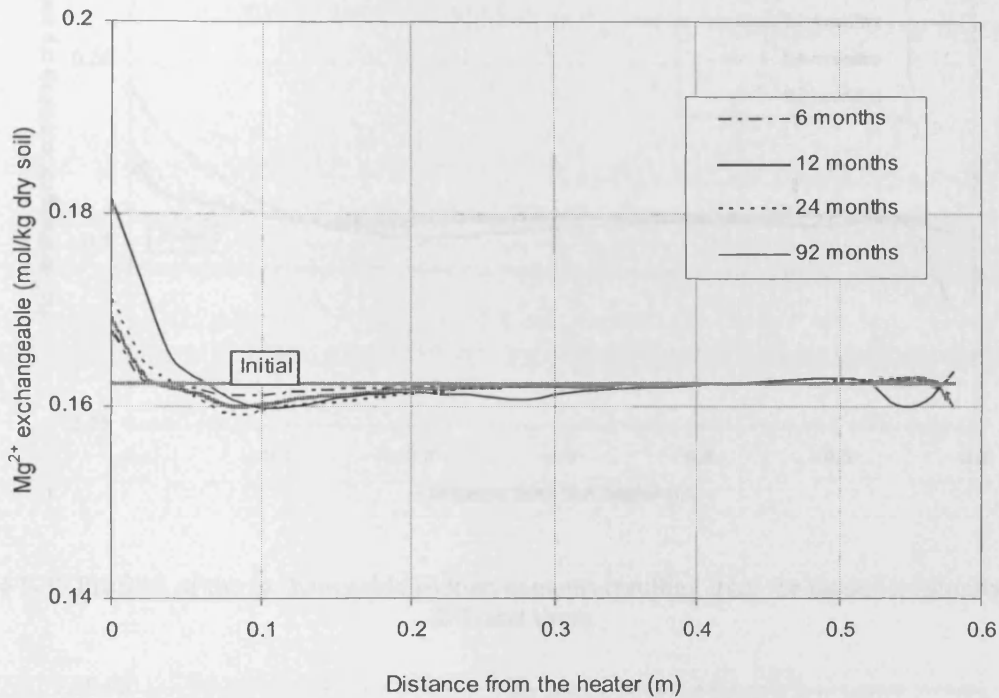


Figure 8.29 Profiles of the exchangeable magnesium contents resulting from the numerical simulation at different times

Close to the heater, exchangeable composition shows higher amount of sodium and magnesium than the initial state. On the other hand calcium and potassium exchangeable ions reduced. In the region close to the heater, precipitation of anhydrite and dissolution of gypsum affects the exchangeable ions composition. The pore fluid in this region was more concentrated with sodium and magnesium than calcium due to the precipitation of anhydrite. This resulted to the replacement of calcium exchangeable ions with sodium and calcium. To a lesser extent potassium exchangeable ions have been also replaced by sodium and magnesium ions in the interlayer, providing the equilibrium condition in exchangeable composition.

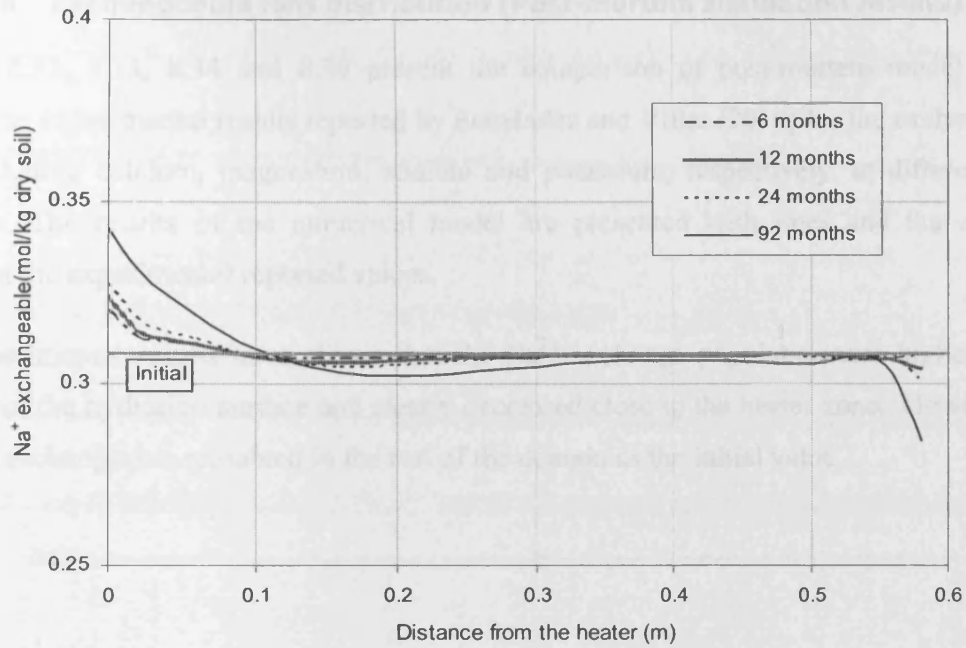


Figure 8.30 Profiles of the exchangeable sodium contents resulting from the numerical simulation at different times

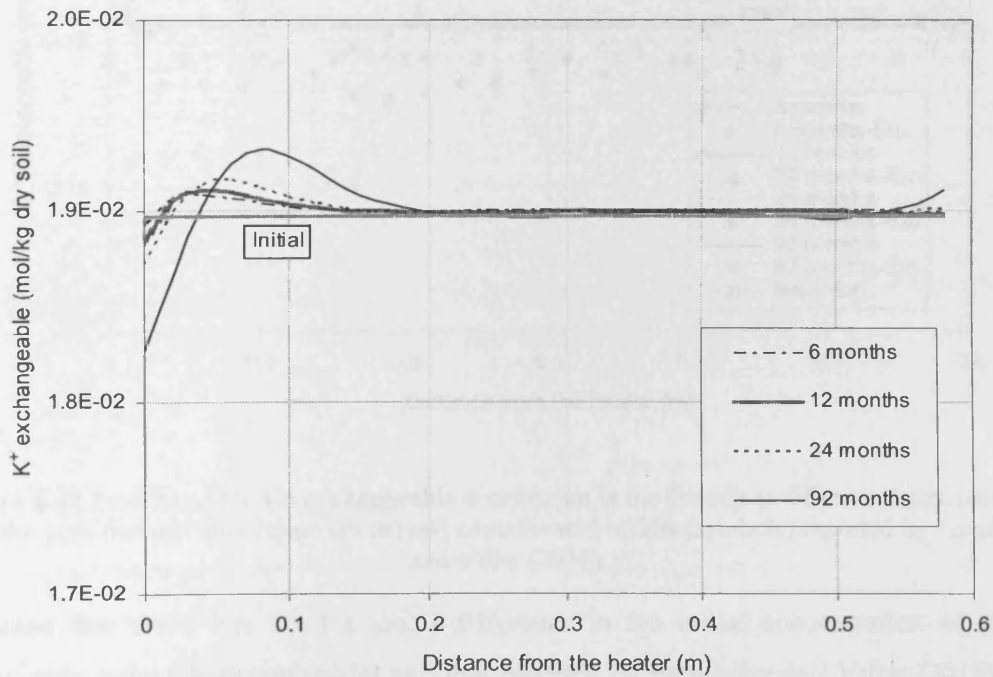


Figure 8.31 Profiles of the exchangeable potassium contents resulting from the numerical simulation at different times

8.5.3.18 Exchangeable ions distribution (Post-mortem simulation results)

Figures 8.32, 8.33, 8.34 and 8.35 present the comparison of post-mortem model results against the experimental results reported by Fernández and Villar (2010) for the exchangeable ions including calcium, magnesium, sodium and potassium, respectively, at different time intervals. The results of the numerical model are presented with lines and the symbols represent the experimental reported values.

The experimental results have shown that the Ca^{2+} exchange population was higher in the vicinity of the hydration surface and clearly decreased close to the heater zone.. However the calcium exchangeable remained in the rest of the domain as the initial value.

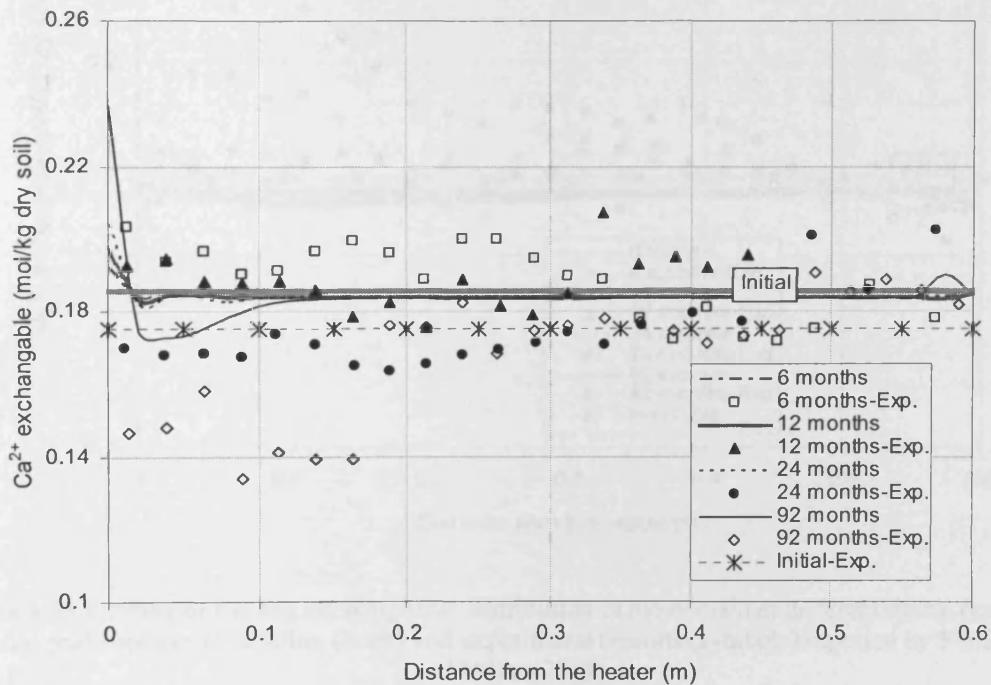


Figure 8.32 Profiles of the Ca exchangeable distribution in the domain at different times, resulted from the post-mortem simulation (lines) and experimental results (symbols) reported by Fernández and Villar (2010)

It is noted that there has been a small difference in the initial concentration of calcium exchangeable values between model and that reported by Fernández and Villar (2010) at the solid/water ratio of 1/4.

As Fernández and Villar (2010) reported, in the case of 92 month test the sum of the exchangeable cations, i.e. CEC, has shown an increase from the original value for FEBEX bentonite from 102 to 106 meq/100gr soil. Therefore they have normalised all the results with respect to the resulted CEC (refer to figure 8.5). However total exchangeable cations remained constant and equal to the initial value in the numerical simulation for all time periods. The general increase from the initial value observed in experimental results for calcium exchangeable can be related to this modification.

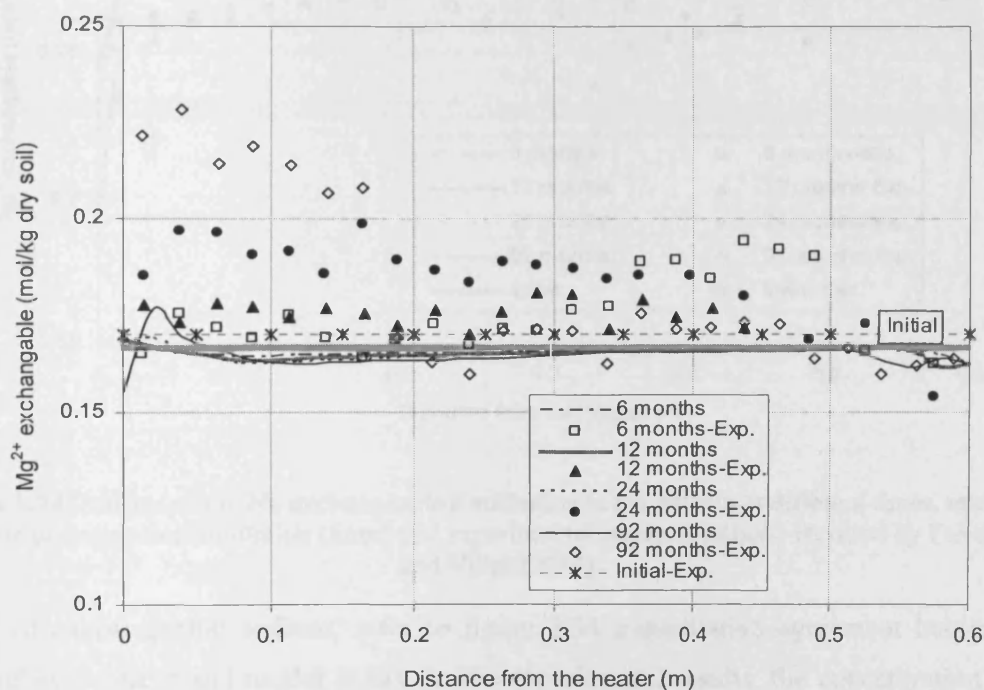


Figure 8.33 Profiles of the Mg exchangeable distribution in the domain at different times, resulting from the post-mortem simulation (lines) and experimental results (symbols) reported by Fernández and Villar (2010)

Experimental results show that exchangeable Mg^{2+} concentration decreased close to the hydration source and increased significantly in the 150 mm closest to the heater. Fernández and Villar (2010) stated that the increase in exchangeable magnesium in the 200 mm closest to the heater observed in the longest test and to a much lesser extent in the 24 months test could be related to the dissolution of dolomite. However since dolomite was not considered in simulation as previously discussed in section 8.5.3.12, the increase in the amount of

exchangeable magnesium can not observed in the numerical model results (refer to figure 8.33).

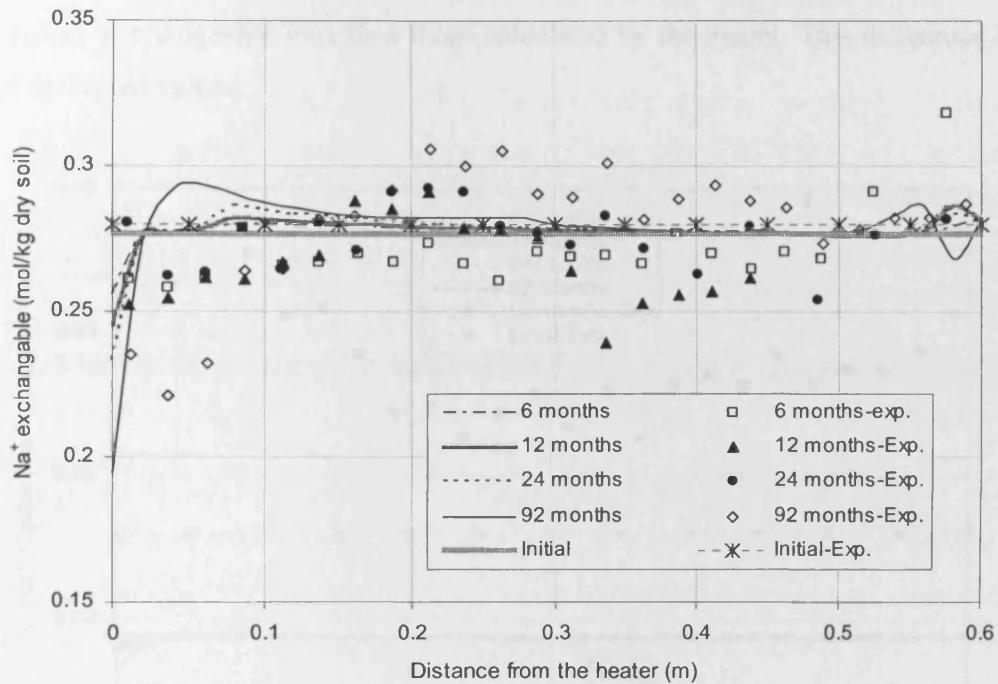


Figure 8.34 Profiles of the Na exchangeable distribution in the domain at different times, resulting from the post-mortem simulation (lines) and experimental results (symbols) reported by Fernández and Villar (2010)

In term of exchangeable sodium, refer to figure 8.34 a qualitative agreement between the results of experiment and model exists. In the experimental results, the concentration of the exchangeable sodium has generally decreased in the area close to the heater. However, the area affected by temperature is more extended in the case of experimental work compared with the numerical simulation.

The decrease and increase in the amount of exchangeable sodium resulted from the numerical simulation can be correlated with those related to exchangeable calcium where the pore fluid contained more calcium in the vicinity of heater which resulted to the replacement of sodium by calcium ions in the interlayer. On the other hand in the distance of 20 to 300 mm, the calcium concentration was reduced in the solution, providing the mechanism of replacement of calcium by sodium ions in the interlayer.

The results of numerical simulation calculated that the exchangeable potassium amount in the interlayer was remained almost as the initial condition. In the experimental results there is an obvious increase in the amount of that. The results of the experiment showed greater values for potassium exchangeable ions than those calculated by the model. This difference is seen even for the initial values.

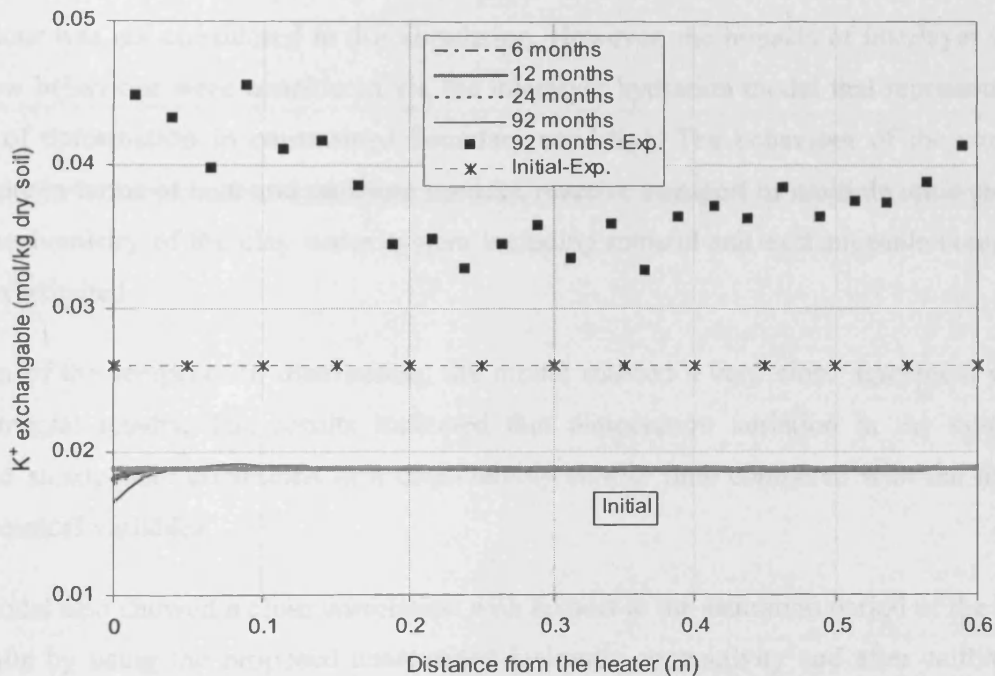


Figure 8.35 Profiles of the K^+ exchangeable distribution in the domain at different times, resulting from the post-mortem simulation (lines) and experimental results (symbols) reported by Fernández and Villar (2010) for the 92 months test

Fernández and Villar (2010) stated that in the case of the K^+ exchange population; although there was a slight increase along the entire bentonite column in the experimental results, it needs to be considered that, due to the experimental procedure of measurement of interlayer cation composition via the $CsNO_3$ method, the K^+ content in all the samples and even in the reference one might be overestimated due to exchangeable potassium displacement with Cs^{2+} ions in interlayer sites.

8.6 Conclusions

This chapter has demonstrated the capability of the developed numerical model (COMPASS-PHREEQC) to simulate the large cell heating and hydration experiment carried out as on compacted bentonite. The long term experimental results, i.e. up to 92 months (7.6 years) provided an opportunity to test and validate the developed model. The numerical simulation was performed under coupled thermal, hydraulic and chemical conditions. Deformation behaviour was not considered in this simulation. However, the impacts of interlayer water in the flow behaviour were considered via the interlayer hydration model that represents major effect of deformation in constrained boundary condition. The behaviour of the compacted bentonite in terms of heat and moisture transfer, reactive transport of multiple ionic chemicals and geochemistry of the clay water system including mineral and exchangeable composition was investigated

In term of the temperature distribution, the model showed a very close agreement with the experimental results. The results indicated that temperature variation in the system has reached steady-state conditions in a considerably shorter time compared with the hydraulic and chemical variables.

The model also showed a close correlation with respect to the saturation period of the FEBEX bentonite by using the proposed unsaturated hydraulic conductivity and after calibration of vapour diffusivity terms. Especially the results of the numerical model and experiment for the 92 months are in close agreement in terms of the degree of saturation which improves the confidence on the hydraulic model to predict the variation of the moisture for longer durations. Similar to the observations reported in chapter 7, the adopted hydraulic conductivity relationship which is coupled with interlayer water content variation has also modified the water transport in the example simulation presented in this chapter. Small discrepancies are observed in the shorter tests, i.e. 6, 12 and 24 months, where model resulted more wetting in the hydration side and more drying in the regions close to the heater in comparison with the experimental results.

In the case of each of chemical behaviour, two series of simulations were performed and the corresponding results were presented. The first type of results is related to the *in-place* condition in the bentonite cell, whilst the second type of the results reported were the *post-*

mortem geochemical analysis results, corresponding to a 1:4 aqueous extract post-analysis. The results of *post-mortem* analysis can be used to check the validity of the model via the comparison with the available experimental results reported by Fernández and Villar (2010). The results of in-place simulation provide the information about the condition of the compacted bentonite under the associated environmental conditions that can not be directly measured in the test.

In comparison between the results of post-mortem analysis between experiment and numerical model the following conclusions can be drawn:

- The simulation results of the chloride ions showed a good qualitative agreement with the experimental results especially for the periods of 6, 12 and 24 months. Chloride behaves as a conservative anion (Fernández and Villar 2010). The low chloride concentration in the results of numerical simulation can be due to the flow regime of moisture in the system, where the cycle of evaporation-condensation mainly controlled the distribution of chloride. In addition, exclusion effects due to the overlapping diffuse layer can be an effective issue in chloride distribution.
- The results for bicarbonate and sulfate spatial distribution are in agreement with the experimental results. Bicarbonate showed a nearly constant value along the domain except at boundary conditions affected by calcite dissolution and precipitation. It has also been found that bicarbonate distribution has been controlled by calcite dissolution reaction. A consistency between pH and bicarbonate behaviour was observed in the model results which is in agreement with experimental observation reported by Fernández and Villar (2010).
- The distribution of sodium ions agreed qualitatively with those reported in the experimental results, showing the accumulation of sodium ions in the heater side. The rest of the cations (Ca^{2+} , Mg^{2+} and K^{+}) showed reasonable correlation with respect to the limited available experimental results. However over prediction of ion concentrations at the hot side for all the cations was observed in simulation results.
- In terms of the exchangeable ion variations, the model also correctly predicted the qualitative distribution of exchangeable Na^{+} and Ca^{2+} ions in the domain. The results

indicated that except in the hot region, the distribution of these exchangeable ions remained close to that of the initial values. Higher concentrations of Na^+ exchangeable is observed in the vicinity of heater than the experiment which indicates more dissolved sodium has been entered to the interlayer of the clay replacing Ca^{2+} ions. In the case of exchangeable Mg^{2+} , the experimental results showed a general increase from the initial value. However such a behaviour was not observed in the model due to the absent of dolomite in the numerical simulation. In the case of K^+ the discrepancy between numerical and experimental results can be related to the experimental method for determination of exchangeable ions which resulted in higher replacement of interlayer potassium as Fernández and Villar (2010) suggested.

- Although there was no quantitative experimental information available for the transient and spatial mineral behaviour, the model showed compatible trends in comparison with the pore fluid composition. Gypsum was dissolved in the area close to the heat boundary, producing considerable amount of dissolved sulfate. As mentioned before, the equilibrium constant of mineral reactions for gypsum and anhydrite are very close whilst their enthalpies of reaction are different, leading to a different behaviour of these two minerals at the regions with higher temperature. The excess amounts of calcium and sulfate, accumulated due to transport process and dissolution of gypsum at hot end, were precipitated as anhydrite mineral.

Key conclusions of the coupled THC simulation on compacted FEBEX bentonite can be summarised as:

- In general the results for thermal, hydraulic and chemical behaviour are in good agreement with the experiment. The results thus have provided improved confidence in the model's ability to simulate the coupled behaviour of compacted smectite clays. Application of the model for long term simulation of the buffer under repository condition can provide information about the performance and the physical and chemical state of the compacted bentonite.
- Elevated temperature in the heater side showed a profound effect on the distribution of ions and minerals especially. Higher flow of water and vaporisation is likely to have occurred in the system, facilitating the migration of major ionic species towards the

heater by advection mechanism. The presence of a high amount of chloride in the vicinity of the heater can enhance the corrosion rate of the canister in a real scenario.

- The small portion of the accessory minerals in FEBEX bentonite such as gypsum and carbonates, showed considerable effects on the distribution of some ions and geochemical behaviour of the system under heating and hydration.
- Except for approximately 100 mm distance from the heater, the composition of exchangeable ions remained the same as the initial condition based on the in-situ simulation results. This indicates the possibility of conversion of FEBEX bentonite from Ca/Mg-smectite clay to Na/Mg smectite. The consequence in long term can affect the swelling pressure predicted for FEBEX.

Finally, it is acknowledged that several simplifications have been made in the simulation work; hence it is expected that improved results can be obtained by including more complexities into the model.

8.7 References

- Cleall, P.J., Seetharam, S.C., and Thomas, H.R. (2007). On the inclusion of some aspects of chemical behaviour of an unsaturated soil in thermo-hydro-chemical-mechanical models: II: Application and transport of soluble salts in compacted bentonite. *Journal of Engineering Mechanics, ASCE*, 133, 348-356.
- Cussler, E.L. (1997). *Diffusion-Mass Transfer in Fluid Systems*. University Press, Cambridge.
- ENRESA. (1995). *Almacenamiento Geológico Profundo de Residuos Radiactivos de Alta Actividad (AGP), Diseños Conceptuales Genéricos*. Technical Publication ENRESA 11/95, Madrid.
- ENRESA. (1998). *FEBEX. Bentonite: origin, properties and fabrication of blocks*. Publicación Técnica ENRESA 4/98, Madrid.
- ENRESA. (2000). *Full-scale engineered barriers experiment for a deep geological repository for high-level radioactive waste in crystalline host rock, FEBEX project*. EUR 19147, Nuclear Science and Technology Series, European Communities, Luxembourg.
- ENRESA. (2006). *Full-Scale Engineered Barriers Experiment, Updated Final Report 1994-2004*. Technical Publication ENRESA 05-0/2006, Madrid.
- Fernández, A.M., Baeyens, B., Bradbury, M., and Rivas, P. (2004). Analysis of the pore water chemical composition of a Spanish compacted bentonite used in an engineered barrier. *Physics and Chemistry of the Earth*, 29, 105-118.
- Fernández, A.M., Cuevas, J., and Rivas, P. (2001). Pore water chemistry of the FEBEX bentonite. *Material Research Society Symposium Proceeding*. 663, 573-588.
- Fernández, A.M., and Villar, M.V. (2010). Geochemical behaviour of a bentonite barrier in the laboratory after up to 8 years of heating and hydration. *Applied Geochemistry*, 25, 809-824.
- García-Gutiérrez, M., Cormenzana, J.L., Missana, T., and Mingarro, M. (2004). Diffusion coefficients and accessible porosity for HTO and ^{36}Cl in compacted FEBEX bentonite. *Applied Clay Science*, 26, 65-73.

- Lasaga, A.C. (1998). *Kinetic Theory in the Earth Science*. Princeton Series in Geochemistry, Princeton University Press.
- Martin, M., Cuevas, J., and Leguey, S. (2000). Diffusion of soluble salts under a temperature gradient after the hydration of compacted bentonite. *Applied Clay Science*, 17, 55-70.
- Mayhew, Y.R., and Rogers, G.F.C. (1976). *Thermodynamic and transport properties of fluids*. 2nd edition, Oxford, Blackwell.
- Melkior, T., Gaucher, E.C., Brouard, C., Yahiaoui, S., Thoby, D., Clinard, C., Ferrage, E., Guyonnet, D., Tournassat, C., and Coelho, D. (2009). Na⁺ and HTO diffusion in compacted bentonite: Effect of surface chemistry and related texture. *Journal of Hydrology*, 370, 9-20.
- Parkhurst, D.L., and Appelo, C.A.J. (1999). *User's guide to PHREEQC (version 2)*, U.S. Geological Survey, Water Resource Investigation Report, 99-4259.
- Philip, J.R., and de Vries, D.A. (1957). Moisture movements in porous materials under temperature gradients. *Transactions American Geophysical Union*, 38(2), 222-232.
- Plummer, L.N., Wigley, T.M.L., and Parkhurst, D.L. (1978). The kinetics of calcite dissolution in CO₂-water systems at 5-60 °C and 0. 0-1.0 atm CO₂. *American Journal of Science*, 278, 179-216.
- Ransom, B., and Helgeson, H.C. (1994). A chemical and thermodynamic model of aluminous dioctahedral 2:1 layer clay minerals in diagenetic processes: Regular solution representation of interlayer dehydration in smectite, *American Journal of Science*, 294, 449-484.
- Revil, A., and Jougnot, D. (2008). Diffusion of ions in unsaturated porous materials. *Journal of Colloid and Interface Science*, 319, 226-235.
- Seetharam, S.C. (2003). *An investigation of the thermo/hydro/chemical/mechanical behaviour of unsaturated soils*. Ph.D. Thesis, Cardiff University, Wales, UK.
- Singh, R.M. (2007). *An experimental and numerical investigation of heat and mass movement in unsaturated clays*. PhD Thesis, Cardiff University, Wales, UK.
- Van Loon, L.R., Glaus, M.A., and Müller, W. (2007). Anion exclusion effects in compacted bentonite: Towards a better understanding of anion diffusion. *Applied Geochemistry*, 22, 2536-2552.

- van Genuchten, M.Th. (1980). A closed-form equation for predicting the hydraulic conductivity of unsaturated soils. *Soil Science Society of America Journal*, 44, 892-898.
- Villar, M.V., Fernández, A.M., Gómez, R., Barrenechea, J.F., Luque, F.J., Martín, P.L., and Barcala, J.M. (2007). State of a bentonite barrier after 8 years of heating and hydration in the laboratory. In: Dunn, D.S., Poinssot, C., Begg, B. (Eds.), *Scientific Basis for Nuclear Waste Management XXX, Material Research Society Symposium Proceedings*, 985, 0985-NN11-19.
- Villar, M.V., Fernández, A.M., Martín, P.L., Barcala, J.M., Gómez-Espina, R., and Rivas, P. (2008b). *Effect of Heating/Hydration on Compacted Bentonite: Tests in 60 cm Long Cells*. Publishing House CIEMAT. Madrid.
- Villar, M.V., Sánchez, M., Gens, A. (2008a). Behaviour of a bentonite barrier in the laboratory: experimental results up to 8 years and numerical simulation. *Physics and Chemistry of the Earth*, 33, S476-S485.

Chapter 9

Conclusions and Suggestions for Further Research

9.1 Conclusions

In order to investigate the hydro-geochemical processes in unsaturated soils a coupled THCM numerical model has been developed in this thesis. This chapter aims to synthesise the conclusions pertinent to the developments in this thesis and relate them to the objectives presented at the start of this work. Key contributions and advancements will be highlighted throughout this chapter followed with opportunities for further work. The following conclusions can be drawn from the work presented in this thesis.

9.1.1 Theoretical and numerical formulation

A theoretical formulation for coupled flow of moisture, heat, air, multicomponent chemicals and deformation have been developed in the framework of coupled THCM modelling as presented in chapter 3. In particular, the formulations of hydraulic and chemical/geochemical behaviour have been advanced. In terms of hydraulic behaviour, the chemical osmosis potential was included in the governing equations for water and vapour, incorporating an explicit coupling between hydraulic behaviour and dissolved chemical variations in the formulation. The inclusion of chemo-osmosis in the governing equation of moisture flow, assisted with an important step towards understanding the effects of chemistry on water and vapour flow in unsaturated soils. According to the developed model, if the dissolved concentrations of chemicals vary in pore fluid, the variation of moisture in soil due to the chemo-osmosis is evaluated using the proposed formulation and knowing the osmosis properties of the soil.

Based on the state of the art review presented in chapter 2, different rate of diffusion for anionic and cationic species has been found in experimental investigations in compacted clays. This effect requires the modelling of the diffusion under different effective coefficients combined with electrostatic balance of pore fluid. It was realised that this effect and the quantitative evaluation in transport of chemicals in compacted clay especially under non-isothermal conditions has received limited attention and is yet to be investigated in detail. A transport formulation of multicomponent chemicals was developed in which various potentials on diffusion of multiple chemicals were included in the governing equation considering overall charge conservation. Transport of multicomponent ions was explained via

coupled electrochemical diffusion potential and thermal diffusion potential (i.e. the Soret effect). To the knowledge of the author, this is a novel formulation which enables modelling the diffusion of ionic species in multiple species systems either under isothermal or non-isothermal conditions.

The thermal diffusion coefficient or the Soret coefficient was addressed in the formulation via a theoretical approach. The adopted theory to evaluate the Soret coefficient provides a novel modelling platform for the assessment of the impact of transport of temperature on transport of ionic species in multicomponent system and under different diffusion coefficients. In the case of compacted clay buffer, the proposed transport formulation significantly improves the capability to assess the fate of chemicals under non-isothermal condition especially in long-term studies.

A major contribution to the reactive transport model was made via coupling an advanced geochemical model, PHREEQC version 2, to calculate the chemical reaction sink/source in the governing equation. The inclusion of PHREEQC model to the transport formulation offers various capabilities to the reactive transport formulation of the model. The ability of the PHREEQC to model mixed equilibrium and kinetically controlled chemical reactions, various homogeneous and heterogeneous reactions such as mineral reactions, ion exchange and, the activity coefficients of ions in high ionic solutions, and the availability of various databases are among the key potential advantages of this model in the framework of the modelling geochemical processes. The developed reactive transport model, benefits from the advances both in the transport module under coupled THCM framework, COMPASS and in the reaction module where PHREEQC provides a wide range of advantages to model geochemical reactions.

An important development was initiated to couple chemical/geochemical with mechanical behaviour in the theoretical basis of the model. Accordingly the effects of mineral precipitation/dissolution on flow parameters were implemented as a porosity modification feed-back from the geochemical model. In other words, flow properties such as hydraulic conductivity, was modified due to variation in porosity with mineral precipitation or dissolution. This inclusion has improved the abilities of the model to evaluate the hydro-chemical behaviour in low porosity materials where long-term issues related to the mineral precipitation or dissolution can alter the flow regime in the system.

A numerical approximation was adopted to solve the series of the governing equations for all primary variables related to the flow and deformations. A finite element solution was employed for spatial discretisation based on Galerkin weighted residual method. A finite difference scheme for temporal discretisation was employed based on a forwards difference, mid-interval time stepping algorithm. Based on the comprehensive review on the computational aspects of the reactive transport of chemical, presented in chapter 2, sequential approach was found to be efficient to solve the governing equations for transport and chemical reactions. Hence, the coupling between the transport and geochemical models was achieved with adaptation of a sequential non-iterative approach. The developed theoretical formulation and the numerical solution present a robust and advanced computational approach to study the hydro-geochemical processes in the framework of coupled THCM behaviour.

9.1.2 Verification and validation of the numerical model

A series of verification exercises have been presented on the developments to the hydro-geochemical formulation implemented in THCM model. Analytical solutions, alternative numerical solutions or the experimental data have been used to verify different developments made in the theoretical/numerical formulation of the model. Three classes of problems were verified under the development context of this thesis, which included:

Two verifications were provided on the effects of coupling chemical processes with moisture flow via the chemo-osmosis phenomena. In the first example, implementation of the osmotic potential effects on water transport in the model was tested against the results of an analytical solution under steady-state condition. In the second example, osmosis driven vapour transport was validated against a series of experimental results. The comparison indicated the mathematical correctness of the approach adopted in chemo-osmosis inclusion in the model under the conditions of the specified examples.

Two verifications were presented dealing with the transport of multiple ionic species under isothermal conditions. Based on these examples, the implementation of coupling between electrical and chemical potential effects on diffusion was examined. The results of multicomponent approach for modelling the diffusion in binary and ternary solutions were

compared with the results of modelling the diffusion of same problem based on Fick's law of diffusion using analytically derived diffusion coefficient. Non-isothermal multicomponent chemical diffusion was also explored via a series of simulations based on available experimental data on diffusion of multi-ions under thermal gradients. In this series of simulations, the theoretical approach adopted for calculating the Soret coefficient was also validated in multiple ionic systems. Within the conditions of the presented simulation examples, the formulation adopted for multicomponent diffusion due to the electrochemical potential was verified.

Coupling the geochemical reaction model PHREEQC with the transport model was verified for the geochemical reactions including mineral dissolution/precipitation and ion exchange. Verification on the transport of binary solution with mineral reaction under both equilibrium and kinetics was conducted against the results of an analytical solution. Verification was also carried out on multicomponent transport and multiple precipitation/dissolution reactions. The reactive transport of chemicals with ion exchange reactions was checked based on the results of a similar simulation using well established example of PHREEQC version 2. In addition, a preliminary simulation example was presented to demonstrate the effect of coupling between mineral reaction and porosity variation and the effects on chemical transport.

Within the verification/validation tests presented in chapter 4, each development in the theoretical formulation of hydraulic and chemical behaviour was explored and the accuracy of the implementation was examined over a particular range of conditions under consideration. Hence, confidence was built in the theoretical approach and numerical implementation for further applications and exploration of the developments provided in the model.

9.1.3 Reactive transport under coupled THC conditions

A series of simulations was carried out using the developed model to investigate the reactive transport of chemicals under coupled thermo-hydro-chemical conditions. The simulation aimed mainly to study the reactive transport of chemicals with emphasis on coupled electrochemical and thermal diffusions. In fact, the simulations were designed to investigate the effects related to thermal diffusion potential, i.e. the Soret effect, in a binary ionic system in equilibrium with mineral reactions. The theoretical approach for calculation of the Soret

coefficient was used in these series of simulations. The simulations were carried out on two different conditions in terms of the effective diffusion coefficient of chemicals in the system. In addition, the magnitude of the thermal diffusion effects was investigated via a same simulation in each series, once with considering the Soret effect and once without that.

The simulation results verified the charge conservation condition implemented in the model under variable saturated and non-isothermal conditions where the transport of chemicals takes place due to simultaneous advection and diffusion in the system. These series of simulations provided interesting information about the magnitude and importance of the thermal diffusion effects and the way it affects the hydro-geochemistry of the system. Modelling results showed that the distribution of the dissolved chemicals and precipitated minerals can be affected by thermal diffusion impacts, particularly, after completing the re-saturation of the clay system. Under the saturated condition, a combination of diffusion due to the concentration gradient and the thermal diffusion potential controls the transport of chemicals depending on the effective diffusion coefficient.

The simulation examples also indicated that the contribution of the Soret effect in the overall process of reactive diffusion could change the distribution of minerals, especially in the boundary regions close to the heat source where a high degree of precipitation of minerals was expected. The overall impact of thermal diffusion was found to be dependent on the effective diffusion coefficient in the system. This series of simulations assisted to explore the developments to the modelling of temperature impacts on the reactive diffusive transport of chemicals in a clay system where limited information and analysis is available.

9.1.4 Transport Processes in compacted bentonite and microstructure evolution

The state of the art review, presented in chapter 2, on the behaviour of compacted smectite clays indicated that the moisture and chemical transport processes are highly linked with the microstructure evolution of the smectite minerals and the surface interactions. It has been suggested that when water is adsorbed to the interlayer pore space of the smectite, the available pore space for water and chemical flow reduces significantly. A lack of a robust model for calculation of the amount and the rate of water exchange between immobile

interlayer and mobile water/vapour especially under variable suction and temperature has been reported. This area was identified as a critical issue towards modelling the hydro-geochemistry of compacted swelling clays.

A theoretical approach was presented for modelling the hydration/dehydration process and the pore water/porosity evolution in compacted swelling clays (smectite). The developed model is based on a thermodynamic approach in which the hydration/dehydration of smectite was treated as a geochemical solid solution reaction.

Based on the proposed model, the amount of interlayer water and micro/macro porosity evolution was calculated for a compacted bentonite. It was shown that the developed model can estimate the interlayer water content for a given bentonite and its variation with suction and temperature. The model was adopted for the case of a compacted sodium bentonite and the distribution of water in micro and meso/macro levels in saturated compacted bentonite at different dry densities was evaluated using the developed model. The results indicated a good correlation between the model and those estimated and reported in the literature.

An exclusive advantage of the developed model is the capability to evaluate the variation of the interlayer water and micro/macro porosity under variable suction and temperature conditions. To assess that, the variation of the interlayer water content with suction and temperature was modelled for a compacted sodium rich bentonite using the developed model. The model results suggested that even at high suction values, there is a possibility of coexistence of the water in the interlayer and intralayer/interparticle space. The model was also explored under non-isothermal conditions which indicated the water transfer between the interlayer and intralayer/interparticle due to temperature variation which is an important issue in the assessment and understanding of temperature impacts on flow processes.

A modified form of the unsaturated hydraulic conductivity relationship was proposed for compacted swelling clays where the microstructure changes via micro/macro porosity in response to changes in suction and temperature. Accordingly, the proposed model for interlayer hydration/dehydration of smectite was coupled with the unsaturated hydraulic conductivity to calculate the corresponding values of the interlayer porosity. The hydraulic behaviour of compacted bentonite using the developed unsaturated hydraulic conductivity was investigated via a simulation of two series of small scale experiments, one the under

hydraulic gradient and the second under a thermo-hydraulic gradient. In comparison with the experimental data, the model response with modified unsaturated hydraulic conductivity relationship was tested against the standard hydraulic conductivity relationship. The results of the modelling using the modified relationship indicated significant improvements against the results of same simulation via the adopted standard relationship. In particular, the hydraulic behaviour of the model for the highly compacted bentonite in the long term was improved, i.e. the gradients of saturation were improved which may in turn yield significantly improved long term predictions. In fact the microstructure evolution through the interlayer hydration and swelling was found as the dominant potential to delay the re-saturation of the buffer material. This gives increased confidence in longer term predictions made using numerical simulation. The developed model for hydration/dehydration is a novel approach which included some aspects of microstructure evolution of compacted swelling clay in the hydro-chemical transport modelling.

9.1.5 Simulation of a heating and hydration experiment of a compacted bentonite

A numerical simulation was carried out on hydro-geochemical behaviour of compacted bentonite of a large-cell heating and hydration experiment using the developed numerical model. The behaviour of the compacted bentonite in terms of heat and moisture transfer, reactive transport of multiple ionic chemicals and geochemistry of the clay water system including mineral and exchangeable composition was investigated for a period of up to 92 months (7.6 years). The impacts of microstructure swelling and shrinkage in the flow behaviour were considered via the developed interlayer hydration model that represents the major effect related to the deformation under constrained boundary conditions.

The results of the simulation demonstrated a close agreement with the experimental results in terms of temperature profile. The model also showed a good correlation with respect to the saturation degree of the FEBEX bentonite using the modified hydraulic conductivity with interlayer water model, proposed in chapter 7 and with calibration of vapour diffusivity terms. The results of the numerical model and experiment for the 92 months are in close agreement in terms of the degree of saturation which improve confidence in the hydraulic behaviour of

the model. With regards to geochemical behaviour, two series of simulation were performed representing *in-place* and *post-mortem* conditions in the bentonite cell experiment. The results of in-place simulation provided the information about the condition of the compacted bentonite under the associated environmental condition in the test while the post-mortem analysis was utilised to validate the model against the experimental results.

A good qualitative agreement was observed regarding chloride distribution, especially for the periods of 6, 12 and 24 months by comparison between the post-mortem results of the simulation and those reported from the experiment,. The results for the bicarbonate and sulphate spatial distribution are also in reasonable agreement with the experimental results. Bicarbonate showed a nearly constant value along the domain except at boundary conditions affected by calcite dissolution and precipitation. The distribution of sodium ions qualitatively agreed well with those reported in the experimental results, showing the accumulation of sodium ions in the heater side. The rest of the cations (Ca^{2+} , Mg^{2+} and K^{+}) showed reasonable correlation with respect to the limited available experimental results. However, over-prediction of some ions at the hot side for the cations was observed in simulation results. In terms of the exchangeable ion variations, the model also correctly predicted the qualitative distribution of exchangeable Na^{+} and Ca^{2+} ions in the domain.

The in-place chemical and geochemical results of the simulation indicated that the small portion of the accessory minerals in bentonite such as gypsum and carbonate has considerable effects on the distribution of some dissolved ions and the geochemical behaviour of the system under heating and hydration. In particular gypsum has been dissolved in the area close to the heat boundary, which was resulted in producing considerable amount of dissolved sulfate. Excess amounts of calcium and sulfate, accumulated in the region close to the heater due to the combined effects related to the ion transport and dissolution of gypsum at hot side. The model capability for considering kinetically controlled geochemical reactions has provided important and more realistic information about fate of calcite and its precipitation/dissolution behaviour.

It was found from the in-place simulation results that the behaviour of pH follows the same pattern as the bicarbonate in the hydration zone where high amount of bicarbonate was accumulated. The pH variation was found to be correlated with dissolution of gypsum and precipitation of anhydrite during the heating and hydration experiment. The results indicated

that the distribution of the exchangeable ions remained close to that of the initial values, except for a limited region close to the heater.

The results of post-mortem analysis assisted to explore the accuracy of the model and to validate the developed model under complex conditions of experimental work considered. Accordingly it can be claimed that the developed model has successfully simulated the hydro-geochemical behaviour of the studied compacted clay under coupled and complex THC framework. In addition, the in-place chemical/geochemical condition of the simulation bench mark provided important information especially with regards to the accessory minerals and exchangeable ions distribution. Overall the model results have been satisfactory and thus have provided improved confidence in the ability of the developed model to simulate the thermal, hydraulic and chemical/geochemical behaviour of bentonite type soil.

9.1.6 Overall conclusions

In terms of overall conclusions that can be drawn from the research performed, the following observations are presented:

- Several aspects relating to the theoretical modelling of the hydraulic and chemical behaviour of unsaturated soils have been developed in this thesis. For example a description of chemo-osmosis phenomenon has been achieved, which explicitly explains water and vapour flow induced by chemical variations. In the author's opinion, the formulation developed for the transport of multicomponent chemicals is a new theoretical solution for the modelling the diffusion of multiple ionic species due to combined chemical, electrical and thermal potentials.
- Coupling of the robust geochemical model PHREEQC (version 2) to the THCM model significantly improves the capability to simulate the reactive transport of chemicals under mixed equilibrium/kinetically controlled chemical reactions. Advanced geochemical features are thus introduced into the coupled THCM model.
- Verification and validation of the developed model has been pursued, exploring the accuracy of the theoretical formulations and the numerical approach. The results indicated that the techniques, adopted to solve the governing equations for flow and

deformation, and the sequential scheme, implemented to solve the governing equations for reactive transport of chemicals, provide an efficient solution for the problems considered.

- The effect of thermal diffusion on the reactive transport of chemicals under coupled THC conditions was investigated via a series of simulations using the new model. The results indicate the importance of the Soret effect on the distribution of chemicals and minerals in the system. The dependency of the Soret effect on the effective diffusion coefficient of the chemicals in soil is also revealed.
- The inclusion of a hydration/dehydration model in a modified form of unsaturated hydraulic conductivity, significantly improved the prediction of water transport and re-saturation time of a compacted bentonite under both isothermal and non-isothermal water infiltration. In the author's opinion the proposed model provides a novel framework, based on a flexible geochemical approach. Improved understanding and modelling of effects related to microstructural and porosity evolution on flow processes in swelling clays has thus been achieved.
- Simulation of hydro-geochemical processes under simultaneous heating and hydration of compacted bentonite demonstrated the capabilities of the new model. The results achieved have been in agreement with experimental results, providing improved confidence in the ability of the model to simulate the thermal, hydraulic and chemical/geochemical behaviour under the presence of multicomponent chemicals and mixed geochemical processes. Results obtained from the simulations of coupled thermo-hydraulic and thermo-hydro-chemical behaviour of compacted bentonite have improved the quality of modelling of the physical and chemical processes in compacted swelling clays.
- As the result of this study, it is claimed that a new model has been developed, which is an advanced tool for assessing hydro-geochemical processes under variable physical, chemical and mechanical conditions in unsaturated soils. Applications of the work to the case of compacted swelling clays have been carried out throughout this thesis. The developed model has thus been shown to be an appropriate model for such compacted swelling clays.

9.2 Suggestions for further research

The developed model was applied in this thesis to simulate the hydro-geochemical processes under coupled THCM behaviour of compacted swelling clays. However, the numerical code is under constant development to improve and test its capabilities. The following suggestions are made for further research and developments especially for modelling the coupled processes in compacted bentonite:

Utilising the proposed model for interlayer water/porosity evolution, the transport formulation of multicomponent chemical can be extended considering different diffusion classes in different porosity levels in compacted bentonite. In other words, the diffusion can be considered in three different porosity levels including interlayer, diffuse layer and free water. This provides a platform to investigate the coupled diffusion with surface complexation/ion exchange provided by PHREEQC. This modification can be utilised for the assessment of radionuclides diffusion in compacted bentonite.

The interlayer hydration/dehydration model presented in chapter 7 has a significant potential for further development and applications in modelling the hydraulic and chemical/geochemical behaviour in compacted swelling clays. Implementation of this model to the flow parameters can further be extended. A kinetic approach for modelling hydration/dehydration may provide better estimation for temporal variation of the interlayer water and the consequences on flow parameters. Since major aqueous geochemical reactions are thought to be occurred in macropore water, the interlayer water model can be adopted to re-visit the geochemical analysis of the pore fluid composition. It is anticipated that it results with high ionic concentration pore fluid in compacted bentonite that the capability of PHREEQC to geochemical modelling the solution with high ionic strength encountering further analysis in combination with interlayer porosity model.

The coupling between porosity/permeability variations with geochemical reactions via mineral dissolution/precipitation has been implemented in the model. However, the scheme for coupling porosity variation with geochemistry required further verification/validation. In particular, the efficiency of porosity feed back from geochemical model under SNIA coupling algorithm needs to be evaluated. The feedback of chemical reactions on transport properties adds another non-linearity to the system, requiring efficient algorithms to reach an accurate

solution in reasonable computer time. Other coupling schemes suggested in the literature, in particular sequential partly iterative approach (SPIA) and sequential iterative approach (SIA) are suggested to check the numerical efficiency and improve the scheme adopted in this work.

Chapters 7 and 8 presented the simulations results of laboratory scales TH and THC behaviour using developed theory and numerical model, showing the predictive capabilities of the model. Further applications of the model for the hydro-geochemical behaviour of compacted bentonite under coupled THCM condition for longer thermal period is proposed to investigate the major processes. Indeed inclusion of more capabilities of PHREEQC in modelling geochemical reactions into the coupled THCM model such as surface complexation, explicit calculation of the diffuse layer composition, and redox reactions can improve the capabilities of the model.

The developed hydro-geochemical model is a robust and flexible computational tool which incorporated advanced theoretical and experimental knowledge in the field of unsaturated soils into the coupled physico-chemical and mechanical modelling. The model in general can be extended for applications related to the other porous materials and in the engineering of recent challenges in geoenvironment such as geological sequestration of CO₂.

